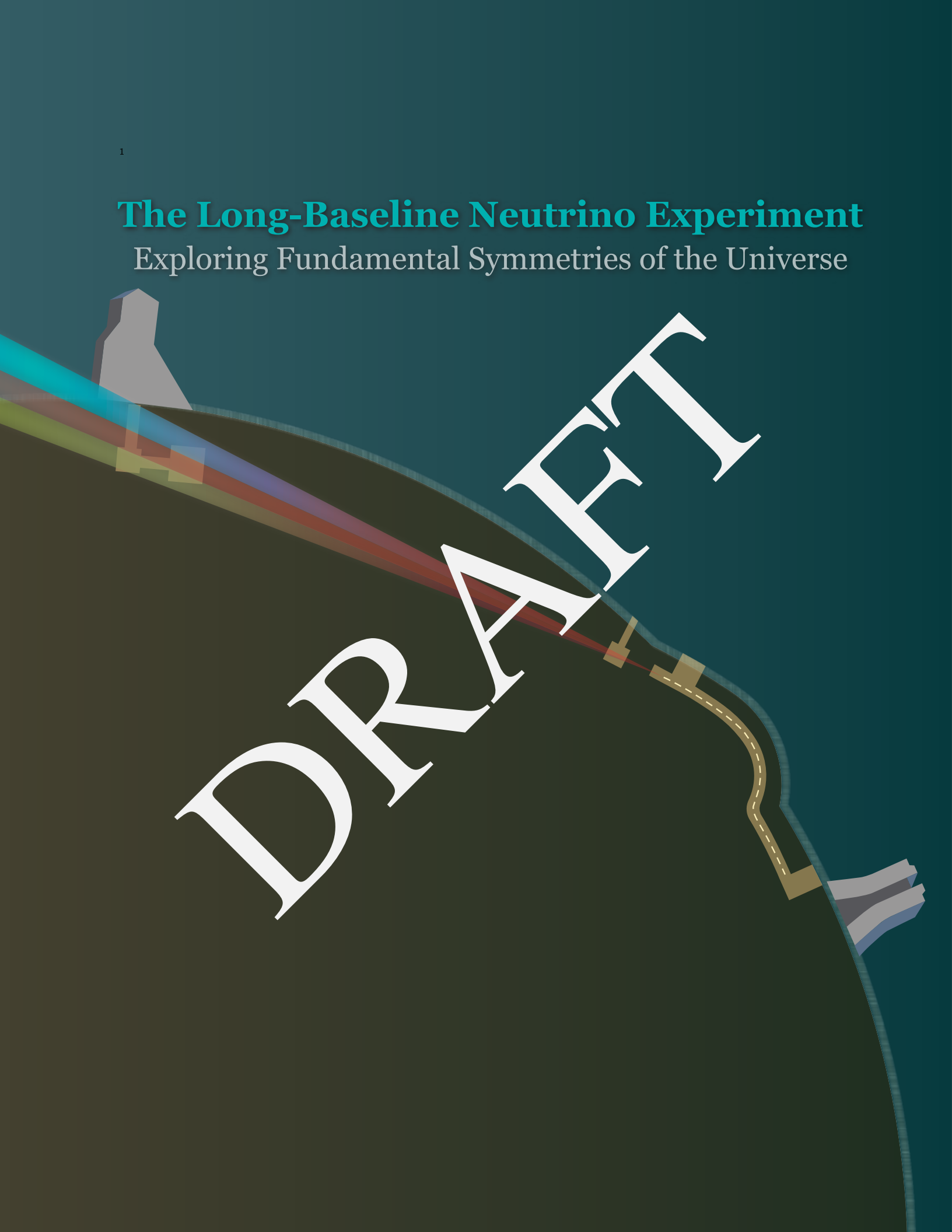


# The Long-Baseline Neutrino Experiment

Exploring Fundamental Symmetries of the Universe



DRAFT



# The Long-Baseline Neutrino Experiment

1 Exploring Fundamental Symmetries of the Universe

2 March 12, 2014

DRAFT

<sup>1</sup> Cover design by Diana Brandonisio, Fermilab Visual Media Services

<sup>2</sup> Typeset in L<sup>A</sup>T<sub>E</sub>X

## The LBNE Collaboration

1

2 C. Adams<sup>85</sup>, D. Adams<sup>7</sup>, T. Akiri<sup>24</sup>, T. Alion<sup>68</sup>, K. Anderson<sup>26</sup>, C. Andreopoulos<sup>41</sup>,  
3 M. Andrews<sup>26</sup>, I. Anghel<sup>34</sup>, J. C. C. d. Anjos<sup>14</sup>, M. Antonello<sup>37</sup>, E. Arrieta-Diaz<sup>47</sup>, M. Artuso<sup>75</sup>,  
4 J. Asaadi<sup>75</sup>, X. Bai<sup>70</sup>, B. Baibussinov<sup>57</sup>, M. Baird<sup>33</sup>, B. Balantekin<sup>84</sup>, B. Baller<sup>26</sup>, B. Baptista<sup>33</sup>,  
5 D. Barker<sup>69</sup>, G. Barker<sup>82</sup>, W. A. Barletta<sup>46</sup>, G. Barr<sup>56</sup>, L. Bartoszek<sup>42</sup>, A. Bashyal<sup>77</sup>, M. Bass<sup>19</sup>,  
6 V. Bellini<sup>13</sup>, P. A. Benetti<sup>59</sup>, B. E. Berger<sup>19</sup>, M. Bergevin<sup>8</sup>, E. Berman<sup>26</sup>, H. Berns<sup>8</sup>, A. Bernstein<sup>40</sup>,  
7 R. Bernstein<sup>26</sup>, B. Bhandari<sup>31</sup>, V. Bhatnagar<sup>58</sup>, B. Bhuyan<sup>32</sup>, J. Bian<sup>50</sup>, M. Bishai<sup>7</sup>, A. Blake<sup>11</sup>,  
8 F. Blaszczyk<sup>43</sup>, E. Blaufuss<sup>45</sup>, B. Bleakley<sup>72</sup>, E. Blucher<sup>15</sup>, S. Blusk<sup>75</sup>, V. Bocean<sup>26</sup>, F. Boffelli<sup>59</sup>,  
9 J. Boissevain<sup>42</sup>, T. Bolton<sup>36</sup>, M. Bonesini<sup>49</sup>, S. Boyd<sup>82</sup>, A. Brandt<sup>77</sup>, R. Breedon<sup>8</sup>, C. Bromberg<sup>47</sup>,  
10 R. Brown<sup>7</sup>, G. Brunetti<sup>26</sup>, N. Buchanan<sup>19</sup>, B. Bugg<sup>76</sup>, J. Busenitz<sup>2</sup>, E. Calligarich<sup>59</sup>,  
11 L. Camilleri<sup>20</sup>, G. Carminati<sup>9</sup>, R. Carr<sup>20</sup>, C. Castromonte<sup>27</sup>, F. Cavanna<sup>85</sup>, S. Centro<sup>57</sup>, A. Chen<sup>26</sup>,  
12 H. Chen<sup>7</sup>, K. Chen<sup>7</sup>, D. Cherdack<sup>19</sup>, C. Chi<sup>20</sup>, S. Childress<sup>26</sup>, B. C. Choudhary<sup>22</sup>,  
13 C. Christofferson<sup>70</sup>, E. Church<sup>85</sup>, D. Cline<sup>10</sup>, T. Coan<sup>73</sup>, A. Cocco<sup>52</sup>, J. Coelho<sup>79</sup>, S. Coleman<sup>18</sup>,  
14 J. M. Conrad<sup>46</sup>, M. Convery<sup>65</sup>, R. Corey<sup>70</sup>, L. Corwin<sup>70</sup>, D. Cronin-Hennessy<sup>50</sup>, A. Curioni<sup>49</sup>,  
15 H. da Motta<sup>14</sup>, T. Davenne<sup>66</sup>, G. S. Davies<sup>34</sup>, S. Dazeley<sup>40</sup>, K. De<sup>77</sup>, A. de Gouvea<sup>54</sup>,  
16 J. K. de Jong<sup>56</sup>, D. Demuth<sup>50</sup>, C. Densham<sup>66</sup>, M. Diwan<sup>7</sup>, Z. Djurcic<sup>4</sup>, R. Dolfini<sup>59</sup>, J. Dolph<sup>7</sup>,  
17 G. Drake<sup>4</sup>, S. Dye<sup>30</sup>, H. Dyuang<sup>68</sup>, D. Edmunds<sup>47</sup>, S. Elliott<sup>42</sup>, M. Elnimr<sup>2</sup>, S. Eno<sup>45</sup>,  
18 S. Enomoto<sup>83</sup>, C. O. Escobar<sup>26</sup>, J. Evans<sup>44</sup>, A. Falcone<sup>59</sup>, L. Falk<sup>74</sup>, A. Farbin<sup>77</sup>, C. Farnese<sup>57</sup>,  
19 A. Fava<sup>57</sup>, J. Felde<sup>45</sup>, S. Fernandes<sup>2</sup>, F. Ferroni<sup>59</sup>, F. Feyzi<sup>84</sup>, L. Fields<sup>54</sup>, A. Finch<sup>38</sup>, M. Fitton<sup>66</sup>,  
20 B. Fleming<sup>85</sup>, J. Fowler<sup>24</sup>, W. Fox<sup>33</sup>, A. Friedland<sup>42</sup>, S. Fuess<sup>26</sup>, B. Fujikawa<sup>39</sup>, H. Gallagher<sup>79</sup>,  
21 R. Gandhi<sup>29</sup>, G. Garvey<sup>42</sup>, V. M. Gehman<sup>39</sup>, G. d. Geronimo<sup>7</sup>, D. Gibin<sup>57</sup>, R. Gill<sup>7</sup>,  
22 R. A. Gomes<sup>27</sup>, M. C. Goodman<sup>4</sup>, J. Goon<sup>69</sup>, N. Graf<sup>61</sup>, M. Graham<sup>65</sup>, R. Gran<sup>51</sup>, C. Grant<sup>8</sup>,  
23 N. Grant<sup>38</sup>, H. Greenlee<sup>26</sup>, L. Greenler<sup>84</sup>, S. Grullon<sup>60</sup>, E. Guardincerri<sup>42</sup>, V. Guarino<sup>4</sup>,  
24 E. Guarnaccia<sup>81</sup>, G. Guedes<sup>25</sup>, R. Guenette<sup>85</sup>, A. Guglielmi<sup>57</sup>, M. M. Guzzo<sup>12</sup>, A. T. Habig<sup>51</sup>,  
25 R. W. Hackenburg<sup>7</sup>, H. Hadavand<sup>77</sup>, A. Hahn<sup>26</sup>, M. Haigh<sup>82</sup>, T. Haines<sup>42</sup>, T. Handler<sup>76</sup>, S. Hans<sup>7</sup>,  
26 J. Hartnell<sup>74</sup>, J. Harton<sup>19</sup>, R. Hatcher<sup>26</sup>, A. Hatzikoutelis<sup>76</sup>, S. Hays<sup>26</sup>, E. Hazen<sup>6</sup>, M. Headley<sup>71</sup>,  
27 A. Heavey<sup>26</sup>, K. Heeger<sup>85</sup>, J. Heise<sup>71</sup>, R. Hellauer<sup>45</sup>, J. Hewes<sup>44</sup>, A. Himmel<sup>24</sup>, M. Hogan<sup>19</sup>,  
28 P. Holanda<sup>12</sup>, A. Holin<sup>80</sup>, G. Horton-Smith<sup>36</sup>, J. Howell<sup>26</sup>, P. Hurh<sup>26</sup>, J. Huston<sup>47</sup>, J. Hysten<sup>26</sup>,  
29 R. Imlay<sup>43</sup>, J. Insler<sup>43</sup>, G. Introzzi<sup>59</sup>, Z. Isvan<sup>7</sup>, C. Jackson<sup>77</sup>, J. Jacobsen<sup>45</sup>, D. E. Jaffe<sup>7</sup>,  
30 C. James<sup>26</sup>, C. Jen<sup>81</sup>, M. Johnson<sup>26</sup>, R. Johnson<sup>16</sup>, R. Johnson<sup>18</sup>, S. Johnson<sup>18</sup>, W. Johnston<sup>19</sup>,  
31 J. Johnstone<sup>26</sup>, B. J. Jones<sup>46</sup>, H. Jostlein<sup>26</sup>, T. Junk<sup>26</sup>, R. Kadel<sup>39</sup>, K. Kaess<sup>51</sup>, G. Karagiorgi<sup>20</sup>,  
32 J. Kaspar<sup>83</sup>, T. Katori<sup>46</sup>, B. Kayser<sup>26</sup>, E. Kearns<sup>6</sup>, P. Keener<sup>60</sup>, E. Kemp<sup>12</sup>, S. H. Kettell<sup>7</sup>,  
33 M. Kirby<sup>26</sup>, J. Klein<sup>60</sup>, G. Koizumi<sup>26</sup>, S. Kopp<sup>78</sup>, L. Kormos<sup>38</sup>, W. Kropp<sup>9</sup>, V. A. Kudryavtsev<sup>67</sup>,  
34 A. Kumar<sup>58</sup>, J. Kumar<sup>30</sup>, T. Kutter<sup>43</sup>, F. La Zia<sup>13</sup>, K. Lande<sup>60</sup>, C. Lane<sup>23</sup>, K. Lang<sup>78</sup>, F. Lanni<sup>7</sup>,  
35 R. Lanza<sup>46</sup>, T. Latorre<sup>60</sup>, J. Learned<sup>30</sup>, D. Lee<sup>42</sup>, K. Lee<sup>10</sup>, Q. Li<sup>26</sup>, S. Li<sup>7</sup>, Y. Li<sup>7</sup>, Z. Li<sup>24</sup>, J. Libo<sup>68</sup>,  
36 S. Linden<sup>6</sup>, J. Ling<sup>7</sup>, J. Link<sup>81</sup>, L. Littenberg<sup>7</sup>, H. Liu<sup>31</sup>, Q. Liu<sup>42</sup>, T. Liu<sup>73</sup>, J. Losecco<sup>55</sup>,  
37 W. Louis<sup>42</sup>, B. Lundberg<sup>26</sup>, T. Lundin<sup>26</sup>, J. Lundy<sup>77</sup>, A. A. Machado<sup>28</sup>, C. Maesano<sup>8</sup>, S. Magill<sup>4</sup>,  
38 G. Mahler<sup>7</sup>, S. Malys<sup>53</sup>, F. Mammoliti<sup>13</sup>, S. K. Mandal<sup>22</sup>, A. Mann<sup>79</sup>, P. Mantsch<sup>26</sup>,

1 A. Marchionni<sup>26</sup>, W. Marciano<sup>7</sup>, C. Mariani<sup>81</sup>, J. Maricic<sup>30</sup>, A. Marino<sup>18</sup>, M. Marshak<sup>50</sup>,  
2 J. Marshall<sup>11</sup>, S. Matsuno<sup>30</sup>, C. Mauger<sup>42</sup>, K. Mavrokoridis<sup>41</sup>, N. Mayer<sup>79</sup>, N. McCauley<sup>41</sup>,  
3 E. McCluskey<sup>26</sup>, K. McDonald<sup>62</sup>, K. McFarland<sup>64</sup>, D. McKee<sup>36</sup>, R. McKeown<sup>17</sup>, R. McTaggart<sup>72</sup>,  
4 R. Mehdiyev<sup>78</sup>, D. Mei<sup>69</sup>, A. Menegolli<sup>59</sup>, G. Meng<sup>57</sup>, Y. Meng<sup>10</sup>, D. Mertins<sup>2</sup>, M. Messier<sup>33</sup>,  
5 W. Metcalf<sup>43</sup>, R. Milincic<sup>30</sup>, W. Miller<sup>50</sup>, G. Mills<sup>42</sup>, S. R. Mishra<sup>68</sup>, N. Mokhov<sup>26</sup>,  
6 C. Montanari<sup>59</sup>, D. Montanari<sup>26</sup>, C. Moore<sup>26</sup>, J. Morfin<sup>26</sup>, B. Morgan<sup>82</sup>, W. Morse<sup>7</sup>, Z. Moss<sup>46</sup>,  
7 C. A. Moura<sup>1</sup>, S. Mufson<sup>33</sup>, D. Muller<sup>65</sup>, J. Musser<sup>33</sup>, D. Naples<sup>61</sup>, J. Napolitano<sup>63</sup>,  
8 M. Newcomer<sup>60</sup>, R. Nichol<sup>80</sup>, T. Nicholls<sup>66</sup>, E. Niner<sup>33</sup>, B. Norris<sup>26</sup>, J. Nowak<sup>38</sup>, H. O’Keeffe<sup>38</sup>,  
9 R. Oliveira<sup>12</sup>, T. Olson<sup>79</sup>, B. Page<sup>47</sup>, S. Pakvasa<sup>30</sup>, O. Palamara<sup>85</sup>, J. Paley<sup>4</sup>, V. Paolone<sup>61</sup>,  
10 V. Papadimitriou<sup>26</sup>, S. Park<sup>77</sup>, Z. Parsa<sup>7</sup>, K. Partyka<sup>85</sup>, B. Paulos<sup>84</sup>, Z. Pavlovic<sup>42</sup>, S. Peeters<sup>74</sup>,  
11 A. Perch<sup>80</sup>, G. Perdue<sup>64</sup>, J. D. Perkin<sup>67</sup>, R. Petti<sup>68</sup>, A. Petukhov<sup>70</sup>, F. Pietropaolo<sup>57</sup>, R. Plunkett<sup>26</sup>,  
12 C. Polly<sup>26</sup>, S. Pordes<sup>26</sup>, M. Potekhin<sup>7</sup>, R. Potenza<sup>13</sup>, A. Prakash<sup>46</sup>, O. Prokofiev<sup>26</sup>, X. Qian<sup>7</sup>,  
13 J. L. Raaf<sup>26</sup>, V. Radeka<sup>7</sup>, I. Rakhno<sup>26</sup>, Y. Ramachers<sup>82</sup>, R. Rameika<sup>26</sup>, J. Ramsey<sup>42</sup>, A. Rappoldi<sup>59</sup>,  
14 G. Raselli<sup>59</sup>, P. Ratoff<sup>38</sup>, S. Ravindra<sup>77</sup>, B. Rebel<sup>26</sup>, J. Reichenbacher<sup>2</sup>, D. Reitzner<sup>26</sup>, S. Rescia<sup>7</sup>,  
15 M. Richardson<sup>67</sup>, K. Rielage<sup>42</sup>, K. Riesselmann<sup>26</sup>, M. Robinson<sup>67</sup>, L. Rochester<sup>65</sup>, M. Ronquest<sup>42</sup>,  
16 M. Rosen<sup>30</sup>, M. Rossella<sup>59</sup>, C. Rubbia<sup>28</sup>, R. Rucinski<sup>26</sup>, S. Sahijpal<sup>58</sup>, H. Sahoo<sup>4</sup>, P. Sala<sup>48</sup>,  
17 D. Salmiera<sup>59</sup>, N. Samios<sup>7</sup>, M. Sanchez<sup>34</sup>, A. Scaramelli<sup>48</sup>, H. Schellman<sup>54</sup>, R. Schmitt<sup>26</sup>,  
18 D. Schmitz<sup>15</sup>, J. Schneps<sup>79</sup>, K. Scholberg<sup>24</sup>, E. Segreto<sup>37</sup>, S. Seibert<sup>60</sup>, L. Sexton-Kennedy<sup>26</sup>,  
19 M. Shaevitz<sup>20</sup>, P. Shanahan<sup>26</sup>, R. Sharma<sup>7</sup>, T. Shaw<sup>26</sup>, N. Simos<sup>7</sup>, V. Singh<sup>5</sup>, G. Sinnis<sup>42</sup>,  
20 W. Sippach<sup>20</sup>, T. Skwarnicki<sup>75</sup>, M. Smy<sup>9</sup>, H. Sobel<sup>9</sup>, M. Soderberg<sup>75</sup>, J. Sondericker<sup>7</sup>,  
21 W. Sondheim<sup>42</sup>, A. Sousa<sup>16</sup>, N. J. Spooner<sup>67</sup>, M. Stancari<sup>26</sup>, I. Stancu<sup>2</sup>, D. Stefan<sup>37</sup>, A. Stefanik<sup>26</sup>,  
22 J. Stewart<sup>7</sup>, S. Stone<sup>75</sup>, J. Strait<sup>26</sup>, M. Strait<sup>15</sup>, S. Striganov<sup>26</sup>, G. Sullivan<sup>45</sup>, Y. Sun<sup>30</sup>, L. Suter<sup>4</sup>,  
23 A. Svenson<sup>68</sup>, R. Svoboda<sup>8</sup>, B. Szczerbinska<sup>21</sup>, A. Szec<sup>85</sup>, M. Szydagis<sup>8</sup>, S. Söldner-Rembold<sup>44</sup>,  
24 R. Talaga<sup>4</sup>, M. Tamsett<sup>74</sup>, S. Tariq<sup>26</sup>, R. Tayloe<sup>33</sup>, C. Taylor<sup>42</sup>, D. Taylor<sup>71</sup>, A. Teymourian<sup>10</sup>,  
25 H. Themann<sup>7</sup>, M. Thiesse<sup>67</sup>, J. Thomas<sup>80</sup>, L. F. Thompson<sup>67</sup>, M. Thomson<sup>11</sup>, C. Thorn<sup>7</sup>,  
26 M. Thorpe<sup>66</sup>, X. Tian<sup>68</sup>, D. Tiedt<sup>70</sup>, W. Toki<sup>19</sup>, N. Tolich<sup>83</sup>, M. Torti<sup>59</sup>, M. Toups<sup>46</sup>,  
27 C. Touramanis<sup>41</sup>, M. Tripathi<sup>8</sup>, I. Tropin<sup>26</sup>, Y. Tsai<sup>65</sup>, C. Tull<sup>39</sup>, M. Tzanov<sup>43</sup>, J. Urheim<sup>33</sup>,  
28 S. Usman<sup>53</sup>, M. Vagins<sup>35</sup>, G. A. Valdivieso<sup>3</sup>, R. Van Berg<sup>60</sup>, R. Van de Water<sup>42</sup>, F. Varanini<sup>57</sup>,  
29 G. Varner<sup>30</sup>, K. Vaziri<sup>26</sup>, G. Velev<sup>26</sup>, S. Ventura<sup>57</sup>, C. Vignoli<sup>37</sup>, B. Viren<sup>7</sup>, D. Wahl<sup>84</sup>,  
30 A. Waldron<sup>74</sup>, C. W. Walter<sup>24</sup>, H. Wang<sup>10</sup>, W. Wang<sup>17</sup>, T.K. Warburton<sup>67</sup>, D. Warner<sup>19</sup>,  
31 R. Wasserman<sup>19</sup>, B. Watson<sup>77</sup>, A. Weber<sup>56</sup>, W. Wei<sup>69</sup>, D. Wells<sup>70</sup>, M. Wetstein<sup>15</sup>, A. White<sup>77</sup>,  
32 H. White<sup>42</sup>, L. Whitehead<sup>31</sup>, D. Whittington<sup>33</sup>, J. Willhite<sup>71</sup>, R. J. Wilson<sup>19</sup>, L. Winslow<sup>10</sup>,  
33 K. Wood<sup>68</sup>, E. Worcester<sup>7</sup>, M. Worcester<sup>7</sup>, T. Xin<sup>34</sup>, K. Yarritu<sup>42</sup>, J. Ye<sup>73</sup>, M. Yeh<sup>7</sup>, B. Yu<sup>7</sup>, J. Yu<sup>77</sup>,  
34 T. Yuan<sup>18</sup>, A. Zani<sup>59</sup>, G. P. Zeller<sup>26</sup>, C. Zhang<sup>7</sup>, C. Zhang<sup>69</sup>, E. D. Zimmerman<sup>18</sup>, and R. Zwaska<sup>26</sup>

35 <sup>1</sup>ABC Federal University, Santo André –SP, 09210-580,

36 <sup>2</sup>Univ. of Alabama (Tuscaloosa), Tuscaloosa, AL 35487-0324, USA

37 <sup>3</sup>Univ. Federal de Alfenas em Poços de Caldas, 11999, CEP 37715-900 Poços de Caldas-MG,  
38 Brazil

39 <sup>4</sup>Argonne National Laboratory, Argonne, IL 60439, USA

- 1 <sup>5</sup>Banaras Hindu University, Dept. of Physics, Varanasi UP 221005, India  
2 <sup>6</sup>Boston University, Boston, MA 02215, USA  
3 <sup>7</sup>Brookhaven National Laboratory, Upton, NY 11973-5000, USA  
4 <sup>8</sup>Univ. of California (Davis), Davis, CA 95616, USA  
5 <sup>9</sup>Univ. of California (Irvine), Irvine, CA 92697-4575, USA  
6 <sup>10</sup>Univ. of California (Los Angeles), Los Angeles, CA 90095-1547, USA  
7 <sup>11</sup>Univ. of Cambridge, JJ Thomson Avenue, Cambridge CB3 0HE, UK  
8 <sup>12</sup>Univ. de Campinas, Av. Sérgio Buarque de Holanda, 777 CEP 13083-859 Campinas-SP, Brazil  
9 <sup>13</sup>Univ. di Catania, Corso Italia, I-95129 Catania, Italy  
10 <sup>14</sup>Centro Brasileiro de Pesquisas Físicas, Rio de Janeiro, BR-22290-180, Brazil  
11 <sup>15</sup>Univ. of Chicago, Chicago, IL 60637-1434, USA  
12 <sup>16</sup>University of Cincinnati, Cincinnati, OH 45221-0011, USA  
13 <sup>17</sup>College Of William And Mary, Williamsburg, VA 23187-8795, USA  
14 <sup>18</sup>Univ. of Colorado, Boulder, CO 80309, USA  
15 <sup>19</sup>Colorado State University, Fort Collins, CO 80523, USA  
16 <sup>20</sup>Columbia University, New York, NY 10027, USA  
17 <sup>21</sup>Dakota State University, Madison, SD 57042, USA  
18 <sup>22</sup>Univ. of Delhi, Department of Physics and Astrophysics, Delhi 110007, India  
19 <sup>23</sup>Drexel University, Philadelphia, PA 19104, USA  
20 <sup>24</sup>Duke University, Durham, NC 27706, USA  
21 <sup>25</sup>Univ. Estadual de Feira de Santana, 44036-900, Feira de Santana-BA, Brazil  
22 <sup>26</sup>Fermilab, Batavia, IL 60510-0500, USA  
23 <sup>27</sup>Univ. Federal de Goias, Goiania, Goias, Brazil  
24 <sup>28</sup>INFN, Laboratori Nazionali del Gran Sasso, I-67010 Assergi, AQ, Italy  
25 <sup>29</sup>Harish-Chandra Research Institute, Jhansi, Allahabad 211 019, India  
26 <sup>30</sup>Univ. of Hawaii, Honolulu, HI 96822-2219, USA  
27 <sup>31</sup>Univ. of Houston, Houston, TX 77204, USA  
28 <sup>32</sup>Indian Institute of Technology Guwahati, Guwahati, 781 039, India  
29 <sup>33</sup>Indiana University, Bloomington, IN 47405-7105, USA  
30 <sup>34</sup>Iowa State University, Ames, IO 50011, USA  
31 <sup>35</sup>Kavli Institute For The Physics And Mathematics Of The Universe, University Of Tokyo,  
32 Kashiwa Shi, Chiba 277-8568, Japan  
33 <sup>36</sup>Kansas State University, Manhattan, KS 66506, USA  
34 <sup>37</sup>Laboratori Nazionali del Gran Sasso, I-67010 Assergi, AQ, Italy  
35 <sup>38</sup>Lancaster University, Bailrigg, Lancaster LA1 4YB, UK  
36 <sup>39</sup>Lawrence Berkeley National Lab., Berkeley, CA 94720-8153, USA  
37 <sup>40</sup>Lawrence Livermore National Lab., Livermore, CA 94551, USA  
38 <sup>41</sup>Univ. of Liverpool, L69 7ZE, Liverpool, UK  
39 <sup>42</sup>Los Alamos National Lab., Los Alamos, NM 87545, USA



1  
2  
3  
4  
5

<sup>81</sup>Virginia Tech., Blacksburg, VA 24061-0435, USA

<sup>82</sup>Univ. of Warwick, Coventry CV4 7AL, UK

<sup>83</sup>Univ. Of Washington, Seattle, WA 98195-1560, USA

<sup>84</sup>Univ. Of Wisconsin, Madison, WI 53706, USA

<sup>85</sup>Yale University, New Haven, CT 06520, USA

DRAFT



## Abstract

Understanding the source of the matter-antimatter asymmetry of the Universe, the dynamics of the supernova bursts that produced the heavy elements necessary for the chemistry of life and determining whether protons will eventually decay stand among the grand questions of physics — keys to understanding the early evolution of our Universe, its current state, and eventually its fate. **FIXME:** *I would change to 'its eventual fate'* The Long-Baseline Neutrino Experiment (LBNE) is a mature, well-developed, world-class experiment whose principal goal is to address these questions that are at the forefront of particle physics and astrophysics.

Experiments carried out over the past half century have revealed that neutrinos are found in three forms or “flavors”, and can transform (oscillate) from one flavor into another. These discoveries indicate that the neutrino flavor states are mixtures of different nonzero mass states and to date offer the most compelling evidence for physics beyond the Standard Model. In a single experiment, LBNE will enable a broad exploration of the three-flavor model of neutrino physics with unprecedented detail. Chief among its potential discoveries is that of matter-antimatter asymmetries in neutrino flavor mixing — a step toward unraveling the mystery of matter generation in the early Universe. **FIXME:** *now this sounds repetitive to me* Independently, determination of the unknown neutrino mass ordering and precise measurement of neutrino mixing parameters by LBNE may reveal new fundamental symmetries of Nature.

Grand Unified Theories, which attempt to describe the unification of the known forces of Nature, predict rates for proton decay that cover a range directly accessible with the next generation of large underground detectors such as the massive 34-kt neutrino detector envisioned for LBNE. LBNE’s sensitivity to key proton decay channels, in particular, will offer unique opportunities for observing this ground-breaking phenomenon.

Neutrinos emitted in the first few seconds of a core-collapse supernova carry with them the potential for great insight into the evolution of the Universe. LBNE’s capability to collect and analyze this high-statistics neutrino signal from a supernova within our galaxy would provide a rare opportunity to peer inside a newly-formed neutron star and potentially witness the birth of a black hole.

To achieve its goals, LBNE is conceived around three central components: (1) a new, high-intensity neutrino source generated from a megawatt-class proton accelerator at Fermi National Accelerator Laboratory, (2) a fine-grained near neutrino detector installed just downstream of the source, and (3) a massive liquid argon time-projection chamber deployed as a far detector deep underground at the Sanford Underground Research Facility. This facility, located at the site of the former Homestake Mine in Lead, South Dakota, is  $\sim 1,300$  km from the neutrino source at Fermilab — a distance (baseline) that delivers optimal sensitivity to neutrino charge-parity symmetry violation (the mechanism responsible for matter-antimatter asymmetries) and mass ordering effects.

LBNE is an experiment whose relevance, importance, and probability of unearthing critical and exciting physics continues to increase with time and is attractive for developing major international partnerships. LBNE will greatly expand our understanding of the most abundant known particle of matter and probe the fundamental forces that shaped our Universe from its first moments of creation.



# Contents

3	<b>List of Figures</b>	<b>v</b>
4	<b>List of Tables</b>	<b>ix</b>
5	<b>How to Read this Document</b>	<b>xi</b>
6	<b>1 Introduction and Executive Summary</b>	<b>1</b>
7	1.1 Overview	2
8	1.2 Development of a World-Class Experiment	5
9	1.2.1 Long-Term Vision	6
10	1.2.2 Present Status of the LBNE Project	7
11	1.2.3 Global Partnerships	7
12	1.2.4 Context for Discussion of Physics Sensitivities	8
13	1.3 The LBNE Physics Program	9
14	1.3.1 Neutrino Mixing, Mass Hierarchy and CP Violation	10
15	1.3.2 Nucleon Decay Physics Motivated by Grand Unified Theories	13
16	1.3.3 Supernova-Neutrino Physics and Astrophysics	14
17	1.3.4 Precision Measurements with a High-Intensity Neutrino Source and High-Resolution Near Detector	14
18	1.4 Summary	15
19		
20	<b>2 The Science of LBNE</b>	<b>17</b>
21	2.1 Scientific Objectives of LBNE	18
22	2.2 Neutrino Three-Flavor Mixing, CP Violation and the Mass Hierarchy	20
23	2.2.1 CP Violation in the Quark and Lepton Sectors	24
24	2.2.2 Observation of CP-Violating Effects in Neutrino Oscillation Experiments	26
25	2.2.3 Probing the Neutrino Mass Hierarchy via the Matter Effect	30
26	2.2.4 Disentangling CP-Violating and Matter Effects	31
27	2.2.5 Optimization of the Oscillation Baseline for CPV and Mass Hierarchy	33
28	2.2.6 Physics from Precision Measurements of Neutrino Mixing	35
29	2.2.7 Oscillation Physics with Atmospheric Neutrinos	36
30	2.3 Nucleon Decay Physics Motivated by Grand Unified Theories	38

1	2.3.1	Theoretical Motivation from GUTs . . . . .	38
2	2.3.2	Proton Decay Modes . . . . .	39
3	2.4	Supernova-Neutrino Physics and Astrophysics . . . . .	41
4	<b>3</b>	<b>Project and Design</b>	<b>45</b>
5	3.1	LBNE and the U.S. Neutrino Physics Program . . . . .	46
6	3.2	Near Site: Fermi National Accelerator Laboratory . . . . .	48
7	3.3	Far Site: Sanford Underground Research Facility . . . . .	54
8	3.4	Beamline . . . . .	63
9	3.5	Near Detector . . . . .	70
10	3.6	Far Detector . . . . .	74
11	3.6.1	The 10-kt Detector Design . . . . .	76
12	3.6.2	The 34-kt Detector Design . . . . .	79
13	<b>4</b>	<b>Neutrino Mixing, Mass Hierarchy, and CP Violation</b>	<b>83</b>
14	4.1	Experimental Requirements Based on Oscillation Phenomenology . . . . .	83
15	4.2	Experiment Simulation . . . . .	85
16	4.2.1	Neutrino Rates . . . . .	85
17	4.2.2	Detector Simulation using the GLoBES Package . . . . .	88
18	4.3	Measurements of Mass Hierarchy and the CP-Violating Phase . . . . .	92
19	4.3.1	Interpretation of Mass Hierarchy Sensitivities . . . . .	96
20	4.3.2	Sensitivities and Systematics . . . . .	100
21	4.3.3	Summary of CP and Mass Hierarchy Sensitivities . . . . .	111
22	4.3.4	Mass Hierarchy and CP Sensitivities with Increased Exposures . . . . .	113
23	4.4	Measurement of $\theta_{23}$ and Determination of the Octant . . . . .	116
24	4.5	Precision Measurements of the Oscillation Parameters in the Three-Flavor Model	118
25	4.6	Oscillation Studies Using Atmospheric Neutrinos . . . . .	122
26	4.7	Searches for Physics Beyond the Standard Three-Flavor Neutrino Oscillation Model	131
27	4.7.1	Search for Nonstandard Interactions . . . . .	132
28	4.7.2	Search for Long-Range Interactions . . . . .	132
29	4.7.3	Search for Active-Sterile Neutrino Mixing . . . . .	134
30	4.7.4	Sensitivity to Large Extra Dimensions . . . . .	135
31	4.8	Comparison of LBNE Sensitivities to other Proposed Neutrino Oscillation Experi-	
32		ments . . . . .	135
33	<b>5</b>	<b>Nucleon Decay Physics Motivated by Grand Unified Theories</b>	<b>139</b>
34	5.1	LBNE and the Current Experimental Context . . . . .	139
35	5.2	Signatures for Nucleon Decay in Liquid Argon . . . . .	140
36	5.3	Background Levels and Rejection Capabilities . . . . .	143
37	5.3.1	Cosmic-Ray Muon Backgrounds . . . . .	143

1	5.3.2	Background from Atmospheric Neutrino Interactions . . . . .	145
2	5.4	Summary of Expected Sensitivity to Key Nucleon Decay Modes . . . . .	149
3	<b>6</b>	<b>Core-Collapse Supernova Neutrinos</b>	<b>153</b>
4	6.1	The Neutrino Signal and Astrophysical Phenomena . . . . .	153
5	6.2	Expected Signal and Detection in Liquid Argon . . . . .	156
6	6.3	Low-Energy Backgrounds . . . . .	160
7	6.3.1	Cosmic Rays . . . . .	160
8	6.3.2	Local Radiation Sources . . . . .	160
9	6.3.3	Intrinsic Radioactive Background Mitigation . . . . .	162
10	6.4	Summary of Core-Collapse Supernova Sensitivities . . . . .	163
11	<b>7</b>	<b>Precision Measurements with a High-Intensity Neutrino Beam</b>	<b>165</b>
12	7.1	Precision Measurements with Long-Baseline Oscillations . . . . .	165
13	7.1.1	Relative Neutrino and Antineutrino Flux . . . . .	166
14	7.1.2	Flavor Content of the Beam: $\nu_\mu, \bar{\nu}_\mu, \nu_e, \bar{\nu}_e$ . . . . .	167
15	7.1.3	Constraining the Unoscillated $\nu$ Spectral Shape with the QE Interaction	168
16	7.1.4	Low-Energy Absolute Flux: Neutrino-Electron NC Scattering . . . . .	169
17	7.1.5	High-Energy Absolute Flux: Neutrino-Electron CC Scattering . . . . .	169
18	7.1.6	Low-Energy Absolute Flux: QE in Water and Heavy-Water Targets . . .	170
19	7.1.7	Neutral Pions, Photons, and $\pi^\pm$ in NC and CC Events . . . . .	170
20	7.1.8	Signal and Background Predictions for the Far Detector . . . . .	171
21	7.2	Electroweak Precision Measurements . . . . .	172
22	7.2.1	Deep Inelastic Scattering . . . . .	172
23	7.2.2	Elastic Scattering . . . . .	175
24	7.3	Observation of the Nucleon's Strangeness Content . . . . .	177
25	7.3.1	Extraction of the Strange Form Factors in the LBNE ND . . . . .	178
26	7.4	Nucleon Structure and QCD Studies . . . . .	181
27	7.4.1	Determination of the $F_3$ Structure Function and GLS Sum Rule . . . . .	181
28	7.4.2	Determination of the Longitudinal Structure Function $F_L(x, Q^2)$ . . .	182
29	7.4.3	Determination of $F_2^n$ and the $d/u$ Ratio of Quark Distribution Functions	183
30	7.4.4	Measurement of Nucleon Structure Functions in the LBNE ND . . . . .	184
31	7.5	Tests of Isospin Physics and Sum-Rules . . . . .	186
32	7.6	Studies of (Anti)Neutrino-Nucleus Interactions . . . . .	187
33	7.7	Search for Heavy Neutrinos . . . . .	189
34	7.8	Search for High $\Delta m^2$ Neutrino Oscillations . . . . .	192
35	7.9	Light (sub-GeV) Dark Matter Searches . . . . .	194
36	<b>8</b>	<b>Additional Far Detector Physics Opportunities</b>	<b>197</b>
37	8.1	Solar Neutrinos . . . . .	197

1	8.2	Indirect Searches for WIMP Dark Matter . . . . .	201
2	8.3	Supernova Relic Neutrinos . . . . .	203
3	8.4	GUT Monopoles . . . . .	205
4	8.5	Neutron-Antineutron Oscillations ( $\Delta B = 2$ ) . . . . .	206
5	8.6	Geo and Reactor $\bar{\nu}_e$ 's . . . . .	206
6	<b>9</b>	<b>Summary and Conclusion</b>	<b>207</b>
7	9.1	Staging Scenarios and Timeline . . . . .	207
8	9.2	Science Impact . . . . .	210
9	9.3	Uniqueness of Opportunity . . . . .	211
10	9.4	Broader Impacts . . . . .	212
11	9.4.1	Intensity Frontier Leadership . . . . .	212
12	9.4.2	Inspirational Project for a New Generation . . . . .	213
13	9.5	Concluding Remarks . . . . .	213
14	<b>A</b>	<b>LBNE Detector Simulation and Reconstruction</b>	<b>215</b>
15	A.1	Far Detector Simulation . . . . .	215
16	A.1.1	Tools and Methods . . . . .	215
17	A.1.2	Low-energy Neutrino Response Studies with LArSoft . . . . .	218
18	A.2	Far Detector Reconstruction . . . . .	220
19	A.3	Fast Monte Carlo . . . . .	223
20	A.4	Simulation of Cosmic-Ray Background for a 10-kt Surface Detector . . . . .	231
21	<b>B</b>	<b>Neutrino-Nucleon Scattering Kinematics</b>	<b>235</b>
22		<b>Acknowledgments</b>	<b>237</b>
23		<b>References</b>	<b>239</b>

## 2 List of Figures

3	1.1	Summary of mass hierarchy sensitivities . . . . .	11
4	1.2	Expected $1\sigma$ resolution for $\delta_{\text{CP}}$ as a function of exposure . . . . .	12
5	1.3	Sensitivity to the decay $p \rightarrow K^+\bar{\nu}$ with liquid argon detectors . . . . .	13
6	2.1	Standard Model particles . . . . .	20
7	2.2	Neutrino mass eigenstate components of flavor eigenstates . . . . .	21
8	2.3	$\nu$ oscillation probabilities versus $E$ and baseline for various $\delta_{\text{CP}}$ , normal MH . . . . .	28
9	2.4	$\nu$ oscillation probabilities versus $E$ and baseline and for various $\delta_{\text{CP}}$ , inverted MH . . . . .	29
10	2.5	CP asymmetry versus baseline . . . . .	32
11	2.6	$\nu/\bar{\nu}$ oscillation asymmetries versus $\delta_{\text{CP}}$ at the first two oscillation nodes . . . . .	33
12	2.7	Fraction of $\delta_{\text{CP}}$ values covered at a given significance for CPV and MH vs baseline . . . . .	34
13	2.8	Atmospheric neutrino flux and spectrum . . . . .	36
14	2.9	Probabilities of atmospheric $\nu_\mu \rightarrow \nu_e$ oscillations vs zenith angle . . . . .	37
15	2.10	Proton decay modes from gauge-mediation and SUSY GUT models . . . . .	40
16	2.11	Proton decay lifetime limits compared to lifetime ranges predicted by GUTs . . . . .	41
17	2.12	Number of supernova neutrino interactions in a LAr detector vs distance . . . . .	44
18	3.1	Three frontiers of particle physics in the U.S. . . . .	46
19	3.2	Fermilab's accelerator chain . . . . .	49
20	3.3	NuMI beamline performance . . . . .	50
21	3.4	Possible flux ramp-up scenario for Intensity Frontier experiments . . . . .	50
22	3.5	Proton beam power versus beam energy . . . . .	51
23	3.6	Site layout of PIP- II . . . . .	53
24	3.7	Location of Lead, South Dakota . . . . .	55
25	3.8	Former Homestake Mine vertical long-section . . . . .	56
26	3.9	Sanford Underground Research Facility campuses . . . . .	57
27	3.10	Layout at the 4,850-ft level in the Sanford Underground Research Facility . . . . .	58
28	3.11	Predicted cosmic-ray flux at the far site . . . . .	59
29	3.12	Geologic long-section of Sanford Underground Research Facility . . . . .	60
30	3.13	Photos from the Sanford Underground Research Facility . . . . .	61
31	3.14	Experiment timeline for the Sanford Underground Research Facility . . . . .	62
32	3.15	Overall LBNE Project layout at Fermilab . . . . .	65

1	3.16	Longitudinal section of the LBNE beamline facility. . . . .	65
2	3.17	Neutrino beamline components . . . . .	66
3	3.18	Neutrino fluxes from the LBNE beam . . . . .	67
4	3.19	Neutrino beam spectra from different beam tunes . . . . .	68
5	3.20	System of tertiary-beam muon detectors . . . . .	71
6	3.21	Magnetized straw-tube tracker near detector design . . . . .	72
7	3.22	Schematic drawing of near detector ECAL . . . . .	73
8	3.23	View of a 10-kt far detector showing the two vessels . . . . .	77
9	3.24	The LBNE TPC modular construction concept . . . . .	78
10	3.25	Schematic of a 34-kt LArTPC design . . . . .	80
11	3.26	Layout of the 10-kt + 24-kt LArTPC detector halls at the 4,850-ft level . . . . .	81
12	3.27	Far site geotechnical site investigation plan . . . . .	81
13	4.1	Unoscillated spectrum of $\nu_\mu$ events and $\nu_\mu \rightarrow \nu_e$ oscillation probabilities . . . . .	86
14	4.2	Disappearance spectra in a LArTPC . . . . .	90
15	4.3	Event spectra of neutrino interactions in a LArTPC . . . . .	91
16	4.4	Sensitivity to MH and CP violation in a 10-kt LArTPC . . . . .	94
17	4.5	Sensitivity to MH and CP violation in a 34-kt LArTPC . . . . .	95
18	4.6	$\Delta\chi^2_{\text{MH=NH}}$ and $\Delta\chi^2_{\text{MH=IH}}$ distributions for LBNE from toy MC studies . . . . .	98
19	4.7	The expected $\sqrt{ \Delta\chi^2 }$ values for the typical LBNE experiment . . . . .	100
20	4.8	Flow chart of $\nu_e$ appearance analysis method . . . . .	101
21	4.9	MH and CP violation sensitivities from shape, rate, and shape+rate . . . . .	106
22	4.10	MH and CP violation sensitivities as a function of exposure in kt · year . . . . .	109
23	4.11	Variation of sensitivity to MH and CP violation with $\theta_{13}$ . . . . .	110
24	4.12	Variation of sensitivity to MH and CP violation with $\theta_{23}$ . . . . .	111
25	4.13	Variation of sensitivity to MH and CP violation with $\Delta m^2_{31}$ . . . . .	111
26	4.14	Sensitivity to MH versus $\sin^2 \theta_{23}$ . . . . .	112
27	4.15	Measurement of the mixing parameters from Capozzi <i>et al.</i> . . . . .	114
28	4.16	Mass hierarchy and CPV versus exposure in mass, beam power and time . . . . .	115
29	4.17	CPV determination versus $\delta_{\text{CP}}$ . . . . .	116
30	4.18	Measurement of $\theta_{23}$ and $\Delta m^2_{31}$ with LBNE 10 . . . . .	117
31	4.19	Sensitivity to the determination of the $\theta_{23}$ octant . . . . .	118
32	4.20	Sensitivity to determination of $\theta_{23}$ octant with increased exposures . . . . .	119
33	4.21	Measurement of $\delta_{\text{CP}}$ and $\theta_{13}$ in LBNE with increased exposures . . . . .	120
34	4.22	Expected $1\sigma$ resolution on three-flavor oscillation parameters, 1.2 MW beam . . . . .	121
35	4.23	L/E distribution of high-resolution $\mu$ -like atmospheric $\nu$ events, 340kt · year . . . . .	125
36	4.24	Reconstructed zenith angle distributions in several ranges of energy . . . . .	126
37	4.25	Reconstructed zenith angle distributions for events of 6-10 GeV . . . . .	126
38	4.26	Sensitivity for atmospheric neutrino data to MH as a function of $\delta_{\text{CP}}$ , 340 kt · year . . . . .	128
39	4.27	Sensitivity to mass hierarchy using atmospheric neutrinos . . . . .	128

1	4.28	Sensitivity to $\theta_{23}$ octant and CPV using atmospheric neutrinos . . . . .	129
2	4.29	Sensitivity to MH using atmospheric and beam neutrinos as a function of $\delta_{CP}/\pi$	129
3	4.30	Sensitivity to MH using atmospheric and beam neutrinos as a function of $\sin^2 \theta_{23}$	130
4	4.31	Sensitivity to $\theta_{23}$ octant and CPV using atmospheric and beam neutrinos . . . . .	131
5	4.32	Sensitivity to nonstandard interactions . . . . .	133
6	4.33	Long-range interactions in LBNE . . . . .	134
7	4.34	CPV in LBNE and other proposed experiments . . . . .	136
8	4.35	Resolution on $\delta_{CP}$ in LBNE and other experiments . . . . .	137
9	4.36	MH sensitivity in LBNE with time compared to other proposed experiments . .	138
10	5.1	Decaying kaon observed during the ICARUS run at CNGS . . . . .	142
11	5.2	3D construction of decaying kaon in the ICARUS detector . . . . .	143
12	5.3	$dE/dx$ profile of decaying kaon in the ICARUS CNGS run . . . . .	147
13	5.4	Proton decay lifetime limit for $p \rightarrow K^+ \bar{\nu}$ versus time . . . . .	149
14	5.5	Proton decay lifetime limits achievable by 34-kt LBNE; comparison to others .	150
15	6.1	Expected core-collapse neutrino signal . . . . .	154
16	6.3	SN $\nu$ event rates in 34 kt of LAr for a core collapse at 10 kpc, GKVM . . . . .	157
17	6.4	Garching flux signal with neutronization burst . . . . .	158
18	6.5	Comparison of total event rates, normal and inverted MH, for WCD and LAr . .	159
19	6.6	Observed $\nu_e$ spectra in 34 kt of LAr for a 10-kpc core collapse . . . . .	159
20	6.7	Avg $\nu_e$ energy, SNOWGLOBES-smearred, pinched-thermal spectrum, 34 kt, 10 kpc	160
21	6.8	Cosmogenic backgrounds in the LArTPC at the 4850-ft level . . . . .	161
22	7.1	Feynman diagrams for the three main NC processes . . . . .	172
23	7.2	Expected near detector sensitivity to $\sin^2 \theta_W$ for a 1.2-MW beam . . . . .	176
24	7.3	Sensitivity of NC/CC to the strange contribution to spin of nucleon . . . . .	179
25	7.4	Feynman diagrams pertaining to sterile neutrinos . . . . .	190
26	7.5	Near detector constraints on heavy Majorana neutrinos . . . . .	191
27	7.6	Production mechanisms for dark matter at neutrino beam experiments . . . . .	195
28	7.7	Regions of nucleon-WIMP cross section versus WIMP mass . . . . .	196
29	8.1	The solar PP cycle and solar $\nu$ spectrum . . . . .	198
30	8.2	$^{40}\text{Cl}$ production rates produced by (n,p) reaction per depth, 10 kt . . . . .	200
31	8.3	Measurements of the solar MSW transition . . . . .	201
32	8.4	Solar neutrino day/night effect and dependence on $\Delta m_{21}^2$ . . . . .	202
33	8.5	Relic supernova spectra and key neutrino backgrounds . . . . .	204
34	8.6	Proton decay catalyzed by a GUT monopole . . . . .	205
35	9.1	Typical DOE Acquisition Management System for line item capital asset projects	208
36	A.1	Event displays of beam interactions in a LArTPC . . . . .	216

1	A.2	Typical 20-MeV event in the LBNE 35-t prototype geometry . . . . .	219
2	A.3	Comparisons of energy resolution . . . . .	220
3	A.4	2D clusterings of hits created by particles in two CC neutrino interactions in LAr . . . . .	222
4	A.5	Distributions of residuals between reconstructed and MC primary vertices . . . . .	222
5	A.6	kNN discriminant for removal of $\nu_\tau$ -CC-induced backgrounds . . . . .	226
6	A.7	Energy distributions for $\nu_e$ - and $\bar{\nu}_e$ appearance signals . . . . .	227
7	A.8	Energy distributions for $\nu_\mu$ - and $\bar{\nu}_\mu$ disappearance signals . . . . .	227
8	A.9	Selection efficiency and sample purities for $\nu_e$ appearance in a LArTPC . . . . .	228
9	A.10	Selection efficiency and sample purities for $\nu_\mu$ disappearance in a LArTPC . . . . .	229
10	A.11	CPV sensitivity with and without allowed variations in CC $M_A^{res}$ . . . . .	230
11	A.12	Cosmic-ray background event distribution in the 10-kt surface detector . . . . .	234
12	B.1	Schematic of the neutrino-nucleon scattering . . . . .	235

## 2 List of Tables

3	2.1	Best-fit values of the neutrino mixing parameters in the PMNS matrix . . . . .	24
4	3.1	Partial U/Th/K assay results for far site rock samples . . . . .	61
5	3.2	Parameters for LBNE beamline reference design at CD-1 . . . . .	64
6	3.3	Impact of the beam improvements on the neutrino $\nu_\mu \rightarrow \nu_e$ . . . . .	70
7	3.4	Summary of the performance for the fine-grained tracker configuration . . . . .	73
8	3.5	Parameters for the fine-grained tracker . . . . .	74
9	3.6	Parameters for LArTPC far detector . . . . .	75
10	4.1	Raw $\nu$ oscillation event rates at the LBNE far site with $E_\nu < 10$ GeV . . . . .	87
11	4.2	Range of detector efficiencies and background rejection based on handscan studies	89
12	4.3	Expected number of $\nu$ oscillation signal and beam background events . . . . .	90
13	4.4	Achieved systematic error performance in prior $\nu_\mu \rightarrow \nu_e$ oscillation experiments	96
14	4.5	$\nu_e$ appearance signal dominant systematic uncertainties MINOS/T2K/LBNE . .	102
15	4.6	Near detector precisions for in situ $\nu_\mu$ and $\nu_e$ flux measurements . . . . .	104
16	4.7	Exposures to reach $3\sigma$ and $5\sigma$ sensitivity to CPV for $\geq 50\%$ of $\delta_{CP}$ values . . .	109
17	4.8	Summary of 10-kt and 34-kt far detector sensitivities . . . . .	113
18	4.9	Summary of CPV sensitivities with PIP II, mass upgrades and beyond . . . . .	115
19	4.10	Oscillation parameters used in the atmospheric neutrino analysis . . . . .	122
20	4.11	Expected atmospheric $\nu$ interaction rates in 100 kt · year with a LArTPC . . . .	123
21	4.12	Performance assumptions for atmospheric and combined atmospheric+beam $\nu$ .	123
22	4.13	Atmospheric neutrino event rates in 100 kt · year with oscillations . . . . .	124
23	4.14	Systematic errors in the atmospheric and beam+atmospheric $\nu$ analysis . . . . .	127
24	5.1	Efficiencies and background rates for nucleon decay modes . . . . .	141
25	5.2	Sensitivity for $p \rightarrow K^+ \bar{\nu}$ with different background rates . . . . .	150
26	6.1	Event rates for different models in 34 kt of LAr for a core-collapse at 10 kpc . .	157
27	7.1	Interaction rates, for neutrino mode, per ton for $1 \times 10^{20}$ POT, 459 m, 120 GeV	166
28	7.2	Uncertainties on the $\mathcal{R}^\nu$ measurement, NuTeV versus LBNE . . . . .	173
29	7.3	Expected proton range for the low-density tracker . . . . .	180
30	7.4	Past experiments' structure function measurements . . . . .	184

1	8.1	Solar neutrino rates in a LArTPC . . . . .	200
2	A.1	Cosmic-ray-induced background in the surface 10-kt detector . . . . .	233

DRAFT

# How to Read this Document

2 The LBNE science document is intended to inform a diverse readership about the goals and capa-  
3 bilities of the LBNE experiment. Your approach to reading this document will depend upon your  
4 purpose as well as your level of knowledge about high energy and neutrino physics.



5 The colored boxes distributed throughout the document highlight the important take-away points. They are integral to the document, but to the extent possible, are written in language accessible to the nonscientist.



6 The three chapters exec-sum-chap Chapter 1 *Introduction and Executive Summary*, project-chap Chapter 3 *Project and Design*  
7 and Chapter 9 conclusion-chap *Summary and Conclusion* together provide a comprehensive overview of LBNE's  
8 scientific objectives, its place in the landscape of neutrino physics experiments world-wide, the  
9 technologies it will incorporate and the capabilities it will possess. Much of the information in these  
10 chapters is accessible to the lay reader, but of course, the scientific concepts, goals and methods  
11 around which LBNE is designed are by their nature highly specialized, and the text in certain  
12 sections is correspondingly technical.



13 In Chapter 2 intro-chap *The Science of LBNE*, the initial paragraphs in each section provide some introductory  
14 information, but in general this chapter assumes a working knowledge of high energy physics and,  
15 ideally, familiarity with neutrino physics.

16 The three chapters that delve into the areas corresponding to the scientific objectives of LBNE:  
17 Chapter 4 nu-oscil-chap *Neutrino Mixing, Mass Hierarchy and CP Violation*, Chapter 5 pdk-chap *Nucleon Decay Physics*  
18 *Motivated by Grand Unified Theories* and Chapter 6 sn-chap *Core-Collapse Supernova Neutrinos*, assume  
19 a working knowledge of high energy physics and particle astrophysics. This is also true of Chap-  
20 ter 7 nd-physics-chap *Precision Measurements with a High-Intensity Neutrino Beam* and Chapter 8 chap-other-goals *Additional Far*  
21 *Detector Physics Opportunities*, as well as the appendices.

DRAFT

1

The Long-Baseline Neutrino Experiment (LBNE) will provide a unique, world-leading program for the exploration of key questions at the forefront of particle physics and astrophysics.

Chief among its potential discoveries is that of matter-antimatter symmetry violation in neutrino flavor mixing — a step toward unraveling the mystery of matter generation in the early Universe. Independently, determination of the neutrino mass ordering and precise measurement of neutrino mixing parameters by LBNE may reveal new fundamental symmetries of Nature.

To achieve its ambitious physics objectives as a world-class facility, LBNE has been conceived around three central components:

1. an intense, wide-band neutrino beam
2. a fine-grained *near* neutrino detector just downstream of the neutrino source
3. a massive liquid argon time-projection chamber (LArTPC) deployed as a *far* neutrino detector deep underground, 1,300 km downstream; this distance between the neutrino source and far detector — the *baseline* — is measured along the line of travel through the Earth

The neutrino beam and near detector will be installed at the Fermi National Accelerator Laboratory (Fermilab), in Batavia, Illinois. The far detector will be installed at the Sanford Underground Research Facility in Lead, South Dakota.

The location of its massive high-resolution far detector deep underground will enable LBNE to significantly expand the search for proton decay as predicted by Grand Unified Theories, as well as study the dynamics of core-collapse supernovae through observation of their neutrino bursts, should any occur in our galaxy during LBNE's operating lifetime.

The near neutrino detector will enable high-precision measurements of neutrino oscillations, thereby enhancing the sensitivity to matter-antimatter symmetry violations and will exploit the potential of high-intensity neutrino beams as probes of new physics.

With its extensively developed design and flexible configuration, LBNE provides a blueprint for an experimental program made even more relevant by recent neutrino mixing parameter measurements.

2

## 1.1 Overview

Although neutrinos are the most abundant of known matter particles (fermions) in the Universe, their properties are the least well understood. The very existence of neutrino mass constitutes evidence of physics beyond the Standard Model. Understanding the nature of neutrinos has consequently become an essential goal for particle physics.

Observations of oscillations of neutrinos from one type (flavor) to another in numerous recent experiments have provided evidence for neutrino flavor mixing and for small, but nonzero, neutrino masses. The framework characterizing these observations is similar to that describing corresponding phenomena in the quark sector, but with a very different pattern of mixing-angle values. As in the quark case, this framework involves a phase parameter,  $\delta_{\text{CP}}$ , that changes sign under combined charge conjugation and parity (CP) reversal operations and thus would lead to CP symmetry-violating asymmetries between the pattern of oscillations for neutrinos and antineutrinos. While groundbreaking on its own, the observation of such asymmetries would also provide an experimental underpinning for the basic idea of leptogenesis\* as an explanation for the Baryon Asymmetry of the Universe (BAU).

Neutrino oscillation data so far tell us about differences in the squared masses of the neutrino mass states, and about the sign of the mass-squared difference between two of the states, but not about the difference of those with respect to the third, which may be heavier (*normal* ordering) or lighter (*inverted* ordering) than the other two. Resolving this neutrino mass hierarchy ambiguity, along with precise measurements of neutrino mixing angles, would have significant theoretical, cosmological and experimental implications. One important consequence of mass hierarchy determination, in particular, would be the impact on future experiments designed to determine whether — uniquely among the fundamental fermions — neutrinos are their own antiparticles, so-called *Majorana* particles. Though long suspected, this hypothesis that neutrinos are Majorana particles has yet to be either established or ruled out. Strong evidence for the *inverted* hierarchy would establish conditions required by the next generation of neutrinoless double-beta decay searches to settle this question even with a null result (no observation). Because the forward scattering of neutrinos in matter alters the oscillation pattern in a hierarchy-dependent way, the long baseline of LBNE — with the neutrinos traveling through the Earth’s mantle — enables a decisive determination of the hierarchy, independent of the value of  $\delta_{\text{CP}}$ .

Additionally, the high-precision determination of oscillation parameters such as mixing angles and squared-mass differences will provide insight into the differences between the quark and lepton mixing patterns, which is necessary for deciphering the flavor structure of physics in the Standard Model. Taken together, the above suite of measurements will thoroughly test the standard three-neutrino flavor paradigm that guides our current understanding, and will provide greatly extended

\*Leptogenesis refers to the mechanisms that generated an asymmetry between leptons and antileptons in the early Universe, described in Section 2.2.1.

1 sensitivity to signatures for nonstandard neutrino interactions in matter.

2 The arena of non-accelerator physics using massive underground detectors such as the LBNE far  
3 detector is also ripe with discovery potential. The observation of nucleon decay would be a wa-  
4 tershed event for the understanding of physics at high energy scales. Neutrinos from supernovae  
5 are expected to provide key insights into the physics of gravitational collapse, and may also reveal  
6 fundamental properties of the neutrino.

7 Among massive detectors designed for neutrino and nucleon decay physics, the LArTPC technol-  
8 ogy offers unmatched capabilities for position and energy resolution and for high-precision recon-  
9 struction of complex interaction topologies over a broad energy range. It also provides a compact,  
10 scalable approach for achieving the required sensitivity to the primary physics signatures to be  
11 explored by LBNE. As these capabilities are also important for non-accelerator neutrino physics,  
12 LBNE will complement the large, underground water Cherenkov and/or scintillator-based detec-  
13 tors that may be operating in parallel. LArTPC detectors are especially well-suited to proton decay  
14 modes such as the supersymmetry-favored  $p \rightarrow K^+\bar{\nu}$  mode, uniquely providing detection effi-  
15 ciency and background rejection sufficient to enable a discovery with a single well-reconstructed  
16 event. With regard to supernova neutrino detection, liquid argon detectors are primarily sensitive  
17 to the  $\nu_e$  component of the flux, while  $\bar{\nu}_e$  interactions dominate for water and scintillator-based  
18 detectors. Thus, LBNE will be sensitive to different features of the supernova-neutrino production  
19 process. Finally, the LArTPC technology opens up an avenue for precision studies of oscillation  
20 physics with atmospheric neutrinos, thereby augmenting the results of the beam-based measure-  
21 ments at the core of the experiment.

22 The highly capable near detector will measure the absolute flux and energy scales of all four  
23 neutrino species in the LBNE beam, as well as neutrino cross sections on argon, water, and other  
24 nuclear targets in the beam's energy range. These measurements are needed to attain the ultimately  
25 desired precision of the oscillation parameter measurements. Additionally, the near detector will  
26 enable a broad range of precision neutrino-interaction measurements, thereby adding a compelling  
27 scientific program of its own.

28 The unique combination in LBNE of a 1,300-km baseline, exceptional resolution, large target  
29 mass and deep underground location offers opportunity for discovery of entirely unanticipated  
30 phenomena. History shows that ambitious scientific endeavors with leading-edge instruments have  
31 often been rewarded with unexpected signatures of new physics.

32 LBNE is an extensively developed experiment whose execution will have substantial impact on the  
33 overall direction of high energy physics (HEP) in the U.S. The U.S. Department of Energy (DOE)  
34 has endorsed the science objectives of LBNE, envisioning the experiment as a phased program,  
35 and has given first stage (CD-1) approval with a budget of \$867M towards the initial phase. The  
36 science scope of this and subsequent phases will depend on the level of investment by additional  
37 national and international partners.

1 This document outlines the LBNE physics program and how it may evolve in the context of long-  
2 term planning studies [1]. The physics reach of this program is summarized under scenarios that are  
3 consistent with short-, medium- and long-term considerations. The general conclusions regarding  
4 the scientific capabilities of LBNE in a phased program are twofold:

- 5 1. A fully realized LBNE will provide an exciting broad-based physics program with excep-  
6 tional capabilities for all of the identified core physics objectives, and many additional ones.
- 7 2. A first phase with a LArTPC far detector of fiducial<sup>†</sup> mass 10 kt<sup>‡</sup> or greater will substantially  
8 advance the field of neutrino oscillation physics while laying the foundations for a broader  
9 physics program in a later phase.

10 Section [1.2](#) provides the context for development of LBNE as a phased program that maintains  
11 flexibility for enhancements in each of its stages through the contributions of additional partners.  
12 The physics reach of LBNE at various stages is summarized in Section [1.3](#).

---

<sup>†</sup>In neutrino experiments, not all neutrino interactions in the instrumented (active) volume of a detector are used for physics studies. Only interactions that are well contained within the instrumented volume are used. The smaller volume of detector that encompasses the neutrino interactions is known as the *fiducial volume* and the target mass contained within it is known as the *fiducial mass*. Unless otherwise noted, this document will use fiducial mass to characterize the far detector size.

<sup>‡</sup>The *kt* refers to a metric kiloton, equivalent to 1,000 kg.

## 1.2 Development of a World-Class Experiment

To achieve the transformative physics goals of LBNE in an era of highly constrained funding for basic research in the U.S., the conceptual design has evolved so as to provide a scalable, phased and global approach, while maintaining a U.S. leadership role as the host for a global facility. International partnerships are being actively pursued to both enhance and accelerate the project.

LBNE's primary beamline is designed to operate initially with a beam power of 1.2 MW, upgradeable to 2.3 MW. This beamline extracts protons with energies from 60 to 120 GeV from the Fermilab Main Injector. The protons collide with a target to generate a secondary beam of charged particles, which in turn decay to generate the neutrino beam.

The liquid argon TPC far detector technology combines fine-grained tracking with total absorption calorimetry. Installed 4,850 ft underground to minimize backgrounds, this detector will be a powerful tool for long-baseline neutrino oscillation physics and underground physics such as proton decay, supernova neutrinos and atmospheric neutrinos. The far detector design is scalable and flexible, allowing for a phased approach, with an initial fiducial mass of at least 10 kt and a final configuration of at least 34 kt.

A high-precision near detector is planned as a separate facility allowing maximal flexibility in phasing and deployment.

The concept of a high-intensity neutrino beam directed toward a distant, massive underground detector to simultaneously investigate the nature of the neutrino, proton decay and astrophysical sources of neutrinos has been under serious investigation since the late 1990s. Since that time both the science goals and concepts for implementation have been the subject of intense study and review by distinguished panels. These panels include the National Academies Neutrino Facilities Assessment Committee in 2003 [2], the National Science and Technology Council Committee on Science in 2004 [3], the National Academies EPP2010 panel in 2006 [4], the HEPAP/NSAC Neutrino Scientific Assessment Group in 2007 [5], the HEPAP Particle Physics Project Prioritization Panel (P5) in 2008 [6], the National Academies ad hoc Committee to Assess the Science Proposed for DUSEL in 2011 [7], and most recently the HEPAP Facilities Subpanel in 2013 [8]. High-level studies performed in Europe and Asia have come to similar conclusions (e.g., [9]) about the merits and feasibility of such a program.

### 1.2.1 Long-Term Vision

LBNE as described in this document has been developed by a collaboration formally established in 2009, which currently comprises over 475 collaborators from over 80 institutions in six countries. In January 2010 the DOE formally recognized the LBNE science objectives with approval of the mission need statement (CD-0) [10]. This action established LBNE as a DOE project. Fermilab has recognized LBNE as a central component of its long-term future program.

The central role of LBNE within the U.S. particle physics program has been acknowledged in other documents prepared for the 2013 particle physics community planning exercise [1], including the Project X Physics Book [11] and the reports from Intensity Frontier working groups on neutrino physics [12] and baryon number violation [13].

The LBNE conceptual design reflects a flexible and cost-effective approach to next-generation neutrino physics experiments that maintains a world-leadership role for the U.S. over the long term. The full-scope LBNE includes a 34-kt fiducial mass (50-kt total) far detector located in a new experimental area to be excavated at the 4,850-ft level of the Sanford Underground Research Facility<sup>§</sup> in the former Homestake Mine, and a fine-grained near neutrino detector located on the Fermilab site. Simultaneous construction of a new neutrino beamline at Fermilab would permit operation with an initial beam power of 1.2 MW, enabled by upgrades to the front end of the accelerator complex carried out within the Proton Improvement Plan-II (PIP-II) program [14]. In anticipation of potential enhancements beyond PIP-II [15], the beamline is designed to support upgrades to accommodate a beam power of 2.3 MW. The 1,300-km baseline is in the optimal range for the neutrino oscillation program. The cosmic ray shielding provided by the deep underground site for the far detector enables the non-accelerator portion of the physics program, including proton decay searches, detailed studies of neutrino bursts from galactic supernovae, and precision analyses of atmospheric neutrino samples.

The overall physics reach of LBNE is predominantly limited by detector mass. From the outset, a guiding principle of the far detector design has been scalability. The conceptual design for the full-scope detector, consisting of two identical 17-kt (25-kt total) TPC modules housed within separate vessels (cryostats), employs technology developed by the liquefied natural gas (LNG) storage and transport industry. The TPC modules themselves consist of arrays of modular anode and cathode plane assemblies (APAs and CPAs) that are suspended from rails affixed to the top of the cryostats. The APA/CPA dimensions are chosen for ease of transportation and installation. The modularity of the detectors allows flexibility in the geometry and phased construction of the LBNE far detector complex. Cost-effective designs for larger detector masses are readily obtained by increasing the vessel size and simply adding APA/CPA units, thereby also exploiting economies of scale and benefiting from an increased ratio of volume to surface area. Detector mass may also be increased through the addition of distinct detectors of the same or a different technology, either during initial

<sup>§</sup>Much larger detectors could also be accommodated at this facility.

1 construction or in a later phase.

## 2 1.2.2 Present Status of the LBNE Project

3 Since DOE CD-0 approval, a complete conceptual design for the full-scope LBNE has been de-  
4 veloped, consisting of a 34-kt LArTPC far detector located 4,850 feet underground, a 1,300-km  
5 baseline, a highly capable near neutrino detector, and a multi-megawatt-capable neutrino beamline.  
6 This design has been thoroughly reviewed, and found to be sound, most recently at a Fermilab Di-  
7 rector's CD-1 Readiness Review in March 2012 [16]. Since then, considerable effort has been  
8 devoted to understanding how the project can be staged so as to accommodate anticipated budget  
9 conditions while maintaining compelling physics output at each stage [17]. This process led to a  
10 *Phase 1* configuration that was reviewed by the DOE in October [18] and November [19] 2012, and  
11 that received CD-1 approval [20] in December 2012. This configuration [21,22,23,24,25,26] main-  
12 tained the most important aspects of LBNE: the 1,300-km baseline to the Sanford Underground  
13 Research Facility, a large — of order tens of kilotons in fiducial mass — LArTPC far detector  
14 design, and a multi-megawatt-capable, wide-band neutrino/antineutrino beam. However, the far  
15 detector size was limited at CD-1 to 10 kt and placed at the surface under minimal overburden, and  
16 the near detector was deferred to a later phase.

17 The DOE CD-1 approval document [20] explicitly allows adjustment of the LBNE Phase 1 scope  
18 in advance of CD-2 if additional partners bring significant contributions to LBNE. *Using the CD-*  
19 *1 DOE funding as the foundation, the goal for the first phase of LBNE is a deep underground*  
20 *far detector of at least 10 kt, placed in a cavern that will accommodate up to a 34-kt detector,*  
21 *coupled with a 1.2-MW neutrino beamline, and a highly capable near detector.* This goal has  
22 been endorsed by the LBNE Collaboration, the LBNE Project, the Fermilab directorate, and the  
23 DOE Office of High Energy Physics. Since a large portion of the LBNE project cost is in civil  
24 infrastructure, funding contributions from new partners could have considerable impact on the  
25 experimental facilities, and therefore the physics scope, in the first phase.

## 26 1.2.3 Global Partnerships

27 Global conditions are favorable for significant international partnerships in developing and build-  
28 ing LBNE. As an example, the 2013 update [9] of the European Strategy for Particle Physics doc-  
29 ument places long-baseline neutrino physics among the highest-priority large-scale activities for  
30 Europe, recognizing that it requires “significant resources, sizeable collaborations and sustained  
31 commitment.” It includes the primary recommendation of exploring “the possibility of major par-  
32 ticipation in leading long-baseline neutrino projects in the U.S. and Japan.” As of March 2014 the  
33 LBNE Collaboration includes institutions from the U.S., Brazil, India, Italy, Japan and the United  
34 Kingdom. Discussions with a number of potential international partners are underway — some al-  
35 ready at an advanced stage. A summary of recent progress in these discussions can be found in the

:global-partner

1 presentation of LBNE status to the U.S. Particle Physics Projects Prioritization Panel in November  
2 2013 [27].  
wilson-nov2013

### 3 **1.2.4 Context for Discussion of Physics Sensitivities**

4 To reflect the physics reach of various phasing scenarios, this document presents many of the  
5 parameter sensitivities for the accelerator-based neutrino topics as functions of exposure, defined  
6 as the product of detector fiducial mass, beam power and run time. As needed, the capabilities  
7 of both a 10-kt Phase 1 configuration and the full 34-kt configuration are explicitly highlighted,  
8 each benchmarked for six to ten years of operations with a 1.2-MW beam power from the PIP-  
9 II accelerator upgrades at Fermilab. Since the U.S. program planning exercises currently under  
10 way look beyond the present decade, this document also presents the long-term physics impact of  
11 the full-scope LBNE operating with the 2.3-MW beam power available with further anticipated  
12 upgrades to the Fermilab accelerator complex.

## 1.3 The LBNE Physics Program

exec-sum-physics

The technologies and configuration of the planned LBNE facilities offer excellent sensitivity to a range of physics processes:

- The muon-neutrino ( $\nu_\mu$ ) beam produced at Fermilab with a peak flux at 2.5 GeV, coupled to the baseline of 1,300 km, will present near-optimal sensitivity to neutrino/antineutrino charge-parity (CP) symmetry violation effects.
- The long baseline of LBNE will ensure a large matter-induced asymmetry in the oscillations of neutrinos and antineutrinos, thus providing a clear, unambiguous determination of the mass ordering of the neutrino states.
- The near detector located just downstream of the neutrino beamline at Fermilab will enable high-precision long-baseline oscillation measurements as well as precise measurements and searches for new phenomena on its own using the high-intensity neutrino beam.
- The deep-underground LArTPC far detector will provide superior sensitivities to proton decay modes with kaons in the final states, modes that are favored by many Grand Unified and supersymmetric theoretical models.
- Liquid argon as a target material will provide unique sensitivity to the electron-neutrino component of the initial burst of neutrinos from a core-collapse supernova.
- The excellent energy and directional resolution of the LArTPC will allow novel physics studies with atmospheric neutrinos.

2

3 This section summarizes LBNE's potential for achieving its core physics objectives based on  
4 the current experimental landscape, scenarios for staging LBNE, and the technical capabilities  
5 of LBNE at each stage.

6 LBNE's capability to achieve the physics objectives described in this document has been sub-  
7 ject to extensive review over a number of years. In addition to the various reviews of the LBNE  
8 Project described in Section 1.2, reviews that focused strongly on LBNE's science program in-  
9 clude the DOE Office of Science Independent Review of Options for Underground Science in the  
10 spring of 2011 [28], the LBNE Science Capabilities Review (by an external panel commissioned  
11 by LBNE) [29] in the fall of 2011, and the LBNE Reconfiguration Review [17] in the summer of  
12 2012.

### 1.3.1 Neutrino Mixing, Mass Hierarchy and CP Violation

**Neutrino Mass Hierarchy** The 1,300-km baseline establishes one of LBNE’s key strengths: sensitivity to the matter effect. This effect leads to a large discrete asymmetry in the  $\nu_\mu \rightarrow \nu_e$  versus  $\bar{\nu}_\mu \rightarrow \bar{\nu}_e$  oscillation probabilities, the sign of which depends on the mass hierarchy (MH). At 1,300 km this asymmetry is approximately  $\pm 40\%$  in the region of the peak flux; this is larger than the maximal possible CP-violating asymmetry associated with  $\delta_{\text{CP}}$ , meaning that both the MH and  $\delta_{\text{CP}}$  can be determined unambiguously with high confidence within the same experiment using the beam neutrinos.

In detail, the sensitivity of LBNE depends on the actual values of poorly known mixing parameters (mainly  $\delta_{\text{CP}}$  and  $\sin^2 \theta_{23}$ ), as well as the true value of the MH itself. The discrimination between the two MH hypotheses is characterized as a function of the *a priori* unknown true value of  $\delta_{\text{CP}}$  by considering the difference, denoted  $\Delta\chi^2$ , between the  $-2 \log \mathcal{L}$  values calculated for a dataset with respect to these hypotheses, considering all possible values of  $\delta_{\text{CP}}$ <sup>¶</sup>. In terms of this test statistic, the MH sensitivity of LBNE with 34 kt, and running three years each in  $\nu$  and  $\bar{\nu}$  modes in a 1.2-MW beam is illustrated in Figure 1.1 for the case of normal hierarchy for two different values of  $\sin^2 \theta_{23}$ . Across the overwhelming majority of the parameter space for the mixing parameters that are not well known (mainly  $\delta_{\text{CP}}$  and  $\sin^2 \theta_{23}$ ), LBNE’s determination of the MH will be definitive, but even for unfavorable combinations of the parameter values, a statistically ambiguous outcome is highly unlikely.

The least favorable scenario corresponds to a true value of  $\delta_{\text{CP}}$  in which the MH asymmetry is maximally offset by the leptonic CP asymmetry, and where, independently,  $\sin^2 \theta_{23}$  takes on a value at the low end of its experimentally allowed range. For this scenario, studies indicate that with a 34-kt LArTPC operating for six years in a 1.2-MW beam, LBNE on its own can (in a typical data set) distinguish between normal and inverted hierarchy with  $|\Delta\chi^2| = \overline{|\Delta\chi^2|} = 25$ . This corresponds to a  $\geq 99.9996\%$  probability of determining the correct hierarchy. In  $> 97.5\%$  of data sets, LBNE will measure  $|\Delta\chi^2| > 9$  in this scenario, where measuring  $|\Delta\chi^2| = 9$  with an expected value of 25 corresponds to a significance in excess of three Gaussian standard deviations.

Concurrent analysis of the corresponding atmospheric neutrino samples in an underground detector will improve the precision with which the MH is resolved. It is important to note that for the initial stages of LBNE, a greatly improved level of precision in the determination of the MH can be achieved by incorporating constraints from  $\text{NO}\nu\text{A}$  and T2K data. With an initial 10-kt detector, for half the range of possible  $\delta_{\text{CP}}$  values, the expected significance exceeds  $\overline{\Delta\chi^2} = 25$ ; again this corresponds to a  $\geq 99.9996\%$  probability of determining the correct hierarchy. To put this in context, it is notable that even an extended  $\text{NO}\nu\text{A}$  program [30] at four times its nominal exposure

<sup>¶</sup>For the case of the MH determination, the usual association of this test statistic with a  $\chi^2$  distribution for one degree of freedom is incorrect; additionally the assumption of a Gaussian probability density implicit in this notation is not exact. The discussion in Chapter 4 provides a brief description of the statistical considerations.

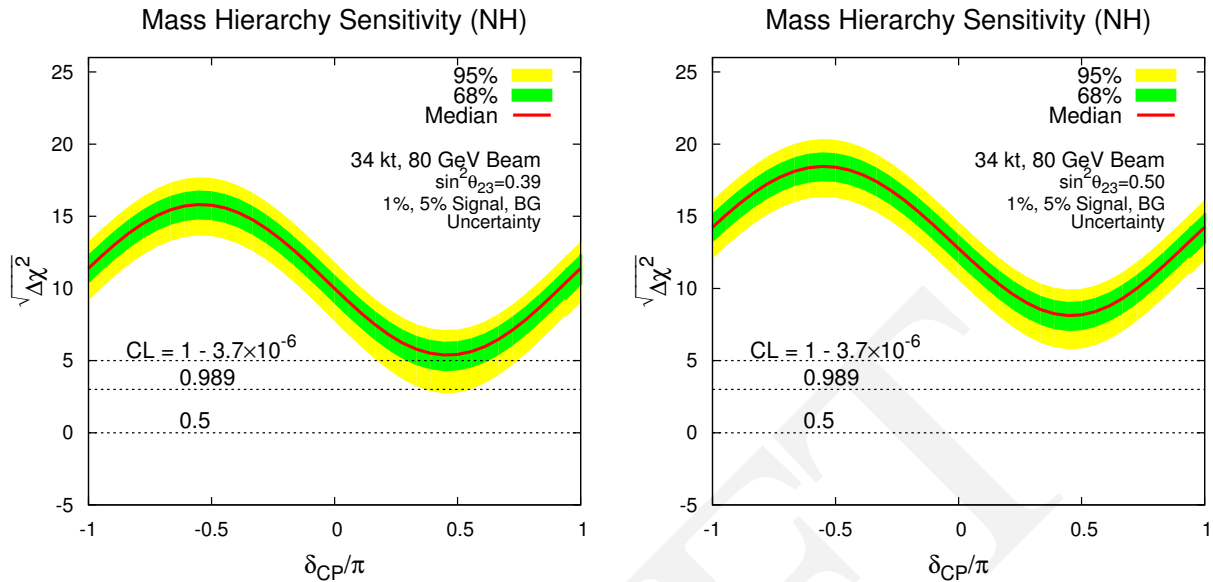


fig:mhexec

**Figure 1.1:** The square root of the mass hierarchy discrimination metric  $\Delta\chi^2$  is plotted as a function of the unknown value of  $\delta_{CP}$  for the full LBNE with 34 kt, 3+3 years of  $\nu + \bar{\nu}$  running in a 1.2-MW beam, assuming normal hierarchy. The plot on the left is for an assumed value of  $\sin^2 \theta_{23} = 0.39$  (based on global fits and assuming worst-case  $\theta_{23}$  octant), while that on the right is for  $\sin^2 \theta_{23} = 0.5$  (maximal mixing). In each plot, the red curve represents the median experimental value expected ( $\sqrt{\Delta\chi^2}$ ), estimated using a data set absent statistical fluctuations, while the green and yellow bands represent the range of  $\Delta\chi^2$  values expected in 68% and 95% of all possible experimental instances, respectively. For certain values of  $\sqrt{\Delta\chi^2}$ , horizontal lines are shown, indicating the corresponding confidence levels ( $1 - \alpha$  in the language of hypothesis testing) with which a typical experiment ( $\beta = 0.5$ ) correctly determines the MH, computed according to a Bayesian statistical formulation (see Section 4.3.1 for further discussion).

1 (of six years of operation at 700 kW), would have coverage at the  $\overline{\Delta\chi^2} = 9$  level or better for only  
 2 40% of the  $\delta_{CP}$  range.

3 **CP Violation and the Measurement of  $\delta_{CP}$**  The LBNE program has two somewhat distinct  
 4 objectives with regard to CP symmetry violation in the  $\nu_{\mu} \rightarrow \nu_e$  oscillation channel. First, LBNE  
 5 aims to make a precise determination of the value of  $\delta_{CP}$  within the context of the standard three-  
 6 flavor mixing scenario described by the PMNS matrix (discussed in Section 2.2). Second, and  
 7 perhaps more significantly, LBNE aims to observe a signal for leptonic CP violation, independent  
 8 of the underlying nature of neutrino oscillation phenomenology. Within the standard three-flavor  
 9 mixing scenario, such a signal will be observable, provided  $\delta_{CP}$  is not too close to either of the  
 10 values for which there is no CP violation (zero and  $\pi$ ). Together, the pursuit of these two goals  
 11 provides a thorough test of the standard three-flavor scenario.

12 Figure 1.2 shows the expected  $1\sigma$  resolution for  $\delta_{CP}$  as a function of exposure for a proton beam  
 13 power of 1.2 MW. At this beam power, in a six-year run, a 10-kt far detector will be able to measure  
 14  $\delta_{CP}$  to  $\pm 20^\circ - 30^\circ$  (depending on its value), independent of other experiments. A full-scope LBNE

- 1 operating with multi-megawatt beam power in a later phase, will achieve a precision better than  
 2  $\pm 10^\circ$ , comparable to the current precision on the CP phase in the CKM matrix in the quark sector.

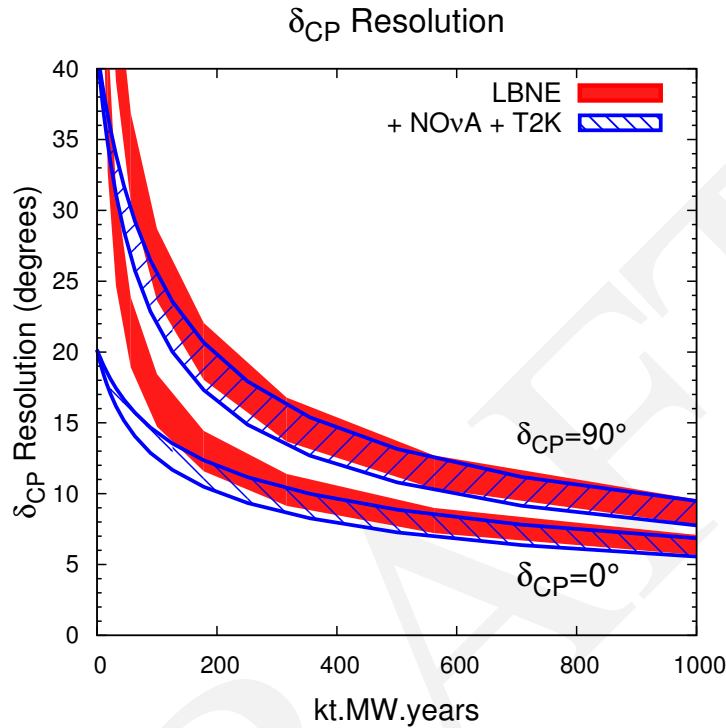


**Figure 1.2:** The expected  $1\sigma$  resolution for  $\delta_{CP}$  as a function of exposure in detector mass (kiloton)  $\times$  beam power (MW)  $\times$  time (years). The red curve is the precision that could be obtained from LBNE alone, while the blue curve represents the combined precision from LBNE plus the T2K and NO $\nu$ A experiments. The width of the bands represents variation with the range of beamline design parameters and proton energy values being considered.

- 3  
 4 LBNE with a 10-kt detector, in combination with T2K and NO $\nu$ A, will determine leptonic CP  
 5 violation with a precision of  $3\sigma$  or greater for  $\approx 40\%$  of  $\delta_{CP}$  values in a six-year run with 1.2 MW  
 6 beam power. It is important to note that LBNE alone dominates the combined sensitivity and that  
 7 T2K and NO $\nu$ A have very limited sensitivity to CP violation on their own. To reach  $5\sigma$  for an  
 8 appreciable fraction of the range of  $\delta_{CP}$ , the full-scope LBNE will be needed to control systematic  
 9 errors while accumulating large enough samples in the far detector to reach this level of sensitivity.  
 10 No experiment can provide coverage at 100%, since CP violation effects vanish as  $\delta_{CP} \rightarrow 0$  or  $\pi$ .

- 11 **Determination of  $\sin^2 2\theta_{23}$  and Octant Resolution** In long-baseline experiments with  $\nu_\mu$  beams,  
 12 the magnitude of  $\nu_\mu$  disappearance and  $\nu_e$  appearance signals is proportional to  $\sin^2 2\theta_{23}$  and  
 13  $\sin^2 \theta_{23}$ , respectively, in the standard three-flavor mixing scenario. Current  $\nu_\mu$  disappearance data  
 14 are consistent with maximal mixing,  $\theta_{23} = 45^\circ$ . To obtain the best sensitivity to both the magnitude  
 15 of its deviation from  $45^\circ$  as well as its sign ( $\theta_{23}$  octant), a combined analysis of the two channels is

needed [31]. As demonstrated in Chapter 4, a 10-kt LBNE detector will be able to resolve the  $\theta_{23}$  octant at the  $3\sigma$  level or better for  $\theta_{23}$  values less than  $40^\circ$  or greater than  $50^\circ$ , provided  $\delta_{\text{CP}}$  is not too close to zero or  $\pi$ . A full-scope LBNE will measure  $\theta_{23}$  with a precision of  $1^\circ$  or less, even for values within a few degrees of  $45^\circ$ .

### 1.3.2 Nucleon Decay Physics Motivated by Grand Unified Theories

The LBNE far detector will significantly extend lifetime sensitivity for specific nucleon decay modes by virtue of its high detection efficiency relative to water Cherenkov detectors and its low background rates. As an example, LBNE has enhanced capability for detecting the  $p \rightarrow K^+\bar{\nu}$  channel, where lifetime predictions from supersymmetric models extend beyond, but remain close to, the current (preliminary) Super-Kamiokande limit of  $\tau/B > 5.9 \times 10^{33}$  year (90% CL) from a 260-kt · year exposure [32]<sup>||</sup>. The signature for an isolated semi-monochromatic charged kaon in a LArTPC is distinctive, with multiple levels of redundancy. A 34-kt LBNE far detector deep underground will reach a limit of  $3 \times 10^{34}$  year after ten years of operation (see Figure 1.3), and would see nine events with a background of 0.3 should  $\tau/B$  be  $1 \times 10^{34}$  year, just beyond the current limit. Even a 10-kt detector (placed underground) would yield an intriguing signal of a few events after a 10-year exposure in this scenario.

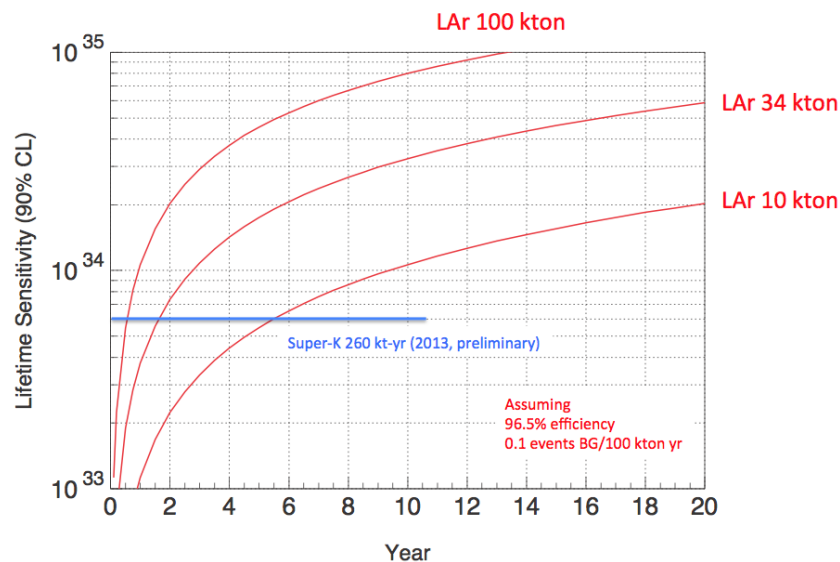
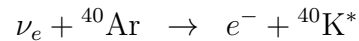


**Figure 1.3:** Sensitivity to the decay  $p \rightarrow K^+\bar{\nu}$  as a function of time for underground liquid argon detectors with different masses.

<sup>||</sup>The lifetime shown here is divided by the branching fraction for this decay mode,  $\tau/B$ , and as such is a *partial lifetime*.

### 1.3.3 Supernova-Neutrino Physics and Astrophysics

The neutrinos from a core-collapse supernova are emitted in a burst of a few tens of seconds duration, with about half in the first second. Energies are in the range of a few tens of MeV, and the luminosity is divided roughly equally between the three known neutrino flavors. Currently, experiments worldwide are sensitive primarily to electron antineutrinos ( $\bar{\nu}_e$ ), with detection through the inverse-beta decay process on free protons\*\*, which dominates the interaction rate in water and liquid-scintillator detectors. Liquid argon has a unique sensitivity to the electron-neutrino ( $\neq$ ) component of the flux, via the absorption interaction on  $^{40}\text{Ar}$  as follows:



This interaction can be tagged via the coincidence of the emitted electron and the accompanying photon cascade from the  ${}^{40}\text{K}^*$  de-excitation. About 900 events would be expected in a 10-kt fiducial mass liquid argon detector for a supernova at a distance of 10 kpc. In the neutrino channel the oscillation features are in general more pronounced, since the  $\nu_e$  spectrum is always significantly different from the  $\nu_\mu$  ( $\nu_\tau$ ) spectra in the initial core-collapse stages, to a larger degree than is the case for the corresponding  $\bar{\nu}_e$  spectrum. Detection of a large neutrino signal in LBNE would help provide critical information on key astrophysical phenomena such as

1. the neutronization burst
2. formation of a black hole
3. shock wave effects
4. shock instability oscillations
5. turbulence effects

### 1.3.4 Precision Measurements with a High-Intensity Neutrino Source and High-Resolution Near Detector

The near neutrino detector will provide precision measurements of neutrino interactions, which in the medium to long term are essential for controlling the systematic uncertainties in the long-baseline oscillation physics program. The near detector, which will include argon targets, will measure the absolute flux and energy-dependent shape of all four neutrino species,  $\nu_\mu$ ,  $\bar{\nu}_\mu$ ,  $\nu_e$  and  $\bar{\nu}_e$  to accurately predict for each species the far/near flux ratio as a function of energy. It will also measure the four-momenta of secondary hadrons, such as charged and neutral mesons, produced

\*\*This refers to neutrino interactions with the nucleus of a hydrogen atom in  $\text{H}_2\text{O}$  in water detectors or in hydrocarbon chains in liquid scintillator detectors.

1 in the neutral and charged current interactions that constitute the dominant backgrounds to the  
2 oscillation signals.

3 With 240,000 (85,000)  $\nu_\mu$  ( $\bar{\nu}_\mu$ ) charged current and 90,000 (35,000) neutral current interactions per  
4 ton per  $1 \times 10^{20}$  protons-on-target at 120 GeV in the  $\nu(\bar{\nu})$  beam, the near detector will also be the  
5 source of data for a rich program of neutrino interaction physics in its own right. These numbers  
6 correspond to  $10^7$  neutrino interactions per year for the range of beam configurations and near de-  
7 tector designs under consideration. Measurement of fluxes, cross sections and particle production  
8 over a large energy range of 0.5 GeV to 50 GeV (which can also help constrain backgrounds to pro-  
9 ton decay signals from atmospheric neutrinos) are the key elements of this program. Furthermore,  
10 since the near detector data will feature very large samples of events that are amenable to preci-  
11 sion reconstruction and analysis, they can be exploited for sensitive studies of electroweak physics  
12 and nucleon structure, as well as for searches for new physics in unexplored regions (heavy sterile  
13 neutrinos, high- $\Delta m^2$  oscillations, light Dark Matter particles, and so on).

## 14 1.4 Summary

The LBNE physics program has been identified as a priority of the global HEP community for the coming decades. The facilities available in the U.S. are the best suited internationally to carry out this program and the substantially developed LBNE design is at the forefront of technical innovations in the field. Timely implementation of LBNE will significantly advance the global HEP program and assure continued intellectual leadership for the U.S. within this community.

15  
16 This chapter has touched only briefly on the most prominent portion of the full suite of physics  
17 opportunities enabled by LBNE. The following chapters cover these in detail, as well as topics that  
18 were omitted here in the interest of brevity and focus. In Chapter 9 conclusion-chap progress toward LBNE physics  
19 milestones is addressed, based on one potential scenario for the operation of successive stages of  
20 LBNE detector and PIP-II implementations, and the broad role of LBNE is discussed in the context  
21 of such scenarios. The present chapter concludes with a summary of its key points.

22 The primary science goals of LBNE are drivers for the advancement of particle physics. The ques-  
23 tions being addressed are of wide-ranging consequence: the origin of flavor and the generation  
24 structure of the fermions (i.e., the existence of three families of quark and lepton flavors), the phys-  
25 ical mechanism that provides the CP violation needed to generate the Baryon Asymmetry of the  
26 Universe, and the high energy physics that would lead to the instability of matter. Achieving these  
27 goals requires a dedicated, ambitious and long-term program. No other proposed long-baseline  
28 neutrino oscillation program with the scientific scope and sensitivity of LBNE is as advanced in  
29 terms of engineering development and project planning. A phased program with a far detector of

1 even modest size in the initial stage (e.g., 10 kt) will enable exciting physics in the intermedi-  
2 ate term, including a definitive mass hierarchy determination and a measurement of the CP phase  
3 without ambiguities, while providing the fastest route toward achieving the full range of LBNE's  
4 science objectives. Should LBNE find that the CP phase is not zero or  $\pi$ , it will have found strong  
5 indications ( $> 3\sigma$ ) of leptonic CP violation. Global interest is favorable for contributions from  
6 international partners to accelerate and enhance this program, including the LBNE Phase 1 scope.

7 Implementing the vision that has brought LBNE to this point will allow the U.S. to host this world-  
8 leading program, bringing together the world's neutrino community to explore key questions at the  
9 forefront of particle physics and astrophysics. Moreover, the excitement generated by both the  
10 technical challenges of mounting LBNE and the potential physics payoffs are widely shared —  
11 among the generation of scientists who have been paving the way for these innovations, as well as  
12 the young scientists for whom LBNE will provide numerous research opportunities over the next  
13 two decades.

1

The Standard Model of particle physics describes all of the known fundamental particles and the electroweak and strong forces that, in combination with gravity, govern today's Universe. The observation that neutrinos have mass is one demonstration that the Standard Model is incomplete. By exploring physics beyond the Standard Model, LBNE will address fundamental questions about the Universe:

**What is the origin of the matter-antimatter asymmetry in the Universe?** Immediately after the Big Bang, matter and antimatter were created equally, yet matter now dominates. By studying the properties of neutrino and antineutrino oscillations, LBNE is pursuing the most promising avenue for understanding this asymmetry.

**What are the fundamental underlying symmetries of the Universe?** Resolution by LBNE of the detailed mixing patterns and ordering of neutrino mass states, and comparisons to the corresponding phenomena in the quark sector, could reveal underlying symmetries that are as yet unknown.

**Is there a Grand Unified Theory of the Universe?** Experimental evidence hints that the physical forces observed today were unified into one force at the birth of the Universe. Grand Unified Theories (GUTs), which attempt to describe the unification of forces, predict that protons should decay, a process that has never been observed. LBNE will probe proton lifetimes predicted by a wide range of GUT models.

**How do supernovae explode?** The heavy elements that are the key components of life — such as carbon — were created in the super-hot cores of collapsing stars. LBNE's design will enable it to detect the neutrino burst from core-collapse supernovae. By measuring the time structure and energy spectrum of a neutrino burst, LBNE will be able to elucidate critical information about the dynamics of this special astrophysical phenomenon.

**What more can LBNE discover about the Standard Model?** The high intensity of the LBNE neutrino beam will provide a unique probe for precision tests of Standard Model processes as well as searches for new physics in unexplored regions.

2

3 LBNE has been designed to address a wide range of scientific topics using well-characterized,  
4 high-intensity, accelerator-based neutrino beams, a long baseline for neutrino oscillations, and a  
5 very large, deep-underground detector with excellent particle identification capabilities over a large  
6 range of energies. While maximizing the reach for a core set of scientific objectives, its design —

described in Chapter 3 — accommodates the flexibility to extend the scope of measurements as additional resources become available.

## 2.1 Scientific Objectives of LBNE

The scientific objectives of LBNE have been categorized into primary, secondary, and additional secondary objectives according to priorities developed and agreed upon by the LBNE community and accepted as part of the CD-0 (Mission Need) approval by the U.S. Department of Energy [33].

**Primary objectives** of LBNE, in priority order, are the following measurements:

1. precision measurements of the parameters that govern  $\nu_\mu \rightarrow \nu_e$  oscillations; this includes precision measurement of the third mixing angle  $\theta_{13}$ , measurement of the charge-parity (CP) violating phase  $\delta_{\text{CP}}$ , and determination of the neutrino mass ordering (the sign of  $\Delta m_{31}^2 = m_3^2 - m_1^2$ ), the so-called *mass hierarchy*
2. precision measurements of the mixing angle  $\theta_{23}$ , including the determination of the octant in which this angle lies, and the value of the mass difference,  $|\Delta m_{32}^2|$ , in  $\nu_\mu \rightarrow \nu_{e,\mu}$  oscillations
3. search for proton decay, yielding significant improvement in the current limits on the partial lifetime of the proton ( $\tau/\text{BR}$ ) in one or more important candidate decay modes, e.g.,  $p \rightarrow K^+\bar{\nu}$
4. detection and measurement of the neutrino flux from a core-collapse supernova within our galaxy, should one occur during the lifetime of LBNE

In a phased approach to LBNE, the goal of the first phase is to maximize the effectiveness of the facility to achieve the first two objectives, above. The mass hierarchy determination and the precision determination of  $\theta_{23}$  will most likely be complete in the first phase of LBNE; while the precision determination of CP violation will require the full-scope LBNE, an initial measurement of the CP phase parameter  $\delta_{\text{CP}}$  will be performed in earlier phases.

**Secondary objectives**, which may also be enabled by the facility designed to achieve the primary objectives, include:

1. other accelerator-based, neutrino oscillation measurements; these could include further sensitivity to Beyond Standard Model (BSM) physics such as nonstandard interactions
2. measurements of neutrino oscillation phenomena using atmospheric neutrinos
3. measurement of other astrophysical phenomena using medium-energy neutrinos

1 **Additional secondary objectives**, the achievement of which may require upgrades to the facility  
2 that is designed to achieve the primary physics objectives (e.g., deployment of additional detector  
3 mass or alternate detector technologies), include:

- 4 1. detection and measurement of the diffuse supernova-neutrino flux
- 5 2. measurements of neutrino-oscillation phenomena and of solar physics using solar neutrinos
- 6 3. measurements of astrophysical and geophysical neutrinos of low energy

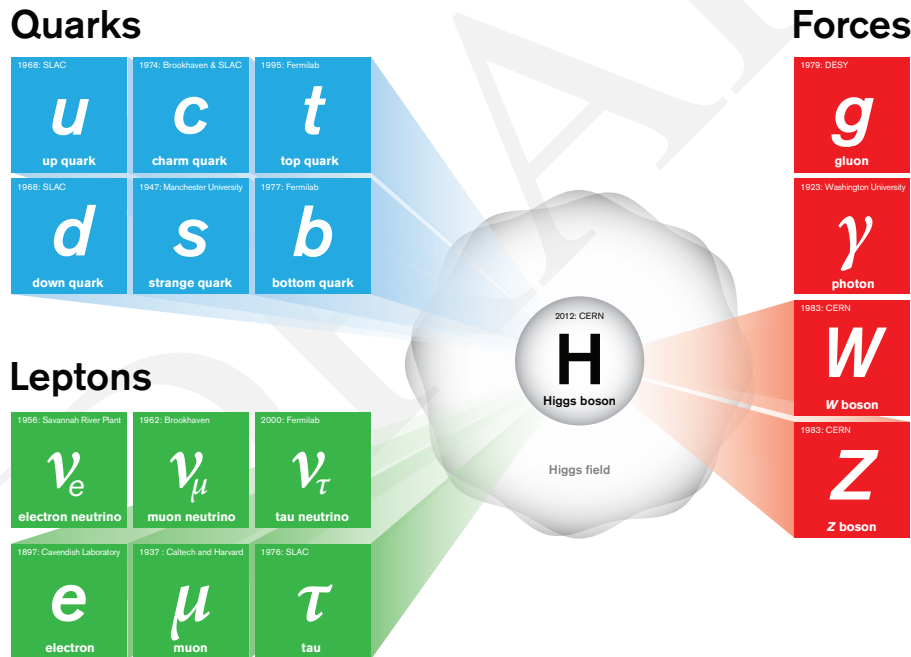
7 In addition, a rich set of science objectives enabled by a sophisticated near neutrino detector have  
8 been identified. A primary and a secondary objective, respectively, are:

- 9 1. measurements necessary to achieve the primary physics research objectives listed above
- 10 2. studies of neutrino interactions that may be enabled either by the facility designed to achieve  
11 the primary objectives or by future upgrades to the facility and detectors; these include pre-  
12 cision studies of the weak interaction, studies of nuclear and nucleon structure, and searches  
13 for new physics

## 2.2 Neutrino Three-Flavor Mixing, CP Violation and the Mass Hierarchy

scphysics

The Standard Model of particle physics (see Figure 2.1) presents a remarkably accurate description of the elementary particles and their interactions. However, its limitations beg deeper questions about Nature. The unexplained patterns of quarks, leptons, flavors and generations imply that a more fundamental underlying theory must exist. LBNE plans to pursue a detailed study of neutrino mixing, resolve the neutrino mass ordering, and search for CP violation in the lepton sector by studying the oscillation patterns of high-intensity  $\nu_\mu$  and  $\bar{\nu}_\mu$  beams measured over a long baseline.



standardmodel

**Figure 2.1:** Known particles and forces in the Standard Model of particle physics. There are three known neutrino mass states  $\nu_1, \nu_2, \nu_3$  which are mixtures of the three neutrino flavors  $\nu_e, \nu_\mu, \nu_\tau$  shown in this figure.

Results from the last decade, indicating that the three known types of neutrinos have nonzero mass, mix with one another and oscillate between generations, imply physics beyond the Standard Model [34]. Each of the three flavors of neutrinos,  $\nu_e, \nu_\mu$  and  $\nu_\tau$  (Figure 2.1), is known to be a different mix of three mass eigenstates  $\nu_1, \nu_2$  and  $\nu_3$  (Figure 2.2). In the Standard Model, the simple Higgs mechanism, which has now been confirmed by the observation of the Higgs boson [35,36], is responsible for both quark and lepton masses, mixing and charge-parity (CP) violation (the mechanism responsible for matter-antimatter asymmetries). However, the small size of neutrino masses and their relatively large mixing bears little resemblance to quark masses and mixing, suggesting that different physics — and possibly different mass scales — in the two sectors may be present, and motivating precision study of mixing and CP violation in the lepton sector.

1

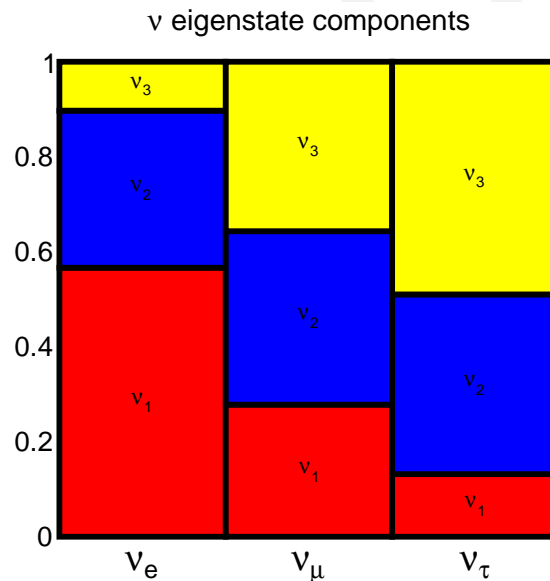


fig:pmns

**Figure 2.2:** The neutrino mass eigenstate components of the known flavor eigenstates.

Neutrino oscillation arises from mixing between the flavor and mass eigenstates of neutrinos, corresponding to the weak and gravitational interactions, respectively. This three-flavor-mixing scenario can be described by a rotation between the weak-interaction eigenstate basis  $(\nu_e, \nu_\mu, \nu_\tau)$  and the basis of states of definite mass  $(\nu_1, \nu_2, \nu_3)$ . In direct correspondence with mixing in the quark sector, the transformations between basis states is expressed in the form of a complex unitary matrix, known as the PMNS matrix :

$$\begin{pmatrix} \nu_e \\ \nu_\mu \\ \nu_\tau \end{pmatrix} = \underbrace{\begin{pmatrix} U_{e1} & U_{e2} & U_{e3} \\ U_{\mu1} & U_{\mu2} & U_{\mu3} \\ U_{\tau1} & U_{\tau2} & U_{\tau3} \end{pmatrix}}_{U_{\text{PMNS}}} \begin{pmatrix} \nu_1 \\ \nu_2 \\ \nu_3 \end{pmatrix}. \quad (2.1)$$

eqn:pmns0

The PMNS matrix in full generality depends on just three mixing angles and a CP-violating phase. The mixing angles and phase are designated as  $(\theta_{12}, \theta_{23}, \theta_{13})$  and  $\delta_{\text{CP}}$ . This matrix can be parameterized as the product of three two-flavor mixing matrices as follows, where  $c_{\alpha\beta} = \cos \theta_{\alpha\beta}$  and  $s_{\alpha\beta} = \sin \theta_{\alpha\beta}$ :

$$U_{\text{PMNS}} = \underbrace{\begin{pmatrix} 1 & 0 & 0 \\ 0 & c_{23} & s_{23} \\ 0 & -s_{23} & c_{23} \end{pmatrix}}_{\text{I}} \underbrace{\begin{pmatrix} c_{13} & 0 & e^{i\delta_{\text{CP}}} s_{13} \\ 0 & 1 & 0 \\ -e^{i\delta_{\text{CP}}} s_{13} & 0 & c_{13} \end{pmatrix}}_{\text{II}} \underbrace{\begin{pmatrix} c_{12} & s_{12} & 0 \\ -s_{12} & c_{12} & 0 \\ 0 & 0 & 1 \end{pmatrix}}_{\text{III}} \quad (2.2) \quad \text{eqn: pmns}$$

- 1 The parameters of the PMNS matrix determine the probability amplitudes of the neutrino oscillation phenomena that arise from mixing.
- 2

The relationship between the three mixing angles  $\theta_{12}$ ,  $\theta_{23}$ , and  $\theta_{13}$  and the mixing between the neutrino flavor and mass states can be described as follows [37]:

$$\tan^2 \theta_{12} : \frac{\text{amount of } \nu_e \text{ in } \nu_2}{\text{amount of } \nu_e \text{ in } \nu_1} \quad (2.3)$$

$$\tan^2 \theta_{23} : \text{ratio of } \nu_\mu \text{ to } \nu_\tau \text{ in } \nu_3 \quad (2.4)$$

$$\sin^2 \theta_{13} : \text{amount of } \nu_e \text{ in } \nu_3 \quad (2.5)$$

The frequency of neutrino oscillation among the weak-interaction (flavor) eigenstates depends on the difference in the squares of the neutrino masses,  $\Delta m_{ij}^2 \equiv m_i^2 - m_j^2$ ; a set of three neutrino mass states implies two independent mass-squared differences ( $\Delta m_{21}^2$  and  $\Delta m_{32}^2$ ). The ordering of the mass states is known as the *neutrino mass hierarchy*. An ordering of  $m_1 < m_2 < m_3$  is known as the *normal hierarchy* since it matches the ordering of the quarks in the Standard Model, whereas an ordering of  $m_3 < m_1 < m_2$  is referred to as the *inverted hierarchy*.

Since each flavor eigenstate is a mixture of three mass eigenstates, there can be an overall phase difference between the quantum states, referred to as  $\delta_{\text{CP}}$ . A nonzero value of this phase implies that neutrinos and antineutrinos oscillate differently — a phenomenon known as charge-parity (CP) violation.  $\delta_{\text{CP}}$  is therefore often referred to as the *CP phase* or the *CP-violating phase*.

- 3
- 4 The entire complement of neutrino experiments to date has measured five of the mixing parameters:
- 5 the three angles  $\theta_{12}$ ,  $\theta_{23}$  and (recently)  $\theta_{13}$ , and the two mass differences  $\Delta m_{21}^2$  and  $\Delta m_{32}^2$ . The sign
- 6 of  $\Delta m_{21}^2$  is known, but not that of  $\Delta m_{32}^2$ , which is the crux of the mass-hierarchy ambiguity. The
- 7 values of  $\theta_{12}$  and  $\theta_{23}$  are large, while  $\theta_{13}$  is smaller [38]. The value of  $\delta_{\text{CP}}$  is unknown. The real
- 8 values of the entries of the PMNS mixing matrix, which contains information on the strength of

1 flavor-changing weak decays in the lepton sector, can be expressed in approximate form as

$$|U_{\text{PMNS}}| \sim \begin{pmatrix} 0.8 & 0.5 & 0.2 \\ 0.5 & 0.6 & 0.6 \\ 0.2 & 0.6 & 0.8 \end{pmatrix}. \quad (2.6) \text{ eq: pmnsma}$$

2 The three-flavor-mixing scenario for neutrinos is now well established. However, the mixing pa-  
 3 rameters are not known to the same precision as are those in the corresponding quark sector, and  
 4 several important quantities, including the value of  $\delta_{\text{CP}}$  and the sign of the large mass splitting, are  
 5 still undetermined. In addition, several recent anomalous experimental results count among their  
 6 possible interpretations phenomena that do not fit this model [39,40,41,42].

The relationships between the values of the parameters in the neutrino and quark sectors suggest that mixing in the two sectors is qualitatively different. Illustrating this difference, the value of the entries of the CKM quark-mixing matrix (analogous to the PMNS matrix for neutrinos, and thus indicative of the strength of flavor-changing weak decays in the quark sector) can be expressed in approximate form as

$$|V_{\text{CKM}}| \sim \begin{pmatrix} 1 & 0.2 & 0.004 \\ 0.2 & 1 & 0.04 \\ 0.008 & 0.04 & 1 \end{pmatrix} \quad (2.7) \text{ eq: ckmmat}$$

7 and compared to the entries of the PMNS matrix given in Equation 2.6. As discussed in [43], the  
 8 question of why the quark mixing angles are smaller than the lepton mixing angles is an important  
 9 part of the “flavor problem.”

10 Quoting the discussion in [12], “while the CKM matrix is almost proportional to the identity matrix  
 11 plus hierarchically ordered off-diagonal elements, the PMNS matrix is far from diagonal and, with  
 12 the possible exception of the  $U_{e3}$  element, all elements are  $\mathcal{O}(1)$ .” One theoretical method often  
 13 used to address this question involves the use of non-Abelian discrete subgroups of  $SU(3)$  as flavor  
 14 symmetries; the popularity of this method comes partially from the fact that these symmetries can  
 15 give rise to the nearly *tri-bi-maximal*\* structure of the PMNS matrix. Whether employing these  
 16 flavor symmetries or other methods, any theoretical principle that attempts to describe the funda-  
 17 mental symmetries implied by the observed organization of quark and neutrino mixing — such as  
 18 those proposed in unification models — leads to testable predictions such as sum rules between  
 19 CKM and PMNS parameters [43,12,34,45]. Data on the patterns of neutrino mixing are already  
 20 proving crucial in the quest for a relationship between quarks and leptons and their seemingly ar-  
 21 bitrary generation structure. Table 2.1 displays the comparison between quark and lepton mixing

\*Tri-bi-maximal mixing refers to a form of the neutrino mixing matrix with effective bimaximal mixing of  $\nu_\mu$  and  $\nu_\tau$  at the atmospheric scale ( $L/E \sim 500 \text{ km/ GeV}$ ) and effective trimaximal mixing for  $\nu_e$  with  $\nu_\mu$  and  $\nu_\tau$  at the solar scale ( $L/E \sim 15,000 \text{ km/ GeV}$ ) [44].

- 1 in terms of the fundamental parameters and the precision to which they are known<sup>†</sup>, highlighting
- 2 the limited precision of the neutrino-mixing parameter measurements.

**Table 2.1:** Best-fit values of the neutrino mixing parameters in the PMNS matrix (assumes normal hierarchy) from [46], their  $1\sigma$  uncertainties and comparison to the analogous values in the CKM matrix [47].  $\Delta M^2$  is defined as  $m_3^2 - (m_1^2 + m_2^2)/2$ .

Parameter	Value (neutrino PMNS matrix)	Value (quark CKM matrix)
$\theta_{12}$	$34 \pm 1^\circ$	$13.04 \pm 0.05^\circ$
$\theta_{23}$	$38 \pm 1^\circ$	$2.38 \pm 0.06^\circ$
$\theta_{13}$	$8.9 \pm 0.5^\circ$	$0.201 \pm 0.011^\circ$
$\Delta m_{21}^2$	$+(7.54 \pm 0.22) \times 10^{-5} \text{ eV}^2$	
$ \Delta M^2 $	$(2.43_{-0.06}^{+0.10}) \times 10^{-3} \text{ eV}^2$	$m_3 \gg m_2$
$\delta_{\text{CP}}$	$-170 \pm 54^\circ$	$67 \pm 5^\circ$

- 3 Clearly much work remains in order to complete the standard three-flavor mixing picture, partic-
- 4 ularly with regard to  $\theta_{23}$  (is it less than, greater than, or equal to  $45^\circ$ ?), mass hierarchy (normal
- 5 or inverted?) and  $\delta_{\text{CP}}$ . Additionally, there is great value in obtaining a set of measurements for
- 6 multiple parameters *from a single experiment*, so that correlations and systematic uncertainties can
- 7 be handled properly. Such an experiment would also be well positioned to extensively test the
- 8 standard picture of three-flavor mixing. LBNE is designed to be this experiment.

### 9 2.2.1 CP Violation in the Quark and Lepton Sectors

In the parameterization of the PMNS matrix shown in Equation 2.2, the middle factor, labeled ‘II’, describes the mixing between the  $\nu_1$  and  $\nu_3$  mass states, and depends on the CP-violating phase  $\delta_{\text{CP}}$ . In the three-flavor model, the interference of contributions from terms in this factor containing  $\delta_{\text{CP}}$  causes oscillation effects with both CP-conserving (CP-even) and CP-violating (CP-odd) components. The presence of nonzero CP-odd terms (which requires  $\delta_{\text{CP}} \neq 0$  or  $\pi$ ) in the interference patterns would result in an asymmetry in neutrino versus antineutrino oscillations. The magnitude of the CP-violating terms in the oscillation depends most directly on the size of the Jarlskog Invariant [48], a function that was introduced to provide a measure of CP violation independent of mixing-matrix parameterization. In terms of the three mixing angles and the (as yet unmeasured) CP-violating phase, the Jarlskog Invariant is:

$$J_{\text{CP}}^{\text{PMNS}} \equiv \frac{1}{8} \sin 2\theta_{12} \sin 2\theta_{13} \sin 2\theta_{23} \cos \theta_{13} \sin \delta_{\text{CP}}. \quad (2.8)$$

- 10 The relatively large values of the mixing angles in the lepton sector imply that leptonic CP-
- 11 violation effects may be quite large — depending on the value of the phase  $\delta_{\text{CP}}$ , which is currently

<sup>†</sup>A global fit [46] to existing results from current experiments sensitive to neutrino oscillation effects is the source for the PMNS matrix values.

unknown. Experimentally, it is unconstrained at the  $2\sigma$  level by the global fit [46]. Many theoretical models, examples of which include [49,50,51,52,53,54], provide predictions for  $\delta_{CP}$ , but these predictions range over all possible values so do not yet provide any guidance.

Given the current best-fit values of the mixing angles [46] and assuming normal hierarchy,

$$J_{CP}^{\text{PMNS}} \approx 0.03 \sin \delta_{CP}. \quad (2.9)$$

This is in sharp contrast to the very small mixing in the quark sector, which leads to a very small value of the corresponding quark-sector Jarlskog Invariant [47],

$$J_{CP}^{\text{CKM}} \approx 3 \times 10^{-5}, \quad (2.10)$$

despite the large value of  $\delta_{CP}^{\text{CKM}} \approx 70^\circ$ .

To date, all observed CP-violating effects have occurred in experiments involving systems of quarks, in particular strange and  $b$ -mesons [47]. Furthermore, in spite of several decades of experimental searches for other sources of CP violation, all of these effects are explained by the CKM quark-mixing paradigm, and all are functions of the quark-sector CP-phase parameter,  $\delta_{CP}^{\text{CKM}}$ . In Cosmology, successful synthesis of the light elements after the Big Bang [55,56] (Big Bang Nucleosynthesis) requires that there be an imbalance in the number of baryons and antibaryons of at least one part in a billion when the Universe is a few minutes old [57]. CP violation in the quark sector has not, however, been able to explain the observed Baryon Asymmetry of the Universe (BAU), due to the small value of  $J_{CP}^{\text{CKM}}$ .

Baryogenesis [58] is a likely mechanism for generating the observed matter-antimatter asymmetry of our Universe. One way that it is elegantly achieved is by first having *leptogenesis* in the very early Universe. That mechanism can come about from the production and decay of very heavy right-handed neutrinos, if they are Majorana states (i.e. do not conserve lepton number), CP symmetry is violated in their decays (thus distinguishing particles and antiparticles) and the Universe is in non-equilibrium. Leptogenesis will lead to an early dominance of antileptons over leptons. When the cooling Universe reaches the electroweak phase transition,  $T \sim 250 \text{ GeV}$ , a baryon number excess is generated from the lepton asymmetry by a  $B - L$  ‡ conserving mechanism (analogous to proton decay in that it violates  $B$  and  $L$  separately but conserves  $B - L$ ) already present in the Standard Model.

The heavy Majorana right-handed neutrino states that could give rise to leptogenesis in the very early Universe are also a natural consequence of the GUT-based *seesaw* mechanism [59] — the simplest and most natural explanation of the observed super-light neutrino mass scales. The seesaw mechanism is a theoretical attempt to reconcile the very small masses of neutrinos to the much larger masses of the other elementary particles in the Standard Model. The seesaw mechanism achieves this unification by assuming an unknown new physics scale that connects the observed

‡  $B$  and  $L$  refer to Baryon and Lepton number respectively.

1 low-energy neutrino masses with a higher mass scale that involves very heavy sterile neutrino  
 2 states. The seesaw mechanism as generator of neutrino mass is in addition to the Higgs mechanism  
 3 that is now known to be responsible for the generation of the quark, charged lepton, and vector  
 4 boson masses.

5 The no-equilibrium leptogenesis ingredient is expected in a hot Big Bang scenario, but the Majorana  
 6 nature of the heavy neutrinos and needed CP violation can only be indirectly inferred from  
 7 light neutrino experiments by finding lepton number violation (validating their Majorana nature  
 8 via neutrinoless double beta decay) and observing CP violation in ordinary neutrino oscillations.  
 9

Recent theoretical advances have demonstrated that CP violation, necessary for the generation of the Baryon Asymmetry of the Universe at the GUT scale (baryogenesis), can be directly related to the low-energy CP violation in the lepton sector that could manifest in neutrino oscillations. As an example, the theoretical model described in [60] predicts that leptogenesis, the generation of the analogous lepton asymmetry, can be achieved if

$$|\sin \theta_{13} \sin \delta_{\text{CP}}| \gtrsim 0.11 \quad (2.11)$$

This implies  $|\sin \delta_{\text{CP}}| \gtrsim 0.7$  given the latest global fit value of  $|\sin \theta_{13}|$  [61].

10  
 11 The goal of establishing an experimental basis for assessing this possibility ranks very high on the  
 12 list of programmatic priorities within particle physics, and can be effectively addressed by LBNE.

### 13 2.2.2 Observation of CP-Violating Effects in Neutrino Oscillation Experiments

oscil-cpv  
 14 Whereas the Standard Model allows for violation of charge-parity (CP) symmetries in weak interactions,  
 15 CP transformations followed by time-reversal transformations (CPT) are invariant. Under  
 16 CPT invariance, the probabilities of neutrino oscillation and antineutrino oscillation are equivalent,  
 17 i.e.,  $P(\nu_l \rightarrow \nu_l) = P(\bar{\nu}_l \rightarrow \bar{\nu}_l)$  where  $l = e, \mu, \tau$ . Measurements of  $\nu_l \rightarrow \nu_l$  oscillations in which  
 18 the flavor of the neutrino before and after oscillations remains the same are referred to as *disappearance*  
 19 or *survival* measurements. CPT invariance in neutrino oscillations was recently tested  
 20 by measurements of  $\nu_\mu \rightarrow \nu_\mu$  and  $\bar{\nu}_\mu \rightarrow \bar{\nu}_\mu$  oscillations [62]; no evidence for CPT violation was  
 21 found. Therefore, asymmetries in neutrino versus antineutrino oscillations arising from CP violation  
 22 effects can only be accessed in *appearance* experiments, defined as oscillations of  $\nu_l \rightarrow \nu_{l'}$ , in  
 23 which the flavor of the neutrino after oscillations has changed. Because of the intrinsic challenges  
 24 of producing and detecting  $\nu_\tau$ 's, the oscillation modes  $\nu_{\mu,e} \rightarrow \nu_{e,\mu}$  provide the most promising  
 25 experimental signatures of leptonic CP violation.

For  $\nu_{\mu,e} \rightarrow \nu_{e,\mu}$  oscillations that occur as the neutrinos propagate through matter, as in terrestrial

long-baseline experiments, the coherent forward scattering of  $\nu_e$ 's on electrons in matter modifies the energy and path-length dependence of the vacuum oscillation probability in a way that depends on the magnitude *and* sign of  $\Delta m_{32}^2$ . This is the Mikheyev-Smirnov-Wolfenstein (MSW) effect [63,64] that has already been observed in solar neutrino oscillation (disappearance) experiments [65,66,67,68]. The oscillation probability of  $\nu_{\mu,e} \rightarrow \nu_{e,\mu}$  through matter, in a constant density approximation, keeping terms up to second order in  $\alpha \equiv |\Delta m_{21}^2|/|\Delta m_{31}^2|$  and  $\sin^2 \theta_{13}$ , is [69,47]:

$$P(\nu_{\mu} \rightarrow \nu_e) \cong P(\nu_e \rightarrow \nu_{\mu}) \cong P_0 + \underbrace{P_{\sin \delta}}_{\text{CP violating}} + P_{\cos \delta} + P_3 \quad (2.12)$$

1 where

$$P_0 = \sin^2 \theta_{23} \frac{\sin^2 2\theta_{13}}{(A-1)^2} \sin^2[(A-1)\Delta], \quad (2.13)$$

$$P_3 = \alpha^2 \cos^2 \theta_{23} \frac{\sin^2 2\theta_{12}}{A^2} \sin^2(A\Delta), \quad (2.14)$$

$$P_{\sin \delta} = \alpha \frac{8J_{cp}}{A(1-A)} \sin \Delta \sin(A\Delta) \sin[(1-A)\Delta], \quad (2.15)$$

$$P_{\cos \delta} = \alpha \frac{8J_{cp} \cot \delta_{CP}}{A(1-A)} \cos \Delta \sin(A\Delta) \sin[(1-A)\Delta], \quad (2.16)$$

and where

$$\Delta = \Delta m_{31}^2 L/4E, \text{ and } A = \sqrt{3}G_F N_e 2E/\Delta m_{31}^2.$$

2 In the above, the CP phase  $\delta_{CP}$  appears (via  $J_{cp}$ ) in the expressions for  $P_{\sin \delta}$  (the CP-odd term)  
3 which switches sign in going from  $\nu_{\mu} \rightarrow \nu_e$  to the  $\bar{\nu}_{\mu} \rightarrow \bar{\nu}_e$  channel, and  $P_{\cos \delta}$  (the CP-conserving  
4 term) which does not. The matter effect also introduces a neutrino/antineutrino asymmetry, the  
5 origin of which is simply the presence of electrons and absence of positrons in the Earth.

6 Recall that in Equation 2.2, the CP phase appears in the PMNS matrix through the mixing of  
7 the  $\nu_1$  and  $\nu_3$  mass states. The physical characteristics of an appearance experiment are therefore  
8 determined by the baseline and neutrino energy at which the mixing between the  $\nu_1$  and  $\nu_3$  states  
9 is maximal, as follows:

$$\frac{L(\text{km})}{E_{\nu}(\text{GeV})} = (2n-1) \frac{\pi}{2} \frac{1}{1.27 \times \Delta m_{31}^2 (\text{eV}^2)} \quad (2.17)$$

$$\approx (2n-1) \times 510 \text{ km/GeV} \quad (2.18)$$

10 where  $n = 1, 2, 3, \dots$  denotes the oscillation nodes at which the appearance probability is maximal.  
11 The dependences on  $E_{\nu}$  of the oscillation probability for the LBNE baseline of  $L = 1,300$  km are  
12 plotted on the right in Figures 2.3 and 2.4. The colored curves demonstrate the variation in the  $\nu_e$   
13 appearance probability as a function of  $E_{\nu}$ , for three different values of  $\delta_{CP}$ .

The variation in the  $\nu_{\mu} \rightarrow \nu_e$  oscillation probabilities with the value of  $\delta_{CP}$  indicates that it is experimentally possible to measure the value of  $\delta_{CP}$  at a fixed baseline using only the observed

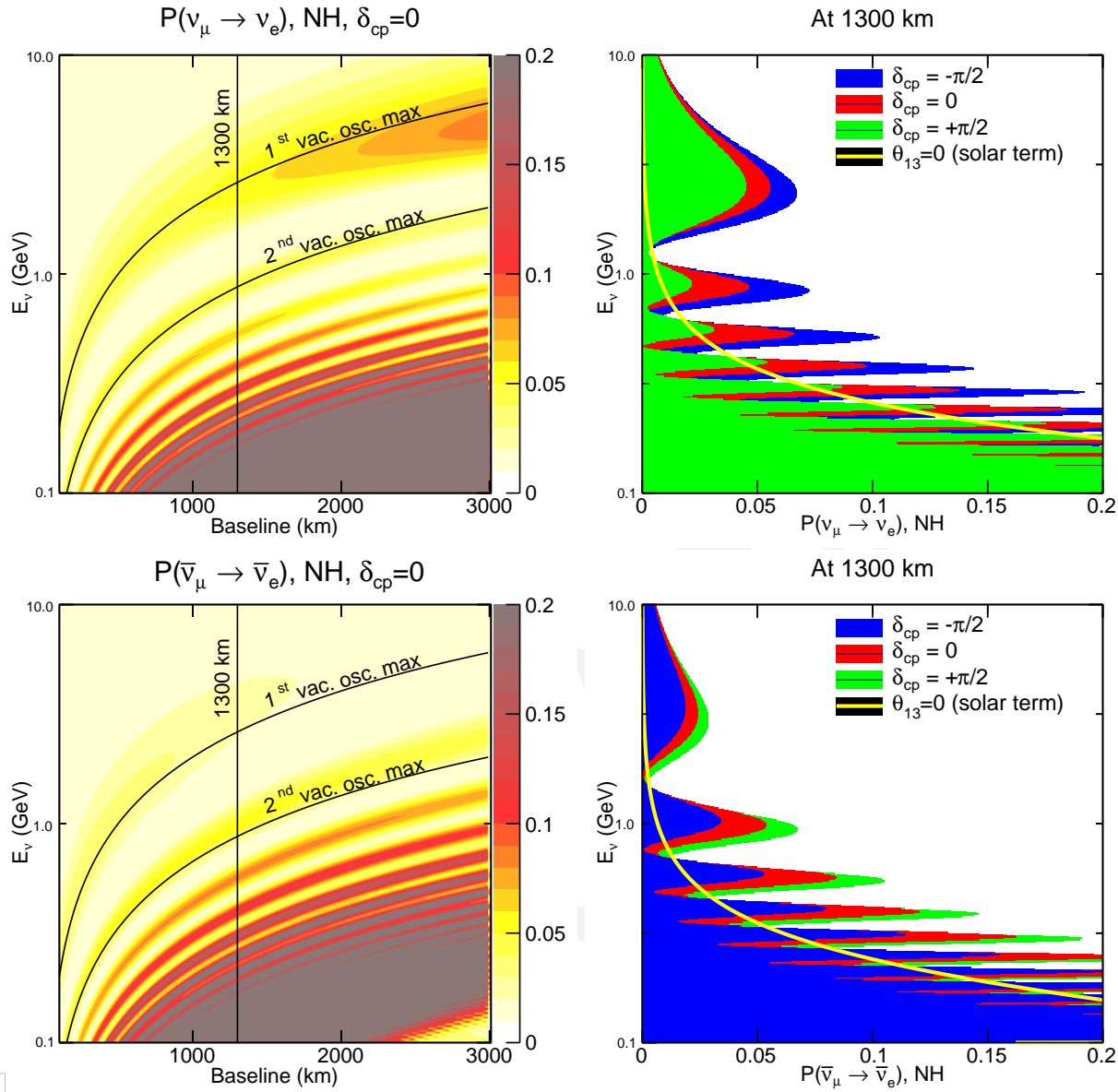


**Figure 2.3:** Neutrino oscillation probabilities as a function of energy and baseline, for different values of  $\delta_{CP}$ , *normal hierarchy*. The oscillograms on the left show the  $\nu_\mu \rightarrow \nu_e$  oscillation probabilities as a function of baseline and energy for *neutrinos* (top left) and *antineutrinos* (bottom left) with  $\delta_{CP} = 0$ . The figures on the right show the projection of the oscillation probability on the neutrino energy axis at a baseline of 1,300 km for  $\delta_{CP} = 0$  (red),  $\delta_{CP} = +\pi/2$  (green), and  $\delta_{CP} = -\pi/2$  (blue) for neutrinos (top right) and antineutrinos (bottom right). The yellow curve is the  $\nu_e$  appearance solely from the “solar term” due to  $\nu_1$  to  $\nu_2$  mixing as given by Equation 2.14.

shape of the  $\nu_\mu \rightarrow \nu_e$  or the  $\bar{\nu}_\mu \rightarrow \bar{\nu}_e$  appearance signal measured over an energy range that encompasses at least one full oscillation interval. A measurement of the value of  $\delta_{CP} \neq 0$  or  $\pi$ , assuming that neutrino mixing follows the three-flavor model, would imply CP violation. The CP

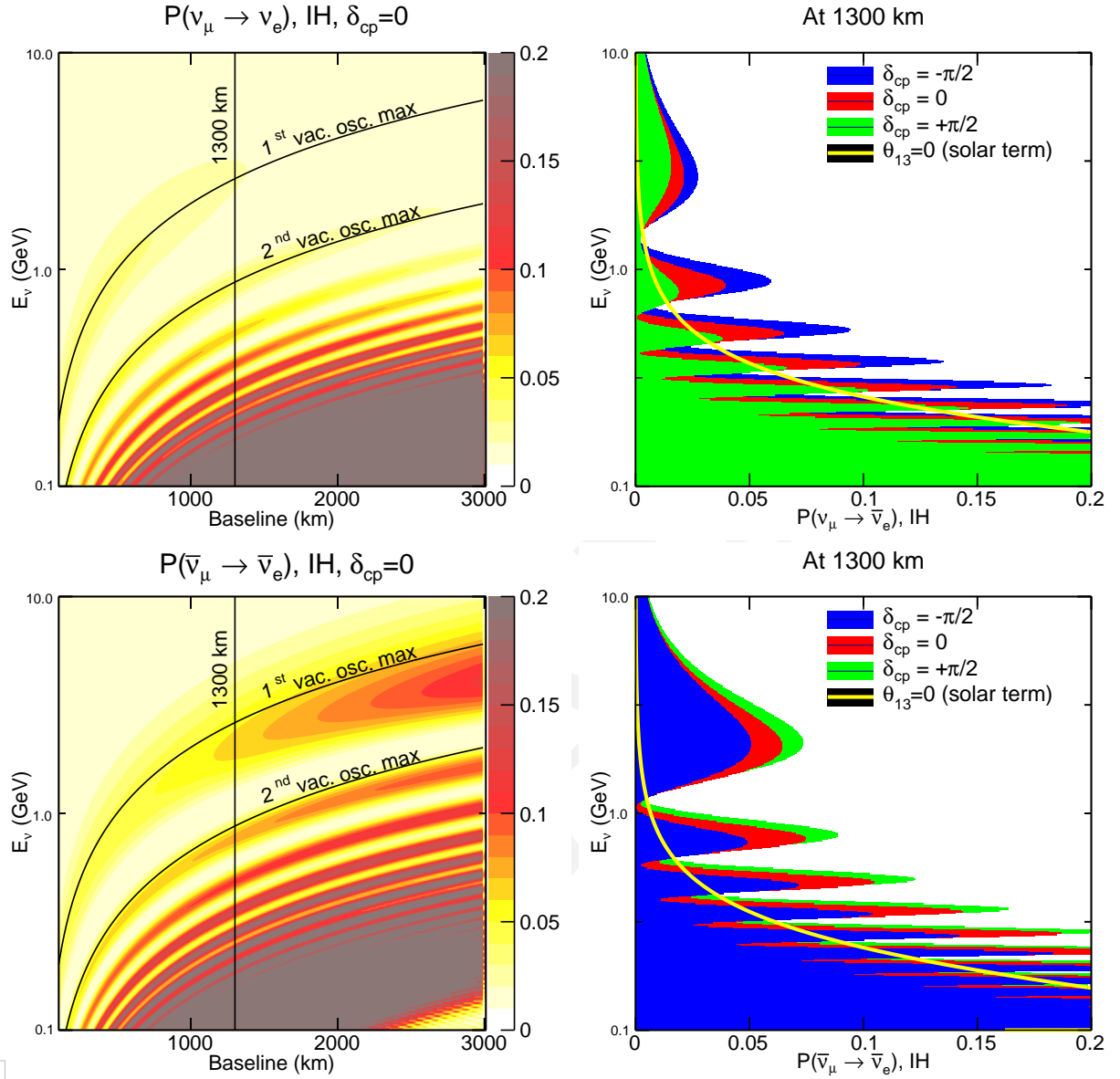


**Figure 2.4:** Neutrino oscillation probabilities as a function of energy and baseline, for different values of  $\delta_{CP}$ , *inverted hierarchy*. The oscillograms on the left show the  $\nu_\mu \rightarrow \nu_e$  oscillation probabilities as a function of baseline and energy for *neutrinos* (top left) and *antineutrinos* (bottom left) with  $\delta_{CP} = 0$ . The figures on the right show the projection of the oscillation probability on the neutrino energy axis at a baseline of 1,300 km for  $\delta_{CP} = 0$  (red),  $\delta_{CP} = +\pi/2$  (green), and  $\delta_{CP} = -\pi/2$  (blue) for neutrinos (top right) and antineutrinos (bottom right). The yellow curve is the  $\nu_e$  appearance solely from the “solar term” due to  $\nu_1$  to  $\nu_2$  mixing as given by Equation 2.14.

asymmetry,  $\mathcal{A}_{CP}$ , is defined as

$$\mathcal{A}_{CP} = \frac{P(\nu_\mu \rightarrow \nu_e) - P(\bar{\nu}_\mu \rightarrow \bar{\nu}_e)}{P(\nu_\mu \rightarrow \nu_e) + P(\bar{\nu}_\mu \rightarrow \bar{\nu}_e)}. \quad (2.19)$$

In the three-flavor model the asymmetry can be approximated to leading order in  $\Delta m_{21}^2$  as [70]:

$$\mathcal{A}_{CP} \sim \frac{\cos \theta_{23} \sin 2\theta_{12} \sin \delta_{CP}}{\sin \theta_{23} \sin \theta_{13}} \left( \frac{\Delta m_{21}^2 L}{4E_\nu} \right) + \text{matter effects} \quad (2.20)$$

Regardless of the value obtained for  $\delta_{CP}$ , it is clear that the explicit observation of an asymmetry between  $P(\nu_l \rightarrow \nu_{l'})$  and  $P(\bar{\nu}_l \rightarrow \bar{\nu}_{l'})$  is sought to directly demonstrate the leptonic CP violation effect that a value of  $\delta_{CP}$  different from zero or  $\pi$  implies. For long-baseline experiments such as LBNE, where the neutrino beam propagates through the Earth's mantle, the leptonic CP-violation effects must be disentangled from the matter effects.

### 2.2.3 Probing the Neutrino Mass Hierarchy via the Matter Effect

The asymmetry induced by matter effects as neutrinos pass through the Earth arises from the change in sign of the factors proportional to  $\Delta m_{31}^2$  (namely  $A$ ,  $\Delta$  and  $\alpha$ ; see Equations 2.12 to 2.16) in going from the normal to the inverted neutrino mass hierarchy. This sign change provides a means for determining the currently unknown mass hierarchy. The oscillation probabilities given in these approximate equations for  $\nu_\mu \rightarrow \nu_e$  as a function of baseline in kilometers and energy in GeV are calculated numerically with an exact formalism [71] and shown in the oscillograms of Figure 2.3 and 2.4 for  $\delta_{CP} = 0$ , for normal and inverted hierarchies, respectively. The oscillograms include the matter effect, assuming an Earth density and electron fraction described by [72]. These values are taken as a constant average over paths through regions of the Earth with continuous density change. Any baseline long enough to pass through a discontinuity is split into three or more segments each of constant average density and electron fraction. The solid black curves in the oscillograms indicate the location of the first and second oscillation maxima as given by Equation 2.18, assuming oscillations in a vacuum; matter effects will change the neutrino energy values at which the mixing between the  $\nu_1$  and  $\nu_3$  mass states is maximal.

The significant impact of the matter effect on the  $\nu_\mu \rightarrow \nu_e$  and  $\bar{\nu}_\mu \rightarrow \bar{\nu}_e$  oscillation probabilities at longer baselines (Figures 2.3 and 2.4) implies that  $\nu_e$  appearance measurements over long distances through the Earth provide a powerful probe into the neutrino mass-hierarchy question: is  $m_1 > m_3$  or vice-versa?

The dependence of the matter effect on the mass hierarchy is illustrated in the oscillograms plotted on the left hand side of Figures 2.3 and 2.4, and can be characterized as follows:

- For normal hierarchy,  $P(\nu_\mu \rightarrow \nu_e)$  is enhanced and  $P(\bar{\nu}_\mu \rightarrow \bar{\nu}_e)$  is suppressed. The effect increases with baseline at a fixed  $L/E$ .
- For inverted hierarchy,  $P(\nu_\mu \rightarrow \nu_e)$  is suppressed and  $P(\bar{\nu}_\mu \rightarrow \bar{\nu}_e)$  is enhanced. The effect increases with baseline at a fixed  $L/E$ .

- 1     o The matter effect has the largest impact on the probability amplitude at the first oscillation
- 2        maximum.
- 3     o The matter effect introduces a phase shift in the oscillation pattern, shifting it to a lower
- 4        energy for a given baseline when the hierarchy changes from normal to inverted. The shift is
- 5        approximately  $-100$  MeV.

#### 6   2.2.4   Disentangling CP-Violating and Matter Effects

7   In Figure [fig:oscnodes2](#), the asymmetries induced by matter and maximal CP violation (at  $\delta_{\text{CP}} = \pm\pi/2$ ) are  
8   shown separately as 2D oscillograms in baseline and neutrino energy. The matter effect induces an  
9   asymmetry in  $P(\nu_l \rightarrow \nu_l')$  and  $P(\bar{\nu}_l \rightarrow \bar{\nu}_l')$  that adds to the CP asymmetry. At longer baselines  
10  ( $> 1000$  km), the matter asymmetry in the energy region of the first oscillation node is driven  
11  primarily by the change in the  $\nu_e$  appearance amplitude. At shorter baselines ( $\mathcal{O}(100$  km)) the  
12  asymmetry is driven by the phase shift. In general:

$$\mathcal{A}_{\text{cp}} \propto L/E, \quad (2.21)$$

$$\mathcal{A}_{\text{matter}} \propto L \times E. \quad (2.22)$$

13  The phenomenology of  $\nu_\mu \rightarrow \nu_e$  oscillations described in Section 2.2.2 implies that the experimen-  
14  tal sensitivity to CP violation and the mass hierarchy from measurements of the total asymmetry  
15  between  $P(\nu_l \rightarrow \nu_l')$  and  $P(\bar{\nu}_l \rightarrow \bar{\nu}_l')$  requires the disambiguation of the asymmetry induced  
16  by the matter effect and that induced by CP violation. This is particularly true for experiments  
17  designed to access mixing between the  $\nu_1$  and  $\nu_3$  mass states using neutrino beams of  $\mathcal{O}(1$  GeV).  
18  Such beams require baselines of at least several hundred kilometers, at which the matter asymme-  
19  tries are significant. The currently known values of the oscillation parameters permit calculation  
20  of the magnitude of the matter asymmetry within an uncertainty of  $< 10\%$ ; only the sign of the  
21  asymmetry, which depends on the sign of  $\Delta m_{31}^2$ , is unknown. Since the magnitude of the mat-  
22  ter asymmetry is known, baselines at which the size of the matter asymmetry exceeds that of the  
23  maximal possible CP asymmetry are required in order to separate the two effects.

24  Figure [fig:oscnodes4](#) illustrates the ambiguities that can arise from the interference of the matter and CP  
25  asymmetries. The plots show the total asymmetry as a function of  $\delta_{\text{CP}}$  at four baseline values  
26  (clockwise from top left): 290 km, 810 km, 2,300 km and 1,300 km. The curves in black and red  
27  illustrate the asymmetries at the first and second oscillation nodes, respectively. The solid lines  
28  represent normal hierarchy, and the dashed lines represent inverted hierarchy. The plots demon-  
29  strate that experimental measurements of the asymmetry (Equation 2.19) [eqn:cp-asymm](#) at the first oscillation  
30  node could yield ambiguous results for short baselines if the hierarchy is unknown. This occurs in  
31  regions of the  $(L, E, \delta_{\text{CP}})$  phase space where the matter and CP asymmetries cancel partially or  
32  totally. For example, the green lines in Figure 2.6 [fig:oscnodes4](#) indicate the asymmetry at the first node for max-  
33  imal CP violation ( $\delta_{\text{CP}} = \pi/2$ ) with an inverted hierarchy. At a baseline of 290 km, the measured

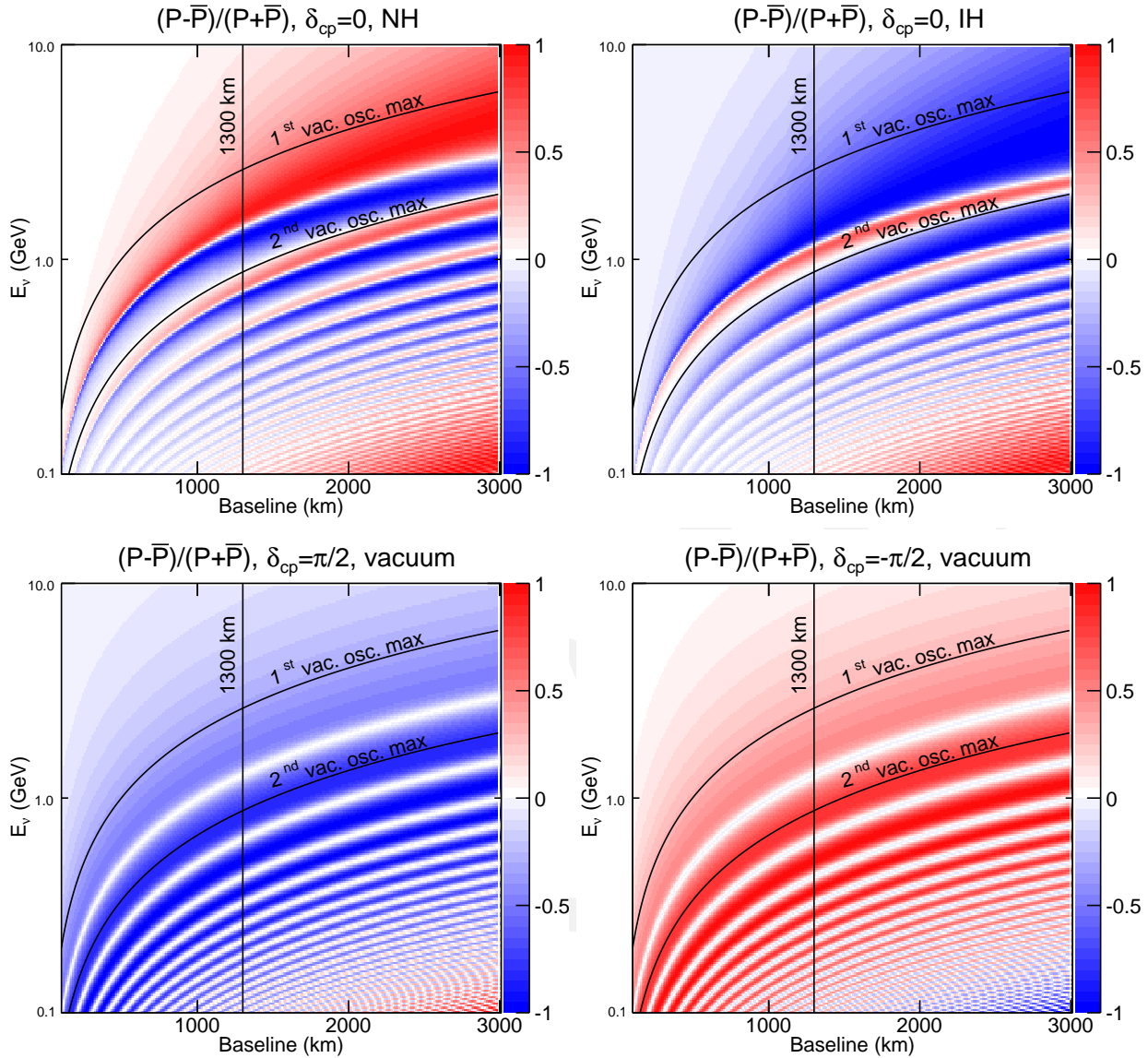


**Figure 2.5:** The  $\nu\mu/\bar{\nu}$  oscillation probability asymmetries as a function of baseline. The top two figures show the asymmetry induced by the matter effect only for normal (top left) and inverted (top right) hierarchies. The bottom figures show the asymmetry induced through the CP-violating phase  $\delta_{CP}$  in vacuum, for  $\delta_{CP} = +\pi/2$  (bottom left) and  $\delta_{CP} = -\pi/2$  (bottom right)

- 1 asymmetry at  $\delta_{CP} = \pi/2$  (inverted hierarchy) is degenerate with that at  $\delta_{CP} \sim 0$  (normal hierar-
- 2 chy) at the first node. Measurements of the asymmetry at different  $L/E$  or at different baselines can
- 3 break the degeneracies (Equation 2.22). At very long baselines, for which the matter asymmetry
- 4 exceeds the maximal CP asymmetry at the first oscillation node, there are no degeneracies and the
- 5 mass hierarchy and CP asymmetries can be resolved within the same experiment. For the current
- 6 best-fit values of the oscillation parameters, the matter asymmetry exceeds the maximal possible
- 7 CP asymmetry at baselines of  $\geq 1,200$  km.

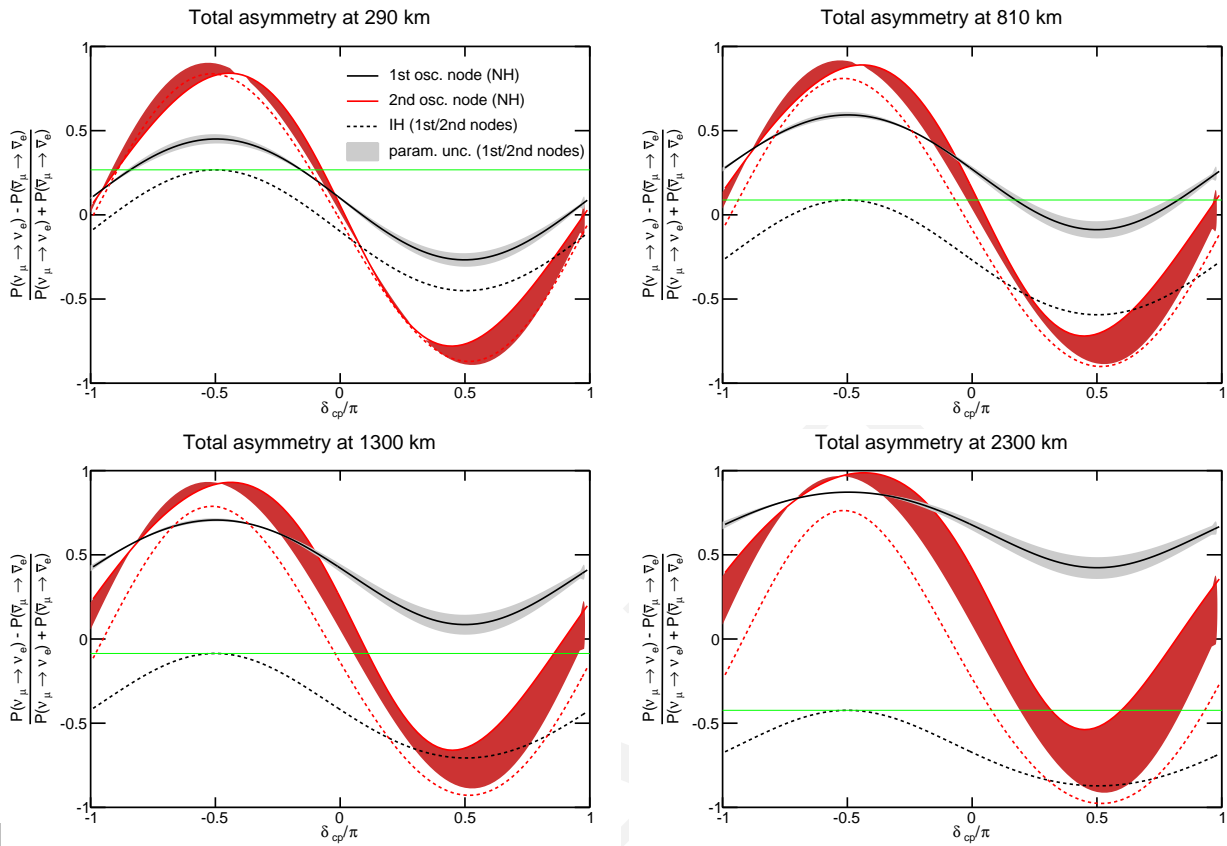


**Figure 2.6:** The  $\nu\mu/\bar{\nu}$  oscillation probability asymmetries versus  $\delta_{\text{CP}}$  at the first two oscillation nodes. Clockwise from top left: 290 km, 810 km, 2,300 km and 1,300 km. The solid/dashed black line is the total asymmetry at the first oscillation node for normal/inverted hierarchy. The red lines indicate the asymmetries at the second node.

### 1 2.2.5 Optimization of the Oscillation Baseline for CPV and Mass Hierarchy

2 The simple arguments above suggest that a baseline  $\geq 1,200$  km is required to search for CP viola-  
3 tion and determine the mass hierarchy simultaneously in a single long-baseline neutrino oscilla-  
4 tion experiment. To understand the performance of a long-baseline experiment as a function of baseline  
5 using realistic neutrino beamline designs, a study of the sensitivities to CP violation and the mass  
6 hierarchy as a function of baseline was carried out using a neutrino beamline design optimized  
7 individually for each baseline. A 34-kt LArTPC neutrino detector at the far site was assumed since  
8 it has a high  $\nu_e$ -identification efficiency that is flat over a large range of energies (see Chapter 4).  
9 The beamline design was based on the NuMI beamline utilizing the 120-GeV, 1.2-MW proton  
10 beam from the Fermilab Main Injector and was fully simulated using GEANT3 [73]. Varying the  
11 distance between the target and the first horn allowed selection of a beam spectrum that covered  
12 the first oscillation node and part of the second. The design incorporated an evacuated decay pipe  
13 of 4-m diameter and a length that varied from 280 to 580 m. For baselines less than 1,000 m, the  
14 oscillation occurs at neutrino energies where on-axis beams produce too little flux. Therefore, off-

- 1 axis beams — which produce narrow-band, low-energy neutrino fluxes — were simulated for these  
 2 baselines, with the off-axis angle chosen to provide the most coverage of the first oscillation node.  
 3 The results of this study are summarized in Figure 2.7. The sensitivity to CP violation (bottom plot)  
 4 assumes that the mass hierarchy is unknown. An updated study with more detail is available [74].  
 The baseline study indicates that with realistic experimental conditions, baselines between 1,000

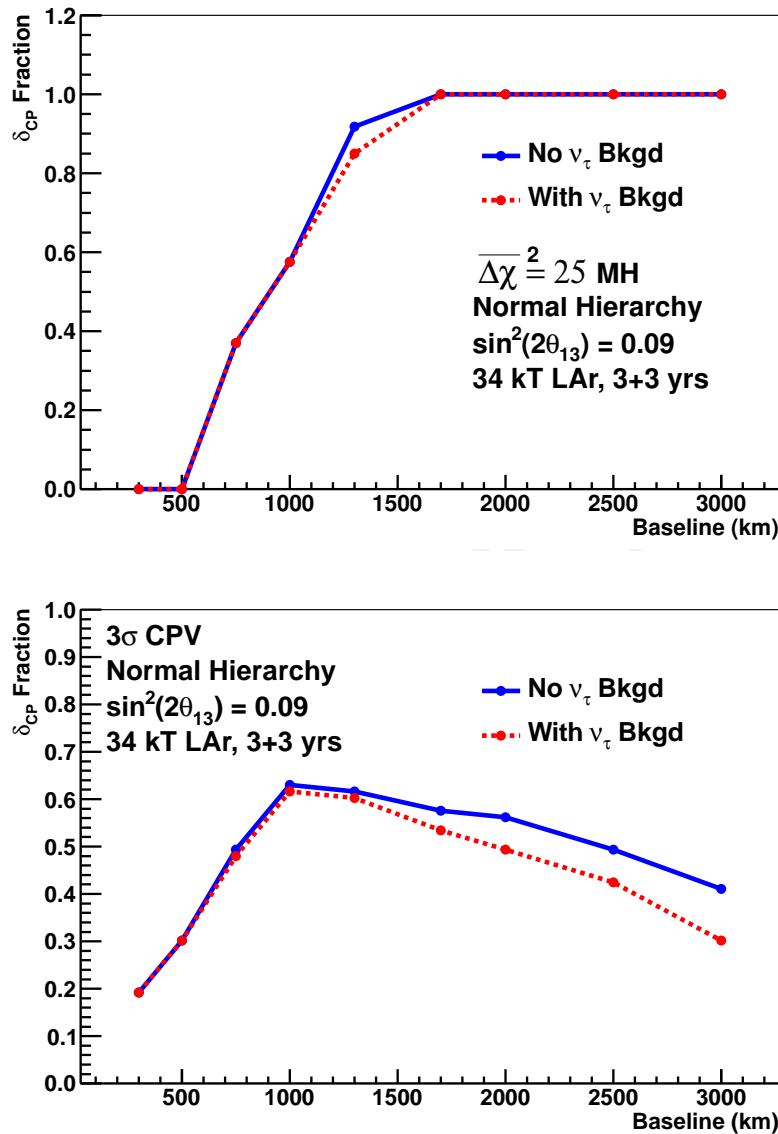


**Figure 2.7:** The fraction of  $\delta_{CP}$  values for which the mass hierarchy can be determined with an average  $|\Delta\chi^2| = 25$  or greater as a function of baseline (top) and the fraction of  $\delta_{CP}$  values which CP violation can be determined at the  $3\sigma$  level or greater as a function of baseline (bottom). A NuMI based beam design with a 120-GeV beam was optimized for each baseline. Projections assume  $\sin^2 2\theta_{13} = 0.09$  and a 34-kt LArTPC as the far detector [75]. An exposure of 3yrs+3yrs of neutrino+antineutrino running with 1.2-MW beam power is assumed.

and 1,300 km are near optimal for determination of CP violation. With baselines  $> 1,500$  km, the correct mass hierarchy could be determined with a probability greater than 99% for all values of  $\delta_{\text{CP}}$  with a large LArTPC far detector. However, at very long baselines, in one of the neutrino beam polarities ( $\nu/\bar{\nu}$  for inverted/normal hierarchy) the event rate suppression due to the beam's traversal through matter becomes very large, making it difficult to observe an explicit CP-violation asymmetry.

### 2.2.6 Physics from Precision Measurements of Neutrino Mixing

Precision measurements of the neutrino mixing parameters in long-baseline oscillations not only reveal the neutrino mixing patterns in greater detail, but also serve as probes of new physics that manifests as perturbations in the oscillation patterns driven by three-flavor mixing.

The determination of whether there is maximal mixing between  $\nu_\mu$  and  $\nu_\tau$  — or a measurement of the deviation from maximal — is of great interest theoretically [76,77,78,51,79,80]. Models of quark-lepton universality propose that the quark and lepton mixing matrices (Equations 2.7 and 2.6, respectively) are given by

$$U^{\text{CKM}} = 1 + \epsilon_{\text{Cabbibo}} \text{ and} \quad (2.23)$$

$$U^{\text{PMNS}} = T + \epsilon_{\text{Cabbibo}}, \quad (2.24)$$

where  $T$  is determined by Majorana physics [81] and  $\epsilon_{\text{Cabbibo}}$  refers to small terms driven by the Cabbibo weak mixing angle ( $\theta_C = \theta_{12}^{\text{CKM}}$ ). In such models  $\theta_{23} \sim \pi/4 + \Delta\theta$ , where  $\Delta\theta$  is of order the Cabbibo angle,  $\theta_C$ , and  $\theta_{13} \sim \theta_C/\sqrt{2}$ . It is therefore important to determine experimentally both the value of  $\sin^2 \theta_{23}$  and the octant of  $\theta_{23}$  if  $\theta_{23} \neq 45^\circ$ .

Studying  $\nu_\mu$  disappearance probes  $\sin^2 2\theta_{23}$  and  $|\Delta m_{32}^2|$  with very high precision. Disappearance measurements can therefore determine whether  $\nu_\mu$ - $\nu_\tau$  mixing is maximal or near maximal such that  $\sin^2 2\theta_{23} = 1$ , but they cannot resolve the octant of  $\theta_{23}$  if  $\nu_\mu$ - $\nu_\tau$  mixing is less than maximal. Combining the  $\nu_\mu$  disappearance signal with the  $\nu_e$  appearance signal can help determine the  $\theta_{23}$  octant and constrain some of the theoretical models of quark-lepton universality.

Direct unitarity tests, in which the individual components of the PMNS matrix are measured separately, are challenging due to limited experimentally available oscillation channels [82,83]. Application of the “proof by contradiction” principle offers another way to perform the unitarity tests. In these tests, the mixing angles are extracted from the data by assuming unitarity in the standard three-flavor framework. If measurements of the same mixing angle by two different processes are inconsistent, then the standard three-flavor framework is insufficient and new physics beyond this

framework is required. Observation of unitarity violation will constrain the phase space of possible new physics. In particular, the precision measurement of  $\sin^2 2\theta_{13}$  provides the most promising unitarity test [83] for the PMNS matrix. It is important to note that several theoretical models of new physics, such as the existence of sterile neutrinos or nonstandard interactions, could lead to apparent deviations of the  $\sin^2 2\theta_{13}$  value measured in  $\nu_e$  appearance experiments from that measured in reactor ( $\bar{\nu}_e$  disappearance) experiments.

Precision measurements of  $\nu_\mu$  and  $\bar{\nu}_\mu$  survival over long baselines could reveal nonstandard physics driven by new interactions in matter. Examples of some of these effects and the experimental signatures in long-baseline oscillations are discussed in Chapter 4.

In addition, experiments with long enough baselines and sufficient neutrino flux at  $E_\nu > 3$  GeV, coupled with high-resolution tracking detectors, as in the LBNE design, can also probe  $\nu_\mu \rightarrow \nu_\tau$  appearance with higher precision than is currently possible using  $\nu_\tau$  charged-current interactions. The combination of  $\nu_\mu \rightarrow \nu_\mu$ ,  $\nu_\mu \rightarrow \nu_e$ , and  $\nu_\mu \rightarrow \nu_\tau$  can ultimately over-constrain the three-flavor model of neutrino oscillations both in neutrino and antineutrino modes.

## 2.2.7 Oscillation Physics with Atmospheric Neutrinos

Atmospheric neutrinos are unique among sources used to study oscillations; the flux contains neutrinos and antineutrinos of all flavors, matter effects play a significant role, both  $\Delta m^2$  values contribute to the oscillation patterns, and the oscillation phenomenology occurs over several orders of magnitude in both energy (see Figure 2.8) and path length. These characteristics make atmospheric neutrinos ideal for the study of oscillations and provide a laboratory suitable to search for exotic phenomena for which the dependence of the flavor-transition and survival probabilities on energy and path length can be defined. The probabilities of atmospheric  $\nu_\mu \rightarrow \nu_e$  and  $\bar{\nu}_\mu \rightarrow \bar{\nu}_e$  oscillations

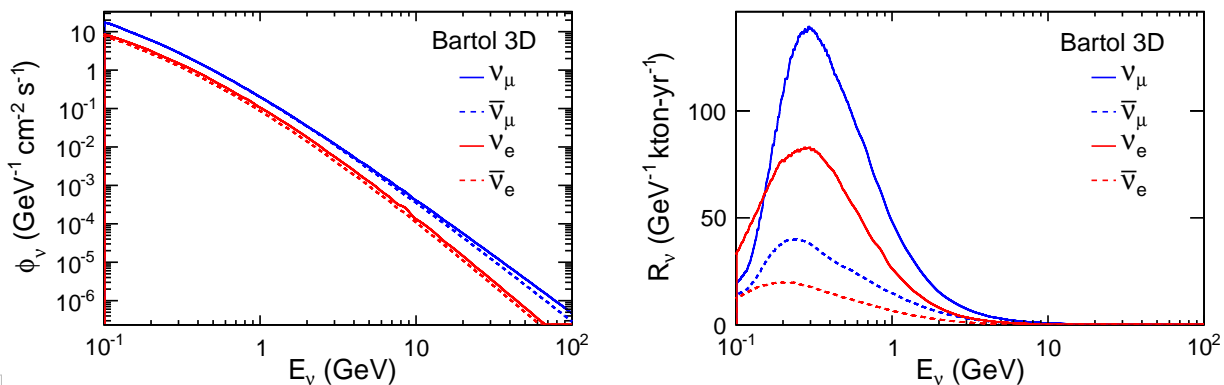


**Figure 2.8:** The atmospheric neutrino flux in neutrinos per second per square centimeter as a function of neutrino energy for different flavors (left). The atmospheric neutrino spectrum per GeV per kt per year for the different species (right).

for normal and inverted hierarchies are shown as a function of zenith angle in Figure 2.9.

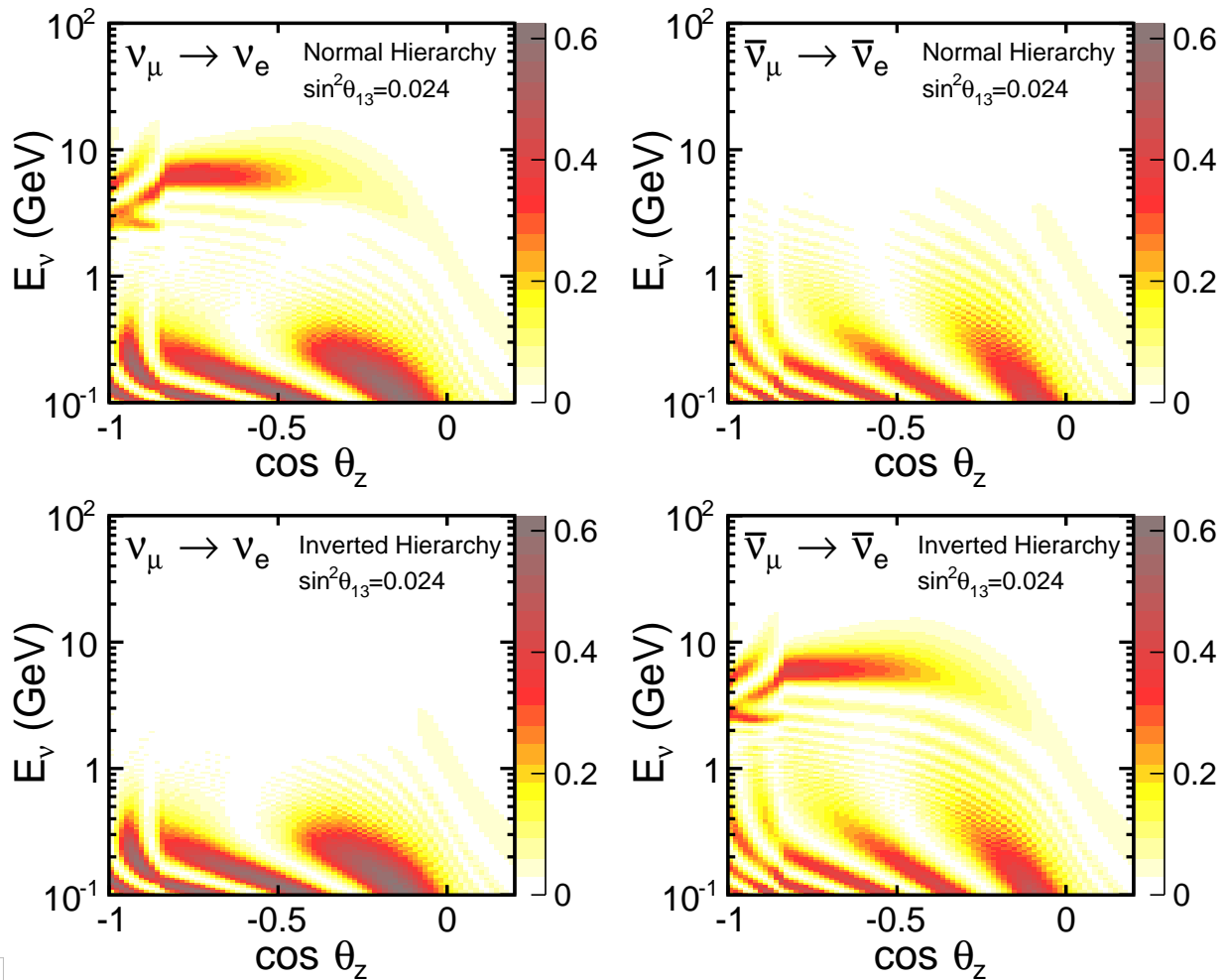


fig:oscatm

**Figure 2.9:** The probabilities of atmospheric  $\nu_\mu \rightarrow \nu_e$  (left) and  $\bar{\nu}_\mu \rightarrow \bar{\nu}_e$  (right) oscillations for normal (top) and inverted (bottom) hierarchies as a function of zenith angle.

- 1 Even with dedicated long-baseline experiments exploring the large mass splitting ( $\Delta m_{32}^2$ ) for
- 2 nearly a decade, atmospheric data continues to contribute substantially to our understanding of
- 3 the neutrino sector. Broadly speaking:
  - 4 ○ The data demonstrate *complementarity* with beam results via two- and three-flavor fits and
  - 5 the measurement of a  $\nu_\tau$  appearance signal consistent with expectations.
  - 6 ○ The data serve to increase measurement *precision* through global fits, given that the sensi-
  - 7 tivity of atmospheric neutrinos to the mass hierarchy is largely independent of  $\delta_{CP}$  and the
  - 8 octant of  $\theta_{23}$ .
  - 9 ○ *New physics* searches with atmospheric neutrinos have placed limits on CPT violation, non-
  - 10 standard interactions, mass-varying neutrinos and Lorentz-invariance violation.

1 Atmospheric neutrinos can continue to play these roles in the LBNE era given LBNE's deep-  
 2 underground far detector. In particular, complementarity will be vital in a future where, worldwide,  
 3 the number of high-precision, long-baseline beam/detector facilities is small. The physics potential  
 4 of a large underground liquid argon detector for measuring atmospheric neutrinos is discussed in  
 5 Section 4.6.

## 6 2.3 Nucleon Decay Physics Motivated by Grand Unified 7 Theories

Searches for proton decay, bound-neutron decay and similar processes such as di-nucleon decay and neutron-antineutron oscillations test the apparent but unexplained conservation law of baryon number. These decays are already known to be rare based on decades of prior searches, all of which have produced negative results. If measurable event rates or even a single-candidate event were to be found, it would be sensible to presume that they occurred via unknown virtual processes based on physics beyond the Standard Model. The impact of demonstrating the existence of a baryon-number-violating process would be profound.

### 9 2.3.1 Theoretical Motivation from GUTs

10 The class of theories known as Grand Unified Theories (GUTs) make predictions about both  
 11 baryon number violation and proton lifetime that may be within reach of the full-scope LBNE  
 12 experiment. The theoretical motivation for the study of proton decay has a long and distinguished  
 13 history [84,85,86] and has been reviewed many times [87,88,89]. Early GUTs provided the original  
 14 motivation for proton decay searches in kiloton-scale detectors placed deep underground to limit  
 15 backgrounds. The 22.5-kt Super-Kamiokande experiment extended the search for proton decay by  
 16 more than an order of magnitude relative to the previous generation of experiments. Contemporary  
 17 reviews [90,91,92] discuss the strict limits already set by Super-Kamiokande and the context of  
 18 the proposed next generation of larger underground experiments such as Hyper-Kamiokande and  
 19 LBNE.

20 Although no evidence for proton decay has been detected, the lifetime limits from the current  
 21 generation of experiments already constrain the construction of many contemporary GUT models.  
 22 In some cases, these lifetime limits are approaching the upper limits allowed by GUT models. This  
 23 situation points naturally towards continuing the search with new, larger detectors. These searches  
 24 are motivated by a range of scientific issues:

- 25 ○ Conservation laws arise from underlying symmetries in Nature [93]. Conservation of baryon

- 1 number is therefore unexplained since it corresponds to no known long-range force or sym-  
2 metry.
- 3 ○ Baryon number non-conservation has cosmological consequences, such as a role in inflation  
4 and the matter-antimatter asymmetry of the Universe.
  - 5 ○ Proton decay is predicted at some level by almost all GUTs.
  - 6 ○ Some GUTs can accommodate neutrinos with nonzero mass and characteristics consistent  
7 with experimental observations.
  - 8 ○ GUTs incorporate other previously unexplained features of the Standard Model such as the  
9 relationship between quark and lepton electric charges.
  - 10 ○ The unification scale is suggested both experimentally and theoretically by the apparent  
11 convergence of the running coupling constants of the Standard Model. The unification scale  
12 is in excess of  $10^{15}$  GeV.
  - 13 ○ The unification scale is not accessible by any accelerator experiment; it can only be probed  
14 by virtual processes such as with proton decay.
  - 15 ○ GUTs usually predict the relative branching fractions of different nucleon decay modes.  
16 Testing these predictions would, however, require a sizeable sample of proton decay events.
  - 17 ○ The dominant proton decay mode of a GUT is often sufficient to roughly identify the likely  
18 characteristics of the GUT, such as gauge mediation or the involvement of supersymmetry.

The observation of even a single unambiguous proton decay event would corroborate the idea of unification and the signature of the decay would give strong guidance as to the nature of the underlying theory.

### 20 2.3.2 Proton Decay Modes

21 From the body of literature, two decay modes (shown in Figure <sup>pdk feyn</sup>2.10) emerge that dominate the  
22 LBNE experimental design. The more well-known of the two, the decay mode of  $p \rightarrow e^+\pi^0$ ,  
23 arises from gauge mediation. It is often predicted to have the higher branching fraction and is also  
24 demonstrably the more straightforward experimental signature for a water Cherenkov detector. In  
25 this mode, the total mass of the proton is converted into the electromagnetic shower energy of the  
26 positron and two photons from  $\pi^0$  decay, with a net momentum vector near zero.

27 The second key mode is  $p \rightarrow K^+\bar{\nu}$ . This mode is dominant in most supersymmetric GUTs, many  
28 of which also favor additional modes involving kaons in the final state. This decay mode with a

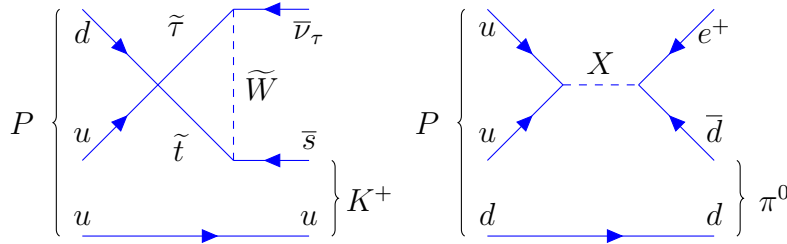


**Figure 2.10:** Feynman diagrams for proton decay modes from gauge-mediation GUT models,  $p^+ \rightarrow K^+ \bar{\nu}$  (left) and supersymmetric GUT,  $p^+ \rightarrow e^+ \pi^0$  (right).

1 charged kaon is uniquely interesting; since stopping kaons have a higher ionization density than  
 2 other particles, a LArTPC could detect it with extremely high efficiency, as described in Chapter 5.  
 3 In addition, many final states of  $K^+$  decay would be fully reconstructable in a LArTPC.

4 There are many other allowed modes of proton or bound neutron into antilepton plus meson decay  
 5 that conserve  $B - L$ <sup>§</sup>, but none of these will influence the design of a next-generation experiment.  
 6 The most stringent limits, besides those on  $p \rightarrow e^+ \pi^0$ , include the lifetime limits on  $p \rightarrow \mu^+ \pi^0$   
 7 and  $p \rightarrow e^+ \eta$ , both of which are greater than  $4 \times 10^{33}$  years. Any experiment that will do well  
 8 for  $p \rightarrow e^+ \pi^0$  will also do well for these decay modes. The decays  $p \rightarrow \bar{\nu} \pi^+$  or  $n \rightarrow \bar{\nu} \pi^0$  may  
 9 have large theoretically predicted branching fractions, but they are experimentally difficult due to  
 10 the sizeable backgrounds from atmospheric-neutrino interactions. The decay  $p \rightarrow \mu^+ K^0$  can be  
 11 detected relatively efficiently by either water Cherenkov or LArTPC detectors.

12 A number of other possible modes exist, such as those that conserve  $B + L$ , that violate only baryon  
 13 number, or that decay into only leptons. These possibilities are less well-motivated theoretically,  
 14 as they do not appear in a wide range of models, and are therefore not considered here.

15 Figure 2.11 shows a comparison of experimental limits, dominated by recent results from Super-  
 16 Kamiokande to the ranges of lifetimes predicted by an assortment of GUTs. At this time, the theory  
 17 literature does not attempt to precisely predict lifetimes, concentrating instead on suggesting the  
 18 dominant decay modes and relative branching ratios. The uncertainty in the lifetime predictions  
 19 comes from details of the theory, such as masses and coupling constants of unknown heavy parti-  
 20 cles, as well as poorly known details of matrix elements for quarks within the nucleon.

21 It is apparent from Figure 2.11 that a continued search for proton decay is by no means assured  
 22 of obtaining a positive result. With that caveat, an experiment with sensitivity to proton lifetimes  
 23 between  $10^{33}$  and  $10^{35}$  years is searching in the right territory over virtually all GUTs; even if no  
 24 proton decay is detected, stringent lifetime limits will provide strong constraints on such models.  
 25 Minimal SU(5) was ruled out by the early work of IMB and Kamiokande and minimal SUSY SU(5)  
 26 is considered to be ruled out by Super-Kamiokande. In most cases, another order of magnitude in

<sup>§</sup> $B$  and  $L$  refer to baryon number and lepton number; in these models, the quantum number  $B - L$  is expected to be conserved even though  $B$  and  $L$  are not individually conserved.

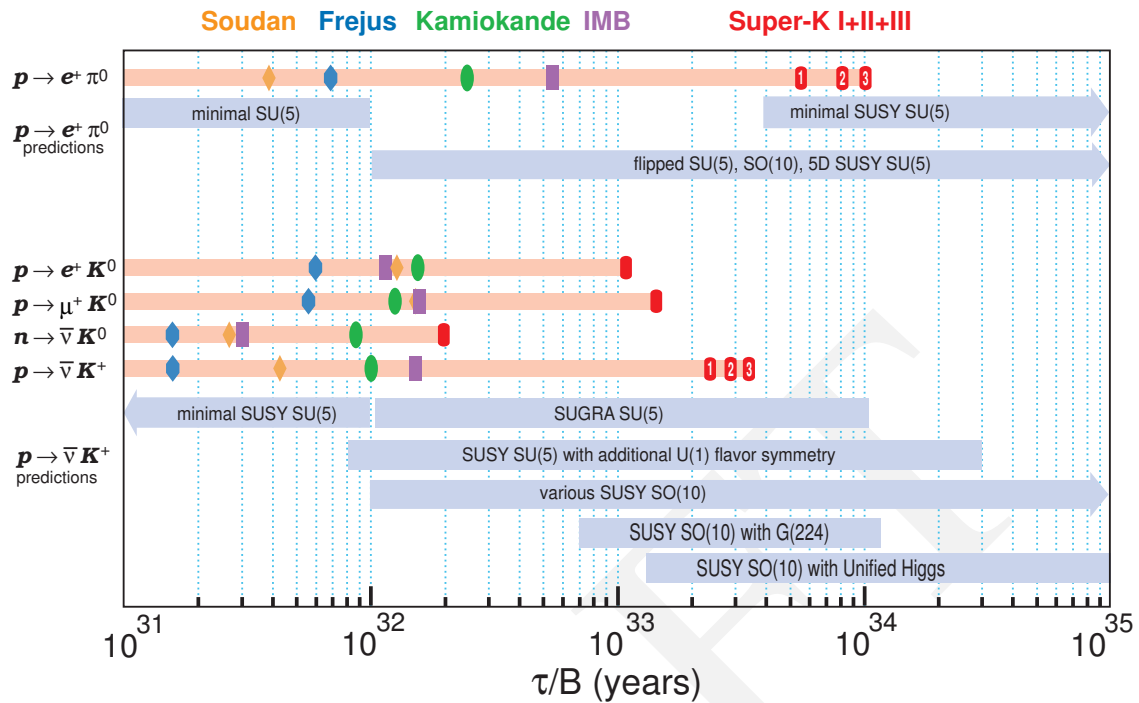


**Figure 2.11:** Proton decay lifetime limits compared to lifetime ranges predicted by Grand Unified Theories. The upper section is for  $p \rightarrow e^+ \pi^0$ , most commonly caused by gauge mediation. The lower section is for SUSY-motivated models, which commonly predict decay modes with kaons in the final state. The marker symbols indicate published experimental limits, as indicated by the sequence and colors on top of the figure.

- 1 improved limits will not rule out specific models but will constrain their allowed parameters; this
- 2 could allow identification of models which must be fine-tuned in order to accommodate the data,
- 3 and are thus less favored.
- 4 As Chapter 5 will show, the performance and scalability of the LArTPC technology opens up
- 5 nucleon decay channels that are not as readily accessible in existing and proposed water Cherenkov
- 6 detectors, providing LBNE with a unique and compelling opportunity for discovery.

## 2.4 Supernova-Neutrino Physics and Astrophysics

For over half a century, researchers have been grappling to understand the physics of the neutrino-driven core-collapse supernova. The interest in observing the core-collapse supernova explosion mechanism comes from the key role supernovae of this type have played in the history of the Universe. Without taking supernova feedback into account, for example, modern simulations of galaxy formation cannot reproduce the structure of our galactic disk. More poetically, the heavy elements that are the basis of life on Earth were synthesized inside stars and ejected by supernova explosions.

Neutrinos from a core-collapse supernova are emitted in a burst of a few tens of seconds duration,

1 with about half emitted in the first second. They record the information about the physical processes  
2 in the center of the explosion during the first several seconds — as it is happening. Energies are in  
3 the few-tens-of-MeV range and luminosity is divided roughly equally between flavors. The basic  
4 model of core collapse was confirmed by the observation of neutrino events from SN1987A, a  
5 supernova in the Large Magellanic Cloud — outside the Milky Way — 50 kpc (kiloparsecs) away.  
6 Nineteen events were detected in two water Cherenkov detectors [94,95] and additional events  
7 were reported in a scintillator detector [96]. The neutrino signal from a core-collapse supernova in  
8 the Milky Way is expected to generate a high-statistics signal from which LBNE could extract a  
9 wealth of information [97,98].

10 The explosion mechanism is thought to have three distinct stages: the collapse of the iron core,  
11 with the formation of the shock and its breakout through the neutrinosphere; the accretion phase,  
12 in which the shock temporarily stalls at a radius of about 200 km while the material keeps raining  
13 in; and the cooling stage, in which the hot proto-neutron star loses its energy and trapped lepton  
14 number, while the re-energized shock expands to push out the rest of the star. Each of these three  
15 stages is predicted to have a distinct signature in the neutrino signal. Thus, it should be possible to  
16 directly observe, for example, how long the shock is stalled. More exotic features of the collapse  
17 may be observable in the neutrino flux as well, such as possible transitions to quark matter or to a  
18 black hole. (An observation in conjunction with a gravitational wave detection would be especially  
19 interesting; see, e.g. [99,100].)

20 Core-collapse supernovae are rare events: the expected rate is two to three per century in the Milky  
21 Way [101,102]. The large LBNE detector, once constructed, may operate for decades. On this time  
22 scale, the likelihood of a supernova event in our galaxy is significant.

In a 20-year experimental run, LBNE's probability of observing neutrinos from a core-collapse supernova in the Milky Way is about 40%. The detection of thousands of supernova-burst neutrinos from this event would dramatically expand the science reach of the experiment, allowing observation of the development of the explosion in the star's core and probing the equation-of-state of matter at nuclear densities. In addition, independent measurements of the neutrino mass hierarchy and the  $\theta_{13}$  mixing angle are possible, as well as additional constraints on physics beyond the Standard Model.

Each of the topics that can be addressed by studying supernova-burst neutrinos represent important outstanding problems in modern physics, each worthy of a separate, dedicated experiment, and the neutrino physics and astrophysics communities would receive payback simultaneously. The opportunity of targeting these topics in a single experiment is very attractive, especially since it may come only at incremental cost to the LBNE project.

23  
24 Over the last two decades, neutrino flavor oscillations have been firmly established in solar neutri-

nos and a variety of terrestrial sources. The physics of the oscillations in the supernova environment promises to be much richer than in any of the cases measured to date, for a variety of reasons:

- Neutrinos travel through the changing profile of the explosion with stochastic density fluctuations behind the expanding shock and, due to their coherent scattering off of each other, their flavor states are coupled.
- The oscillation patterns come out very differently for the normal and inverted mass hierarchies.
- The expanding shock and turbulence leave a unique imprint in the neutrino signal.
- Additional information on oscillation parameters, free of supernova model-dependence, will be available if matter effects due to the Earth can be observed in detectors at different locations around the world [103,104].
- The observation of this potentially copious source of neutrinos will also allow limits on coupling to axions, large extra dimensions, and other exotic physics (e.g., [105,106]).
- The oscillations of neutrinos and antineutrinos from a core-collapse supernova manifest very differently. In the neutrino channel, the oscillation features are in general more pronounced, since the initial spectra of  $\nu_e$  and  $\nu_\mu$  ( $\nu_\tau$ ) are always significantly different. It would be extremely valuable to detect both neutrino and antineutrino channels with high statistics.

Only about two dozen neutrinos were observed from SN1987A, which occurred in a nearby galaxy; in contrast, the currently proposed next-generation detectors would register thousands or tens of thousands of interactions from a core-collapse supernova in our galaxy. The type of observed interactions will depend on the detector technology: a water-Cherenkov detector is primarily sensitive to  $\bar{\nu}_e$ 's, whereas a LArTPC detector has excellent sensitivity to  $\nu_e$ 's. In each case, the high event rate implies that it should be possible to measure not only the time-integrated spectra, but also their second-by-second evolution. This is a key feature of the supernova-burst physics potential of the planned LBNE experiment.

Currently, experiments worldwide are sensitive primarily to  $\bar{\nu}_e$ 's, via inverse-beta decay on free protons, which dominates the interaction rate in water and liquid-scintillator detectors. Liquid argon exhibits a unique sensitivity to the  $\nu_e$  component of the flux, via the absorption interaction on  $^{40}\text{Ar}$ ,  $\nu_e + ^{40}\text{Ar} \rightarrow e^- + ^{40}\text{K}^*$ . In principle, this interaction can be tagged via the coincidence of the electron and the  $^{40}\text{K}^*$  de-excitation gamma cascade. About 900 events would be expected in a 10-kt fiducial liquid argon detector for a core-collapse supernova at 10 kpc. The number of signal events scales with mass and the inverse square of distance, as shown in Figure 2.12. For a collapse in the Andromeda galaxy, massive detectors of hundreds of kilotons would be required to observe a handful of events. However, for supernovae within the Milky Way, even a relatively small 10-kt detector would gather a significant  $\nu_e$  signal.

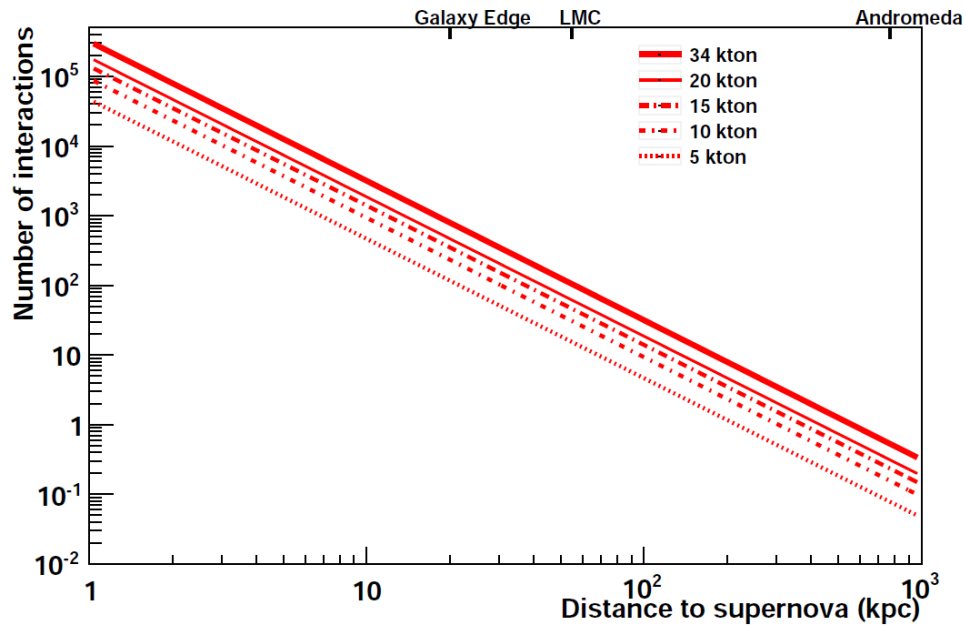


**Figure 2.12:** Number of supernova neutrino interactions in a liquid argon detector as a function of distance to the supernova for different detector masses. Core collapses are expected to occur a few times per century, at a most-likely distance from 10 kpc to 15 kpc.

- 1 Because the neutrinos emerge promptly after core collapse, in contrast to the electromagnetic
- 2 radiation which must beat its way out of the stellar envelope, an observation could provide a
- 3 prompt supernova alert [107,108], allowing astronomers to find the supernova in early light turn-on
- 4 stages, which could yield information about the progenitor (in turn, important for understanding
- 5 oscillations). Further, observations and measurements by multiple, geographically separated de-
- 6 tectors during a core collapse — of which several are expected to be online over the next few
- 7 decades [97,109] — will enhance the potential science yield from such a rare and spectacular
- 8 event [103].

1

The LBNE Project was formed to design and construct the Long-Baseline Neutrino Experiment. The experiment will comprise a new, high-intensity neutrino source generated from a megawatt-class proton accelerator at Fermi National Accelerator Laboratory (Fermilab) directed at a large far detector at the Sanford Underground Research Facility in Lead, SD. A near detector will be located about 500 m downstream of the neutrino production target. LBNE is currently planned as a phased program, with increased scientific capabilities at each phase.

- The experimental facilities are designed to meet the primary scientific objectives of the experiment: (1) fully characterize neutrino oscillations, including measuring the value of the unknown CP phase,  $\delta_{CP}$ , and determining the ordering of the neutrino mass states, (2) significantly improve proton decay lifetime limits, and (3) measure the neutrino flux from potential core-collapse supernovae in our galaxy.
- The LBNE beamline, based on the existing *Neutrinos at the Main Injector* (NuMI) beamline design, is designed to deliver a wide-band, high-purity  $\nu_\mu$  beam with a peak flux at 2.5 GeV, which optimizes the oscillation physics potential at the 1,300-km baseline. The beamline will operate initially at 1.2 MW and is upgradeable to 2.3 MW utilizing a proton beam with energy tunable from 60 to 120 GeV.
- The full-scope LBNE far detector is a liquid argon time-projection chamber (LArTPC) of fiducial mass 34 kt.

The TPC design is modular, allowing flexibility in the choice of initial detector size.

- The LBNE far detector will be located 4,850 feet underground, a depth favorable for LBNE's search for proton decay and detection of the neutrino flux from a core-collapse supernova.
- The high-precision near detector and its conventional facilities can be built as an independent project, at the same time as the far detector and beamline, or later.

2

## 3.1 LBNE and the U.S. Neutrino Physics Program

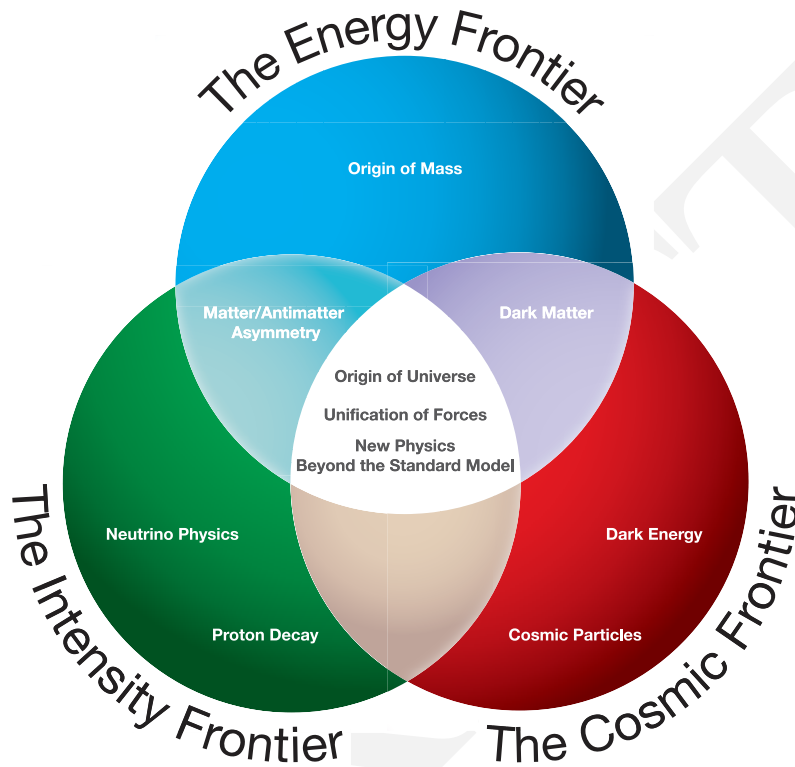


**Figure 3.1:** Three frontiers of research in particle physics form an interlocking framework that addresses fundamental questions about the laws of Nature and the cosmos. Each frontier, essential to the whole, has a unique approach to making discoveries [6].

In its 2008 report, the U.S. Particle Physics Project Prioritization Panel (P5)\* recommended a world-class neutrino physics program as a core component of a U.S. particle physics program that revolves around three research frontiers as shown in Figure 3.1. Included in the report is the long-term vision of a large far detector at the site of the former Homestake Mine in Lead, SD, and a high-intensity, broad-band neutrino source at Fermilab. At the time, the proposed Deep Underground Science and Engineering Laboratory (DUSEL) was planned to occupy the site of the former mine; it is now the Sanford Underground Research Facility.

\*P5 is an advisory panel to the two main funding bodies for particle physics in the United States, the Department of Energy (DOE) and the National Science Foundation (NSF).

1 On January 8, 2010 the DOE approved the Mission Need [10] statement<sup>†</sup> for a new long-baseline  
2 neutrino experiment that would enable this world-class program and firmly establish the U.S. as  
3 the leader in neutrino science. The LBNE experiment is designed to meet this Mission Need.

4 With the facilities provided by the LBNE Project and the unique features of the experiment —  
5 in particular the long baseline of 1,300 km, the broad-band beam and the high-resolution, un-  
6 derground far detector — LBNE will conduct a broad scientific program addressing key physics  
7 questions concerning the nature of our Universe as described in Chapter 2. The focus of the long-  
8 baseline neutrino program will be the explicit demonstration of leptonic CP violation, if it exists,  
9 and the determination of the neutrino mass hierarchy.

The 1,300-km baseline has been determined to provide optimal sensitivity to CP violation and the measurement of  $\delta_{CP}$ , and is long enough to enable an unambiguous determination of the neutrino mass hierarchy [74].

11 The focus of the non-beam scientific program will be to search for proton decay, to enable detailed  
12 studies of atmospheric neutrinos, and to detect and measure the neutrino flux from a supernova,  
13 should one occur within our galaxy.

14 It is currently planned to implement LBNE as a phased program, with increased scientific capabil-  
15 ities at each phase. The initial phase (also referred to as Phase 1) of LBNE will achieve significant  
16 advances with respect to its primary scientific objectives as compared to current experiments. The  
17 *goal* for the initial phase of LBNE is:

- 18 1. a new neutrino beamline at Fermilab driven by a 60 to 120 GeV proton beam with power of  
19 up to 1.2 MW
- 20 2. a liquid argon time-projection chamber (LArTPC) detector of fiducial mass at least 10 kt  
21 located at the Sanford Underground Research Facility at a depth of 4,850 feet
- 22 3. a high-precision near neutrino detector on the Fermilab site

23 The cost for this initial phase (with a 10-kt far detector) is estimated to be 1.2B U.S.\$ according to  
24 DOE standard project accounting.

25 In December of 2012, the DOE issued CD-1 (Conceptual Design Phase) approval for a budget  
26 of 867M\$ U.S. based on a reduced scope that excluded the near neutrino detector and the un-  
27 derground placement of the far detector. Domestic and international partners are being sought to  
28 enable construction of the full first-phase scope outlined above. Subsequent phases of LBNE are  
29 expected to include additional far detector mass and upgrades of the beam to  $\geq 2.3$ -MW capability.

<sup>†</sup>A Mission Need statement initiates the process and provides initial funding towards developing the conceptual design of a DOE scientific project.

## 3.2 Near Site: Fermi National Accelerator Laboratory

ntro-fnal

Fermilab, located 40 miles west of Chicago, Illinois, is a DOE-funded laboratory dedicated to high energy physics. The laboratory builds and operates accelerators, detectors and other facilities that physicists from all over the world use to carry out forefront research.

Dramatic discoveries in high energy physics have revolutionized our understanding of the interactions of the particles and forces that determine the nature of matter in the Universe. Two major components of the Standard Model of Fundamental Particles and Forces were discovered at Fermilab: the bottom quark (May-June 1977) and the top quark (February 1995). In July 2000, Fermilab experimenters announced the first direct observation of the tau neutrino, thus filling the final slot in the lepton sector of the Standard Model. Run II of the Fermilab Tevatron Collider was inaugurated in March 2001. The Tevatron was the world's highest-energy particle accelerator and collider until the Large Hadron Collider at CERN came online in 2011.

While CERN now hosts the world's highest-energy particle collider, the Fermilab accelerator complex is being retooled to produce the world's highest-intensity beams of protons, muons and neutrinos. Scientists from around the world can exploit this capability to pursue cutting-edge research in the lepton sector of the Standard Model where strong hints of new physics have surfaced.

The beamline and near detector for LBNE will be constructed at Fermilab, referred to as the *Near Site*.

Fermi National Accelerator Laboratory, originally named the National Accelerator Laboratory, was commissioned by the U.S. Atomic Energy Commission, under a bill signed by President Lyndon B. Johnson on November 21, 1967. On May 11, 1974, the laboratory was renamed in honor of 1938 Nobel Prize winner Enrico Fermi, one of the preeminent physicists of the atomic age.

Today, the DOE operates national laboratories throughout the United States, including Fermilab. The DOE awarded to Fermi Research Alliance (FRA) the management and operating contract for Fermilab, effective January 1, 2007. The FRA is a tax-exempt, limited liability company (LLC) organized and operated for charitable, scientific and educational purposes under Section 501(c)(3) of the Internal Revenue Code. The two members of FRA are the University of Chicago and the Universities Research Association (URA). FRA has earned extensions to the Fermilab contract through Dec. 31, 2015.

At Fermilab, a robust scientific program pushes forward on the three interrelated scientific frontiers specified by the P5 panel in 2008 [6] and illustrated in Figure 3.1:

- 1 1. At the Energy Frontier, Fermilab scientists are significant contributors to the LHC and to the  
2 CMS experiment.
- 3 2. At the Intensity Frontier, Fermilab operates two neutrino beams that support a number of ex-  
4 periments. In the next few years several new neutrino and muon experiments will be coming  
5 online, of which LBNE will be the largest.
- 6 3. At the Cosmic Frontier, Fermilab runs and/or participates in several experiments, with in-  
7 struments installed in North America, South America and Europe.

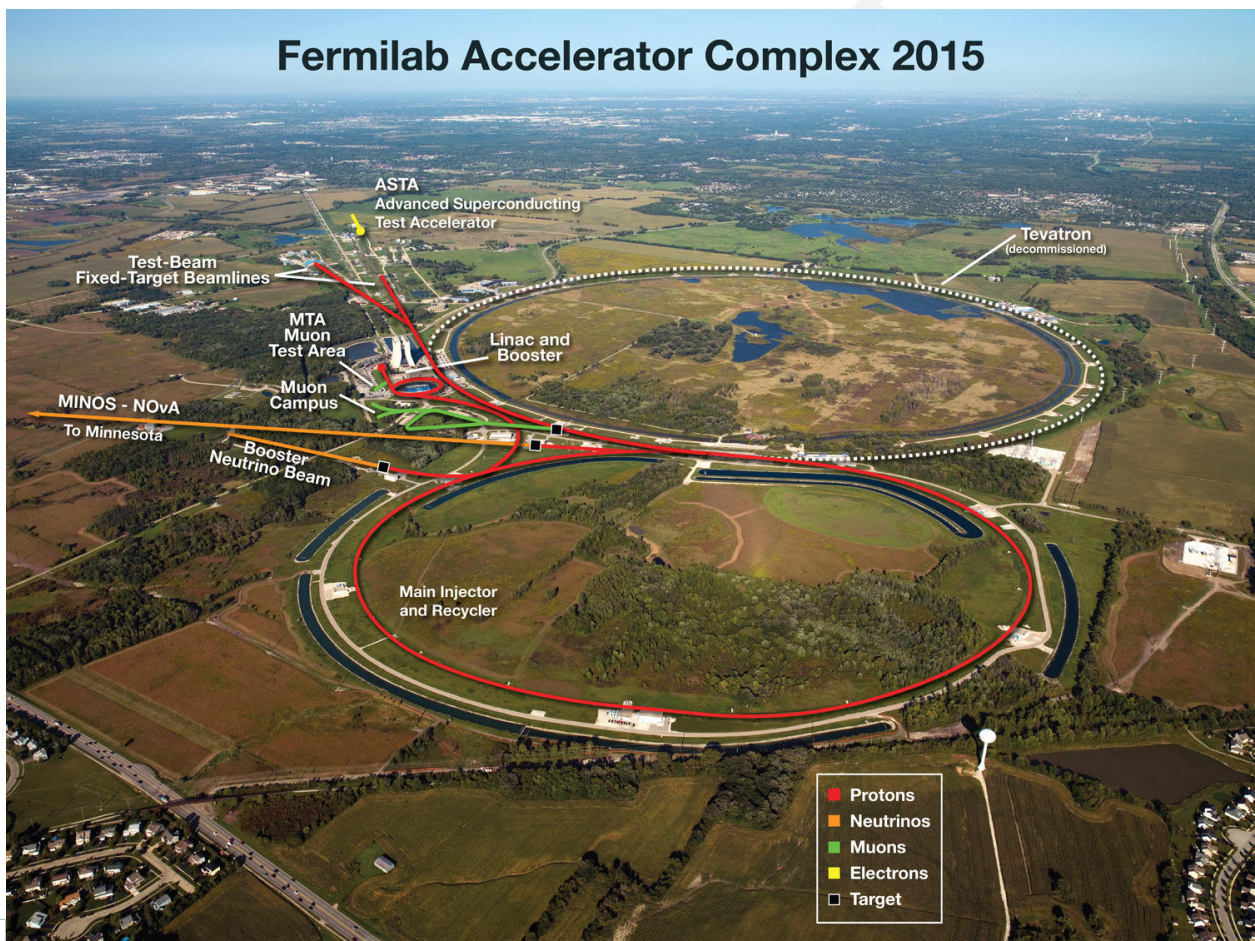


fig:accels

**Figure 3.2:** The accelerator chain at Fermi National Accelerator Laboratory. A 400-MeV linear accelerator (linac) feeds into the 15-Hz Booster, which produces an 8-GeV beam. The Booster beam is used for the Booster Neutrino Beamline experiments. The Booster feeds into the 120-GeV Main Injector. The Main Injector is the source for the NuMI beamline, which supplies a high-power, high-energy neutrino beam to the MINOS/MINOS+ and NO $\nu$ A experiments.

8 The neutrino beams at Fermilab come from two of the lab's proton accelerators (see the 2012 site  
9 layout in Figure 3.2), the 8-GeV Booster, which feeds the *Booster Neutrino Beamline* (BNB), and  
10 the 120-GeV Main Injector (MI), which feeds the NuMI beamline. The LBNE beamline, described  
11 in Section 3.4, will utilize the MI beam.

1 NuMI, on which LBNE’s beamline design is based, is a high-energy neutrino beam that has been  
 2 operating since 2004. It was designed for steady 400-kW operation and achieved that goal by the  
 3 end of the MINOS experimental run in 2012. As shown in Figure 3.3, the NuMI beamline was  
 4 running with an average of  $9 \times 10^{18}$  protons per week ( $\approx 2.7 \times 10^{20}$  protons-on-target per year) in  
 mid 2012.

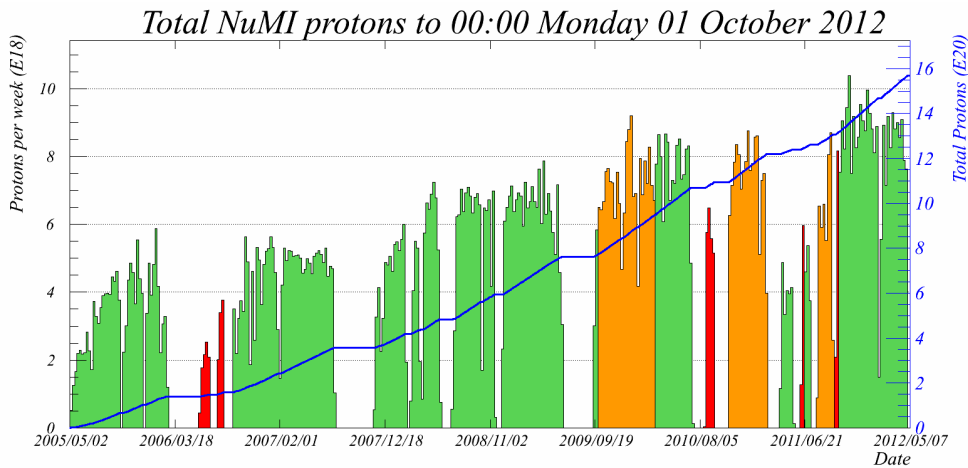


Figure 3.3: The NuMI beamline performance

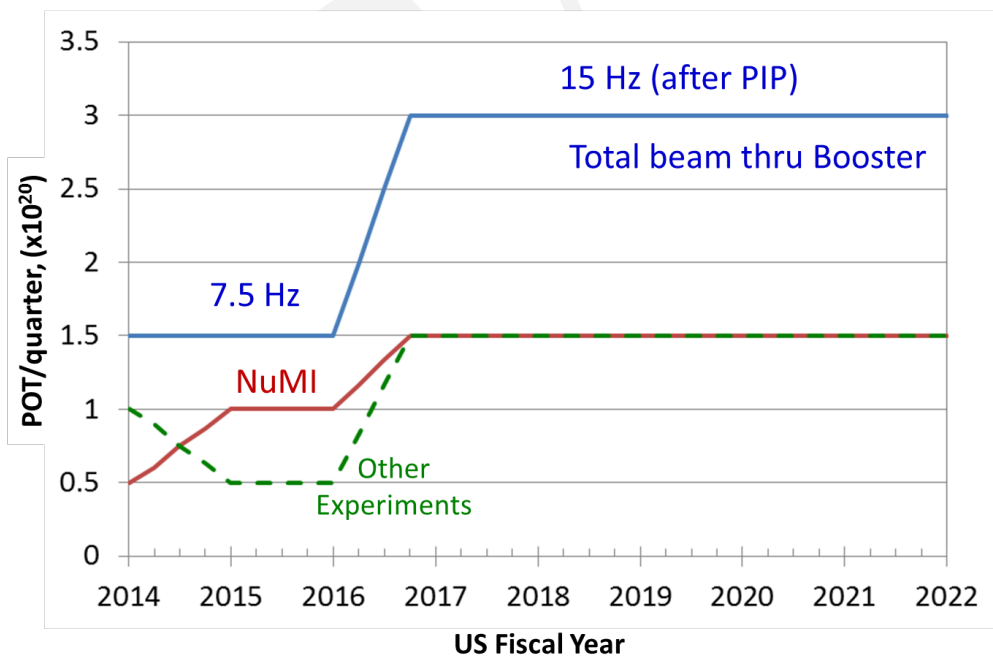


Figure 3.4: A possible ramp-up scenario for proton flux from Fermilab’s proton source for the Intensity Frontier experiments.

- 1 Upgrades to the Recycler<sup>‡</sup> and MI as part of the NO $\nu$ A Project, as well as the Proton Improve-  
 2 ment Plan (PIP) that is currently underway, comprise a set of improvements to the existing Linac,  
 3 Booster and MI aimed at supporting 15-Hz beam operations from the Booster (see Figure 3.4).  
 4 In combination, the NO $\nu$ A upgrades and the PIP create a capability of delivering 700 kW from the  
 5 MI at 120 GeV ( $\approx 6 \times 10^{20}$  proton-on-target per year) by 2016. The proton beam power expected  
 6 to be available as a function of MI beam energy after completion of the PIP upgrades is shown in  
 Figure 3.5.

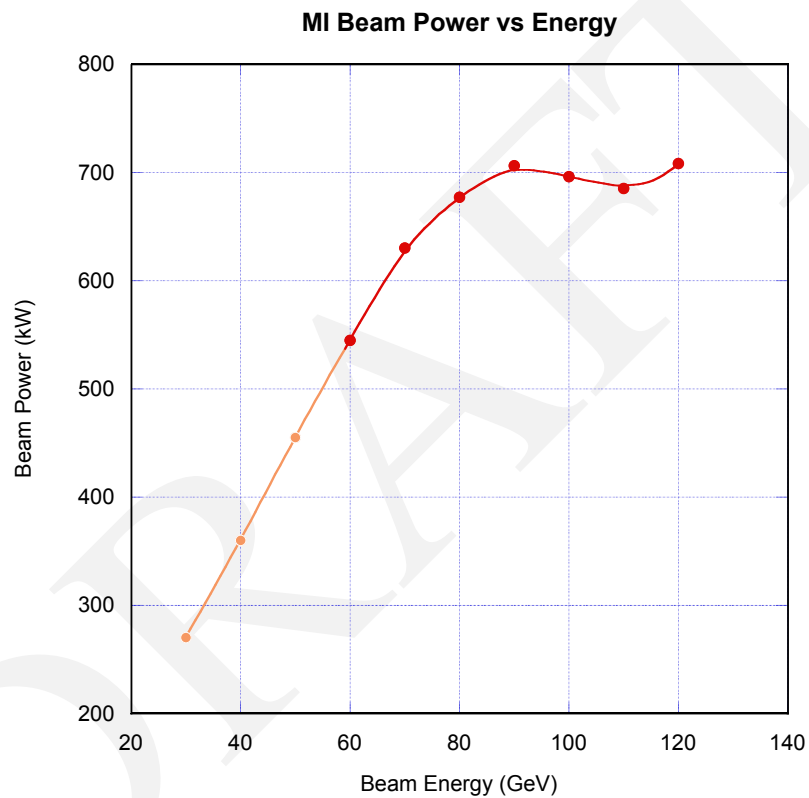


fig:pippower

**Figure 3.5:** Proton beam power expected to be available as a function of MI beam energy after proton-improvement-plan (PIP) upgrades.

7

- 8 A conceptual plan for further upgrades to the Fermilab accelerator complex has been completed.  
 9 Called the *Proton Improvement Plan-II* (PIP-II) [14], its goal is to increase the capabilities of  
 10 the existing accelerator complex to support delivery of 1.2 MW of beam power to the LBNE  
 11 production target at the initiation of operations, while simultaneously providing a platform for  
 12 subsequent upgrades of the complex to multi-MW capability. The starting point of this plan is the  
 13 *Project X Reference Design Report* [15].

<sup>‡</sup>The Recycler, a fixed 8-GeV kinetic energy storage ring located directly above the MI beamline, stores protons from the 8-GeV Booster during MI ramp up.

1 The primary bottleneck to providing increased beam power at Fermilab is the Fermilab Booster,  
2 limited by space-charge forces at injection. In the intermediate term the most cost-effective ap-  
3 proach to removing this bottleneck is to increase the injection energy into the Booster. The PIP-II  
4 meets this goal via an 800-MeV superconducting linear accelerator (linac), operated at low duty  
5 factor, but constructed of accelerating modules that are capable of continuous-wave (CW) oper-  
6 ations if provided with sufficient cryogenic cooling and appropriate RF power. This is expected  
7 to increase the beam intensity delivered from the Booster by 50% relative to current operations.  
8 Shortening the MI cycle time to 1.2 s yields a beam power of 1.2 MW at 120 GeV. The conceptual  
9 site layout of PIP-II is shown in Figure 3.6. Further possible upgrades beyond PIP-II would require  
10 replacing the 8-GeV Booster with a superconducting linac injecting into the MI at energies be-  
11 tween 6 and 8 GeV as shown in Figure 3.6, eventually increasing the power from the MI to 2.0–2.3  
12 MW at 60–120 GeV.

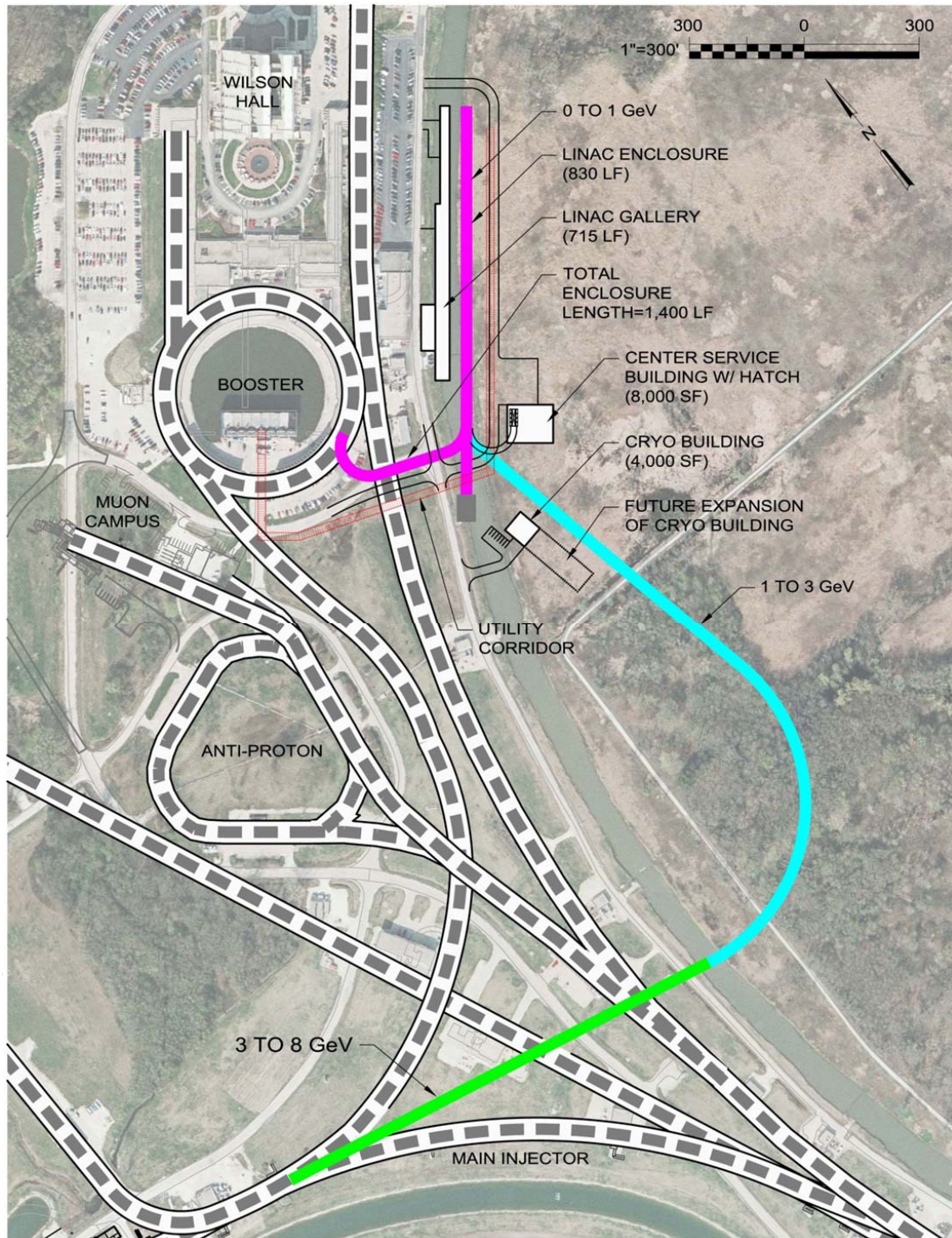


fig: pip2-layout

**Figure 3.6:** Site layout of PIP- II is shown as the magenta line which is the 800 MeV linac enclosure and transfer line. New construction includes the linac enclosure, transfer line enclosure, linac gallery, center service building, utility corridor, and cryo building. Dashed areas represent existing or planned underground enclosures. Further possible upgrades to the Fermilab complex beyond PIP- II are shown in the bottom half of the figure: cyan is a 1-3 GeV CW linac and transfer line, and green is a 3-8 GeV pulsed linac [14].

### 3.3 Far Site: Sanford Underground Research Facility

The Sanford Underground Research Facility [110] is a laboratory located on the site of the former Homestake gold mine in Lead, SD that is dedicated to underground science. This laboratory has been selected as the location of the far detector for LBNE, and is referred to as the *Far Site*.

Underground neutrino experiments in the former mine date back to 1967 when nuclear chemist Ray Davis installed a solar neutrino experiment 4,850 feet below the surface [111]. Ray Davis earned a share of the Nobel Prize for physics in 2002 for his experiment, which ran until 1993.

LBNE is envisioned as the next-generation, multi-decade neutrino experiment at this site seeking groundbreaking discoveries.

In 2006, Barrick Gold Corporation donated the Homestake Gold Mine site, located in Lead, South Dakota (see map in Figure 3.7) to the State of South Dakota, following over 125 years of mining. Mining operations created over 600 km of tunnels and shafts in the facility, extending from the surface to over 8,000 feet below ground. The mining levels are distributed  $\sim 150$  feet apart and are referenced by their depth below the facility entrance, e.g., the level 4,850 feet below ground is referred to as the *4850L*. This former mine encompasses the deepest caverns in the western hemisphere, offering extensive drifts both vertically and laterally. A detailed vertical cross section of the 60 underground levels developed for mining is shown in Figure 3.8.

In 2004, the South Dakota state legislature created the South Dakota Science and Technology Authority (SDSTA) to foster scientific and technological investigations, experimentation and development in South Dakota. A six-member board of directors appointed by the governor of South Dakota directs the SDSTA. The SDSTA's first task was to reopen the former Homestake site to the 4,850-foot level for scientific research. At this site, the SDSTA now operates and maintains the Sanford Underground Research Facility through a contract managed and overseen by a dedicated operations office at Lawrence Berkeley National Laboratory as a deep-underground research laboratory. The Sanford Underground Research Facility property comprises 186 acres on the surface and 7,700 acres underground. The surface campus includes approximately 253,000 gross square feet of existing structures. A surface schematic of the campus is shown in Figure 3.9.

The state legislature has since committed more than \$40 million in state funds to the development of the Sanford Underground Research Facility, and the state has also obtained a \$10 million Community Development Block Grant to help rehabilitate the site. In addition, a \$70 million donation from philanthropist T. Denny Sanford has been used to reopen the site for science and to establish the Sanford Center for Science Education. The initial concepts for the facility were developed with

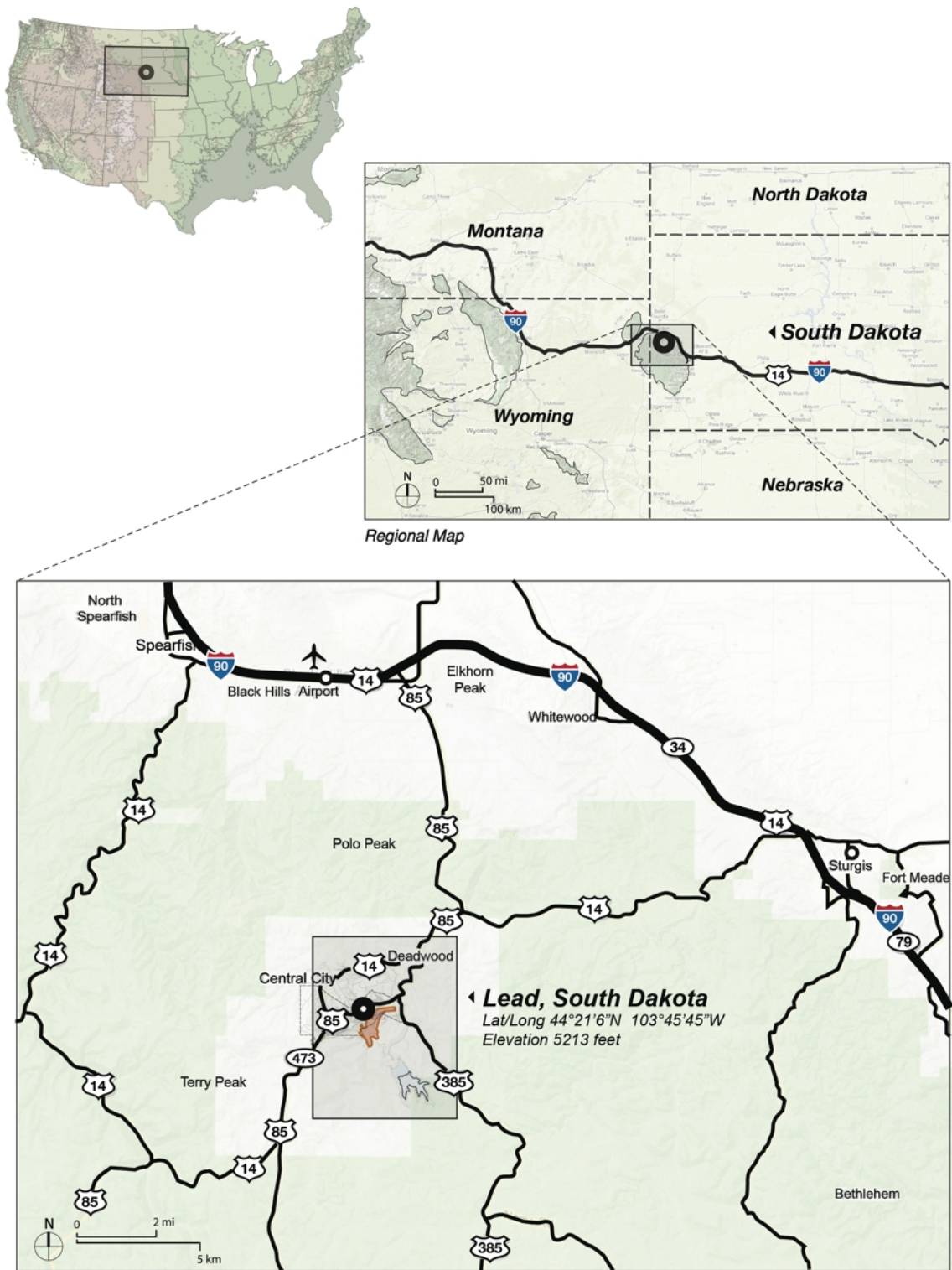
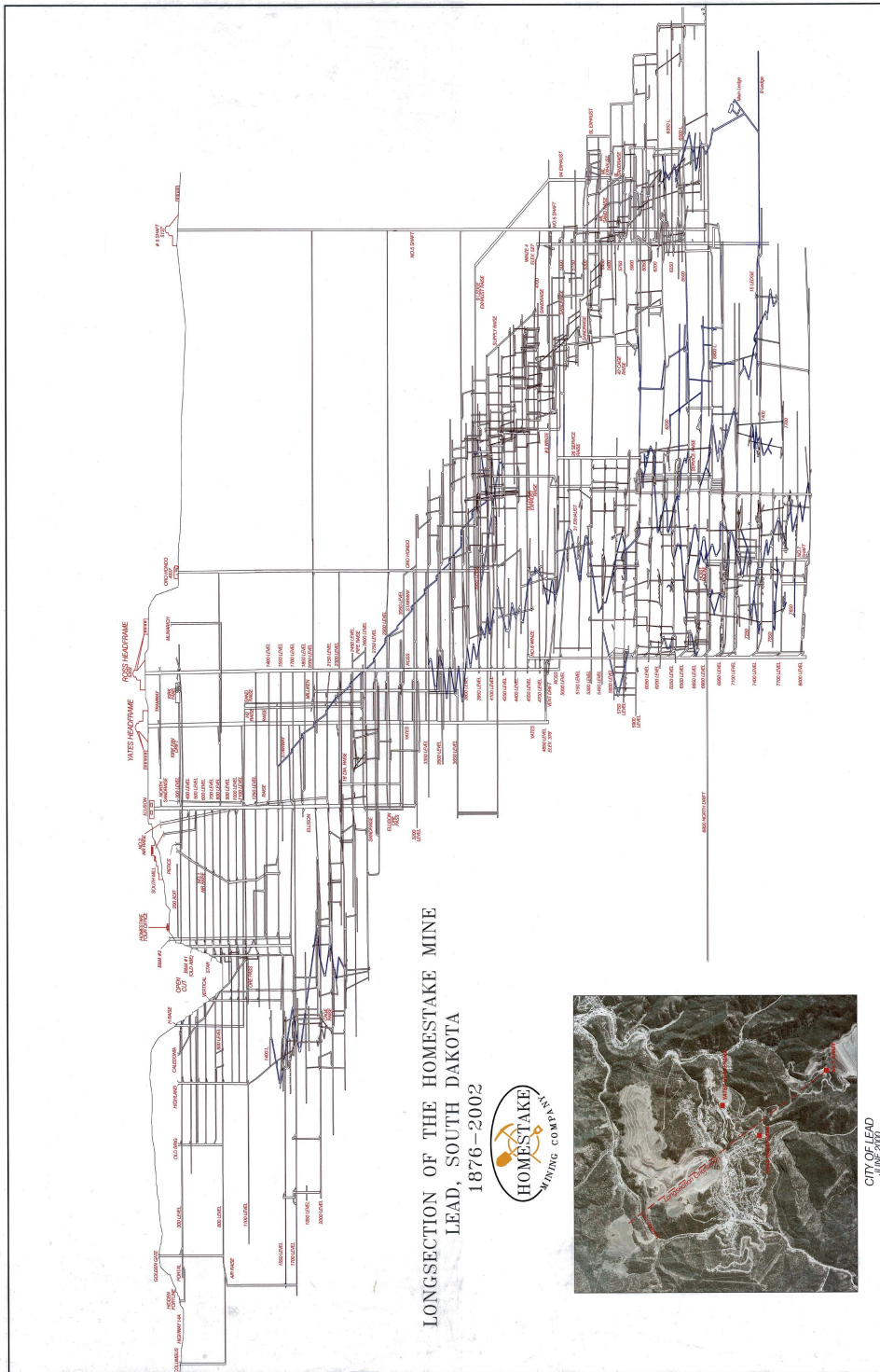
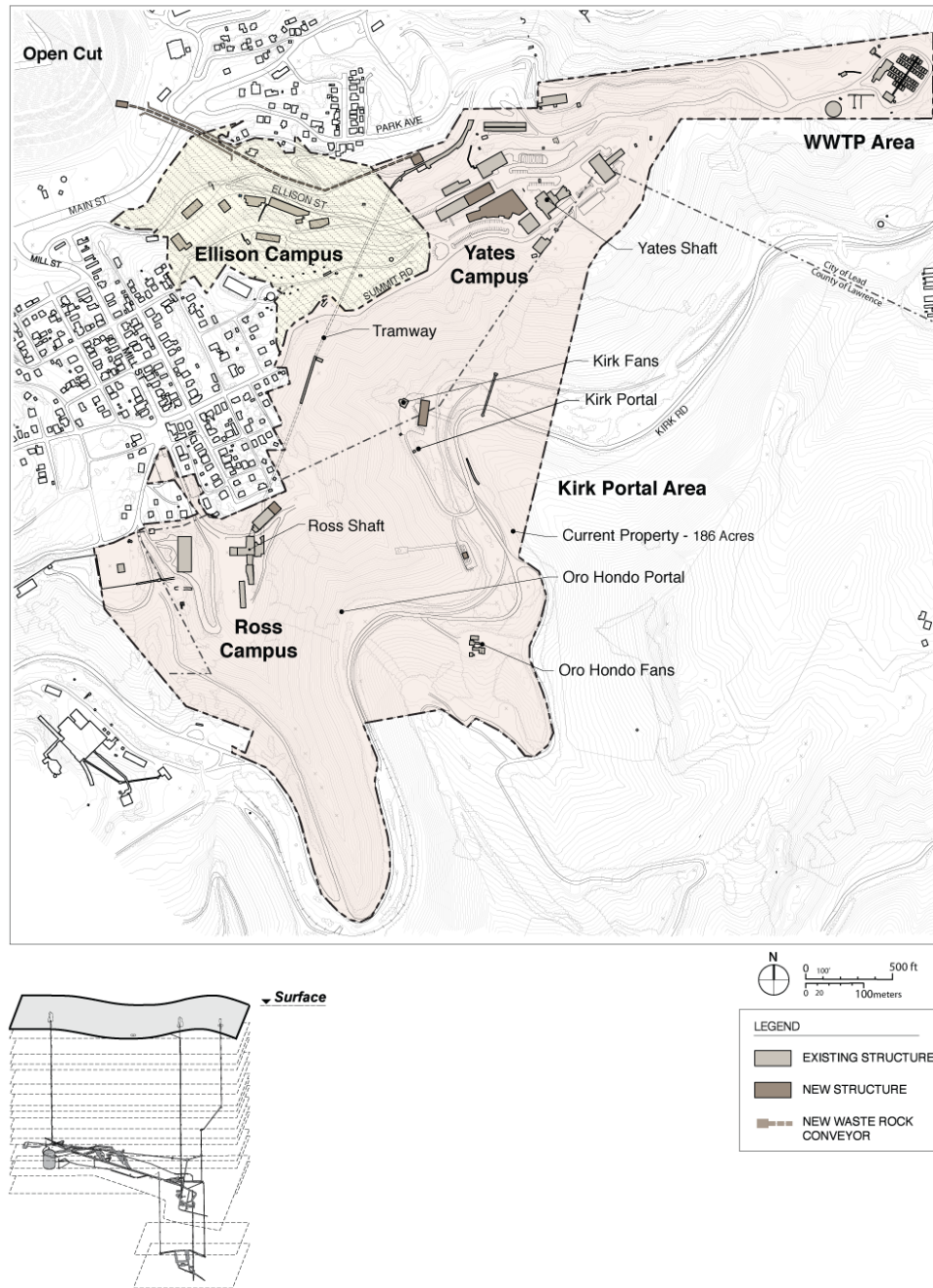


fig:lead

Figure 3.7: Location of the town of Lead, South Dakota - the site of the former Homestake Gold Mine.



**Figure 3.8:** The long section of the former Homestake Gold Mine. This figure illustrates the 60 underground levels extending to depths greater than 8,000 feet. The location of cross section is indicated in the inset along a NW to SE plane. The projection extends for 5.2 km along this plane



5.1.2.1 Major Surface Elements

fig:surf\_larloc

**Figure 3.9:** The surface and underground campuses of the Sanford Underground Research Facility. The 3D inset image illustrates the plans to develop the 4850L and 7400L. Most current experiments are at the 4850L.

**The Long-Baseline Neutrino Experiment**

1 the support of the U.S. National Science Foundation (NSF) as the primary site for the NSF's Deep  
 2 Underground Science and Engineering Laboratory (DUSEL). With the National Science Board's  
 3 decision to halt development of the NSF-supported underground laboratory, the DOE now supports  
 4 the operation of the facility in addition to state and private funding. Both the NSF and the DOE  
 5 support experiments at the site.

6 Access to the underground areas has been reestablished and the primary access rehabilitated and  
 7 improved. The facility has been stabilized and the accumulated underground water has been pumped  
 8 out below 5,680 ft. The area around the Davis cavern at the 4850L, named for the late Ray Davis,  
 9 has been enlarged and adapted primarily for current and next-generation dark matter and neutri-  
 10 noless double-beta decay experiments. This upgraded area of the 4850L is now called the Davis  
 11 Campus. Additional science efforts are located throughout the facility, including an ultrapure de-  
 12 tector development laboratory, geophysics and geological efforts, and a public outreach program.  
 A 3D schematic highlighting the planned development of the 4850L is shown in Figure 3.10. The

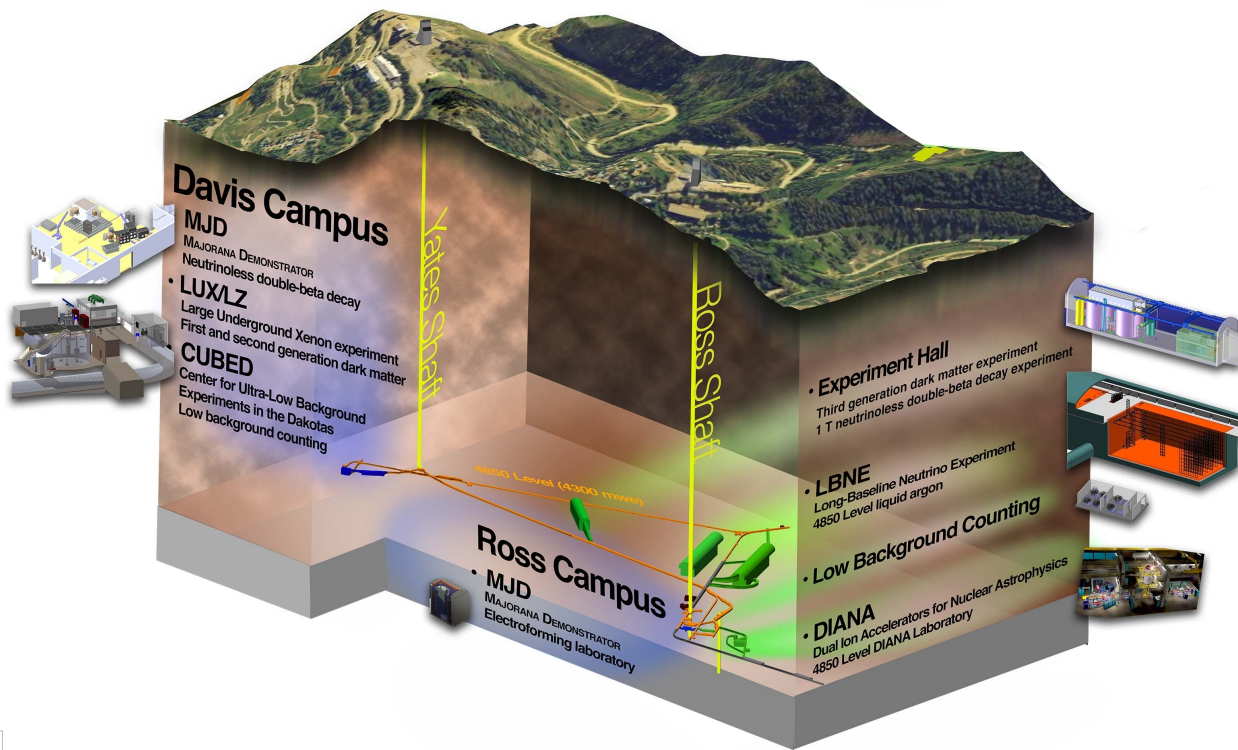
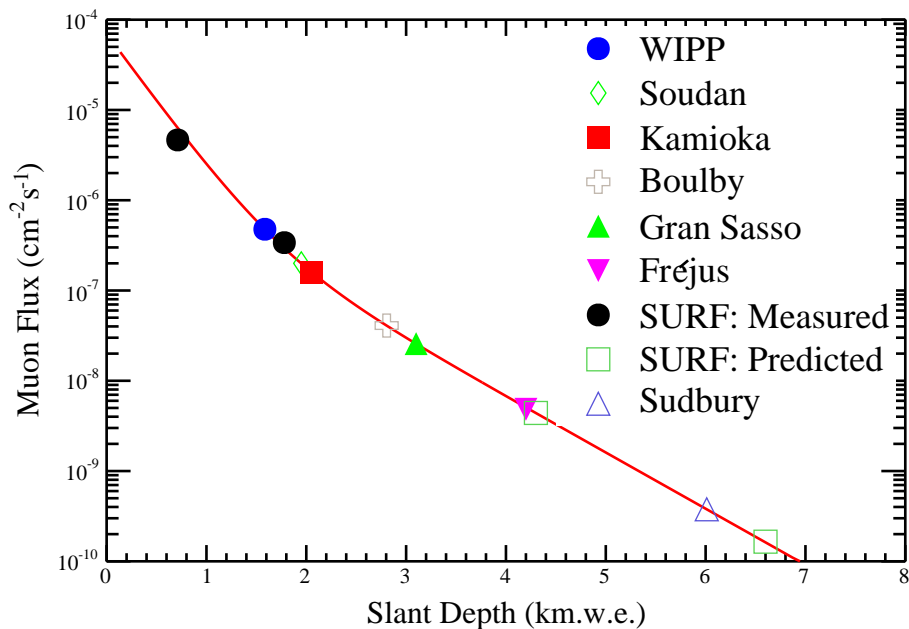


fig:48501

**Figure 3.10:** Layout of experiments at the 4,850-ft level in the Sanford Underground Research Facility

13  
 14 LBNE far detector will be located in new excavated spaces near the bottom of the Ross Shaft, about  
 15 1 km from the Davis Campus. The 4,850-ft depth makes it an extremely competitive location in  
 16 terms of cosmic-ray background suppression for undertaking the nucleon decay and supernova  
 17 neutrino studies that LBNE plans to address. Figure 3.11 shows the predicted cosmic-ray flux at  
 18 this site [112] as compared to other underground laboratories worldwide.



**Figure 3.11:** Closed green squares indicate the predicted integrated cosmic muon flux at the 4,850-ft level (left) and 8,000-ft level (right) at the Sanford Underground Research Facility (SURF) site. Values for other underground laboratories are also shown [112].

Another advantage of the 4850L Sanford Underground Research Facility site for LBNE is the low level of rock radioactivity that could contribute backgrounds to the supernova burst neutrino signal and other low-energy physics searches. It was found that the U/Th/K radioactivity for the underground bedrocks at Homestake is in general very low when compared to common construction materials such as concrete and shotcrete; some samples are in the sub-ppm levels. However, samples from Rhyolite intrusions, *a very small fraction of the total*, show a relatively high content of U, Th, and K more typical of the levels found in other laboratories, in particular those in granitic formations. Regions of potential Rhyolite intrusions have been identified and documented as shown in Figure 3.12. In some cases local shielding significantly mitigates the impact of the Rhyolite intrusions. Table 3.1 presents some of the assay results, obtained by direct gamma counting for rock samples from the mine, including those collected close to the 4850L [113].

The Large Underground Xenon (LUX) experiment is now operating in the cavern first excavated for Davis in the 1960s. LUX is the most sensitive detector yet to search for dark matter [114]. The Majorana Demonstrator experiment (MJD), also being installed in a newly excavated space adjacent to the original Davis cavern, will search for neutrinoless double-beta decay. Figure 3.13 shows four photographs of facilities and activities at the Sanford Underground Research Facility related to the LUX and MJD at the 4850L. The LBNE far detector will benefit from the common infrastructure being developed to house large experiments underground. The layout of the different proposed experiments at the 4850L, including the LBNE detector, is shown in Figure 3.10.

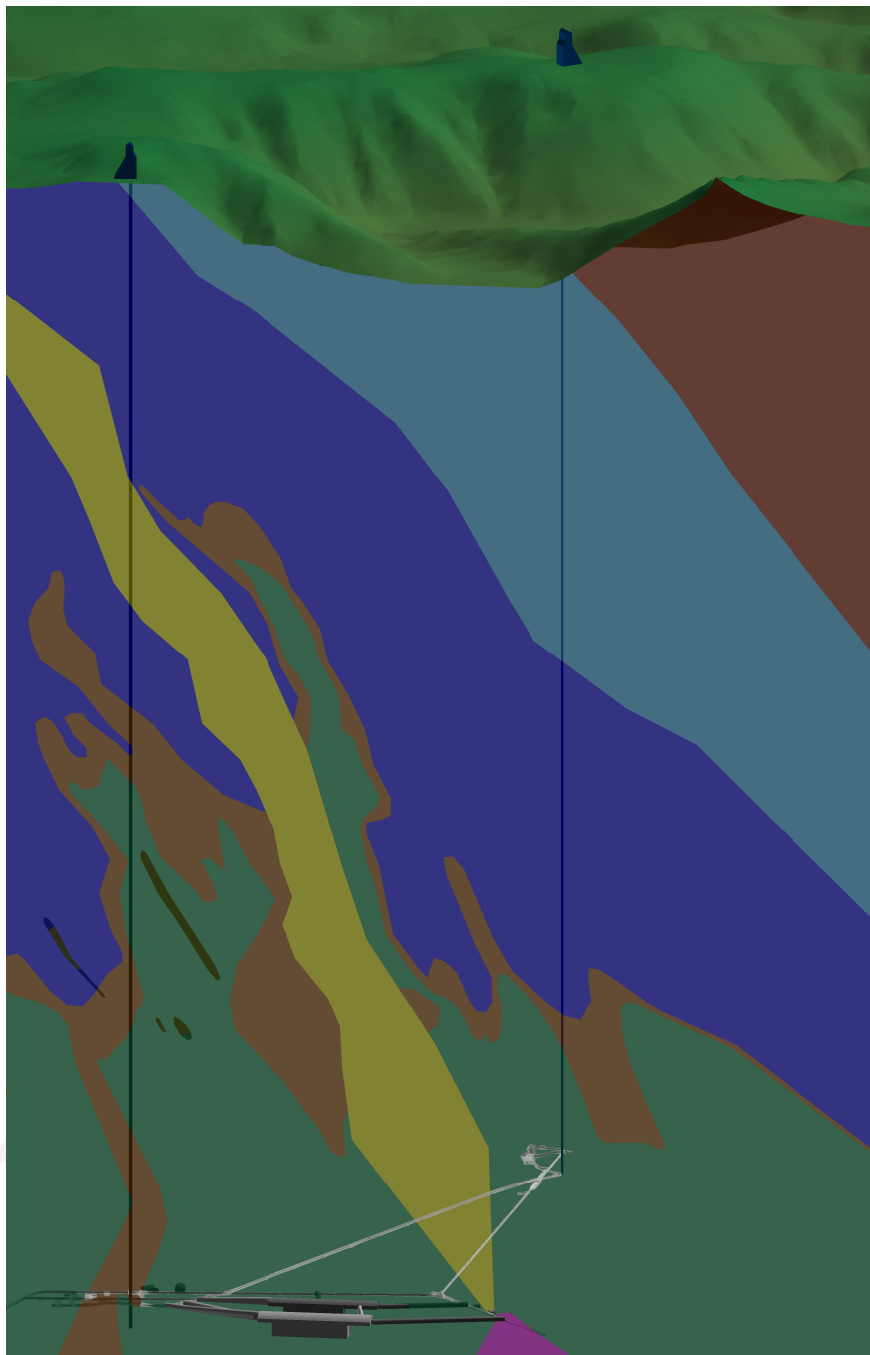


**Figure 3.12:** Geologic long-section of Sanford Underground Research Facility showing the main rock formations and the location of the LBNE cavern. The dark green rock is the Poorman formation, and the yellow areas indicate a projected rhyolite swarm. The proposed location of two LBNE detector caverns are shown in the foreground.

- 1 In addition to LBNE, LUX and MJD, the Sanford Underground Research Facility science pro-
- 2 gram for the coming five to ten years consists of the expansion of the LUX dark matter search,
- 3 the Center for Ultralow Background Experiments at Dakota (CUBED), and the geoscience instal-

**Table 3.1:** Partial U/Th/K assay results for Sanford Underground Research Facility rock samples. Overall errors estimated to be  $\sim 10\text{-}20\%$ . Also shown are results for various construction materials (shotcrete/concrete).

tab:rockrad

	Uranium (ppm) Ave. [Range]	Thorium (ppm) Ave. [Range]	Potassium (%) Ave. [Range]
<b>U/G Country Rock</b>	0.22 [0.06-0.77]	0.33 [0.24-1.59]	0.96 [0.10-1.94]
<b>Shotcrete</b>	1.89 [1.74-2.23]	2.85 [2.00-3.46]	0.88 [0.41-1.27]
<b>Concrete Blocks</b>	2.16 [2.14-2.18]	3.20 [3.08-3.32]	1.23 [1.27-1.19]
<b>Rhyolite Dike</b>	8.75 [8.00-10.90]	10.86 [8.60-12.20]	4.17 [1.69-6.86]

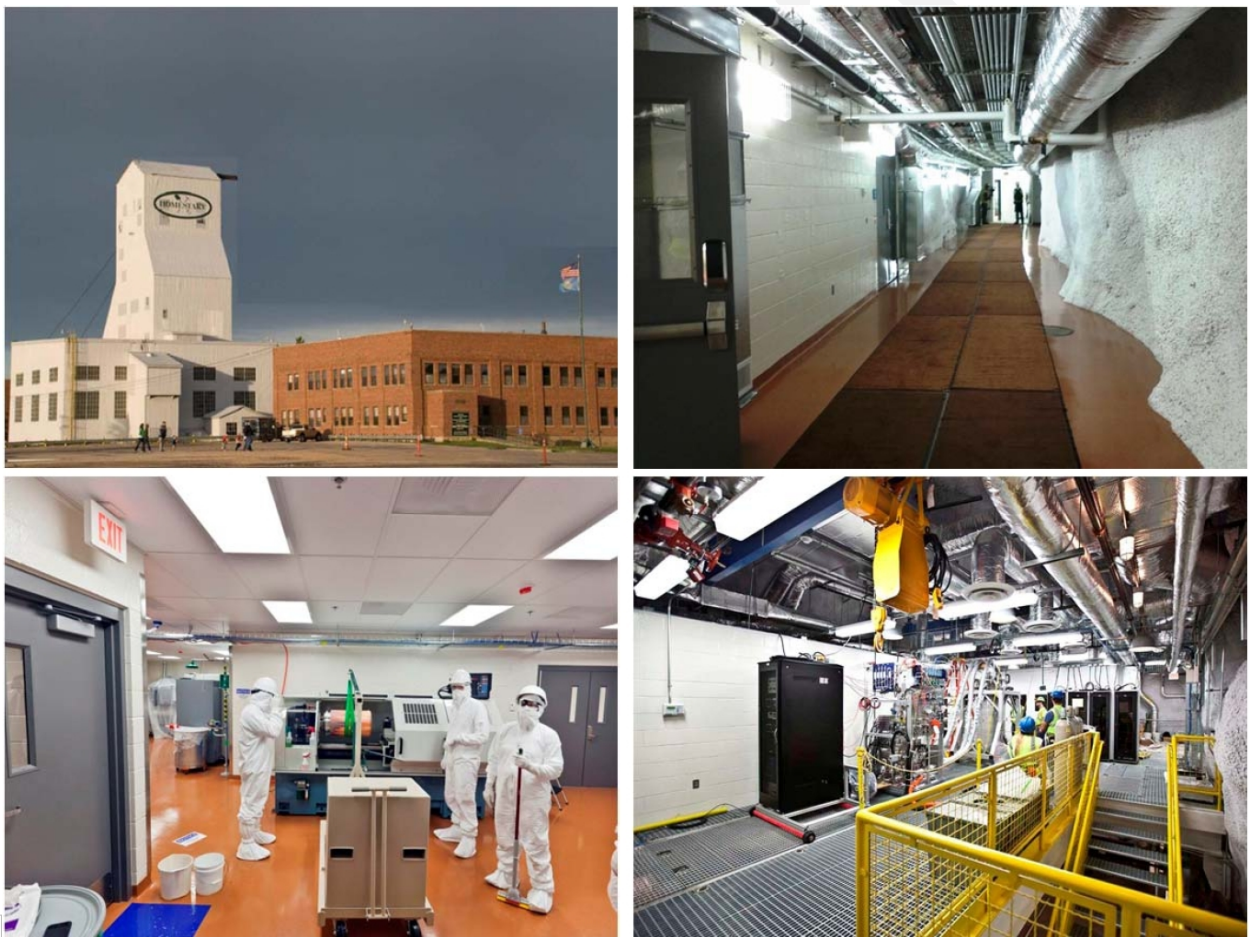
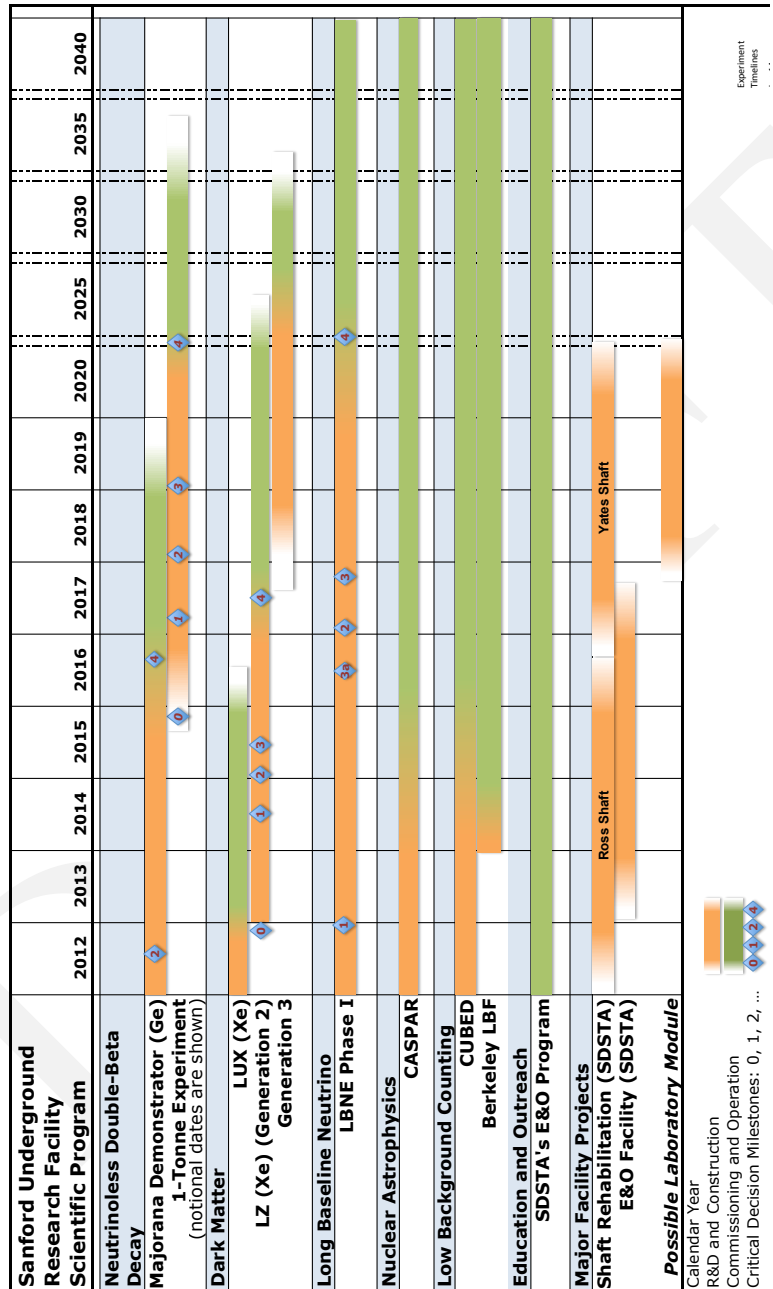


fig:lux

**Figure 3.13:** Sanford Underground Research Facility: Administration building and Yates shaft headframe (top left); corridor at 4,850 ft (1,480 m) depth leading to clean rooms and experimental halls (top right); billet of radiopure electroformed copper for the MJD experiment being placed on a lathe in a clean room at 4,850 ft depth (bottom left); LUX experiment at 4,850 ft depth (bottom right).

- 1 lations. Long-term plans are being developed to host a nuclear astrophysics program involving
- 2 underground particle accelerators (CASPAR and DIANA), and second- and third-generation dark

1 matter experiments. Figure 3.14 illustrates the long-term potential for experiments at the Sanford Underground Research Facility.



**Figure 3.14:** Timeline exploring the long-term potential of deep science experiments at the Sanford Underground Research Facility. Figure courtesy of Mike Headley, the Sanford Underground Research Facility.

## 3.4 Beamline

beamline-chap

The LBNE neutrino beamline, located at Fermilab, utilizes a conventional horn-focused neutrino beam produced from pion decay-in-flight, based largely on the highly successful NuMI beamline design:

- The primary beam utilizes 60- to 120-GeV protons from the Main Injector accelerator. The primary beamline is embedded in an engineered earthen embankment — a novel construction concept to reduce costs and improve radiological controls.
- The beamline is designed to operate at 1.2 MW and to support an upgrade to 2.3-MW operation.
- The beamline will generate a wide-band, high-purity beam, selectable for muon neutrinos or muon antineutrinos. Its tunable energies from 60 to 120 GeV will be well matched to the 1,300-km neutrino oscillation baseline.

The LBNE beamline facility will aim a beam of neutrinos toward the LBNE far detector located 1,300 km away at the Sanford Underground Research Facility. The beamline facility, which will be fully contained within Fermilab property, will consist of a primary (proton) beamline, a neutrino beamline, and conventional facilities to support the technical components of the primary and neutrino beamlines [22]. The LBNE beamline reference design parameters approved at CD-1 are summarized in Table 3.2. Improvements to this design that have been made or are being considered are described in this section, including the important change to an initial beam power of 1.2 MW, enabled by the planned PIP-II. The beamline needed for the full-scope LBNE will be fully realized in the first phase of LBNE and is upgradeable to 2.3 MW.

The primary beam, composed of protons in the energy range of 60-120 GeV, will be extracted from the MI-10 straight section of the Main Injector using single-turn extraction. The beam will then be transported to the target area within a beam enclosure embedded in an engineered earthen embankment (hill). The primary-beam transport section is designed for very low losses. The embankment's dimensions are designed to be commensurate with the bending strength of the required dipole magnets so as to provide a net  $5.8^\circ$  downward vertical bend to the neutrino beam (see Figures 3.15 and 3.16). The beamline is then buried by soil shielding that is placed at a stable angle of repose, resulting in the embankment final geometry.

For 120-GeV operation and with the MI upgrades implemented for the NO $\nu$ A experiment [117], the fast, single-turn extraction will deliver  $4.9 \times 10^{13}$  protons to the LBNE target in a 10- $\mu$ s pulse. With a 1.33-s cycle time, the beam power for NO $\nu$ A is 700 kW. Additional accelerator upgrades planned as PIP-II [14] will increase the protons per cycle to  $7.5 \times 10^{13}$  and reduce the cycle

**Table 3.2:** Partial set of parameters for the elements of the LBNE Beamline reference design at CD-1 from Volume 2 of the CDR [22]. The reference design described a 700 kW beam; it has since been changed to 1.2 MW. For each parameter the third column lists the range that had been studied prior to CD-1. Distances between beam elements are given from the upstream face (the end facing the proton beam) with respect to the upstream (front) face of Horn 1.

Element	Parameter	Range studied	Reference design value (700 kW)
<b>Proton Beam</b>	energy	60 GeV to 120 GeV	120 GeV
	protons per pulse		$4.9 \times 10^{13}$
	cycle time between pulses		1.33 s
	size at target $\sigma_{x,y}$	1 mm to 2 mm	1.3 mm
	duration		$1.0 \times 10^{-5}$ sec
	POT per year		$6.5 \times 10^{20}$
<b>Target</b>	material	graphite, beryllium hybrid [115]	graphite
	length	$\geq 2$ interaction lengths	966 mm
	profile	rectangular, round ( $r = 5$ mm to 16 mm)	rectangular 7.4 mm x 15.4 mm
	dist. from Horn 1 (front)	0 cm to -250 cm	-35 cm to -285 cm
<b>Focusing Horn 1 [116]</b>	shape	cylindrical-parabolic, double-parabolic	double-parabolic (NuMI)
	length (focusing region)	2,500 mm to 3,500 mm	3,000 mm
	current	180 kA to 350 kA	200 kA
	minimum inner radius		9.0 mm
	maximum outer radius		174.6 mm
<b>Focusing Horn 2</b>	shape	double-parabolic	NuMI Horn 2
	length (focusing region)	3,000 mm to 4,000 mm	3,000 mm
	current	180 kA to 350 kA	200 kA
	minimum inner radius		39.0 mm
	maximum outer radius		395.4 mm
	dist. from Horn 1 (front)	4,000 mm to 10,000 mm	6,600 mm
<b>Decay Pipe</b>	length	200 m to 350 m	204 m
	radius	1.0 m to 3.0 m	2 m
	atmosphere	Air, He, vacuum	air at atm. pressure
	dist. from Horn 1 (front)	11 m to 23 m	17.3 m

- 1 time to 1.2 s, resulting in an initial beam power for LBNE of 1.2 MW. The LBNE beamline is
- 2 designed to support additional beam power upgrades beyond PIP-II, discussed in Section 3.2, that
- 3 can increase the beam power up to 2.3 MW. At 1.2-MW operation the accelerator and primary
- 4 beamline complex are expected to deliver  $11 \times 10^{20}$  protons per year to the target.
- 5 Approximately 85% of the protons interact with the solid target, producing pions and kaons that
- 6 subsequently get focused by a set of magnetic horns into a decay pipe where they decay into muons
- 7 and neutrinos (Figure 3.17). The neutrinos form a wide-band, sign-selected neutrino or antineutrino

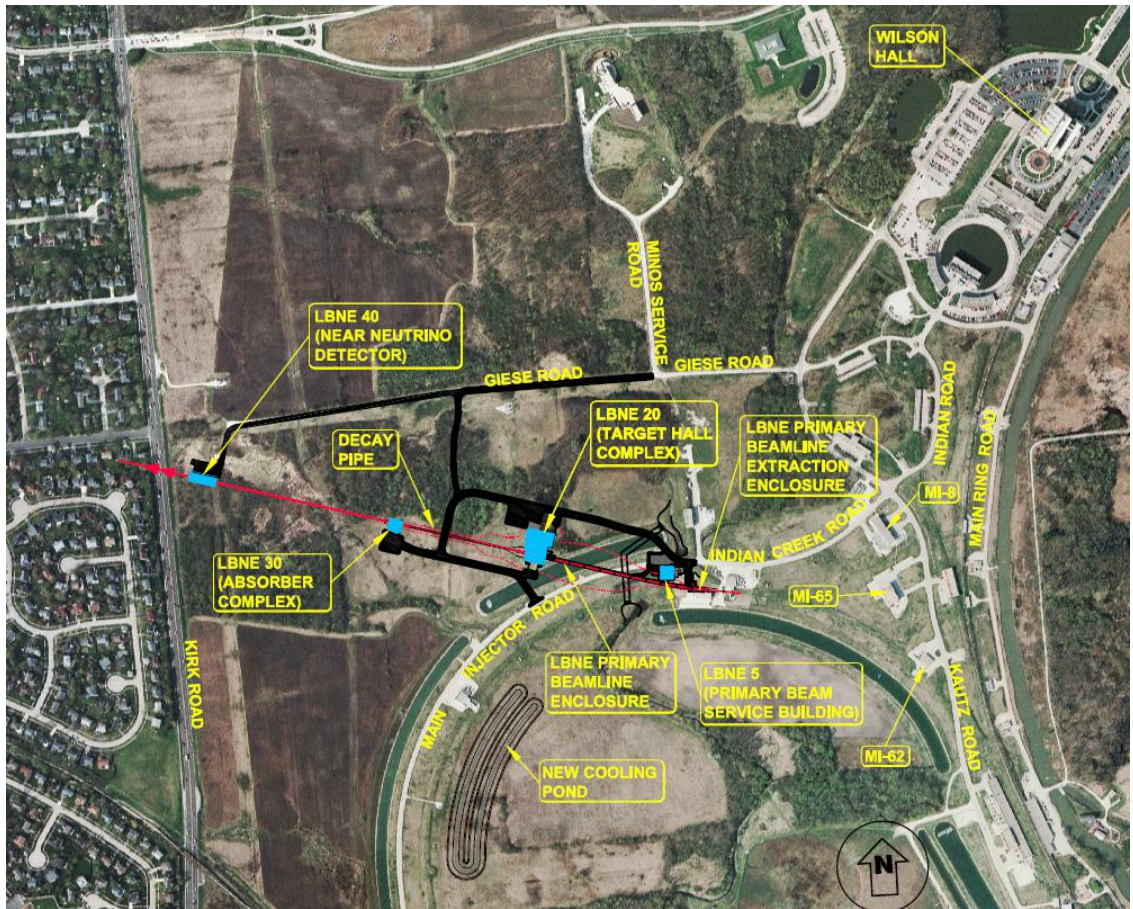
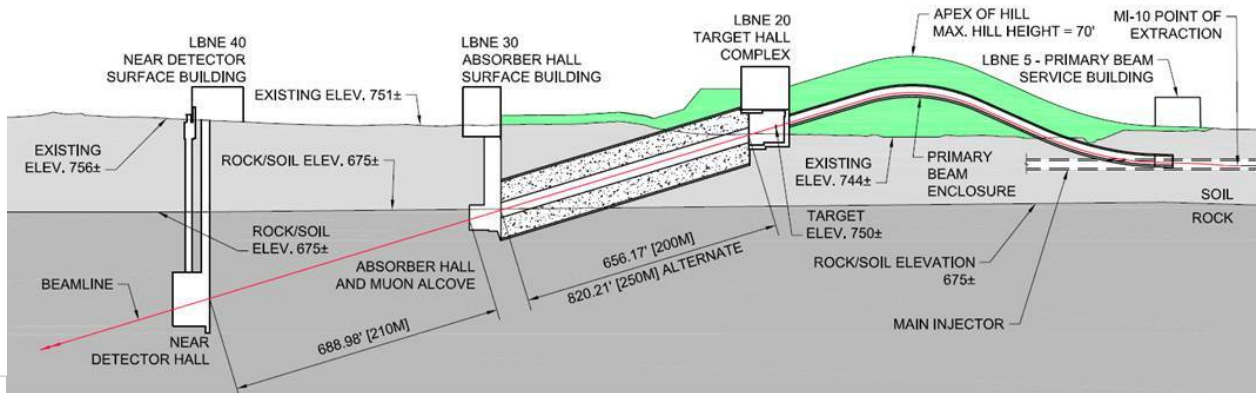


fig:nscf\_layout

**Figure 3.15:** Plan view of the overall Near Site Project layout showing locations for the LBNE Beamline extraction point from the MI, the primary beamline, target hall, decay pipe, absorber and near neutrino detector.



o\_elev\_overview

**Figure 3.16:** Longitudinal section of the LBNE Beamline facility. The beam enters from the right in the figure, the protons being extracted from the MI-10 extraction point at the Main Injector.

- 1 beam, designed to provide flux in the energy range of 0.5 to 5 GeV. This energy range will cover the  
 2 first and second neutrino-oscillation maxima, which for a 1,300-km baseline are at approximately  
 2.5 and 0.8 GeV, respectively.

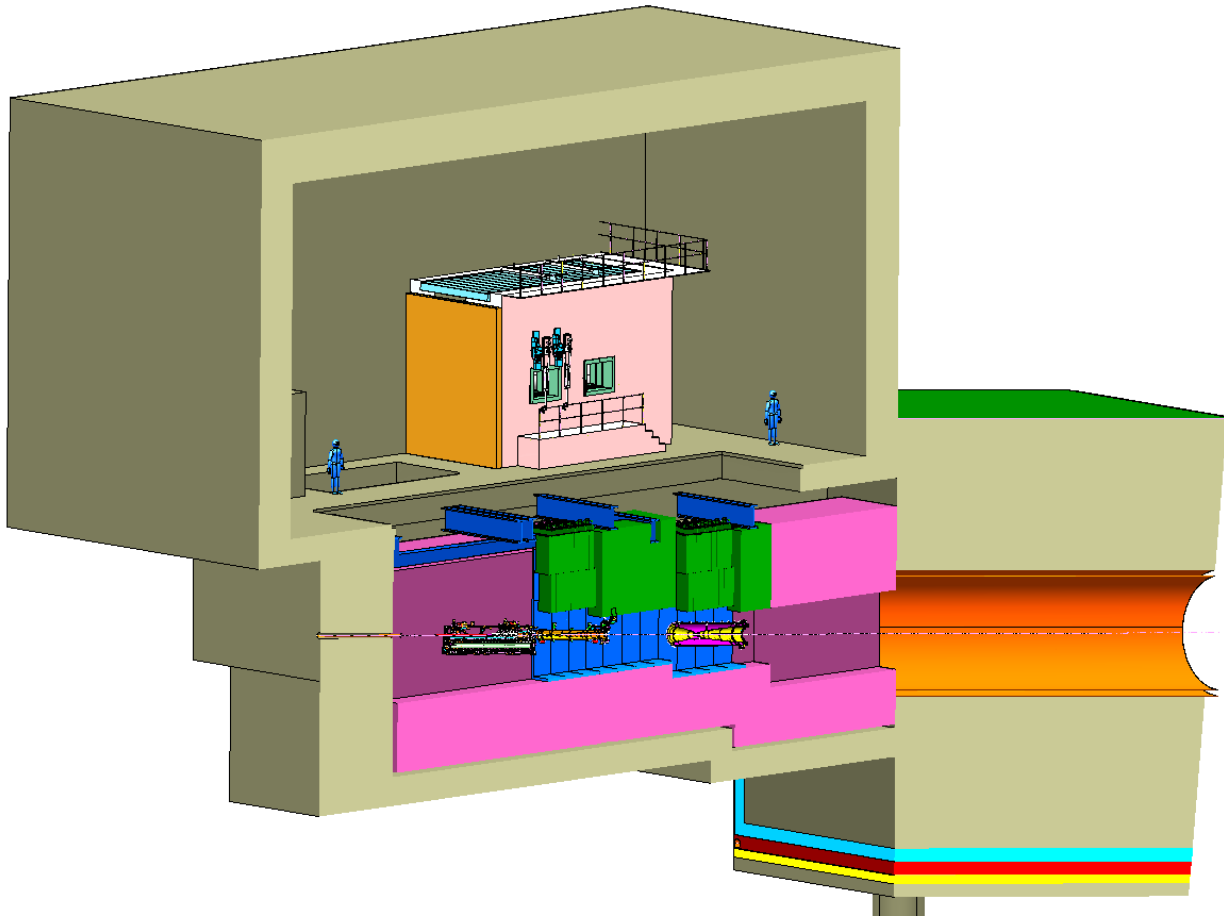


**Figure 3.17:** Schematic of the upstream portion of the LBNE neutrino beamline showing the major components of the neutrino beam. The target chase bulk steel shielding is shown in magenta. Inside the target chase from left to right (the direction of the beam) pointing downwards: the beam window, horn-protection baffle and target mounted on a carrier, the two toroidal focusing horns (the green custom shielding blocks are part of the horn support modules that are not shown) and the decay pipe (orange). Above the chase and to the right is the work cell for horn and target system repairs. The beige areas indicate concrete shielding.

- 3
- 4 The reference target design for LBNE is an upgraded version of the NuMI-LE (Low Energy) target  
 5 that was used for eight years to deliver beam to the MINOS experiment. The target consists of 47  
 6 segments, each 2 cm long, of POCO graphite ZXF-5Q. Focusing of charged particles is achieved  
 7 by two magnetic horns in series, the first of which partially surrounds the target. They are both  
 8 NuMI/NO $\nu$ A-design horns with double-paraboloid inner conductor profiles. The NuMI/NO $\nu$ A-  
 9 design horns currently operate at 185 kA to 200 kA. The horns have been evaluated and found to  
 10 be operable with currents up to 230 kA but the striplines that supply the horn currents are still under  
 11 evaluation. Additional development of the target and horns is required to adapt the existing designs

1 from the 700-kW beam power used by NO $\nu$ A to 1.2 MW for LBNE. The horn current polarity can  
 2 be changed to selectively focus positive or negative hadrons, thus producing high purity ( $> 90\%$   
 3 in oscillation region)  $\nu_\mu$  or  $\bar{\nu}_\mu$  beams. Each beam polarity will have a  $< 10\%$  contamination of  
 4 neutrinos of the “wrong sign” in the oscillation energy region ( $\bar{\nu}$ 's in the  $\nu$  beam and vice-versa)  
 5 from decays of wrong-sign hadrons that propagate down the center of the focusing horns — where  
 6 there is no magnetic field — into the decay volume. In addition, a  $\leq 1\%$  contamination of  $\nu_e$   
 7 and  $\bar{\nu}_e$  in the  $\nu_e$  appearance signal region is produced by the decays of tertiary muons from pion  
 8 decays, and decays of kaons. The neutrino flux components from the LBNE CD-1 beamline design  
 produced using a full GEANT4 simulation of both horn polarities are shown in Figure 3.18. The

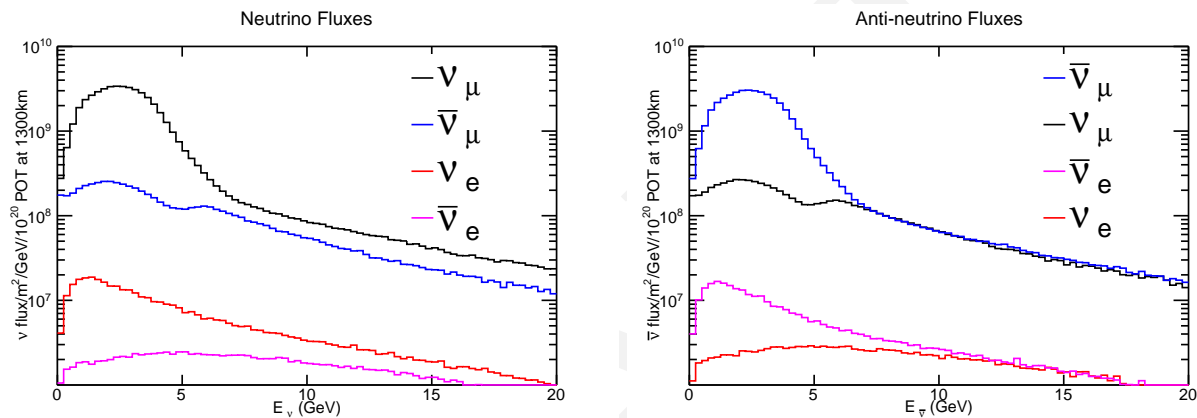


fig:cdflux

**Figure 3.18:** The neutrino beam fluxes (top) and antineutrino beam fluxes (bottom) produced by a Geant4 simulation of the LBNE beamline. The horn current assumed is 200 kA, the target is located  $-35$  cm from the front face of horn 1, the decay pipe is air-filled, 4 m in diameter and 204 m in length.

9  
 10 beamline design provides a wide-band neutrino beam with a peak flux at 2.5 GeV, which matches  
 11 the location of the first  $\nu_\mu \rightarrow \nu_e$  oscillation maximum. The NuMI reference target design used for  
 12 LBNE allows the target to be moved with respect to Horn 1. The location of the upstream face  $\S$   
 13 of the target with respect to the upstream face of Horn 1 can be varied from  $-35$  cm (default  
 14 location) to  $-2.85$  m, thus the LBNE beamline can produce a wide range of beam spectra. Three  
 15 possible far-site beam spectra, produced by moving the target from  $-35$  cm (low-energy) to  $-1.5$  m  
 16 (medium-energy) to  $-2.5$  m (high energy) are shown in Figure 3.19.

17 The decay volume design for LBNE is a helium-filled, air-cooled pipe of circular cross section  
 18 with a diameter of 4 m and length from 204 m to 250 m optimized such that decays of the pions  
 19 and kaons result in neutrinos in the energy range useful for the experiment. A 250-m decay pipe is  
 20 the maximum length that will allow the near neutrino detector complex to fit within the Fermilab  
 21 site boundaries. At the end of the decay region, the absorber, a water-cooled structure of aluminum  
 22 and steel, is designed to remove any residual hadronic particles; it must absorb a large fraction of  
 23 the incident beam power of up to 2.3 MW. Instrumentation immediately upstream of the absorber

$\S$ The proton beam direction determines the upstream and downstream conventions. The upstream (front) face of Horn 1 is therefore the Horn 1 face closest to the proton beam window.

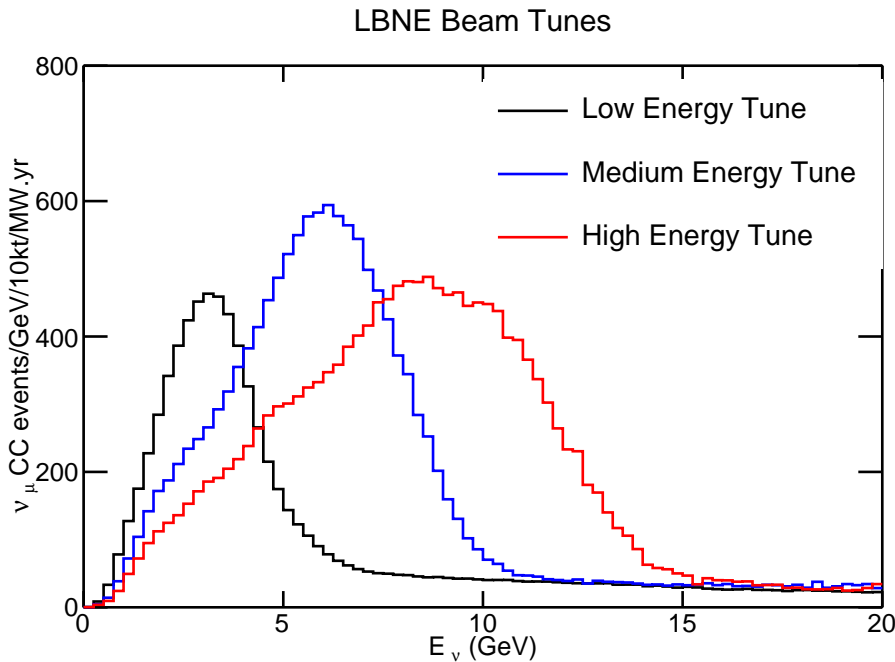


**Figure 3.19:** Event rates at the LBNE far detector in the absence of oscillations from a 120 GeV proton beam for several target positions relative to Horn 1. The black curve the default low-energy tune (LE) where the upstream face of the target is located  $-35$  cm from the front face of Horn 1, the blue curve is a sample medium-energy (ME) tune with the target located  $-1.5$  m from Horn 1 and the red curve is the high energy tune (HE) with the target located  $-2.5$  m upstream of Horn 1. The horn current assumed is 200 kA, the decay pipe is air-filled, 4 m in diameter and 204 m in length.

1 measures the transverse distribution of the resultant hadronic showers to monitor the beam on a  
2 pulse-by-pulse basis.

3 An array of muon detectors in a small alcove immediately downstream of the absorber measures  
4 tertiary-beam muons and thereby indirectly provides information on the direction, profile and flux  
5 of the neutrino beam. This will be described in Section 3.5.

6 The beamline conventional facilities include the civil construction required to house the beam-  
7 line components in their planned layout as shown in Figures 3.15 and 3.16. Following the beam  
8 from southeast to northwest, or roughly from right to left in Figure 3.15, the elements include the  
9 underground Extraction Enclosure, the Primary Beam Enclosure (inside the embankment) and its  
10 accompanying surface-based Service Building (LBNE 5), the Target Complex (LBNE 20) located  
11 in the embankment, the Decay Pipe, the underground Absorber Hall with the muon alcove, and  
12 its surface-based Service Building (LBNE 30). The embankment will need to be approximately  
13 290 m long and 18 m above grade at its peak. The planned near neutrino detector facility is located  
14 as near as is feasible to the west site boundary of Fermilab, along the line-of-sight indicated in red  
15 in Figure 3.15.

16 The parameters of the beamline facility were determined taking into account several factors includ-

ing the physics goals, the Monte Carlo modeling of the facility, spatial and radiological constraints and the experience gained by operating the NuMI facility at Fermilab. The relevant radiological concerns, prompt dose, residual dose, air activation and tritium production have been extensively modeled and the results implemented in the system design. The beamline facility design described above minimizes expensive underground construction and significantly enhances capability for ground-water radiological protection. In general, components of the LBNE beamline system that cannot be replaced or easily modified after substantial irradiation are being designed for 2.3-MW operation. Examples of such components are the shielding of the target chase and decay pipe, and the absorber with its associated shielding.

The following LBNE beamline design improvements beyond the CD-1 conceptual design are being assessed:

- An increase in the length of the decay pipe up to 250 m (the maximum length allowed by the existing Fermilab site boundaries), and also possibly an increase in its diameter up to 6 m. Increases to the decay pipe size would require additional cost of the order several tens of millions of dollars. Increasing the length of the decay pipe from 200 to 250 m increases the overall event rate in the oscillation region by 12%. Increases in the decay pipe diameter produce a 6% increase in the low-energy neutrino event rate as shown in Table 3.3.
- It has recently been decided to fill the decay pipe with helium instead of air. The total  $\nu_\mu$  event rate increases by about 11%, with a decrease in  $\bar{\nu}$  contamination in the neutrino beam. Introducing helium in the decay pipe requires the design and construction of a decay pipe window.
- An increase in the horn current of the horns by a modest amount (from 200 kA to 230 kA); this is expected to increase the neutrino event rates by about 10-12% at the first oscillation maximum [118]. A Finite Element Analysis simulation and a cooling test of the horns are underway to evaluate this option.
- Use of an alternate material to the POCO graphite for the target to increase the target longevity. This would involve additional R&D effort and design work. A beryllium target, for example, could be made shorter, potentially improving the horn focusing.
- Development of more advanced horn designs that could boost the low-energy flux in the region of the second oscillation maximum. It should be noted that the target and horn systems can be modified or replaced even after operations have begun if improved designs enable higher beam flux.

Table 3.3 summarizes the impact of the beam design improvements after CD-1 and the additional costs required. Together, the changes are anticipated to result in an increase of  $\sim 50\%$  in the  $\nu_e$  appearance signal rate at the far detector. A 30% increase in signal event rate at the far detector

- 1 can be achieved for  $< 10$  M\$ without changing the CD-1 decay pipe size (4 m diameter  $\times$  204 m  
 2 length) by changing from an air-filled to a helium-filled decay pipe. Increasing the decay pipe size  
 3 to 6 m diameter  $\times$  250 m length would result in an additional 15% increase in flux but would cost  
 an additional  $\sim 47$  M\$ — this includes the cost of a redesigned absorber.

**Table 3.3:** Impact of the beam improvements under study on the neutrino  $\nu_\mu \rightarrow \nu_e$  CC appearance rates at the far detector in the range of the first and second oscillation maxima, shown as the ratio of appearance rates: the “improved” rate divided by the rate from the beam design described in the Conceptual Design Report.

Changes	0.5 to 2 GeV	2 to 5 GeV	Extra Cost
Horn current 200 kA $\rightarrow$ 230 kA	1.00	1.12	none
Proton beam 120 $\rightarrow$ 80 GeV at constant power	1.14	1.05	none
Target NuMI-style graphite $\rightarrow$ Be cylinder	1.10	1.00	$< 1$ M\$
Decay pipe Air $\rightarrow$ He	1.07	1.11	$\sim 8$ M\$
Decay pipe diameter 4 m $\rightarrow$ 6 m	1.06	1.02	$\sim 17$ M\$
Decay pipe length 200 m $\rightarrow$ 250 m	1.04	1.12	$\sim 30$ M\$
<b>Total</b>	<b>1.48</b>	<b>1.50</b>	

### 3.5 Near Detector

A high-resolution near neutrino detector located approximately 500 m downstream of the LBNE neutrino production target, as shown in Figure 3.16, is a key component of the full LBNE scientific program:

- The near neutrino detector will enable the LBNE experiment to achieve its primary scientific goals — in particular discovery-level sensitivity to CP violation and high-precision measurements of the neutrino oscillation parameters, including the unknown CP-violating phase,  $\delta_{CP}$ .
- A rich program of LBNE physics measurements at the near detector will exploit the potential of high-intensity neutrino beams as probes of new physics.

To achieve the precision required to make a significant advancement in the measurement of neutrino oscillation parameters over current experiments and to reach the desired  $5\sigma$  sensitivity to CP violation (discussed in Chapters 4 and 7), LBNE will need to measure the unoscillated flux spectrum, to a few percent, for all neutrino species in the beam:  $\nu_\mu$ ,  $\nu_e$ ,  $\bar{\nu}_\mu$  and  $\bar{\nu}_e$ . This requires a high-resolution, magnetized near neutrino detector with high efficiency for identifying and measuring electrons and muons. To measure the small  $\nu_e$  contamination in the beam with greater precision,

1 the detector would need to be able to distinguish  $e^+$  from  $e^-$ ; this would require a low-density  
 2 detector with a commensurately long physical radiation length. In addition, use of an argon target  
 3 nucleus — similar to the far detector — would allow cancellation of systematic errors. A reference  
 4 design has been developed for a near neutrino detector that will meet these requirements; in par-  
 5 ticular it will measure the neutrino event rates and cross sections on argon, water and other nuclear  
 6 targets for both  $\nu_e$  and  $\nu_\mu$  charged current (CC) and neutral current (NC) scattering events.

7 In addition to the near neutrino detector, a sophisticated array of muon detectors will be placed just  
 8 downstream of the absorber. The muon detectors, shown in Figure 3.20, detect mostly muons from  
 9 the two-body decays of  $\pi^{+(-)} \rightarrow \mu^{+(-)}\nu_\mu(\bar{\nu}_\mu)$  in the beamline, thus the measured muon and  $\nu_\mu$  flux  
 10 distributions are highly correlated. The ionization chamber array will provide pulse-by-pulse mon-  
 11 itoring of the beam profile and direction. The variable-threshold gas Cherenkov detectors will map  
 12 the energy spectrum of the muons exiting the absorber on an on-going basis. The stopped muon  
 13 detectors will sample the lowest-energy muons, which are known to correlate with the neutrino  
 14 flux above 3 GeV — equivalent to about half the neutrino flux near the first oscillation maximum  
 15 — and a decreasing fraction of it at lower energy. This system, together with the existing level of  
 16 understanding of the similar NuMI beam and experience in previous neutrino oscillation experi-  
 17 ments, will provide additional constraints on the understanding of the neutrino beam, and will thus  
 18 support and complement the near neutrino detector measurements.

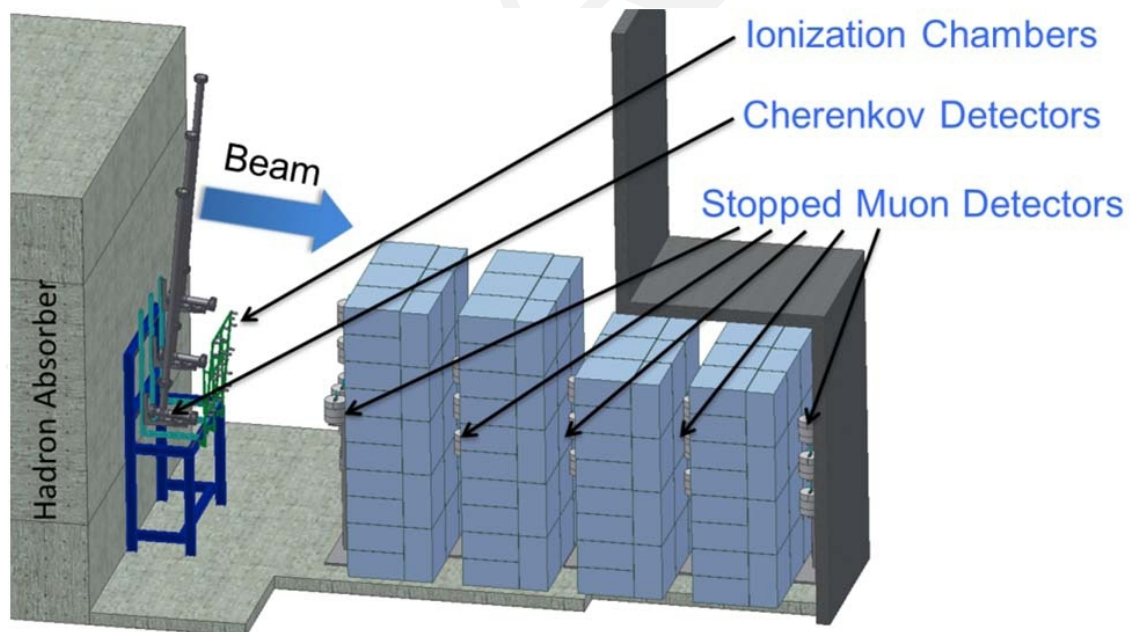
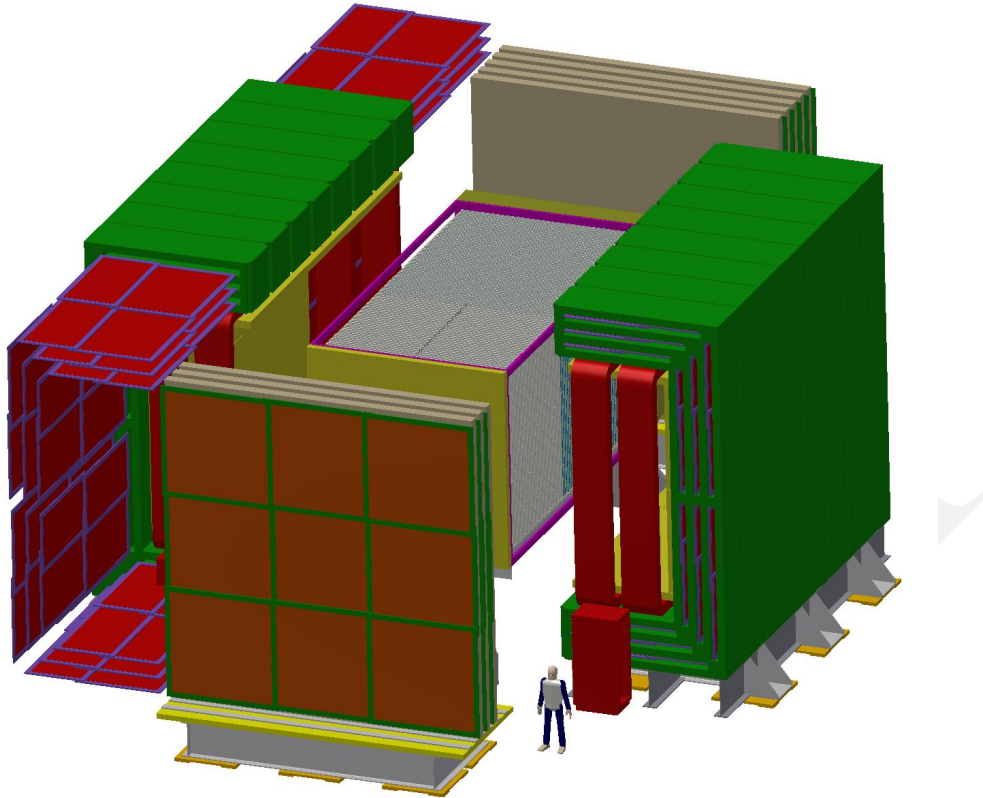


fig:muons

**Figure 3.20:** System of tertiary-beam muon detectors, located downstream of the LBNE beamline absorber, for monitoring the muon flux from the LBNE beamline.

19 The reference design for the near neutrino detector is a fine-grained tracker [119], illustrated in Fig-  
 20 ure 3.21. It consists of a  $3 \times 3 \times 7.04 \text{ m}^3$  straw-tube tracking detector (STT) and electromagnetic  
 21 calorimeter inside of a 0.4-T dipole magnet, illustrated in Figure 3.22, and resistive plate chambers



**Figure 3.21:** The LBNE near neutrino detector reference design with the dipole magnet open to show the straw-tube tracker (grey) and electromagnetic calorimeter (yellow). RPCs for muon identification (red squares) are embedded in the yoke steel and up- and downstream steel walls.

1 for muon identification (MuID) located in the steel of the magnet and also upstream and down-  
 2 stream of the tracker. High-pressure argon gas targets, as well as water and other nuclear targets,  
 3 are embedded in the upstream part of the tracking volume. The nominal active volume of the STT  
 4 corresponds to eight tons of mass. The STT is required to contain sufficient mass of argon gas in  
 5 tubes (Al or composite material) to provide at least a factor of ten more statistics than expected in  
 6 the far detector. Table 3.4 summarizes the performance for the fine-grained tracker's configuration,  
 7 and Table 3.5 lists its parameters.

8 Figure 3.22 shows the locations of the electromagnetic calorimeter and MuID next to the magnet  
 9 steel and magnet coils. The fine-grained tracker has excellent position and angular resolutions due  
 10 to its low-density ( $\sim 0.1 \text{ g/cm}^3$ ), high-precision STT. The low density and magnetic field allow it to  
 11 distinguish  $e^+$  from  $e^-$  on an event-by-event basis. The high resolution is important for determining  
 12 the neutrino vertex and determining whether the neutrino interaction occurs in a water or argon  
 13 target. Electrons are distinguished from hadrons using transition radiation.

14 The design of the near neutrino detector is the subject of study by the LBNE Collaboration, and  
 15 alternatives such as a magnetized liquid argon TPC will be investigated further. A detailed descrip-

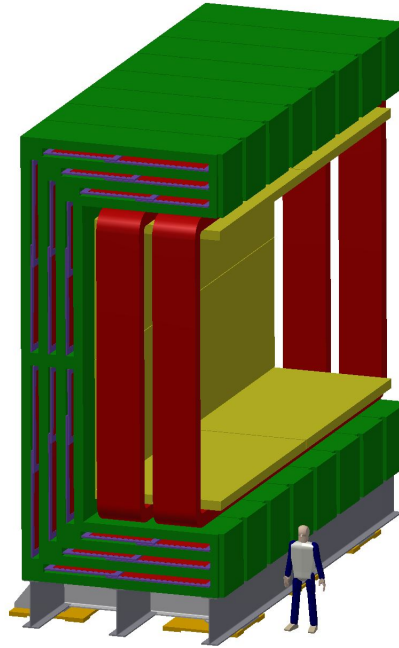


**Figure 3.22:** A schematic drawing of the ECAL (yellow modules) next to the magnet coils (red) and MuID (blue modules) interspersed in the magnet steel (green).

**Table 3.4:** Summary of the performance for the fine-grained tracker configuration

Performance Metric	Value
<b>Vertex resolution</b>	0.1 mm
<b>Angular resolution</b>	2 mrad
<b><math>E_e</math> resolution</b>	5%
<b><math>E_\mu</math> resolution</b>	5%
<b><math>\nu_\mu/\bar{\nu}_\mu</math> ID</b>	Yes
<b><math>\nu_e/\bar{\nu}_e</math> ID</b>	Yes
<b>NC<math>\pi^0</math>/CCe rejection</b>	0.1%
<b>NC<math>\gamma</math>/CCe rejection</b>	0.2%
<b>NC<math>\mu</math>/CCe rejection</b>	0.01%

tion of the fine-grained tracker can be found in [120], and descriptions of it and the alternative LArTPC design are presented in the March 2012 LBNE CDR (Volume 3 of [23]).

High-intensity neutrino beams can be used as probes of new physics and given the broad energy range of the LBNE beam, a diverse range of physics measurements is possible in the high-resolution near neutrino detector. These potentially wide-ranging physics measurements would complement other physics programs, such as those at Jefferson Laboratory, that are using proton, electron or ion beams from colliders and fixed-target facilities. A detailed discussion of the physics capabilities of a high-resolution near detector is presented in Chapter 7 and in [120].

Table 3.5: Parameters for the fine-grained tracker.

Parameter	Value
STT detector volume	$3 \times 3 \times 7.04 \text{ m}^3$
STT detector mass	8 tons
Number of straws in STT	123,904
Inner magnetic volume	$4.5 \times 4.5 \times 8.0 \text{ m}^3$
Targets	1.27-cm thick argon ( $\sim 50 \text{ kg}$ ), water and others
Transition radiation radiators	2.5 cm thick
ECAL $X_0$	10 barrel, 10 backward, 18 forward
Number of scintillator bars in ECAL	32,320
Dipole magnet	2.4-MW power; 60-cm steel thickness
Magnetic field and uniformity	0.4 T; $< 2\%$ variation over inner volume
MuID configuration	32 RPC planes interspersed between 20-cm thick layers of steel

## 3.6 Far Detector

The full-scope LBNE far detector is a liquid argon time-projection chamber of 34 kt fiducial mass located at the 4,850-ft level of the Sanford Underground Research Facility. The LArTPC technology allows for high-precision identification of neutrino flavors, offers excellent sensitivity to proton decay modes with kaons in the final state and provides unique sensitivity to electron neutrinos from a core-collapse supernova. The full detector size, and its location at a depth of 4,850 feet will enable LBNE to meet the primary scientific goals — in particular, to find evidence for CP violation over a large range of  $\delta_{\text{CP}}$  values, and to significantly advance proton-decay lifetime limits. Conceptual designs of the 34-kt underground detector are well developed.

The liquid argon TPC technology chosen for LBNE combines fine-grained tracking with total absorption calorimetry to provide a detailed view of particle interactions, making it a powerful tool for neutrino physics and underground physics such as proton decay and supernova-neutrino observation. It provides millimeter-scale resolution in 3D for all charged particles. Particle types can be identified both by their  $dE/dx$  and by track patterns, e.g., the decays of stopping particles. The modest radiation length (14 cm) is sufficiently short to identify and contain electromagnetic showers from electrons and photons, but long enough to provide good  $e/\gamma$  separation by  $dE/dx$  (one versus two minimum ionizing particles) at the beginning of the shower. In addition, photons can be distinguished from electrons emanating from an event vertex by the flight path before their first interaction. These characteristics allow the LArTPC to identify and reconstruct signal events with high efficiency while rejecting backgrounds to provide a high-purity data sample. The principal

design parameters of the full-scope LBNE LArTPC far detector are given in Table 3.6. tab: param-summ-larfd

**Table 3.6:** Principal design parameters of the full-scope LBNE LArTPC far detector from [24]. CDRv4

Parameter	Value
Total/Active/Fiducial Mass	50/40/34 kt
Number of Detector Modules (Cryostats)	2
Drift Cell Configuration within Module	3 wide $\times$ 2 high $\times$ 18 long drift cells
Drift Cell Dimensions	2 $\times$ 3.7 m wide (drift) $\times$ 7 m high $\times$ 2.5 m long
Detector Module Dimensions	22.4 m wide $\times$ 14 m high $\times$ 45.6 m long
Anode Wire Spacing	$\sim$ 5 mm
Wire Planes (Orientation from vertical)	Grid (0°), Induction 1 (45°), Induction 2 (-45°) Collection (0°)
Drift Electric Field	500 V/cm
Maximum Drift Time	2.3 ms

1

2 Scalability has been a design consideration of critical importance for the LBNE Project, and for  
3 the far detector in particular, since the Project's inception in 2009. A 10-kt LArTPC far detector  
4 configuration has been identified as the minimal initial configuration of LBNE that can make sig-  
5 nificant advances towards the primary scientific goals of LBNE. Because of the scalability built  
6 into the LBNE design, other, more capable, configurations could be accomplished either in the  
7 initial phase with the identification of additional resources, or at a later stage.

8 Other important considerations for the construction of LBNE's large LArTPC far detector include:

- 9 1. cryogenic safety and the elimination of hazards associated with large cryogenic liquid vol-  
10 umes
- 11 2. attainment of stringent argon purity requirements with respect to electronegative contami-  
12 nants (e.g.,  $< 0.2$  ppb O<sub>2</sub> concentration)
- 13 3. ease of transport and assembly of TPC mechanical systems
- 14 4. efficient deployment of high-sensitivity/low-noise electronics for readout of the ionization  
15 signal

16 The far detector complex for both the first-phase ( $\geq 10$ -kt) and full 34-kt options will be outfitted  
17 with two separately instrumented detector vessels instead of a single, larger vessel — an approach  
18 which has several benefits. First, this design enables each cryostat and TPC to be filled and com-  
19 missioned while the other remains available for liquid storage, allowing for repairs to be made after  
20 the start of commissioning, should that be necessary. Secondly, it allows deployment of TPCs of  
21 different designs. This would enable, for example, international partners to contribute a detector

1 of an alternate design, based on their own experience, or one that would emphasize a particular  
2 research interest.

3 The detector vessels will be constructed using technology standards from the liquefied natural gas  
4 (LNG) industry. With similar requirements and geometries, adaptation of industrial LNG cryostat  
5 design provides a high-performance, extensively tested approach to the challenge of liquid argon  
6 containment for LBNE. The cryostats in large LNG tanker ships are constructed using a thin (1–2  
7 mm), polished, stainless steel inner membrane surrounded by thick foam passive insulation. With  
8 stainless steel as the only wetted surface, this is an inherently clean design, ideal for liquid argon  
9 detectors where high purity is essential.

10 The underground detector placement at the 4850L of the Sanford Underground Research Facility  
11 was studied in detail during the conceptual design phase of LBNE and presented at the Fermilab  
12 Director’s Independent Conceptual Design Review in March of 2012 [16]. Significant effort has  
13 been invested to minimize the (dominant) cost of the far site conventional facilities.

### 14 3.6.1 The 10-kt Detector Design

- The far detector for the initial phase of LBNE will have *at least* 10 kt fiducial mass. This mass allows for high probability determination of the neutrino mass hierarchy and can provide evidence for CP violation, if this effect is large.
- The detector needs to be located deep underground to provide sensitivity for proton decay searches in the kaon modes and for measuring neutrinos from potential supernovae in the galaxy.
- A conceptual design for a 10-kt LArTPC has been developed, thoroughly reviewed and found to be sound.
- LBNE is working with international partners in an effort to deploy a more massive far detector in the initial phase.

15  
16 A conceptual design for the initial 10-kt far detector for the first-phase LBNE Project has been  
17 developed that is easily scalable to larger detectors. Many of the detector elements, in particular  
18 the modular TPC design and readout electronics, utilize full-scale modules and designs that can  
19 easily be replicated in larger numbers to instrument a larger detector. This design consists of two  
20 9.4-kt liquid argon vessels [24], each designed to hold a 5-kt fiducial-mass LArTPC as shown in  
21 Figure 3.23.

22 The cryogenics systems for the 10-kt detector will consist of two 85-kW liquid nitrogen liquefac-

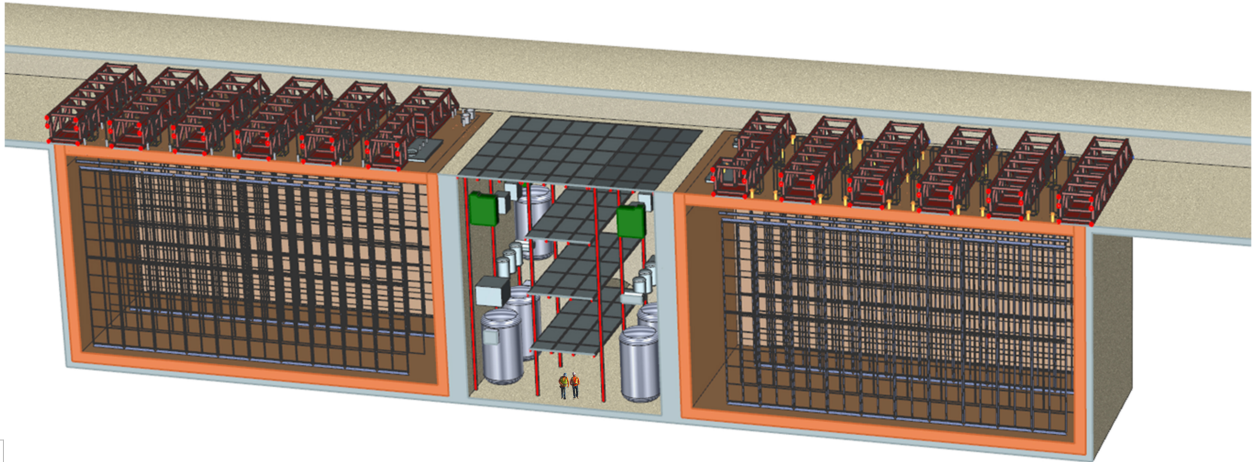


fig:10kton

**Figure 3.23:** 3D view of the 10-kt far detector showing a lateral cross section of the two 5-kt fiducial-mass LArTPC vessels

1 tion plants, a liquid argon receiving station, a liquid argon circulation system with liquid purifiers,  
 2 and a liquid argon re-condensing system. All the cryogenics systems are similar to large-scale  
 3 systems found in industrial applications.

4 The LBNE TPC design for the 10-kt detector consists of three rows of cathode plane assemblies  
 5 (CPAs) interspersed with two rows of anode plane assemblies (APAs), similar to the layout concept  
 6 shown in Figure 3.24 bottom right, with readout electronics mounted directly on the APA frames  
 7 (Figure 3.24, left). These elements run the length of a cryostat module, save for space at one  
 8 end allocated to the cryogenics systems. A field cage for shaping the electric field covers the  
 9 top, bottom, and ends of the detector. The spacing between the CPA and APA rows is 3.48 m  
 10 and the cathode planes will be operated at 173 kV, establishing a drift field of 500 V/cm and a  
 11 corresponding maximum drift time of 2.16 ms.

12 The APAs and CPAs are designed in a modular fashion as illustrated in Figure 3.24, top right.  
 13 Each APA/CPA is constructed with a support frame 2.5 m long and 7 m high; these dimensions are  
 14 chosen for ease of transportation to the detector site and installation within the cryostat. During  
 15 installation, two APAs are connected end-to-end to form a 14 m tall, 2.5 m long unit, which is  
 16 transported to its final position in the detector and suspended there using a rail system at the top  
 17 of the detector. Pairs of CPAs are installed in a similar fashion. This system of 2.5 m long detector  
 18 elements is easily scalable to any desired detector size. A total of 40 APAs and 60 CPAs per cryostat  
 19 are needed for the 10-kt detector design, configured as two rows of APAs, ten APA pairs long.

20 Three sense wire planes (two *induction* planes and one *collection* plane) with wire pitches of 4.8  
 21 mm are mounted on each side of an APA frame, for sensitivity to ionization signals originating  
 22 within the TPC cell on either side. The wires on these planes are oriented vertically (collection)

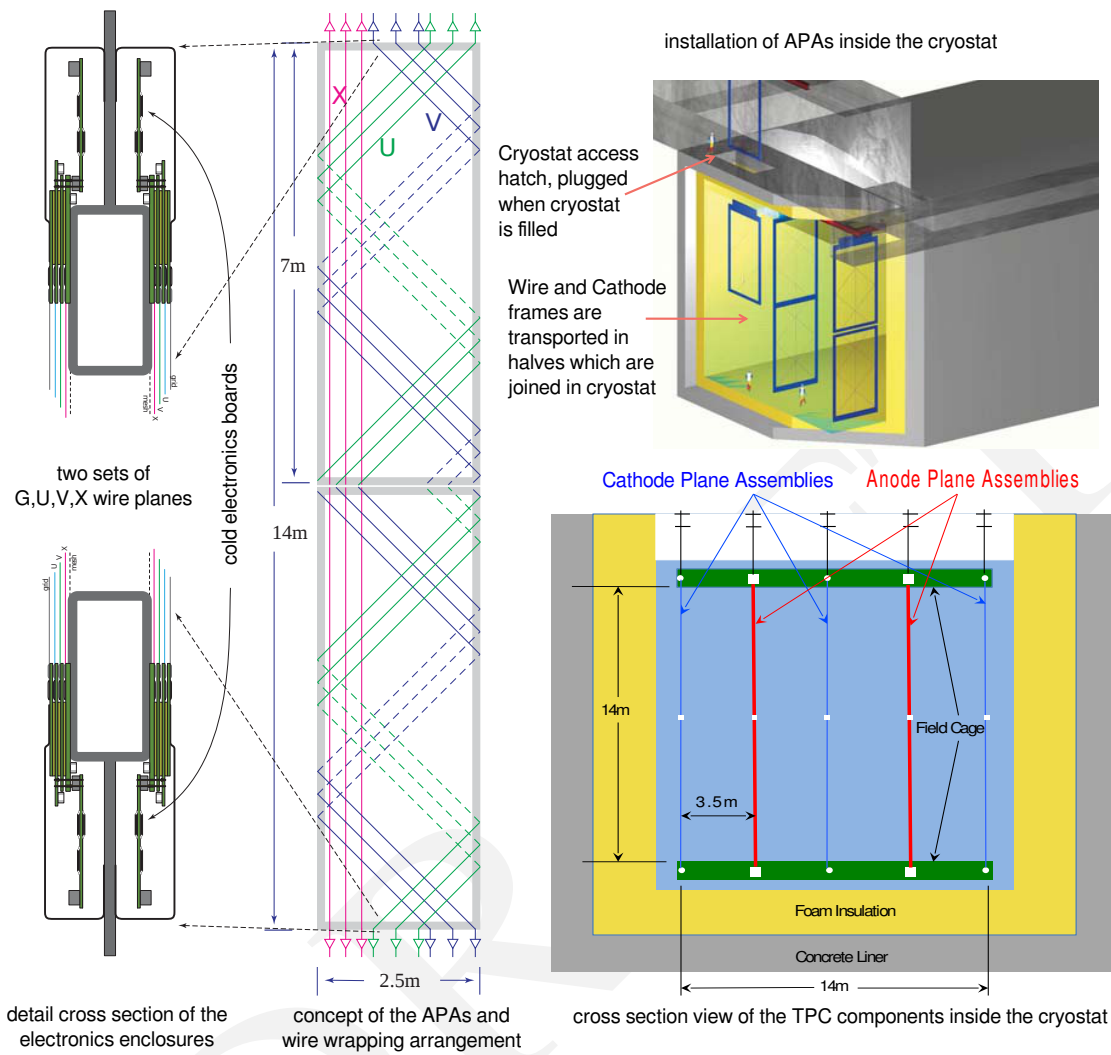


**Figure 3.24:** The LBNE TPC modular construction concept

- 1 and at  $\pm 45^\circ$  (induction)<sup>¶</sup>. The induction plane wires are wrapped around the APA frame, and are
- 2 therefore sensitive to charge arriving from either side of the APA, depending on where the charge
- 3 arrives along the length of the wires. This configuration allows placement of readout electronics
- 4 at the top and bottom of each two-APA unit. (Cables from the bottom APA are routed up through
- 5 the support frame, thereby eliminating any obstruction they would otherwise cause.) In this way,
- 6 adjacent APA-pairs can be abutted so as to minimize the uninstrumented region in the gaps between
- 7 them along the length of the detector.
- 8 Low-noise, low-power CMOS (Complementary Metal Oxide Semiconductor) preamplifier and

<sup>¶</sup>The current design uses a  $36^\circ$  orientation to remove hit assignment ambiguities.

1 ADC ASICS (Application Specific Integrated Circuit) have been developed for deployment on  
2 circuit boards mounted directly on the APA frames. This scheme ensures good signal-to-noise  
3 performance, even allowing for some attenuation of long-drift ionization signals due to residual  
4 impurities in the argon. It also offers the possibility of digital signal processing, including multi-  
5 plexing and zero suppression at the front end, thereby limiting the cable plant within the cryostat  
6 and the number of penetrations required, while also easing requirements on the downstream read-  
7 out/DAQ systems located outside the cryostat. The ASICS have been laid out following design  
8 rules developed explicitly for long-term operation at cryogenic temperatures.

9 In order to separate neutrino beam events from other interactions — particularly for proton decay  
10 and supernova neutrino signals — it is necessary to accurately determine the event time relative  
11 to the neutrino beam time window or an incoming cosmic muon. If the event time is known at the  
12 microsecond level then out-of-time cosmic-ray backgrounds for beam neutrinos can be rejected to  
13 the level of  $10^{-5}$  (the beam spill duty factor). The slow ionization-electron drift velocity gives the  
14 TPC its 3D imaging capability, but an independent fast signal is required to localize events in time  
15 and in space along the drift direction. The excellent scintillation properties of liquid argon ( $\mathcal{O}(10^4)$   
16 photons per MeV of energy deposition) are exploited to address this issue. A photon detection  
17 system is planned for detection of the 128-nm scintillation light that, in turn, allows determination  
18 of the event timing. Several photon detector designs are under study. The most advanced design  
19 uses cast acrylic bars coated with wavelength shifter, and SiPMs (silicon photomultipliers) at the  
20 ends for read-out. These bars will be assembled into paddles of dimensions 10 cm by 2 m, and  
21 mounted on the APA frames, fitting within the 5-cm gap between the sets of wire planes located on  
22 both sides of the frames. Initial studies indicate a light yield of 0.1 to 0.5 photoelectrons per MeV.

### 23 3.6.2 The 34-kt Detector Design

24 One possible design of a 34-kt detector is two 17-kt modules placed end-to-end in a common  
25 cavern at the 4,850-ft level of the Sanford Underground Research Facility, as shown in Figure 3.25.  
26 This design was reviewed at the Fermilab Director’s Independent Conceptual Design Review in  
27 March of 2012 [16].

28 Alternatively, the 34-kt detector can be realized by adding a roughly 24-kt detector of essentially  
29 the same design as the 10-kt detector, housed in a set of two cryostats, each holding 12 kt (20 kt  
30 total) of liquid argon. In this configuration the additional cryostats each have three APA rows (total  
31 84 APAs) and four CPA rows (total 112 CPAs), making them wider than the 10-kt design described  
32 in Section 3.6.1. The APA-to-CPA row spacing is expanded to 3.77 m and the length of each is  
33 increased to 14 APA units long. The cryogenics system installed for the 10-kt design will simply  
34 be expanded from two to four 85-kW refrigerators to service both the 10-kt and the 24-kt detector.  
35 The 24-kt detector hall will be excavated parallel to the 10-kt detector hall as shown in Figure 3.26.

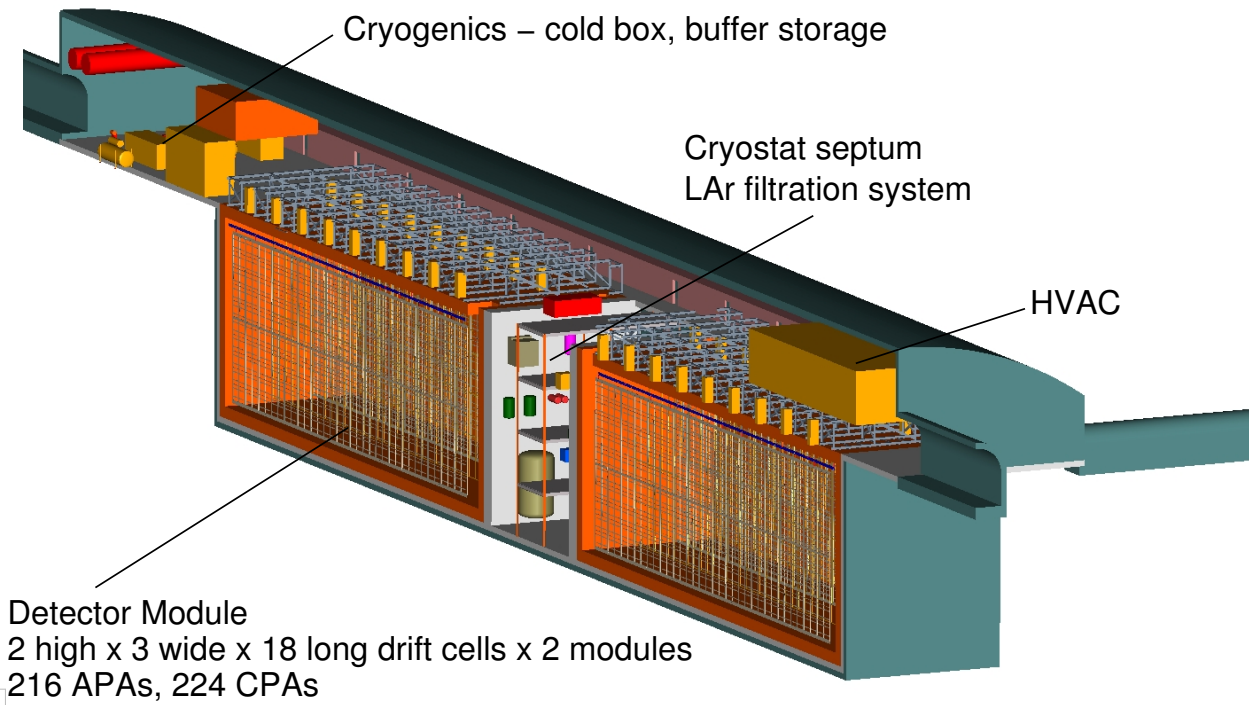


**Figure 3.25:** Schematic of a 34-kt LArTPC design. The detector comprises two 17-kt LArTPC vessels.

1 Given the modular design of the detector and the use of industrial technologies in the cryogenics  
 2 system, there is a great deal of flexibility in possible contributions from new partners to expand the  
 3 size of the detector. The details of any scope change would depend on the interests, capabilities  
 4 and resources of the new partners.

5 A full geotechnical site investigation is underway to characterize the rock mass in which it is  
 6 planned to site the LBNE far detector. Mapping of existing drifts in the vicinity of the proposed  
 7 detector location has been completed and a core boring program was launched in early 2014. This  
 8 investigation will explore the area with enough breadth to allow flexibility in siting and sizing  
 9 detector modules in the future before design work begins. The proposed boring layouts are shown  
 10 in Figure 3.27 overlaid with possible 34-kt and 70-kt modules to demonstrate the large capacity of  
 11 this location.

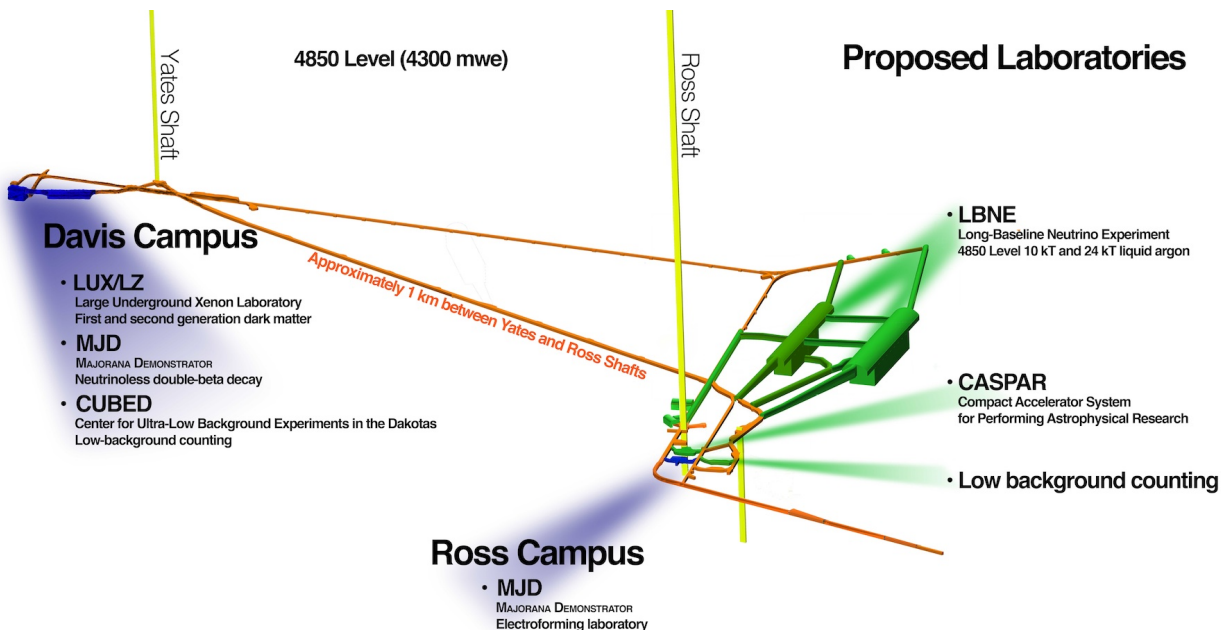
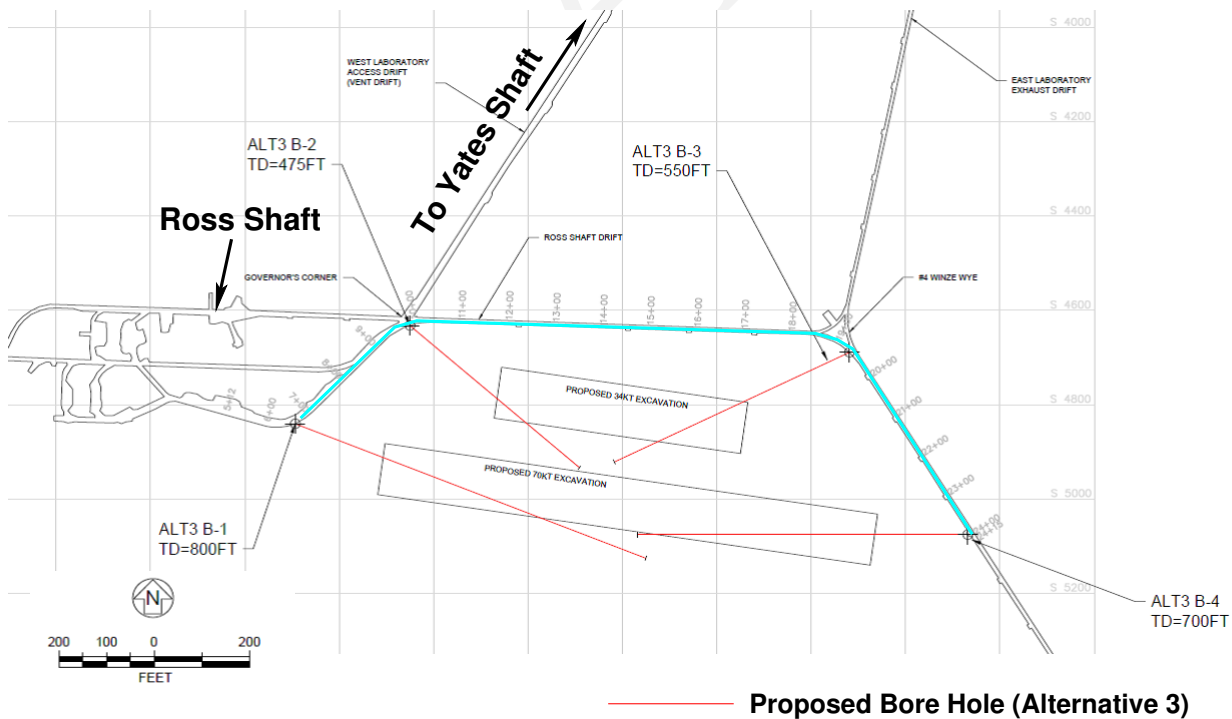


fig:fd\_4850

**Figure 3.26:** Layout of the 10-kt + 24-kt LArTPC detector halls at the 4,850-ft level of the Sanford Underground Research Facility.



g:fd\_4850\_100kt

**Figure 3.27:** Geotechnical site investigation plan, showing the drifts that have been mapped (blue) and the planned core borings (red) overlaid on possible locations of caverns that would accommodate the 34-kt or larger (70 kt shown as an example) LArTPC detectors.

DRAFT

# Chapter Neutrino Mixing, Mass Hierarchy and CP Violation

## 4

nu-oscil-chap

LBNE is designed to address the science of neutrino oscillations with superior sensitivity to many mixing parameters in a single experiment, in particular,

1. precision measurements of the parameters that govern  $\nu_\mu \rightarrow \nu_e$  and  $\bar{\nu}_\mu \rightarrow \bar{\nu}_e$  oscillations; this includes precision measurement of the third mixing angle  $\theta_{13}$ , measurement of the CP violating phase  $\delta_{\text{CP}}$ , and determination of the mass ordering (the sign of  $\Delta m_{32}^2$ )
2. precision measurements of  $\sin^2 2\theta_{23}$  and  $|\Delta m_{32}^2|$  in the  $\nu_\mu/\bar{\nu}_\mu$  disappearance channel
3. determination of the  $\theta_{23}$  octant using combined precision measurements of the  $\nu_e/\bar{\nu}_e$  appearance and  $\nu_\mu/\bar{\nu}_\mu$  disappearance channels
4. search for nonstandard physics that can manifest itself as differences in higher-precision measurements of  $\nu_\mu$  and  $\bar{\nu}_\mu$  disappearance over long baselines

### 4.1 Experimental Requirements Based on Oscillation Phenomenology

The experimental requirements for designing a neutrino oscillation experiment to simultaneously address neutrino CP violation and the mass hierarchy can be extrapolated as follows from the phenomenology summarized in Chapter 2:

1. *Phenomenology: An appearance experiment is necessary to extract the CP-violating effects.*

Experimental requirements:

- The experiment will probe oscillations of  $\nu_{\mu,e} \rightarrow \nu_{e,\mu}$ .
  - The experiment will identify  $\nu_e$  and  $\nu_\mu$  with high efficiency and purity in order to tag (or otherwise know) the flavor of the neutrino before and after flavor transformations.
  - The experiment requires  $E_\nu > 100 \text{ MeV}$  so that it will be possible to perform flavor-tagging of muon neutrinos using the lepton flavor produced in a charged-current interaction ( $\nu_\mu + N \rightarrow \mu N' X$ ).
2. *Phenomenology: In the three-flavor mixing model, the CP-violating Jarlskog invariant arises in the interference term  $P_{\sin \delta}$  as given by Equation 2.15; the oscillation scale where the*

interference term is maximal is that determined by the mixing between the  $\nu_1$  and  $\nu_3$  states.

Experimental requirements:

- The experimental baseline and corresponding neutrino energy are chosen according to Equation 2.18 such that  $L/E$  equals 510 km/GeV to maximize sensitivity to the CP-violating term in the neutrino flavor mixing.
- Flavor-tagging of muon neutrinos that can be produced either at the source or after flavor-mixing requires  $E_\nu > 100$  MeV; therefore, the experimental baselines over which to measure neutrino oscillations are  $L > 50$  km\*.

3. *Phenomenology: In the three-flavor model  $\nu_{\mu,e} \rightarrow \nu_{e,\mu}$  oscillations depend on all parameters in the neutrino mixing matrix as well as on the mass differences, as shown in Equations 2.12 to 2.15.*

Experimental requirements:

- The precision with which  $\delta_{CP}$  can be determined — and the sensitivity to small CP-violating effects or CP violation outside the three-flavor model — requires precision determination of all the other mixing parameters, preferably in the same experiment. The experiment will be designed so as to minimize dependence on external measurements of the oscillation parameters.

4. *Phenomenology: Observation of CP violation requires the explicit observation of an asymmetry between  $P(\nu \rightarrow \nu)$  and  $P(\bar{\nu} \rightarrow \bar{\nu})$ .*

Experimental requirements:

- The experiment will probe the oscillations of both neutrinos and antineutrinos in an unambiguous way.
- The experiment will be capable of charge tagging in addition to flavor tagging. Charge tagging can be achieved at detection using the lepton charge and/or at production by selecting beams purely of neutrinos or antineutrinos.
- The experiment will be capable of resolving degeneracies between matter and CP asymmetries in order to determine the mass hierarchy. This can be achieved by using a baseline greater than 1,000 km or with measurements probing oscillations over a range of  $L/E$  values.

5. *Phenomenology: CP asymmetries are maximal at the secondary oscillation nodes.*

Experimental requirements:

---

\*Neutrino experiments using beams from pion decay-at-rest experiments such as DAE $\delta$ ALUS are exceptions since the  $\bar{\nu}_\mu$  production spectrum is well known and only the  $\bar{\nu}_e$  flavor after oscillations is tagged through inverse-beta decay. The neutrino energies are  $\sim 50$  MeV below the CC muon production threshold.

- 1 ○ Coverage of the  $L/E$  scale of the secondary oscillation nodes improves experimental  
2 sensitivity to small values of  $\delta_{\text{CP}}$  by enabling measurements of the asymmetry at the  
3 secondary nodes where the CP asymmetries are much larger and where there is no  
4 degeneracy with the matter asymmetries. The experiment will be performed with a  
5 wide-band beam to provide sensitivity to the  $L/E$  scale of both the first and second  
6 oscillation nodes.
- 7 ○ The experimental baseline will be  $>150$  km, given that muon flavor tagging is required  
8 at either production or detection. The secondary oscillation nodes are located at scales  
9 set by Equation 2.18 where  $n > 1$ . The second oscillation maximum is located at scales  
10 given by  $L/E \sim 1,500$  km/GeV.

11 Based on the experimental requirements prescribed by the neutrino oscillation phenomenology  
12 detailed above, pursuit of the primary science objectives for LBNE dictates the need for a very  
13 large mass (10 kt to 100 kt) neutrino detector located at a distance greater than 1,000 km from  
14 the neutrino source. A large mass coupled with a powerful wide-band beam and long exposures  
15 is required to accumulate enough neutrino interactions —  $\mathcal{O}(1,000)$  events — to make precision  
16 measurements of the parameters that govern the subdominant  $\nu_\mu \rightarrow \nu_e$  oscillations. At 1,300 km,  
17 the baseline chosen for LBNE, both the first and second oscillation nodes are at neutrino energies  
18  $> 0.5$  GeV, as shown in Figure 4.1. This places both neutrino oscillation nodes in a region that is  
19 well matched to the energy spectrum of the high-power conventional neutrino beams that can be  
20 obtained using the 60 GeV to 120 GeV Main Injector (MI) proton accelerator at Fermilab.

## 21 4.2 Experiment Simulation

sec:expt-sim

22 To evaluate the sensitivity of LBNE and to optimize the experiment design, it is important to  
23 accurately predict the neutrino flux produced by the neutrino beamline, the neutrino interaction  
24 rate at the far detector, and the far detector performance. This is achieved using Monte Carlo (MC)  
25 simulations and the GLoBES [121,122] package. The simulations and experimental assumptions  
26 that are used to evaluate the sensitivity of LBNE to neutrino mixing parameters, to the neutrino  
27 mass hierarchy and to CP violation are described in this section.

### 28 4.2.1 Neutrino Rates

29 The LBNE beamline design, described in Section 3.4, is simulated using GEANT4 [123]. The  
30 simulated  $\nu_\mu$  spectrum (unoscillated flux  $\times$  cross section) at 1,300 km obtained from the LBNE  
31 beamline using 80-GeV protons from the MI is shown as the black histogram in Figure 4.1. At this  
32 baseline, there is no degeneracy between matter and CP asymmetries at the first oscillation node  
33 where the LBNE neutrino beam spectrum peaks. The wide coverage of the oscillation patterns  
34 enables the search for physics beyond the three-flavor model because new physics effects may

1 interfere with the standard oscillations and induce a distortion in the oscillation patterns. As a  
 2 next-generation neutrino oscillation experiment, LBNE aims to study in detail the spectral shape  
 3 of neutrino mixing over the range of energies where the mixing effects are largest. This is crucial  
 4 for advancing the science beyond the current generation of experiments, which depend primarily  
 on rate asymmetries.

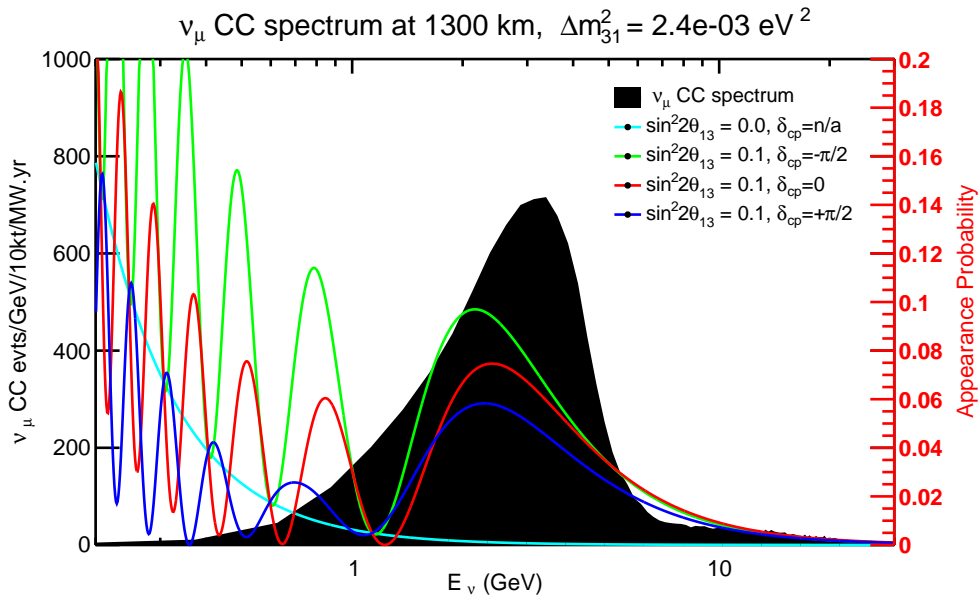


**Figure 4.1:** The simulated unoscillated spectrum of  $\nu_\mu$  events from the LBNE beam (black histogram) overlaid with the  $\nu_\mu \rightarrow \nu_e$  oscillation probabilities (colored curves) for different values of  $\delta_{CP}$  and normal hierarchy.

5  
 6 The LBNE reconfiguration study [17] determined that the far detector location at the Sanford  
 7 Underground Research Facility provides an optimal baseline for precision measurement of neutrino  
 8 oscillations using a conventional neutrino beam from Fermilab. The 1,300-km baseline optimizes  
 9 sensitivity to CP violation and is long enough to resolve the mass hierarchy with a high level of  
 10 confidence, as shown in Figure 2.7.

11 Table 4.1 lists the beam neutrino interaction rates for all three known species of neutrinos as ex-  
 12 pected at the LBNE far detector. This table shows only the raw interaction rates using the neutrino  
 13 flux from the GEANT4 simulations of the LBNE beamline and the default interaction cross sec-  
 14 tions included in the GLoBeS package [121] with *no detector effects included*. A tunable LBNE  
 15 beam spectrum, obtained by varying the distance between the target and the first focusing horn  
 16 (Horn 1), is assumed. The higher-energy tunes are chosen to enhance the  $\nu_\tau$  appearance signal and  
 17 improve the oscillation fits to the three-flavor paradigm. To estimate the NC event rates based on  
 18 visible energies above 0.5 GeV, a true-to-visible energy smearing function based on output from  
 19 the GENIE neutrino MC generator [124] is used. For comparison, the rates at current neutrino  
 20 oscillation experiments such as T2K [125], MINOS [126] and NO $\nu$ A [117] are shown for simi-

**Table 4.1:** Raw  $\nu$  oscillation event rates at the LBNE far site with  $E_\nu < 10$  GeV. Assumes  $1.8 \times 10^7$  seconds/year (Fermilab). Oscillation parameters used are:  $\theta_{12} = 0.587$ ,  $\theta_{13} = 0.156$ ,  $\theta_{23} = 0.670$ ,  $\Delta m_{21}^2 = 7.54 \times 10^{-5} \text{ eV}^2$ , and  $\Delta m_{31}^2 = +2.47 \times 10^{-3} \text{ eV}^2$  (normal hierarchy). The NC event rate is for events with visible energy  $> 0.5$  GeV. For comparison, the rates at other neutrino oscillation experiments (current and proposed) are shown for similar exposure in mass and time. No detector effects are included.

lbl\_event\_rates

Expt. details	Baseline km	$\nu_\mu$ unosc. CC	$\nu_\mu$ osc. CC	$\nu_e$ beam CC	$\nu_\mu$ NC	$\nu_\mu \rightarrow \nu_\tau$ CC	$\nu_\mu \rightarrow \nu_e$ CC	$\delta_{\text{CP}} = -\frac{\pi}{2}, 0, \frac{\pi}{2}$
<b>LBNE LE</b> 80 GeV, 1.2 MW $1.5 \times 10^{21}$ POT/year	1,300							
50 kt · year $\nu$		12721	4339	108	3348	156	605	480 350
50 kt · year $\bar{\nu}$		4248	1392	34	1502	48	51	86 106
<b>LBNE ME</b> 120 GeV, 1.2 MW $1 \times 10^{21}$ POT/year	1,300							
50 kt · year $\nu$		19613	12317	72	5808	686	435	399 293
<b>T2K</b> 30 GeV, 750 kW $9 \times 10^{20}$ POT/year	295							
50 kt · year $\nu$		2100	898	41	360	$< 1$	73	58 39
<b>MINOS LE</b> 120 GeV, 700 kW $6 \times 10^{20}$ POT/year	735							
50 kt · year $\nu$		17574	11223	178	4806	115	345	326 232
50 kt · year $\bar{\nu}$		5607	3350	56	2017	32	58	85 88
<b>NOvA ME</b> 120 GeV, 700 kW $6 \times 10^{20}$ POT/year	810							
50 kt · year $\nu$		4676	1460	74	1188	10	196	168 116
50 kt · year $\bar{\nu}$		1388	428	19	485	2	22	35 41
<b>LBNO</b> 50 GeV $\sim$ 2 MW $3 \times 10^{21}$ POT/year	2,300							
50 kt · year $\nu$		8553	2472	48	2454	570	534	426 336
50 kt · year $\bar{\nu}$		3066	828	15	1140	255	24	45 54
$\nu$ -Factory details		$\nu_\mu$ unosc. CC	$\nu_\mu$ osc. CC		$\nu_\mu$ NC	$\nu_\mu \rightarrow \nu_\tau$ CC	$\nu_e \rightarrow \nu_\mu$ CC	$\delta_{\text{CP}} = -\frac{\pi}{2}, 0, \frac{\pi}{2}$
<b>NuMAX I</b> 3 GeV, 1 MW $0.94 \times 10^{20}$ $\mu$ /year	1,300							
50 kt · year $\mu^+$		1039	339		484	28	71	97 117
50 kt · year $\mu^-$		2743	904		945	89	24	19 12
<b>NuMAX II</b> 3 GeV, 3 MW $5.6 \times 10^{20}$ $\mu$ /year	1,300							
50 kt · year $\mu^+$		6197	2018		2787	300	420	580 700
50 kt · year $\mu^-$		16349	5390		5635	534	139	115 85

lar exposure in mass and time and using the same interaction cross sections. The raw interaction rates from other proposed neutrino oscillation experiments such as LBNO [127] and the NuMAX neutrino factory designs [128] are also shown<sup>†</sup>. It is important to note that the duty factors for the JPARC and CERN beams are  $\sim 1/3$  and  $\sim 1/2$  of NuMI/LBNE respectively. For LBNO, the event rates are obtained using the optimized beam from the HP-PS2 50-GeV synchrotron [129] with an exposure of  $3 \times 10^{21}$  POT/year. The LBNO duty cycle is assumed to be  $\sim 10^7$  seconds/year, which corresponds to a beam power of 2 MW. Note that for Stage 1 and Stage 2 of the NuMAX neutrino factory proposal [128], Project X beams [15] at 3 GeV with 1 and 3 MW, respectively, are needed<sup>‡</sup>. It is clear that the LBNE beam design and baseline produce high rates of  $\nu_e$  appearance coupled with large rate asymmetries when CP-violating effects are included. For example, LBNE has significantly higher appearance rates with a Main Injector 1.2-MW beam when compared to Stage 1 of the NuMAX neutrino factory with a 1-MW beam from a 3-GeV linac. The  $\nu_e$  appearance rates are very similar in LBNE and LBNO with normal hierarchy, but the  $\bar{\nu}_e$  appearance rates (normal hierarchy) in LBNO are  $\approx 1/2$  that of LBNE due to the suppression from the larger matter effect (longer baseline) in LBNO.

#### 4.2.2 Detector Simulation using the GLoBES Package

For the sensitivity studies presented here, the GLoBES package [121,122] was used to simulate the detector response using simple smearing and using detector efficiency values based on results from ICARUS and earlier simulation efforts as documented in [21]. The values used in GLoBES are shown in Table 4.2.

Studies from ICARUS have estimated and measured single-particle energy resolutions in liquid argon (LAr). Below 50 MeV, the energy resolution of electrons is  $11\%/\sqrt{E[\text{MeV}]} + 2\%$ . The energy resolution of an electromagnetic shower with energy in the range (50–5000) MeV is  $33\%/\sqrt{E(\text{MeV})} + 1\%$  [130], and that of hadronic showers is  $\approx 30\%/\sqrt{E(\text{GeV})}$ . A significant fraction of the  $\nu_e$  CC signal in LBNE in the range of 1 GeV to 6 GeV is non-quasi-elastic CC interactions with a large component of the visible energy in the hadronic system. From recent simulations of neutrino interactions in the region of 1 GeV to 6 GeV it has been determined that  $\langle E_{\text{lepton}}/E_\nu \rangle \approx 0.6$ . For this reason, the total electron-neutrino energy resolution for the neutrino oscillation sensitivity calculation is chosen to be  $15\%/\sqrt{E(\text{GeV})}$ . In a non-magnetized LArTPC, the muon momentum can be obtained from measurements of range and multiple scattering. The muon momentum resolution for partially contained muons is found to be in the range 10 – 15% [131,132] for muons in the 0.5 GeV to 3 GeV range. The  $\nu_\mu$  total energy resolution in LBNE is, therefore, assumed to be  $20\%/\sqrt{E(\text{GeV})}$ ; the resolution will be significantly better than this for the small subsample of events in which muons are fully contained by the detector.

<sup>†</sup>T2K uses a JPARC neutrino beam, MINOS and NO $\nu$ A use the Fermilab NuMI neutrino beam and LBNO uses a CERN neutrino beam.

<sup>‡</sup>Project X has been superseded by PIP-II as of late 2013; PIP-II is briefly described in Section 3.4.

**Table 4.2:** Estimated range of the LArTPC detector performance parameters for the primary oscillation physics. Signal efficiencies, background levels, and resolutions are obtained from ICARUS and earlier simulation efforts (middle column) and the value chosen for the baseline LBNE neutrino oscillation sensitivity calculations (right column).

Parameter	Range of Values	Value Used for LBNE Sensitivities For $\nu_e$ CC appearance studies
$\nu_e$ CC efficiency	70-95%	80%
$\nu_\mu$ NC mis-identification rate	0.4-2.0%	1%
$\nu_\mu$ CC mis-identification rate	0.5-2.0%	1%
Other background	0%	0%
Signal normalization error	1-5%	1-5%
Background normalization error	2-15%	5-15%
For $\nu_\mu$ CC disappearance studies		
$\nu_\mu$ CC efficiency	80-95%	85%
$\nu_\mu$ NC mis-identification rate	0.5-10%	1%
Other background	0%	0%
Signal normalization error	1-10%	5-10%
Background normalization error	2-20%	10-20%
For $\nu$ NC disappearance studies		
$\nu$ NC efficiency	70-95%	90%
$\nu_\mu$ CC mis-identification rate	2-10%	10%
$\nu_e$ CC mis-identification rate	1-10%	10%
Other background	0%	0%
Signal normalization error	1-5%	under study
Background normalization error	2-10%	under study
Neutrino energy resolutions		
$\nu_e$ CC energy resolution	$15\%/\sqrt{E(\text{GeV})}$	$15\%/\sqrt{E(\text{GeV})}$
$\nu_\mu$ CC energy resolution	$20\%/\sqrt{E(\text{GeV})}$	$20\%/\sqrt{E(\text{GeV})}$
$E_{\nu_e}$ scale uncertainty	under study	under study
$E_{\nu_\mu}$ scale uncertainty	1-5%	2%

Figures 4.2 and 4.3 show the predicted spectra of observed signal and background events in LBNE produced from the GLOBES implementation, including the effects of neutrino oscillation. Figure 4.2 shows the  $\nu_\mu$  and  $\bar{\nu}_\mu$ -CC sample and Figure 4.3 shows the  $\nu_e$  and  $\bar{\nu}_e$ -CC appearance sample. Table 4.3 shows the expected LBNE signal and background event rates in  $\nu_\mu$  disappearance and  $\nu_e$  appearance mode for neutrinos and antineutrinos, for normal and inverted hierarchy. The rates are given per 10 kt of fiducial LArTPC mass.

The GLOBES implementation used in the sensitivity studies presented here appears to be in good agreement with more recent results from the Fast MC, described in Appendix A. Updated sensi-

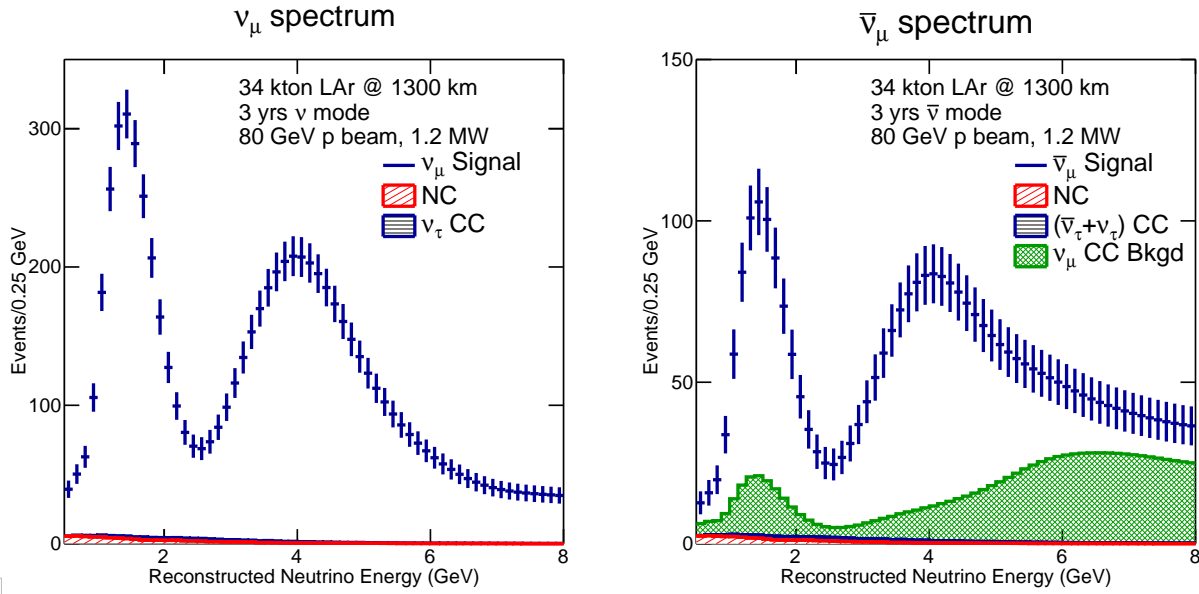


**Figure 4.2:** The expected spectrum of  $\nu_\mu$  or  $\bar{\nu}_\mu$  events in a 34-kt LArTPC for three years of neutrino (left) and antineutrino (right) running with a 1.2-MW beam.

**Table 4.3:** Expected number of neutrino oscillation signal and background events in the energy range 0.5 GeV to 8.0 GeV at the far detector after detector smearing and event selection. The calculation assumes  $\sin^2(2\theta_{13}) = 0.09$  and  $\delta_{CP} = 0$ . The event rates are given per 10-kt LArTPC and three years of running with the improved 80-GeV LBNE beam at 1.2 MW. For the background estimates,  $\nu$  and  $\bar{\nu}$  events are combined. The mass hierarchy has negligible impact on  $\nu_\mu$  disappearance signals.

Beam	Hierarchy	Signal Events		Background Events			Total
		$\nu_x/\bar{\nu}_x$ CC	$\nu_\mu$ NC	$\nu_\mu$ CC	$\nu_e$ Beam	$\nu_\tau$ CC	
<b><math>\nu_\mu \rightarrow \nu_{x=\mu}</math> (disappearance)</b>							
Neutrino	-	2056/96	23	N/A	-	18	41
Antineutrino	-	280/655	10	N/A	-	10	20
<b><math>\nu_\mu \rightarrow \nu_{x=e}</math> (appearance)</b>							
Neutrino	Normal	229/3	21	25	47	14	107
Neutrino	Inverted	101/5	21	25	49	17	112
Antineutrino	Normal	15/41	11	11	24	9	55
Antineutrino	Inverted	7/75	11	11	24	9	55

- 1 tivity and systematic studies are currently underway using the Fast MC for detector simulation and
- 2 customized, GLOBES-based software for the oscillation fits and propagation of systematics. A full
- 3 MC simulation of the far detector and automated event reconstruction is being developed; this is
- 4 also described in Appendix A. [app-sim](#)

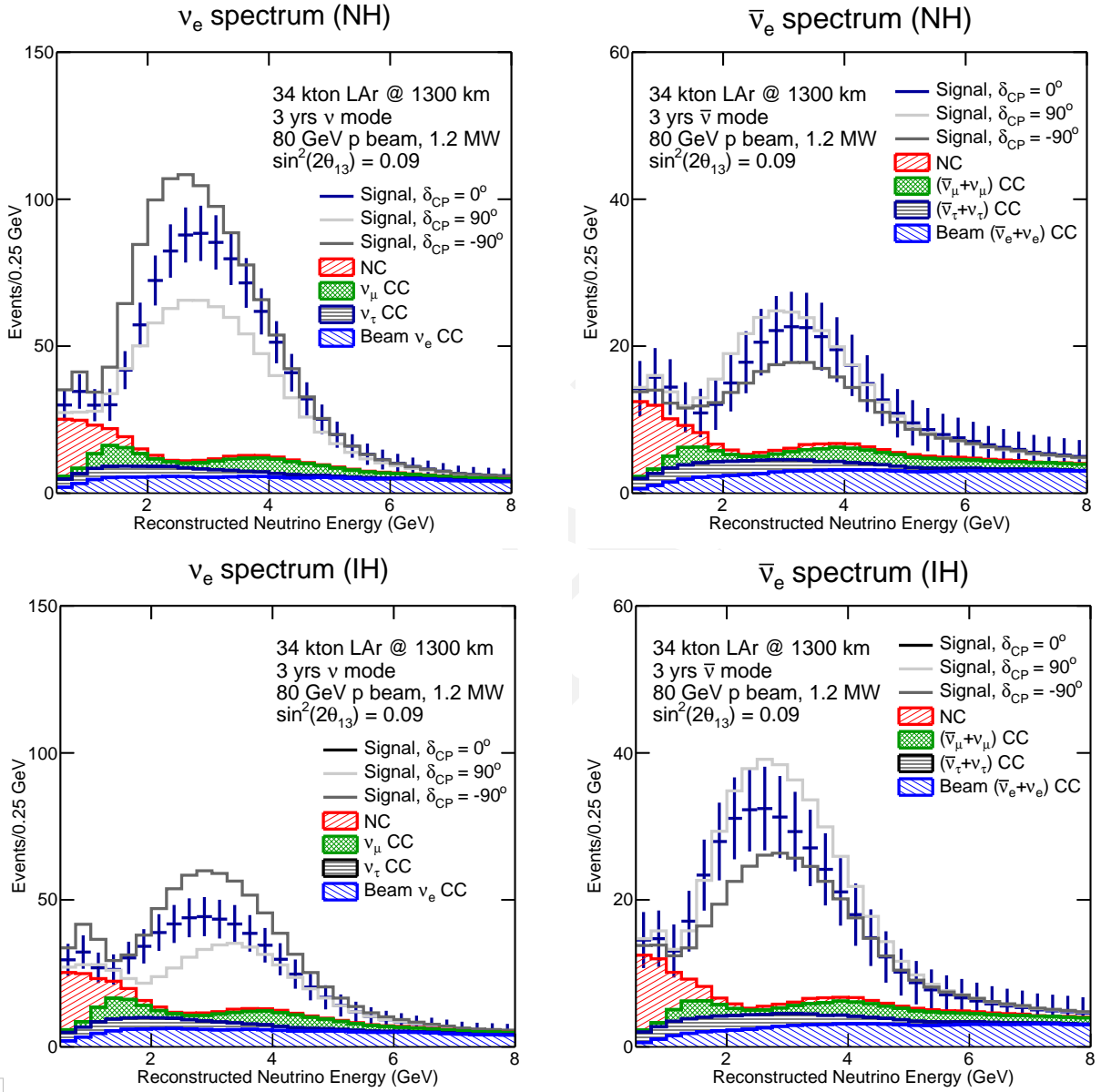


**Figure 4.3:** The expected spectrum of  $\nu_e$  or  $\bar{\nu}_e$  oscillation events in a 34-kt LArTPC for three years of neutrino (left) and antineutrino (right) running with a 1.2-MW, 80-GeV beam assuming  $\sin^2(2\theta_{13}) = 0.09$ . The plots on the top are for normal hierarchy and the plots on the bottom are for inverted hierarchy.

-event-spectrum

## 4.3 Measurements of Mass Hierarchy and the CP-Violating Phase

The neutrino mass hierarchy and the value of the CP violating phase,  $\delta_{CP}$ , are currently unknown. Knowledge of the mass hierarchy has significant theoretical, cosmological and experimental implications. A determination of the  $\delta_{CP}$  value to be neither zero (0) nor  $\pi$  would constitute the first observation of CP violation in the lepton sector.

The expected performance of a 10-kt LArTPC far detector 1,300 km downstream from a Main Injector neutrino beam is detailed in the LBNE Conceptual Design Report Volume 1 [21]. Estimated sensitivities to the determination of the mass hierarchy and discovery of CP violation, presented both here and in the CDR, are calculated using the GLOBES package. The detector response assumed in these calculations is summarized in Table 4.2. The sensitivities are obtained by simultaneously fitting the  $\nu_\mu \rightarrow \nu_\mu$ ,  $\bar{\nu}_\mu \rightarrow \bar{\nu}_\mu$ ,  $\nu_\mu \rightarrow \nu_e$ , and  $\bar{\nu}_\mu \rightarrow \bar{\nu}_e$  oscillated spectra, examples of which are shown in Figures 4.2 and 4.3. The  $\nu_\tau$  background is not used in the sensitivity calculations since it is expected that further analysis will reduce this background to negligible levels.

In these calculations, experimental sensitivity is quantified using  $\Delta\chi^2$  parameters, which are determined by comparing the predicted spectra for various scenarios. These quantities are defined, differently for neutrino mass hierarchy and CP-violation sensitivity, to be:

$$\Delta\chi_{MH}^2 = |\chi_{MH}^{2\text{test}=IH} - \chi_{MH}^{2\text{test}=NH}|, \quad (4.1)$$

$$\Delta\chi_{CPV}^2 = \min\left(\Delta\chi_{CP}^2(\delta_{CP}^{\text{test}} = 0), \Delta\chi_{CP}^2(\delta_{CP}^{\text{test}} = \pi)\right), \text{ where} \quad (4.2)$$

$$\Delta\chi_{CP}^2 = \chi_{\delta_{CP}}^{2\text{test}} - \chi_{\delta_{CP}}^{2\text{true}}. \quad (4.3)$$

These sensitivities are evaluated separately for true normal and inverted neutrino mass hierarchy. Since the true value of  $\delta_{CP}$  is unknown, a scan is performed over all possible values of  $\delta_{CP}^{\text{true}}$ . The individual  $\chi^2$  values are calculated using

$$\chi^2(\mathbf{n}^{\text{true}}, \mathbf{n}^{\text{test}}, f) = 2 \sum_i^{N_{\text{reco}}} \left( n_i^{\text{true}} \ln \frac{n_i^{\text{true}}}{n_i^{\text{test}}(f)} + n_i^{\text{test}}(f) - n_i^{\text{true}} \right) + f^2, \quad (4.4)$$

where  $\mathbf{n}$  are event rate vectors in  $N_{\text{reco}}$  bins of reconstructed energy and  $f$  represents a nuisance parameter to be profiled. Nuisance parameters include the values of mixing angles, mass splittings, and signal and background normalization. The nuisance parameters are constrained by Gaussian priors; in the case of the oscillation parameters, the Gaussian prior has standard deviation determined by taking 1/6 of the  $3\sigma$  range allowed by the global fit [46].

With the exception of results reported in Section 4.3.1, where more information on the statistical interpretation of mass hierarchy sensitivity is provided, the sensitivities presented here are for the ‘‘typical experiment’’ with no statistical fluctuations considered. In the absence of statistical

1 fluctuations, the  $\chi^2$  value for the “true” spectra is identically zero. Statistical fluctuations are in-  
 2 corporated by repeatedly varying the contents of each energy bin in each sample by drawing from  
 3 a Poisson distribution with the expected number of events in that bin as the mean.

4 This section presents the sensitivities of various LBNE configurations to determination of the mass  
 5 hierarchy and CP violation. In particular, a 10-kt far detector and the full-scope 34-kt far detector  
 6 are considered. In each case, the performance of LBNE with both the 120-GeV beamline design  
 7 presented in the CDR [22] as well as the upgraded 80-GeV beam described in Section 3.4 is  
 8 studied. In addition, the sensitivities at different possible stages of LBNE with increases to far  
 9 detector mass and Main Injector beam upgrades are estimated.

10 Figure 4.4 summarizes the sensitivities for determining the mass hierarchy and CP violation ( $\delta_{CP} \neq$   
 11  $0$  or  $\pi$ ) as a function of the true value of  $\delta_{CP}$  with a 10-kt LArTPC. The red band shows the  
 12 sensitivity that is achieved with an exposure of six years with equal exposures in  $\nu$  and  $\bar{\nu}$  mode in a  
 13 1.2-MW beam. The cyan band shows the sensitivity obtained by combining LBNE 10 kt with T2K  
 14 and NO $\nu$ A, where the T2K exposure is  $7.8 \times 10^{21}$  protons-on-target in  $\nu$  mode only and the NO $\nu$ A  
 15 exposure is six years with equal exposures in  $\nu$  and  $\bar{\nu}$  mode. The bands indicate the sensitivity  
 16 range corresponding to different levels of signal and background normalization uncertainties and  
 17 different possible beam designs. The gray curves are the expected sensitivities for the combination  
 18 of NO $\nu$ A and T2K. The known mixing parameters are allowed to float in the fit, but are constrained  
 19 (using a Gaussian prior) by the uncertainties from the 2012 global best fits [46]. The reactor mixing  
 20 angle,  $\sin^2 2\theta_{13}$ , is constrained to be  $0.094 \pm 0.005$ . The uncertainty is equal to the size of the current  
 21 systematic uncertainty from Daya Bay and is used as a conservative estimate of the precision that  
 22 will be achieved by the current generation of reactor experiments. Figure 4.5 shows the sensitivities  
 23 for determining the mass hierarchy and CP violation ( $\delta_{CP} \neq 0$  or  $\pi$ ) as a function of the true value  
 24 of  $\delta_{CP}$  after six years of running in the LBNE 34-kt configuration under the same assumptions.

25 The sensitivity bands in Figures 4.4 and 4.5 represent the variation in sensitivity as a function of  
 26 the beam design and normalization uncertainties on the signal and background. The solid curve  
 27 at the lower end of the red band represents the beamline design described in the LBNE CDR  
 28 Volume 2 [22] for the case in which there is no near detector. The dashed line above the solid curve  
 29 represents the sensitivity with the beam design improvements currently under study as described in  
 30 Section 3.4, still without a near detector. The dashed line at the upper end of the red band represents  
 31 the case in which both the beam design improvements and a high-resolution, highly capable near  
 32 detector are implemented. The key design goal of the LBNE near detector and beamline simulation  
 33 software is to enable a prediction of the far detector unoscillated flux with a precision of  $\leq 2\%$ .  
 34 Therefore, the total signal and background normalization uncertainties on the  $\nu_\mu$  disappearance  
 35 signal are assumed to be 5% and 10%, respectively. The default  $\nu_e$  appearance signal *uncorrelated*  
 36 normalization uncertainties for the full-scope LBNE presented in this chapter are assumed to be  
 37 1%. The  $\nu_e$  appearance background uncertainty is expected to be at least as good as the  $\sim 5\%$  [133]  
 38 achieved by the  $\nu_e$  appearance search in the MINOS experiment.

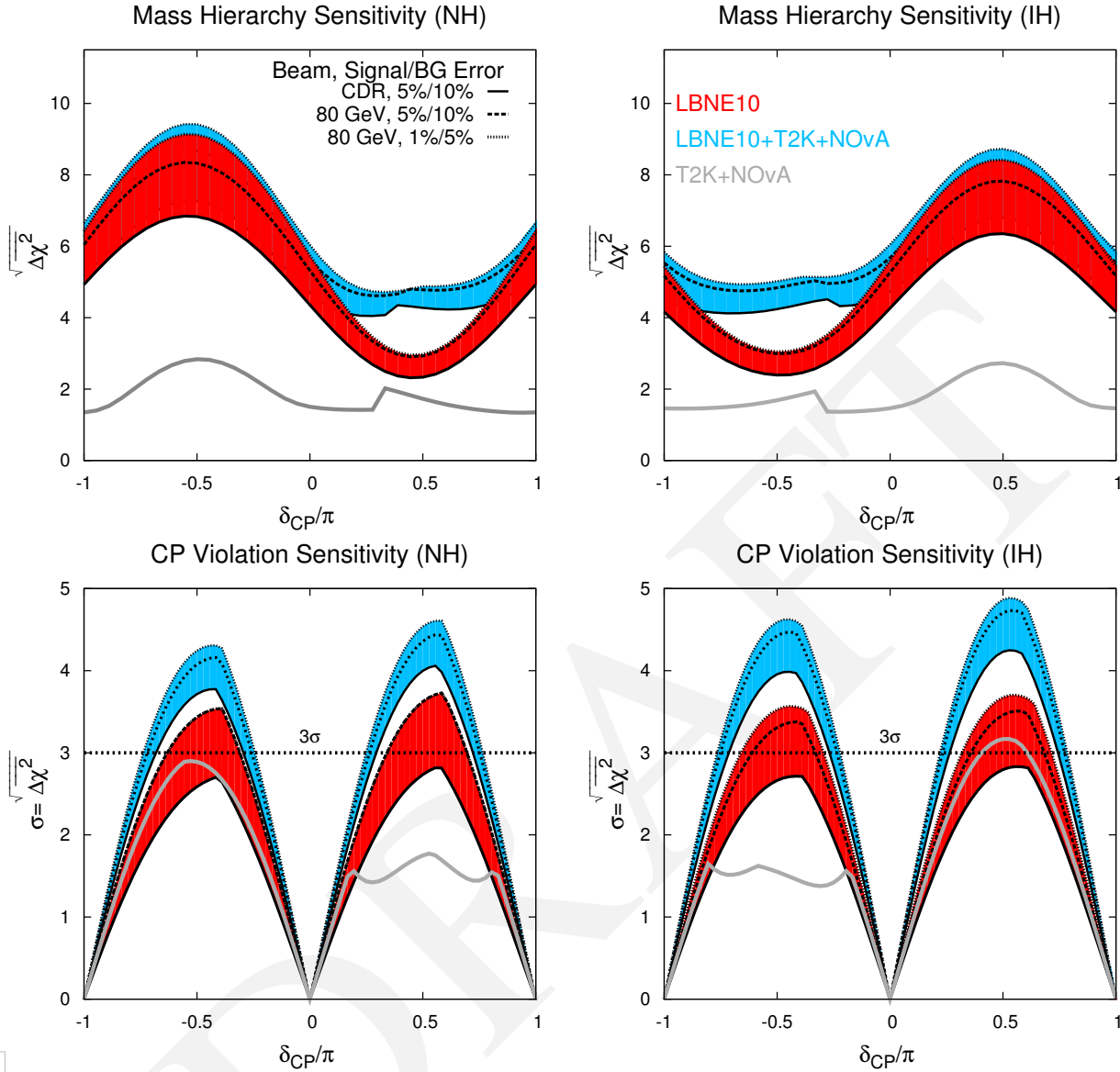


**Figure 4.4:** The significance with which the mass hierarchy (top) and CP-violation (for  $\delta_{CP} \neq 0$  or  $\pi$ , bottom) can be determined as a function of the value of  $\delta_{CP}$ . The plots on the left are for normal hierarchy and the plots on the right are for inverted hierarchy. The red band shows the sensitivity that is achieved by a typical experiment with the LBNE 10-kt configuration alone, where the width of the band shows the range of sensitivities obtained by varying the beam design and the signal and background uncertainties as described in the text. The cyan band shows the sensitivity obtained by combining LBNE 10-kt with T2K and NO $\nu$ A, and the gray curves are the expected sensitivities for the combination of NO $\nu$ A and T2K; the assumed exposures for each experiment are described in the text. For the CP-violation sensitivities, the mass hierarchy is assumed to be unknown.

- 1 A detailed discussion of the systematics assumptions for LBNE is presented in Section 4.3.2. <sup>sec:sys</sup>
- 2 In the case that LBNE has no near neutrino detector, the uncertainties on signal and background are
- 3 expected to be 5% and 10%, respectively, extrapolating from the performance and detailed knowl-
- 4 edge of the NuMI beam on which the LBNE beamline is modeled, in-situ measurements of the

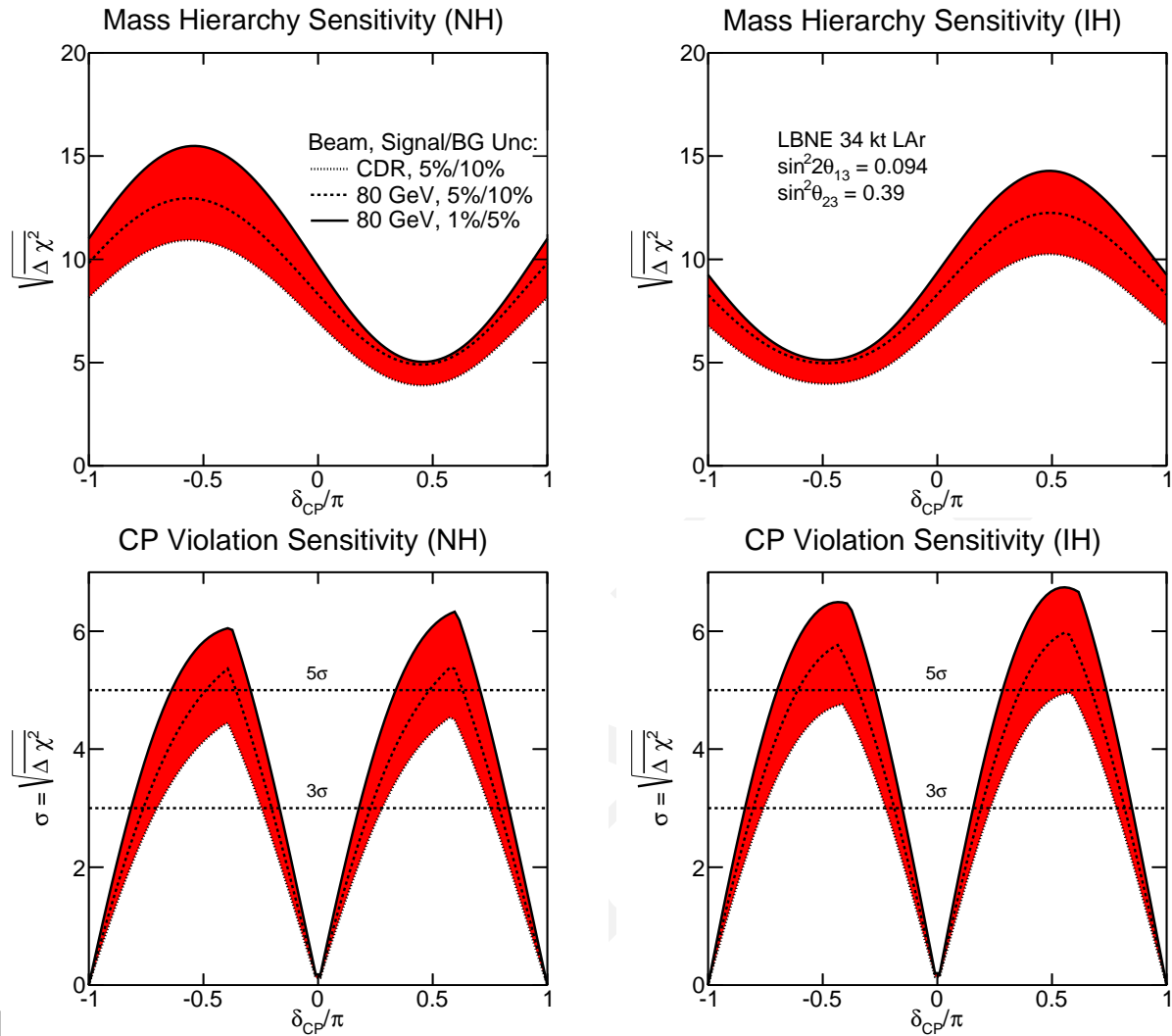


fig:35kton

**Figure 4.5:** The significance with which the mass hierarchy (top) and CP-violation (for  $\delta_{CP} \neq 0$  or  $\pi$ , bottom) can be determined by a typical LBNE experiment with a 34-kt far detector as a function of the value of  $\delta_{CP}$ . The plots on the left are for normal hierarchy and the plots on the right are for inverted hierarchy. The width of the red band shows the range of sensitivities that can be achieved by LBNE when varying the beam design and the signal and background uncertainties as described in the text.

- 1 muon flux at the near site as described in [21], the expectation of improved hadron production
- 2 measurements with the NA61 and MIPP, experiments, and the experience of previous  $\nu_e$  appear-
- 3 ance experiments as summarized in Table 4.4.

**Table 4.4:** Summary of achieved systematic error performance in several select prior  $\nu_\mu \rightarrow \nu_e$  oscillation experiments. These numbers were extracted from publications and may not correspond exactly to the description in the text. NBB/WBB indicates a narrow/wide band beam. “No ND” indicates there was no near detector, and “ND-FD” indicates a two (near-far) detector experiment with extrapolation of the expected background and signal from the near to the far detector. In the case of T2K, the quoted systematic (\*) is actually the total uncertainty on the observed events, which are predominately signal.

Experiment	Year	$\nu_\mu$ -NC/CC Events	$\nu_e$ -CC Events	Background Syst.Error	Comment
BNL E734 [134]	1985	235	418	20%	No ND
BNL E776(89)(NBB) [135]		10	9	20%	No ND
BNL E776 (WBB) [136]	1992	95	40	14%	No ND
NOMAD [137]	2003	<300	5500	< 5%	No ND
MiniBooNE [138]	2008	460	380	9%	No ND
MiniBooNE [40]	2013	536	782	5%	SciBooNE
MINOS [133]	2013	111	36	4%	ND-FD
T2K [139]	2013	1.1	26	9%*	ND-FD

### 4.3.1 Interpretation of Mass Hierarchy Sensitivities

LBNE will be definitive in its ability to discriminate between normal and inverted mass ordering for the allowed range of unknown parameters such as  $\delta_{CP}$  and  $\sin^2 \theta_{23}$ . To assess the sensitivity of LBNE to this physics, particularly for the case of less favorable parameter values, detailed understanding of statistical significance is essential.

At the true values of  $\delta_{CP}$  for which the mass hierarchy asymmetry is maximally offset by the leptonic CP asymmetry, LBNE’s sensitivity to the mass hierarchy is at its minimum. Even in this case, with a 34-kt LArTPC operating for six years in a 1.2-MW beam, the  $|\Delta\chi^2|$  value obtained in a typical data set will exceed 25, allowing LBNE on its own to rule out the incorrect mass ordering at a confidence level above  $1 - 3.7 \times 10^{-6}$ . Considering fluctuations, LBNE will measure, in  $\geq 97.5\%$  of all possible data sets for this least favorable scenario, a value of  $|\Delta\chi^2|$  equal to 9 or higher, which corresponds to a  $\geq 99\%$  probability of ruling out the incorrect hierarchy hypothesis.

In the mass hierarchy determination, only two possible results are considered, as the true mass hierarchy is either normal or inverted. Reference [140] presents the statistical considerations of determining the sensitivity of an experiment to the mass hierarchy, framed partly in the context of two separate but related questions:

1. Given real experimental data, with what significance can the mass hierarchy be determined?

- 1 2. When evaluating future experimental sensitivities, what is the probability that a particular  
2 experimental design will be able to determine the mass hierarchy with a given significance?

3 Once data is in hand, a number of techniques based either within Bayesian or frequentist statistics  
4 make it possible to determine the level of confidence at which one MH hypothesis or the other can  
5 be ruled out.

6 In assessing the sensitivity of future experiments, it is common practice to generate a simulated  
7 data set (for an assumed true mass hierarchy) that does not include statistical fluctuations. The  
8 expected sensitivity can be reported as  $\overline{\Delta\chi^2}$ , representative of the mean or the most likely value  
9 of  $\Delta\chi^2$  that would be obtained in an ensemble of experiments for a particular true hierarchy. With  
10 the exception of Figure 4.7, the sensitivity plots in this document have been generated using this  
11 method.

12 However, addressing the expected sensitivity of an experiment per the second question above re-  
13 quires consideration of the effect of statistical fluctuations and variations in systematics. If the  
14 experiment is repeated many times, a distribution of  $\Delta\chi^2$  values will appear. Studies in [140] and  
15 elsewhere (e.g., [141]) show that the  $\Delta\chi^2$  metric employed here *does not* follow the commonly  
16 expected  $\chi^2$  function for one degree of freedom, which has a mean of  $\overline{\Delta\chi^2}$  and can be interpreted  
17 using a Gaussian distribution with a standard deviation of  $\sqrt{|\overline{\Delta\chi^2}|}$ . Rather, these studies show that  
18 when the observed counts in the experiment are large enough, the distribution of  $\Delta\chi^2$  used here  
19 approximately follows a Gaussian distribution with a mean and standard deviation of  $\overline{\Delta\chi^2}$  and  
20  $2\sqrt{|\overline{\Delta\chi^2}|}$ , respectively [140].

21 Figure 4.6 shows the expected distribution of  $\Delta\chi^2$  values in LBNE from toy Monte Carlo studies.  
22 The interpretation of pairs of distributions, such as those in the various panels of this figure, de-  
23 pends on the information being sought. For example, one is not necessarily interested simply in the  
24 fraction of experiments where  $\Delta\chi^2$  has the “right” sign. (An experiment that obtains a small value  
25 of  $\Delta\chi^2$ , even with the “right” sign, would not be particularly constraining since there is no way  
26 *a priori* to know which is the right sign — this is what the experiment is attempting to measure.)  
27 It should also be noted that in general  $|\overline{\Delta\chi^2_{\text{MH=NH}}}|$  for the case of true normal hierarchy is not  
28 necessarily equal to  $|\overline{\Delta\chi^2_{\text{MH=IH}}}|$  for the case of true inverted hierarchy, nor do the corresponding  
29 distributions necessarily have the same shape. For some ranges in  $\delta_{\text{CP}}$ , for example, the event rate  
30 in LBNE is sufficiently different for the two MH hypotheses that the corresponding distributions  
31 in  $\Delta\chi^2$  are quite distinct.

32 The plots shown on the left in Figure 4.6 illustrate the case for a true value of  $\delta_{\text{CP}} = 0^\circ$ , where the  
33  $\Delta\chi^2$  distributions for NH and IH scenarios are similar. Shown on the right are the corresponding  
34 distributions for the case of  $\delta_{\text{CP}} = 90^\circ$ , where for normal hierarchy the matter asymmetry is  
35 maximally offset by the CP asymmetry, leading to poorer MH discrimination. For the inverted  
36 hierarchy case, these effects go in the same direction, leading to better MH discrimination. The  
37 converse is the case for  $\delta_{\text{CP}} = -90^\circ$ . Since the true value of  $\delta_{\text{CP}}$  is unknown (although a best-fit

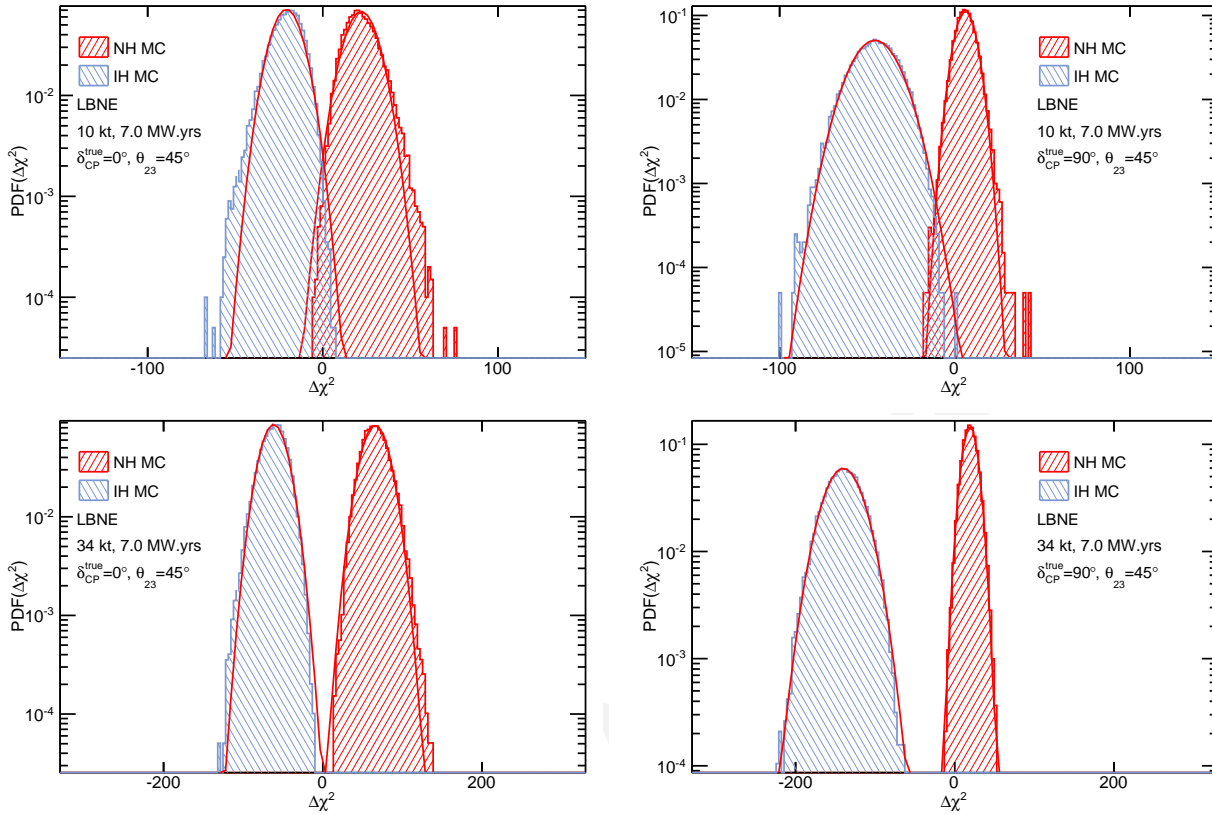


**Figure 4.6:**  $\Delta\chi^2_{\text{MH}=\text{NH}}$  (red) and  $\Delta\chi^2_{\text{MH}=\text{IH}}$  (blue) distributions for LBNE from Toy MC studies. The top set of figures are for a 10-kt detector operating six years in a 1.2-MW beam. The bottom set is for a 34-kt detector operating six years in a 1.2-MW beam. The figures on the left are for  $\delta_{\text{CP}}^{\text{true}} = 0^\circ$  and the figures on the right are for  $\delta_{\text{CP}}^{\text{true}} = 90^\circ$ . The value of  $\delta_{\text{CP}}$  is unconstrained in the fit.

1 value and confidence interval will emerge from the analysis of the data collected), comparison of a  
 2 given value of  $\Delta\chi^2$  with expected distributions for NH and IH cases for the *same* value of  $\delta_{\text{CP}}$  does  
 3 not in general provide the appropriate test. For simplicity, following [141], the discussion below  
 4 focuses on the respective values of  $\delta_{\text{CP}}$  for which the experiment will have poorest sensitivity for  
 5 NH ( $+90^\circ$ ) and IH ( $-90^\circ$ ) scenarios.

6 Given the above introduction to the statistical fluctuation issues, it is natural to employ the statisti-  
 7 cal language of hypothesis testing in projecting LBNE's MH sensitivity. Specifically,  $\alpha$  is defined  
 8 as the desired Type-I error rate — that is, the probability of rejecting a particular hypothesis, e.g.,  
 9 normal hierarchy (NH), in the case where this is the true hypothesis. One can then ask what the  
 10 corresponding Type-II error rate  $\beta$  would be, defined as the probability of accepting the hypothesis  
 11 being tested (NH in this example), when in fact the alternate hypothesis (IH) is true. The pair of  
 12  $\alpha$  and  $\beta$  would correspond to a particular value of  $\overline{\Delta\chi^2}$  chosen (in advance of the experiment) as  
 13 a criterion for deciding whether to rule out the NH (or IH). Historically, many experiments have  
 14 characterized their anticipated sensitivity by reporting  $\alpha$  for the case of  $\beta = 0.5$ , which is noth-  
 15 ing more than that given by the median value of the test statistic (in this case,  $\Delta\chi^2 = \overline{\Delta\chi^2}$ ) as

described above. Sometimes, the sensitivity is also reported as the square root of  $\overline{\Delta\chi^2}$ .

Due to the approximate symmetry of the mass hierarchy ambiguity as a function of  $\delta_{\text{CP}}$  for the two MH scenarios and the desire to be able to reject exactly one of the two possible mass orderings [141], it is also natural to report a value of  $\alpha$  for an experiment such that  $\alpha = \beta$  [142,143,141]. In this way, it is possible to express just how “unlucky” an experiment can be while maintaining a corresponding sensitivity  $\alpha$ . In the case of LBNE, a reasonable benchmark for comparison corresponds to  $\overline{\Delta\chi^2} = 36$ . For this case, specifying  $\alpha = \beta$  yields  $\alpha = 0.0013$ , which means that the experiment will have a 0.13% probability of ruling out the true MH hypothesis and of accepting the wrong MH hypothesis.

As described above, and as is evident in the plots presented, such as those in Figures 4.4 and 4.5, the sensitivity of LBNE is strongly dependent on the true value of  $\delta_{\text{CP}}$ ; Figure 4.12 shows that it also depends on the true value of  $\sin^2 \theta_{23}$ . While plotting the value of  $\alpha$  (for some choice of  $\beta$ , such as  $\beta = 0.5$  or  $\beta = \alpha$ ) as a function of these parameters encapsulates the sensitivity, a visually helpful presentation is obtained by plotting the expected mean value,  $\overline{\Delta\chi^2}$ , as well as ranges of possible values corresponding to the expected distribution in  $\Delta\chi^2$ . Thus, Figure 4.7 shows the dependence of  $\sqrt{|\overline{\Delta\chi^2}|}$  on the true value of  $\delta_{\text{CP}}$  for the typical LBNE data set, for two possible values of  $\sin^2 \theta_{23}$ , as well as the corresponding expectation bands within which 68% (green) and 95% (yellow) of LBNE sensitivities will fall. These expectation bands give a semi-quantitative picture of the likely range of outcomes for the experiment.

The horizontal dashed lines on Figure 4.7 specify the confidence level of an experiment with a particular value of  $\Delta\chi^2$  such that:

$$\text{CL} = P(\text{favored MH}|\text{data } x) / (P(\text{favored MH}|\text{data } x) + P(\text{unfavored MH}|\text{data } x)), \quad (4.5)$$

following the convention in [140], where the notation  $P(A|B)$  represents the probability of A given condition B and these probabilities are inferred from the corresponding likelihoods via Bayes’ Theorem. Alternatively, the  $\Delta\chi^2$  values shown in these plots can be approximately translated to sensitivities in terms of  $\alpha$ , for whatever choice of  $\beta$  is desired, following, for example, the prescription described in [141].

As seen in Figure 4.7, a typical LBNE data set with a 34-kt detector can determine the mass hierarchy with  $|\overline{\Delta\chi^2}| \geq 25$  for all values of  $\delta_{\text{CP}}$  (for the left plot, where  $\sin^2 \theta_{23} = 0.39$ ). From a Bayesian analysis, the probability that an experiment measuring  $|\overline{\Delta\chi^2}| = 25$  has ruled out the true MH hypothesis is  $3.7 \times 10^{-6}$ , as indicated for the corresponding horizontal dashed line in the plots in this figure. When considering the effect of statistical fluctuations, for the same value of  $\theta_{23}$ , about 97.5% of experiments will determine the mass hierarchy with  $|\overline{\Delta\chi^2}| > 9$  for the worst-case value of  $\delta_{\text{CP}}$ , where  $|\overline{\Delta\chi^2}| = 9$  corresponds to a CL of 98.9%.

For the bulk of the range of  $\delta_{\text{CP}}$ , the sensitivity of LBNE is vastly better than for the worst-case value described above. Furthermore, newer data prefer values of  $\theta_{23}$  closer to maximal [61], which

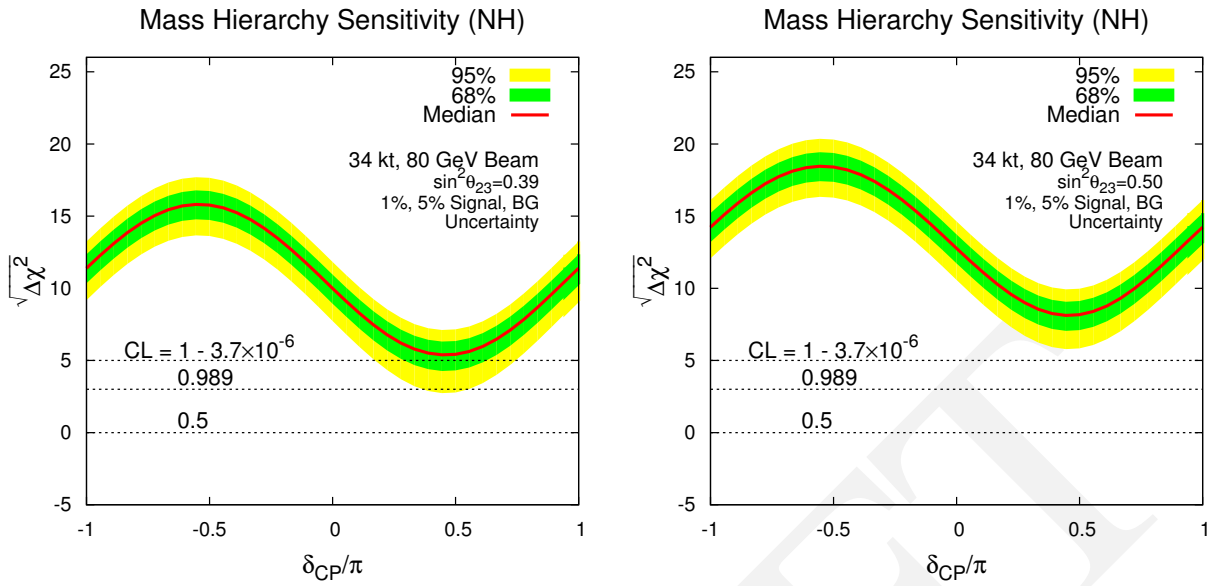


**Figure 4.7:** The square root of the mass hierarchy discrimination metric  $\Delta\chi^2$  is plotted as a function of the unknown value of  $\delta_{CP}$  for the full LBNE with 34-kt,  $\nu + \bar{\nu}$  3+3 yrs of running in a 1.2-MW beam, for true normal hierarchy. The red curve represents the most likely experimental value obtained, estimated using a data set absent statistical fluctuations, while the green and yellow bands represent the range of  $\Delta\chi^2$  values expected in 68% and 95% of all possible experimental cases, respectively. The horizontal lines indicate the probability that an experiment with that value of  $\Delta\chi^2$  correctly determines the mass hierarchy, computed according to a Bayesian statistical formulation. The plot on the left assumes a value of  $\sin^2\theta_{23} = 0.39$  [46], while that on the right assumes  $\sin^2\theta_{23} = 0.50$  (maximal  $\nu_\mu$ - $\nu_\tau$  mixing).

1 results in significantly enhanced LBNE mass hierarchy sensitivity (see Figure 4.12). As shown in  
 2 the right-hand plot of Figure 4.7, if  $\sin^2\theta_{23} = 0.5$ , the expected mass hierarchy sensitivity for  
 3 the typical LBNE experiment at the least favorable  $\delta_{CP}$  point is  $|\overline{\Delta\chi^2}| \approx 64$ , which is significantly  
 4 larger than the sensitivity of  $|\overline{\Delta\chi^2}| \approx 25$  expected for the same value of  $\delta_{CP}$  if  $\sin^2\theta_{23} = 0.39$ . This  
 5 suggests that a typical LBNE data set will determine the mass hierarchy with  $|\overline{\Delta\chi^2}|$  well above the  
 6 benchmark value of 36 mentioned above for even the worst-case values of  $\delta_{CP}$ .

7 In addition to detailed LBNE-specific frequentist studies reported in [141], an LBNE-specific up-  
 8 date (using both Bayesian and frequentist approaches) to the general statistical studies reported  
 9 in [140] is in preparation.

### 10 4.3.2 Sensitivities and Systematics

11 The main systematic uncertainties in any experiment are determined by the analysis strategy em-  
 12 ployed and the performance of the detector. Figure 4.8 outlines the analysis strategy commonly  
 13 employed to extract oscillation parameters in two-detector long-baseline neutrino oscillation ex-  
 14 periments. The measured spectrum of  $\nu_\mu$  events in the near detector,  $N_{ND}^{data}(\nu_\mu)$  is extrapolated to  
 15 the far detector and is used to predict both the  $\nu_\mu$ - and  $\nu_e$  appearance signals in the far detector,  
 16  $N_{FD}^{expected}(\nu_\mu)$  and  $N_{FD}^{expected}(\nu_e)$  respectively. The measured spectrum of  $\nu_e$  candidates in the near

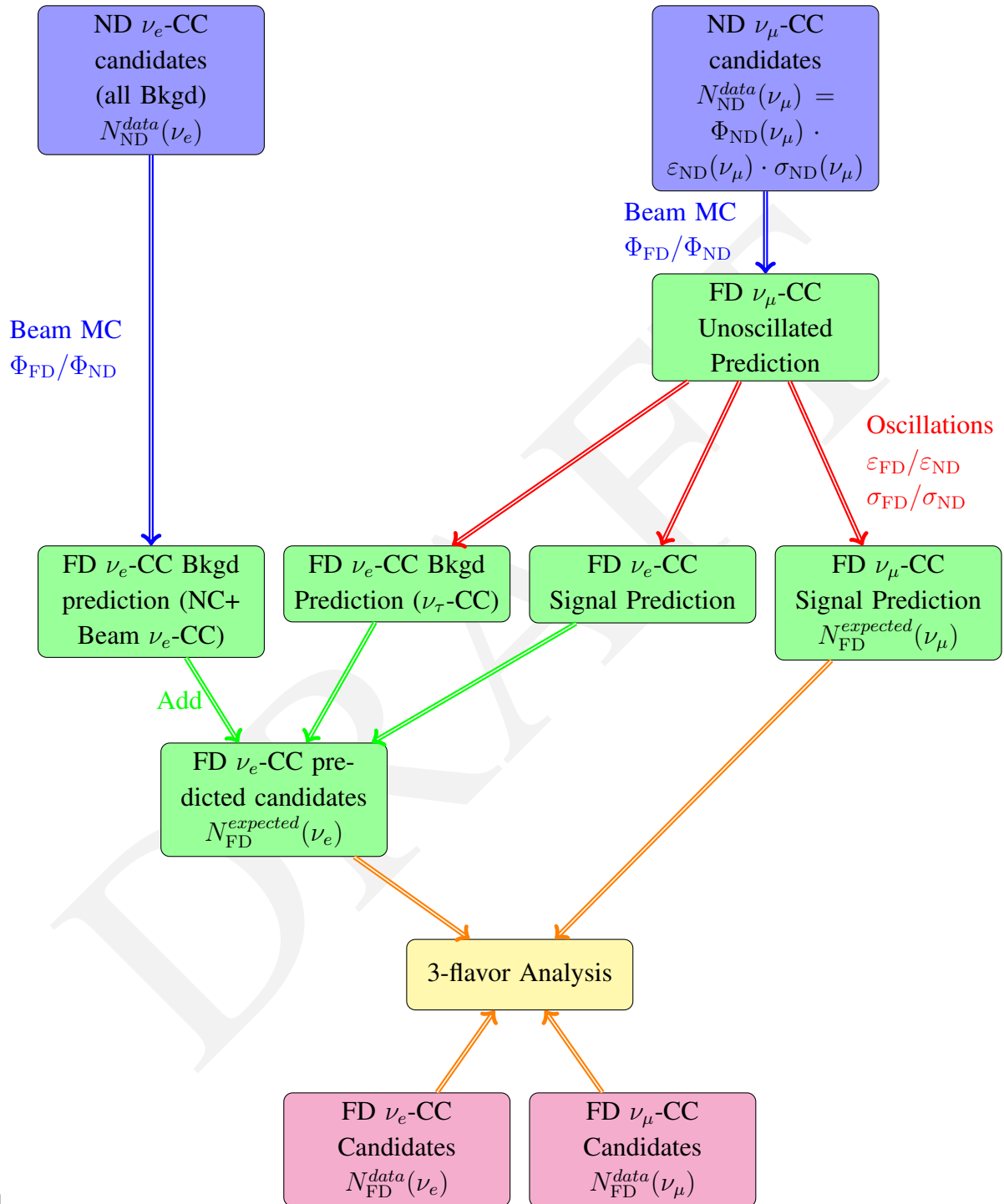


**Figure 4.8:** Flow chart of the  $\nu_e$  appearance analysis method in a two-detector long-baseline experiment.  $\Phi$  refers to the beam flux,  $\varepsilon$  refers to detector efficiencies and smearing, and  $\sigma$  refers to neutrino interaction modeling. The terms ND and FD refer to the near and far detector, respectively.

- 1 detector  $N_{\text{ND}}^{\text{data}}(\nu_e)$ , which comprises mostly the beam  $\nu_e$  events and NC  $\pi^0$  misidentified events, is  
 2 used to predict the background to the  $\nu_e$  appearance signal in the far detector. In LBNE, neutrino  
 3 oscillation parameters will be extracted using a fit to four far detector data samples:  $\nu_e$ ,  $\bar{\nu}_e$ ,  $\nu_\mu$ , and  
 4  $\bar{\nu}_\mu$ , which will allow for partial cancellation of uncertainties.

**Table 4.5:** The dominant systematic uncertainties on the  $\nu_e$  appearance signal prediction in MINOS and T2K and a conservative projection of the expected uncertainties in LBNE. For the MINOS uncertainties *absolute* refers to the total uncertainty and  $\nu_e$  is the effect on the  $\nu_e$  appearance signal only. The LBNE uncertainties are the total *expected* uncertainties on the  $\nu_e$  appearance signal which include both correlated and uncorrelated uncertainties in the three-flavor fit.

Source of Uncertainty	MINOS Absolute/ $\nu_e$	T2K $\nu_e$	LBNE $\nu_e$	Comments
<b>Beam Flux after N/F extrapolation</b>	3%/0.3%	2.9%	2%	MINOS is normalization only. LBNE normalization and shape highly correlated between $\nu_\mu/\nu_e$ .
Detector effects				
<b>Energy scale (<math>\nu_\mu</math>)</b>	7%/3.5%	included above	(2%)	Included in LBNE $\nu_\mu$ sample uncertainty only in three-flavor fit. MINOS dominated by hadronic scale.
<b>Absolute energy scale (<math>\nu_e</math>)</b>	5.7%/2.7%	3.4% includes all FD effects	2%	Totally active LArTPC with calibration and test beam data lowers uncertainty.
<b>Fiducial volume</b>	2.4%/2.4%	1%	1%	Larger detectors = smaller uncertainty.
Neutrino interaction modeling				
<b>Simulation includes: hadronization cross sections nuclear models</b>	2.7%/2.7%	7.5%	$\sim 2\%$	Hadronization models are better constrained in the LBNE LArTPC. N/F cancellation larger in MINOS/LBNE. X-section uncertainties larger at T2K energies. Spectral analysis in LBNE provides extra constraint.
<b>Total</b>	<b>5.7%</b>	<b>8.8%</b>	<b>3.6%</b>	<b>Uncorrelated <math>\nu_e</math> uncertainty in full LBNE three-flavor fit = 1-2%.</b>

- 5 In the current generation of experiments, the measured spectrum of neutrino events in the near  
 6 detector is a product of beam flux ( $\Phi$ ), detector efficiency and smearing ( $\varepsilon$ ), and neutrino inter-  
 7 action dynamics ( $\sigma$ ). To extrapolate the observed spectra in the near detector to the far detector,  
 8 corrections have to be made for:

- 9 1. Differences in the beam flux in the near and far detectors,  $\Phi_{\text{FD}}/\Phi_{\text{ND}}$ : The near detector is  
 10 much closer to the neutrino beamline and sees an extended source of neutrinos from the de-  
 11 cay pipe as compared to the far detector, which observes a point source. A beam MC is used

to correct for these differences. Uncertainties arise from inaccuracies in the simulation of the hadron production from the target, the focusing of the horns, the material in the beamline (which absorbs hadrons before they can decay), and the decay channel geometry.

2. Differences in near and far detector smearing and efficiencies,  $\varepsilon_{\text{FD}}/\varepsilon_{\text{ND}}$ : The largest uncertainties arise from the different event selection efficiencies in the near and far detectors and, in particular, the imperfect modeling of the energy scales of the near and far detectors. Identical near and far detectors allow most of these uncertainties to cancel in the extrapolation in the case of the  $\nu_\mu$ -signal prediction. The  $\nu_e$ -signal prediction is extrapolated from  $N_{\text{ND}}^{\text{data}}(\nu_\mu)$ ; thus there are irreducible residual uncertainties arising from different criteria used to select  $\nu_e$  and  $\nu_\mu$  candidate events and different detector response functions.
3. Differences in the interactions of neutrinos in the near and far detector,  $\sigma_{\text{FD}}/\sigma_{\text{ND}}$ : In the case in which both near and far detectors use the same target nucleus, the differences cancel for extrapolation of the  $\nu_\mu$  signal from the near detector to the far detector. When using the  $\nu_\mu$  signal in the near detector to predict the  $\nu_e$  (and  $\nu_\tau$ ) signals in the far detector, uncertainties arising from differences in  $\nu_e$  ( $\nu_\tau$ ) and  $\nu_\mu$  interactions,  $\sigma_{\text{FD}}(\nu_e)/\sigma_{\text{ND}}(\nu_\mu)$ , dominate. These uncertainties are limited by theoretical uncertainties and are typically smaller at higher energies.

The estimation of the expected signals at the far detector can be summarized thus:

$$N_{\text{ND}}^{\text{data}}(\nu_\mu) = \Phi_{\text{ND}}(\nu_\mu) \otimes \varepsilon_{\text{ND}}(\nu_\mu) \otimes \sigma_{\text{ND}}(\nu_\mu) \quad (4.6)$$

$$N_{\text{FD}}^{\text{expected}}(\nu_\mu) = N_{\text{ND}}^{\text{data}}(\nu_\mu) \otimes \frac{\Phi_{\text{FD}}(\nu_\mu)}{\Phi_{\text{ND}}(\nu_\mu)} \otimes P(\nu_\mu \rightarrow \nu_\mu) \otimes \frac{\varepsilon_{\text{FD}}(\nu_\mu)}{\varepsilon_{\text{ND}}(\nu_\mu)} \otimes \frac{\sigma_{\text{FD}}(\nu_\mu)}{\sigma_{\text{ND}}(\nu_\mu)} \quad (4.7)$$

$$N_{\text{FD}}^{\text{expected}}(\nu_e) = N_{\text{ND}}^{\text{data}}(\nu_\mu) \otimes \frac{\Phi_{\text{FD}}(\nu_e)}{\Phi_{\text{ND}}(\nu_\mu)} \otimes P(\nu_\mu \rightarrow \nu_e) \otimes \frac{\varepsilon_{\text{FD}}(\nu_e)}{\varepsilon_{\text{ND}}(\nu_\mu)} \otimes \frac{\sigma_{\text{FD}}(\nu_e)}{\sigma_{\text{ND}}(\nu_\mu)} \quad (4.8)$$

Expected signal events

$$+ N_{\text{ND}}^{\text{data}}(\nu_e) \otimes \frac{\Phi_{\text{FD}}(\nu_e)}{\Phi_{\text{ND}}(\nu_e)} \otimes P(\nu_e \rightarrow \nu_e) \otimes \frac{\varepsilon_{\text{FD}}(\nu_e)}{\varepsilon_{\text{ND}}(\nu_e)} \otimes \frac{\sigma_{\text{FD}}(\nu_e)}{\sigma_{\text{ND}}(\nu_e)}$$

Beam  $\nu_e$  events

$$+ \text{NC background extrapolated from } N_{\text{ND}}^{\text{data}}(\nu_e)$$

$$+ \nu_\tau \text{ background extrapolated from } N_{\text{ND}}^{\text{data}}(\nu_\mu)$$

Expected systematic uncertainties on the LBNE  $\nu_e$  appearance and  $\nu_\mu$ -signal samples in the three-flavor fit for LBNE (Table 4.2) are extrapolated from the current performance of the MINOS [133,144]

and T2K [139] experiments. The dominant uncertainties on the current  $\nu_e$  appearance analysis from MINOS and T2K and the expected corresponding uncertainties in LBNE are shown in Table 4.5.

The categorization of the dominant experimental uncertainties in Table 4.5 are not always in exact

1 correspondence since T2K and MINOS are very different experiments and deploy different analy-  
 2 sis techniques. A detailed description of the expected LBNE performance on each of the dominant  
 3 uncertainties follows.

4 **Beam flux uncertainties:** The LBNE high-resolution near detector is being designed with the  
 5 goal of accurately measuring the unoscillated beam *flux* at the near site with a precision  $\leq 2\%$  for  
 6 both shape and absolute normalization. Table 4.6 summarizes the precision that can be achieved  
 7 using different near detector analysis techniques, described in detail in Section 7.1, to measure  
 the absolute normalization and shape of the different components of this flux. It is important to

**Table 4.6:** Precisions achievable from in situ  $\nu_\mu$  and  $\nu_e$  flux measurements in the fine-grained, high-resolution ND with different techniques.

Technique	Flavor	Absolute normalization	Relative flux $\Phi(E_\nu)$	Near Detector requirements
<b>NC Scattering</b> $\nu_\mu e^- \rightarrow \nu_\mu e^-$	$\nu_\mu$	2.5%	$\sim 5\%$	$e^-$ ID $\theta_e$ Resolution $e^-/e^+$ Separation
<b>Inverse muon decay</b> $\nu_\mu e^- \rightarrow \mu^- \nu_e$	$\nu_\mu$	3%		$\mu^-$ ID $\theta_\mu$ Resolution 2-Track ( $\mu+X$ ) Resolution $\mu$ energy scale
<b>CC QE</b> $\nu_\mu n \rightarrow \mu^- p$ $Q^2 \rightarrow 0$	$\nu_\mu$	3 – 5%	5 – 10%	$D$ target $p$ Angular resolution $p$ energy resolution Back-Subtraction
<b>CC QE</b> $\bar{\nu}_\mu p \rightarrow \mu^+ n$ $Q^2 \rightarrow 0$	$\bar{\nu}_\mu$	5%	10%	$H$ target Back-Subtraction
<b>Low-<math>\nu_0</math></b>	$\nu_\mu$		2.0%	$\mu^-$ vs $\mu^+$ $E_\mu$ -Scale Low- $E_{Had}$ Resolution
<b>Low-<math>\nu_0</math></b>	$\bar{\nu}_\mu$		2.0%	$\mu^-$ vs $\mu^+$ $E_\mu$ -Scale Low- $E_{Had}$ Resolution
<b>Low-<math>\nu_0</math></b>	$\nu_e/\bar{\nu}_e$	1-3%	2.0%	$e^-/e^+$ Separation ( $K_L^0$ )
<b>CC</b>	$\nu_e/\nu_\mu$	<1%	$\sim 2\%$	$e^-$ ID & $\mu^-$ ID $p_e/p_\mu$ Resolution
<b>CC</b>	$\bar{\nu}_e/\bar{\nu}_\mu$	<1%	$\sim 2\%$	$e^+$ ID & $\mu^+$ ID $p_e/p_\mu$ Resolution
<b>Low-<math>\nu_0</math>/CohPi</b>	$\bar{\nu}_\mu/\nu_\mu$	$\sim 2\%$	$\sim 2\%$	$\mu^+$ ID & $\mu^-$ ID $p_\mu$ Resolution $E_{Had}$ Resolution

note that several of these techniques have already been used and *proven to work* in neutrino experiments such as MINOS [145] and NOMAD [146,147]. In particular, the inclusive neutrino charged-current cross section measurement in the MINOS near detector reported in [145] has already achieved a normalization uncertainty of  $\sim 2\%$  in the range of  $3 < E_\nu < 9$  GeV using the low- $\nu_0$  method described in Section 7.1. The total systematic uncertainty on the NuMI neutrino flux measurements by the MINOS near detector reported in [145] are  $\sim 6\%$  and were limited by the detector performance. Recent independent studies on extraction of the neutrino flux using the low- $\nu_0$  method [148] indicate that the technique can be reliably extended down to 1 GeV.

The LBNE high-resolution near detector is being designed to significantly improve performance relative to the current generation of high-intensity neutrino detectors. A detailed beamline simulation will enable the extrapolation of the LBNE near-detector flux measurements to the unoscillated far detector spectrum with high precision using techniques similar to those used by MINOS [149]. The near-to-far  $\nu_\mu$  unoscillated-spectrum extrapolation uncertainties already achieved by MINOS are  $< 3\%$  in the MINOS (and also in the LBNE) appearance signal range of  $1 < E_\nu < 8$  GeV [150,149]. The MINOS extrapolation does not include any independent constraints on the hadron production spectrum from the proton target or information on the horn focusing performance from the muon flux measurements at the near site. The NuMI beamline — the design of which is very similar to LBNE's — is expected to operate for more than a decade with improved flux measurements using the much more capable MINER $\nu$ A detector [151] in both the low-energy and high-energy tunes. MINER $\nu$ A is designed to measure the absolute NuMI flux with a precision of  $\sim 5\%$  or better; data from MINER $\nu$ A will be used to further improve the accuracy of the LBNE beamline simulation, reducing the uncertainties on the extrapolation of the flux. A new program of hadron production measurements at the NA61/SHINE [152] experiment will also reduce the near-far extrapolation uncertainties from the LBNE beamline simulation. The combination of LBNE near detector flux measurements and improved beamline simulation is expected to enable a prediction of the far detector  $\nu_e$  appearance signal with a precision of  $< 2\%$  total normalization and shape uncertainty. Since this uncertainty is highly correlated between the four data samples in the three-flavor fit, the final uncorrelated uncertainty on the  $\nu_e$ -signal sample will be significantly smaller.

**$\nu_\mu$  energy-scale uncertainty:** Both T2K and MINOS use the reconstructed  $\nu_\mu$  event spectrum in the near detector to predict the  $\nu_e$  appearance signal at the far detector. Therefore the  $\nu_\mu$  energy-scale uncertainty in the near detector is propagated as an uncertainty on the  $\nu_e$  appearance signal at the far detector. In MINOS — which has a high proportion of non-QE events — the  $\nu_\mu$  energy-scale uncertainty is dominated by uncertainty in the hadronic energy scale (7% for  $E_\nu < 3$  GeV) [153] and the muon energy scale (2.5%). Utilization of the low- $\nu$  method for energies less than 3 GeV in LBNE reduces the hadronic energy-scale contribution to the uncertainty in the  $\nu_\mu$  energy scale in the near detector. As discussed in Chapter 7, it is expected that both the muon and hadronic energy-scale uncertainties in the near detector will be  $< 1\%$ , so far-detector energy-scale uncertainties will dominate the uncertainty in the  $\nu_\mu$ -signal prediction. The high-resolution LArTPC far detector and

1 an active program of hadron test-beam experiments planned for LBNE will reduce far-detector  
 2 hadronic energy-scale uncertainties, which also contribute to uncertainty in the energy scale of the  
 3 far detector  $\nu_\mu$  signal used in the three-flavor analysis. Extrapolating from MINOS, the LBNE  $\nu_\mu$   
 4 energy-scale uncertainty is thus estimated to be  $\sim 2\%$ .

5 In MINOS, the 7%  $\nu_\mu$  energy-scale uncertainty resulted in a residual uncertainty of 3.5% on the  
 6  $\nu_e$  signal prediction. In the LBNE full three-flavor analysis, this uncertainty is 100% correlated  
 7 between the predicted  $\nu_\mu$  and  $\nu_e$  signal samples; therefore a  $E_{\nu_\mu}$  energy-scale uncertainty of 2%  
 8 is assigned to the  $\nu_\mu$  signal prediction in LBNE. The residual uncorrelated uncertainty on the  $\nu_e$   
 9 signal prediction is considered to be negligible.

10 **Absolute  $\nu_e$  energy-scale uncertainties:** In Figure 4.9, the mass hierarchy and CP-violation sensi-  
 11 tivity obtained using a rate-only, a shape-only and a rate+shape analysis of  $\nu_e$  appearance is shown.  
 12 This study demonstrates that a critical component of LBNE's oscillation sensitivity is an accurate  
 measurement of the shape of the  $\nu_e$  appearance signal. This measurement depends on the precision

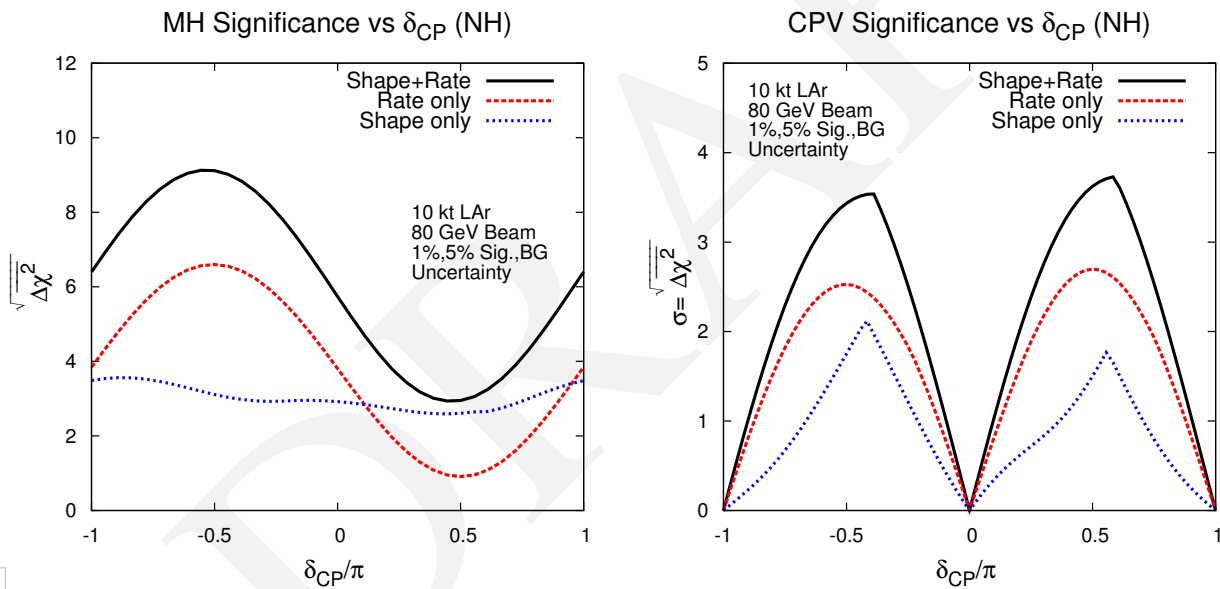


**Figure 4.9:** The mass hierarchy (left) and CP violation (right) sensitivities from shape, rate, and shape+rate. The sensitivity is for a 10-kt detector, 1.2-MW beam, 3+3 ( $\nu + \bar{\nu}$ ) years, for true normal hierarchy.

13 with which the detector response to  $\nu_e$  interactions is understood. The  $\nu_e$  energy-scale uncertainty,  
 14 which is not yet included in the current sensitivity calculation with the GLOBES framework, is  
 15 therefore expected to be an important systematic uncertainty in the LBNE oscillation analysis.

16 The effect of  $\nu_e$  energy-scale uncertainty on the  $\nu_e$  signal normalization, determined by the pre-  
 17 cision of detector calibration, was 2.7% in MINOS and 3.4% in T2K, where the T2K uncertainty  
 18 actually includes most far detector effects. LBNE's LArTPC detector technology is expected to  
 19 outperform both the MINOS sampling calorimeter and the T2K water Cherenkov detector in recon-  
 20 struction of the  $\nu_e$  interaction. For example, the proton produced from the  $\nu_e$  QE interaction — the  
 21

1 interaction with potentially the best  $\nu_e$  energy resolution — is clearly visible in a LArTPC [154],  
2 whereas it is often below Cherenkov threshold in T2K. An active program of test beam experi-  
3 ments with LArTPCs is currently being planned to address the detector response to electrons and  
4 hadrons. Results from the test beam experiments and the projected performance of the in situ cali-  
5 bration will enable LBNE to limit the detector energy-scale uncertainties below the level achieved  
6 by the current generation of experiments.

7 Hadronic energy is expected to contribute more than half of the total energy deposit for many  $\nu_e$  and  
8  $\nu_\mu$  interactions in LBNE. The hadronic energy scale does not depend on neutrino flavor; it should  
9 be identical for  $\nu_e$  and  $\nu_\mu$  interactions, so this portion of the absolute energy-scale uncertainty is  
10 expected to largely cancel in the LBNE three-flavor analysis. This cancellation may be reduced to  
11 the extent that event-selection criteria vary the hadronic energy fraction among the samples.

12 **Simulation uncertainties:** The simulation uncertainties listed in Table 4.5 refer primarily to un-  
13 certainties in modeling neutrino interactions with the target nucleus in the near and far detectors.  
14 These uncertainties include  $\nu_e$  and  $\nu_\mu$  cross section uncertainties, uncertainties arising from the  
15 modeling of the structure of the target nucleus, modeling of final-state interactions within the nu-  
16 cleus, and hadronization model uncertainties arising from the break up of the target nucleus in  
17 higher-energy inelastic interactions. The deployment of identical nuclear targets in the MINOS  
18 (iron) and LBNE (argon) near and far detectors allows for a larger cancellation of the simulation  
19 uncertainties as compared to T2K, which used dissimilar target nuclei in its near detector (carbon)  
20 and far detector (oxygen). A high-resolution near detector such as that being designed for LBNE  
21 will enable further constraints on the hadronization models by resolving many of the individual  
22 particles produced in resonance and deep inelastic interactions, which represent  $\sim 75\%$  of LBNE  
23 neutrino interactions.

24 The MINOS  $\nu_e$  appearance analysis achieved a 2.7% residual uncertainty from simulation after  
25 the near-to-far extrapolation. The MINOS simulation uncertainty is dominated by hadronization  
26 uncertainties, because cross section uncertainties largely cancel between the identical nuclei in the  
27 near and far detectors. The T2K residual uncertainty after near-to-far extrapolation is 7%. The near-  
28 to-far cancellation of simulation uncertainties is less pronounced in T2K compared to MINOS due  
29 to the different target nuclei in its near and far detectors. Additionally, the T2K analysis includes  
30 more sources of cross section uncertainties than MINOS and, at the lower T2K energies, larger  
31 differences in  $\nu_\mu/\nu_e$  cross sections (2.9 %) persist after extrapolating the  $\nu_\mu$  spectrum in the near  
32 detector to the  $\nu_e$  signal prediction in the far.

33 The LBNE near detector design is required to achieve a cancellation of near-to-far cross section  
34 and hadronization-model uncertainties at the same level as MINOS or better. The  $\nu_e$  appearance  
35 signal in LBNE peaks at 2.5 GeV; these higher energies will result in lower uncertainties from the  
36 cross section effects considered by T2K. In addition, since cross section variations impact the ob-  
37 served  $\nu_e$  and  $\nu_\mu$  spectra differently when compared to oscillation effects, the fit to the broad-band  
38 spectrum in LBNE could constrain some of these uncertainties further. Therefore, it is expected

1 that LBNE could reduce the total  $\nu_e$  appearance simulation uncertainties to a level of 2%. Prelimi-  
 2 nary results from the LBNE Fast MC simulation described in Appendix A indicate that many cross  
 3 section uncertainties cancel out when combining the  $\nu_\mu$  disappearance and  $\nu_e$  appearance signal  
 4 samples in a three-flavor fit, resulting in a much smaller uncorrelated uncertainty on the  $\nu_e$  signal  
 5 sample.

6 It is important to note that some  $\nu/\bar{\nu}$  simulation uncertainties may not cancel out in the near-to-far  
 7 extrapolation or in the combined fit; in particular, uncertainties due to nuclear models and intra-  
 8 nuclear effects are different for  $\nu/\bar{\nu}$  interactions. New models of intra-nuclear effects are being  
 9 evaluated to determine the size of these irreducible residual uncertainties. Additionally, there are  
 10 uncertainties at the level of 1-2% in the cross sections that will not cancel between  $\nu_e$  and  $\nu_\mu$  [155].  
 11 In the absence of theoretical progress, these should also be considered irreducible.

12 **Fiducial volume uncertainties:** One of the dominant uncertainties in the MINOS  $\nu_\mu$  disappear-  
 13 ance analysis — a high-precision oscillation analysis based on a detailed spectral shape — was the  
 14 fiducial-volume uncertainty, which included near and far detector reconstruction uncertainties. The  
 15 uncertainty on the fiducial volume of the MINOS far detector alone was 2.4%. T2K, with a much  
 16 larger far detector (22.5 kt fiducial), was able to reduce this uncertainty to the 1% level. It is ex-  
 17 pected that LBNE will be able to achieve this level of uncertainty on the  $\nu_e$  appearance signal. With  
 18 the combination of all four signal samples ( $\nu_\mu, \bar{\nu}_\mu, \nu_e, \bar{\nu}_e$ ) in a three-flavor fit, the  $\nu_e$  uncorrelated  
 19 portion of this uncertainty is expected to be smaller than 1%.

20  **$\nu_e$  appearance background systematic uncertainties:** The  $\nu_e$  appearance normalization uncer-  
 21 tainty is expected to be at least as good as the  $\sim 5\%$  [133] achieved by the  $\nu_e$  appearance search  
 22 in the MINOS experiment, using the technique of predicting intrinsic-beam and neutral-current  
 23 background levels from near-detector measurements. Additionally, the LBNE far detector should  
 24 be able to provide additional constraints on the background level by independently measuring  
 25 neutral-current and  $\nu_\tau$  background.

26 In Figure 4.10, the mass hierarchy and CP-violation sensitivities as a function of exposure are  
 27 evaluated using three different sets of assumptions regarding the uncorrelated  $\nu_e$  signal/background  
 28 normalization uncertainties: 1%/5% (the goal of the LBNE scientific program), 2%/5% and 5%/10%.  
 29 The last is a conservative estimate of the uncertainties that can be achieved in LBNE without un-  
 30 oscillated neutrino beam measurements at the near site. The impact of signal and background  
 31 normalization uncertainties on the mass hierarchy sensitivity is small even at high exposures given  
 32 the large  $\nu/\bar{\nu}$  asymmetry at 1,300 km and the fact that much of the sensitivity to mass hierarchy  
 33 comes from analysis of the spectral shapes (see Figure 4.9). For CP violation, however, the impact  
 34 of normalization uncertainties is significant at exposures  $\geq 100 \text{ kt} \cdot \text{MW} \cdot \text{years}$ .

35 Table 4.7 summarizes the LBNE exposures required to reach  $3\sigma$  and  $5\sigma$  sensitivity to CP vio-  
 36 lation for at least 50% of all possible values of  $\delta_{\text{CP}}$ . The resolution on  $\delta_{\text{CP}}$  is also shown. The  
 37 exposures vary depending on the assumptions made about the normalization uncertainties that

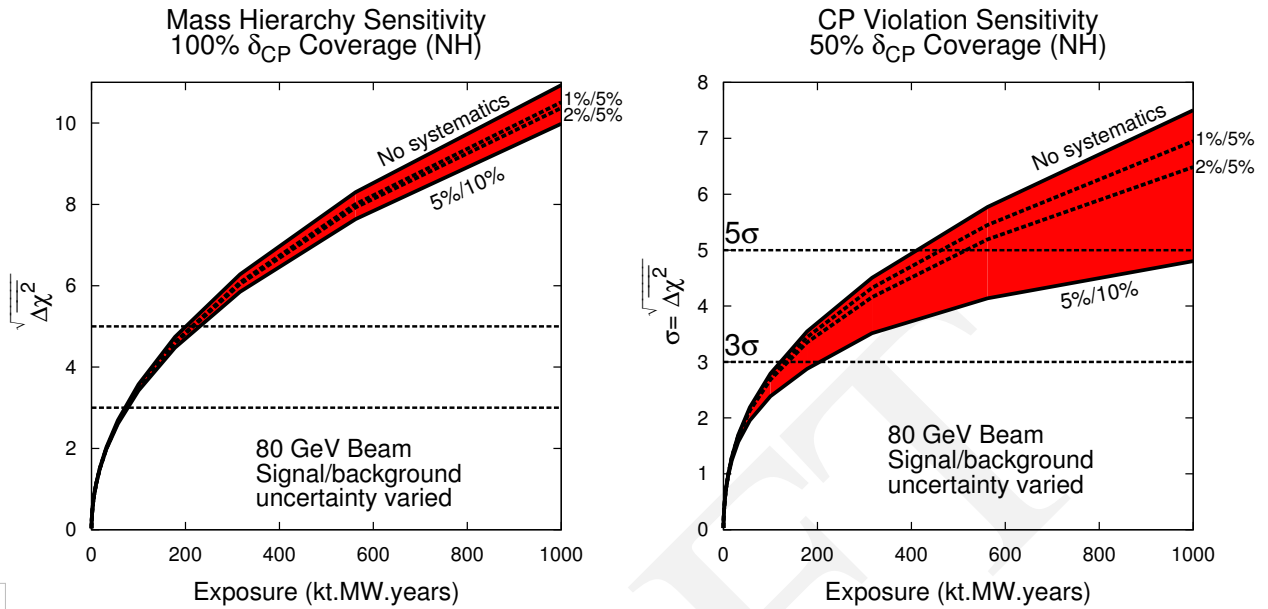


fig:systs

**Figure 4.10:** The mass hierarchy (left) and CP violation (right) sensitivities as a function of exposure in  $\text{kt} \cdot \text{year}$ , for true normal hierarchy. The band represents the range of signal and background normalization errors.

- 1 can be achieved in LBNE. The normalization uncertainty assumptions range from 1-2%/5% on  
 2 signal/background to 5%/10%. The uncertainties listed in Table 4.7 and shown in the sensitivity

**Table 4.7:** The exposures required to reach  $3\sigma$  and  $5\sigma$  sensitivity to CP violation for at least 50% of all possible values of  $\delta_{\text{CP}}$  as a function of systematic uncertainties assumed on the  $\nu_e$  appearance signal. The uncertainties varied are the uncorrelated signal normalization uncertainty (Sig) and the background normalization uncertainty (Bkgd).

tab:senssysts

Systematic uncertainty	CP Sensitivity		Required Exposure
	$\delta_{\text{CP}}$ Fraction	$(\sqrt{\Delta\chi^2})$	
<b>0 (statistical only)</b>	50% $\delta_{\text{CP}}$	$3\sigma$	100 $\text{kt} \cdot \text{MW} \cdot \text{year}$
	50% $\delta_{\text{CP}}$	$5\sigma$	400 $\text{kt} \cdot \text{MW} \cdot \text{year}$
<b>1%/5% (Sig/bkgd)</b>	50% $\delta_{\text{CP}}$	$3\sigma$	100 $\text{kt} \cdot \text{MW} \cdot \text{year}$
	50% $\delta_{\text{CP}}$	$5\sigma$	450 $\text{kt} \cdot \text{MW} \cdot \text{year}$
<b>2%/5% (Sig/bkgd)</b>	50% $\delta_{\text{CP}}$	$3\sigma$	120 $\text{kt} \cdot \text{MW} \cdot \text{year}$
	50% $\delta_{\text{CP}}$	$5\sigma$	500 $\text{kt} \cdot \text{MW} \cdot \text{year}$
<b>5%/10% (no near <math>\nu</math> det.)</b>	50% $\delta_{\text{CP}}$	$3\sigma$	200 $\text{kt} \cdot \text{MW} \cdot \text{year}$

- 2  
 3 figures pertain to the  $\nu_e$  appearance signal and background normalization. In Figure 4.9 the sen-  
 4 sivities obtained from the rate only, shape only and rate+shape of the appearance spectrum are  
 5 shown for a 10-kt detector with an 80-GeV beam. For CP violation (right), the rate information  
 6 dominates the sensitivity, but the shape information enables the detector to exceed  $3\sigma$  sensitivity  
 7 for large CP violation. For the mass hierarchy sensitivity, Figure 4.9 (left) demonstrates that the

1 sensitivity in the least favorable range of  $\delta_{\text{CP}}$  values is dominated by the shape information. Further  
 2 analysis has shown that it is the region of the second oscillation node that is responsible for this  
 3 effect. The shape of the signal in this region will enable LBNE to determine the sign of  $\delta_{\text{CP}}$ , which  
 4 is sufficient to break the degeneracy with mass hierarchy effects and determine the correct sign of  
 5 the mass ordering.

6 Figures 4.11, 4.12, and 4.13 show the variation in sensitivity to CP violation and mass hierarchy  
 7 when the true value of the oscillation parameters  $\theta_{13}$ ,  $\theta_{23}$  and  $\Delta m_{31}^2$  are varied within the  $3\sigma$  range  
 8 allowed by the 2012  $3\nu$  global fit [46]. These sensitivities are calculated for six years with equal  
 9 exposures in  $\nu$  and  $\bar{\nu}$  mode in a 1.2-MW beam for the case in which an upgraded 80-GeV beam  
 and a near detector have both been implemented.

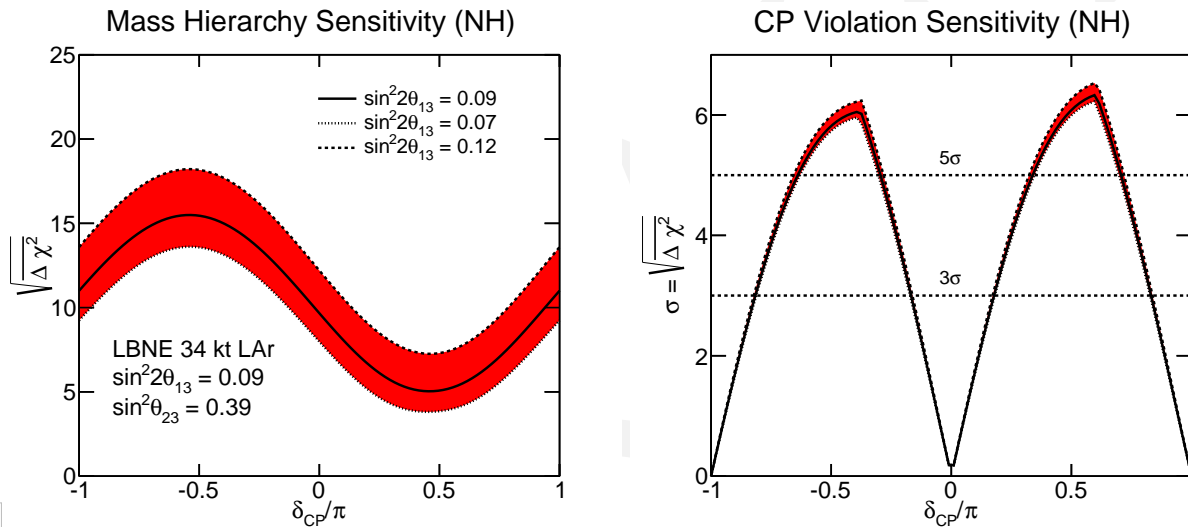


**Figure 4.11:** The significance with which the mass hierarchy (left) and CP violation, i.e.,  $\delta_{\text{CP}} \neq 0$  or  $\pi$ , (right) can be determined by a typical LBNE experiment as a function of the value of  $\delta_{\text{CP}}$  for an allowed range of  $\theta_{13}$  values and for normal hierarchy; assumes a 34-kt far detector.

10

11 In comparing Figures 4.11, 4.12 and 4.13, the dependence on the true value of  $\theta_{23}$  is particularly  
 12 striking. As  $\sin^2 \theta_{23}$  increases, the sensitivity to CP violation decreases because the CP asymmetry  
 13 that LBNE measures is inversely proportional to  $|\sin \theta_{23}|$  as demonstrated in Equation 2.20. For the  
 14 same reason, as  $\theta_{23}$  increases, the degeneracy between the CP and matter asymmetries is broken,  
 15 which increases the LBNE sensitivity to neutrino mass hierarchy. The explicit dependence of mass  
 16 hierarchy sensitivity on the value of  $\sin^2 \theta_{23}$  is shown in Figure 4.14. As this plot makes clear,  
 17 LBNE resolves the mass hierarchy with a significance of  $\sqrt{\Delta\chi^2} > 6$  for nearly all allowed values  
 18 of  $\sin^2 \theta_{23}$  and  $\delta_{\text{CP}}$ .

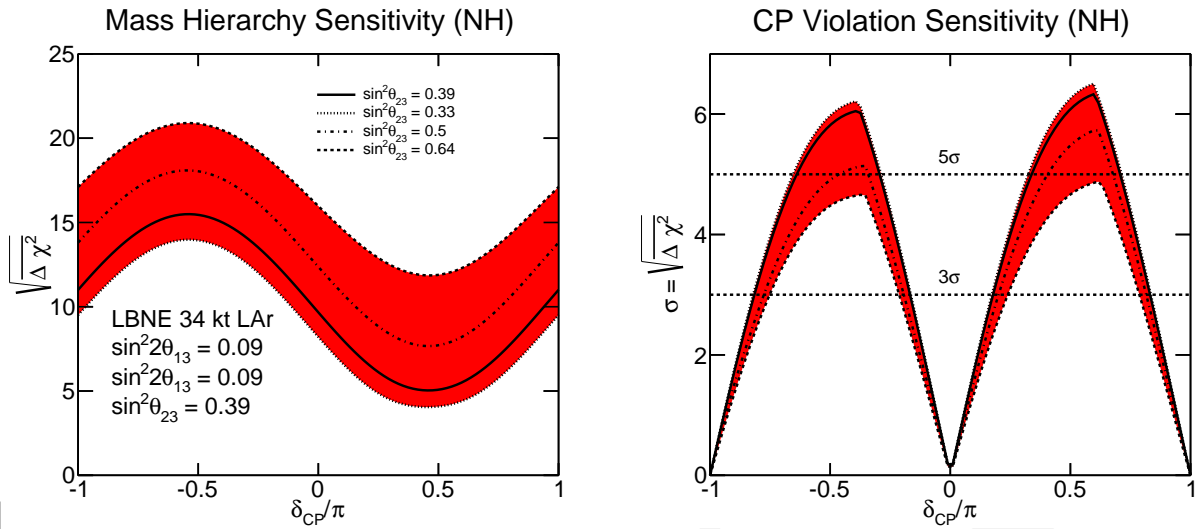


**Figure 4.12:** The significance with which the mass hierarchy (left) and CP violation, i.e.,  $\delta_{CP} \neq 0$  or  $\pi$ , (right) can be determined by a typical LBNE experiment as a function of the value of  $\delta_{CP}$  for an allowed range of  $\theta_{23}$  values and for normal hierarchy; assumes a 34-kt far detector.

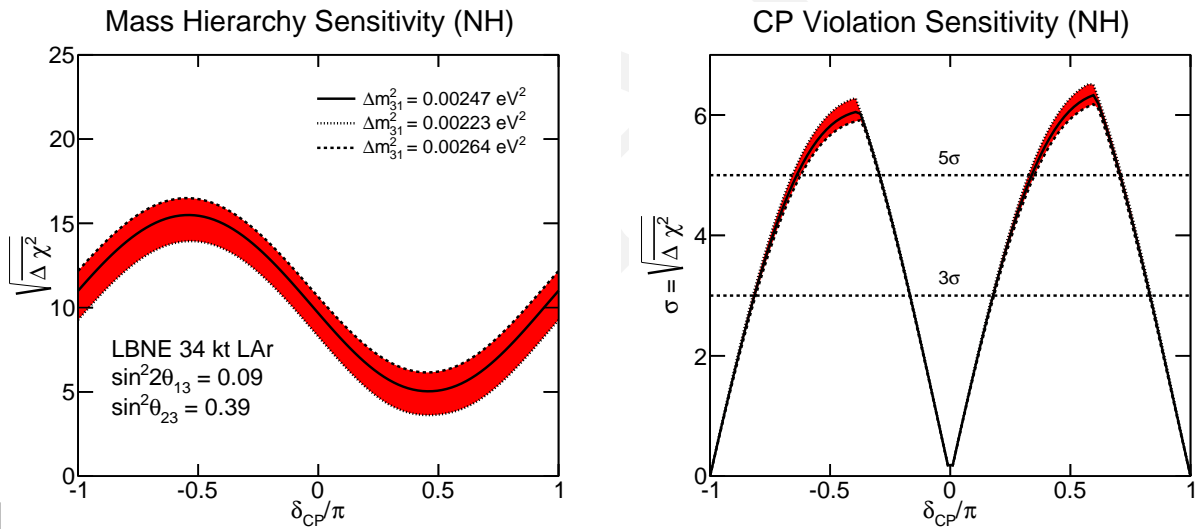


**Figure 4.13:** The significance with which the mass hierarchy (left) and CP violation, i.e.,  $\delta_{CP} \neq 0$  or  $\pi$ , (right) can be determined by a typical LBNE experiment as a function of the value of  $\delta_{CP}$  for an allowed range of  $\Delta m_{31}^2$  values and for normal hierarchy; assumes a 34-kt far detector.

### 1 4.3.3 Summary of CP and Mass Hierarchy Sensitivities

- 2 For LBNE 10 kt, the statistical uncertainties are much larger than the systematic uncertainties.  
 3 Combining the sensitivity from LBNE 10 kt with expected knowledge from the NO $\nu$ A and T2K  
 4 experiments would allow a 10-kt detector to achieve a  $\geq 4\sigma$  sensitivity for detecting CP violation  
 5 for 30% of the allowed values of  $\delta_{CP}$  and a  $\geq 3\sigma$  sensitivity for 50% of these values. It is clear  
 6 that the LBNE 10 kt sensitivity would be the dominant contribution in the combined sensitivities

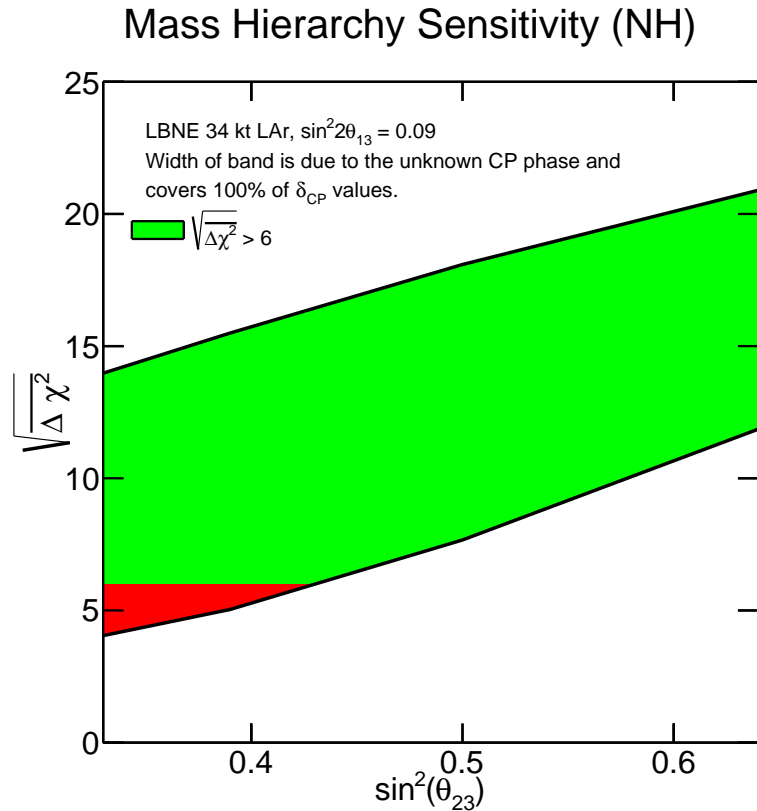


**Figure 4.14:** The significance with which the mass hierarchy can be determined by a typical LBNE experiment as a function of the value of  $\sin^2 \theta_{23}$ , for the  $3\sigma$  allowed range of  $\sin^2 \theta_{23}$ , for true normal hierarchy. The width of the band is due to the unknown value of  $\delta_{CP}$  and covers all possible values of  $\delta_{CP}$ . The green region shows the parameter space for which  $\sqrt{\Delta\chi^2} > 6$ . Assumes a 34-kt far detector with 6 years of running in a 1.2 MW beam.

1 and would therefore represent a significant advance in the search for leptonic CP violation over the  
 2 current generation of experiments, particularly in the region where the CP and matter effects are  
 3 degenerate.

4 The combination with T2K and NO $\nu$ A would allow the mass hierarchy to be determined with a  
 5 *minimum* precision of  $|\overline{\Delta\chi^2}| \geq 25$  over 60%  $\delta_{CP}$  values and  $|\overline{\Delta\chi^2}| \geq 16$  for all possible values  
 6 of  $\delta_{CP}$ . Due to the low event statistics in these experiments, the combination with NO $\nu$ A and T2K  
 7 only helps the sensitivity in the region of  $\delta_{CP} > 0$  (normal hierarchy) or  $\delta_{CP} < 0$  (inverted hier-  
 8 archy) where there are residual degeneracies between matter and CP-violating effects. As will be  
 9 discussed in Section 4.6, the combination with atmospheric neutrino oscillation studies can also be  
 10 used to improve the mass hierarchy sensitivity in this region using the LBNE 10-kt configuration.

11 Table 4.8 summarizes the mass hierarchy and CP sensitivities that can be reached by a typical  
 12 experiment with the LBNE 10 kt and 34 kt configurations assuming a running time of 3+3 ( $\nu + \bar{\nu}$ )  
 13 years with a 1.2 MW beam under a variety of scenarios.

**Table 4.8:** The mass hierarchy and CP sensitivities that can be reached with a typical data set from the LBNE 10 kt and 34 kt configurations with a 1.2 MW beam, no near neutrino detector (ND) unless otherwise stated, and a run time of  $3+3 \nu + \bar{\nu}$  years under a variety of beam and systematic scenarios, for normal hierarchy. Note that the sensitivities for inverted hierarchy are similar but not identical. As discussed in the text, the significance of the mass hierarchy determination should not be interpreted using Gaussian probabilities.

tab:10ktsens

Scenario ( $\sin^2 \theta_{23} = 0.39$ )	MH sensitivity		CP sensitivity	
	$\delta_{\text{CP}}$ Fraction	$(\sqrt{\Delta\chi^2})$	$\delta_{\text{CP}}$ Fraction	$(\sqrt{\Delta\chi^2})$
LBNE 10 kt, CDR beam	50%	$\geq 4$	40%	$\geq 2\sigma$
	100%	$\geq 2$	-	-
LBNE 10 kt, 80-GeV upgraded beam	50%	$\geq 5$	23%	$\geq 3\sigma$
	100%	$\geq 3$	55%	$\geq 2\sigma$
LBNE 10 kt, 80-GeV beam, with $\nu$ ND	50%	$\geq 5$	33%	$\geq 3\sigma$
	100%	$\geq 3$	60%	$\geq 2\sigma$
+ NO $\nu$ A (6 yrs), T2K ( $7.8 \times 10^{21}$ P.O.T)	75%	$\geq 5$	30%	$\geq 4\sigma$
	100%	$\geq 4$	50%	$\geq 3\sigma$
LBNE 34 kt, CDR beam	50%	$\geq 7$	20%	$\geq 4\sigma$
	100%	$\geq 4$	50%	$\geq 3\sigma$
LBNE 34 kt, 80-GeV upgraded beam	50%	$\geq 8$	15%	$\geq 5\sigma$
	100%	$\geq 5$	35%	$\geq 4\sigma$
LBNE 34 kt, 80-GeV beam, with $\nu$ ND	50%	$\geq 9$	35%	$\geq 5\sigma$
	100%	$\geq 5$	50%	$\geq 4\sigma$

Assuming the normal hierarchy, the most recent global fit of experimental data for the three-neutrino paradigm favors a value of  $\delta_{\text{CP}}$  close to  $-\pi/2$  with  $\sin \delta_{\text{CP}} < 0$  at a confidence level of  $\sim 90\%$  [61] (Figure 4.15). LBNE alone with a 10-kt detector and six years of running would resolve with  $\geq 3\sigma$  precision the question of whether CP is violated for the currently favored value of  $\delta_{\text{CP}}$ . With a 34-kt detector running for six years, LBNE — alone — will achieve a precision approaching  $6\sigma$ .

1

#### 2 4.3.4 Mass Hierarchy and CP Sensitivities with Increased Exposures

3 Figure 4.16 shows the minimum significance with which the mass hierarchy can be resolved and  
 4 CP violation determined by LBNE as a function of increased exposure in units of mass  $\times$  beam  
 5 power  $\times$  time<sup>§</sup>. For this study the LBNE beamline improvements discussed in Section 3.4 are used  
 6 with  $E_p = 80$  GeV, and the signal and background normalization uncertainties are assumed to be  
 7 1% and 5%, respectively. Both  $\nu_e$  and  $\nu_\mu$  appearance signals are used in a combined analysis. Due  
 8 to the long baseline, the determination of the mass hierarchy in LBNE to high precision does not

<sup>§</sup>Time is denoted in years of running at Fermilab. One year of running at Fermilab corresponds to  $\approx 1.7 \times 10^7$  seconds.

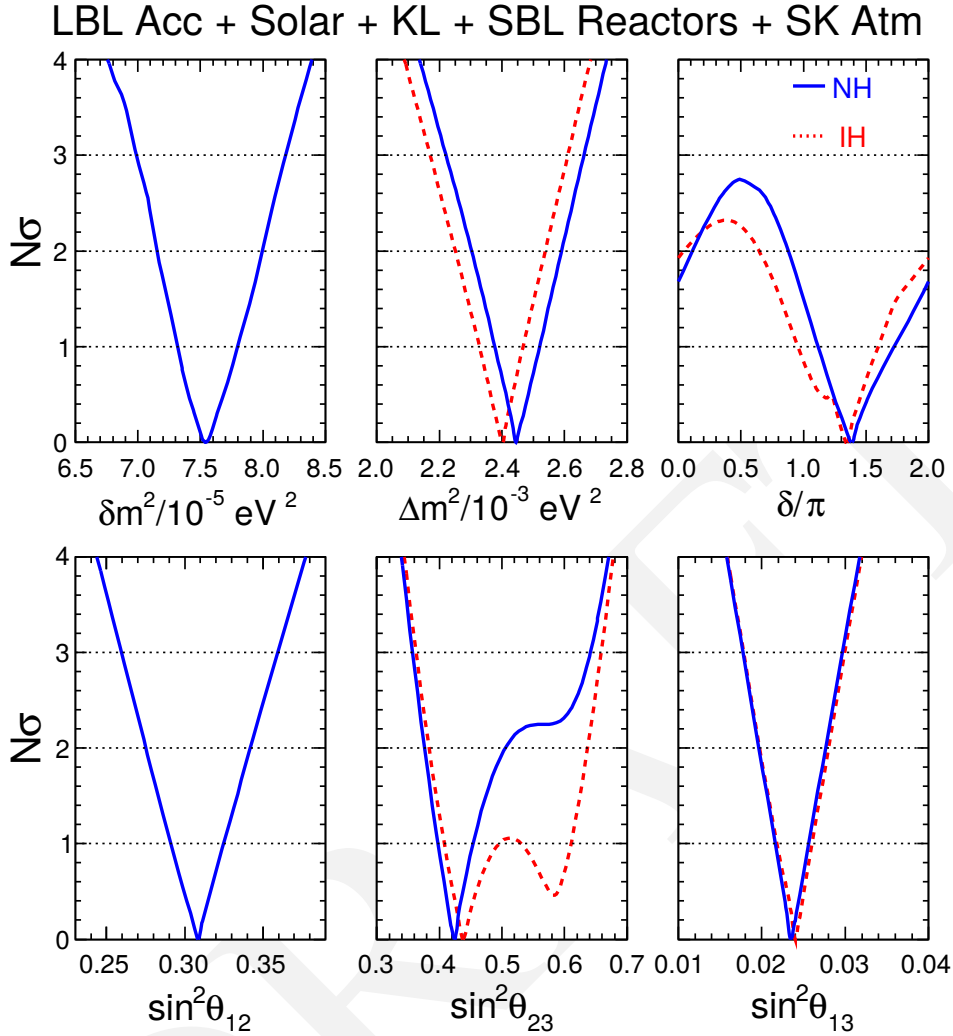


**Figure 4.15:** Results of the 2013 global analysis from Capozzi *et al.* shown as  $N\sigma$  bounds on the six parameters governing three  $\nu$  flavor oscillations. Blue (solid) and red (dashed) curves refer to NH and IH, respectively. Figure is from reference [61].

- 1 require a large exposure; a sensitivity of  $\sqrt{\Delta\chi^2} = 5$  for the worst case (NH,  $\delta_{\text{CP}} = \pi/2$  or IH,
- 2  $\delta_{\text{CP}} = -\pi/2$ ) requires an exposure of  $\sim 200 \text{ kt} \cdot \text{MW} \cdot \text{years}$ , but  $\sqrt{\Delta\chi^2} = 5$  sensitivity can be
- 3 reached for 50% of the allowed values of  $\delta_{\text{CP}}$  with an exposure of less than  $100 \text{ kt} \cdot \text{MW} \cdot \text{years}$ . On
- 4 the other hand, reaching discovery-level sensitivity ( $\geq 5\sigma$ ) to leptonic CP violation for at least 50%
- 5 of the possible values of  $\delta_{\text{CP}}$  will require large exposures of  $\approx 450 \text{ kt} \cdot \text{MW} \cdot \text{years}$ . Figure 4.17
- 6 demonstrates the sensitivity to CP violation as a function of  $\delta_{\text{CP}}$  and exposure that can be achieved
- 7 with various stages of the Fermilab Proton-Improvement-Plan (PIP-II and upgrades to PIP-II). In
- 8 this study, the PIP-II upgrades are assumed to provide LBNE with  $1.2 \text{ MW}$ <sup>¶</sup> at 80 GeV, followed

<sup>¶</sup>The assumed exposures are only accurate to the level of 15% due to incomplete knowledge of the PIP-II final design parameters and running conditions.

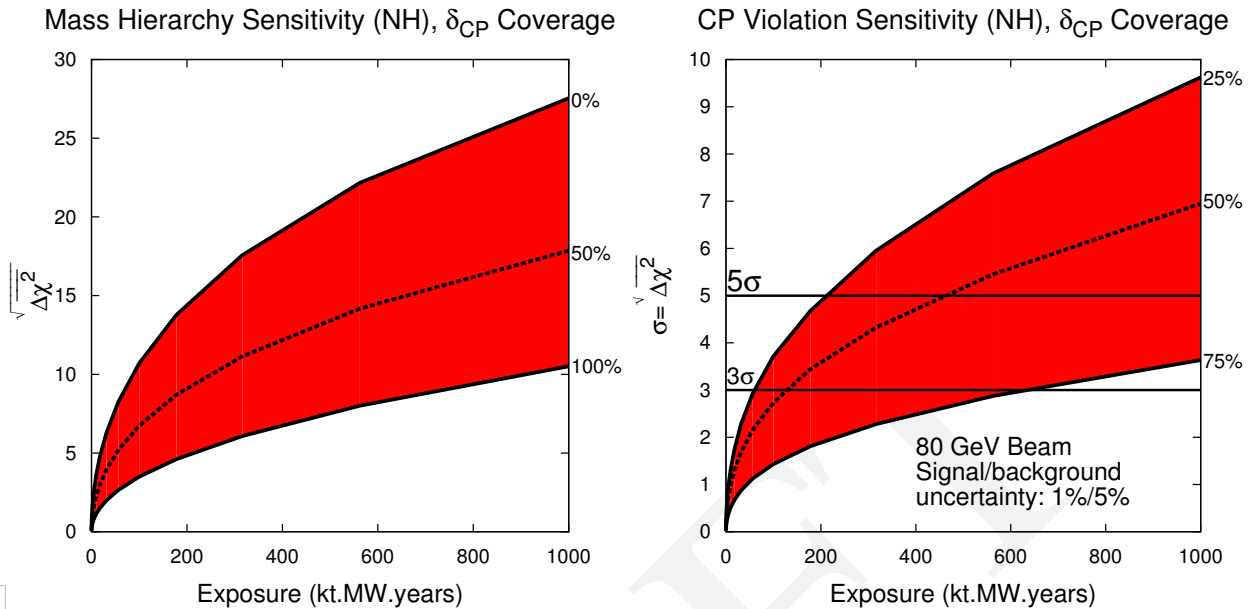


**Figure 4.16:** The minimum significance with which the mass hierarchy (left) and CP violation (right) can be resolved as a function of exposure in detector mass (kiloton)  $\times$  beam power (MW)  $\times$  time (years), for true normal hierarchy. The red band represents the fraction of  $\delta_{CP}$  values for which the sensitivity can be achieved with at least the minimal significance on the y-axis.

- 1 by further upgrades in which the booster is replaced with a linac which will provide 2.3 MW from
- 2 the Main Injector, also at 80 GeV. The study demonstrates that it is possible to reach  $5\sigma$  sensitivity
- 3 to CP violation over at least 40% of  $\delta_{CP}$  values running for a little over 10 years, starting with the
- 4 PIP-II Main Injector power and a LArTPC greater than 10 kt, and phasing in more detector mass.
- 5 Other possible staging scenarios of detector mass and beam power are discussed in Chapter 9.

**Table 4.9:** The CP violation sensitivities that can be reached by LBNE alone starting with the LBNE 10 kt configuration with a 1.2-MW beam and a run time of 3+3 ( $\nu + \bar{\nu}$ ) years and phasing in additional far detector mass and beam power upgrades beyond the current PIP-II. In all cases, the sensitivities are calculated using the 80 GeV upgraded beam and 1%/5% signal/background normalization uncertainties, for true normal hierarchy. The sensitivity for each stage includes exposure from the previous stage(s) of the experiment.

Exposure	Possible Scenario	CP sensitivity	
		$\delta_{CP}$ Fraction	( $\sqrt{\Delta\chi^2}$ )
60 kt $\cdot$ years 1.2 MW beam	PIP-II, 10 kt, 6 years	60% $\delta_{CP}$	$\geq 2\sigma$
		33% $\delta_{CP}$	$\geq 3\sigma$
+ 200 kt $\cdot$ years 1.2 MW beam	PIP-II, 34 kt, 6 years	40% $\delta_{CP}$	$\geq 5\sigma$
+ 200 kt $\cdot$ years 2.3 MW beam	Booster replaced, 34 kt, 6 years	60% $\delta_{CP}$	$\geq 5\sigma$

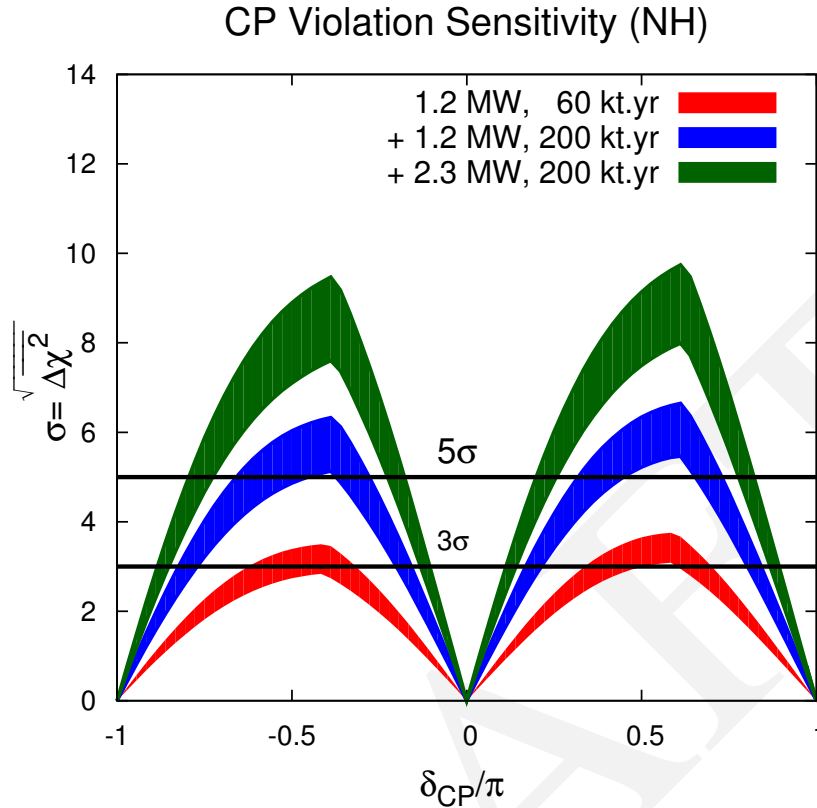


**Figure 4.17:** The significance with which CP violation —  $\delta_{CP} \neq 0$  or  $\pi$  — can be determined as a function of  $\delta_{CP}$ . The different color curves represent possible exposures from different stages of PIP and detector mass upgrades as follows: 1.2 MW, 60 kt-years (red), 1.2 MW, 200 kt-years (blue) + 2.3 MW, 200 kt-years (green). The sensitivity for each higher exposure is in addition to that from all lower exposures. The bands represent the range of sensitivities obtained from the improvements to the CDR beamline design.

## 4.4 Measurement of $\theta_{23}$ and Determination of the Octant

- The value of  $\sin^2 2\theta_{23}$  is measured to be  $> 0.95$  at 90% C.L. using atmospheric neutrino oscillations [156]. This corresponds to a value of  $\theta_{23}$  near  $45^\circ$ , but leaves an ambiguity as to whether the value of  $\theta_{23}$  is in the lower octant (less than  $45^\circ$ ), the upper octant (greater than  $45^\circ$ ) or exactly  $45^\circ$ . The value of  $\sin^2 \theta_{23}$  from the 2013 global fit reported by [61] is  $\sin^2 \theta_{23} = 0.425^{+0.029}_{-0.027}(1\sigma)$  for normal hierarchy, but, as shown in Figure 4.15, the distribution of the  $\chi^2$  from the global fit has another local minimum — particularly if the hierarchy is inverted — at  $\sin^2 \theta_{23} \approx 0.59$ . A *maximal* mixing value of  $\sin^2 \theta_{23} = 0.5$  is therefore still allowed by the data and the octant is still largely undetermined. As discussed in Chapter 2, a value of  $\theta_{23}$  exactly equal to  $45^\circ$  would indicate that  $\nu_\mu$  and  $\nu_\tau$  have equal contributions from  $\nu_3$ , which could be evidence for a previously unknown symmetry. It is therefore important experimentally to determine the value of  $\sin^2 \theta_{23}$  with sufficient precision to determine the octant of  $\theta_{23}$ .

1 The measurement of  $\nu_\mu \rightarrow \nu_\mu$  oscillations is sensitive to  $\sin^2 2\theta_{23}$ , whereas the measurement of  
 2  $\nu_\mu \rightarrow \nu_e$  oscillations is sensitive to  $\sin^2 \theta_{23}$ . A combination of both  $\nu_e$  appearance and  $\nu_\mu$  disappear-  
 3 ance measurements can probe both maximal mixing and the  $\theta_{23}$  octant. With the large statistics and  
 4 rich spectral structure in a wide-band, long-baseline experiment like LBNE (see Figure 4.2), pre-  
 5 cision measurements of  $\sin^2 \theta_{23}$  can be significantly improved compared to existing experiments,  
 particularly for values of  $\theta_{23}$  near  $45^\circ$ . Figure 4.18 demonstrates the measurement precision of  $\theta_{23}$

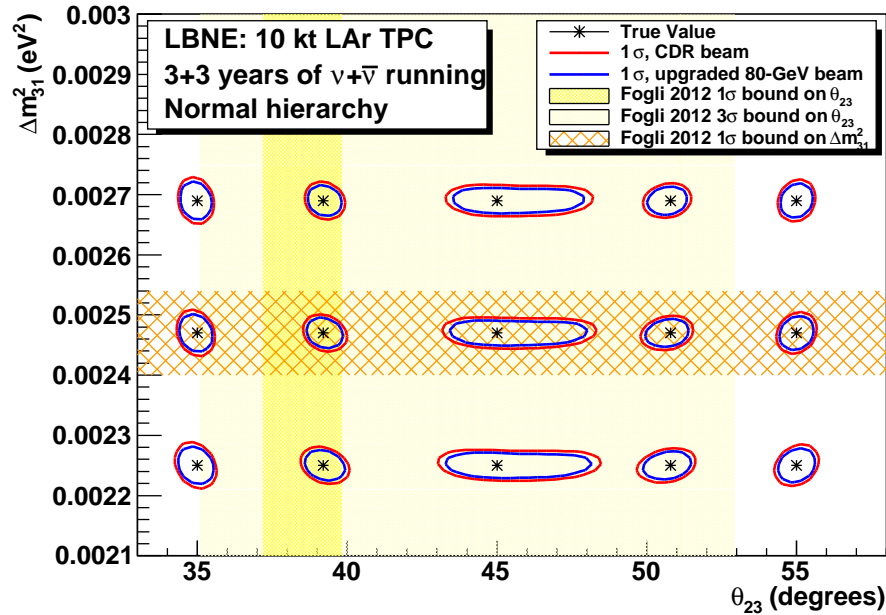


**Figure 4.18:** The precision with which a simultaneous measurement of  $\theta_{23}$  and  $\Delta m_{31}^2$  can be determined with 10 kt and 3+3 years of  $\nu + \bar{\nu}$  running in a 1.2-MW beam. The yellow bands represent the 1 $\sigma$  and 3 $\sigma$  allowed ranges of  $\theta_{23}$  and the orange hatched region represents the 1 $\sigma$  allowed range of  $\Delta m_{31}^2$  from [46]

6 and  $\Delta m_{31}^2$  that can be achieved for different true values of these parameters by a 10-kt LBNE  
 7 detector. The subdominant  $\nu_\mu \rightarrow \nu_e$  appearance signal in a 10-kt detector is limited by statistical  
 8 uncertainties.  
 9

10 The significance with which the  $\theta_{23}$  octant can be determined with a 10-kt LBNE detector is shown  
 11 in Figure 4.19. The  $\Delta\chi^2$  metric is defined as:

$$\Delta\chi_{\text{octant}}^2 = |\chi_{\theta_{23}^{\text{test}} > 45^\circ}^2 - \chi_{\theta_{23}^{\text{test}} < 45^\circ}^2|, \quad (4.9)$$

12 where the value of  $\theta_{23}$  in the “wrong” octant is constrained only to have a value within the “wrong”  
 13 octant (i.e., it is not required to have the same value of  $\sin^2 2\theta_{23}$  as the true value). The individual  
 14  $\chi^2$  values are given by Equation 4.4. As in the  $\Delta\chi^2$  metrics for mass hierarchy and CP violation,  
 15 the  $\chi^2$  value for the “true” octant is identically zero in the absence of statistical fluctuations.

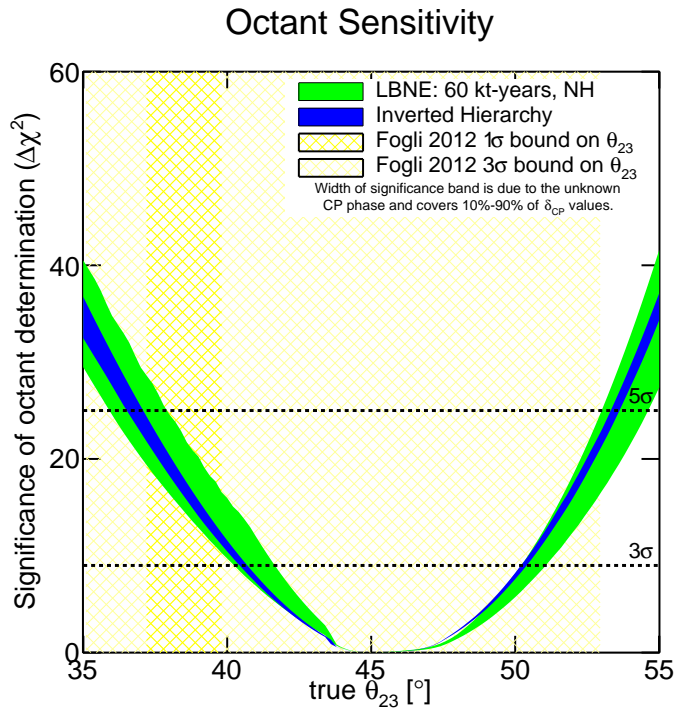


**Figure 4.19:** Significance with which LBNE can resolve the  $\theta_{23}$  octant degeneracy for 3+3 years of  $\nu+\bar{\nu}$  running at 1.2 MW with a 10-kt detector. The bands are for normal (green) and inverted (blue) hierarchy. The widths of the bands correspond to the fraction of  $\delta_{CP}$  values covered at this significance or higher, ranging from 10% to 90%. The yellow bands represent the  $1\sigma$  and  $3\sigma$  allowed ranges of  $\theta_{23}$  from [46].

- 1 If  $\theta_{23}$  is within the  $1\sigma$  bound of the global fit [46], an LBNE 10-kt detector alone will determine
- 2 the octant with  $> 3\sigma$  significance for all values of  $\delta_{CP}$ . Figure 4.20 demonstrates the increasing
- 3 sensitivity to the  $\theta_{23}$  octant for values closer to maximal  $\nu_{\mu}-\nu_{\tau}$  mixing that can be achieved with
- 4 subsequent phases of LBNE coupled with upgrades in beam power from the Main Injector.

With sufficient exposure, LBNE can resolve the  $\theta_{23}$  octant with  $> 3\sigma$  significance even if  $\theta_{23}$  is within a few degrees of  $45^\circ$ , the value at which the mixing between the neutrino states is maximal.

## 4.5 Precision Measurements of the Oscillation Parameters in the Three-Flavor Model

- 8 The rich oscillation structure that can be observed by LBNE and the excellent particle identifi-
- 9 cation capability of the detector will enable precision measurement of all the mixing parameters
- 10 governing the  $\nu_1-\nu_3$  and  $\nu_2-\nu_3$  mixing in a single experiment. As discussed in Chapter 2, theoretic-
- 11 al models probing quark-lepton universality predict specific values of the mixing angles and the

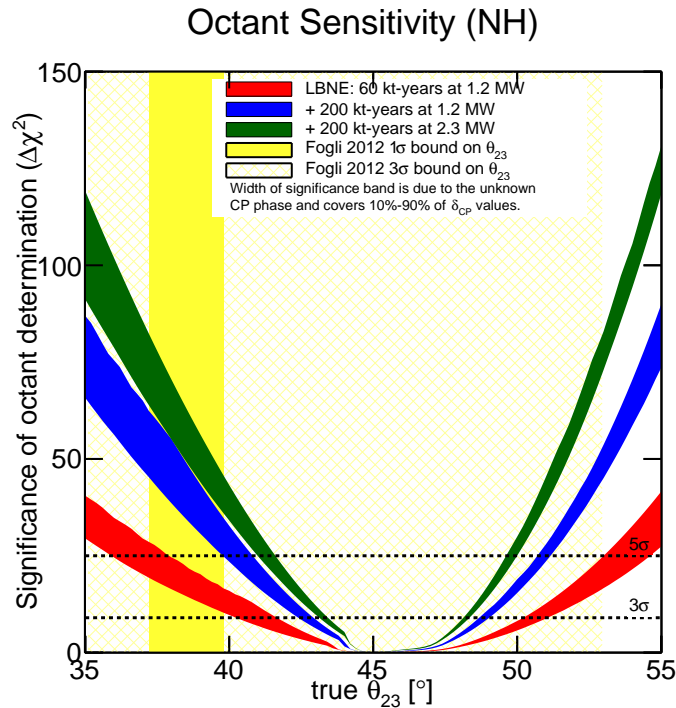


**Figure 4.20:** Significance with which LBNE can resolve the  $\theta_{23}$  octant degeneracy (normal hierarchy) for equal  $\nu+\bar{\nu}$  running with increased exposure from different stages of PIP and detector mass upgrades. The colored bands represent increasing exposures as follows: 1.2 MW, 60 kt·year (red), 1.2 MW, 200 kt·years (blue) + 2.3 MW, 200 kt·years (green). The sensitivity for each higher exposure is in addition to that from all lower exposures. The width of the bands corresponds to the fraction of  $\delta_{CP}$  values covered at this significance or higher, ranging from 10% to 90%.

1 relations between them. The mixing angle  $\theta_{13}$  is expected to be measured accurately in reactor  
 2 experiments by the end of the decade with a precision that will be limited by systematics. The  
 3 systematic uncertainty on the value of  $\sin^2 2\theta_{13}$  from the Daya Bay reactor neutrino experiment,  
 4 which has the lowest systematics, is currently  $\sim 4\%$  [157].

5 While the constraint on  $\theta_{13}$  from the reactor experiments will be important in the early stages  
 6 of LBNE for determining CP violation, measuring  $\delta_{CP}$  and determining the  $\theta_{23}$  octant, LBNE  
 7 itself will eventually be able to measure  $\theta_{13}$  independently with a precision on par with the final  
 8 precision expected from the reactor experiments. Whereas the reactor experiments measure  $\theta_{13}$   
 9 using  $\bar{\nu}_e$  disappearance, LBNE will measure it through  $\nu_e$  and  $\bar{\nu}_e$  appearance, thus providing an  
 10 independent constraint on the three-flavor mixing matrix. Figure 4.21 demonstrates the precision  
 11 with which LBNE can measure  $\delta_{CP}$  and  $\theta_{13}$  simultaneously, with no external constraints on  $\theta_{13}$ , as  
 12 a function of increased exposure, for three different exposures. Both appearance and disappearance  
 13 modes are included in the fit using the upgraded 80-GeV beam. Signal/background normalization  
 14 uncertainties of 1%/5% are assumed. Figure 4.22 shows the expected  $1\sigma$  resolution on different  
 15 three-flavor oscillation parameters as a function of exposure in kt·year in a 1.2-MW beam with  
 16 LBNE alone and LBNE in combination with the expected performance from T2K and NO $\nu$ A. It

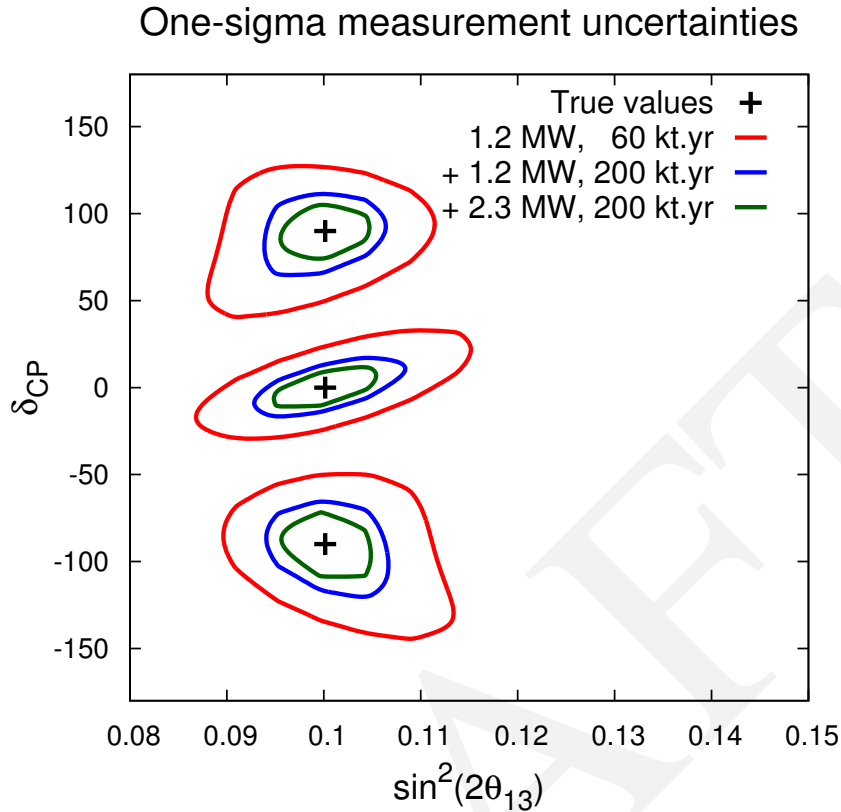


fig:t13dcp

**Figure 4.21:** Measurement of  $\delta_{\text{CP}}$  and  $\theta_{13}$  in LBNE with different exposures, for true normal hierarchy. The different color curves represent one-sigma contours for three possible exposures from different stages of PIP and detector mass upgrades as follows: 1.2 MW, 60 kt-year (red), 1.2 MW, 200 kt-years (blue) + 2.3 MW, 200 kt-years (green). The sensitivity for each higher exposure is in addition to that from all lower exposures.

- 1 should be noted that LBNE alone could reach a precision on  $\sin^2 2\theta_{13}$  of 0.005 with an exposure of
- 2  $\sim 300 \text{ kt} \cdot \text{MW} \cdot \text{years}$ . LBNE can also significantly improve the resolution on  $\Delta m_{32}^2$  beyond what
- 3 the combination of  $\text{NO}\nu\text{A}$  and T2K can achieve, reaching a precision of  $1 \times 10^{-5} \text{ eV}^2$  with an
- 4 exposure of  $\sim 300 \text{ kt} \cdot \text{MW} \cdot \text{years}$ . The precision on  $\Delta m_{23}^2$  will ultimately depend on tight control
- 5 of energy-scale systematics. Initial studies of the systematics reveal that the measurement of  $\nu_\mu$
- 6 disappearance in LBNE over a full oscillation interval with two oscillation peaks and two valleys
- 7 (Figure 4.2), reduces the dependency of the  $\Delta m_{23}^2$  measurement on the energy-scale systematics,
- 8 which limited the measurement precision in MINOS [153].

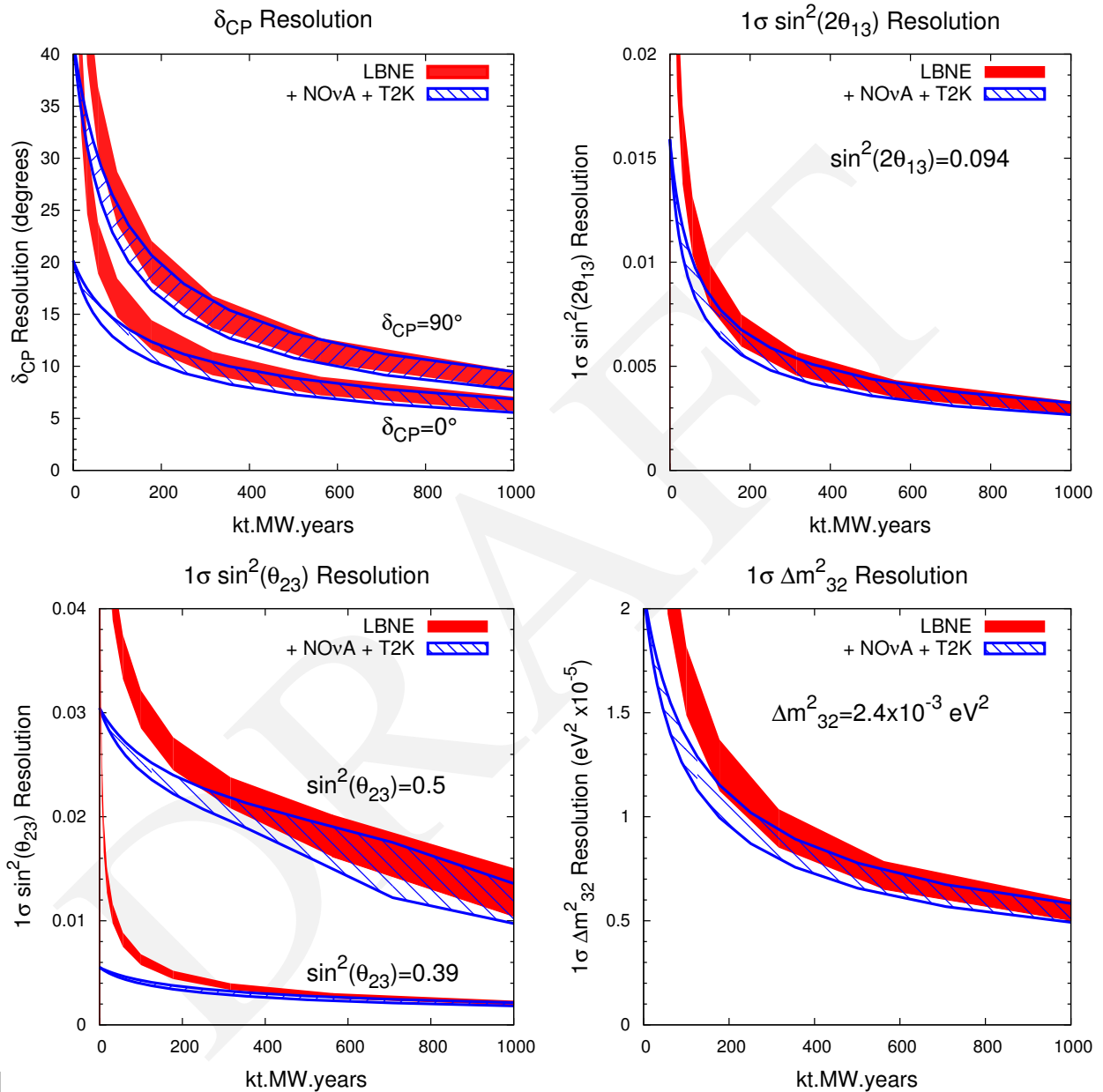


fig:precision

**Figure 4.22:** The expected  $1\sigma$  resolution on different three-flavor oscillation parameters as a function of exposure in kt.MW.years, for true normal hierarchy. The red curve indicates the precision that could be obtained from LBNE alone, and the blue curve represents the combined precision from LBNE and the T2K and NO $\nu$ A experiments. The width of the bands represents the range of performance with the beam improvements under consideration.

## 4.6 Oscillation Studies Using Atmospheric Neutrinos

atmnu

Atmospheric neutrinos are unique among sources used to study oscillations: the flux contains neutrinos and antineutrinos of all flavors, matter effects play a significant role, both  $\Delta m^2$  values contribute, and the oscillation phenomenology occurs over several orders of magnitude each in energy (see Figure 2.8) and path length. These characteristics make atmospheric neutrinos ideal for the study of oscillations (in principle sensitive to all of the remaining unmeasured quantities in the PMNS matrix) and provide a laboratory in which to search for exotic phenomena for which the dependence of the flavor-transition and survival probabilities on energy and path length can be defined. The large LBNE LArTPC far detector, placed at sufficient depth to shield from cosmic-ray background, provides a unique opportunity to study atmospheric neutrino interactions with excellent energy and path-length resolutions.

LBNE has obtained far detector physics sensitivities based on information from atmospheric neutrinos by using a Fast MC and a three-flavor analysis framework developed for the MINOS experiment [158]. Four-vector-level events are generated using the GENIE neutrino event generator [124]. For atmospheric neutrinos the Bartol [159] flux calculation for the Soudan, MN site was used, and for beam neutrinos the 80-GeV, 1.2-MW improved beamline design described in Section 3.4 was used. In this section, unless otherwise specified, the oscillation parameters are as specified in Table 4.10.

**Table 4.10:** Oscillation parameters used in the atmospheric neutrino analysis.

Parameter	value
$\Delta m^2 = 1/2(\Delta m_{32}^2 + \Delta m_{31}^2)$	$+2.40 \times 10^{-3} \text{ eV}^2$
<b>Normal hierarchy</b>	
$\sin^2 \theta_{23}$	<b>0.40</b>
$\Delta m_{21}^2$	$7.54 \times 10^{-5} \text{ eV}^2$
$\sin^2 \theta_{12}$	<b>0.307</b>
$\sin^2 \theta_{13}$	<b>0.0242</b>
$\delta_{CP}$	<b>0</b>

The expected interaction rates in  $100 \text{ kt} \cdot \text{year}$  are shown in Table 4.11. All interactions occur on argon, and are distributed uniformly throughout a toy detector geometry consisting of two modules, each 14.0 m high, 23.3 m wide, and 45.4 m long. For this study, events with interaction vertices outside the detector volume (e.g., events that produce upward-going stopping or through-going muons) have not been considered. Cosmogenic background has not been studied in detail, but since atmospheric neutrinos are somewhat more tolerant of background than proton decay, a depth that

- 1 is sufficient for a proton decay search is expected to also be suitable for atmospheric neutrinos. For  
 2 the 4,850-ft depth at the Sanford Underground Research Facility, a veto should not be necessary,  
 3 and the full fiducial mass of the detector should be usable.

**Table 4.11:** Expected atmospheric  $\nu$  interaction rates in a LArTPC with an exposure of 100 kt · years for the Bartol flux and GENIE Argon cross sections (no oscillations).

mos\_event\_rates

Flavor	CC	NC	Total
$\nu_\mu$	10069	4240	14309
$\bar{\nu}_\mu$	2701	1895	4596
$\nu_e$	5754	2098	7852
$\bar{\nu}_e$	1230	782	2012
<b>Total:</b>	19754	9015	28769

- 4 A Fast MC runs on the produced four-vectors, placing events into containment and flavor cate-  
 5 gories. Containment is evaluated by tracking leptons through the liquid argon detector box geom-  
 6 etry and classifying events as either fully contained (FC) or partially contained (PC). A detection  
 7 threshold of 50 MeV is assumed for all particles. Flavor determination, in which events are placed  
 8 into electron-like or muon-like categories, is based on properties of the primary and secondary par-  
 9 ticles above detection threshold. Electrons are assumed to be correctly identified with 90% proba-  
 10 bility and other electromagnetic particles (e.g.,  $\pi^0$ ,  $\gamma$ ) are misidentified as electrons 5% of the time.  
 11 Muons are identified with 100% probability and charged pions are misidentified as muons 1% of  
 12 the time. Events in which neither of the two leading particles is identified as a muon or electron are  
 13 placed into an *NC-like* category. With these assumptions, the purities of the flavor-tagged samples  
 14 are 97.8% for the FC electron-like sample, 99.7% for the FC muon-like sample, and 99.6% for  
 15 the PC muon-like sample. The NC-like category is not used in this analysis, but would be useful  
 for  $\nu_\tau$  appearance studies. The energy and direction of the event are then assigned by separately

**Table 4.12:** Detector performance assumptions for the atmospheric neutrino and the combined atmo-  
 spheric+beam neutrino analyses.

tab:atmosdpa

Particle	Resolution
<b>Angular Resolutions</b>	
<b>Electron</b>	1°
<b>Muon</b>	1°
<b>Hadronic System</b>	10°
<b>Energy Resolutions</b>	
<b>Stopping Muon</b>	3%
<b>Exiting Muon</b>	15%
<b>Electron</b>	$1\%/\sqrt{E(\text{GeV})} \oplus 1\%$
<b>Hadronic System</b>	$30\%/\sqrt{E(\text{GeV})}$

1 smearing these quantities of the leptonic and hadronic systems, where the width of the Gaussian  
 2 resolution functions for each flavor/containment category are given in Table 4.12. Detector per-  
 3 formance assumptions are taken both from the LBNE CDR [21] and from published results from  
 4 the ICARUS experiment [130,160,161,162]. Including oscillations, the expected number of events  
 in 100 kt · year is summarized in Table 4.13. Figure 4.23 shows the expected L/E distribution

**Table 4.13:** Atmospheric neutrino event rates including oscillations in 100 kt · year with a LArTPC. FC indicates events that are fully contained in the detector fiducial volume, and PC indicates partially contained events.

Sample	Event rate
FC electron-like sample	4,015
FC muon-like sample	5,958
PC muon-like sample	1,963

5  
 6 for *high-resolution* muon-like events from a 350 kt · year exposure; the latest data from Super-  
 7 Kamiokande is shown for comparison. LBNE defines high-resolution events similarly to Super-  
 8 Kamiokande, i.e., either by excluding a region of low-energy events or events pointing towards the  
 9 horizon where the baseline resolution is poor. The data provide excellent resolution of the first two  
 10 oscillation nodes, even when taking into account the expected statistical uncertainty.

11 In performing oscillation fits, the data in each flavor/containment category are binned in energy and  
 12 zenith angle. Figure 4.24 shows the zenith angle distributions for several ranges of reconstructed  
 13 energy, where oscillation features are clearly evident.

14 The power to resolve the mass hierarchy with atmospheric neutrinos comes primarily from the  
 15 MSW enhancement of few-GeV neutrinos at large zenith angles. This enhancement occurs for neu-  
 16 trinos in the normal hierarchy and antineutrinos in the inverted hierarchy. Figure 4.25 shows zenith  
 17 angle distributions of events in the relevant energy range for each of the three flavor/containment  
 18 categories. Small differences are evident in comparing the normal and inverted hierarchy predic-  
 19 tions.

20 Since the resonance peak occurs for neutrinos in the normal hierarchy and antineutrinos in the  
 21 inverted hierarchy, the MH sensitivity can be greatly enhanced if neutrino and antineutrino events  
 22 can be separated. The LBNE detector will not be magnetized; however, the high-resolution imaging  
 23 offers possibilities for tagging features of events that provide statistical discrimination between  
 24 neutrinos and antineutrinos. For the sensitivity calculations that follow, two such tags are included:  
 25 a proton tag and a decay-electron tag. For low-multiplicity events, protons occur preferentially in  
 26 neutrino interactions; protons are tagged with 100% efficiency if their kinetic energy is greater than  
 27 50 MeV. Decay electrons are assumed to be 100% identifiable and are assumed to occur 100% of  
 28 the time for  $\mu^+$  and 25% of the time for  $\mu^-$ , based on the  $\mu^\pm$  capture probability on  $^{40}\text{Ar}$ .

29 In the oscillation analysis, 18 nuisance parameters are included, with detector performance param-

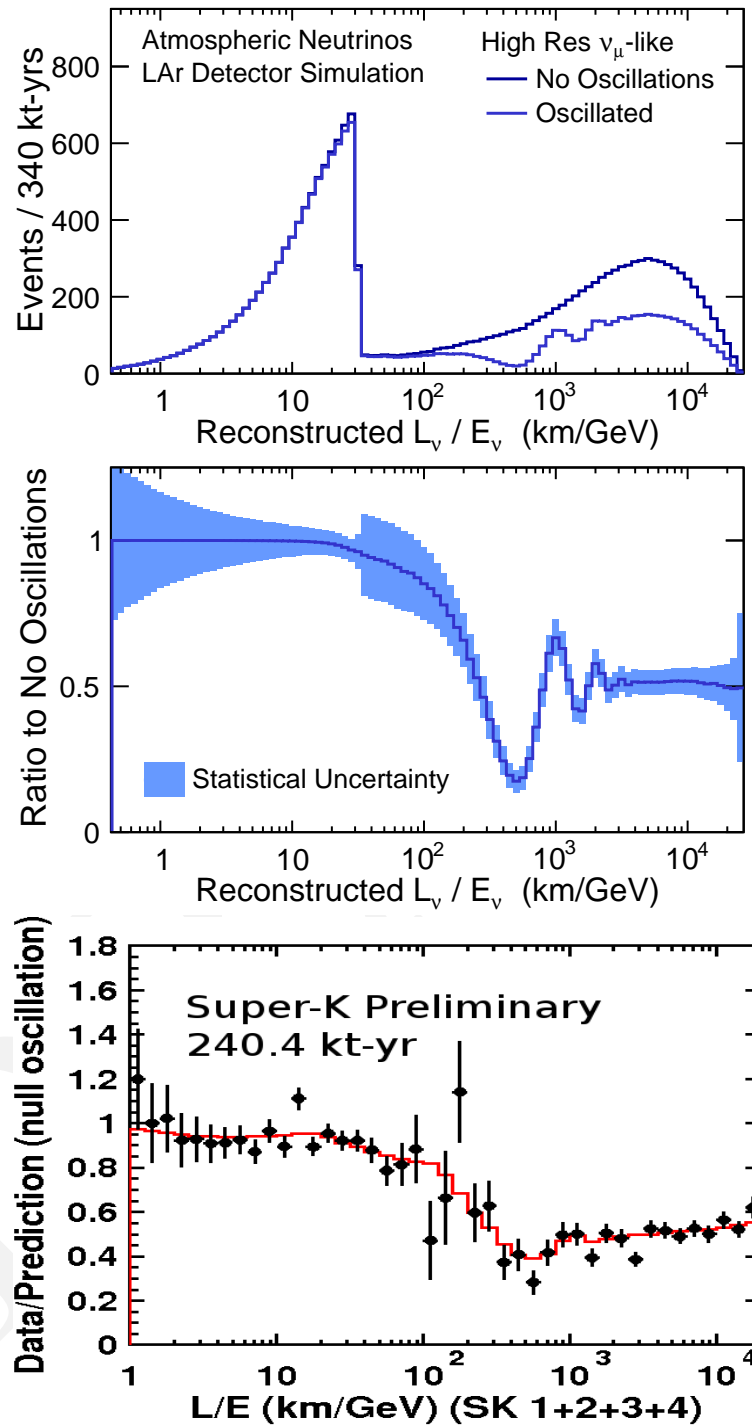
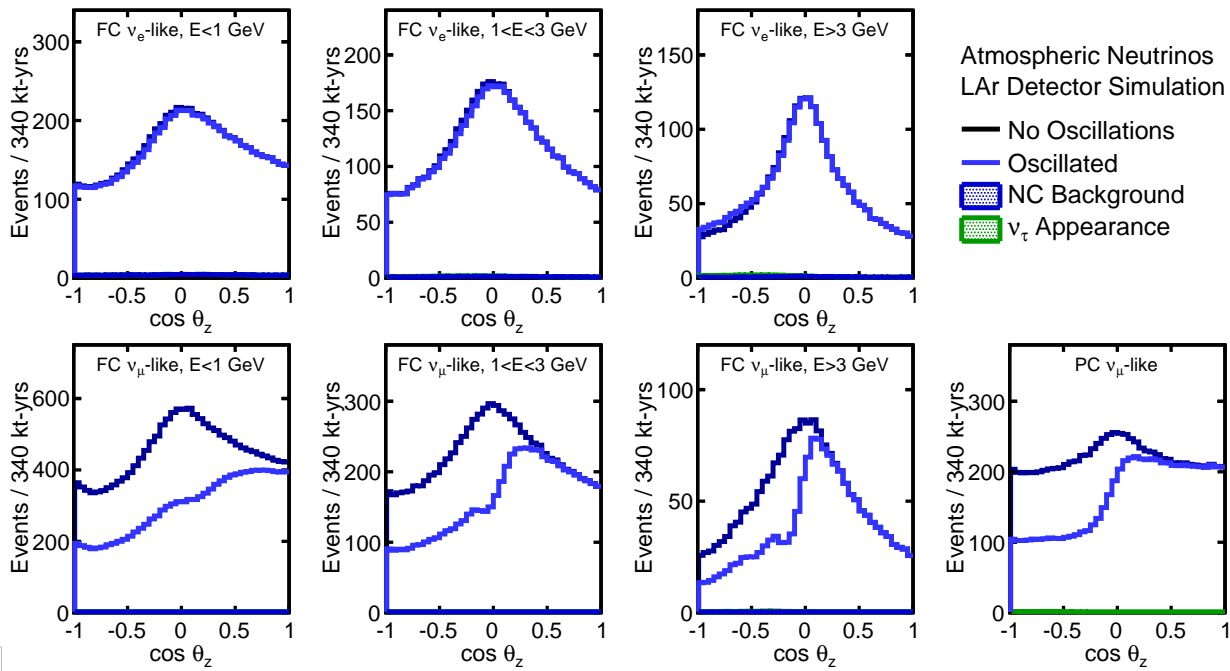
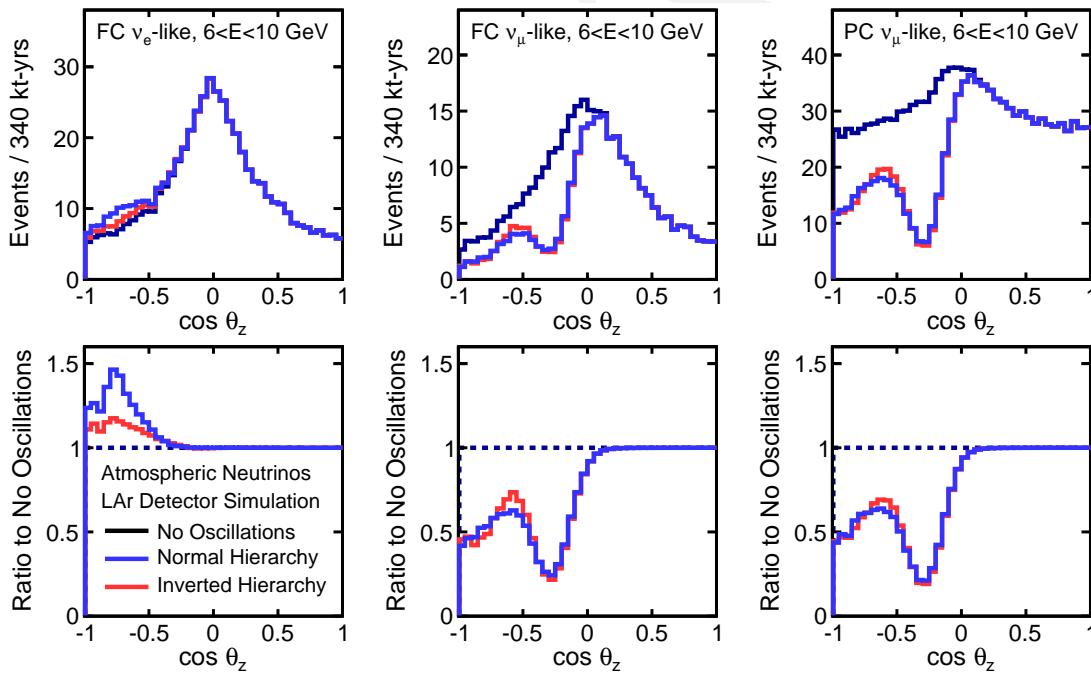


fig:lovere

**Figure 4.23:** Reconstructed  $L/E$  Distribution of “high-resolution”  $\mu$ -like atmospheric neutrino events in LBNE with a 340 kt · year exposure with and without oscillations (top); the ratio of the two, with the shaded band indicating the size of the statistical uncertainty (center); the ratio of observed data over the null oscillation prediction from the Super-Kamiokande detector with 240.4 kt · years of exposure (bottom).



**Figure 4.24:** Reconstructed zenith angle distributions in several ranges of energy for the FC  $e$ -like, FC  $\mu$ -like, and PC  $\mu$ -like samples. The small contributions from NC background and  $\nu_\tau$  are also shown.



**Figure 4.25:** Reconstructed zenith angle distributions for 6- to 10-GeV events in the different FC and PC samples. Top plots show the expected distributions for no oscillations (black), oscillations with normal (blue), and inverted (red) hierarchy. Bottom plots show the ratio of the normal and inverted expectations to the no-oscillation distributions for each category.

eters correlated between beam and atmospheric data. In all cases,  $\sin^2 \theta_{12}$ ,  $\Delta m^2 = 1/2(\Delta m_{32}^2 + \Delta m_{31}^2)$ , and  $\Delta m_{21}^2$  are taken to be fixed at the values given in Table 4.10. The fits then range over  $\theta_{23}$ ,  $\theta_{13}$ ,  $\delta_{CP}$ , and the mass hierarchy. A 2% constraint is assumed on the value of  $\theta_{13}$ ; this value is chosen to reflect the expected ultimate precision of the current generation of reactor-neutrino experiments. The systematic errors included in this analysis are given in Table 4.14.

**Table 4.14:** Systematic errors included in the atmospheric and beam+atmospheric neutrino analysis. The beam values assume the existence of a near detector (ND). Atmospheric spectrum ratios include the combined effect of flux and detector uncertainties (e.g., the up/down flux uncertainty as well as the uncertainty on the detector performance for the up/down ratio). The atmospheric spectrum shape uncertainty functions are applied separately for  $\nu_\mu$ ,  $\nu_e$ ,  $\bar{\nu}_\mu$ ,  $\bar{\nu}_e$ .

tab:atmosyst

	Atmospheric	Beam (Assumes ND)
<b>Normalization</b>	Overall (15%)	$\mu$ -like (5%) e-like (1%)
<b>NC Background</b>	e-like (10%)	$\mu$ -like (10%) e-like (5%)
<b>Spectrum Ratios</b>	up/down (2%) $\nu_e/\nu_\mu$ (2%) $\bar{\nu}_\mu/\nu_\mu$ (5%) $\bar{\nu}_e/\nu_e$ (5%)	
<b>Spectrum Shape</b>	$f(E < E_0) = 1 + \alpha(E - E_0)/E_0$ $f(E > E_0) = 1 + \alpha \log(E/E_0)$ where $\sigma_\alpha=5\%$	
<b>Energy Scales (Correlated)</b>	Muons (stopping 1%, exiting 5%) Electrons (1%) Hadronic System (5%)	

5

For the determination of the mass hierarchy, the  $\overline{\Delta\chi^2}$  value is calculated between the best-fit points in the normal and inverted hierarchies where, at each, the nuisance parameters have been marginalized. The sensitivity in the plots that follow is given as  $\sqrt{\overline{\Delta\chi^2}}$ . Figure 4.26 shows the MH sensitivity from a 340 kt · year exposure of atmospheric neutrino data alone. For all values of the hierarchy and  $\delta_{CP}$ , the hierarchy can be determined at  $\sqrt{\overline{\Delta\chi^2}} > 3$ . The resolution depends significantly on the true value of  $\theta_{23}$ ; the sensitivity for three  $\theta_{23}$  values is shown. The sensitivity depends relatively weakly on the true hierarchy and the true value of  $\delta_{CP}$ . This is in sharp contrast to the MH sensitivity of the beam, which has a strong dependence on the true value of  $\delta_{CP}$ . Figure 4.27 shows the MH sensitivity as a function of the fiducial exposure. Over this range of fiducial exposures, the sensitivity goes essentially as the square root of the exposure, indicating that the measurement is not systematics-limited. Figure 4.28 shows the octant and CPV sensitivity from a 340 kt · year exposure of atmospheric neutrino data alone. For the determination of the octant of  $\theta_{23}$ , the  $\overline{\Delta\chi^2}$  value is calculated between the best-fit points in the lower ( $\theta_{23} < 45^\circ$ ) and higher ( $\theta_{23} > 45^\circ$ ) octants, where at each, the nuisance parameters have been marginalized. The discontinuities in the slopes of the octant sensitivity plot are real features, indicating points at which the best fit moves

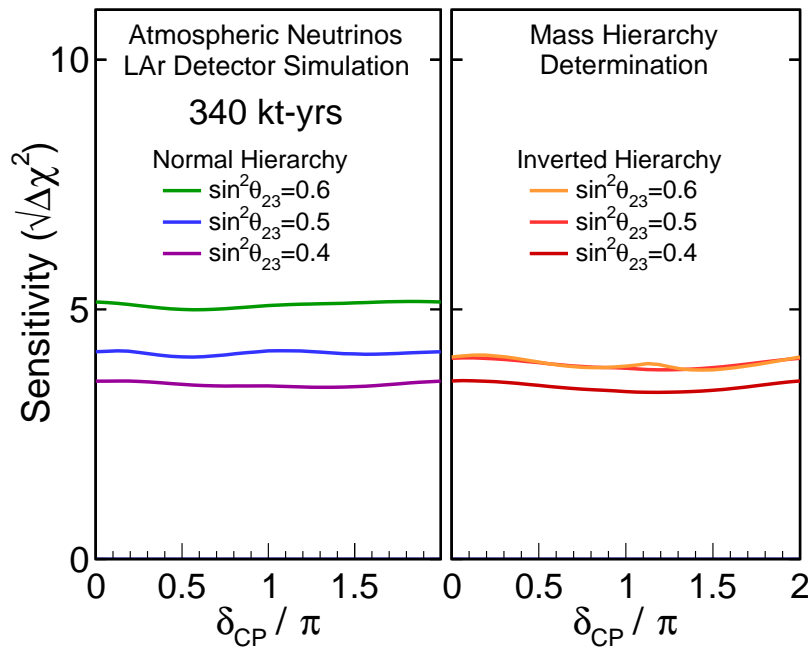


**Figure 4.26:** Sensitivity of 340 kt · years of atmospheric neutrino data to MH as a function of  $\delta_{CP}$  for true normal (left) and inverted (right) hierarchy and different assumed values of  $\sin^2 \theta_{23}$ .

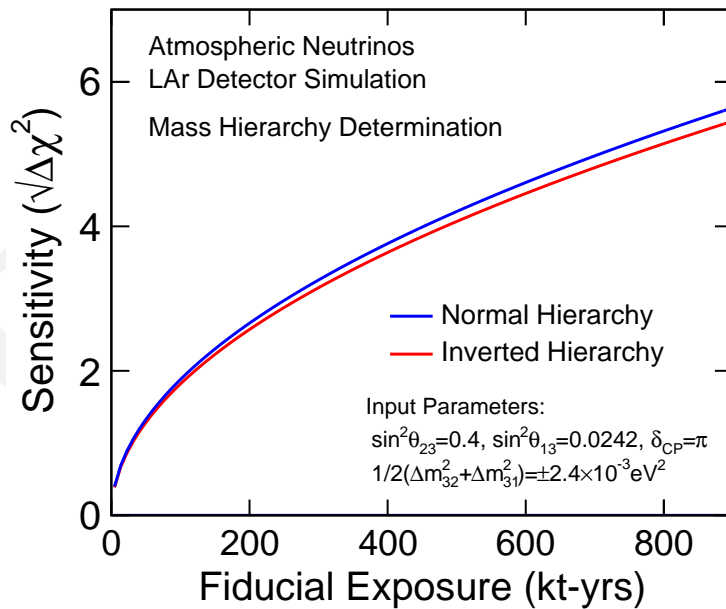


**Figure 4.27:** Sensitivity to mass hierarchy using atmospheric neutrinos as a function of fiducial exposure in a liquid argon detector.

- 1 from one hierarchy to the other. For the detection of CP violation, the  $\overline{\Delta\chi^2}$  exclusion is similarly
- 2 computed for  $\delta_{CP} = (0, \pi)$ .

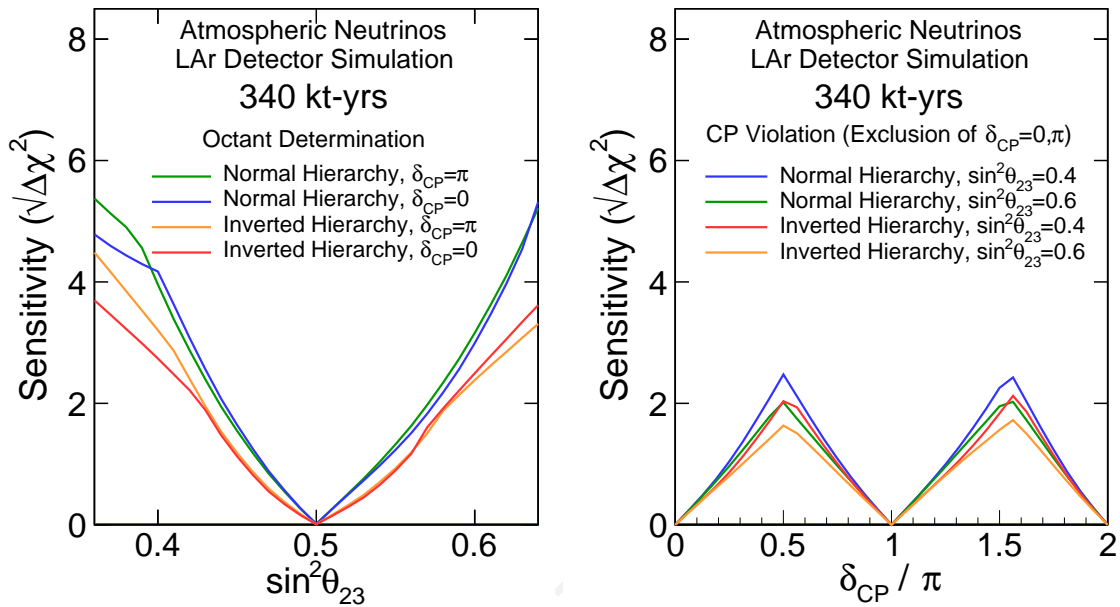


fig:atmnsens3

Figure 4.28: Sensitivity to  $\theta_{23}$  octant (left) and CPV (right) using atmospheric neutrinos.

- Figure 4.29 shows the combined sensitivity to beam and atmospheric neutrinos for determination of the mass hierarchy. This assumes a 10-year run with equal amounts of neutrino and antineutrino running in a 1.2-MW beam.

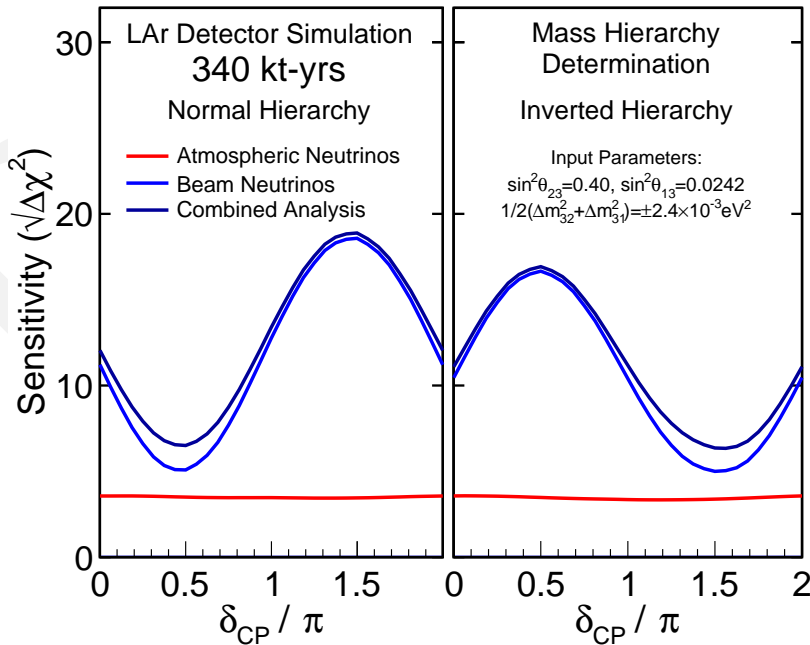
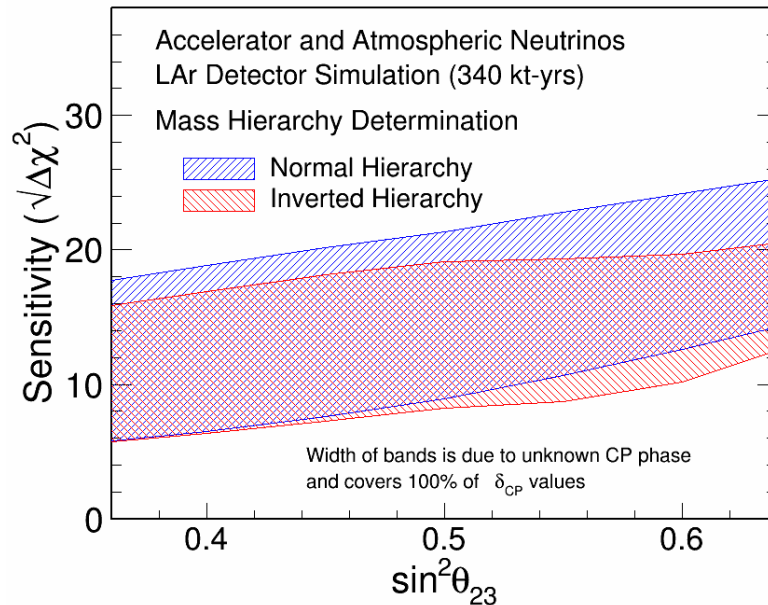


fig:atmnsens4

Figure 4.29: Sensitivity to mass hierarchy using atmospheric neutrinos combined with beam neutrinos with an exposure of 340 kt-years in a 1.2-MW beam.



**Figure 4.30:** Sensitivity to mass hierarchy using atmospheric neutrinos combined with beam neutrinos as a function of the true value of  $\sin^2 \theta_{23}$ , for true normal (blue) and inverted (red) hierarchy. The width of the band is due to the unknown value of  $\delta_{CP}$  and covers all possible values of  $\delta_{CP}$ . Assumes an exposure of 340 kt-years in a 1.2-MW beam.

In the region of  $\delta_{CP}$  where the LBNE neutrino-beam-only analysis is least sensitive to the mass hierarchy, atmospheric neutrinos measured in the same experiment offer comparable sensitivity. The combined beam and atmospheric neutrino mass hierarchy sensitivity is  $|\sqrt{\Delta\chi^2}| > 6$  for all values of  $\delta_{CP}$  ( $\sin^2 \theta_{23} = 0.4$ ) in a 34-kt detector, assuming a 1.2-MW beam running for ten years. It is important to note that the combined sensitivity is better than the sum of the separate  $\chi^2$  values, as the atmospheric data help to remove degeneracies in the beam data.

1

2 Figure [4.30](#) shows the [combined sensitivity to beam and atmospheric neutrinos for determination](#)  
 3 [of mass hierarchy as a function of the true value of  \$\sin^2 \theta\_{23}\$ , for the same 340 kt · year exposure](#)  
 4 [in a 1.2-MW beam. This can be compared to Figure 4.14 in Section 4.3.3, which shows the same](#)  
 5 [sensitivity using only beam neutrinos.](#)

6 Figure [4.31](#) shows the [combined sensitivity to beam and atmospheric neutrinos for the octant de-](#)  
 7 [termination and CPV. The role played by atmospheric data in resolving beam degeneracies is also](#)  
 8 [clear from considering the combined and beam-only sensitivities in these plots.](#)

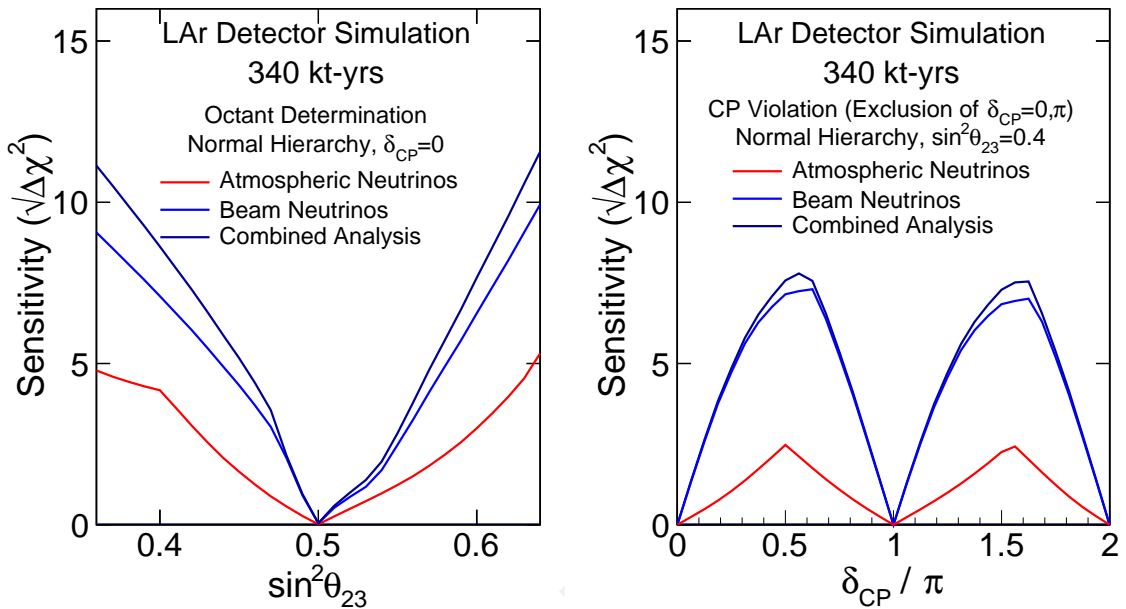


**Figure 4.31:** Sensitivity to octant (left) and CPV (right) using atmospheric neutrinos combined with beam neutrinos with an exposure of 340 kt · year in a 1.2-MW beam.

## 4.7 Searches for Physics Beyond the Standard Three-Flavor Neutrino Oscillation Model

Due to the very small masses and large mixing of neutrinos, their oscillations over a long distance act as an exquisitely precise interferometer with high sensitivity to very small perturbations caused by new physics phenomena, such as:

- nonstandard interactions in matter that manifest in long-baseline oscillations as deviations from the three-flavor mixing model
- new long-distance potentials arising from discrete symmetries that manifest as small perturbations on neutrino and antineutrino oscillations over a long baseline
- sterile neutrino states that mix with the three known active neutrino states
- large compactified extra dimensions from String Theory models that manifest through mixing between the Kaluza-Klein states and the three active neutrino states

Full exploitation of LBNE's sensitivity to such new phenomena will require higher-precision predictions of the unoscillated neutrino flux at the far detector and large exposures.

1 This section explores the potential of the full-scope LBNE design to pursue physics beyond the  
2 three-flavor neutrino oscillation model.

### 3 4.7.1 Search for Nonstandard Interactions

sec:nsi

4 Neutral-current (NC) nonstandard interactions (NSI) can be understood as nonstandard matter ef-  
5 fects that are visible only in a far detector at a sufficiently long baseline. They can be parameterized  
6 as new contributions to the MSW matrix in the neutrino-propagation Hamiltonian:

$$H = U \begin{pmatrix} 0 & & \\ & \Delta m_{21}^2/2E & \\ & & \Delta m_{31}^2/2E \end{pmatrix} U^\dagger + \tilde{V}_{\text{MSW}}, \quad (4.10)$$

with

$$\tilde{V}_{\text{MSW}} = \sqrt{2}G_F N_e \begin{pmatrix} 1 + \epsilon_{ee}^m & \epsilon_{e\mu}^m & \epsilon_{e\tau}^m \\ \epsilon_{e\mu}^{m*} & \epsilon_{\mu\mu}^m & \epsilon_{\mu\tau}^m \\ \epsilon_{e\tau}^{m*} & \epsilon_{\mu\tau}^{m*} & \epsilon_{\tau\tau}^m \end{pmatrix} \quad (4.11)$$

7 Here,  $U$  is the leptonic mixing matrix, and the  $\epsilon$ -parameters give the magnitude of the NSI relative  
8 to standard weak interactions. For new physics scales of a few  $\times 100$  GeV, a value of  $|\epsilon| \lesssim 0.01$  is  
9 expected [Davidson:2003ha, GonzalezGarcia:2007ib, Biggio:2009nt]. LBNE's 1,300-km baseline provides an advantage in the detection of NSI  
10 relative to existing beam-based experiments with shorter baselines. Only atmospheric-neutrino  
11 experiments have longer baselines, but the sensitivity of these experiments to NSI is limited by  
12 systematic effects.

13 To assess the sensitivity of LBNE to NC NSI, the NSI discovery reach is defined in the following  
14 way: the expected event spectra are simulated using GLoBeS, assuming “true” values for the NSI  
15 parameters, and a fit is then attempted assuming no NSI. If the fit is incompatible with the simulated  
16 data at a given confidence level, the chosen “true” values of the NSI parameters are considered to  
17 be within the experimental discovery reach. In Figure 4.32, the NSI discovery reach of LBNE is  
18 shown; only one of the  $\epsilon_{\alpha\beta}^m$  parameters at a time is taken to be non-negligible.

### 19 4.7.2 Search for Long-Range Interactions

20 The small scale of neutrino-mass differences implies that minute differences in the interactions of  
21 neutrinos and antineutrinos with currently unknown particles or forces may be detected through  
22 perturbations to the time evolution of the flavor eigenstates. The longer the experimental baseline,  
23 the higher the sensitivity to a new long-distance potential acting on neutrinos. For example, some  
24 of the models for such long-range interactions (LRI) as described in [166] (see Figure 4.33) could  
25 contain discrete symmetries that stabilize the proton and give rise to a dark-matter candidate parti-  
26 cle, thus providing new connections between neutrino, proton decay and dark matter experiments.

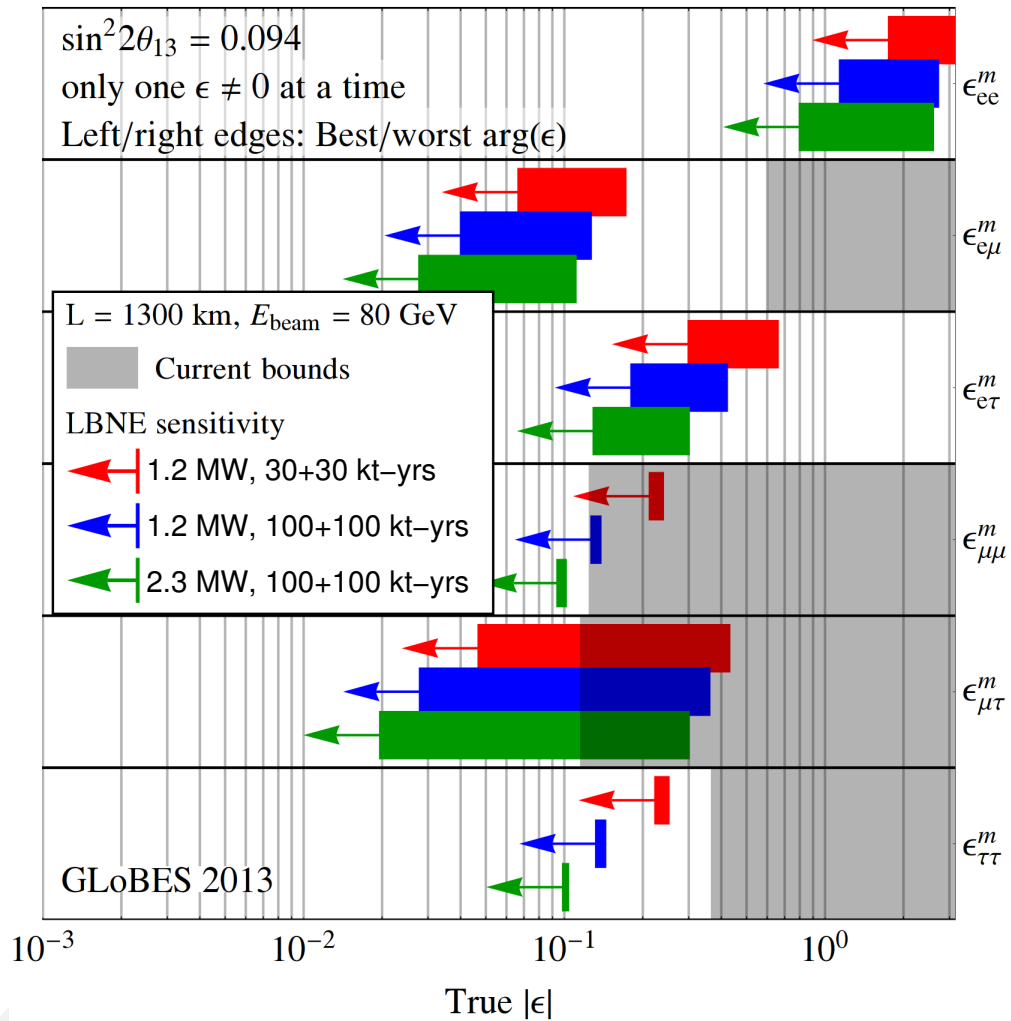
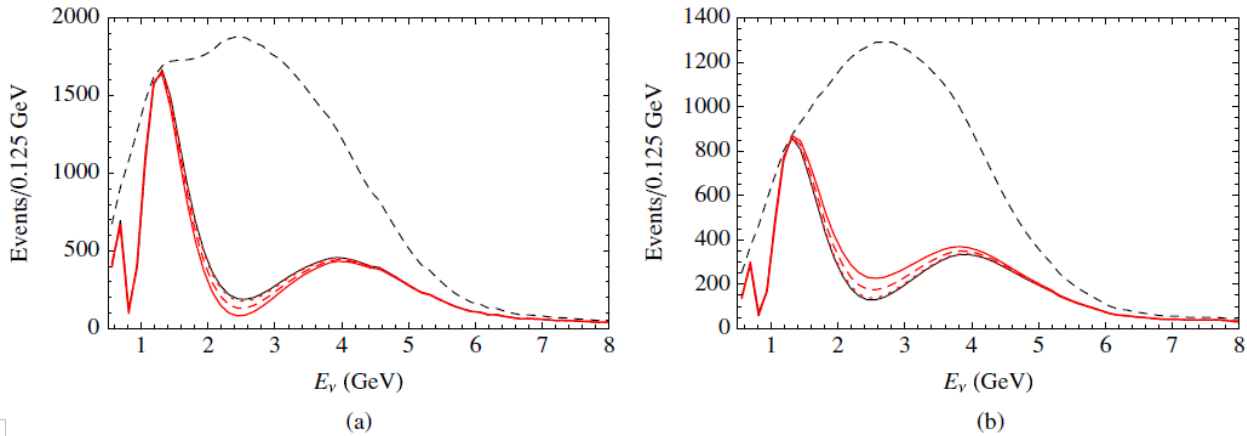
NC NSI discovery reach ( $3\sigma$  C.L.)


fig:LAr-NSI

**Figure 4.32:** Nonstandard interaction discovery reach in LBNE with increasing exposure: 1.2 MW, 60 kt-years (red) + 1.2 MW, 200 kt · year (blue) + 2.3 MW, 200 kt · year (green). The left and right edges of the error bars correspond to the most favorable and the most unfavorable values for the complex phase of the respective NSI parameters. The gray shaded regions indicate the current model-independent limits on the different parameters at  $3\sigma$  [163,164]. For this study the value of  $\sin^2 2\theta_{13}$  was assumed to be 0.09. Figure courtesy of Joachim Kopp.

- 1 The longer baseline of LBNE improves the sensitivity to LRI beyond that possible by the current
- 2 generation of long-baseline neutrino experiments. The sensitivity will be determined by the amount
- 3 of  $\nu_\mu/\bar{\nu}_\mu$  CC statistics accumulated and the accuracy with which the unoscillated and oscillated  $\nu_\mu$
- 4 spectra can be determined.



**Figure 4.33:** Long-range interactions in LBNE. The number of (a) neutrino and (b) antineutrino events versus  $E_\nu$ , in a long-baseline experiment with a 1,300-km baseline. The unoscillated case (top black dashed curves) and the case of no new physics (thin black solid curves) are displayed, as well as the cases with  $\alpha' = (1.0, 0.5, \text{ and } 0.1) \times 10^{-52}$ , corresponding to red solid, dashed, and dotted curves, respectively.  $\alpha'$  is the “fine structure constant” of such interactions, which is constrained to be  $\alpha' \leq 10^{-47}$  [166].

### 1 4.7.3 Search for Active-Sterile Neutrino Mixing

2 Searches for evidence of active-sterile neutrino mixing at LBNE can be conducted by examin-  
 3 ing the NC event rate at the far detector and comparing it to a precise estimate of the expected  
 4 rate extrapolated from  $\nu_\mu$  flux measurements from the near detector and from beam and detector  
 5 simulations. Observed deficits in the NC rate could be evidence for active-sterile neutrino mix-  
 6 ing. The most recent such search in a long-baseline experiment was conducted by the MINOS  
 7 experiment [167].

8 LBNE will provide a unique opportunity to revisit this search with higher precision over a large  
 9 range of neutrino energies and a longer baseline. The expected rate of NC interactions with vis-  
 10 ible energy  $> 0.5$  GeV in a 10-kt detector over three years is approximately 2,000 events (see  
 11 Table 4.1) in the LE beam tune and 3,000 events in the ME beam tune. The NC identification effi-  
 12 ciency is high, with a low rate of  $\nu_\mu$  CC background misidentification as shown in Table 4.2. The  
 13 high-resolution LArTPC far detector will enable a coarse measurement of the incoming neutrino  
 14 energy in a NC interaction by using the event topology and correcting for the missing energy of  
 15 the invisible neutrino. This will greatly improve the sensitivity of LBNE to active-sterile mixing as  
 16 compared to current long-baseline experiments such as MINOS+ since both the energy spectrum  
 17 as well as the rate of NC interactions can be measured at both near and far detectors. Studies are  
 18 currently underway to quantify LBNE’s sensitivity to active-sterile mixing.

#### 4.7.4 Sensitivity to Large Extra Dimensions

Several theoretical models propose that right-handed neutrinos propagate in large compactified extra dimensions, whereas the standard left-handed neutrinos are confined to the four-dimensional brane [168]. Mixing between the right-handed *Kaluza-Klein* modes and the standard neutrinos would change the mixing patterns predicted by the three-flavor model. The effects could manifest, for example, as distortions in the disappearance spectrum of  $\nu_\mu$ . The rich oscillation structure visible in LBNE, measured with its high-resolution detector using both beam and atmospheric oscillations, could provide further opportunities to probe for this type of new physics. Studies are underway to understand the limits that LBNE could impose relative to current limits and those expected from other experiments.

## 4.8 Comparison of LBNE Sensitivities to other Proposed Neutrino Oscillation Experiments

With tight control of systematics, LBNE will reach  $5\sigma$  sensitivity to CP violation for a large fraction of  $\delta_{CP}$  values. LBNE delivers the best resolution of the value of  $\delta_{CP}$  with the lowest combination of power-on-target and far detector mass when compared to other future proposed neutrino oscillation experiments (Figure 4.34).

In Figure 4.34, the CP-violation sensitivity of LBNE is compared to that of other proposed neutrino oscillation experiments from an *independent study* with updated LBNE input based on [169]. The dashed black curve labeled “2020” is the expected sensitivity from the current generation of experiments that could be achieved by 2020. LBNE-Full represents a 34-kt LArTPC running in a 1.2-MW beam for  $3(\nu) + 3(\bar{\nu})$  years. LBNE-PX is LBNE staged with PIP-II and further upgraded beams with power up to 2.3 MW as shown in Figure 4.17. T2HK is a 560-kt (fiducial mass) water Cherenkov detector running in a 1.66-MW beam for  $1.5(\nu) + 3.5(\bar{\nu})$  years [170]. LBNO<sub>100</sub> is a 100-kt LArTPC at a baseline of 2,300 km running in a 0.8-MW beam from CERN for  $5(\nu) + 5(\bar{\nu})$  years [171]. NF-IDS is the Neutrino Factory with a neutrino beam generated from muon decays in a 10-GeV muon storage ring produced from a 4-MW, 8-GeV Project X proton beam coupled with 100-kt magnetized iron detectors at a baseline of 2,000 km ( $\nu + \bar{\nu}$  simultaneously) [172]. LBNE can reach  $5\sigma$  sensitivity to CP violation for a large fraction of  $\delta_{CP}$  values with the lowest combination of power-on-target and far detector mass when compared to current and future proposed neutrino oscillation experiments.

Alone, LBNE can potentially reach a precision on  $\delta_{CP}$  between roughly  $6^\circ$  and  $10^\circ$ , i.e., close to the  $4^\circ$  CKM precision on  $\delta_{CP}^{CKM}$  — but an exposure of  $\sim 700$  kt · MW · years is needed. Nevertheless, as shown in Figure 4.35, wide-band, long-baseline experiments such as LBNE (and LBNO) can

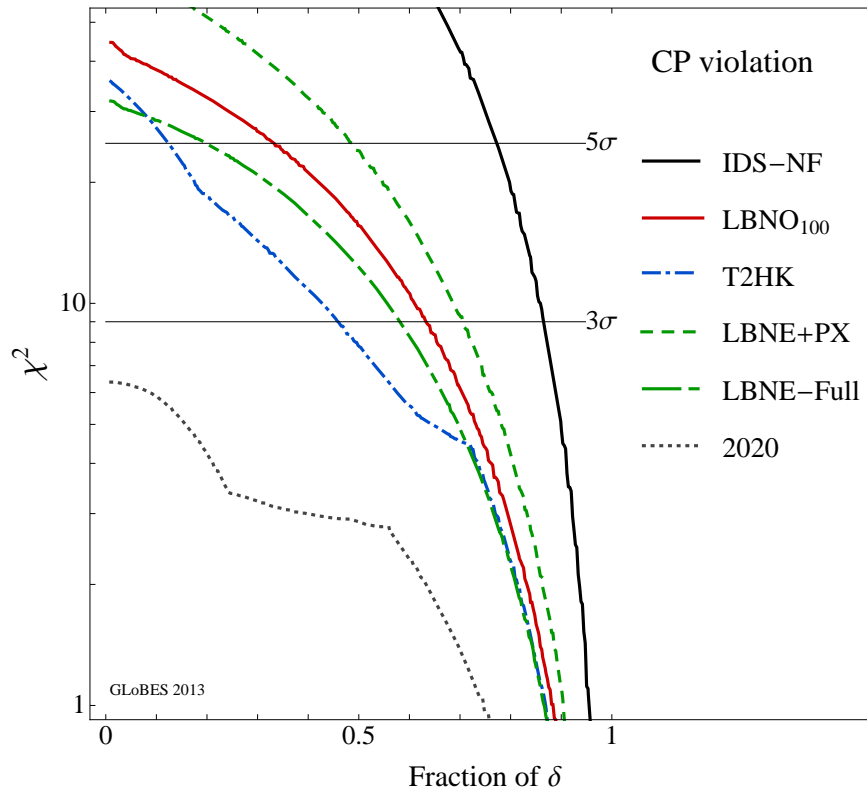


**Figure 4.34:** The minimal CP-violation sensitivity for a given fraction of  $\delta_{\text{CP}}$  values for different proposed neutrino oscillation experiments. The exposure and baseline of each experiment is described in the text. Figure is based on the studies detailed in [169].

1 achieve nearly CKM precision on  $\delta_{\text{CP}}$  with much less exposure than is required for existing ex-  
 2 periments such as  $\text{NO}\nu\text{A}$ , T2K and proposed short-baseline, off-axis experiments such as T2HK.  
 3 With the exception of the NuMAX sensitivity, which is taken from [173], the resolutions in the  
 4 colored bands in Figure 4.35 are calculated independently by LBNE using GLOBES and found  
 5 to be in good agreement with the values reported by the experiments themselves (T2HK [174],  
 6  $\text{NO}\nu\text{A}$  [30], LBNO [175]).

7 It is important to note that the precision on  $\delta_{\text{CP}}$  in the off-axis experiments shown in Figure 4.35  
 8 assumes the mass hierarchy is resolved. If the mass hierarchy is unknown, the resolution of T2K,  
 9  $\text{NO}\nu\text{A}$  and T2HK will be much worse than indicated. LBNE does not require external information  
 10 on the mass hierarchy to reach the precisions described in this section. Only a neutrino factory can  
 11 possibly out-perform a wide-band, long-baseline experiment — but not by much — for equivalent  
 12 power, target mass and years of running. To achieve this precision, however, LBNE will need to  
 13 tightly control the systematic uncertainties on the  $\nu_e$  appearance signal. A high-resolution near  
 14 detector will be needed to reach this level of precision, as described in Section 3.5.

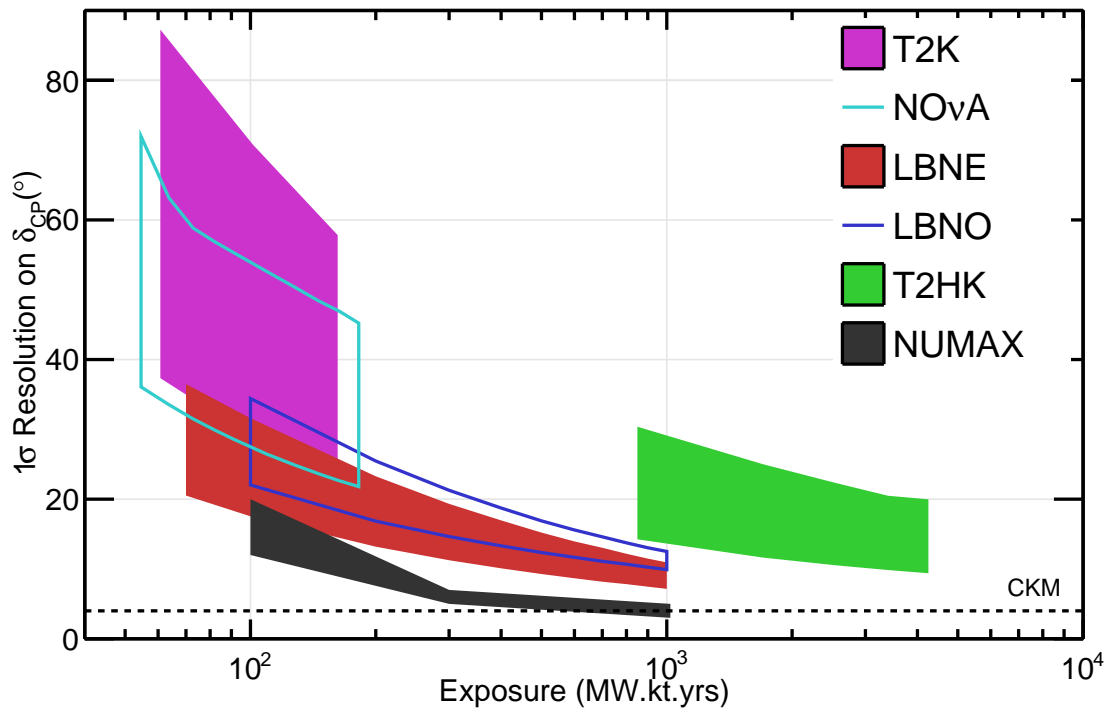


**Figure 4.35:** The  $1\sigma$  resolution on  $\delta_{CP}$  that can be achieved by existing and proposed beamline neutrino oscillation experiments as a function of exposure in terms of mass  $\times$  beam power  $\times$  years of running. The band represents the variation in the resolution as a function of  $\delta_{CP}$  with the lower edge representing the best resolution and the upper edge the worst. The bands start and stop at particular milestones. For example, the LBNE band starts with the resolutions achieved by LBNE 10 kt and ends with the full LBNE running with the 2.3-MW upgrades beyond PIP-II. With the exception of the NuMAX sensitivity, which is taken from [173], the resolutions in the colored bands are calculated independently by LBNE using GLoBES. The dashed line denotes the  $4^\circ$  resolution point which is the resolution of  $\delta_{CP}^{CKM}$  from the 2011 global fits.

- 1 An independent study comparing LBNE's sensitivity to the mass ordering to that of current and
- 2 future proposed experiments highlights the potential of LBNE [141]. The study uses frequentist
- 3 methods of hypothesis testing to define sensitivities. The validity of the approach is tested using
- 4 toy MC simulations of the various experiments. The comparison of expected mass hierarchy sen-
- 5 sitivities for a variety of current and proposed experiments using different approaches with some
- 6 reasonable estimate as to the start time of the different experiments is summarized in Figure 4.36.
- 7 Future upgrades to the Fermilab accelerator complex — in particular the prospect of high-power,
- 8 low-energy proton beams such as the 3-MW, 8-GeV beam originally proposed as Stage 4 of Project
- 9 X — could open up further unique opportunities in LBNE to probe CP violation using on-axis, low-
- 10 energy beams specifically directed at the second oscillation maximum where CP effects dominate
- 11 the asymmetries [176]. Such high-power, low-energy beams could even enable studies in  $\nu_1\text{-}\nu_2$
- 12 mixing in very long-baseline experiments.

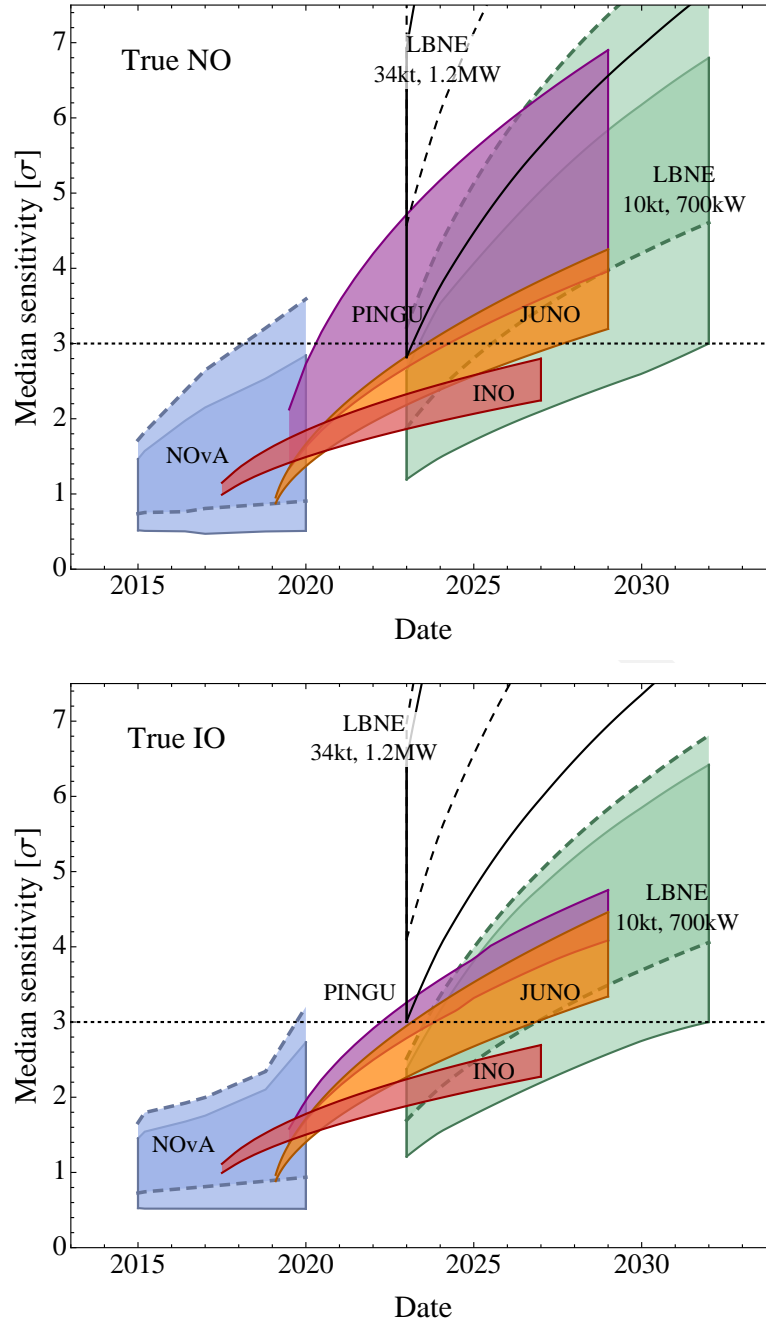


**Figure 4.36:** The top (bottom) figure shows the median sensitivity in number of sigmas for rejecting the inverted (normal) hierarchy if the normal (inverted) hierarchy is true for different facilities as a function of the date. The width of the bands corresponds to different true values of the CP phase  $\delta_{CP}$  for  $NO\nu A$  and LBNE, different true values of  $\theta_{23}$  between  $40^\circ$  and  $50^\circ$  for INO and PINGU, and energy resolution between  $3\%/\sqrt{E}$  (MeV) and  $3.5\%/\sqrt{E}$  (MeV) for JUNO. For the long-baseline experiments, the bands with solid (dashed) contours correspond to a true value for  $\theta_{23}$  of  $40^\circ$  ( $50^\circ$ ). In all cases, octant degeneracies are fully considered. This figure is from the analysis presented in [141], however, for the plots shown here, the beam power for the full-scope, 34-kt LBNE has been changed to 1.2 MW to reflect the Fermilab PIP-II upgrade plan.

pdk-chap

1 Baryon number conservation is an unexplained symmetry in the Universe with deep connections to both cosmology and particle physics. As one of the conditions underlying the observed matter-antimatter asymmetry of the Universe, baryon number *should* be violated. Nucleon decay, which is a manifestation of baryon number violation, is a hallmark of many Grand Unified Theories (GUTs), theories that connect quarks and leptons in ways not envisioned by the Standard Model. Observation of proton or bound-neutron decay would provide a clear experimental signature of baryon number violation.

2 Predicted rates for nucleon decay based on GUTs are uncertain but cover a range directly accessible with the next generation of large underground detectors. LBNE, configured with its massive, deep-underground LArTPC far detector, offers unique opportunities for the discovery of nucleon decay, with sensitivity to key decay channels an order of magnitude beyond that of the current generation of experiments.

## 3 5.1 LBNE and the Current Experimental Context

4 Current limits on nucleon decay via numerous channels are dominated by Super-Kamiokande  
5 (SK) [177], for which the most recently reported preliminary results are based on an overall ex-  
6 posure of 260 kt year. The SK search has so far failed to observe nucleon decay, however it has  
7 established strict limits (90% CL) on the partial lifetimes for decay modes of particular interest to  
8 GUT models such as  $\tau/B(p \rightarrow e^+\pi^0) > 1.3 \times 10^{34}$  yr and  $\tau/B(p \rightarrow K^+\bar{\nu}) > 0.59 \times 10^{34}$  yr [32].  
9 These are significant limits on theoretical models that constrain model builders and set a high  
10 threshold for the next-generation detectors such as LBNE and Hyper-Kamiokande. With more  
11 than ten years of exposure, the SK limits will improve only slowly. A much more massive detector  
12 such as Hyper-Kamiokande — which will have a 560-kt fiducial mass — is required to make a  
13 significant (order-of-magnitude) improvement using the water Cherenkov technique.

14 The uniqueness of proton decay signatures in a LArTPC and the potential for reconstructing them  
15 with redundant information has long been recognized as a key strength of this technology. A  
16 LArTPC can reconstruct all final-state charged particles and make an accurate assessment of par-  
17 ticle type, distinguishing between muons, pions, kaons and protons. Electromagnetic showers are  
18 readily measured, and those that originate from photons generated by  $\pi^0$  decay can be distinguished  
19 to a significant degree from those that originate from charged-current  $\nu_e$  interactions. Kiloton per  
20 kiloton, LArTPC technology is expected to outperform water Cherenkov in both detection effi-  
21 ciency and atmospheric neutrino background rejection for most nucleon decay modes, although

1 intranuclear effects, which can smear out some of the proton decay signal, are smaller for oxygen  
2 and non-existent for hydrogen.

3 When mass and cost are taken into account, water Cherenkov technology is optimum for the  $p \rightarrow$   
4  $e^+\pi^0$  final-state topology, where the signal efficiency is roughly 40% and the background rate is  
5 two events per megaton-year. The efficiency estimate [178] for a LArTPC is 45% with one event  
6 per megaton-year — not a significant enough improvement in efficiency to overcome the penalty  
7 of the higher cost per kiloton for liquid argon.

8 For the  $p \rightarrow K^+\bar{\nu}$  channel, on the other hand, the LArTPC technology is superior based on the  
9 same criteria. In the LArTPC, the  $K^+$  track is reconstructed and identified as a charged kaon.  
10 The efficiency for the  $K^+\bar{\nu}$  mode in a LArTPC is estimated to be as high as 97.5% with a back-  
11 ground rate of one event per megaton-year. In water Cherenkov detectors the efficiency for this  
12 mode is roughly 19% for a low-background search, with a background rate of four events per  
13 megaton-year. Based on these numbers and a ten-year exposure, LBNE's full-scope 34-kt LArTPC  
14 and the 560-kt Hyper-Kamiokande WCD have comparable sensitivity (at 90% CL), but the esti-  
15 mated LArTPC background of 0.3 events is dramatically better than the 22 estimated for Hyper-  
16 Kamiokande (assuming no further improvement in analysis technique past that currently executed  
17 for Super-Kamiokande [32]).

## 18 5.2 Signatures for Nucleon Decay in Liquid Argon

The LBNE LArTPC's superior detection efficiencies for decay modes that produce kaons will outweigh its relatively low mass compared with multi-100-kt water Cherenkov detectors. Because the LArTPC can reconstruct protons that would otherwise be below Cherenkov threshold, it can reject many atmospheric neutrino background topologies by vetoing on the presence of a recoil proton. Due to its high spatial resolution, it also performs better for event topologies with displaced vertices, such as  $p \rightarrow K^+\bar{\nu}$  (for multi-particle  $K^+$  decay topologies) and  $p \rightarrow K^0\mu^+$ . The latter mode is preferred in some SUSY GUTs.

19  
20 For modes with no electron in the final state, the same displaced vertex performance that un-  
21 derpins long-baseline neutrino oscillation measurements allows the rejection of charged current  
22 interactions of atmospheric  $\nu_e$ 's. And, as will be stressed for the key mode of  $p \rightarrow K^+\bar{\nu}$  described  
23 in detail below, the capability to reconstruct the charged kaon with the proper range and  $dE/dx$   
24 profile allows for a high-efficiency, background-free analysis. In general, the above criteria favor  
25 all modes with a kaon, charged or neutral, in the final state. Conversely, the efficiency for decay  
26 modes to a lepton plus light meson will be limited by intranuclear reactions that plague liquid  
27 argon to a greater extent than they do  $^{16}\text{O}$  in a water Cherenkov detector.

1 An extensive survey [178] of nucleon decay efficiency and background rates for large LArTPCs  
 2 with various depth/overburden conditions, published in 2007, provides the starting point for the  
 3 assessment of LBNE’s capabilities. Table 5.1 lists selected modes where LArTPC technology ex-  
 hibits a significant performance advantage (per kiloton) over the water Cherenkov technology. The

**Table 5.1:** Efficiencies and background-rates (events per Mt-yr) for nucleon decay channels of interest for a large underground LArTPC [178], and comparison with water Cherenkov detector capabilities. The entries for the water Cherenkov capabilities are based on experience with the Super-Kamiokande detector [32].

Decay Mode	Water Cherenkov		Liquid Argon TPC	
	Efficiency	Background	Efficiency	Background
$p \rightarrow K^+\bar{\nu}$	19%	4	97%	1
$p \rightarrow K^0\mu^+$	10%	8	47%	< 2
$p \rightarrow K^+\mu^-\pi^+$			97%	1
$n \rightarrow K^+e^-$	10%	3	96%	< 2
$n \rightarrow e^+\pi^-$	19%	2	44%	0.8

tab:pdecay

4  
 5 remainder of this chapter focuses on the capabilities of LBNE for the  $p \rightarrow K^+\bar{\nu}$  channel, as the  
 6 most promising from theoretical and experimental considerations. Much of the discussion that  
 7 follows can be applied to cover the other channels with kaons listed in the table.

8 The key signature for  $p \rightarrow K^+\bar{\nu}$  is the presence of an isolated charged kaon (which would also  
 9 be monochromatic for the case of free protons, with  $p = 340$  MeV). Unlike the case of  $p \rightarrow e^+\pi^0$ ,  
 10 where the maximum detection efficiency is limited to 40–45% because of inelastic intranuclear  
 11 scattering of the  $\pi^0$ , the kaon in  $p \rightarrow K^+\bar{\nu}$  emerges intact (because the kaon momentum is below  
 12 threshold for inelastic reactions) from the nuclear environment of the decaying proton  $\sim 97\%$  of  
 13 the time. Nuclear effects come into play in other ways, however: the kaon momentum is smeared  
 14 by the proton’s Fermi motion and shifted downward by re-scattering [179]. The kaon emerging  
 15 from this process is below Cherenkov threshold, therefore a water detector would need to detect  
 16 it after it stops, via its decay products. Not all  $K$  decay modes are reconstructable, however, and  
 17 even for those that are, insufficient information exists to determine the initial  $K$  momentum. Still,  
 18 water detectors can reconstruct significant hadronic channels such as  $K^+ \rightarrow \pi^+\pi^0$  decay, and the  
 19 6-MeV gamma from de-excitation of  $O^{16}$  provides an added signature to help with the  $K^+ \rightarrow \mu^+\nu$   
 20 channel. The overall detection efficiency in SK [32] thus approaches 20%.

21 In LArTPC detectors, the  $K^+$  can be tracked, its momentum measured by range, and its identity  
 22 positively resolved via detailed analysis of its energy-loss profile. Additionally, all decay modes  
 23 can be cleanly reconstructed and identified, including those with neutrinos, since the decaying  
 24 proton is essentially at rest. With this level of detail, it is possible for a single event to provide  
 25 overwhelming evidence for the appearance of an isolated kaon of the right momentum originating  
 26 from a point within the fiducial volume. The strength of this signature is clear from cosmogenic-  
 27 induced kaons observed by the ICARUS Collaboration in the cosmic-ray test run of half of the

- 1 T600 detector, performed at a surface installation in Pavia [180] and in high-energy neutrino in-  
 2 teractions with the full T600 in the recent CNGS (CERN Neutrinos to Gran Sasso) run [181].  
 3 Figure 5.1 shows a sample event from the CNGS run in which the kaon is observed as a progres-  
 4 sively heavily-ionizing track that crosses into the active liquid argon volume, stops, and decays to  
 5  $\mu\nu$ , producing a muon track that also stops and decays such that the Michel-electron track is also  
 visible. The 3D reconstruction of the event is shown in Figure 5.2.

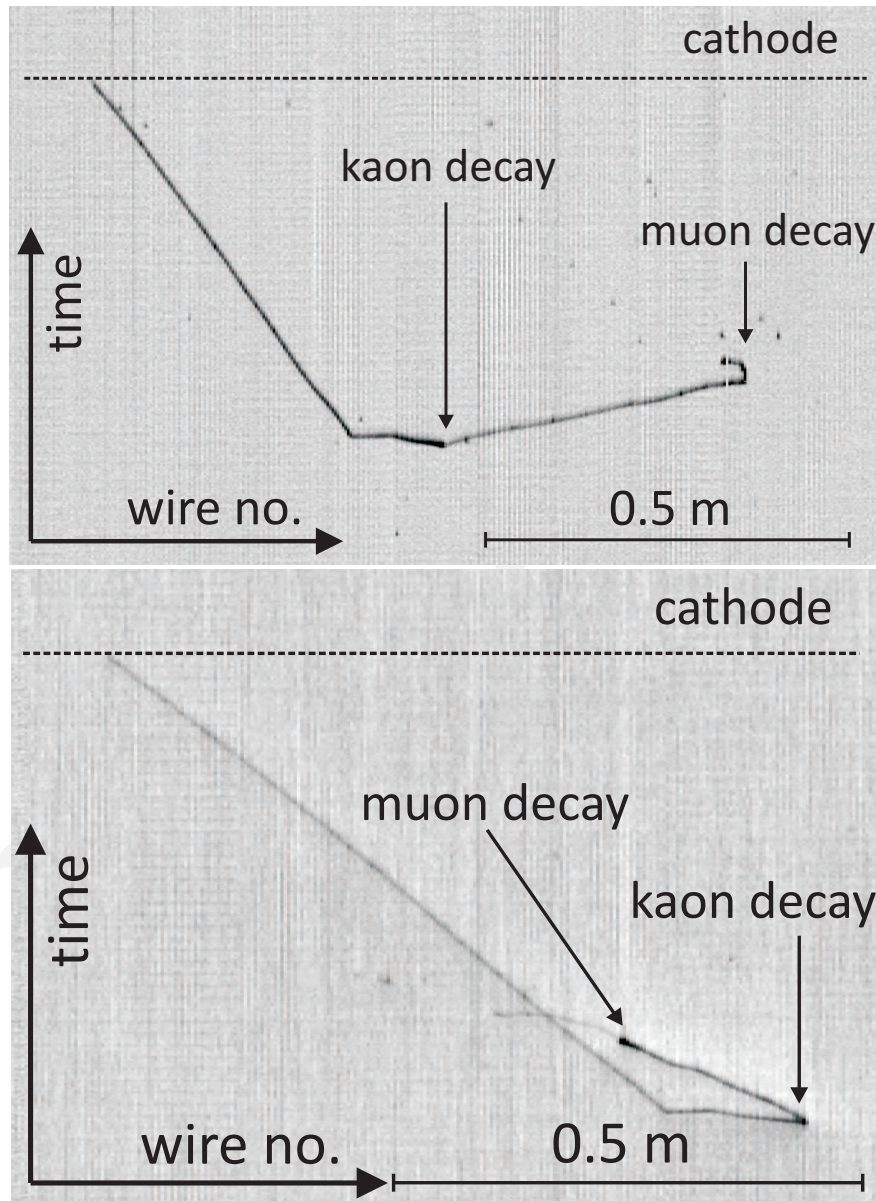


**Figure 5.1:** Event display for a decaying kaon candidate  $K \rightarrow \mu\nu_\mu \mu \rightarrow e\nu_e\nu_\mu$  in the ICARUS T600 detector observed in the CNGS data ( $K$ : 90 cm, 325 MeV;  $\mu$ : 54 cm, 147 MeV;  $e$ : 13 cm, 27 MeV). The top figure shows the signal on the collection plane, and the bottom figure shows the signal on the second induction plane [181].

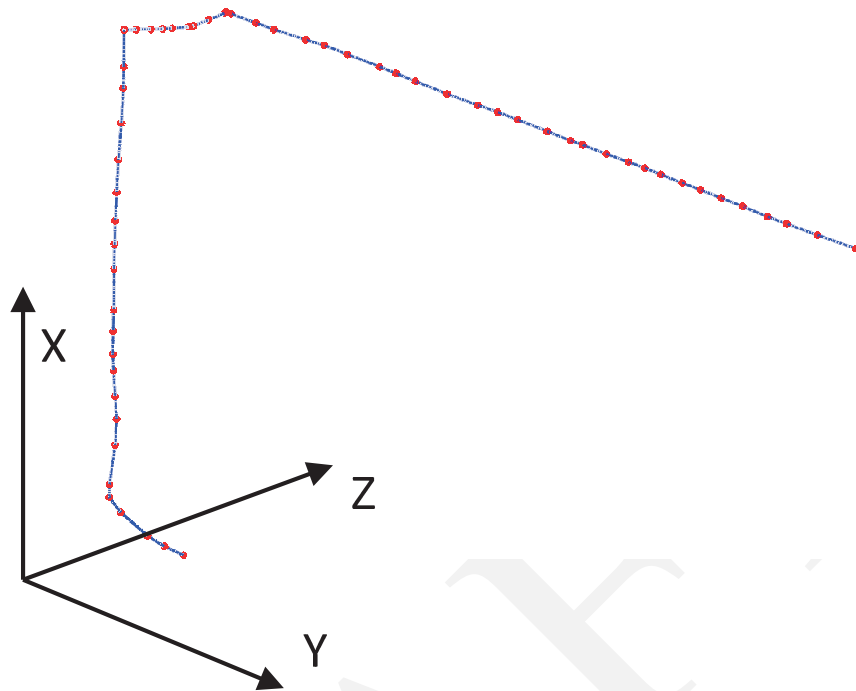


**Figure 5.2:** 3D reconstruction of the decaying kaon event observed in the ICARUS T600 detector and shown in Figure 5.1.

- 1 If it can be demonstrated that background processes mimicking this signature can be rejected at
- 2 the appropriate level, a single  $p \rightarrow K^+ \bar{\nu}$  candidate could constitute evidence for proton decay. The
- 3 background rejection capability of the LBNE far detector is the topic of Section 5.3 below.

## 5.3 Background Levels and Rejection Capabilities

- 5 This section discusses the key background processes and their signatures, focusing on the  $p \rightarrow$
- 6  $K^+ \bar{\nu}$  channel as the benchmark mode\*. The two potential sources of background are cosmic-ray
- 7 muons and atmospheric neutrinos, described separately below.

### 5.3.1 Cosmic-Ray Muon Backgrounds

- 9 Cosmic-ray (CR) muons contribute background signals when they penetrate the detector. Hence,
- 10 the self-shielding feature of the LArTPC and the depth of the site are important assets for control-
- 11 ling the rate of signals that can mimic a proton decay event. Additionally, the energy deposition
- 12 associated with spallation products is well below the hundreds-of-MeV energy range for deposi-
- 13 tions from proton decay final-state particles.

\*Much of this discussion applies equally well to other nucleon decay modes involving charged or neutral kaons.

1 The most pernicious CR muon background in liquid argon for proton decay with kaon final states  
2 thus comes from particular pathological processes. Specifically, cosmic-ray muons that produce  
3 kaons via photonuclear interactions in the rock near the detector or in the liquid argon itself but  
4 outside the active volume are capable of producing signatures that mimic  $p \rightarrow K^+\bar{\nu}$  and other  
5 modes with kaons. Cosmic-ray induced kaon backgrounds as a function of depth have been studied  
6 for liquid argon [178,182,183].

7 In particular, at the 4,850-ft level, the vertical rock overburden will be approximately 4-km water  
8 equivalent, at which depth the muon rate through a 34-kt LArTPC will be approximately  $0.1 \text{ s}^{-1}$ .  
9 This is low enough that a veto on the detection of a muon in the liquid argon volume can be  
10 applied with negligible loss of live-time. Specifically, assuming a maximum drift time of 2 ms,  
11 the probability of a muon passing through the detector in time with any candidate event (i.e., a  
12 candidate for proton decay or other signal of interest) will be  $2 \times 10^{-4}$ . Thus, any candidate event  
13 that coincides in time with a large energy deposition from a muon or muon-induced cascade can be  
14 rejected with a negligible signal efficiency loss of 0.02%. Only background from events associated  
15 with cosmic-ray muons in which the muon itself does not cross the active region of the detector  
16 remain to be considered.

17 One class of such backgrounds involves production of a charged kaon outside the active volume,  
18 which then enters the active region. Assuming unambiguous determination of the drift time (via  
19 the scintillation photon detection system and other cues such as detailed analysis of the  $dE/dx$   
20 profile of the kaon candidate), it will be possible to identify and reject such entering kaons with  
21 high efficiency. It should be noted that, through studies of CR muons that interact within the active  
22 volume of the detector, backgrounds of this type can be well characterized with data from the  
23 detector itself.

24 A potentially less tractable background for the decay mode  $p^+ \rightarrow K^+\bar{\nu}$  occurs when a neutral  
25 particle (e.g., a  $K_L^0$ ) originating in a muon-induced cascade outside the detector propagates into  
26 the detector volume and undergoes a charge-exchange reaction in the fiducial volume. To further  
27 understand the possible rate for this background at LBNE, simulations of cosmic-ray muons and  
28 their secondaries at depth have been run. The rate of positive kaons produced inside the 34-kt  
29 detector by a neutral particle entering from outside (and with no muon inside) has been found to  
30 be 0.9 events per year before any other selection criteria are applied. Further studies included the  
31 following additional selection criteria:

- 32 1. No muon is in the detector active volume.
- 33 2. The  $K^+$  candidate is produced inside the liquid argon active volume at a distance from the  
34 wall greater than 10 cm.
- 35 3. The energy deposition from  $K^+$  and its descendants (excluding decay products) is less than  
36 150 MeV.

- 1 4. The total energy deposition from the  $K^+$ , its descendants and decay products is less than  
2 1 GeV.
- 3 5. Energy deposition from other particles in the muon-induced cascade (i.e., excluding the en-  
4 ergy deposition from the positive kaon, its descendants and decay products) is less than  
5 100 MeV.

6 No event survived the additional selection criteria, resulting in an upper bound on the rate of this  
7 type of background event of 0.07 events per year in a 34-kt LArTPC, equivalent to 2 events per  
8 megaton-year. A key factor contributing to the rejection of cosmic-ray backgrounds to this level  
9 is that although a large number of  $K^+$ 's generated by cosmic rays deposit an energy similar to  
10 that expected from proton decay, the energy depositions from  $K^+$ 's are not the only ones recorded  
11 for these events. Other particles from the cosmic-muon interaction tend also to enter the detector  
12 and deposit additional visible energy, making the rejection of background events simpler than  
13 expectations that assume just the appearance of a kaon in the detector.

14 In addition to the impact of an active veto system for detectors at various depths, the studies  
15 of [178] also consider impacts of progressively restrictive fiducial volume cuts. Together, these  
16 and the above studies demonstrate that proton decay searches in the LBNE LArTPC at the 4,850-ft  
17 level can be made immune to cosmic-ray muon backgrounds, without the requirement of an ex-  
18 ternal active veto system. To the extent that there are uncertainties on the rate of kaon production  
19 in CR muon interactions, one has flexibility to suppress background from this source further by  
20 application of modest fiducial volume cuts.

### 21 5.3.2 Background from Atmospheric Neutrino Interactions

22 Unlike the case of CR muon backgrounds, the contamination of a nucleon decay candidate set  
23 due to interactions of atmospheric neutrinos cannot be directly controlled by changing the depth  
24 or fiducial volume definition of the LBNE detector. Furthermore the atmospheric neutrino flux is  
25 naturally concentrated around the energy range relevant for proton decay. Indeed, in the analysis  
26 of [178], a single simulated neutral current event survived the requirement of having an isolated  
27 single kaon with no additional tracks or  $\pi^0$ 's, and total deposited energy below 800 MeV. This  
28 event is responsible for the estimated background rate of 1.0 per megaton-year.

29 While this rate is acceptable for LBNE, it is natural to ask to what extent simulations are capable  
30 of providing reliable estimates for such rare processes. What if the actual rate for single-kaon  
31 atmospheric neutrino events is higher by a factor of ten or more? Is that even conceivable? To set  
32 the scale, it is useful to recall that the atmospheric neutrino sample size in LBNE is expected to  
33 be of order  $10^5$  per megaton-year of exposure (see Table 4.11). Hence, "rare-but-not-negligible" in  
34 this context denotes a process that occurs at a level of no less than  $10^{-6}$ .

1 Considerable attention to atmospheric neutrino backgrounds has been given by Super–Kamiokande  
 2 in its nucleon decay searches (see, for example [184]). In the SK analyses, data obtained with  
 3 relaxed cuts have been studied to validate the atmospheric neutrino flux and interaction models  
 4 employed. Consequently, the atmospheric neutrino backgrounds for nucleon decay searches are  
 5 well established at the level required for the water Cherenkov detector approach to this physics.

6 For the case of LBNE, however, with a different detector technology, and with a goal of being suffi-  
 7 ciently background-free to enable a discovery based on observation of a single candidate event, one  
 8 would like to go further to understand at a detailed level what the rates for the specific background  
 9 processes are. The first question to ask is what are the physical processes that could produce the  
 10 exact signature as that for a  $p \rightarrow K^+\bar{\nu}$  event? Some possibilities are discussed below.

### 11 **Strange Particle Production in $\Delta S = 0$ Processes**

12 An identified source of background events for Super–Kamiokande [184] involves associated pro-  
 13 duction of a pair of strange hadrons, nominally in the strong decay of a nucleonic resonance excited  
 14 via an inelastic neutral-current neutrino-nucleon interaction. This could be in the form of a kaon  
 15 accompanying a  $\Lambda$  baryon. Again conservation of strangeness holds that the baryon cannot be ab-  
 16 sorbed, and thus a weak decay of the strange quark is guaranteed. For water Cherenkov detectors  
 17 the strange baryon is produced with a small enough momentum that its decay products are typi-  
 18 cally below Cherenkov threshold. For a liquid argon detector, these final state particles should be  
 19 detectable, leaving distinctive signatures that can be reconstructed. Thus in principle, this source of  
 20 background can be suppressed with appropriate event reconstruction and analysis tools. To under-  
 21 stand this prospect in quantitative terms, the range of kinematic distributions are currently under  
 22 investigation.

23 It is possible to imagine yet more contrived scenarios, for example where the meson produced is  
 24 a  $K_L^0$  that escapes detection, while a charged kaon ( $K^-$  in this case) results from the decay of  
 25 an excited  $\Lambda$  or  $\Sigma$  baryon produced in association. However, one would expect such processes to  
 26 be even more rare than those described above. Thus if the rates for (say) the  $K^+\Lambda$  production  
 27 channel described above can be constrained as being sufficiently small, it can be argued that the  
 28 more contrived scenarios can be ignored.

### 29 **Strange Particle Production in $\Delta S = 1$ Processes**

30 A potentially challenging source of background is production of a single charged kaon (in this case  
 31 a  $K^-$ ) in a  $\Delta S = 1$  process. In the simplest case, one could think of it as the Cabibbo-suppressed  
 32 version of single  $\pi$  production in a charged-current anti-neutrino interaction. In this case there is  
 33 no strange baryon produced in association, and so no other hadrons to detect, in contrast with  
 34 the  $\Delta S = 0$  processes described above. (Similarly, one could imagine the kaon originating in  
 35 the decay of a strange baryon resonance produced in a Cabibbo-suppressed neutrino interaction,  
 36 accompanied by a neutron that goes undetected.) On the other hand, such processes can only  
 37 occur in charged-current interactions, and thus a charged lepton will accompany the kaon. Thus,

1 this constitutes a background only for cases where the charged lepton is missed, which should be  
 2 rare. The combination of probabilities associated with (1) Cabibbo-suppression, (2) single hadron  
 3 production, and (3) circumstances causing the charged lepton to be missed, lead to an overall  
 4 suppression of this source of background. Thus it should be possible to rule it out as a source of  
 5 concern for LBNE on the basis of these features alone.

### 6 Mis-Identification of Pions in Atmospheric Neutrino Events

7 One might be concerned about mis-identification of leading pions in atmospheric neutrino scatter-  
 8 ing events as kaons. However, it can be argued that the rate for such mis-identification events can  
 9 be controlled. Key signatures for the kaon are found in the distinctive residual-range dependence  
 10 of its energy deposition near the end of its trajectory (nominally 14 cm) as well as in the explicit  
 11 reconstruction of its decay products. While it is possible to imagine that tails in the measurement  
 12 of  $dE/dx$  could lead a pion track to mimic a kaon, the momentum (30 MeV) and hence range of  
 13 the muon produced in the decay of a stopping pion would not match that of the corresponding  
 14 muon (236 MeV) in a  $K^+ \rightarrow \mu^+ \nu$  decay. Thus, it should be possible to control this background  
 15 experimentally.

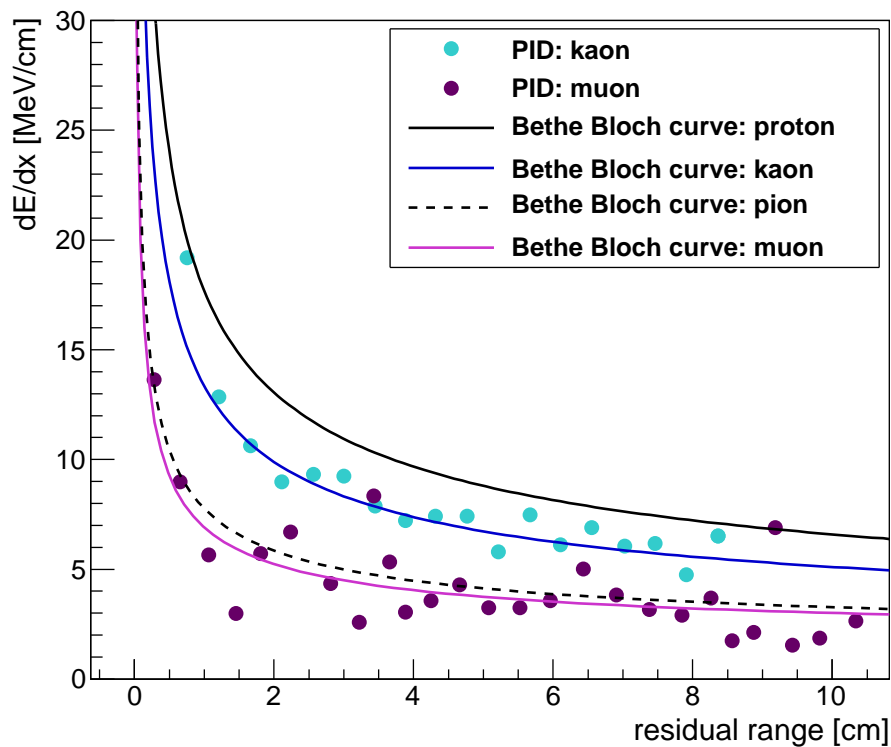


fig:pdkdedx

**Figure 5.3:** Measurements of  $dE/dx$  versus residual range for signals associated with the kaon track in Figure 5.1 (cyan points) and the decay muon (magenta points). Overlaid are the expected  $dE/dx$  profiles for the two particle identities [181].

1 One variant of this background source occurs for the case where the pion decays in flight. Two  
2 experimental handles on this background can be immediately identified. First is the deviation from  
3 the expected  $dE/dx$  profile for a kaon, which will be more dramatic than in the case of the stopping  
4 pion. Second is the correlation of the direction of the decay muon with that of the pion, which is  
5 absent in the decay of a particle at rest. Assessment of the cumulative impact of event rejection  
6 based on these features is under study. However, the decaying kaon observed in the ICARUS  
7 CNGS run displayed in Figure 5.1 can be used to give a sense of the  $\pi/K$  discrimination possible  
8 in a LArTPC via  $dE/dx$ . In Figure 5.3, the measurements of  $dE/dx$  versus residual range for the  
9 anode wires registering signals from the kaon and muon tracks in this event are plotted against the  
10 expected  $dE/dx$  profiles [181]. The data from the kaon track (cyan points) agrees very well with  
11 the expected  $dE/dx$  profile (blue curve) and is quite distinguishable from the expected pion profile  
12 (dashed curve).

### 13 Event Reconstruction Pathologies

14 While consideration of rare event topologies in atmospheric neutrino interactions is important,  
15 it will be equally important to understand ways in which more typical events might be mis-  
16 reconstructed so as to mimic nucleon decay processes. For example, a quasi-elastic charged-current  
17  $\nu_\mu$  interaction will produce a muon and a recoil proton from a common vertex. However, it may  
18 be possible to interpret the vertex as the kink associated with the decay of a stopping kaon, where  
19 the proton track is confused with a kaon traveling in the opposite direction. Tools are still under  
20 development to be able to understand the degree to which this possibility poses a potential back-  
21 ground. Naively, the  $dE/dx$  profile of the proton as a function of residual range will not match the  
22 time-reversed version of this for a kaon, and distributions of kinematic quantities will be distinct.  
23 Additionally, such a background will only affect the portion of the  $p \rightarrow K^+\bar{\nu}$  analysis focused on  
24  $K^+ \rightarrow \mu^+\nu$ ; other  $K^+$  decays will be immune to this pathology.

25 The point of this example is to illustrate that although the exquisite performance characteristics of  
26 the LArTPC technique enables unambiguous identification of nucleon decay signatures, an exten-  
27 sive program of detailed analysis will be required to fully exploit these capabilities.

### 28 Conclusions on Atmospheric Neutrino Backgrounds

29 The above examples suggest that it will be possible to demonstrate the desired level of suppression  
30 of atmospheric neutrino background without undue reliance on simulations via a combination of  
31 arguments based on existing experimental data (from Super-Kamiokande proton decay searches,  
32 as well as data from various sources on exclusive and inclusive neutrino interaction processes  
33 that yield rare topologies), physics considerations, and detailed analysis of anticipated detector  
34 response. For the latter, ongoing LBNE event reconstruction efforts will play a role with simu-  
35 lated atmospheric neutrino samples. Additionally, useful input is expected to come in over the  
36 short/intermediate term from analyses of LArTPC data from ArgoNeuT, MicroBooNE and the  
37 proposed LArIAT. Finally, while the state of neutrino flux and interaction models is already quite

1 advanced, vigorous theoretical work is ongoing to improve these further, exploiting existing data  
 2 from neutrino and electron scattering experiments. In particular, kaon production in neutrino inter-  
 3 actions in relevant energy ranges is receiving renewed attention [185].

## 4 5.4 Summary of Expected Sensitivity to Key Nucleon De- 5 cay Modes

6 Based on the expected signal efficiency and the upper limit on the background rates estimated in  
 7 Section 5.3, the expected limit on the proton lifetime as a function of running time in LBNE for  
 $p \rightarrow K^+\bar{\nu}$  is shown in Figure 5.4.

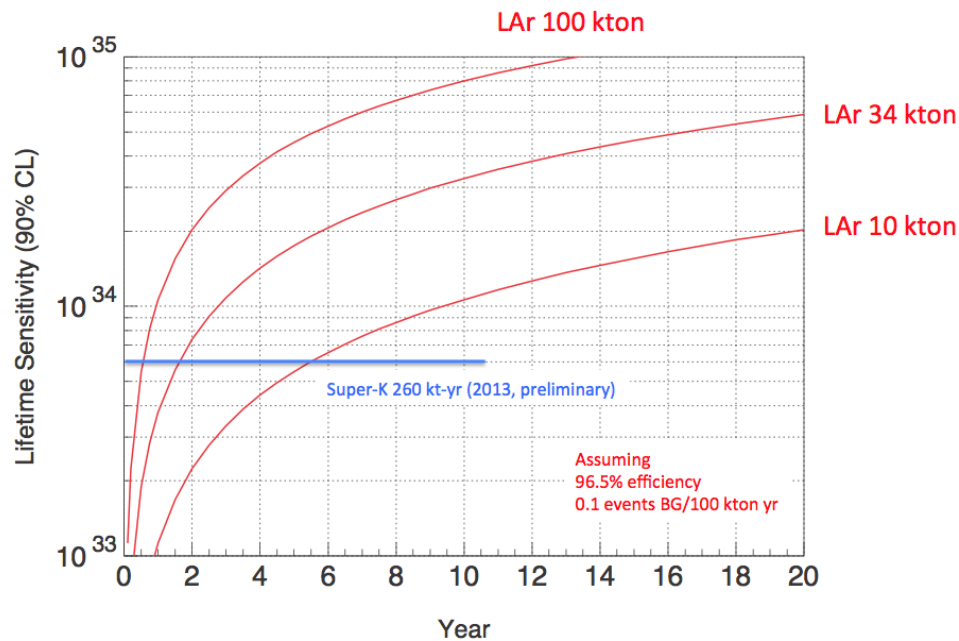


fig:kdklimit

**Figure 5.4:** Proton decay lifetime limit for  $p \rightarrow K^+\bar{\nu}$  as a function of time for underground LArTPCs of fiducial masses 10, 34 and 50 kt. For comparison, the current limit from Super-Kamiokande is also shown. The limits are at 90% C.L., calculated for a Poisson process including background, assuming that the detected events equal the expected background.

8

Figure 5.4 demonstrates that to improve the current limits on the  $p \rightarrow \bar{\nu}K^+$ , set by Super-Kamiokande, significantly beyond that experiment's sensitivity, a LArTPC detector of at least 10 kt, installed deep underground, is needed. A 34-kt detector will improve the current limits by an order of magnitude after running for two decades. Clearly a larger detector mass would improve the limits even more in that span of time.

9

1 While the background rates are thought to be no higher than those assumed in generating the above  
 2 sensitivity projections, it is possible to estimate the impact of higher rates. For  $p \rightarrow K^+\bar{\nu}$ , Table 5.2  
 3 shows a comparison of the 90% CL lower bounds on proton lifetime for an exposure of 340 kt year  
 4 assuming the nominal 1.0 per megaton-year background rate with the corresponding bounds for  
 a rate that is ten times higher, as well as for a fully background-free experiment. While a factor

tab:pdecay-bgvariati

**Table 5.2:** The impact of different assumed background rates on the expected 90% CL lower bound for the partial proton lifetime for the  $p \rightarrow K^+\bar{\nu}$  channel, for a 34-kt detector operating for ten years. The expected background rate is one event per megaton-year. Systematic uncertainties are not included in these evaluations.

Background Rate	Expected Partial Lifetime
0 events/Mt-yr	$3.8 \times 10^{34}$ years
1 events/Mt-yr	$3.3 \times 10^{34}$ years
10 events/Mt-yr	$2.0 \times 10^{34}$ years

5 of ten increase in the background would hurt the sensitivity, useful limits can still be obtained. As  
 6 stated above, however, there is good reason to believe such a case is highly unlikely.  
 7

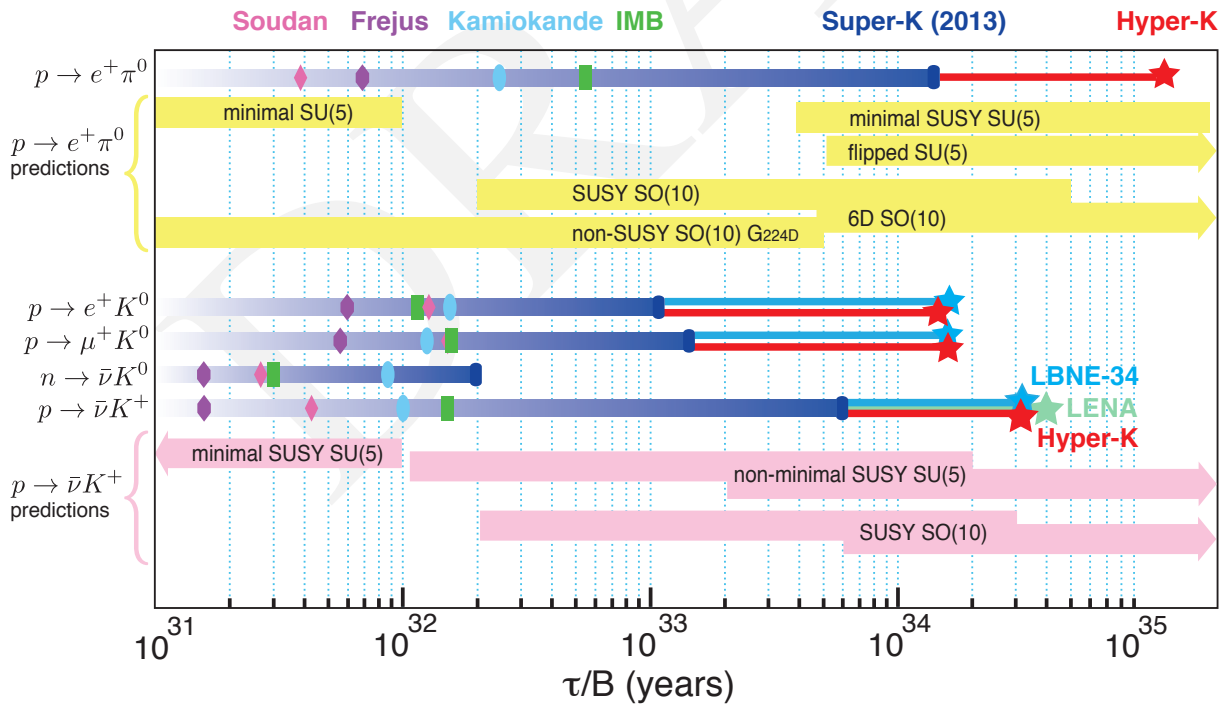


fig:nnn13

**Figure 5.5:** Proton decay lifetime limits that can be achieved by the LBNE 34-kt detector compared to other proposed future experiments. The limits are at 90% C.L., calculated for a Poisson process including background, assuming that the detected events equal the expected background.

- 1 Sensitivities have been computed for some of the other decay channels listed in Table 5.1. The tab:pdecay
- 2 limits that could be obtained from an LBNE 34-kt detector in ten years of running as compared to fig:nnn13
- 3 other proposed future experiments and theoretical expectations are shown in Figure 5.5.

DRAFT

DRAFT



sn-chap

1 Neutrinos emitted in the first few seconds of a core-collapse supernova carry with them  
 2 the potential for great insight into the mechanisms behind some of the most spectacular  
 3 events that play key roles in the evolution of the Universe. Collection and analysis of this  
 4 high-statistics neutrino signal from a supernova within our galaxy would provide a rare  
 5 opportunity to witness the energy and flavor development of the burst as a function of time.  
 6 This would in turn shed light on the astrophysics of the collapse as well as on neutrino  
 7 properties.

## 3 6.1 The Neutrino Signal and Astrophysical Phenomena

4 A core-collapse supernova\* occurs when a massive star reaches the end of its life, and stellar  
 5 burning can no longer support the star's weight. This catastrophic collapse results in a compact  
 6 remnant such as a neutron star, or possibly a black hole, depending on the mass of the progenitor.  
 7 The infall is followed by a “bounce” when sufficiently high core density is reached, and in some  
 8 unknown (but non-zero) fraction of cases, the shock wave formed after the bounce results in a  
 9 bright explosion [186]. The explosion energy represents only a small fraction of the enormous  
 10 total gravitational binding energy of the resulting compact remnant, however — thanks to the  
 11 neutrinos' weak coupling, which allows them to escape — within a few tens of seconds almost all  
 12 of the energy is emitted in the form of neutrinos in the tens-of-MeV range. In spite of their weak  
 13 coupling, the neutrinos are copious enough to (very likely) play a significant role in the explosion.

14 Neutrinos from the celebrated SN1987A core collapse Bionta:1987qt, Hirata:1987hu in the Large Magellanic Cloud out-  
 15 side the Milky Way were observed; however, the statistics were sparse and a great many questions  
 16 remain. A high-statistics observation of a nearby supernova neutrino burst would be possible with  
 17 the current generation of detectors. Such an observation would shed light on the nature of the astro-  
 18 physical event, as well as on the nature of neutrinos themselves. Sensitivity to the different flavor  
 19 components of the flux is highly desirable.

20 The core-collapse neutrino signal starts with a short, sharp *neutronization* (or *break-out*) burst pri-  
 21 marily composed of  $\nu_e$  (originating from  $p + e^- \rightarrow n + \nu_e$ , as protons and electrons get squeezed  
 22 together), and is followed by an “accretion” phase lasting some hundreds of milliseconds, as matter  
 23 falls onto the collapsed core. The later “cooling” phase over  $\sim 10$  seconds represents the main part  
 24 of the signal, over which the proto-neutron star sheds its gravitational binding energy. The neu-

\*“Supernova” always refers to a “core-collapse supernova” in this chapter unless stated otherwise.

trino flavor content and spectra change throughout these phases, and the supernova's temperature evolution can be followed with the neutrino signal (see Figure 6.7). Some fairly generic supernova signal features are illustrated in Figure 6.1, based on [187] and reproduced from [188].

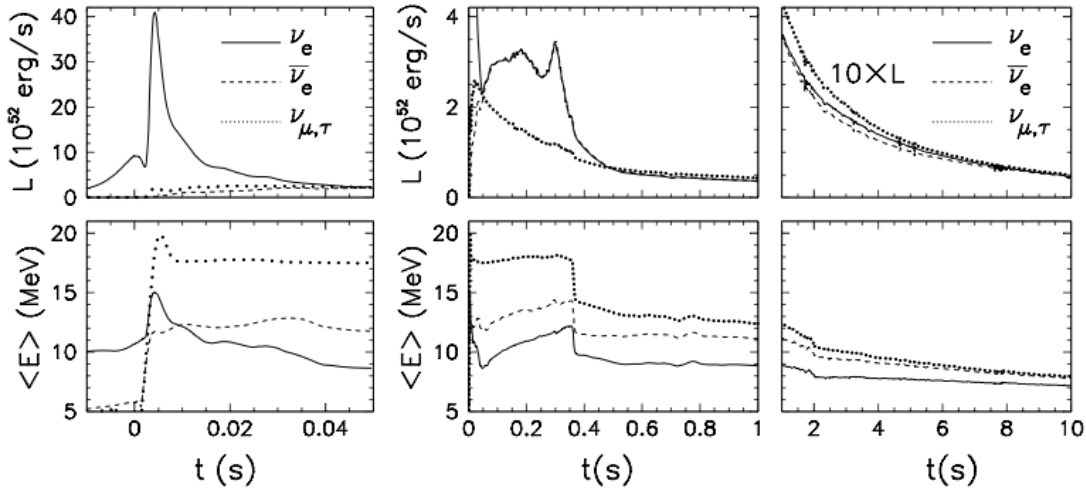


**Figure 6.1:** Expected core-collapse neutrino signal from the “Basel” model [187], for a 10.8  $M_{\odot}$  progenitor. The left plots show the very early signal, including “neutronization burst;” the middle plots show the “accretion phase”, and the right plots show the cooling phase. Across the top, luminosities as a function of time are shown. Across the bottom, the plots show average energy as a function of time for the  $\nu_e$ ,  $\bar{\nu}_e$  and  $\nu_{\mu,\tau}$  flavor components of the flux (fluxes for  $\nu_{\mu}$ ,  $\bar{\nu}_{\mu}$ ,  $\nu_{\tau}$ , and  $\bar{\nu}_{\tau}$  should be identical). Figure courtesy of [188].

The supernova neutrino spectrum at a given moment in time is expected to be well described by a parameterization [189,190] given by:

$$\phi(E_{\nu}) = \mathcal{N} \left( \frac{E_{\nu}}{\langle E_{\nu} \rangle} \right)^{\alpha} \exp \left[ -(\alpha + 1) \frac{E_{\nu}}{\langle E_{\nu} \rangle} \right], \quad (6.1)$$

where  $E_{\nu}$  is the neutrino energy,  $\langle E_{\nu} \rangle$  is the mean neutrino energy,  $\alpha$  is a “pinching parameter”, and  $\mathcal{N}$  is a normalization constant. Large  $\alpha$  corresponds to a more “pinched” spectrum (suppressed high-energy tail). This parameterization is referred to as a “pinched-thermal” form. The different  $\nu_e$ ,  $\bar{\nu}_e$  and  $\nu_x$ ,  $x = \mu, \tau$  flavors are expected to have different average energy and  $\alpha$  parameters and to evolve differently in time.

A wide variety of astrophysical phenomena affect the flavor-energy-time evolution of the spectrum, including neutrino oscillation effects that are determined by the mass hierarchy and “collective” effects due to neutrino-neutrino interactions. A voluminous literature exists exploring these collective phenomena, e.g., [191,192,193,194,195,196,197,198,199].

A number of astrophysical phenomena associated with supernovae are expected to be observable in the supernova neutrino signal, providing a remarkable window into the event, for example:

- The initial burst, primarily composed of  $\nu_e$  and called the “neutronization” or “break-out” burst, represents only a small component of the total signal. However, oscillation effects can manifest themselves in an observable manner in this burst, and flavor transformations can be modified by the “halo” of neutrinos generated in the supernova envelope by scattering [200].
- The formation of a black hole would cause a sharp signal cutoff (e.g., [201,202]).
- Shock wave effects (e.g., [203]) would cause a time-dependent change in flavor and spectral composition as the shock wave propagates.
- The standing accretion shock instability (SASI) [204,205], a “sloshing” mode predicted by three-dimensional neutrino-hydrodynamics simulations of supernova cores, would give an oscillatory flavor-dependent modulation of the flux.
- Turbulence effects [206,207] would also cause flavor-dependent spectral modification as a function of time.

1

2 This list is far from comprehensive. Furthermore, signatures of *collective* effects and signatures that  
 3 depend on the mass hierarchy will make an impact on many of the above signals (examples will be  
 4 presented in Section 6.2). Certain phenomena are even postulated to indicate beyond-the-standard-  
 5 model physics [208] such as axions, extra dimensions and an anomalous neutrino magnetic mo-  
 6 ment; non-observation of these effects, conversely, would enable constraints on these phenomena.

7 The supernova neutrino burst is prompt with respect to the electromagnetic signal and therefore  
 8 can be exploited to provide an early warning to astronomers [107,108]. Additionally, a liquid argon  
 9 signal [209] is expected to provide some pointing information, primarily from elastic scattering on  
 10 electrons.

11 Even non-observation of a burst, or non-observation of a  $\nu_e$  component of a burst in the presence  
 12 of supernovae (or other astrophysical events) observed in electromagnetic or gravitational wave  
 13 channels, would still provide valuable information about the nature of the sources. Further, a long-  
 14 timescale, sensitive search yielding no bursts will also provide limits on the rate of core-collapse  
 15 supernovae.

## 6.2 Expected Signal and Detection in Liquid Argon

The LBNE far detector will use liquid argon technology. As discussed in Section 2.4, liquid argon is known to exhibit a singular sensitivity to the  $\nu_e$  component of a supernova neutrino burst. But LBNE alone will be able to learn only so much; the combination of data from a variety of detectors with different flavor sensitivities will create a much more complete picture of the physics of this phenomenon.

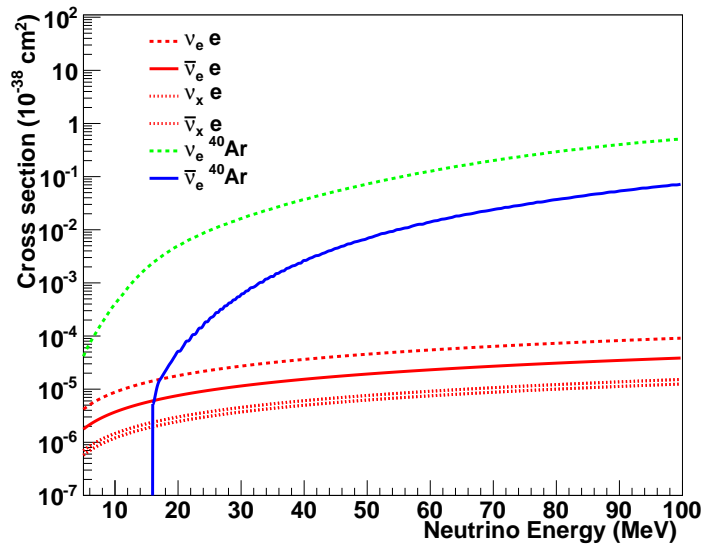


Figure 6.2: Cross sections for supernova-relevant interactions in argon.

The predicted event rate from a supernova burst may be calculated by folding expected neutrino differential energy spectra in with cross sections for the relevant channels, and with detector response. For event rate estimates in liquid argon, a detection threshold of 5 MeV is assumed. The photon detection system of the LBNE LArTPC, coupled with charge collection and simple pattern recognition is expected to provide a highly efficient trigger. Most LBNE supernova physics sensitivity studies so far have been done using parameterized detector responses from [130] implemented in the SNOwGLoBES software package [210]. SNOwGLoBES takes as input fluxes, cross sections (see Figure 6.2), “smearing matrices” (that incorporate both interaction product spectra and detector response) and post-smearing efficiencies. The energy resolution used is

$$\frac{\sigma}{E \text{ (MeV)}} = \frac{11\%}{\sqrt{E \text{ MeV}}} + 2\% \quad (6.2)$$

Work is currently underway using the full Geant4 simulation [123] framework and the LArSoft software package [211] to characterize low-energy response for realistic LBNE detector configurations. Preliminary studies of the detector response with the full simulation are summarized in

1 Section A.1.2 and are found to be consistent with the parameterized response implemented in  
2 SNOwGLoBES.

3 Table 6.1 shows rates calculated with SNOwGLoBES for the dominant interactions in argon for the  
4 “Livermore” model [212], and the “GKVM” model [213]. Figure 6.3 shows the expected observed  
differential event spectra for these fluxes. Clearly, the  $\nu_e$  flavor dominates.

**Table 6.1:** Event rates for different supernova models in 34 kt of liquid argon for a core collapse at 10 kpc, for  $\nu_e$  and  $\bar{\nu}_e$  charged-current channels and elastic scattering (ES) on electrons. Event rates will simply scale by active detector mass and inverse square of supernova distance.

Channel	Events “Livermore” model	Events “GKVM” model
$\nu_e + {}^{40}\text{Ar} \rightarrow e^- + {}^{40}\text{K}^*$	2308	2848
$\bar{\nu}_e + {}^{40}\text{Ar} \rightarrow e^+ + {}^{40}\text{Cl}^*$	194	134
$\nu_x + e^- \rightarrow \nu_x + e^-$	296	178
<b>Total</b>	<b>2794</b>	<b>3160</b>

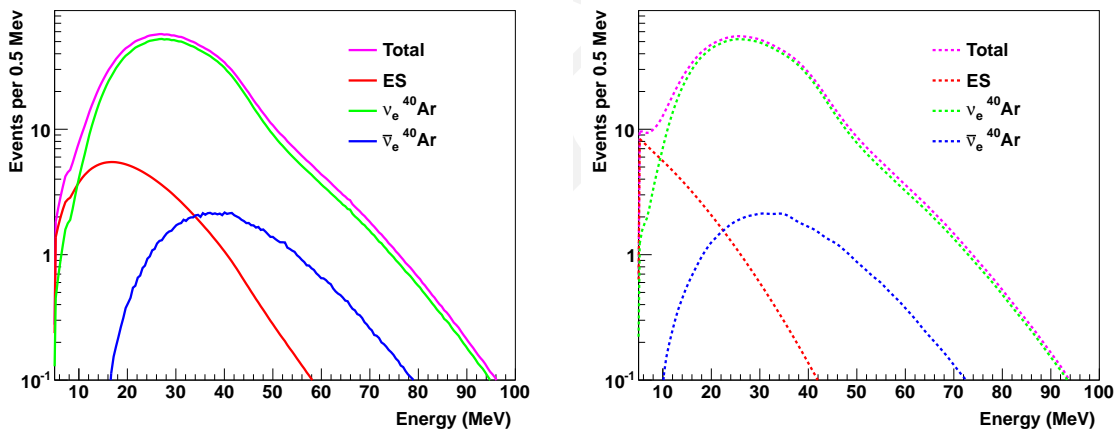


**Figure 6.3:** Supernova neutrino event rates in 34 kt of argon for a core collapse at 10 kpc, for the GKVM model [213] (events per 0.5 MeV), showing three relevant interaction channels. Left: interaction rates as function of true neutrino energy. Right: “smeared” rates as a function of detected energy, assuming resolution from [130].

5  
6 Figure 6.4 gives another example of an expected burst signal, for which a calculation with de-  
7 tailed time dependence of the spectra is available [214] out to 9 seconds post-bounce. This model  
8 has relatively low luminosity but a robust neutronization burst. Note that the relative fraction of  
9 neutronization-burst events is quite high.

10 In Figure 6.5, different oscillation hypotheses have been applied to “Duan” fluxes [199]. The Duan  
11 flux represents only a single late time slice of the supernova burst and not the full flux; hierarchy

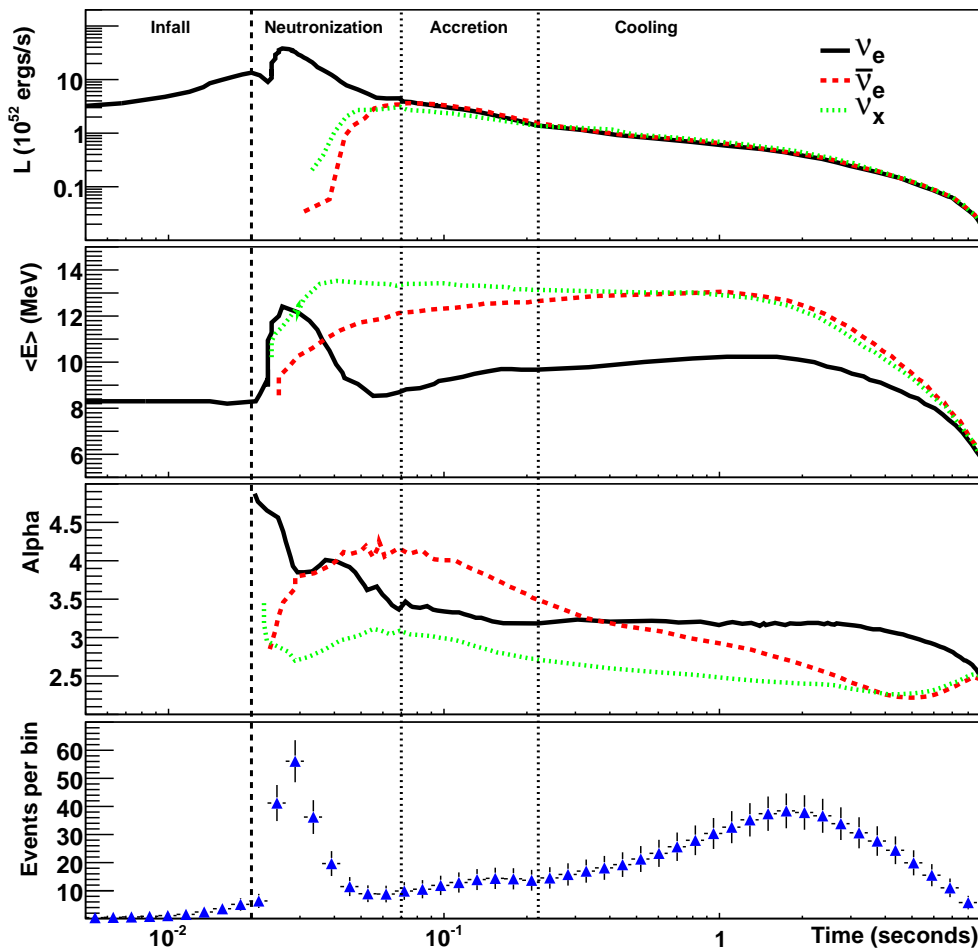


**Figure 6.4:** Expected time-dependent signal for a specific flux model for an electron-capture supernova [214] at 10 kpc. The top plot shows the luminosity as a function of time, the second plot shows average neutrino energy, and the third plot shows the  $\alpha$  (pinching) parameter. The fourth (bottom) plot shows the total number of events (mostly  $\nu_e$ ) expected in 34 kt of liquid argon, calculated using SNOwGLOBES. Note the logarithmic binning in time; the plot shows the number of events expected in the given bin and the error bars are statistical. The vertical dashed line at 0.02 seconds indicates the time of core bounce, and the vertical lines indicate different eras in the supernova evolution. The leftmost time interval indicates the infall period. The next interval, from core bounce to 50 ms, is the neutronization burst era, in which the flux is composed primarily of  $\nu_e$ . The next period, from 50 ms to 200 ms, is the accretion period. The final era, from 0.2 to 9 seconds, is the proto-neutron-star cooling period.

1 information will be encoded in the time evolution of the signal, as well. The figure illustrates, if  
 2 only anecdotally, potential mass hierarchy signatures.

3 Another potential mass hierarchy signature is shown in Figure 6.6, for which a clear time-dependent  
 4 shock-wave-related feature is visible for the normal mass hierarchy case.

5 Figure 6.7 shows yet another example of a preliminary study showing how one might track super-  
 6 nova temperature as a function of time with the  $\nu_e$  signal in liquid argon. Here, a fit is made to the  
 7 pinched-thermal form of Equation 6.1. Not only can the internal temperature of the supernova be

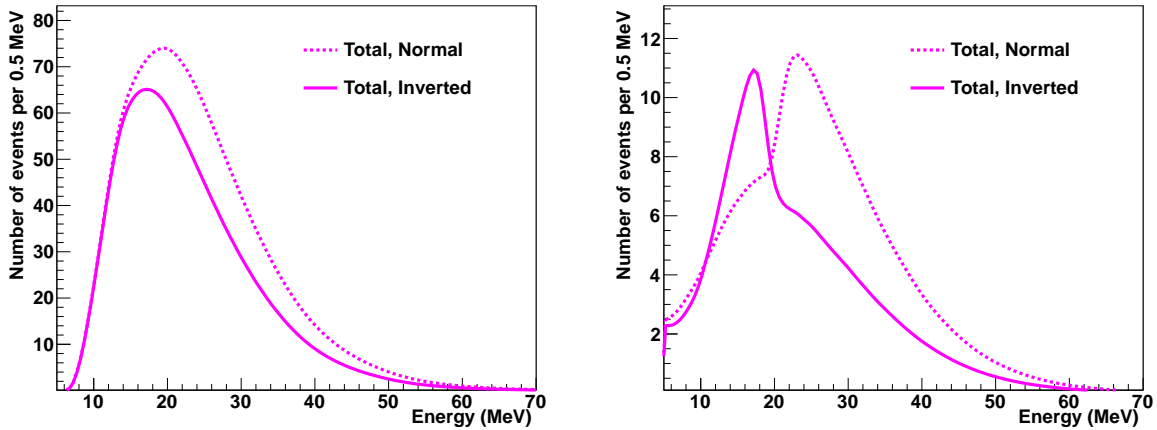


**Figure 6.5:** Comparison of total event rates for normal and inverted hierarchy, for a specific flux example, for a 100-kt water Cherenkov detector (left) and for a 34-kt LArTPC (right) configuration, in events per 0.5 MeV. There are distinctive features in liquid argon for different neutrino mass hierarchies for this supernova model [215].

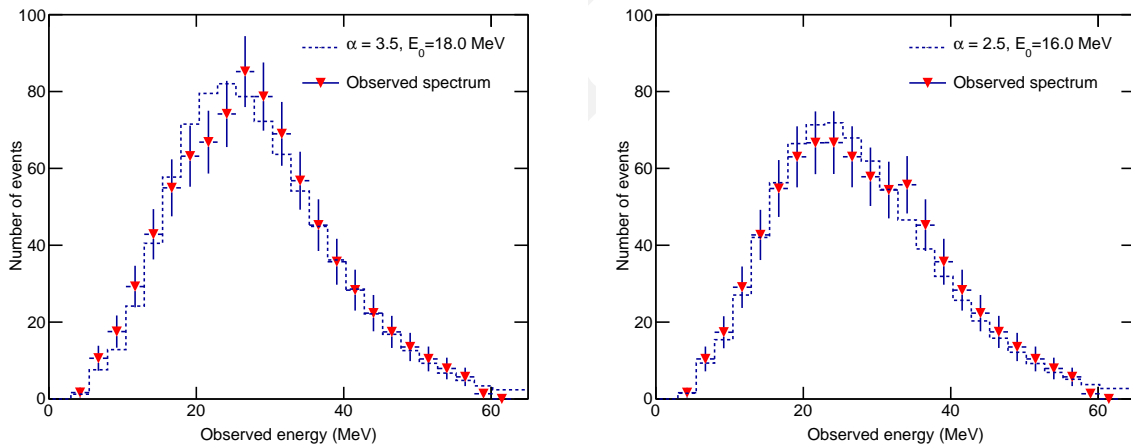


**Figure 6.6:** Observed  $\nu_e$  spectra in 34 kt of liquid argon for a 10-kpc core collapse, representing about one second of integration time each at one-second intervals during the supernova cooling phase. The dashed line represents the best fit to a parameterized pinched-thermal spectrum. Clear “non-thermal” features in the spectrum that change with time are visible, on the left at around 20 MeV and on the right at around 35 MeV. Error bars are statistical. These features are present *only* for normal mass hierarchy.

- effectively measured, but the time evolution is observably different for the different hierarchies.

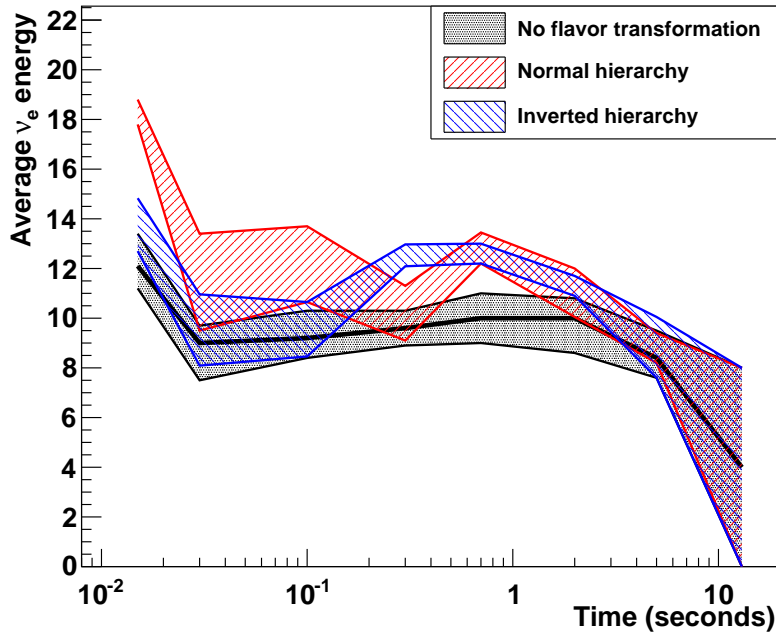


**Figure 6.7:** Average  $\nu_e$  energy from fit to SNOWGLOBES-smearred, pinched-thermal spectrum as a function of time (34 kt at 10 kpc), for a flux model based on [216] and including collective oscillations, for two different hierarchy assumptions. The bands represent  $1\sigma$  error bars from the fit. The solid black line is the truth  $\langle E_\nu \rangle$  for the unoscillated spectrum. Clearly, meaningful information can be gleaned by tracking  $\nu_e$  spectra as a function of time.

## 6.3 Low-Energy Backgrounds

### 6.3.1 Cosmic Rays

Due to their low energy, supernova events are subject to background from cosmic rays, although the nature of the signal — a short-timescale burst — is such that the background from these muons and their associated Michel electrons can in principle be well known, easily distinguished and subtracted. Preliminary studies [217] suggest that the shielding provided by the 4,850-ft depth available at the Sanford Underground Research Facility is acceptable.

### 6.3.2 Local Radiation Sources

It is possible that radioactive decays will directly overlap with the energy spectrum created by supernova neutrino events in LBNE. It is also possible for an ensemble of radioactive-decay events in and around higher-energy particle interactions (e.g., from beam neutrinos) to obscure the edges of electromagnetic showers from highly scattering particles such as electrons and pions; this would appear as the radiological equivalent of dark noise in a digital image, and could potentially in-

1 produce a systematic uncertainty in the energy calculated for events, even at much higher energy  
 2 than the decays themselves. It is therefore very important to calculate the radioactive-decay back-  
 3 grounds in the LBNE far detector with sufficient accuracy to properly account for their presence,  
 4 either as direct backgrounds or as systematic effects in energy calculations. To this end, LBNE  
 5 collaborators are in the process of creating a physics-driven, radioactive-background budget and  
 6 associated event generator for low-energy background events in the far detector.

7 The radioactive background budget will have many components, each of which will fall into one  
 8 of two categories:

- 9 1. intrinsic radioactive contamination in the argon or support materials, or
- 10 2. cosmogenic radioactivity produced in situ from cosmic-ray showers interacting with the ar-  
 11 gon or the support materials.

12 The former is dependent on the materials comprising the detector itself, and is therefore inde-  
 13 pendent of far detector depth. The latter is strongly coupled to the cosmic-ray flux and spectrum.  
 14 A preliminary estimate [218] of the cosmogenic radioactivity from beta emitters produced from  
 15 cosmic-ray interactions with argon in the LBNE LArTPC at the 4,850 ft level of the Sanford Un-  
 16 derground Research Facility is shown in Figure 6.8. Both of these background categories add to

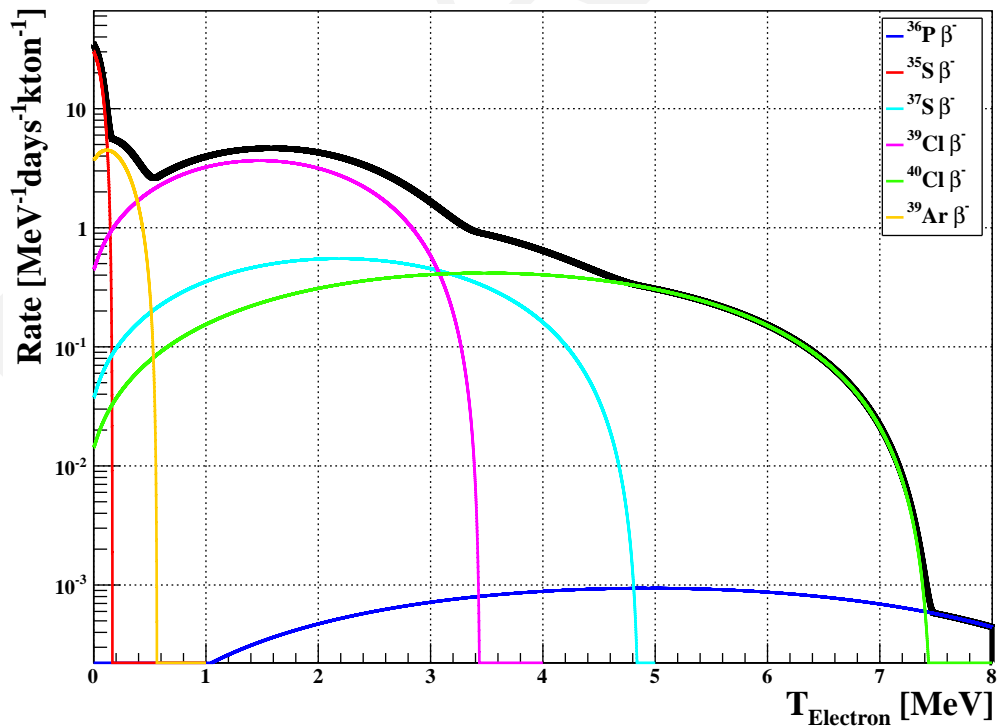


**Figure 6.8:** Cosmogenic background rates in the LBNE LArTPC as a function of the decay beta kinetic energy calculated at the 4,850-ft level of the Sanford Underground Research Facility.

16 the direct energy depositions from cosmic rays themselves and associated showers.  
 17

### 6.3.3 Intrinsic Radioactive Background Mitigation

Intrinsic backgrounds in the far detector come from the radioactive material that is prevalent in the materials comprising the detector (both active and instrumentation/support materials and the cryostat itself), in the cavern walls and in the dust. The isotopes of primary interest are “the usual suspects” in experiments where radioactive backgrounds must be controlled:  $^{232}\text{Th}$  and  $^{238}\text{U}$  (and their associated decay chains),  $^{40}\text{K}$ , and  $^{60}\text{Co}$ . In addition,  $^{39}\text{Ar}$  will contribute a significant component, since it is present in natural argon harvested from the atmosphere at the level of approximately 1 Bq/kg. In consequence, a 10-kt far detector filled with  $^{\text{nat.}}\text{Ar}$  will experience a rate from  $^{39}\text{Ar}$  of approximately 10 MHz across the whole detector. The beta decay spectrum from  $^{39}\text{Ar}$  is thankfully quite low in energy ( $Q_\beta = 0.565$  MeV), so it will not interfere directly with the supernova signal, but it may contribute to the “dark noise” effect. Furthermore, the product of the average beta energy with this rate indicates the level at which the background due to introduction of power into the detector becomes a problem. This radioactive power from  $^{39}\text{Ar}$  is approximately:

$$P_{\text{Rad}} \sim 0.25 \text{ MeV} \times 10 \text{ MHz} = 2.5 \times 10^6 \text{ MeV/s.} \quad (6.3)$$

Because this category of background can come from the cavern walls, the concrete cavern lining, the cryostat materials or the materials comprising the submersed instrumentation, it is important to know which type of radioactive decay is produced by each isotope as well as the total energy it releases. For instance, an alpha decay from an isotope in the U or Th decay chain will deposit its full energy into the detector if it occurs in the active region of the detector, but will deposit no energy if it occurs inside of some macroscopically thick piece of support material because of its very short range ( $\lesssim 1 \mu\text{m}$ ) in most solids. This requires different accounting for energy depositions from intrinsic radioactive contamination measured in different locations (or groups of locations). This is clearly a tractable problem, but one which must be handled with care and forethought.

Since a large body of work has been compiled on the control of radiological backgrounds in previous experiments that have encountered similar conditions, much of the work in this area will be cited from these experiments (e.g., DARKSIDE, ICARUS, BOREXINO, KamLAND and Super Kamiokande). Work remains, however, on understanding backgrounds particular to the LBNE far detector location/depth (radon levels and dust activity, for instance), and on integrating existing and new work into the LBNE simulation, reconstruction and analysis framework.

## 1 6.4 Summary of Core-Collapse Supernova Sensitivities

LBNE, with its high-resolution LArTPC detector, is uniquely sensitive to the  $\nu_e$  component of the neutrino flux from a core-collapse supernova within our galaxy. The  $\nu_e$  component of the neutrino flux dominates the initial neutronization burst of the supernova. Preliminary studies indicate that such a supernova at a distance of 10 kpc would produce  $\sim 3000$  events in a 34-kt LArTPC. The time dependence of the signal will allow differentiation between different neutrino-driven core-collapse dynamical models, and will exhibit a discernible dependence on the neutrino mass hierarchy.

A low energy threshold of  $\sim 5$  MeV will enable the LBNE LArTPC to extract the rich information available from the  $\nu_e$  supernova flux. LBNE's photon detection system is being designed to provide a high-efficiency trigger for supernova events. Careful design and quality control of the detector materials will minimize low-energy backgrounds from radiological contaminants.

2

DRAFT

DRAFT

# Chapter 7 Precision Measurements with a High-Intensity Neutrino Beam

nd-physics-chap

1 High-intensity neutrino beams can be used as probes of new physics and given the broad  
2 energy range of the LBNE beam, a diverse range of physics measurements are possible.  
3 These wide-ranging measurements would complement physics programs, such as those at  
4 the Jefferson Laboratory, that are using proton, electron or ion beams from colliders and  
5 fixed-target facilities.

6 The reduction of systematic uncertainties for the neutrino oscillation program of the full LBNE  
7 scope requires a highly capable near neutrino detector (ND) to provide excellent resolution in  
8 the reconstruction of neutrino events. Combined with the unprecedented neutrino fluxes available  
9 for the LBNE program — which will allow the collection of  $\mathcal{O}(10^8)$  inclusive neutrino charged  
10 current (CC) interactions for  $10^{22}$  protons-on-target (POT) just downstream of the beamline — the  
11 inclusion of a near detector offers a unique opportunity to significantly enhance the LBNE long-  
12 baseline oscillation program and to produce a range of short-baseline neutrino scattering physics  
13 measurements. The combined statistics and precision expected in the ND will allow precise tests  
14 of fundamental interactions resulting in a better understanding of the structure of matter.

15 Table 7.1 lists the expected number of interactions in the neutrino beam at the LBNE near detector  
16 site — located 459 m downstream from the beginning of the decay pipe — per ton of detector.

17 This chapter presents a short description of some of the studies that can be performed at LBNE  
18 with a fine-grained near neutrino detector and gives a flavor of the outstanding physics potential. A  
19 more detailed and complete discussion of the near detector physics potential can be found in [120].

20 Appendix B describes neutrino scattering kinematics and includes definitions of the kinematic  
21 variables used in this chapter.

## 22 7.1 Precision Measurements with Long-Baseline Oscilla- 23 tions

sec-fluxosc

24 From the studies of uncertainties and the impact of the spectral shape presented in Section 4.3.2, it  
25 is evident that to fully realize the goals of the full LBNE scientific program — in particular, sensi-  
26 tivity to CP violation and the precision measurement of the three-flavor oscillation parameters — it  
is necessary to characterize the expected unoscillated neutrino flux with high precision. In addition  
to the precise determination of the neutrino flux, shape and flavor composition, the characterization  
of different neutrino interactions and interaction cross sections on a liquid argon target is necessary

sec:sys

**Table 7.1:** Estimated interaction rates in the neutrino beam per ton of detector (water) for  $1 \times 10^{20}$  POT at 459 m assuming neutrino cross sections predictions from NUANCE [219] and a 120-GeV proton beam. Processes are defined at the initial neutrino interaction vertex and thus do not include final-state effects. These estimates do not include detector efficiencies or acceptance [220,221].

Production mode	$\nu_\mu$ Events	$\bar{\nu}_\mu$ Events
CC QE ( $\nu_\mu n \rightarrow \mu^- p$ )	50,100	3,310
NC elastic ( $\nu_\mu N \rightarrow \nu_\mu N$ )	18,800	1,100
CC resonant $\pi^+$ ( $\nu_\mu N \rightarrow \mu^- N \pi^+$ )	67,800	0
CC resonant $\pi^-$ ( $\bar{\nu}_\mu N \rightarrow \mu^+ N \pi^-$ )	0	3,300
CC resonant $\pi^0$ ( $\nu_\mu n \rightarrow \mu^- p \pi^0$ )	16,200	1,100
NC resonant $\pi^0$ ( $\nu_\mu N \rightarrow \nu_\mu N \pi^0$ )	16,300	1,030
NC resonant $\pi^+$ ( $\nu_\mu p \rightarrow \nu_\mu n \pi^+$ )	6,930	480
NC resonant $\pi^-$ ( $\nu_\mu n \rightarrow \nu_\mu p \pi^-$ )	5,980	390
CC DIS ( $\nu_\mu N \rightarrow \mu^- X$ or $\bar{\nu}_\mu N \rightarrow \mu^+ X, W > 2$ )	66,800	6,610
NC DIS ( $\nu_\mu N \rightarrow \nu_\mu X$ or $\bar{\nu}_\mu N \rightarrow \bar{\nu}_\mu X, W > 2$ )	24,100	2,950
NC coherent $\pi^0$ ( $\nu_\mu A \rightarrow \nu_\mu A \pi^0$ or $\bar{\nu}_\mu A \rightarrow \bar{\nu}_\mu A \pi^0$ )	2,040	212
CC coherent $\pi^+$ ( $\nu_\mu A \rightarrow \mu^- A \pi^+$ )	3,920	0
CC coherent $\pi^-$ ( $\bar{\nu}_\mu A \rightarrow \mu^+ A \pi^-$ )	0	400
NC resonant radiative decay ( $N^* \rightarrow N \gamma$ )	110	7
<b>Cabbibo-suppressed QE hyperon production</b>		
( $\mu^+ \Lambda, \mu^+ \Sigma^0, \mu^+ \Sigma^-$ )	0	240
NC elastic electron ( $\nu_\mu e^- \rightarrow \nu_\mu e^-$ or $\bar{\nu}_\mu e^- \rightarrow \bar{\nu}_\mu e^-$ )	30	3
Inverse Muon Decay ( $\nu_\mu e \rightarrow \mu^- \nu_e$ )	12	0
Other	42,600	2,920
<b>Total CC</b>	<b>236,000</b>	<b>17,000</b>
<b>Total NC+CC</b>	<b>322,000</b>	<b>24,000</b>

- 1 to estimate physics backgrounds to the oscillation measurements. A high-resolution near tracking
- 2 detector such as that described in Section 3.5 can measure the unoscillated flux normalization,
- 3 shape and flavor to a few percent using systematically independent techniques that are discussed
- 4 in the following sections.

### 5 7.1.1 Relative Neutrino and Antineutrino Flux

The most promising method of determining the shape of the  $\nu_\mu$  and  $\bar{\nu}_\mu$  flux is by measuring charged current events with low-hadronic energy deposition (low- $\nu$ ) where  $\nu$  is the total energy of the hadrons that are produced after a neutrino interaction,  $E_\nu - E_\mu$ . It is important to note that not all the hadrons escape the remnant nucleus and intranuclear effects will smear the visible energy of the hadronic system. A method of relative flux determination known as low- $\nu_0$  — where  $\nu_0$  is a given value of visible hadronic energy in the interaction that is selected to minimize the fraction of

the total interaction energy carried by the hadronic system — is well developed [222]. The method follows from the general expression of the  $\nu$ -nucleon differential cross section:

$$\mathcal{N}(\nu < \nu_0) = C\Phi(E_\nu)\nu_0 \left[ \mathcal{A} + \left(\frac{\nu_0}{E_\nu}\right) \mathcal{B} + \left(\frac{\nu_0}{E_\nu}\right)^2 \mathcal{C} + \mathcal{O}\left(\frac{\nu_0}{E_\nu}\right)^3 \right], \quad (7.1)$$

where the coefficients are  $\mathcal{A} = \mathcal{F}_2$ ,  $\mathcal{B} = (\mathcal{F}_2 \pm \mathcal{F}_3)/2$ ,  $\mathcal{C} = (\mathcal{F}_2 \mp \mathcal{F}_3)/6$ , and  $\mathcal{F}_i = \int_0^1 \int_0^{\nu_0} F_i(x) dx d\nu$  is the integral of structure function  $F_i(x)$ . The dynamics of neutrino-nucleon scattering implies that the number of events in a given energy bin with hadronic energy  $E_{\text{had}} < \nu_0$  is proportional to the neutrino (antineutrino) flux in that energy bin up to corrections  $\mathcal{O}(\nu_0/E_\nu)$  and  $\mathcal{O}(\nu_0/E_\nu)^2$ . The number  $\mathcal{N}(\nu < \nu_0)$  is therefore proportional to the flux up to correction factors of the order  $\mathcal{O}(\nu_0/E_\nu)$  or smaller, which are not significant for small values of  $\nu_0$  at energies  $\geq \nu_0$ . The coefficients  $\mathcal{A}, \mathcal{B}, \mathcal{C}$  are determined for each energy bin and neutrino flavor within the ND data.

LBNE's primary interest is the relative flux determination, i.e., the neutrino flux in one energy bin relative to that in another; variations in the coefficients do not affect the relative flux. The prescription for the relative flux determination is simple: count the number of  $\nu$ -CC events below a certain small value of hadronic energy ( $\nu_0$ ). The observed number of events, up to the correction of the order  $\mathcal{O}(\nu_0/E_\nu)$  due to the finite  $\nu_0$  in each total visible energy bin, is proportional to the relative flux. The smaller the factor  $\nu_0/E_\nu$  is, the smaller is the correction. Furthermore, the energy of events passing the low- $\nu_0$  cut is dominated by the corresponding lepton energy.

It is apparent from the above discussion that this method of relative flux determination is not very sensitive to nucleon structure, QCD corrections or types of  $\nu$ -interactions such as scaling or non-scaling. With the excellent granularity and resolution foreseen in the low-density magnetized tracker, it will be possible to use a value of  $\nu_0 \sim 0.5$  GeV or lower, thus allowing flux predictions down to  $E_\nu \sim 0.5$  GeV. A preliminary analysis with the high-resolution tracker achieved a precision  $\leq 2\%$  on the relative  $\nu_\mu$  flux with the low- $\nu_0$  method in the energy region  $1 \leq E_\nu \leq 30$  GeV in the fit with  $\nu_0 < 0.5$  GeV. Similar uncertainties are expected for the  $\bar{\nu}_\mu$  component (the dominant one) in the antineutrino beam mode (negative focusing).

### 7.1.2 Flavor Content of the Beam: $\nu_\mu, \bar{\nu}_\mu, \nu_e, \bar{\nu}_e$

The empirical parameterization of the pion and kaon neutrino parents produced from the proton target, determined from the low- $\nu_0$  flux at the ND, allows prediction of the  $\nu_\mu$  and  $\bar{\nu}_\mu$  flux at the far detector location. This parameterization provides a measure of the  $\pi^+/K^+/\mu^+$  ( $\pi^-/K^-/\mu^-$ ) distributions of neutrino parents of the beam observed in the ND. Additionally, with the capability to identify  $\bar{\nu}_e$ -CC interactions, it is possible to directly extract the elusive  $K_L^0$  content of the beam. Therefore, an accurate measurement of the  $\nu_\mu, \bar{\nu}_\mu$  and  $\bar{\nu}_e$ -CC interactions provides a prediction of the  $\nu_e$  content of the beam, which is an irreducible background for the  $\nu_e$  appearance search in the far detector:

$$\nu_e \equiv \mu^+(\pi^+ \rightarrow \nu_\mu) \oplus K^+(K^+ \rightarrow \nu_\mu) \oplus K_L^0 \quad (7.2)$$

$$\bar{\nu}_e \equiv \mu^-(\pi^- \rightarrow \bar{\nu}_\mu) \oplus K^-(K^- \rightarrow \bar{\nu}_\mu) \oplus K_L^0 \quad (7.3)$$

1 The  $\mu$  component is well constrained from  $\nu_\mu(\bar{\nu}_\mu)$ -CC data at low energy, while the  $K^\pm$  component  
 2 is only partially constrained by the  $\nu_\mu(\bar{\nu}_\mu)$ -CC data at high energy and requires external hadro-  
 3 production measurements of  $K^\pm/\pi^\pm$  ratios at low energy from hadro-production experiments such  
 4 as MIPP [223] and NA61 [152]. Finally, the  $K_L^0$  component can be constrained by the  $\bar{\nu}_e$ -CC data  
 5 and by external dedicated measurements at hadron-production experiments. In the energy range  
 6  $1(5) \leq E_\nu \leq 5(15)$  GeV, the approximate relative contributions to the  $\nu_e$  spectrum are 85% (55%)  
 7 from  $\mu^+$ , 10% (30%) from  $K^+$  and 3% (15%) from  $K_L^0$ .

8 Based on the NOMAD experience, a precision of  $\leq 0.1\%$  on the flux ratio  $\nu_e/\nu_\mu$  is expected at  
 9 high energies. Taking into account the projected precision of the  $\nu_\mu$  flux discussed in the previous  
 10 section, this translates into an absolute prediction for the  $\nu_e$  flux at the level of 2%.

11 Finally, the fine-grained ND can directly identify  $\nu_e$ -CC interactions from the LBNE beam. The  
 12 relevance of this measurement is twofold:

- 13 1. It provides an independent validation for the flux predictions obtained from the low- $\nu_0$   
 14 method.
- 15 2. It can further constrain the uncertainty on the knowledge of the absolute  $\nu_e$  flux.

### 16 7.1.3 Constraining the Unoscillated $\nu$ Spectral Shape with the QE Interaction

17 In any long-baseline neutrino oscillation program, including LBNE, the quasi-elastic (QE) interac-  
 18 tions are special. First, the QE cross section is substantial at lower energies [224]. Second, because  
 19 of the simple topology (a  $\mu^-$  and a proton), the visible interaction energy provides, to first order, a  
 20 close approximation to the neutrino energy ( $E_\nu$ ). In the context of a fine-grained tracker, a precise  
 21 measurement of QE will impose direct constraints on nuclear effects related to both the primary  
 22 and final-state interaction (FSI) dynamics (see Section 7.6), which can affect the overall neutrino  
 23 energy scale and, thus, the entire oscillation program. To this end, the key to reconstructing a high  
 24 quality sample of  $\nu_\mu$ -QE interactions is the two-track topology where both final state particles are  
 25 visible:  $\mu^-$  and  $p$ . A high-resolution ND can efficiently identify the recoil proton and measure  
 26 its momentum vector as well as  $dE/dx$ . Preliminary studies indicate that in a fine-grained track-  
 27 ing detector the efficiency (purity) for the proton reconstruction in QE events is 52% (82%). A  
 28 comparison between the neutrino energy reconstructed from the muon momentum through the QE  
 29 kinematics (assuming a free target nucleon) with the visible neutrino energy measured as the sum  
 30 of  $\mu$  and  $p$  energies is sensitive to both nuclear effects and FSI. Furthermore, comparing the two

- 1 track sample ( $\mu$  and  $p$ ) with the single track one (only  $\mu$  is reconstructed) empirically constraints  
 2 the rate of FSI.

### 3 7.1.4 Low-Energy Absolute Flux: Neutrino-Electron NC Scattering

- 4 Neutrino neutral current (NC) interaction with the atomic electron in the target,  $\nu_\mu e^- \rightarrow \nu_\mu e^-$ ,  
 5 provides an elegant measure of the absolute flux. The total cross section for NC elastic scattering  
 6 off electrons is given by [225]:

$$\sigma(\nu_l e \rightarrow \nu_l e) = \frac{G_\mu^2 m_e E_\nu}{2\pi} \left[ 1 - 4 \sin^2 \theta_W + \frac{16}{3} \sin^4 \theta_W \right], \quad (7.4)$$

$$\sigma(\bar{\nu}_l e \rightarrow \bar{\nu}_l e) = \frac{G_\mu^2 m_e E_\nu}{2\pi} \left[ \frac{1}{3} - \frac{4}{3} \sin^2 \theta_W + \frac{16}{3} \sin^4 \theta_W \right], \quad (7.5)$$

- 7 where  $\theta_W$  is the weak mixing angle (WMA). For the currently known value of  $\sin^2 \theta_W \simeq 0.23$ ,  
 8 the above cross sections are very small:  $\sim 10^{-42} (E_\nu/\text{GeV}) \text{ cm}^2$ . The NC elastic scattering off  
 9 electrons can be used to determine the absolute flux normalization since the cross section only  
 10 depends on the knowledge of  $\sin^2 \theta_W$ . Within the Standard Model, the value of  $\sin^2 \theta_W$  at the  
 11 average momentum transfer expected at LBNE,  $Q \sim 0.07 \text{ GeV}$ , can be extrapolated down from  
 12 the LEP/SLC measurements with a precision of  $\leq 1\%$ . The  $\nu_\mu e^- \rightarrow \nu_\mu e^-$  will produce a single  $e^-$   
 13 collinear with the  $\nu$ -beam ( $\leq 40 \text{ mrad}$ ). The background, dominated by the asymmetric conversion  
 14 of a photon in an ordinary  $\nu$ -nucleon neutral current event, will produce  $e^-$  and  $e^+$  in equal measure  
 15 with much broader angular distribution. A preliminary analysis of the expected elastic scattering  
 16 signal in the high-resolution tracking near detector shows that the scattering signal can be selected  
 17 with an efficiency of about 60% with a small background contaminant. The measurement will be  
 18 dominated by the statistical error. The determination of the absolute flux of the LBNE neutrinos  
 19 is estimated to reach a precision of  $\simeq 2.5\%$  for  $E_\nu \leq 10 \text{ GeV}$ . The measurement of NC elastic  
 20 scattering off electrons can only provide the integral of all neutrino flavors.

### 21 7.1.5 High-Energy Absolute Flux: Neutrino-Electron CC Scattering

- 22 The  $\nu_\mu e^-$ -CC interaction,  $\nu_\mu + e^- \rightarrow \mu^- + \nu_e$  (*inverse muon decay* or *IMD*), offers an elegant way  
 23 to determine the absolute flux. Given the energy threshold needed for this process, IMD requires  
 24  $E_\nu \geq 10.8 \text{ GeV}$ . A high-resolution near detector in the LBNE neutrino beam will observe  $\geq$   
 25 2,000 IMD events in three years. The reconstruction efficiency of the single, energetic forward  
 26  $\mu^-$  will be  $\geq 98\%$ ; the angular resolution of the IMD  $\mu$  is  $\leq 1 \text{ mrad}$ . The background, primarily  
 27 from the  $\nu_\mu$ -QE interactions, can be precisely constrained using control samples. In particular, the  
 28 systematic limitations of the CCFR ([226,227]) and the CHARM-II [228] IMD measurements can  
 29 be substantially alleviated with the proposed near detector design. A preliminary analysis indicates  
 30 that the absolute flux can be determined with an accuracy of  $\approx 3\%$  for  $E_\nu \geq 11 \text{ GeV}$  (average  
 31  $E_\nu \approx 25 \text{ GeV}$ ).

### 1 7.1.6 Low-Energy Absolute Flux: QE in Water and Heavy-Water Targets

Another independent method to extract the absolute flux is through the Quasi-Elastic (QE) CC scattering ( $\nu_\mu n(p) \rightarrow \mu^- p(n)$ ) on deuterium at low  $Q^2$ . Neglecting terms in  $(m_\mu/M_n)^2$  at  $Q^2 = 0$  the QE cross section is independent of neutrino energy for  $(2E_\nu M_n)^{1/2} > m_\mu$ :

$$\frac{d\sigma}{dQ^2} \Big|_{Q^2=0} = \frac{G_\mu^2 \cos^2 \theta_c}{2\pi} [F_1^2(0) + G_A^2(0)] = 2.08 \times 10^{-38} \text{ cm}^2 \text{ GeV}^{-2}, \quad (7.6)$$

2 which is determined by neutron  $\beta$  decay and has a theoretical uncertainty  $< 1\%$ . The flux can be  
 3 extracted experimentally by measuring low  $Q^2$  QE interactions ( $\leq 0.05$  GeV) and extrapolating the  
 4 result to the limit of  $Q^2 = 0$ . The measurement requires a deuterium (or hydrogen for antineutrino)  
 5 target to minimize the smearing due to Fermi motion and other nuclear effects. This requirement  
 6 can only be achieved by using both H<sub>2</sub>O and D<sub>2</sub>O targets embedded in the fine-grained tracker  
 7 and extracting the events produced in deuterium by statistical subtraction of the larger oxygen  
 8 component. The experimental resolution on the muon and proton momentum and angle is crucial.  
 9 Dominant uncertainties of the method are related to the extrapolation to  $Q^2 = 0$ , to the theoret-  
 10 ical cross section on deuterium, to the experimental resolution and to the statistical subtraction.  
 11 Sensitivity studies and the experimental requirements are under study.

### 12 7.1.7 Neutral Pions, Photons, and $\pi^\pm$ in NC and CC Events

13 The principal background to the  $\nu_e$  and  $\bar{\nu}_e$  appearance comes from the NC events where a photon  
 14 from the  $\pi^0$  decay produces a signature similar to that produced by  $\nu_e$ -induced electron; the second  
 15 source of background is due to  $\pi^0$ 's from  $\nu_\mu$ -CC where the  $\mu^-$  evades identification — typically at  
 16 high  $y_{BJ}$ . Since the energy spectra of NC and CC interactions are different, it is critical for the ND  
 17 to measure  $\pi^0$ 's in NC and CC interactions in the full kinematic phase space.

18 The proposed ND is designed to measure  $\pi^0$ 's with high accuracy in three topologies:

- 19 1. both photons convert in the tracker ( $\simeq 25\%$ )
- 20 2. one photon converts in the tracker and the other in the calorimeter ( $\simeq 50\%$ ) and
- 21 3. both photons convert in the calorimeter The first two topologies afford the best resolution  
 22 because the tracker provides precise  $\gamma$ -direction measurement.

23 The  $\pi^0$  reconstruction efficiency in the proposed fine-grained tracker is expected to be  $\geq 75\%$  if  
 24 photons that reach the ECAL are included. By contrasting the  $\pi^0$  mass in the tracker versus in the  
 25 calorimeter, the relative efficiencies of photon reconstruction will be well constrained.

26 Finally, the  $\pi^\pm$  track momentum and  $dE/dx$  information will be measured by the tracker. An in  
 27 situ determination of the charged pions in the  $\nu_\mu/\bar{\nu}_\mu$ -CC events — with  $\mu$ ID and without  $\mu$ ID

1 — and in the  $\nu$ -NC events is crucial to constrain the systematic error associated with the  $\nu_\mu$  ( $\bar{\nu}_\mu$ )  
2 disappearance, especially at low  $E_\nu$ .

### 3 7.1.8 Signal and Background Predictions for the Far Detector

sec-extfd

4 In order to achieve reliable predictions for signal and backgrounds in the far detector, near detec-  
5 tor measurements — including (anti)neutrino fluxes, nuclear cross-sections and detector smearing  
6 — must be unfolded and extrapolated to the far detector location. The geometry of the beam and  
7 detectors (point source versus extended source) as well as the expected neutrino oscillations imply  
8 differences in the (anti)neutrino fluxes in the near and far detectors. These differences, in turn, will  
9 result in increased sensitivity of the long-baseline analysis to cross section uncertainties, in partic-  
10 ular between neutrinos and antineutrinos and for exclusive background topologies. Furthermore,  
11 the much higher event rates at the near site and the smaller detector size (i.e., reduced containment)  
12 make it virtually impossible to achieve identical measurement conditions in both the near and far  
13 detectors. However, as discussed in Sections 7.1.1 to 7.1.7, the energy, angular and space resolution  
14 of the low-density, fine-grained near detector are key factors in reducing the systematic uncertain-  
15 ties achievable on the event predictions for the far detector; the near detector can offer a precise *in*  
16 *situ* measurement of the absolute flux of all flavor components of the beam,  $\nu_\mu, \nu_e, \bar{\nu}_\mu, \bar{\nu}_e$ , resulting  
17 in constraints on the parent  $\pi^\pm/K^\pm/\mu^\pm$  distributions. In addition, measurements of momenta and  
18 energies of final-state particles produced in (anti)neutrino interactions will allow a detailed study  
19 of exclusive topologies affecting the signal and background rates in the far detector. All of these  
20 measurements will be used to cross-check and fine-tune the simulation programs needed for the  
21 actual extrapolation from the near to the far detector.

22 It is important to note that several of these techniques have already been used and *proven to work* in  
23 neutrino experiments such as MINOS [145] and NOMAD [146,147,229]. The higher segmentation  
24 and resolution in the LBNE near detector with respect to past experiments will increase the avail-  
25 able information about the (anti)neutrino event topologies, allowing further reduction of systematic  
26 uncertainties both in the near detector measurements and in the Monte Carlo extrapolation.

27 For a more detailed discussion of the impact of near detector measurements on the long-baseline  
28 oscillation analysis see Section 4.3.2.

## 7.2 Electroweak Precision Measurements

Neutrinos and antineutrinos are the most effective probes for investigating electroweak physics. Interest in a precise determination of the weak mixing angle ( $\sin^2 \theta_W$ ) at LBNE energies via neutrino scattering is twofold: (1) it provides a direct measurement of neutrino couplings to the  $Z$  boson and (2) it probes a different scale of momentum transfer than LEP did by virtue of not being at the  $Z$  boson mass peak.

The weak mixing angle can be extracted experimentally from three main NC physics processes:

1. deep inelastic scattering off quarks inside nucleons:  $\nu N \rightarrow \nu X$
2. elastic scattering off electrons:  $\nu e^- \rightarrow \nu e^-$
3. elastic scattering off protons:  $\nu p \rightarrow \nu p$

Figure 7.1 shows the Feynman diagrams corresponding to the three processes.

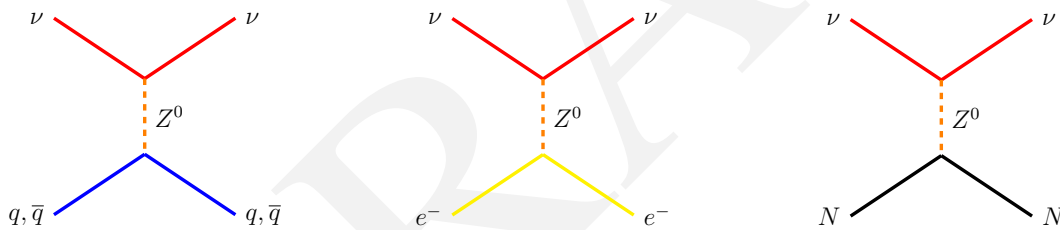


**Figure 7.1:** Feynman diagrams for the three main neutral current processes that can be used to extract  $\sin^2 \theta_W$  with the LBNE near detector. From left, deep inelastic scattering off quarks, elastic scattering off electrons and elastic scattering off nucleons.

### 7.2.1 Deep Inelastic Scattering

The most precise measurement of  $\sin^2 \theta_W$  in neutrino deep inelastic scattering (DIS) comes from the NuTeV experiment, which reported a value that is  $3\sigma$  from the Standard Model [230]. The LBNE ND can perform a similar analysis in the DIS channel by measuring the ratio of NC and CC interactions induced by neutrinos:

$$\mathcal{R}^\nu \equiv \frac{\sigma_{\text{NC}}^\nu}{\sigma_{\text{CC}}^\nu} \simeq \rho^2 \left( \frac{1}{2} - \sin^2 \theta_W + \frac{5}{9} (1+r) \sin^4 \theta_W \right). \quad (7.7)$$

Here  $\rho$  is the relative coupling strength of the neutral-to-charged current interactions ( $\rho = 1$  at tree-level in the Standard Model) and  $r$  is the ratio of antineutrino to neutrino cross section ( $r \sim 0.5$ ).

- 1 The absolute sensitivity of  $\mathcal{R}^\nu$  to  $\sin^2 \theta_W$  is 0.7, which implies that a measurement of  $\mathcal{R}^\nu$  to 1%  
 2 precision would in turn provide a 1.4% precision on  $\sin^2 \theta_W$ . This technique was used by the  
 3 CDHS [231], CHARM [232] and CCFR [233] experiments. In contrast to the NuTeV experiment,  
 4 the antineutrino interactions cannot be used for this analysis at LBNE due to the large number of  
 5  $\nu_\mu$  DIS interactions in the  $\bar{\nu}_\mu$  beam compared to the  $\bar{\nu}_\mu$  DIS interactions.
- 6 The measurement of  $\sin^2 \theta_W$  from DIS interactions can only be performed with the low-density  
 7 magnetized tracker since an accurate reconstruction of the NC event kinematics and of the  $\nu$ -  
 8 CC interactions are crucial for keeping the systematic uncertainties on the event selection under  
 9 control. The analysis selects events in the ND after imposing a cut on the visible hadronic energy  
 10 of  $E_{\text{had}} > 5 \text{ GeV}$  (the CHARM analysis had  $E_{\text{had}} > 4 \text{ GeV}$ ). With an exposure of  $5 \times 10^{21}$  POT  
 11 with 1.2-MW primary beam, about  $7.7 \times 10^6$  CC events and  $2.4 \times 10^6$  NC events are expected,  
 12 giving a statistical precision of 0.074% on  $\mathcal{R}^\nu$  and 0.1% on  $\sin^2 \theta_W$  (Table 7.2).

**Table 7.2:** Comparison of uncertainties on the  $\mathcal{R}^\nu$  measurement between NuTeV and LBNE with a 5 t fiducial mass after an exposure of  $5 \times 10^{21}$  POT (5 year) with the 1.2-MW reference beam at 120 GeV. The corresponding relative uncertainties on  $\sin^2 \theta_W$  must be multiplied by a factor of 1.4, giving for LBNE a projected overall precision of 0.35%.

Source of uncertainty	$\delta R^\nu / R^\nu$		Comments
	NuTeV	LBNE	
<b>Data statistics</b>	0.00176	0.00074	
<b>Monte Carlo statistics</b>	0.00015		
<b>Total Statistics</b>	0.00176	0.00074	
<b><math>\nu_e, \bar{\nu}_e</math> flux (<math>\sim 1.7\%</math>)</b>	0.00064	0.00010	$e^-/e^+$ identification
<b>Energy measurement</b>	0.00038	0.00040	
<b>Shower length model</b>	0.00054	n.a.	
<b>Counter efficiency, noise</b>	0.00036	n.a.	
<b>Interaction vertex</b>	0.00056	n.a.	
<b><math>\bar{\nu}_\mu</math> flux</b>	n.a.	0.00070	Large $\bar{\nu}$ contamination
<b>Kinematic selection</b>	n.a.	0.00060	Kinematic identification of NC
<b>Experimental systematics</b>	0.00112	0.00102	
<b>d,s<math>\rightarrow</math>c, s-sea</b>	0.00227	0.00140	Based on existing knowledge
<b>Charm sea</b>	0.00013	n.a.	
<b><math>r = \sigma^{\bar{\nu}}/\sigma^\nu</math></b>	0.00018	n.a.	
<b>Radiative corrections</b>	0.00013	0.00013	
<b>Non-isoscalar target</b>	0.00010	N.A.	
<b>Higher twists</b>	0.00031	0.00070	Lower $Q^2$ values
<b><math>R_L (F_2, F_T, xF_3)</math></b>	0.00115	0.00140	Lower $Q^2$ values
<b>Nuclear correction</b>		0.00020	
<b>Model systematics</b>	0.00258	0.00212	
<b>TOTAL</b>	<b>0.00332</b>	<b>0.00247</b>	

The use of a low-density magnetized tracker can substantially reduce systematic uncertainties compared to a massive calorimeter. Table 7.2 shows a comparison of the different uncertainties on the measured  $\mathcal{R}^\nu$  between NuTeV and LBNE. While NuTeV measured both  $\mathcal{R}^\nu$  and  $\mathcal{R}^{\bar{\nu}}$ , the largest experimental uncertainty in the measurement of  $\mathcal{R}^\nu$  is related to the subtraction of the  $\nu_e$ -CC contamination from the NC sample. Since the low-density tracker at LBNE can efficiently reconstruct the electron tracks, the  $\nu_e$ -CC interactions can be identified on an event-by-event basis, reducing the corresponding uncertainty to a negligible level. Similarly, uncertainties related to the location of the interaction vertex, noise, counter efficiency and so on are removed by the higher resolution and by changing the analysis selection. The experimental selection at LBNE will be dominated by two uncertainties: the knowledge of the  $\bar{\nu}_\mu$  flux and the kinematic selection of NC interactions. The former is relevant due to the larger NC/CC ratio for antineutrinos. The total experimental systematic uncertainty on  $\sin^2 \theta_W$  is expected to be about 0.14%.

The measurement of  $\mathcal{R}^\nu$  will be dominated by theoretical systematic uncertainties on the structure functions of the target nucleons. The estimate of these uncertainties for LBNE is based upon the extensive work performed for the NOMAD analysis and includes a Next-to-Next-Leading-Order (NNLO) QCD calculation of structure functions (NLO for charm production) [234,235,236], parton distribution functions (PDFs) extracted from dedicated low- $Q$  global fits, high-twist contributions [234], electroweak corrections [237] and nuclear corrections [238,239,240]. The charm quark production in CC, which has been the dominant source of uncertainty in all past determinations of  $\sin^2 \theta_W$  from  $\nu$ N DIS, is reduced to about 4% of the total  $\nu_\mu$ -CC DIS for  $E_{\text{had}} > 5$  GeV with the low-energy beam spectrum at LBNE. This number translates into a systematic uncertainty of 0.14% on  $\mathcal{R}^\nu$  (Table 7.2), assuming the current knowledge of the charm production cross section. It is worth noting that the recent measurement of charm dimuon production by the NOMAD experiment allowed a reduction of the uncertainty on the strange sea distribution to  $\sim 3\%$  and on the charm quark mass  $m_c$  to  $\sim 75$  MeV [229]. The lower neutrino energies available at LBNE reduce the accessible  $Q^2$  values with respect to NuTeV, increasing in turn the effect of non-perturbative contributions (high twists) and  $R_L$ . The corresponding uncertainties are reduced by the recent studies of low- $Q$  structure functions and by improved modeling with respect to the NuTeV analysis (NNLO vs. LO). The total model systematic uncertainty on  $\sin^2 \theta_W$  is expected to be about 0.21% with the reference beam configuration. The corresponding total uncertainty on the value of  $\sin^2 \theta_W$  extracted from  $\nu$ N DIS is 0.35%.

Most of the model uncertainties will be constrained by dedicated in situ measurements using the large CC samples and employing improvements in theory that will have evolved over the course of the experiment. The low-density tracker will collect about 350,000 neutrino-induced inclusive charm events in a 5 year run with the reference 120-GeV 1.2-MW beam. The precise reconstruction of charged tracks will allow measurement of exclusive decay modes of charmed hadrons (e.g.,  $D^{*+}$ ) and measurement of charm fragmentation and production parameters. The average semileptonic branching ratio  $B_\mu$  is of order 5% with the low-energy LBNE beam, and the low-density ND will be able to reconstruct both the  $\mu\mu$  and  $\mu e$  decay channels. Currently, the most precise sample

of 15,400 dimuon events has been collected by the NOMAD experiment. Finally, precision measurements of CC structure functions in the LBNE ND would further reduce the uncertainties on PDFs and on high-twist contributions.

The precision that can be achieved from  $\nu N$  DIS interactions is limited by both the event rates and the energy spectrum of the standard beam configuration. The high-statistics beam exposure with the low-energy default beam-running configuration (described in Chapter 3) combined with a dedicated run with the high-energy beam option would increase the statistics by more than a factor of ten. This major step forward would not only reduce the statistical uncertainty to a negligible level, but would provide large control samples and precision auxiliary measurements to reduce the systematic uncertainties on structure functions. The two dominant systematic uncertainties, charm production in CC interactions and low  $Q^2$  structure functions, are essentially defined by the available data at present. Overall, the use of a high-energy beam with upgraded intensity can potentially improve the precision achievable on  $\sin^2 \theta_W$  from  $\nu N$  DIS to better than 0.2%.

### 7.2.2 Elastic Scattering

A second independent measurement of  $\sin^2 \theta_W$  can be obtained from NC  $\nu_\mu e$  elastic scattering. This channel has lower systematic uncertainties since it does not depend on knowledge of the structure of nuclei, but it has limited statistics due to its very low cross section. The value of  $\sin^2 \theta_W$  can be extracted from the ratio of interactions [225] as follows:

$$\mathcal{R}_{\nu e}(Q^2) \equiv \frac{\sigma(\bar{\nu}_\mu e \rightarrow \bar{\nu}_\mu e)}{\sigma(\nu_\mu e \rightarrow \nu_\mu e)}(Q^2) \simeq \frac{1 - 4 \sin^2 \theta_W + 16 \sin^4 \theta_W}{3 - 12 \sin^2 \theta_W + 16 \sin^4 \theta_W}, \quad (7.8)$$

in which systematic uncertainties related to the selection and the electron identification cancel out. The absolute sensitivity of this ratio to  $\sin^2 \theta_W$  is 1.79, which implies that a measurement of  $\mathcal{R}_{\nu e}$  to 1% precision would provide a measurement of  $\sin^2 \theta_W$  to 0.65% precision.

The best measurement of NC elastic scattering off electrons was performed by CHARM II, which observed  $2677 \pm 82$   $\nu$  and  $2752 \pm 88$   $\bar{\nu}$  events [241]. The CHARM II analysis was characterized by a sizable uncertainty related to the extrapolation of the background into the signal region.

The event selection for NC elastic scattering is described in Section 7.1.4. Since the NC elastic scattering off electrons is also used for the absolute flux normalization, the WMA analysis can be performed only with the low-density magnetized tracker in conjunction with a large liquid argon detector. In the case of the flux normalization measurement, the total reconstructed statistics is limited to about 4,500 (2,800)  $\nu(\bar{\nu})$  events. These numbers do not allow a competitive determination of  $\sin^2 \theta_W$  by using the magnetized tracker alone. However, a 100-t liquid argon detector in the ND would be expected to collect about 90,000 (60,000) reconstructed  $\nu(\bar{\nu})$  events with the standard beam, and an additional factor of two with an upgraded 2.3-MW beam.

A combined analysis of both detectors can achieve the optimal sensitivity: the fine-grained tracker

1 is used to reduce systematic uncertainties (measurement of backgrounds and calibration), while  
 2 the liquid argon detector provides the statistics required for a competitive measurement. Overall,  
 3 the use of the complementary liquid argon detector can provide a statistical accuracy on  $\sin^2 \theta_W$   
 4 of about 0.3%. However, the extraction of the WMA is dominated by the systematic uncertainty  
 5 on the  $\bar{\nu}_\mu/\nu_\mu$  flux ratio in Equation (7.8). This uncertainty has been evaluated with the low- $\nu_0$   
 6 method for the flux extraction and a systematic uncertainty of about 1% was obtained on the ratio  
 7 of the  $\bar{\nu}_\mu/\nu_\mu$  flux integrals. An improved precision on this quantity could be achieved from a  
 8 measurement of the ratios  $\pi^-/\pi^+$  and  $\rho^-/\rho^+$  from coherent production in the fine-grained tracker.  
 9 Due to the excellent angular and momentum resolution and to large cancellations of systematic  
 10 uncertainties, preliminary studies indicate that an overall precision of about 0.3% can be achieved  
 11 on the  $\bar{\nu}_\mu/\nu_\mu$  flux ratio using coherent production.

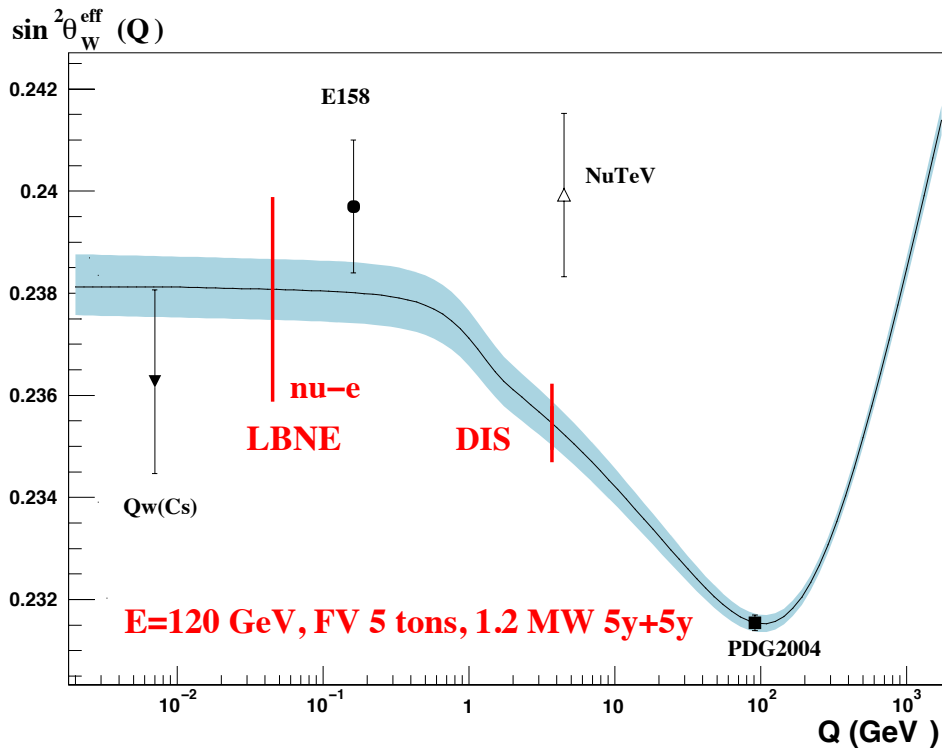


**Figure 7.2:** Expected sensitivity to the measurement of  $\sin^2 \theta_W$  from the LBNE ND with the reference 1.2-MW beam and an exposure of  $5 \times 10^{21}$  POT with a neutrino beam (five years) and  $5 \times 10^{21}$  pot with an antineutrino beam (five years). The curve shows the Standard Model prediction as a function of the momentum scale [242]. Previous measurements from Atomic Parity Violation [243,244], Moeller scattering (E158 [245]),  $\nu$  DIS (NuTeV [230]) and the combined Z pole measurements (LEP/SLC) [244] are also shown for comparison. The use of a high-energy beam tune can reduce the LBNE uncertainties by almost a factor of two.

12 Together, the DIS and the NC elastic scattering channels involve substantially different scales of  
 13 momentum transfer, providing a tool to test the running of  $\sin^2 \theta_W$  in a single experiment. To  
 14 this end, the study of NC elastic scattering off protons can provide additional information since

1 it occurs at a momentum scale that is intermediate between the two other processes. Figure 7.2  
 2 summarizes the target sensitivity from the LBNE ND, compared with existing measurements as a  
 3 function of the momentum scale.

4 In the near future, another precision measurement of  $\sin^2 \theta_W$  is expected from the  $Q_{\text{weak}}$  experi-  
 5 ment [246] at Jefferson Laboratory. From the measurement of parity-violating asymmetry in elastic  
 6 electron-proton scattering, the  $Q_{\text{weak}}$  experiment should achieve a precision of 0.3% on  $\sin^2 \theta_W$  at  
 7  $Q^2 = 0.026 \text{ GeV}^2$ . It should be noted that the  $Q_{\text{weak}}$  measurement is complementary to those from  
 8 neutrino scattering given the different scale of momentum transfer and the fact that neutrino mea-  
 9 surements are the only direct probe of the  $Z$  coupling to neutrinos. With the 12-GeV upgrade of  
 10 Jefferson Laboratory, the  $Q_{\text{weak}}$  experiment [247] could potentially reach precisions on the order  
 11 of 0.2-0.1 %.

## 12 7.3 Observation of the Nucleon's Strangeness Content

sec-deltas

The strange-quark content of the proton and its contribution to the proton spin remain enig-  
 matic. The question is whether the strange quarks contribute substantially to the vector and  
 axial-vector currents of the nucleon. A large observed value of the strange-quark contribu-  
 tion to the nucleon spin (axial current),  $\Delta s$ , would enhance our understanding of the proton  
 structure.

The spin structure of the nucleon also affects the couplings of axions and supersymmetric  
 particles to dark matter.

13

14 The strange quark *vector* elastic form factors of the nucleon have been measured to high precision  
 15 in parity-violating electron scattering (PVES) at Jefferson Lab, Mainz and elsewhere. A recent  
 16 global analysis [248] of PVES data finds a strange magnetic moment  $\mu_s = 0.37 \pm 0.79$  (in units of  
 17 the nucleon magneton), so that the strange quark contribution to proton magnetic moment is less  
 18 than 10%. For the strange electric charge radius parameter,  $\rho_s$ ,

19 one finds a very small value,  $\rho_s = -0.03 \pm 0.63 \text{ GeV}^{-2}$ , consistent with zero. Both results are  
 20 consistent with theoretical expectations based on lattice QCD and phenomenology [249].

21 In contrast, the strange *axial vector* form factors are poorly determined. A global study of PVES  
 22 data [248] finds  $G_A^N(Q^2) = \tilde{g}_A^N (1 + Q^2/M_A^2)^2$ , with the effective proton and neutron axial charges  
 23  $\tilde{g}_A^p = -0.80 \pm 1.68$  and  $\tilde{g}_A^n = 1.65 \pm 2.62$ .

24 The strange axial form factor at  $Q^2 = 0$  is related to the *spin* carried by strange quarks,  $\Delta s$ .  
 25 Currently the world data on the spin-dependent  $g_1$  structure function constrain  $\Delta s$  to be  $\approx -0.055$   
 26 at a scale  $Q^2 = 1 \text{ GeV}^2$ , with a significant fraction coming from the region  $x < 0.001$ .

An independent extraction of  $\Delta_s$ , which does not rely on the difficult measurements of the  $g_1$  structure function at very small values of the Bjorken variable  $x$ , can be obtained from (anti)neutrino NC elastic scattering off protons, see Figure 7.3. Indeed, this process provides the most direct measurement of  $\Delta_s$ . The differential cross section for NC-elastic and CC-QE scattering of (anti)neutrinos from protons can be written as:

$$\frac{d\sigma}{dQ^2} = \frac{G_\mu^2 Q^2}{2\pi E_\nu^2} \left( A \pm BW + CW^2 \right); \quad W = 4E_\nu/M_p - Q^2/M_p^2, \quad (7.9) \text{ eqn:QE}$$

- 1 where the positive (negative) sign is for neutrino (antineutrino) scattering and the coefficients  $A$ ,  $B$ ,  
2 and  $C$  contain the vector and axial form factors as follows:

$$\begin{aligned} A &= \frac{1}{4} \left[ G_1^2 (1 + \tau) - (F_1^2 - \tau F_2^2) (1 - \tau) + 4\tau F_1 F_2 \right] \\ B &= -\frac{1}{4} G_1 (F_1 + F_2) \\ C &= \frac{1}{16} \frac{M_p^2}{Q^2} (G_1^2 + F_1^2 + \tau F_2^2) \end{aligned}$$

The axial-vector form factor,  $G_1$ , for NC scattering can be written as the sum of the known axial form factor  $G_A$  plus a strange form factor  $G_A^s$ :

$$G_1 = \left[ -\frac{G_A}{2} + \frac{G_A^s}{2} \right], \quad (7.10)$$

while the NC vector form factors can be written as:

$$F_{1,2} = \left[ \left( \frac{1}{2} - \sin^2 \theta_W \right) (F_{1,2}^p - F_{1,2}^n) - \sin^2 \theta_W (F_{1,2}^p + F_{1,2}^n) - \frac{1}{2} F_{1,2}^s \right], \quad (7.11)$$

- 3 where  $F_1^{p(n)}$  is the Dirac form factor of the proton (neutron),  $F_2^{p(n)}$  is the corresponding Pauli form  
4 factor, and  $F_{1,2}^s$  are the strange-vector form factors. These latter form factors are expected to be  
5 small from the PVES measurements summarized above. In the limit  $Q^2 \rightarrow 0$ , the differential cross  
6 section is proportional to the square of the axial-vector form factor  $d\sigma/dQ^2 \propto G_1^2$  and  $G_A^s \rightarrow \Delta_s$ .  
7 The value of  $\Delta_s$  can therefore be extracted experimentally by extrapolating the NC differential  
8 cross section to  $Q^2 = 0$ .

### 9 7.3.1 Extraction of the Strange Form Factors in the LBNE ND

- 10 Previous neutrino scattering experiments have been limited by the statistics and by the systematic  
11 uncertainties on background subtraction. One of the earliest measurements available comes from  
12 the analysis of 951 NC  $\nu p$  and 776 NC  $\bar{\nu} p$  collected by the experiment BNL E734 [250,251,252].  
13 There are also more recent results with high statistics from MiniBooNE where a measurement of

$\Delta s$  was carried out using neutrino NC elastic scattering with 94,531  $\nu N$  events [253]. The Mini-BooNE measurement was limited by the inability to distinguish the proton and neutron from  $\nu N$  scattering. The LBNE neutrino beam will be sufficiently intense that a measurement of NC elastic scattering on protons in the fine-grained ND can provide a definitive statement on the contribution of the strange sea to either the axial or vector form factor.

Systematic uncertainties can be reduced by measuring the NC/CC ratios for both neutrinos and antineutrinos as a function of  $Q^2$ :

$$\mathcal{R}_{\nu p}(Q^2) \equiv \frac{\sigma(\nu_{\mu}p \rightarrow \nu_{\mu}p)}{\sigma(\nu_{\mu}n \rightarrow \mu^{-}p)}(Q^2); \quad \mathcal{R}_{\bar{\nu}p}(Q^2) \equiv \frac{\sigma(\bar{\nu}_{\mu}p \rightarrow \bar{\nu}_{\mu}p)}{\sigma(\bar{\nu}_{\mu}p \rightarrow \mu^{+}n)}(Q^2), \quad (7.12)$$

Figure 7.3 shows the absolute sensitivity of both ratios to  $\Delta s$  for different values of  $Q^2$ . The sensitivity for  $Q^2 \sim 0.25 \text{ GeV}^2$  is about 1.2 for neutrinos and 1.9 for antineutrinos, which implies that a measurement of  $\mathcal{R}_{\nu p}$  and  $\mathcal{R}_{\bar{\nu}p}$  of 1% precision would enable the extraction of  $\Delta s$  with an uncertainty of 0.8% and 0.5%, respectively.

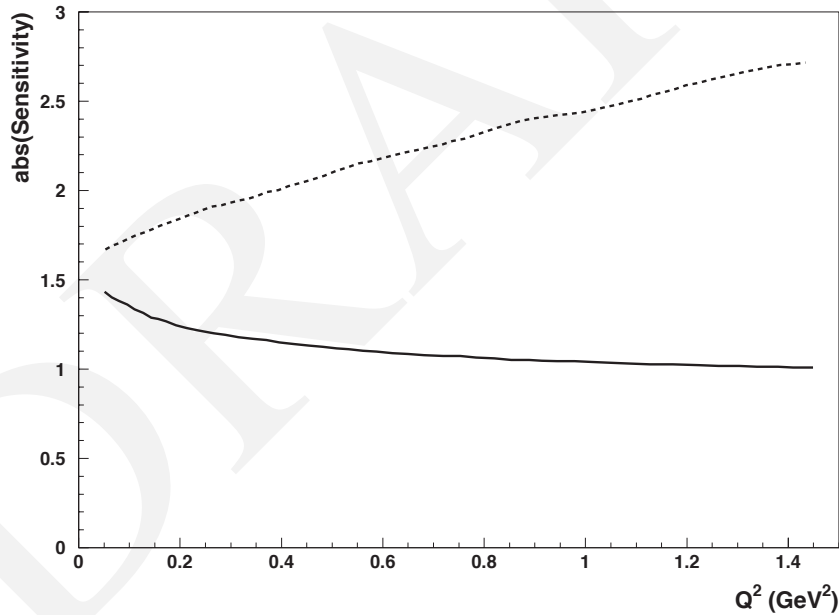


**Figure 7.3:** Absolute sensitivity of the ratios  $\mathcal{R}_{\nu p}$  (solid) and  $\mathcal{R}_{\bar{\nu}p}$  (dashed) to the strange contribution to the spin of the nucleon,  $\Delta s$ , as a function of  $Q^2$ .

The design of the high-resolution tracker ND for LBNE includes several different nuclear targets. Therefore, most of the neutrino scattering is from nucleons embedded in a nucleus, requiring nuclear effects to be taken into account. Fortunately, in the ratio of NC/CC the nuclear corrections are expected to largely cancel out. The  $\Delta s$  analysis requires a good proton reconstruction efficiency as well as high resolution on both the proton angle and energy. To this end, the low-density magnetized tracker at LBNE can increase the range of the protons inside the ND, allowing the

- 1 reconstruction of proton tracks down to  $Q^2 \sim 0.07 \text{ GeV}^2$ . This capability will reduce the uncer-  
 2 tainties in the extrapolation of the form factors to the limit  $Q^2 \rightarrow 0$ .
- 3 Table 7.3 summarizes the expected proton range for the low-density ( $\rho \sim 0.1 \text{ g cm}^{-3}$ ) straw tube  
 4 tracker (STT) in the ND tracking detector design described in Section 3.5. About  $2.0(1.2) \times 10^6$   
 5  $\nu p(\bar{\nu} p)$  events are expected after the selection cuts in the low-density tracker, yielding a statistical  
 6 precision on the order of 0.1%.

**Table 7.3:** Expected proton range for the low-density ( $\rho \sim 0.1 \text{ g cm}^{-3}$ ) tracker. The first column gives the proton kinetic energy and the last column the proton momentum. The  $Q^2$  value producing  $T_p$  is calculated assuming the struck nucleon is initially at rest.

$T_p$ MeV	$Q^2$ $\text{GeV}^2/c^2$	Range STT cm	$P_p$ GeV/c
20	0.038	4.2	0.195
40	0.075	14.5	0.277
60	0.113	30.3	0.341
80	0.150	50.8	0.395
100	0.188	75.7	0.445

- 7 The determination of  $\Delta s$  in the straw-tube tracker ND utilizes analysis techniques performed by  
 8 the FINeSSE collaboration [254] and used by the SciBooNE experiment. In particular, based on the  
 9 latter, LBNE expects a purity of about 50%, with background contributions of 20% from neutrons  
 10 produced outside of the detector, 10%  $\nu n$  events and 10% NC pion backgrounds. The dominant  
 11 systematic uncertainty will be related to the background subtraction. The low-energy beam spec-  
 12 trum at LBNE provides the best sensitivity for this measurement since the external background  
 13 from neutron-induced proton recoils will be reduced by the strongly suppressed high-energy tail.  
 14 The low-density magnetized tracker is expected to increase the purity by reducing the neutron  
 15 background and the NC pion background. The outside neutron background, it should be noted, can  
 16 be determined using the  $n \rightarrow p + \pi^-$  process in the STT. The sensitivity analysis is still in progress,  
 17 however LBNE is confident of achieving a precision on  $\Delta s$  of about 0.02–0.03.

## 7.4 Nucleon Structure and QCD Studies

sec-nucleon

Precision measurements of (anti)neutrino differential cross sections in the LBNE near detector will provide additional constraints on several key nucleon structure functions that are complementary to results from electron scattering experiments.

In addition, these measurements would directly improve LBNE's oscillation measurements by providing accurate simulation of neutrino interactions in the far detector and offer an estimate of all background processes that are dependent upon the angular distribution of the outgoing particles in the far detector. Furthermore, certain QCD analyses — i.e., global fits used for extraction of parton distribution functions (PDFs) via the differential cross sections measured in ND data — would constrain the systematic error in precision electroweak measurements. This would apply not only in neutrino physics but also in hadron collider measurements.

### 7.4.1 Determination of the $F_3$ Structure Function and GLS Sum Rule

For quantitative studies of inclusive deep-inelastic lepton-nucleon scattering, it is vital to have precise measurements of the  $F_3$  structure functions as input into global PDF fits. Because it depends on weak axial quark charges, the  $F_3$  structure function can only be measured with neutrino and antineutrino beams and is unique in its ability to differentiate between the quark and antiquark content of the nucleon. On a proton target, for instance, the neutrino and antineutrino  $F_3$  structure functions (at leading order in  $\alpha_s$ ) are given by

$$xF_3^{\nu p}(x) = 2x(d(x) - \bar{u}(x) + s(x) + \dots), \quad (7.13)$$

$$xF_3^{\bar{\nu} p}(x) = 2x(u(x) - \bar{d}(x) - \bar{s}(x) + \dots), \quad (7.14)$$

$$xF_3^{\nu n}(x) = 2x(u(x) - \bar{d}(x) + s(x) + \dots), \quad (7.15)$$

$$xF_3^{\bar{\nu} n}(x) = 2x(d(x) - \bar{u}(x) - \bar{s}(x) + \dots). \quad (7.16)$$

where  $u_v = u - \bar{u}$  and  $d_v = d - \bar{d}$  are the valence sea quark distributions. Under the assumption of a symmetric strange sea, i.e.,  $s(x) = \bar{s}(x)$ , the above expressions show that a measurement of the average  $xF_3 = (xF_3^{\nu N} + xF_3^{\bar{\nu} N})/2$  for neutrino and antineutrino interactions on isoscalar targets provides a direct determination of the valence quark distributions in the proton. This measurement is complementary to the measurement of Drell-Yan production at colliders, which is essentially proportional to the sea quark distributions.

The first step in the structure function analysis is the measurement of the differential cross-section:

$$\frac{1}{E_\nu} \frac{d\sigma^2}{dx dQ^2} = \frac{N(x, Q^2, E_\nu) \sigma_{\text{tot}}/E_\nu}{N(E_\nu) dx dQ^2} \quad (7.17)$$

where  $N(x, Q^2, E_\nu)$  is the number of events in each  $(x, Q^2, E_\nu)$  bin and  $N(E_\nu)$  is the number of events in each  $E_\nu$  bin integrated over  $x$  and  $Q^2$ . The average  $xF_3$  structure function can be extracted by taking the difference between neutrino and antineutrino differential cross sections:

$$\frac{1}{E_\nu} \frac{d^2\sigma^\nu}{dx dQ^2} - \frac{1}{E_\nu} \frac{d^2\sigma^{\bar{\nu}}}{dx dQ^2} = 2 \left[ y \left(1 - \frac{y}{2}\right) \frac{y}{Q^2} \right] xF_3 \quad (7.18)$$

- 1 where  $xF_3$  denotes the sum for neutrino and antineutrino interactions.
- 2 The determination of the  $xF_3$  structure functions will, in turn, allow a precision measurement of
- 3 the Gross-Llewellyn-Smith (GLS) QCD sum rule:

$$\begin{aligned} S_{\text{GLS}}(Q^2) &= \frac{1}{2} \int_0^1 \frac{1}{x} \left[ xF_3^{\nu N} + xF_3^{\bar{\nu} N} \right] dx \\ &= 3 \left[ 1 - \frac{\alpha_s(Q^2)}{\pi} - a(n_f) \left( \frac{\alpha_s(Q^2)}{\pi} \right)^2 - b(n_f) \left( \frac{\alpha_s(Q^2)}{\pi} \right)^3 \right] + \Delta\text{HT} \end{aligned} \quad (7.19)$$

- 4 where  $\alpha_s$  is the strong coupling constant,  $n_f$  is the number of quark flavors,  $a$  and  $b$  are known func-
- 5 tions of  $n_f$ , and the quantity  $\Delta\text{HT}$  represents higher-twist contributions. The equation above can be
- 6 inverted to determine  $\alpha_s(Q^2)$  from the GLS sum rule. The most precise determination of the GLS
- 7 sum rule was obtained by the CCFR experiment on an iron target [255]  $S_{\text{GLS}}(Q^2 = 3 \text{ GeV}^2) =$
- 8  $2.50 \pm 0.018 \pm 0.078$ . The use of a high-resolution ND in LBNE combined with the unprecedented
- 9 statistics would substantially reduce the systematic uncertainty on the low- $x$  extrapolation of the
- 10  $xF_3$  structure functions entering the GLS integral. In addition, the presence of different nuclear
- 11 targets, as well as the availability of a target with free protons will allow investigation of isovector
- 12 and nuclear corrections, and adding a tool to test isospin (charge) symmetry (see Section 7.5).

#### 13 7.4.2 Determination of the Longitudinal Structure Function $F_L(x, Q^2)$

The structure function  $F_L$  is directly related to the gluon distribution  $G(x, Q^2)$  of the nucleon, as can be seen from the Altarelli-Martinelli relation:

$$F_L(x, Q^2) = \frac{\alpha_s(Q^2)}{\pi} \left[ \frac{4}{3} \int_x^1 \frac{dy}{y} \left( \frac{x}{y} \right)^2 F_2(x, Q^2) + n_f \int_x^1 \frac{dy}{y} \left( \frac{x}{y} \right)^2 \left( 1 - \frac{x}{y} \right) G(y, Q^2) \right] \quad (7.20)$$

where  $n_f$  is the number of parton flavors. In the leading order approximation the longitudinal structure function  $F_L$  is zero, while at higher orders a non-zero  $F_L(x, Q^2)$  is originated as a consequence of the violation of the Callan-Gross relation:

$$F_L(x, Q^2) = \left( 1 + \frac{4M^2 x^2}{Q^2} \right) F_2(x, Q^2) - 2xF_1(x, Q^2) \quad (7.21)$$

1 where  $2xF_1 = F_T$  is the transverse structure function. A measurement of  $R = F_L/F_T$  is therefore  
 2 both a test of perturbative QCD at large  $x$  and a clean probe of the gluon density at small  $x$   
 3 where the quark contribution is small. A poor knowledge of  $R$ , especially at small  $x$ , results in  
 4 uncertainties in the structure functions extracted from deep inelastic scattering cross sections, and  
 5 in turn, in electroweak measurements. It is instructive to compare the low- $Q^2$  behavior of  $R$  for  
 6 charged-lepton versus neutrino scattering. In both cases CVC implies that  $F_T \propto Q^2$  as  $Q^2 \rightarrow 0$ .  
 7 However, while  $F_L \propto Q^4$  for the electromagnetic current, for the weak current  $F_L$  is dominated  
 8 by the finite PCAC (partial conservation of the axial current) contribution [239]. The behavior  
 9 of  $R$  at  $Q^2 \ll 1 \text{ GeV}^2$  is therefore very different for charged-lepton and neutrino scattering. A  
 10 new precision measurement of the  $Q^2$  dependence of  $R$  with (anti)neutrino data would also clarify  
 11 the size of the high-twist contributions to  $F_L$  and  $R$ , which reflect the strength of multi-parton  
 12 correlations (qq and qg).

The ratio of longitudinal to transverse structure functions can be measured from the  $y$  dependence  
 of the deep inelastic scattering data. Fits to the following function:

$$F(x, Q^2, \epsilon) = \frac{\pi(1-\epsilon)}{y^2 G_F^2 M E_\nu} \left[ \frac{d^2\sigma^\nu}{dx dy} + \frac{d^2\sigma^{\bar{\nu}}}{dx dy} \right] = 2xF_1(x, Q^2) [1 + \epsilon R(x, Q^2)] \quad (7.22)$$

13 have been used by CCFR and NuTeV to determine  $R = \sigma_L/\sigma_T$ . In this equation  $\epsilon \simeq 2(1-y)/(1+$   
 14  $(1-y)^2)$  is the polarization of the virtual  $W$  boson. This equation assumes  $x F_3^\nu = x F_3^{\bar{\nu}}$ , and a  
 15 correction must be applied if this is not the case. The values of  $R$  are extracted from linear fits to  
 16  $F$  versus  $\epsilon$  at fixed  $x$  and  $Q^2$  bins.

### 17 7.4.3 Determination of $F_2^n$ and the $d/u$ Ratio of Quark Distribution Functions

18 Because of the larger electric charge on the  $u$  quark than on the  $d$ , the electromagnetic proton  $F_2$   
 19 structure function data provide strong constraints on the  $u$ -quark distribution, but are relatively  
 20 insensitive to the  $d$ -quark distribution. To constrain the  $d$ -quark distribution a precise knowledge  
 21 of the corresponding  $F_2^n$  structure functions of free neutrons is required, which in practice is cur-  
 22 rently extracted from inclusive deuterium  $F_2$  data. At large values of  $x$  ( $x > 0.5$ ) the nuclear  
 23 corrections in deuterium become large and, more importantly, strongly model-dependent, leading  
 24 to large uncertainties on the resulting  $d$ -quark distribution. Using the isospin relation  $F_2^{\bar{\nu}p} = F_2^{\nu n}$   
 25 and  $F_2^{\nu p} = F_2^{\bar{\nu}n}$  it is possible to obtain a direct determination of  $F_2^{\nu n}$  and  $F_2^{\bar{\nu}n}$  with neutrino and  
 26 antineutrino scattering off a target with free protons. This determination is free from model uncer-  
 27 tainties related to nuclear targets. The extraction of  $F_2^{\nu n}$  and  $F_2^{\bar{\nu}n}$  will allow a precise extraction on  
 28 the  $d$ -quark distribution at large  $x$ . Existing neutrino data on hydrogen have relatively large errors  
 29 and do not extend beyond  $x \sim 0.5$  [256,257].

30 The  $F_2^{\bar{\nu}p}$  and  $F_2^{\nu p}$  structure functions can be obtained from interactions on a target with free protons  
 31 after subtracting the contributions from  $x F_3$  and  $R$ . These latter can either be modeled within global  
 32 PDF fits or taken from the other two measurements described above. As discussed in Section 7.5

1 the LBNE ND can achieve competitive measurements of  $F_2^{\bar{\nu}p}$  and  $F_2^{\nu p}$  with an increase of statistics  
2 of three orders of magnitude with respect to the existing hydrogen data [256,257].

### 3 7.4.4 Measurement of Nucleon Structure Functions in the LBNE ND

4 At present neutrino scattering measurements of cross sections have considerably larger uncertain-  
5 ties than those of the electromagnetic inclusive cross sections. The measurement of the differential  
6 cross sections [224] is dominated by three uncertainties: (1) muon energy scale; (2) hadron energy  
7 scale; and (3) knowledge of the input (anti)neutrino flux. Table 7.4 shows a comparison of past  
8 and present experiments and the corresponding uncertainties on the energy scales. The most pre-  
9 cise measurements are from the CCFR, NuTeV and NOMAD experiments, which are limited to a  
statistics of about  $10^6$  neutrino events.

**Table 7.4:** Summary of past experiments performing structure function measurements. The expected num-  
bers in the LBNE near detector for a five-year run with the 1.2-MW 120-GeV reference beam ( $5 \times 10^{21}$  pot)  
are also given for comparison.

Experiment	Mass	$\nu_\mu$ -CC Stat.	Target	$E_\nu$ (GeV)	$\Delta E_\mu$	$\Delta E_H$
CDHS [258]	750 t	$10^7$	p,Fe	20-200	2.0%	2.5%
BEBC [259,260]	various	$5.7 \times 10^4$	p,D,Ne	10-200		
CCFR [261,262]	690 t	$1.0 \times 10^6$	Fe	30-360	1.0%	1.0%
NuTeV [263]	690 t	$1.3 \times 10^6$	Fe	30-360	0.7%	0.43%
CHORUS [264]	100 t	$3.6 \times 10^6$	Pb	10-200	2.5%	5.0%
NOMAD [146]	2.7 t	$1.3 \times 10^6$	C	5-200	0.2%	0.5%
[229]	18 t	$1.2 \times 10^7$	Fe	5-200	0.2%	0.6%
MINOS ND [145]	980 t	$3.6 \times 10^6$	Fe	3-50	2-4%	5.6%
LBNE ND	5 t	$5.9 \times 10^7$	$(C_3H_6)_n$	0.5-30	$< 0.2\%$	$< 0.5\%$

10

11 The MINER $\nu$ A [151] experiment is expected to provide new structure function measurements on a  
12 number of nuclear targets including He, C, Fe and Pb in the near future. Since the structure function  
13 measurement mainly involves DIS events, the MINER $\nu$ A measurement will achieve a competitive  
14 statistics after the completion of the new run with the medium-energy beam. MINER $\nu$ A will fo-  
15 cus on a measurement of the ratio of different nuclear targets to measure nuclear corrections in  
16 (anti)neutrino interactions. It must be noted that the MINER $\nu$ A experiment relies on the MINOS  
17 ND for muon identification. The corresponding uncertainty on the muon-energy scale (Table 7.4)  
18 is substantially larger than that in other modern experiments, e.g., NuTeV and NOMAD, thus limit-  
19 ing the potential of absolute structure function measurements. Furthermore, the muon-energy scale  
20 is also the dominant source of uncertainty in the determination of the (anti)neutrino fluxes with the  
21 low- $\nu$  method. Therefore, the flux uncertainties in MINER $\nu$ A are expected to be larger than in  
22 NOMAD and NuTeV.

Given its reference beam design and 1.2-MW proton-beam power, LBNE expects to collect about  $2.3 \times 10^7$  neutrino DIS events and about  $4.4 \times 10^6$  antineutrino DIS events in the ND. These numbers correspond to an improvement by more than one order of magnitude with respect to the most precise past experiments, e.g., NuTeV [263] and NOMAD [146,229]. With these high-statistics samples, LBNE will be able to significantly reduce the gap between the uncertainties on the weak and electromagnetic structure functions. A possible high-energy run with the upgraded 2.3-MW beam would offer a further increase by more than a factor of ten in statistics.

In addition to the large data samples, the use of a high-resolution, low-density spectrometer allows LBNE to reduce systematic uncertainties with respect to previous measurements. The LBNE ND is expected to achieve precisions better than 0.2% and 0.5% on the muon- and hadron-energy scales, respectively. These numbers are based on the results achieved by the NOMAD experiment (see Table 7.4), which had much lower statistics and worse resolution than is expected in the LBNE ND. The calibration of the momentum and energy scales will be performed with the large sample of reconstructed  $K_S^0 \rightarrow \pi\pi$ ,  $\Lambda \rightarrow p\pi$ , and  $\pi^0 \rightarrow \gamma\gamma$  decays. In addition, the overall hadronic energy scale can be calibrated by exploiting the well-known structure of the Bjorken  $y$  distribution in (anti)neutrino DIS interactions [146,265]. The relative fluxes as a function of energy can be extracted to a precision of about 2% with the low- $\nu$  method, due to the small uncertainty on the muon-energy scale. The world average absolute normalization of the differential cross-sections  $\sigma_{\text{tot}}/E$ , is known to 2.1% precision [47]. However, with the 1.2-MW beam available from the PIP-II upgrades, it will be possible to improve the absolute normalization using  $\nu$ -e NC elastic scattering events, coherent meson production, etc. An overall precision of 1-2% would make (anti)neutrino measurements comparable to or better than the complementary ones from charged-lepton DIS.

On the time scale of the LBNE project, comparable measurements from (anti)neutrino experiments are not expected, primarily due to the low energy of competing beamlines (J-PARC neutrino beamline in Japan [266] or to the poorer resolution of the detectors used (MINER $\nu$ A [151], T2K [125], NO $\nu$ A [117]). The experimental program most likely to compete with the LBNE ND measurements is the 12-GeV upgrade at Jefferson Laboratory (JLab) [267]. However, it must be emphasized that the use of electron beams at JLab makes this program *complementary* to LBNE's. In particular, the three topics discussed above are specific to the (anti)neutrino interactions.

Several planned experiments at JLab with the energy-upgraded 12-GeV beam will measure the  $d/u$  ratio from D targets up to  $x \sim 0.85$ , using different methods to minimize the nuclear corrections. The LBNE measurement in the ND will be competitive with the proposed JLab 12-GeV experiments, since the large statistics expected will allow a precise determination of  $F_2^{\nu n}$  and  $F_2^{\bar{\nu}n}$  up to  $x \sim 0.85$ . Furthermore, the use of a weak probe coupled with a wide-band beam will provide a broader  $Q^2$  range than in JLab experiments, thus allowing a separation of higher twist and other sub-leading effects in  $1/Q^2$ .

## 7.5 Tests of Isospin Physics and Sum-Rules

c-isospin

One of the most compelling physics topics accessible to a high-resolution near detector in LBNE is the isospin physics using neutrino and antineutrino interactions. This physics involves the Adler sum rule and tests isospin (charge) symmetry in nucleons and nuclei.

The Adler sum rule relates the integrated difference of the antineutrino and neutrino  $F_2$  structure functions to the isospin of the target:

$$\mathcal{S}_A(Q^2) = \int_0^1 dx \left[ F_2^{\bar{\nu}}(x, Q^2) - F_2^{\nu}(x, Q^2) \right] / (2x) = 2 I_z, \quad (7.23) \text{ ASR}$$

where the integration is performed over the entire kinematic range of the Bjorken variable  $x$  and  $I_z$  is the projection of the target isospin vector on the quantization axis ( $z$  axis). For the proton  $\mathcal{S}_A^p = 1$  and for the neutron  $\mathcal{S}_A^n = -1$ .

In the quark-parton model the Adler sum is the difference between the number of valence  $u$  and  $d$  quarks of the target. The Adler sum rule survives the strong-interaction effects because of the conserved vector current (CVC) and provides an exact relation to test the local current commutator algebra of the weak hadronic current. In the derivation of the Adler sum rule the effects of both non-conservation of the axial current and heavy-quark production are neglected.

Experimental tests of the Adler sum rule require the use of a hydrogen target to avoid nuclear corrections to the bound nucleons inside the nuclei. The structure functions  $F_2^{\bar{\nu}}$  and  $F_2^{\nu}$  have to be determined from the corresponding differential cross sections and must be extrapolated to small  $x$  values in order to evaluate the integral. The test performed in bubble chambers by the BEBC collaboration — the only test available — is limited by the modest statistics; it used about 9,000  $\bar{\nu}$  and 5,000  $\nu$  events collected on hydrogen [260].

The LBNE program can provide the first high-precision test of the Adler sum rule. To this end, the use of the high-energy beam tune shown in Figure 3.19, although not essential, would increase the sensitivity, allowing attainment of higher  $Q^2$  values. Since the use of a liquid  $H_2$  bubble chamber is excluded in the ND hall due to safety concerns, the (anti)neutrino interactions off a hydrogen target can only be extracted with a subtraction method from the composite materials of the ND targets. Using this technique to determine the position resolution in the location of the primary vertex is crucial to reducing systematic uncertainties. For this reason, a precision test of the Adler sum rule is best performed with the low-density magnetized ND.

A combination of two different targets — the polypropylene  $(C_3H_6)_n$  foils placed in front of the STT modules and pure carbon foils — are used in the low-density magnetized ND to provide a fiducial hydrogen mass of about 1 t. With the LBNE fluxes from the standard exposure of  $5.0(1.5) \times 10^6 \pm 13(6.6) \times 10^3$  (*sub.*) — where the quoted uncertainty is dominated by the statistical subtraction

1 procedure —  $\nu(\bar{\nu})$ -CC events would be collected on the hydrogen target. The level of precision that  
 2 can be achieved is sufficient to open up the possibility of making new discoveries in the quark and  
 3 hadron structure of the proton. No other comparable measurement is expected on the timescale of  
 4 LBNE.

## 5 7.6 Studies of (Anti)Neutrino-Nucleus Interactions

sec-nuclear

6 An integral part of the physics program envisioned for the LBNE ND involves detailed measure-  
 7 ments of (anti)neutrino interactions in a variety of nuclear targets. The LBNE ND detector of-  
 8 fers substantially larger statistics coupled with a much higher resolution and, in turn, lower sys-  
 9 tematic uncertainties with respect to past experiments (Table 7.4) or ongoing and future ones  
 10 (MINER $\nu$ A [151], T2K [125], NO $\nu$ A [117]). The most important nuclear target is of course  
 11 the argon target that comprises the LBNE far detector. Regarding the ND, the standard target is  
 12 polypropylene ( $C_3H_6$ ) $_n$ , largely provided by the mass of the STT radiators. An additional proposed  
 13 ND target is argon gas in pressurized aluminum tubes with sufficient mass to provide  $\simeq 10$  times the  
 14  $\nu_\mu$ -CC and NC statistics as expected in the LBNE far detector. Equally important nuclear targets  
 15 are carbon (graphite), which is essential in order to get (anti)neutrino interactions on free proton  
 16 through a statistical subtraction procedure from the main polypropylene target (see Section 7.5),  
 17 and calcium. In particular, this latter target has the same atomic weight ( $A = 40$ ) of argon but is  
 18 isoscalar. One additional nuclear target is iron, which is used in the proposed India-based Neu-  
 19 trino Observatory (INO) [268]. The modularity of the STT provides for successive measurements  
 20 using thin nuclear targets (thickness  $< 0.1X_0$ ), while the excellent angular and space resolution  
 21 allows a clean separation of events originating in different target materials. Placing an arrange-  
 22 ment of different nuclear targets upstream of the detector provides the desired nuclear samples in  
 23 (anti)neutrino interactions. For example, a single 7 mm-thick calcium layer at the upstream end of  
 24 the detector will provide about  $3.1 \times 10^5$   $\nu_\mu$ -CC interactions in one year.

25 Potential ND studies in nuclear effects include the following:

- 26 ○ nuclear modifications of form factors
- 27 ○ nuclear modifications of structure functions
- 28 ○ mechanisms for nuclear effects in coherent and incoherent regimes
- 29 ○ a dependence of exclusive and semi-exclusive processes
- 30 ○ effect of final-state interactions
- 31 ○ effect of short-range correlations
- 32 ○ two-body currents

The study of nuclear effects in (anti)neutrino interactions off nuclei is directly relevant for the long-baseline oscillation studies. The use of heavy nuclei like argon in the LBNE far detector requires a measurement of nuclear cross sections on the same targets in the ND in order to reduce signal and background uncertainties in the oscillation analyses. Cross section measurements obtained from other experiments using different nuclei are not optimal; in addition to the different  $p/n$  ratio in argon compared to iron or carbon where measurements from other experiments exist, nuclear modifications of cross sections can differ from 5% to 15% between carbon and argon for example, while the difference in the final-state interactions could be larger. Additionally, nuclear modifications can introduce a substantial smearing of the kinematic variables reconstructed from the observed final-state particles. Detailed measurements of the dependence on the atomic number  $A$  of different exclusive processes are then required in order to understand the absolute energy scale of neutrino event interactions and to reduce the corresponding systematic uncertainties on the oscillation parameters.

It is worth noting that the availability of a free-proton target through statistical subtraction of the  $(\text{C}_3\text{H}_6)_n$  and carbon targets (Section 7.5) will allow for the first time a direct model-independent measurement of nuclear effects — including both the primary and final-state interactions — on the argon target relevant for the far detector oscillation analysis.

Furthermore, an important question in nuclear physics is how the structure of a nucleon is modified when said nucleon is inside the medium of a heavy nucleus as compared to a free nucleon like the proton in a hydrogen nucleus. Studies of the ratio of structure functions of nuclei to those of free nucleons (or in practice, the deuteron) reveal nontrivial deviations from unity as a function of  $x$  and  $Q^2$ . These have been well explored in charged-lepton scattering experiments, but little empirical information exists from neutrino scattering. Measurements of structure using neutrino scattering are complementary to those in charged-lepton scattering.

Another reason to investigate the nuclear-medium modifications of neutrino structure functions is that most neutrino scattering experiments are performed on nuclear targets, from which information on the free nucleon is inferred by performing a correction for the nuclear effects. In practice this often means applying the same nuclear correction as for the electromagnetic structure functions, which introduces an inherent model-dependence in the result. In particular, significant differences between photon-induced and weak-boson-induced nuclear structure functions are predicted, especially at low  $Q^2$  and low  $x$ , which have not been tested. A striking example is offered by the ratio  $R$  of the longitudinal-to-transverse structure functions [239]. While the electromagnetic ratio tends to zero in the photoproduction limit,  $Q^2 \rightarrow 0$ , by current conservation, the ratio for neutrino structure functions is predicted to be *finite* in this limit. Thus, significant discovery potential exists in the study of neutrino scattering from nuclei.

The comparison of argon and calcium targets ( $^{18}_{40}\text{Ar}$  and  $^{20}_{40}\text{Ca}$ ) in the LBNE ND would be particularly interesting. Since most nuclear effects depend on the atomic weight  $A$ , inclusive properties of (anti)neutrino interactions are expected to be the same for these two targets [269,270,271,239].

This fact would allow the use of both targets to model signal and backgrounds in the LBNE far detector (argon target), as well as to compare LBNE results for nuclear effects on argon with the extensive data on calcium from charged lepton DIS. In addition, a high-precision measurement of (anti)neutrino interactions in both argon and calcium opens the possibility for studying a potential flavor and isovector dependence of nuclear effects and to further test the isospin (charge symmetry) in nuclei (see Section 7.5). Evidence for any of these effects would constitute important discoveries.

Finally, the extraction of (anti)neutrino interactions on deuterium from the statistical subtraction of  $\text{H}_2\text{O}$  from  $\text{D}_2\text{O}$ , which is required to measure the fluxes (Section 7.1), would allow the first direct measurement of nuclear effects in deuterium. This measurement can be achieved since the structure function of a free isoscalar nucleon is given by the average of neutrino and antineutrino structure functions on hydrogen ( $F_2^{\nu n} = F_2^{\bar{\nu} p}$ ). A precise determination of nuclear modifications of structure functions in deuterium would play a crucial role in reducing systematic uncertainties from the global PDF fits.

## 7.7 Search for Heavy Neutrinos

The most economical way to handle the problems of neutrino masses, dark matter and baryon asymmetry of the Universe in a unified way may be to add to the SM three Majorana singlet fermions with masses roughly on the order of the masses of known quarks and leptons using the seesaw mechanism [59]. The appealing feature of this theory (called the  $\nu$ MSM for *Neutrino Minimal SM*) [272] is that every left-handed fermion has a right-handed counterpart, leading to a consistent way of treating quarks and leptons.

The most efficient mechanism proposed for producing these heavy sterile singlet states experimentally is through weak decays of heavy mesons and baryons, as can be seen from the left-hand diagram in Figure 7.4, showing some examples of relevant two- and three-body decays [273]. These heavy mesons can be produced by energetic protons scattering off the LBNE beamline target and the heavy singlet neutrinos from their decays detected in the LBNE ND.

The lightest of the three new singlet fermions in the  $\nu$ MSM, is expected to have a mass from 1 keV to 50 keV [274] and could play the role of the dark matter particle [275]. The two other neutral fermions are responsible for giving masses to ordinary neutrinos via the seesaw mechanism at the *electroweak scale* and for creation of the baryon asymmetry of the Universe (for a review see [274]). The masses of these particles and their coupling to ordinary leptons are constrained by particle physics experiments and cosmology [273,276] They should be almost degenerate, thus nearly forming Dirac fermions (this is dictated by the requirement of successful baryogen-

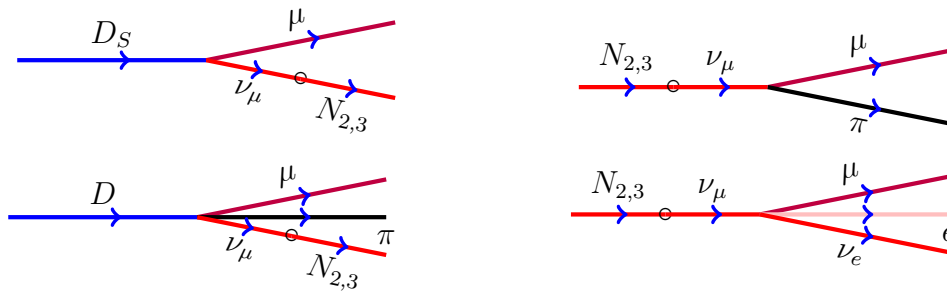


**Figure 7.4:** Left: Feynman diagrams of meson decays producing heavy sterile neutrinos. Right: Feynman diagrams of sterile neutrino decays.

esis). Different considerations indicate that their mass should be in the region of  $\mathcal{O}(1)$  GeV [277]. The mixing angle,  $U^2$ , between the singlet fermions and the three active neutrino states must be small [278,272] — otherwise the large mixing would have led to equilibration of these particles in the early Universe above the electroweak temperatures, and, therefore, to erasing of the baryon asymmetry — explaining why these new particles have not been seen previously.

Several experiments have conducted searches for heavy neutrinos, for example BEBC [279], CHARM [280], NuTeV [281] and the CERN PS191 experiment [282,283] (see also discussion of different experiments in [276]). In the search for heavy neutrinos, the strength of the LBNE high-resolution ND, compared to earlier experiments, lies in reconstructing the exclusive decay modes, including electronic, hadronic and muonic. Furthermore, the detector offers a means to constrain and measure the backgrounds using control samples.

In case of the LBNE experiment the relevant heavy mesons are charmed. With a typical lifetime (in the rest frame) of about  $10^{-10}$  s, these mesons mostly decay before further interaction, yielding the sterile neutrino flux. Since these sterile neutrinos are very weakly interacting they can cover quite a large distance before decay, significantly exceeding the distance of 459 m from the target to the near LBNE near detector. Neutrino decays into SM particles due to mixing with active neutrinos can be searched for in the ND, provided a sufficiently long instrumented decay region is available. Two examples of the interesting decay modes are presented on the right panel of Figure 7.4. More examples can be found in [273].

An estimate of sterile neutrino events that can be observed in the LBNE near detector,  $N_{signal}^{LBNE}$ , is obtained by comparing the relevant parameters of the LBNE and CHARM experiments. The number of events grows linearly with the number of protons on target, the number of produced charmed mesons, the detector length (decay region) and the detector area. In particular, this latter linear increase is valid if the angular spread of the neutrino flux, which is on the order of  $N_m M_D / E_{beam}$ , is larger than the angle at which the ND is seen from the target. Here  $N_m$  is the multiplicity of the produced hadrons, and the above condition is valid for both LBNE and CHARM. The number of events decreases linearly when the energy increases, since this increases the lifetime, reducing the

- 1 decay probability within the detector. Finally, the number of mesons decreases quadratically with
- 2 the distance between the target and the detector.

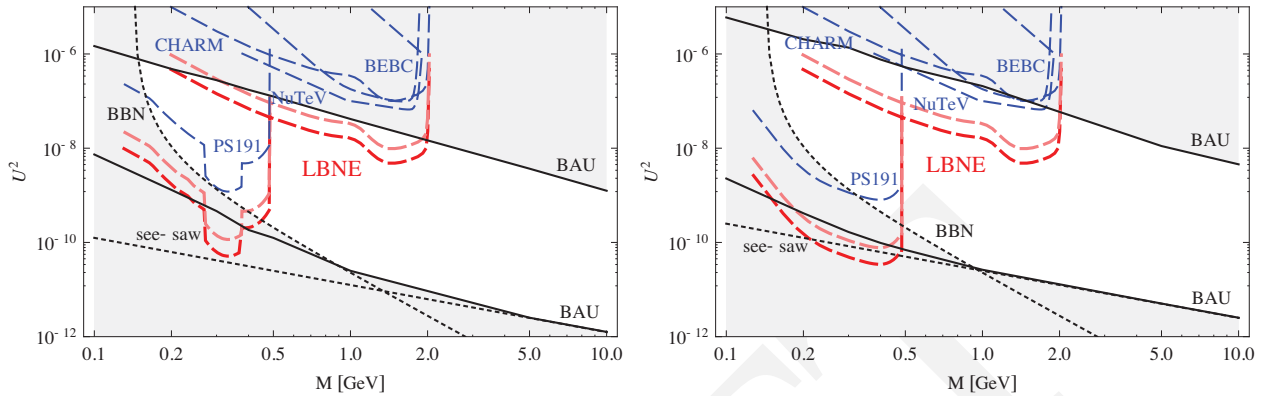


fig:heavyneu

**Figure 7.5:** Constraints on  $U^2$ , the mixing angle between heavy sterile neutrinos and the light active states, coming from the Baryon Asymmetry of the Universe (solid lines), from the seesaw mechanism (dotted line) and from the Big Bang nucleosynthesis (dotted line). The regions corresponding to different experimental searches are outlined by blue dashed lines. Left panel: normal hierarchy; right panel: inverted hierarchy (adopted from [284]). Pink and red curves indicate the expected sensitivity of the LBNE near detector with an exposure of  $5 \times 10^{21}$  pot ( $\sim 5$  years) with the 1.2-MW reference beam at 120 GeV for detector lengths of 7 m and 30 m, respectively (see text for details).

3 The considerations above imply that a search for  $\nu$ MSM sterile neutrinos in the LBNE ND can be  
 4 competitive after only five years of running with the reference beam, corresponding to an overall  
 5 integrated exposure of about  $5 \times 10^{21}$  POT with a proton energy of 120 GeV. The use of a low-  
 6 density, high-resolution spectrometer in the ND substantially reduces backgrounds and allows the  
 7 detection of both leptonic and hadronic decay modes. Assuming a fiducial length of the magnetized  
 8 tracker of 7 m as decay region, the ratio between the signal event to be observed in the LBNE ND  
 9 and those in the CHARM experiment can be estimated to be more than a factor of 50 after only  
 10 four years of running. Since both production and decay rates are proportional to the square of  
 11 the neutrino mixing angles, the corresponding improvement in the square of the neutrino mixing  
 12 angle  $U^2$  will be about a factor of seven with respect to the CHARM experiment. Figure 7.5 shows  
 13 the projected LBNE sensitivity in the  $(U^2, M)$  plane. At lower values of the mass of the heavy  
 14 neutrinos, additional constraints can be obtained for kaons by comparing the LBNE and PS191  
 15 experiments, as shown in Figure 7.5.

16 It must be noted that exploitation of the complete  $5 \nu + 5 \bar{\nu}$  years of data taking would further  
 17 improve the number of expected events by a factor of 2, since it scales linearly with the number of  
 18 protons on target. With the beam upgrade to 2.3 MW, this improvement would become a factor of  
 19 four with respect to the initial five year run and the 1.2 MW beam.

20 A better sensitivity to  $\nu$ MSM can be achieved by instrumenting the upstream region of the ND  
 21 hall (e.g., with the liquid argon detector and some minimal tracking device upstream). The fiducial  
 22 volume of the new detector will need to be empty (material-free) or fully sensitive in order to

1 suppress background events. The geometry of the ND hall would allow a maximal decay length  
 2 of about 30 m. The sensitivity of this configuration can be estimated by rescaling the expected  
 3 limits on mixing  $U^2$ . The expected number of signal events with a total decay length of  $\sim 30$  m  
 4 exceeds by about 200 (800) times the number of events in CHARM after a five (5 +5) year run  
 5 with the standard (upgraded) beam. In turn, this implies an improvement by a factor of 15 (28) in  
 6 the sensitivity to  $U^2$  with respect to the CHARM experiment.

7 It must be noted that if the magnetic moment of the sterile neutrinos is sizeable, the dominant  
 8 decay channel would be a radiative electromagnetic decay into  $\gamma\nu$ , which has also been proposed  
 9 as a possible explanation for the observed MiniBooNE low-energy excess [138]. This possibility,  
 10 in turn, requires a detector capable of identifying and reconstructing single photon events. The low-  
 11 density ND in LBNE can achieve an excellent sensitivity to this type of search as demonstrated by  
 12 a similar analysis in NOMAD [285].

## 13 7.8 Search for High $\Delta m^2$ Neutrino Oscillations

14 The evidence for neutrino oscillations obtained from atmospheric, long-baseline accelerator, so-  
 15 lar and long-baseline reactor data from different experiments consistently indicates two different  
 16 scales, with  $\Delta m_{32}^2 \sim 2.4 \times 10^{-3} \text{ eV}^2$  defining the atmospheric oscillations (also long-baseline ac-  
 17 celerator and short-baseline reactor scales) and  $\Delta m_{21}^2 \sim 7.9 \times 10^{-5} \text{ eV}^2$  defining the solar oscil-  
 18 lations (and long-baseline reactor oscillations). The only way to accommodate oscillations with  
 19 relatively high  $\Delta m^2$  at the  $\text{eV}^2$  scale as suggested by the results from the LSND experiment [286]  
 20 is therefore to add one or more sterile neutrinos to the conventional three light neutrinos.

21 Recently, the MiniBooNE experiment reported that its antineutrino data might be consistent with  
 22 the LSND  $\bar{\nu}_\mu \rightarrow \bar{\nu}_e$  oscillation with  $\Delta m^2 \sim \text{eV}^2$  [287]. Contrary to the antineutrino data, the neu-  
 23 trino data seem to exclude high  $\Delta m^2$  oscillations, possibly indicating a different behavior between  
 24 neutrinos and antineutrinos.

25 Models with five (3+2) or six (3+3) neutrinos can potentially explain the MiniBooNE results. In  
 26 addition to the cluster of the three neutrino mass states (accounting for *solar* and *atmospheric* mass  
 27 splitting), two (or three) states at the eV scale are added, with a small admixture of  $\nu_e$  and  $\nu_\mu$  to  
 28 account for the LSND signal. One distinct prediction from such models is a significant probability  
 29 for  $\bar{\nu}_\mu$  disappearance into sterile neutrinos, on the order of 10%, in addition to the small probability  
 30 for  $\bar{\nu}_e$  appearance.

Given a 460-m baseline and a low-energy beam, the LBNE ND can reach the same value  $L/E_\nu \sim 1$  as MiniBooNE and LSND. The large fluxes and the availability of fine-grained detectors make the LBNE program well suited to search for active-sterile neutrino oscillations beyond the three-flavor model with  $\Delta m^2$  at the eV<sup>2</sup> scale.

1

2 Due to the potential differences between neutrinos and antineutrinos, four possibilities have to be  
 3 considered in the analysis:  $\nu_\mu$  disappearance,  $\bar{\nu}_\mu$  disappearance,  $\nu_e$  appearance and  $\bar{\nu}_e$  appearance.  
 4 As discussed in Section 7.1, the search for high  $\Delta m^2$  oscillations has to be performed simultane-  
 5 ously with the in situ determination of the fluxes.

6 To this end, an independent prediction of the  $\nu_e$  and  $\bar{\nu}_e$  fluxes starting from the measured  $\nu_\mu$ - and  
 7  $\bar{\nu}_\mu$ -CC distributions are required since the  $\nu_e$  and  $\bar{\nu}_e$ -CC distributions could be distorted by the  
 8 appearance signal. The low- $\nu_0$  method can provide such predictions if external measurements for  
 9 the  $K_L^0$  component are available from hadro-production experiments (Section 7.1).

10 The study will implement an iterative procedure:

- 11 1. extraction of the fluxes from  $\nu_\mu$ - and  $\bar{\nu}_\mu$ -CC distributions assuming no oscillations are present
- 12 2. comparison with data and determination of oscillation parameters (if any)
- 13 3. new flux extraction after subtraction of the oscillation effect
- 14 4. iteration until convergence

15 The analysis has to be performed separately for neutrinos and antineutrinos due to potential CP or  
 16 CPT violation according to MiniBooNE/LSND data.

The ratio of  $\nu_e$ -CC events to  $\nu_\mu$ -CC events will be measured:

$$\mathcal{R}_{e\mu}(L/E) \equiv \frac{\# \text{ of } \nu_e N \rightarrow e^- X}{\# \text{ of } \nu_\mu N \rightarrow \mu^- X}(L/E); \quad \bar{\mathcal{R}}_{e\mu}(L/E) \equiv \frac{\# \text{ of } \bar{\nu}_e N \rightarrow e^+ X}{\# \text{ of } \bar{\nu}_\mu N \rightarrow \mu^+ X}(L/E) \quad (7.24)$$

17 This is then compared with the predictions obtained from the low- $\nu_0$  method. Deviations of  $\mathcal{R}_{e\mu}$  or  
 18  $\bar{\mathcal{R}}_{e\mu}$  from the expectations as a function of  $L/E$  would provide evidence for oscillations. It must be  
 19 noted that this procedure only provides a relative measurement of  $\nu_e(\bar{\nu}_e)$  versus  $\nu_\mu(\bar{\nu}_\mu)$ ; since the  
 20 fluxes are extracted from the observed  $\nu_\mu$ - and  $\bar{\nu}_\mu$ -CC distributions, an analysis of the  $\mathcal{R}_{e\mu}(\bar{\mathcal{R}}_{e\mu})$   
 21 ratio cannot distinguish between  $\nu_\mu(\bar{\nu}_\mu)$  disappearance and  $\nu_e(\bar{\nu}_e)$  appearance.

The process of NC elastic scattering off protons (Section 7.3) can provide the complementary mea-  
 surement needed to disentangle the two hypotheses of  $\nu_\mu(\bar{\nu}_\mu)$  disappearance into sterile neutrinos

and  $\nu_e(\bar{\nu}_e)$  appearance. In order to cancel systematic uncertainties, the NC/CC ratio with respect to quasi-elastic scattering will be measured:

$$\mathcal{R}_{NC}(L/E) \equiv \frac{\# \text{ of } \nu p \rightarrow \nu p}{\# \text{ of } \nu_\mu n \rightarrow \mu^- p}(L/E); \quad \overline{\mathcal{R}}_{NC}(L/E) \equiv \frac{\# \text{ of } \bar{\nu} p \rightarrow \bar{\nu} p}{\# \text{ of } \bar{\nu}_\mu p \rightarrow \mu^+ n}(L/E) \quad (7.25)$$

1 It is possible to reconstruct the neutrino energy from the proton angle and momentum under the  
 2 assumption that the nuclear smearing effects are small enough to neglect (the same for the neutrino  
 3 CC sample). In the oscillation analysis, only the *relative* distortions of the ratio  $\mathcal{R}_{NC}(\overline{\mathcal{R}}_{NC})$  as a  
 4 function of  $L/E$  are of interest, not their absolute values. For  $Q^2 > 0.2 \text{ GeV}^2$  the relative shape of  
 5 the total cross sections is not very sensitive to the details of the form factors. To improve the energy  
 6 resolution, it is possible to use neutrino interaction events originating from the deuterium inside  
 7 the  $\text{D}_2\text{O}$  target embedded into the fine-grained tracker. These events have better energy resolution  
 8 due to the smaller nuclear smearing effects in  $\text{D}_2\text{O}$ .

9 An improved oscillation analysis is based on a simultaneous fit to both  $\mathcal{R}_{e\mu}(\overline{\mathcal{R}}_{e\mu})$  and  $\mathcal{R}_{NC}(\overline{\mathcal{R}}_{NC})$ .  
 10 The first ratio provides a measurement of the oscillation parameters while the latter constrains the  
 11  $\nu_e(\bar{\nu}_e)$  appearance versus the  $\nu_\mu(\bar{\nu}_\mu)$  disappearance. This analysis imposes two main requirements  
 12 on the ND:

- 13 ○  $e^+/e^-$  separation to provide an unambiguous check of the different behavior between neu-  
 14 trinos and antineutrinos suggested by MiniBooNE
- 15 ○ accurate reconstruction of proton momentum and angle

16 Validation of the unfolding of the high  $\Delta m^2$  oscillations from the in situ extraction of the (anti)neutrino  
 17 flux would also require changes to the beam conditions, since the ND cannot be easily moved. This  
 18 would require a short run with a high-energy beam and the capability to change or switch off the  
 19 beam focusing system.

## 20 7.9 Light (sub-GeV) Dark Matter Searches

21 According to the latest cosmological and astrophysical measurements, nearly eighty percent of  
 22 the matter in the Universe is in the form of cold, non-baryonic dark matter (DM) [288,289]. The  
 23 search to find evidence of the particle (or particles) that make up DM, however, has so far turned up  
 24 empty. Direct detection experiments and indirect measurements at the LHC, however, are starting  
 25 to severely constrain the parameter space of Weakly-Interacting Massive Particles (WIMPs), one  
 26 of the leading candidates for DM. The lack of evidence for WIMPs at these experiments has forced  
 27 many in the theory community to reconsider.

28 Some theories consider an alternative possibility to the WIMP paradigm in which the DM mass is  
 29 much lighter than the electroweak scale (e.g., below the GeV level). In order to satisfy constraints

1 on the relic density of DM, these theories require that DM particles be accompanied by light  
 2 “mediator” particles that would have allowed for efficient DM annihilation in the early Universe.  
 3 In the simplest form of these theories an extra U(1) gauge field mixes with the Standard Model  
 4 (SM) U(1) gauge field, but with an additional kinetic term. This mixing term provides a “portal”  
 5 from the dark sector to the charged particles of the SM. In this model, the mediators are called  
 6 “dark photons” and are denoted by  $V$ .

Recently, a great deal of interest has been paid to the possibility of studying models of light  
 (sub-GeV) Dark Matter at low-energy, fixed-target experiments [290,291,292,293]. High-  
 flux neutrino beam experiments — such as LBNE — have been shown to potentially provide  
 coverage of DM+mediator parameter space which cannot be covered by either direct  
 detection or collider experiments.

7

8 Upon striking the target, the proton beam can produce the dark photons either directly through  
 9  $pp(pn) \rightarrow V$  as in the left-hand diagram of Figure 7.6 or indirectly through the production of a  
 10  $\pi^0$  or a  $\eta$  meson which then promptly decays into a SM photon and a dark photon as in the center  
 11 diagram in the figure. For the case where  $m_V > 2m_{DM}$ , the dark photons will quickly decay into  
 a pair of DM particles.

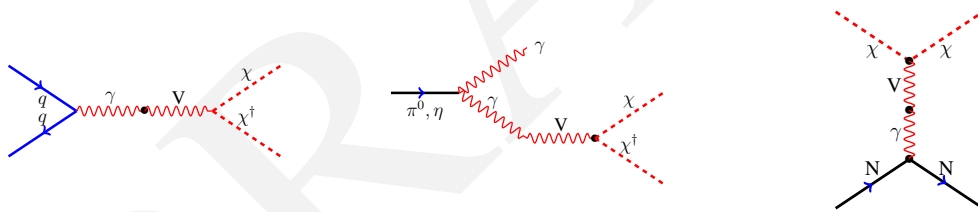


fig:dm

**Figure 7.6:** On the left is shown the direct production of a dark photon, while, in the center, the dark photon is produced via the decay of a neutral pion or eta meson. In both cases, the dark photon promptly decays into a pair of DM particles. Right: Tree-level scattering of a DM particle off of nuclei. Analogous interactions with electrons in the detector are also possible.

12

13 The LBNE ND and high-intensity beam together will provide an excellent setup for making this  
 14 measurement. These relativistic DM particles from the beam will travel along with the neutrinos  
 15 to the LBNE near detector. The DM particles can then be detected through neutral-current-like  
 16 interactions either with electrons or nucleons in the detector, as shown in the right-hand diagram of  
 17 Figure 7.6. Since the signature of a DM event looks similar to that of a neutrino event, the neutrino  
 18 beam provides the major source of background for the DM signal.

19 Several ways have been proposed to suppress neutrino backgrounds using the unique character-  
 20 istics of the DM beam. Since DM will travel much more slowly than the much lighter neutrinos,  
 21 DM events in the near detector will arrive out of time with the proton beam pulse. In addition,  
 22 since the electrons struck by DM will be in a much more forward direction compared to neutrino

- 1 interactions, the angle of these electrons may be used to reduce backgrounds, taking advantage of  
 2 the ND's fine angular resolution.
- 3 Finally, a special run can be devised to turn off the focusing horn to significantly reduce the charged  
 4 particle flux that will produce neutrinos. Figure 7.7 shows the expected sensitivity of the Mini-  
 5 BooNE DM search using this technique [293]. With a wider-band, higher-energy more intense  
 6 beam, LBNE is expected to not only cover the MiniBooNE sensitivity region with higher statis-  
 7 tics, but will also extend the sensitivity to cover the region between MiniBooNE and the direct  
 DM searches. If the LBNE ND were a LArTPC and the entire detector volume active, the effective

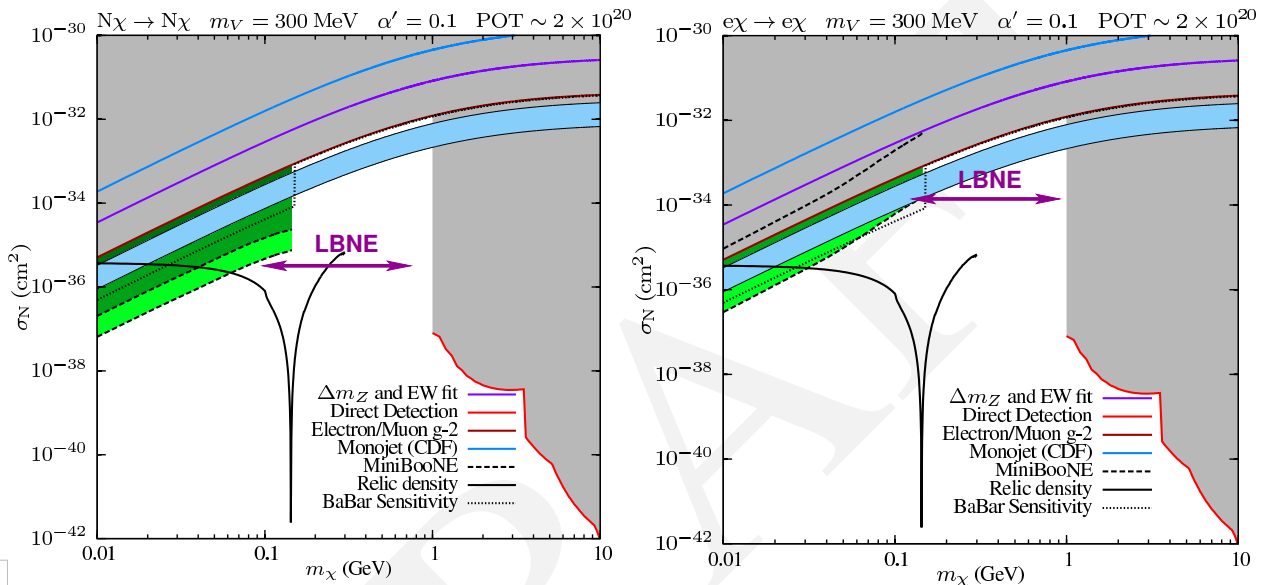


**Figure 7.7:** Regions of nucleon-WIMP scattering cross section (corresponding to dark matter in the lab moving with  $v = 10^{-3}c$ ). The plot uses  $m_\nu = 300\text{MeV}$  and  $\alpha' = 0.1$ . Constraints are shown from different experiments. The left plot shows the exclusion regions expected from MiniBooNE given 1-10 (light green), 10-1000 (green), and more than 1000 (dark green) elastic scattering events off nucleons. The right panel shows the same for elastic scattering off electrons. The magenta arrows indicate the region where LBNE can extend the MiniBooNE sensitivity. Figure is based on studies in [293].

- 8  
 9 number of DM events detected would be much higher when compared to a MINOS-like detector  
 10 of the same mass. Much more thorough studies must be conducted to obtain reliable sensitivities.  
 11 This requires an integration of theoretical predictions into a simulation package for the detector.

The deep underground location of LBNE's LArTPC far detector will expand the range of science opportunities it can pursue to potentially include observation of solar and other low-energy neutrinos, dark matter, magnetic monopoles and nucleon-antinucleon transitions.

## 8.1 Solar Neutrinos

sec:SolNu

In the early 20<sup>th</sup> century, Arthur Stanley Eddington suggested that nuclear reactions of protons fuel energy production in the sun. After the discovery of the neutron, Hans Bethe [294] proposed that the first stage of these nuclear reactions involves the weak interaction: a  $\beta$  decay of a proton into a neutron, a positron and a neutrino accompanied by the fusion of that neutron with another proton to form deuterium. This  $pp$  reaction  $p+p \rightarrow {}^1_1\text{H}+e^++\nu_e$  is the origin of most solar neutrinos (called  $pp$  neutrinos). In 0.2% of the cases deuterium is produced by the corresponding three-body reaction  $p+e^-+p \rightarrow {}^1_1\text{H}+\nu_e$  (called  $pep$ ) which produces mono-energetic solar neutrinos at 1.4 MeV. The  $pp$  reaction is the starting point of a chain of nuclear reactions which converts four protons into a  ${}^4_2\text{He}$  nucleus, two positrons, and two neutrinos. This reaction chain, shown in Figure 8.1, produces 98% of the energy from the Sun. In addition to  $pp$  and  $pep$ , neutrinos are produced by the reactions  ${}^7_4\text{Be}+e^- \rightarrow {}^7_3\text{Li}+\nu_e$  ( ${}^7\text{Be}$  neutrinos) and  ${}^3_2\text{He}+p \rightarrow {}^4_2\text{He}+e^++\nu_e$  (hep neutrinos) as well as the  $\beta$  decay  ${}^8_5\text{B} \rightarrow {}^8_4\text{Be}+e^++\nu_e \rightarrow {}^4_2\text{He}+{}^4_2\text{He}+e^++\nu_e$  ( ${}^8\text{B}$  neutrinos). Carl-Friedrich von Weizsäcker [295] complemented the  $pp$ -chain with a cyclical reaction chain dubbed *CNO cycle* after the principle elements involved (shown in the top right illustration of Figure 8.1). Although theorized to be responsible for only 2% of energy production in the Sun, the CNO cycle plays the dominant role in the energy production of stars heavier than 1.3 solar masses.

The expected spectra of neutrinos from the proton-proton reaction chain [296] are shown as solid curves in the bottom diagram of Figure 8.1. Neutrinos from the CNO cycle are shown as dashed blue curves.

The chief motivation of Raymond Davis to build his pioneering solar neutrino detector in the Homestake mine was the experimental verification of stellar energy production by the observation of the neutrinos from these nuclear processes. While he succeeded in carrying out the first measurements of solar neutrinos — and shared the 2002 Nobel Prize in physics for the results — the measured flux [111] fell short of solar model calculations: the “solar neutrino problem”. Data from the Super-Kamiokande and SNO [297,298] experiments eventually explained this mystery 30 years later as due to flavor transformation. However, intriguing questions in solar neutrino

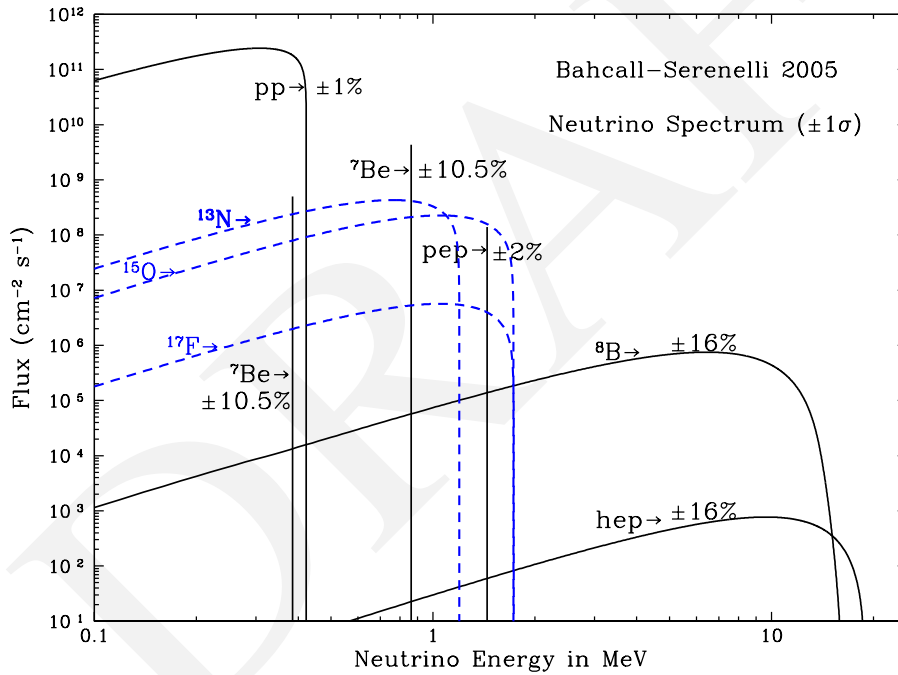
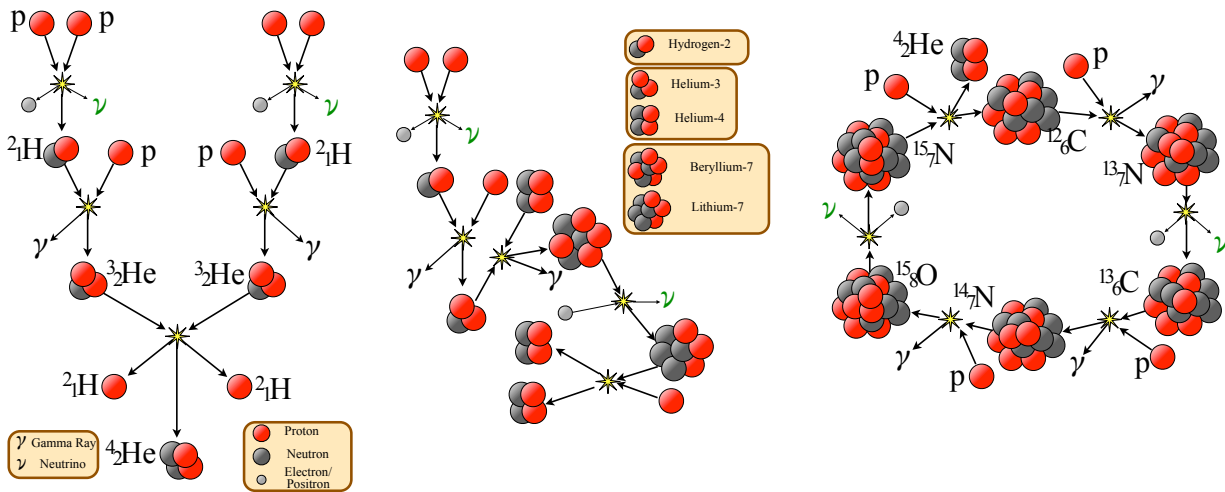


**Figure 8.1:** Top: The proton-proton and CNO reaction chain in the Sun. Bottom: solar neutrino fluxes from [296].

- 1 physics remain. Some unknowns, such as the fraction of energy production via the CNO cycle in
- 2 the Sun, flux variation due to helio-seismological modes that reach the solar core, or long-term
- 3 stability of the solar core temperature, are astrophysical in nature. Others directly impact particle
- 4 physics. Can the MSW model explain the amount of flavor transformation as a function of energy,
- 5 or are non-standard neutrino interactions required? Do solar neutrinos and reactor antineutrinos

oscillate with the same parameters? Experimental data expected in the immediate future (e.g., further data from Borexino [299] and Super-Kamiokande as well as SNO+ [300]) will address some questions, but the high-statistics measurements necessary to further constrain alternatives to the standard oscillation scenario may need to wait for a more capable experiment such as LBNE.

Detection of solar and other low-energy neutrinos is challenging in a LArTPC because of high intrinsic detection energy thresholds for the charged-current interaction on argon ( $>5$  MeV). To be competitive, this physics requires either a very low visible energy threshold ( $\sim 1$  MeV) or a very large mass (50 kt). However, compared with other technologies, a LArTPC offers a large cross section and unique signatures from de-excitation photons. Aggressive R&D efforts in low-energy triggering and control of background from radioactive elements may make detection in LBNE possible, and a large detector mass would make the pursuit of these measurements worthwhile.

5

The solar neutrino physics potential of a large LArTPC depends primarily on its energy threshold and depth. The energy threshold is not only determined by the ability to pick up a low-energy electron, but also by the light collection of the photon-triggering system as well as background suppression. Only at a deep underground location will it have a reasonable chance of detecting solar neutrinos. In any detector of this kind, the decay of the naturally occurring  $^{39}\text{Ar}$  produces  $\beta$ 's with a 567-keV endpoint and an expected rate of 10 MHz per 10 kt of liquid argon. This limits the fundamental reach of LBNE to neutrino interactions with visible energies above 1 MeV. Possible signatures of solar neutrinos in LBNE are:

**Elastic scattering of  $^8\text{B}$  neutrinos with electrons:** This signature would only reproduce the Super-Kamiokande data, which has already accumulated large statistics ( $>60,000$  solar neutrino events). An energy threshold of about 1 MeV (lower than the Super-Kamiokande threshold which is currently 3.5 MeV [301]) would be required for a more interesting measurement of *pep* (defined in Figure 8.1) and CNO fluxes. Such solar neutrino interactions are difficult to detect, as only low-energy single electrons (and neutrinos) are produced.

**Charged-current interactions with argon:** The signature for this interaction is:



This signal is more interesting experimentally, as there is a signature of de-excitation photons and the visible energy is directly correlated with the neutrino energy; however, the reaction has an energy threshold of 5 MeV.

Cosmic-muon and fast-neutrino interactions with the  $^{40}\text{Ar}$  nucleus (which are rather complex compared to interactions on  $^{16}\text{O}$  or  $^{12}\text{C}$ ) are likely to generate many long-lived spallation products that

could limit the detection threshold for low-energy neutrinos. Studies of the spallation background in the LBNE LArTPC are underway. The production rate of  $^{40}\text{Cl}$ , a beta emitter with an endpoint of 7.48 MeV that is a dominant source of background at energies above 5 MeV, is shown in Figure 8.2 as a function of depth. The cosmogenic background rates as a function of beta kinetic

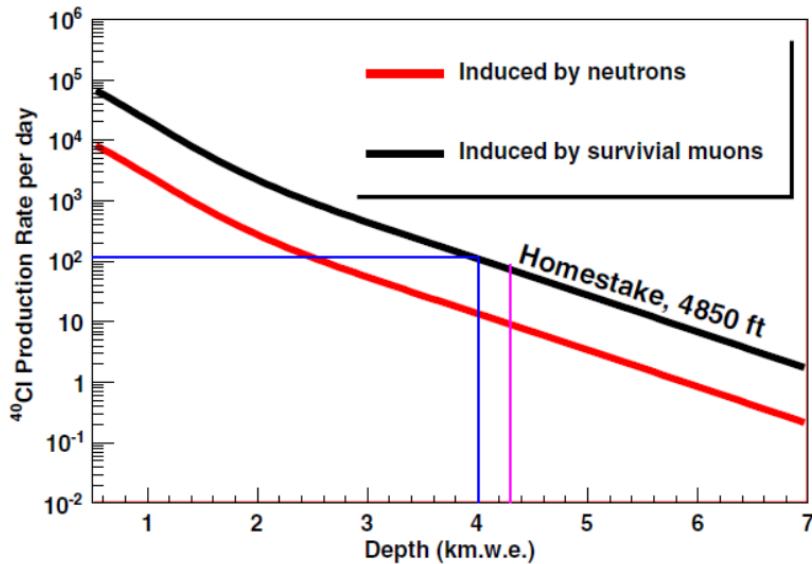


**Figure 8.2:**  $^{40}\text{Cl}$  production rates in a 10-kt detector produced by (n,p) reaction as a function of depth.

energy from several other beta emitters at the 4,850-ft level of Sanford Underground Research Facility are shown in Figure 6.8.

In Table 8.1 the solar neutrino event rate in a 34-kt LArTPC is shown, assuming a 4.5-MeV neutrino energy threshold and 31%  $\nu_e$ .

**Table 8.1:** Solar neutrino event rates in a 34-kt LArTPC assuming a 4.5-MeV neutrino energy threshold and 31%  $\nu_e$

Transition	Rate (evts/day)
Fermi	31
Gamow-Teller	88

The ICARUS collaboration has reported a 10-MeV threshold [304]. Assuming the detector itself has low enough radioactivity levels, this threshold level would enable a large enough detector to measure the electron flavor component of the solar  $^8\text{B}$  neutrino flux with high statistical accuracy. It could thereby further test the MSW flavor transformation curve (see Figure 8.3) with higher statistical precision and potentially better energy resolution.

In addition to these solar matter effects, solar neutrinos also probe terrestrial matter effects with the variation of the  $\nu_e$  flavor observed with solar zenith angle while the Sun is below the horizon

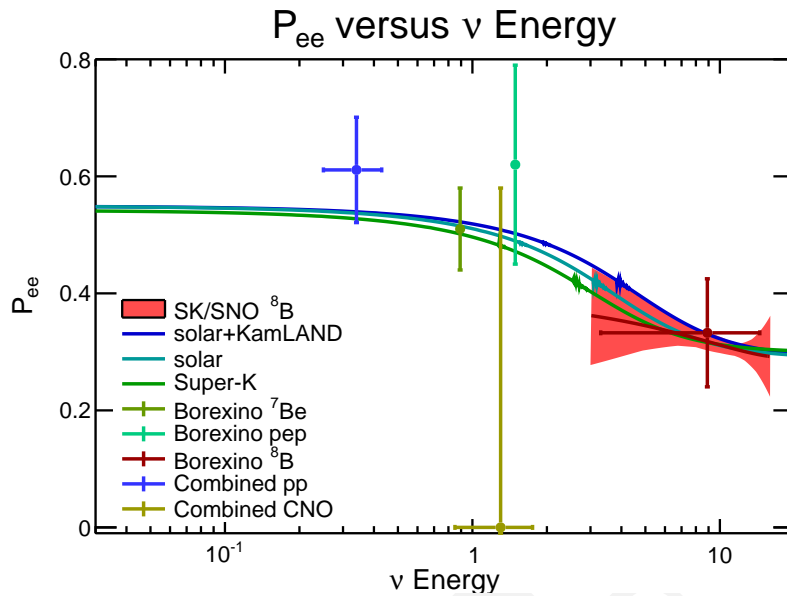


fig:solmsw

**Figure 8.3:** Measurements of the solar MSW transition. The red band combines SK and SNO  $^8\text{B}$  data [67], the green measurements of  $^7\text{Be}$  and pep are from Borexino [299,302] and the red error bar is Borexino's  $^8\text{B}$  measurement [303]. The blue  $pp$  point and the yellow error bar (CNO) combine all solar data. MSW resonance curves for three different parameters are overlaid.

1 — the *day/night effect*. A sizable effect is predicted only for the highest solar-neutrino energies, so  
 2 while the comparatively high energy threshold is a handicap for testing the solar MSW resonance  
 3 curve, it has a smaller impact on the high-statistics test of terrestrial matter effects. Recently, in-  
 4 dication of the existence of the terrestrial matter effects were reported [68]. Measurements of this  
 5 effect currently give the best constraints on the solar mass ( $\Delta m_{21}^2$ ) splitting (see Figure 8.4) using  
 6 neutrinos rather than antineutrinos [305].

7 The comparison of neutrino disappearance to antineutrino disappearance tests CPT invariance. For  
 8 good sensitivity to either solar-neutrino measurement, a liquid argon far detector of at least 34 kt is  
 9 required.

## 10 8.2 Indirect Searches for WIMP Dark Matter

sec:wimp

11 If the true nature of Dark Matter (DM) involves a weakly-interacting particle (WIMP) with a mass  
 12 on the order of 1 GeV, an experiment could look for anomalous signals in astrophysical data from  
 13 the annihilation (or decay) of DM into Standard Model particles, e.g., neutrinos [306]. Neutrinos  
 14 produced by DM decay are expected to come from such distant objects as the galactic center, the  
 15 center of the Sun or even from the Earth.

16 As our solar system moves through the DM halo, WIMPs interact with the nuclei of celestial  
 17 bodies and become trapped in a body's gravitational well. Over time, the WIMPs accumulate

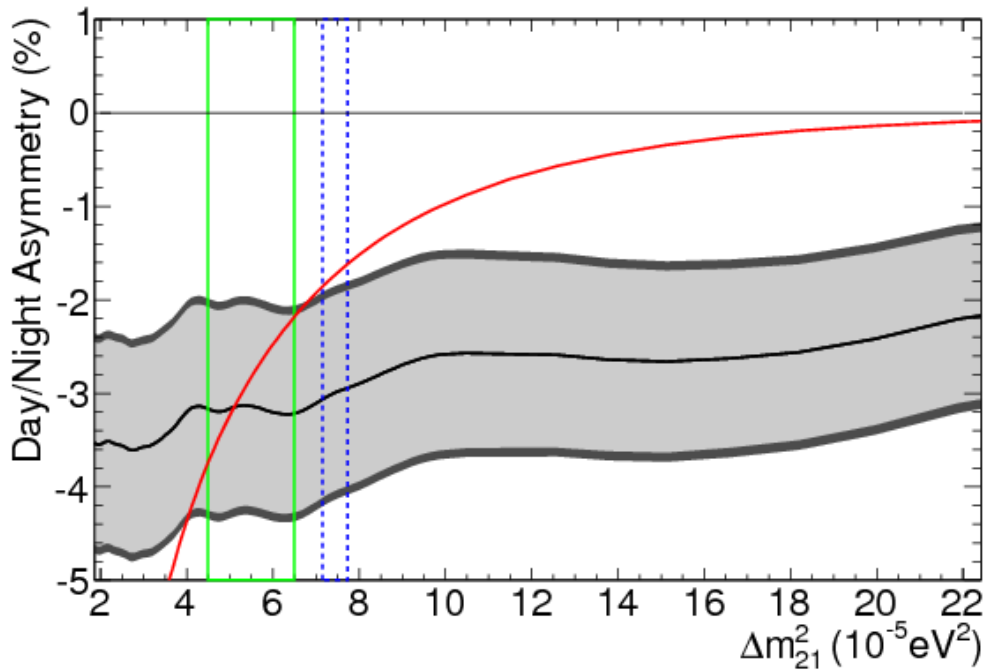


**Figure 8.4:** Dependence of the measured day/night asymmetry (fitted day/night amplitude times the expected day/night asymmetry in red) on  $\Delta m_{21}^2$ , for  $\sin^2 \theta_{12} = 0.314$  and  $\sin^2 \theta_{13} = 0.025$ . The  $1\sigma$  statistical uncertainties from the recent measurements by Super-Kamiokande are given by the light grey band. The additional dark grey width to the band shows the inclusion of the systematic uncertainties. Overlaid are the  $1\sigma$  allowed ranges from the solar global fit (solid green) and the KamLAND experiment (dashed blue). Figure is courtesy of [68]

- 1 near the core of the body, enhancing the possibility of annihilation. The high-energy neutrinos
- 2 ( $E \sim m_{\text{WIMP}}$ ) from these annihilations can free-stream through the astrophysical body and emerge
- 3 roughly unaffected, although oscillation and matter effects can slightly alter the energy spectrum.
- 4 Neutrinos produced via the nuclear-fusion processes in the Sun have energies close to 1 MeV,
- 5 much lower than likely DM-decay neutrino energies.

The LBNE far detector's large mass and directional tracking capabilities will enable it to act as a *neutrino telescope* and search for neutrino signals produced by annihilations of dark matter particles in the Sun and/or the core of the Earth. Detection of high-energy neutrinos coming exclusively from the Sun's direction, for example, would provide clear evidence of dark matter annihilation [307].

- 7 IMB [308], IceCube [309] and Super-Kamiokande, all water Cherenkov-based detectors, have
- 8 searched for signals of DM annihilations coming from these sources, so far with negative results. A
- 9 LArTPC can provide much better angular resolution than can water Cherenkov detectors, therefore
- 10 providing better separation of the directional solar WIMP signal from the atmospheric neutrino

1 background. More thorough studies [Blennow:2013pva, 310] are needed to determine whether LBNE could provide a  
 2 competitive detection of dark matter.

### 3 8.3 Supernova Relic Neutrinos

sec:SRN

4 Galactic supernovae are relatively rare, occurring somewhere between once and four times a cen-  
 5 tury (Chapter 6). In the Universe at large, however, thousands of neutrino-producing explosions  
 6 occur every hour. The resulting neutrinos — in fact most of the neutrinos emitted by all the su-  
 7 pernovae since the onset of stellar formation — suffuse the Universe. Known both as *supernova*  
 8 *relic neutrinos (SRN)* and as the *diffuse supernova neutrino background (DSNB)*, their energies are  
 9 in the few-to-30-MeV range. SRN have not yet been observed, but an observation would greatly  
 10 enhance our understanding of supernova-neutrino emission and the overall core-collapse rate.

A liquid argon detector such as LBNE's far detector is sensitive to the  $\nu_e$  component of the diffuse relic supernova neutrino flux, whereas water Cherenkov and scintillator detectors are sensitive to the  $\bar{\nu}_e$  component. However, backgrounds in liquid argon are as yet unknown, and a huge exposure ( $>500$  kt · years) would likely be required for observation. Given a detector of the scale required to achieve these exposures (50 kt to 100 kt) together with tight control of backgrounds, LBNE — in the long term — could play a unique and complementary role in the physics of relic neutrinos.

11  
 12 In the current LBNE design, the irreducible background from solar neutrinos will limit the search  
 13 for these relic neutrinos to an energy threshold greater than 18 MeV. Similarly, a search for relic an-  
 14 tineutrinos is limited by the reactor antineutrino background to a threshold greater than  $\sim 10$  MeV.  
 15 The lower threshold and the smaller average  $\nu_e$  energy relative to that for  $\bar{\nu}_e$  (see Figure 8.5) leads  
 16 to the need for a larger detector mass.

17 A small but dedicated industry devotes itself to trying to predict the flux of these relic supernova  
 18 neutrinos here on Earth [Potani:1995dw, Sato:1997sc, Hartmann:1997qe, Malaney:1996ar, Kaplinghat:1999xi, And  
 19 SRN spectra are shown in Figure 8.5, along with some of the key physics backgrounds from other  
 20 neutrino sources.

In the LBNE LArTPC, relic supernova electron neutrinos would be detected primarily via the charged current process as described by Equation 8.1. The electron track should be accompanied by evidence of ionization from the de-excitation of the potassium, e.g., shorter tracks sharing a common vertex; this is expected to help reduce backgrounds, but a detailed study has not yet been undertaken. In water Cherenkov and scintillator detectors, it is the electron-antineutrino SRN flux that is detected through the process of inverse-beta decay. Unlike inverse-beta decay, for which the cross section is known to the several-percent level in the energy range of interest [Vogel:1999zy, Strumia

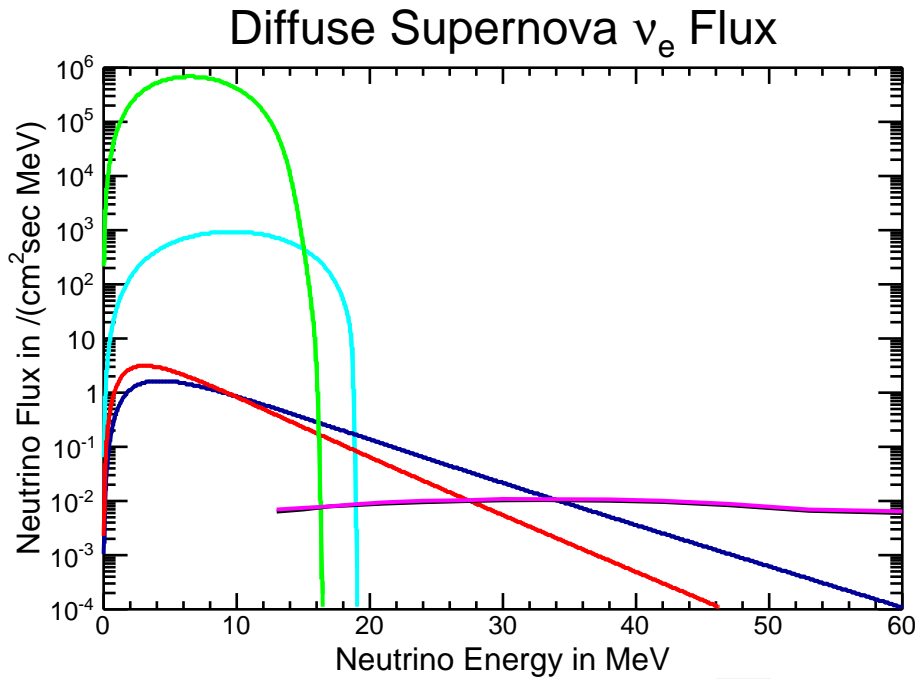


**Figure 8.5:** Predicted relic supernova  $\nu_e$  spectra from two different models (red and blue) and some key neutrino backgrounds:  ${}^8\text{B}$  solar  $\nu_e$  (green), hep solar  $\nu_e$  (cyan) and atmospheric  $\nu_e$  (magenta).

the cross section for neutrino interactions on argon is uncertain at the 20% level [321,322,323]. Another limitation is that the solar hep neutrinos (defined in Figure 8.1), which have an endpoint at 18.8 MeV, will determine the lower bound of the SRN search window ( $\sim 16$  MeV). The upper bound is determined by the atmospheric  $\nu_e$  flux as shown in Figure 8.5 and is around 40 MeV. Although the LArTPC provides a unique sensitivity to the electron-neutrino component of the SRN flux, early studies indicate that due to this lower bound of  $\sim 16$  MeV LBNE would need a huge mass of liquid argon — of order 100 kt — to get more than  $4\sigma$  evidence for the diffuse supernova flux in five years [324]. The expected number of relic supernova neutrinos,  $N_{\text{SRN}}$ , that could be observed in a 100-kt LArTPC detector in five years [324] assuming normal hierarchy is:

$$N_{\text{SRN}} = 57 \pm 12 \quad 16 \text{ MeV} \leq E_e \leq 40 \text{ MeV} \quad (8.2)$$

- 1 where  $E_e$  is the energy of the electron from the CC interaction as shown in Equation 8.1. The
- 2 estimate of the SRN rate shown in Equation 8.2 has a weak dependence on the value of  $\sin^2 \theta_{13}$ .
- 3 The above calculation is valid for values of  $\sin^2 \theta_{13} > 10^{-3}$ . The main challenge for detection of
- 4 such a low rate of relic neutrinos in a LArTPC is understanding how much of the large spallation
- 5 background from cosmic-ray interactions with the heavy argon nucleus (some of which are shown
- 6 in Figure 6.8) leaks into the SRN search window.

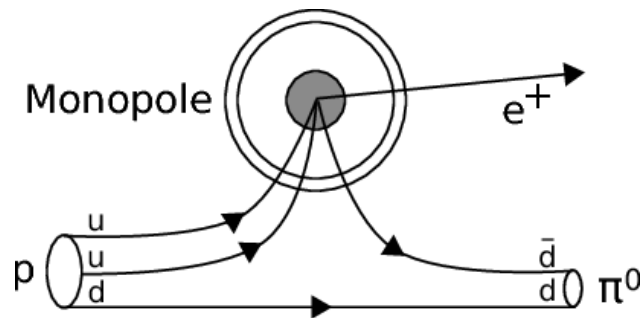


**Figure 8.6:** Illustration of a proton decay into a positron and a neutral pion catalyzed by a GUT monopole [328].

## 8.4 GUT Monopoles

- Searches for massive, slow-moving magnetic monopoles produced in the early universe continue to be of pressing interest. Magnetic monopoles left over from the big bang are predicted by Grand Unified Theories, but to date have not been observed. Because of the very large masses set by the GUT scale, these monopoles are normally non-relativistic, however searches for relativistic and ultra-relativistic monopoles are also of interest.
- Relativistic monopoles are expected to be heavily ionizing, and hence best suited for detection in the large-area, neutrino-telescope Cherenkov detectors deployed in natural bodies of water or ice (see, e.g., [325,326]). With its much smaller active area, LBNE will most likely not be competitive in searches for fast monopoles.
- Massive GUT monopoles are also postulated to catalyze nucleon decay (see Figure 8.6). It is possible that large underground detectors could detect this type of signal from transiting monopoles [327,328] via a signature consisting of multiple proton decays concurrent with the monopole's passage through the detector. Proton decay catalyzed by magnetic monopoles may be easier to observe in a LArTPC due to its superior imaging capability as compared to Cherenkov detectors, namely its high detection efficiency for a wider variety of proton decay modes, and its low energy thresholds. Whether these features are sufficient to overcome the limitation of smaller detector area relative to the very large neutrino telescopes has yet to be studied.
- It should also be possible for LBNE to detect slow-moving monopoles via time-of-flight measurements, thereby eliminating reliance on the assumption of a proton-decay catalysis signature. The most stringent limits from direct searches for GUT monopoles with velocities in the range  $4 \times 10^{-5} < \beta < 1$  have been obtained by the MACRO experiment [329], which has excluded fluxes at the level of  $1.4 \times 10^{-16} \text{ cm}^{-2} \text{ s}^{-1} \text{ sr}^{-1}$ . These limits probe the flux region just beyond that excluded by the existence of the galactic magnetic field (as characterized in variants of the Parker Bound).
- The LBNE LArTPC far detector option provides an opportunity to extend the reach of direct

1 searches for slow monopoles, thanks to excellent timing and ionization measurement capabili-  
 2 ties. Quantitative studies of sensitivity have yet to be carried out, but it is likely that the full-scope  
 3 LBNE far detector will exceed the **FIXME**: *fix units* isotropic-flux acceptance of MACRO.

## 4 8.5 Neutron-Antineutron Oscillations ( $\Delta B = 2$ )

5 Some Grand Unified Theories suggest the existence of double baryon-number-violating transitions  
 6 that change nucleons into antinucleons [330]. The nucleon-antinucleon annihilation resulting from  
 7 such a transition would provide an unmistakable signal in the LBNE LArTPC.

8 The imaging properties of the detector — superior to those of water detectors — would enable  
 9 observation of nucleon annihilation final states in which the signal is broadened by the mix of  
 10 charged and neutral hadrons. This signal could, however, be suppressed in a LArTPC if the neutron-  
 11 to-antineutron transition rate is suppressed for bound neutrons due to interactions with the other  
 12 nucleons.

## 13 8.6 Geo and Reactor $\bar{\nu}_e$ 's

14 Electron antineutrinos ( $\bar{\nu}_e$ 's) produced by radioactive decays of the uranium, thorium and potas-  
 15 sium present in the Earth are referred to as *geo-antineutrinos*. Decays of these three elements  
 16 are currently understood to be the dominant source of the heat that causes mantle convection, the  
 17 fundamental geological process that regulates the thermal evolution of the planet and shapes its sur-  
 18 face. Detection of these geo-antineutrinos near the Earth's surface can provide direct information  
 19 about the deep-Earth uranium and thorium content.

20 Geo-antineutrino energies are typically below 3.5 MeV. Reactor antineutrinos are somewhat more  
 21 energetic, up to 8 MeV.

In a LArTPC, electron antineutrinos can in principle be detected by argon inverse-beta decay,  
 represented by



22 However, the threshold for this reaction is about 8.5 MeV, leading to the conclusion that an  ${}^{40}\text{Ar}$   
 23 detector cannot use this method to detect either geo-antineutrinos or reactor antineutrinos.

24 Interaction via elastic scattering with electrons, another potential avenue, presents other obstacles.  
 25 Not only are the recoil electrons from this interaction produced at very low energies, but solar  
 26 neutrinos scatter off electrons and form an irreducible background roughly a thousand times larger  
 27 than the geo-antineutrino signal. Although LBNE's location far away from any nuclear reactors  
 28 leaves only a small reactor antineutrino background and is thus favorable for geo-antineutrino  
 29 detection, another detector technology (e.g., liquid scintillator) would be required to do so.

conclusion-chap

2 The preceding chapters of this document describe the design of the Long-Baseline Neutrino Ex-  
3 periment, its technical capabilities, and the breadth of physics topics at the forefront of particle  
4 and astrophysics the experiment can address. This chapter concludes the document with several  
5 discussions that look forward in time, specifically:

- 6 ○ First, a consideration of how the design and construction of the LBNE experiment might  
7 unfold from this point on for a general class of staging scenarios.
- 8 ○ Second, within this context of a particular schedule of operations, a summary of the grand  
9 vision for the science of LBNE and its potential for transformative discovery.
- 10 ○ Third, a summary of the compelling reasons — such as LBNE’s current advanced state  
11 of technical development and planning, and its alignment with the national High Energy  
12 Physics (HEP) program — for which *LBNE represents the world’s best chance for address-*  
13 *ing this science on a reasonable timescale.*
- 14 ○ Finally, comments on the broader impacts of LBNE, including the overarching benefits to  
15 the field of HEP, both within and beyond the U.S. program.

## 16 9.1 Staging Scenarios and Timeline

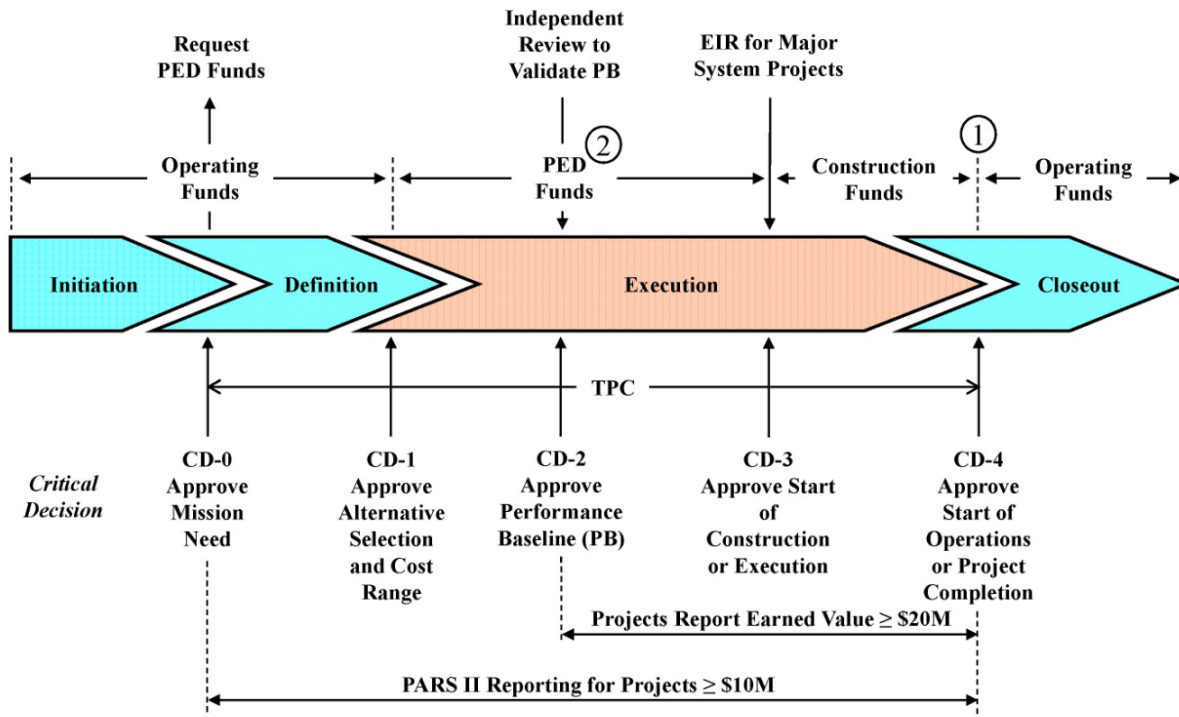
staging-timeline

With DOE CD-1 (“Alternate Selection and Cost Range”) approval in hand, the LBNE Project is working toward its technical design specifications, including detailed costs and schedule, in preparation for CD-2 (“Performance Baseline”). It should be noted that the Project already has fully developed schedules for both the CD-1 scope (10-kt far detector on the surface at the Sanford Underground Research Facility, and no near neutrino detector), and for the full-scope (34-kt far detector located deep underground and full near neutrino detector) for the scenario of full funding from DOE. However, given the current understanding of DOE budgets, contributions from international and non-DOE domestic partners will be required to realize the full-scope LBNE in a timely way.

17

18 Section [1.2.3](#) sec:global-partner has already described the substantial progress that has been achieved so far toward  
19 making LBNE a fully international project. While the specific form and timing of contributions  
20 from new partners are not yet known, there are several plausible scenarios in which the Project can  
21 be implemented to accommodate non-DOE contributions. A review of the DOE project milestones,

- 1 indicating where flexibility and potential for incorporating non-DOE contributions exist, provides
- 2 a starting point.
- 3 DOE-funded projects are subject to several *critical decision (CD)* milestones as shown in Figure 9.1 and explained in DOE Order O 413.3B [331]. At CD-2 the LBNE Phase 1 Project will



**NOTES:**

- 1. Operating Funds may be used prior to CD-4 for transition, startup, and training costs.
- 2. PED funds can be used after CD-3 for design.

**Figure 9.1:** Typical DOE Acquisition Management System for line item capital asset projects [331].

4 be baselined. Currently, the timescale for CD-2 is projected to be toward the end of FY 2016, al-

5 though the DOE has indicated flexibility in the project approval process specifically to allow for

6 incorporation of scope changes enabled by additional partners. For example, it has been suggested

7 that the design and construction approval for different portions of the project can be approved at

8 different times to facilitate proper integration of international partners. It is also expected that CD-

9 3a approval (start of construction/execution) may take place for some parts of the Project before

10 CD-2, thereby authorizing expenditures for long-leadtime components and construction activities,

11 such as the advanced site preparation at Fermilab for the new beamline. The CD-4 milestone (com-

12 pletion of the construction project and transition to experiment operations) is currently projected

13 for 2025. However, it is expected that commissioning and operations for LBNE will have started

14 approximately a year before CD-4, which is considered the formal termination of the construction

15 project.

16

1 The actual timeframe for achieving LBNE science goals will depend on the manner in which a  
2 complex sequence of developments takes place, including the actions of partners as well as imple-  
3 mentation of the milestones above for the DOE-funded elements of the Project. Various scenarios  
4 for incorporating contributions from new partners/sources of funding have been identified [332].

5

Using the current understanding of DOE funding profiles, we provide one plausible long-term timeline that integrates evolution of LBNE detector mass with development of the Fermilab accelerator complex (i.e., PIP-II) and contributions from non-DOE partners. Implicit in this timeline is an assumption that agreements with new partners are put in place on a timescale of three years (by 2017). In this scenario, the milestones that bear on the physics are as follows:

1. LBNE begins operation in 2025 with a 1.2-MW beam and a 15-kt far detector. (In such a scenario, a significant fraction of the far detector mass might be provided in the form of a standalone LArTPC module developed, funded, and constructed by international partners.)
2. Data are recorded for five years, for a net exposure of  $90 \text{ kt} \cdot \text{MW} \cdot \text{year}$ .
3. In 2030, the LBNE far detector mass is increased to 34 kt, and proton beam power is increased to 2.3 MW.
4. After five years of additional running, a net exposure of  $490 \text{ kt} \cdot \text{MW} \cdot \text{year}$  is attained by 2035.

6

7 Physics considerations will dictate the desired extent of operation of LBNE beyond 2035.

8 Not all key experiment milestones are indicated in this very coarse timeline. This is indicative of  
9 the degree of flexibility available for the staging of various elements of LBNE. For example, near  
10 detector construction (and the corresponding funding) could be undertaken by partners outside the  
11 U.S., on a timescale driven by the constraints they face, and could be completed somewhat earlier  
12 or later than the far detector or beamline.

13 With this timeline as a guide, the discussion of LBNE physics milestones can now be anchored by  
14 plausible construction scenarios.

## 9.2 Science Impact

While considering the practical challenges implicit in the discussion in Section 9.1 in realizing LBNE, it is important to reiterate the compelling science motivation in broad terms.

The discovery that neutrinos have mass constitutes the only palpable evidence *within the body of particle physics data* that the Standard Model of electroweak and strong interactions (SM) does not describe all observed phenomena. In the Standard Model, the simple Higgs mechanism — now confirmed with the observation of the Higgs boson — is responsible for quark as well as lepton masses, mixing and CP violation. Puzzling features such as the extremely small masses of neutrinos compared to other fermions and the large extent of mixing in the lepton sector relative to the quark sector, suggest that new physics not included in the current Standard Model is needed to connect the two sectors. These discoveries have moved the study of neutrino properties to the forefront of experimental and theoretical particle physics as a crucial tool for understanding the fundamental nature and underlying symmetries of the physical world.

The measurement of the neutrino mass hierarchy and search for CP violation in LBNE will further clarify the pattern of mixing and mass ordering in the lepton sector and its relation to the patterns in the quark sector. The impact of exposures of 90 kt · MW · year (2030) and 490 kt · MW · year (2035) for Mass Hierarchy and CP-violation signatures is easily extracted from Figure 4.16. Should CP be violated through neutrino mixing effects, the typical signal in LBNE establishing this would have a significance of at least three (2030) and five standard deviations (2035), respectively for 50% of  $\delta_{CP}$  values (and greater than three standard deviations for nearly 75% of  $\delta_{CP}$  by 2035). In such a scenario, the mass hierarchy can be resolved with a sensitivity for a typical experiment of  $\sqrt{\Delta\chi^2} \geq 6$  for 50% (100%) of  $\delta_{CP}$  by 2030 (2035).

If CP is violated maximally with a CP phase of  $\delta_{CP} \sim -\pi/2$  as hinted at by global analyses of recent data [61], the significance would be in excess of  $7\sigma$ . This opportunity to establish the paradigm of leptonic CP violation is highly compelling, particularly in light of the implications for leptogenesis as an explanation for the Baryon Asymmetry of the Universe (BAU). With tight control of systematic uncertainties, additional data taking beyond 2035 would provide an opportunity to strengthen a marginally significant signal should  $\delta_{CP}$  take a less favorable value.

Similarly, the typical LBNE data set will provide evidence for a particular mass ordering by 2030 in the scenario described in Section 9.1, and will exclude the incorrect hypothesis at a high degree of confidence by 2035, over the full range of possible values for  $\delta_{CP}$ ,  $\theta_{23}$  and the mass ordering itself. In addition to the implications for models of neutrino mass and mixing directly following from this measurement, such a result could take on even greater importance. Should LBNE exclude the normal hierarchy hypothesis, the predicted rate for neutrinoless double-beta decay would then

1 be high enough so as to be accessible to the next generation of experiments [333]. A positive result  
2 from these experiments would provide unambiguous — and exciting — evidence that neutrinos are  
3 Majorana particles\*, and that the empirical law of lepton number conservation — an law lacking  
4 deeper theoretical explanation — is not exact. Such a discovery would indicate that there may be  
5 heavier sterile right-handed neutrinos that mix with ordinary neutrinos, giving rise to the tiny ob-  
6 served neutrino masses as proposed by the seesaw mechanism [59]. On the other hand, a rejection  
7 of the normal neutrino mass hierarchy by LBNE coupled with a null result from the next genera-  
8 tion of neutrinoless double-beta decay experiments would lead to the conclusion that neutrinos are  
9 purely Dirac particles. This would be a profound and astonishing realization, since it is extremely  
10 difficult theoretically to explain the tiny masses of Dirac neutrinos. High-precision neutrino os-  
11 cillation measurements carried out by LBNE beyond 2035 may provide evidence for Majorana  
12 neutrino mass effects that are outside of the ordinary Higgs mechanism or for new interactions that  
13 differentiate the various neutrino species.

14 Within the program of underground physics, LBNE’s most exciting milestones would correspond  
15 to observations of rare events. By 2035, LBNE will have been live for galactic supernova neutrino  
16 bursts for ten years in the above scenario. Such an event would provide a spectacular data set that  
17 would likely be studied for years and even decades to follow.

18 For proton decay, the net exposure obtained by 2035 in the above scenario also provides a com-  
19 pelling opportunity. A partial lifetime for  $p \rightarrow K^+ \bar{\nu}$  of  $1 \times 10^{34}$  years, beyond the current limit  
20 from Super-Kamiokande by roughly a factor of two, would correspond to six candidate events  
21 in LBNE by 2035, with 0.25 background events expected. Running for seven more years would  
22 double this sample. (Similarly, one should not ignore the corresponding value of an LBNE con-  
23 struction scenario that has a larger detector mass operating from the start, in 2025). With careful  
24 study of backgrounds, it may also be possible to suppress them further and/or relax fiducial cuts to  
25 gain further in sensitivity.

26 Finally, the proposed high-resolution near detector, operating in the high-intensity LBNE neu-  
27 trino beam, will not only constrain the systematic errors that affect the oscillation physics but  
28 will also conduct comprehensive measurements of neutrino interactions — from cross sections to  
29 electroweak constants — with unmatched precision.

## 30 9.3 Uniqueness of Opportunity

31 Considering the time and overall effort taken to reach the current state of development of LBNE,  
32 it will be challenging for alternative programs of similarly ambitious scope to begin operation be-  
33 fore 2025, particularly in light of the current constrained budget conditions in HEP. It should be  
34 noted that similar-cost alternatives for the first phase of LBNE utilizing the existing NuMI beam

---

\*A Majorana particle is an elementary particle that is also its own antiparticle

1 were considered during the reconfiguration exercise in 2012 [17]. The panel concluded that none  
2 of these alternatives presented a path toward an experiment capable of a CP-violation signal of  
3  $5\sigma$ . Furthermore, a large water Cherenkov far detector option for LBNE was carefully considered  
4 prior to selection of the LArTPC technology [334]. While both detector options are capable of sat-  
5 isfying the scientific requirements, the LArTPC was judged to have a better potential for scientific  
6 performance while also presenting the attraction of an advanced technological approach.

7 In the broader context of planned experimental programs with overlapping aims for portions of the  
8 LBNE science scope, it must be recognized that progress will be made toward some of these during  
9 the period before LBNE operations commence. For example, indications for a preferred neutrino  
10 mass ordering may emerge from currently running experiments and/or from dedicated initiatives  
11 that can be realized on a shorter timescale. Global fits will continue to be done to capitalize, to  
12 the extent possible, on the rich phenomenology of neutrino oscillation physics where disparate  
13 effects are intertwined. At the same time, each experimental arena will be subject to its own set of  
14 systematic uncertainties and limitations.

15 It is in this sense that the power of LBNE is especially compelling. LBNE will on its own be able  
16 to measure the full suite of neutrino mixing parameters, and with redundancy in some cases. To  
17 use the MH example just given, it is notable that LBNE will have sensitivity both with beam and  
18 atmospheric neutrinos. Control of the relative  $\nu_\mu/\bar{\nu}_\mu$  content of the beam as well as the neutrino  
19 energy spectrum itself, provides additional handles and cross-checks absent in other approaches.

## 20 9.4 Broader Impacts

### 21 9.4.1 Intensity Frontier Leadership

22 The U.S. HEP community faces serious challenges to maintain its vibrancy in the coming decades.  
23 As is currently the case with the LHC, the next-generation energy frontier facility is likely to be  
24 sited outside the U.S. It is critical that the U.S. host facilities aimed at pursuing science at the  
25 HEP scientific frontiers (Figure 3.1), the lack of which could result in erosion of expertise in key  
26 technical and scientific sectors (such as accelerator and beam physics).

LBNE represents a world-class U.S.-based effort to address the science of neutrinos with  
technologically advanced experimental techniques. By anchoring the U.S. Intensity Frontier  
program [335], LBNE provides a platform around which to grow and sustain core infras-  
structure for the community. Development of the Fermilab accelerator systems, in particular,  
will not only advance progress towards achieving the science goals of LBNE, it will also  
greatly expand the capability of Fermilab to host other key experimental programs at the  
Intensity Frontier.

### 9.4.2 Inspirational Project for a New Generation

Attracting young scientists to the field demands a future that is rich with ground-breaking scientific opportunities. LBNE provides such a future, both in the technical development efforts required and its physics reach. The unparalleled potential of LBNE to address fundamental questions about the nature of our Universe by making high-precision, unambiguous measurements with the ambitious technologies it incorporates will attract the best and brightest scientists of the next generation to the U.S. HEP effort.

A young scientist excited by these prospects can already participate in current experiments — some of which use medium-scale LArTPCs — and make contributions to leading-edge R&D activities that provide important preparation for LBNE, both scientifically and technically.

## 9.5 Concluding Remarks

Understanding the fundamental nature of fermion flavor, the existence of CP violation in the lepton sector and how this relates to the Baryon Asymmetry of the Universe; knowing whether proton decay occurs and how; and elucidating the dynamics of supernova explosions all stand among the grand questions of physics. The bold approach adopted for LBNE provides the most rapid and cost-effective means of addressing these questions. With the support of the HEP community, the vision articulated in this document can be realized in a way that maintains the level of excitement for particle physics and the inspirational impact it has in the U.S. and worldwide.

DRAFT

app-sim

A 10-kt or larger LArTPC far detector fulfills the high-mass requirement for LBNE and provides excellent particle identification with high signal-selection efficiency ( $\geq 80\%$ ) over a wide range of energies as described in the LBNE Conceptual Design Report Volume 1 [21]. The far detector design is also described in some detail in Section 3.6 of this document. The status of the LBNE LArTPC simulation and reconstruction efforts and their expected performance are summarized in this appendix.

## A.1 Far Detector Simulation

### A.1.1 Tools and Methods

In the full detector simulation, neutrino interactions in the far detector are simulated with Geant4 [123] using the LArSoft [211] package. LArSoft is being developed to provide an integrated, experiment-agnostic set of software tools to perform simulation, data reconstruction and analysis for LArTPC neutrino experiments. Individual experiments provide experiment-specific components including detector geometry description and analysis code and they contribute to the effort to development the LArSoft software itself.

LArSoft is based on *art* [336]. *Art* is an event-processing framework developed and supported by the Fermilab Scientific Computing Division. It is designed to be shared by multiple experiments and is currently used by several intensity frontier experiments, including NO $\nu$ A, Mu2e, MicroBooNE [337], and ArgoNeuT [338]. The latter two experiments have detectors which are based on liquid argon TPCs, and thus share many simulation and reconstruction requirements with LBNE. Reconstruction algorithms developed in LArSoft for the ArgoNeuT and MicroBooNE experiments can readily benefit LBNE. Examples of neutrino beam interactions in a LArTPC obtained from the LArSoft package using the MicroBooNE detector geometry are shown in Figure A.1.

The LBNE far detector design is summarized in Section 3.6. The LBNE far detector geometries that are available in LArSoft currently are the LBNE 10-kt surface detector and the 34-kt underground detector. The 35-t prototype geometry is also included.

The LBNE far detector geometry description is generated in a flexible way that allows the simulation of differing detector design parameters such as the wire spacing and angles, drift distances, and materials. The photon detectors modeled based on the design which uses acrylic bars coated with wavelength-shifting tetraphenyl butadiene (TPB) and which are read out with silicon photomultiplier tubes (SiPM).

Geant4 is used to simulate particles traveling through the active and inactive detector volumes and

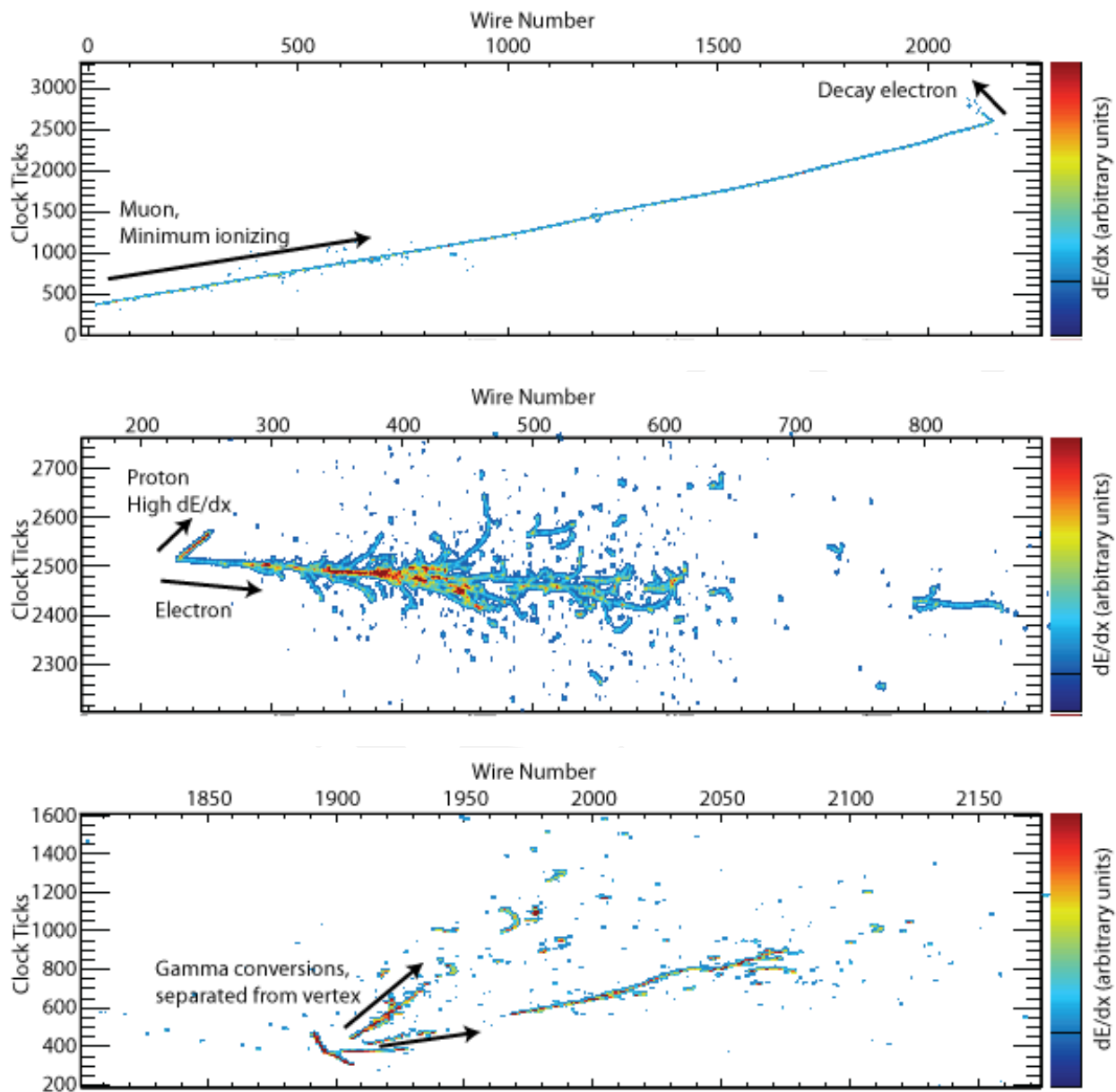


**Figure A.1:** Examples of neutrino beam interactions in a LArTPC obtained from a Geant4 simulation [211]. A  $\nu_\mu$ -CC interaction with a stopped  $\mu$  followed by a decay Michel electron (top), a CCQE  $\nu_e$  interaction with a single electron and a proton (middle), and an NC interaction which produced a  $\pi^0$  that then decayed into two  $\gamma$ 's with separate conversion vertices (bottom).

Church:2013hea

1 the surrounding materials such as the cryostat and rock. The tens of thousands of photons and elec-  
2 trons per MeV of energy deposited that are produced by the ionization of the argon are simulated  
3 using a parameterization rather than a full Geant4 Monte Carlo as tracking them individually would  
4 be prohibitive. The drifting electrons are modeled as many small clouds of charge that diffuse as  
5 they travel towards the collection wires. The response of the channels to the drifting electrons is  
6 parameterized as a function of drift time, with a separate response function for collection and in-  
7 duction wires. The signals on the induction-plane wires result from induced currents and are thus  
8 bipolar as a function of time, as charge drifts past the wires, while the signals on the collection-  
9 plane wires are unipolar. The response functions include the expected response of the electronics.  
10 Noise is simulated using a spectrum measured in the ArgoNeuT detector. The decays of  $^{39}\text{Ar}$  are  
11 included, but some work is required to make them more realistic.

12 For the 10-kt far detector, a 1.5 ms readout of the TPC signals at 2 MHz gives a simulated data  
13 volume of just under 2 GB per event. More data volume will be required if the readout is extended  
14 before and after the drift time including the beam window, which will be required in order to collect  
15 charge deposited by cosmic rays which would otherwise be partially contained. In order to reduce  
16 the data volume and speed up the calculation, long strings of consecutive ADC counts below a  
17 specifiable threshold are suppressed in the readout. Huffman coding of the remaining data is also  
18 included in the digitization [339].

19 The photon detection system likewise requires a full Monte Carlo simulation. Photons propagating  
20 from the TPC to the acrylic bars have been fully simulated using Geant4, and their probabilities  
21 of striking each bar as functions of the emission location and the position along the bar at which  
22 the photon strikes have been computed. Smooth parameterizations of these functions are currently  
23 used in the simulation to compute the average numbers of photons expected to strike a bar as a  
24 function of position along the bar. Given the current design of the optical detectors, approximately  
25 2-3% of VUV (vacuum ultraviolet) photons produced uniformly in the fiducial detector volume  
26 strike the bars. This low number is largely due to the small fraction of the total area in contact  
27 with the argon that is represented by the bars, and the low reflectivity of the stainless steel cathode  
28 planes, field cage, and CuBe wires.

29 A second function is used to parameterize the attenuation of light within the bar as a function  
30 of position along the bar. The expected number of photons surviving propagation, the interaction  
31 with the wavelength shifter (commonly called *downconversion*), attenuation in the bar, and the  
32 detection efficiency of the SiPM is then used as the mean of a Poisson distribution for simulating  
33 individual photon electrons. Measured waveforms for cold SiPMs are used in simulating the digi-  
34 tized response. Measurements in prototype dewars will be used to normalize the yield for signals  
35 in the SiPMs as a function of the incident location of the VUV photon on the bar. The NEST [340]  
36 model, which describes the conversion of ionization energy into both electrons and photons in an  
37 anticorrelated manner, and which has been shown to model a large range of data from noble liquid  
38 detectors, is currently being incorporated into the LBNE detector simulation.

1 A variety of different event generators is available for use in the simulation. Neutrino hard scatter-  
 2 ing interactions and subsequent nuclear breakup are simulated using GENIE [124], though using  
 3 other generators is possible. Cosmic rays are simulated with CRY [341]. Single particles can be  
 4 generated one at a time, and general text-file interfaces are available allowing arbitrary generators  
 5 to be used without linking them with LArSoft.

6 Currently, samples of single electrons, muons, charged and neutral pions, protons and tau leptons  
 7 have been generated and simulated using the 10-kt surface geometry and the 35-ton geometry,  
 8 though without photon-detector simulation. These samples are being used to develop reconstruc-  
 9 tion algorithms.

10 Future planned improvements to the simulation include creating an interface to a calibration database,  
 11 updating the response functions with measured responses from MicroBooNE, which uses an elec-  
 12 tronics design very similar to that of LBNE, simulating the effects of space-charge buildup in the  
 13 drift volume, and creating more detailed maps of the drift in the gaps between the APAs and the  
 14 charge that is deposited between the wire planes.

### 15 A.1.2 Low-energy Neutrino Response Studies with LArSoft

16 Work is currently underway using the LArSoft simulation package to characterize low-energy  
 17 response for realistic LBNE detector configurations. Figure A.2 shows a sample 20-MeV event  
 18 in the LBNE 35-t prototype geometry simulated with LArSoft \*. So far, most studies have been  
 19 done with the MicroBooNE geometry but the results are expected to be generally applicable to  
 20 the larger detector. For a preliminary understanding of achievable energy resolution, isotropic and  
 21 uniform mono-energetic electrons with energies of 5-50 MeV (which should approximate the  $\nu_e$ -  
 22 CC electron products) were simulated and reconstructed with the LArSoft package. The charge of  
 23 reconstructed hits on the collection plane was used to reconstruct the energy of primary electrons.  
 24 (Induction plane charge as well as track-length-based reconstruction were also considered, but  
 25 with inferior results). Figure A.3 shows the results. A correction to compensate for loss of electrons  
 26 during drift,  $Q_{collection} = Q_{production} \times e^{-T_{drift}/T_{electron}}$  (where  $T_{drift}$  is the drift time of the ionization  
 27 electrons, and  $T_{electron}$  is the electron lifetime), using Monte Carlo truth to evaluate  $T_{drift}$ , improved  
 28 resolution significantly. This study indicated that photon time information will be valuable for low-  
 29 energy event reconstruction. Some of the resolution was determined to be due to imperfect hit-  
 30 finding by the nominal reconstruction software. A tuned hit-finding algorithm did somewhat better  
 31 (see Figure A.3), and further improvements for reconstruction algorithms optimized for low-energy  
 32 events are expected.

33 Also under study is the potential for tagging  $\nu_e$ -CC absorption events ( $\nu_e + {}^{40}\text{Ar} \rightarrow e^- + {}^{40}\text{K}^*$ ) using  
 34 the cascade of de-excitation  $\gamma$ -rays, which should serve the dual purposes of rejecting background

\*One of the goals of the 35-t prototype is to test key elements of the TPC module design for the 10-kt and 34-kt detectors including the wrapped wire planes and drift distances.

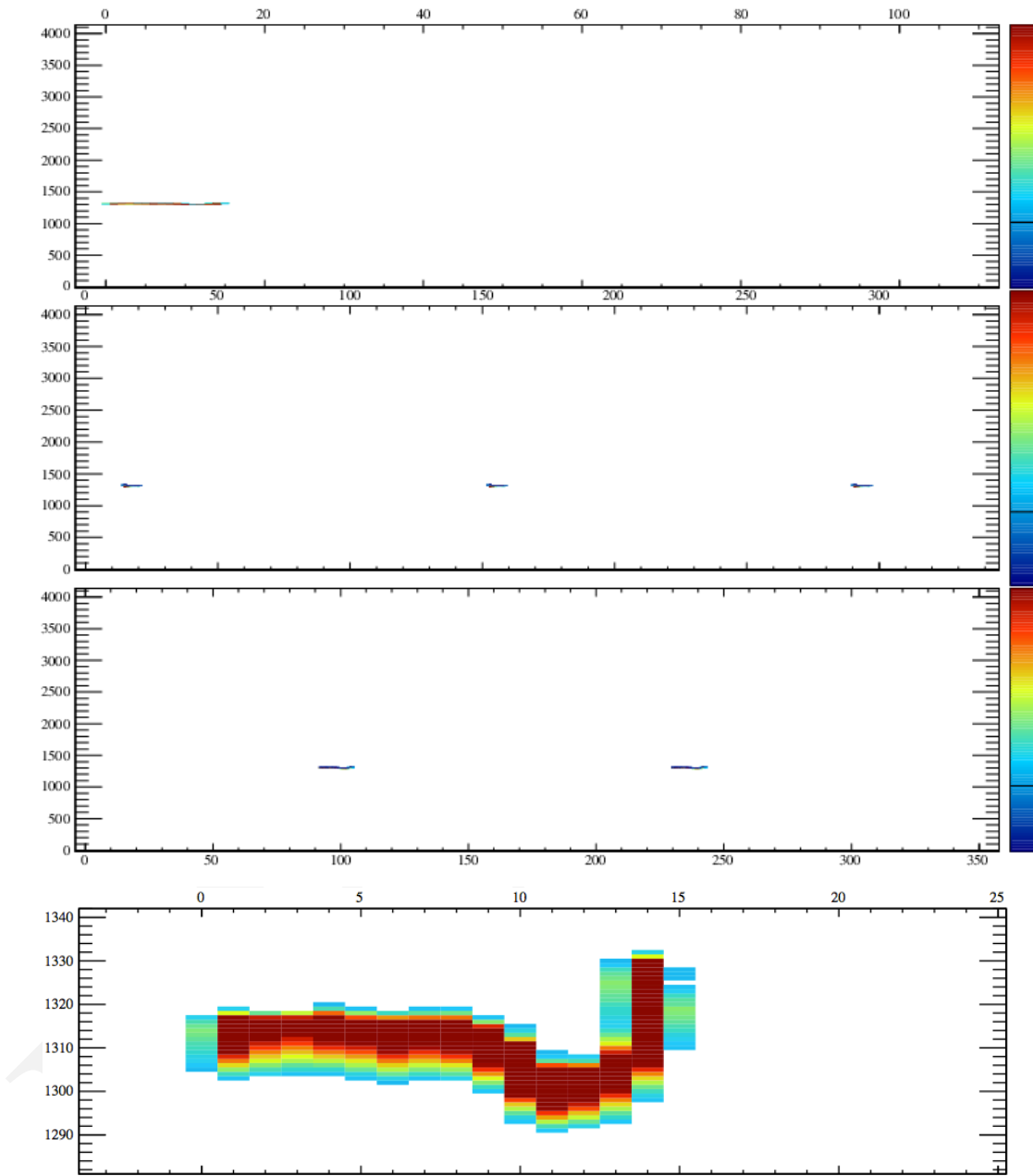


**Figure A.2:** Raw event display of a simulated 20-MeV event in the LBNE 35-t prototype; the top panel shows the collection plane, and the lower two panels show the induction planes (with multiple images due to wire wrapping). The bottom panel shows a zoom of the collection plane image.

1 and isolating the CC component of the signal.

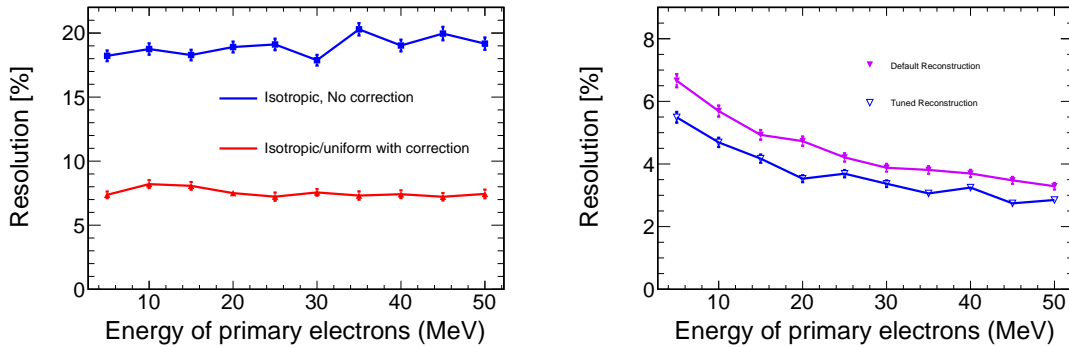


**Figure A.3:** Left: Comparison of energy resolution (defined as  $\sigma/E$ , where  $\sigma$  is the spread of the collection-plane-charge-based event energy  $E$  for a monoenergetic electron), with and without electron lifetime correction, as a function of electron energy. The blue curve is the energy resolution of isotropic and uniform electrons without electron lifetime correction. The red curve is the energy resolution with electron lifetime correction based on MC truth. Right: Comparison of energy resolution before and after tuning the reconstruction algorithm (for fixed position/direction electron events).

## A.2 Far Detector Reconstruction

The first stage of reconstruction of TPC data is unpacking and deconvoluting the electronics and field response of the wire planes. The deconvolution function includes a noise filter that currently is parameterized with ArgoNeuT’s noise, but will be tuned for the eventual noise observed in the LBNE detector. The deconvolution makes sharp, unipolar pulses from the bipolar induction-plane signals and also sharpens the response to collection-plane signals. Hits are then identified in the deconvoluted signals by fitting Gaussian functions, allowing for sums of several overlapping hits in each cluster. In LBNE, because of the large quantity of channels in the far detector, any inefficiency in CPU and memory is magnified. Improvements in the memory-usage efficiency relative to the ArgoNeuT and MicroBooNE implementations have been realized by rearrangement of the processing order and limiting the storage of the intermediate uncompressed raw data and the deconvoluted waveforms.

After signal deconvolution a line-finding and clustering based on a Hough transform in two dimensions is done using an algorithm called “fuzzy clustering” [342]. This clustering is performed separately on data from each induction plane. Since the hit data on LArTPCs are inherently two-dimensional — wire number and arrival time of the charge — the location of the initial ionization point has a two dimensional ambiguity if the deposition time is unknown. For beam events, the  $t_0$  is known, and thus only a one-dimensional ambiguity remains. This 1D ambiguity is broken by angling the induction-plane wires relative to the collection-plane wires, in order to measure the  $y$  location of the hits for which  $t$  (thus  $x$ ) and  $z$  are known. For (non-beam) cosmic-ray signals which arrive uniformly in time, the photon system provides  $t_0$ . After clustering, three-dimensional track-fitting is performed using a Kalman filter [343]. Dedicated algorithms have been developed to optimize electromagnetic shower reconstruction and energy resolution.

1 LBNE poses a unique challenge for reconstruction because the induction-plane wires wrap around  
2 the edges of the APA frames. This introduces discrete ambiguities that are not present in other  
3 LArTPC designs. Whereas a hit on a collection-plane wire identifies uniquely the side of the APA  
4 from which it came, this is not known for a hit on an induction-plane wire. The angles between  
5 the  $U$  and  $V$  plane wires are slightly different from  $45^\circ$  and from each other in order to break  
6 the ambiguities. A combinatoric issue arises, however, if many hits arrive on different wires at  
7 nearly the same time, for instance when a track, or even a track segment, propagates in a plane  
8 parallel to the wire planes (i.e., at constant drift distance). Showers will also contain many hits  
9 on different wires that arrive at similar times. Hits that arrive at different times can be clustered  
10 separately in the  $Z$ ,  $U$ , and  $V$  views without ambiguity, while hits that arrive at similar times must  
11 be associated using a topological pattern-recognition technique. LBNE is developing a version  
12 of the fuzzy clustering tool for use as a pattern-recognition step to allow association of  $Z$ ,  $U$ ,  
13 and  $V$  hits, a step that is needed to assign the correct  $y$  position to a track segment or portion  
14 of a cluster. This process is called “disambiguation” of the induction hits. Misassignment can  
15 affect particle ID performance and reconstructed energy resolution because fully-contained tracks  
16 may appear partially contained and vice versa. After disambiguation has been performed, standard  
17 track, vertex, and cluster reconstruction algorithms are applied.

18 A promising suite of algorithms for event reconstruction is provided by the PANDORA toolkit [344],  
19 which provides a framework for reconstruction algorithms and visualization tools. Currently it is  
20 being used to develop pattern-recognition algorithms and to reconstruct primary vertices. PAN-  
21 DORA’s pattern-recognition algorithm merges hits based on proximity and pointing to form 2D  
22 clusters. Vertices are then identified from the clusters that best connect to the same event. Clus-  
23 ters that best correspond to particles emitted from the primary vertex are identified in 2D. These  
24 particle candidates are then used to seed 3D reconstructed particles, and a 3D primary vertex is  
25 identified. Examples of PANDORA’s 2D clustering are shown in Figure A.4 for two simulated  
26 charged-current neutrino scattering events. Figure A.5 shows the primary vertex spatial resolution  
27 in 3D with well-contained simulated beam neutrino events, using the nominal LBNE spectrum and  
28 MicroBooNE geometry.

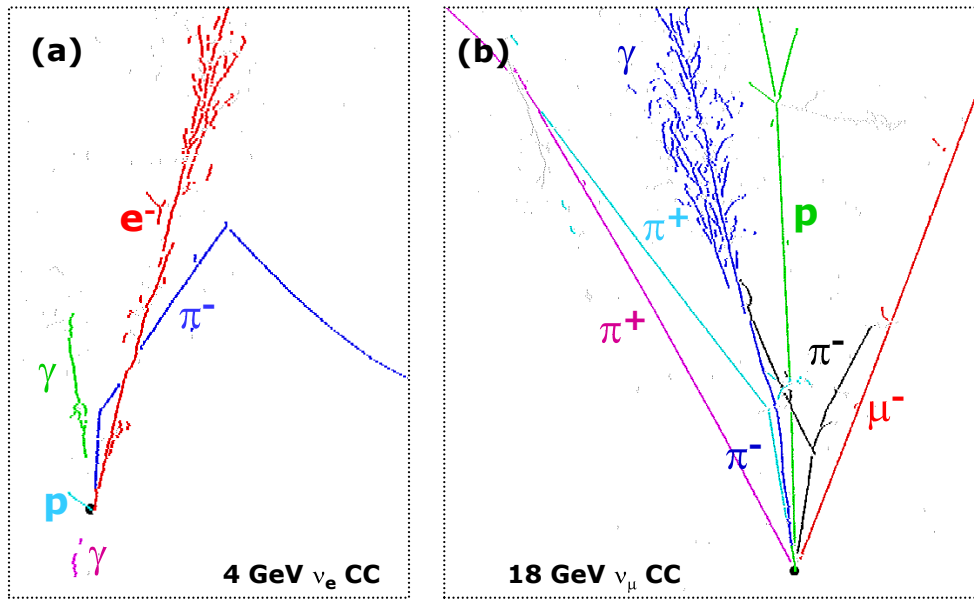


**Figure A.4:** PANDORA's two-dimensional clusterings of hits created by the particles in two charged-current neutrino interactions in liquid argon. Panel (a) shows a 4-GeV  $\nu_e$  interaction, and panel (b) shows an 18-GeV  $\nu_\mu$  interaction. The colors indicate the clusters into which PANDORA has divided the hits, and the particle labels are from the MC truth.

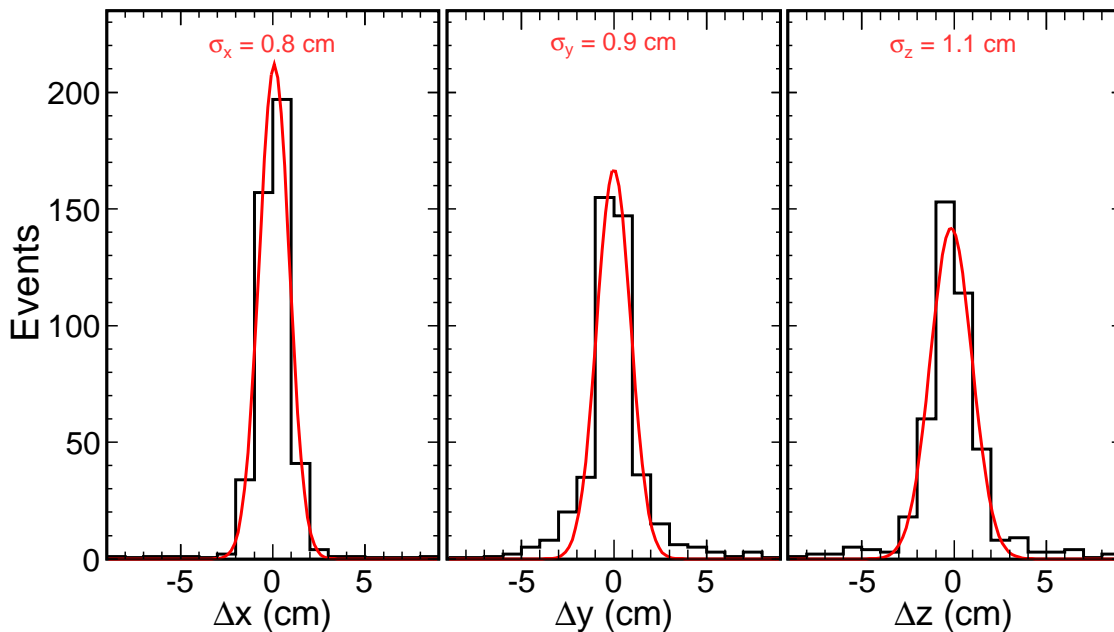


**Figure A.5:** Distributions of the residuals between the reconstructed and the Monte Carlo true locations of primary vertices in neutrino interactions in the MicroBooNE geometry using the LBNE beam spectrum. The  $x$  axis is oriented along the drift field, the  $y$  axis is parallel to the collection-plane wires, and the  $z$  axis points along the beam direction.

## 1 A.3 Fast Monte Carlo

2 The LBNE full Monte Carlo (MC) simulation will use a Geant4 simulation of the beamline to  
3 estimate the neutrino flux, a neutrino interaction generator (e.g., GENIE), and detailed detector  
4 simulation that mimics the real detector output for data events. Both data and MC will have the  
5 same reconstruction algorithms applied to produce quantities that will be used to analyze the data.  
6 The full MC detector simulation and reconstruction algorithms are still under development. Due to  
7 their detailed nature, these algorithms are CPU-intensive and time-consuming to run.

8 In parallel, a Fast Monte Carlo simulation has been developed and is available for use in place  
9 of the full MC to explore long-baseline physics analysis topics. A preliminary version of the Fast  
10 MC is currently available. Results from the latest detector simulations and advancements in recon-  
11 struction algorithms are actively being incorporated to improve the physics models and detector  
12 parameterization. Because the Fast MC replaces CPU-intensive portions of the full MC simulation  
13 with a fast parameterized model, it offers a quick, dynamic alternative which is useful for trying  
14 out new ideas before implementing them in the full MC. This usefulness is expected to remain  
15 even after the full MC simulation is mature.

16 To accurately approximate a full MC simulation, the Fast MC combines the Geant4 LBNE beam-  
17 line flux predictions, the GENIE event interaction generator, and a parameterized detector response  
18 that is used to simulate the measured (reconstructed) energy and momentum of each final-state par-  
19 ticle. The simulated energy deposition of the particles in each interaction is then used to calculate  
20 reconstructed kinematic quantities (e.g., the neutrino energy), and classify the type of neutrino  
21 interaction, including backgrounds and misidentified interactions.

22 The Fast MC is designed primarily to perform detailed sensitivity studies that allow for the prop-  
23 agation of realistic systematic uncertainties. It incorporates effects due to choices of models and  
24 their uncertainties and design decisions and tolerances. The neutrino flux predictions, the neutrino  
25 interaction cross section models, and the uncertainties related to these are also incorporated. The  
26 parameterized detector response is informed by Geant4 simulations of particle trajectories in liq-  
27 uid argon, by studies of detector response simulation in MicroBooNE [337], results reported by  
28 the ICARUS collaboration, and by the expected LBNE detector geometry. The realistic parame-  
29 terization of reconstructed energy and angle resolution, missing energy, and detector and particle  
30 identification acceptances provide a simulation that respects the physics and kinematics of the  
31 interaction and allows for propagation of model changes to final-state reconstructed quantities.

32 Future efforts will allow for propagation of uncertainties in detector effects and of detector design  
33 choices. It should be noted that the same GENIE files generated for the Fast MC can be used as  
34 inputs for the full detector simulation and the results of the two simulations can be compared both  
35 on an event-by-event basis and in aggregate. Studies of this nature can be used to tune the Fast MC  
36 and to cross-check the full simulations.

1 In the current configuration of the Fast MC, GENIE generates interactions on  $^{40}\text{Ar}$  nuclei with  
2 neutrinos selected from the energy spectra predicted by the collaboration's Geant4 flux simula-  
3 tions (described in detail in Section 3.4). For each interaction simulated in GENIE, a record of the  
4 interaction process, its initial kinematics, and the identity and 4-momenta of the final-state particles  
5 is produced. The parameterized detector response applies spatial and energy/momentum smearing  
6 to each of the final-state particles based on the particle properties and encoded detector-response  
7 parameters. Detection thresholds are applied to determine if a final-state particle will deposit en-  
8 ergy in the detector and if that energy deposition will allow for particle identification. The detector  
9 responses for neutrons and charged pions account for a variety of possible outcomes that describe  
10 the way these particles deposit energy in the detector. Neutral pions are decayed into two photons.  
11 Their conversion distance from the point of decay determines the starting position of the resulting  
12 electromagnetic showers. This distance is chosen from an exponential distribution with a charac-  
13 teristic length based on the radiation length of photons in liquid argon. Tau leptons are also decayed  
14 by the Fast MC and their decay products are dealt with appropriately. The spatial extent of tracks  
15 and showers in liquid argon are simulated in Geant4 and encoded as a probability distribution func-  
16 tion (PDF) or parameterization. Combined with vertex placement in a fiducial volume, the fraction  
17 of particle energy and/or track length visible in the detector is determined.

18 Once the Fast MC reconstructs the kinematics of the event ( $E_\nu$ ,  $E_{had}$ ,  $Q^2$ ,  $x$ ,  $y$ , etc.), based on the  
19 smeared four-vectors of particles that are above detection threshold, it searches interaction final-  
20 state particle lists for lepton candidates to be used in event classification algorithms. The resulting  
21 classifications are used to isolate samples for the  $\nu_e$  appearance and the  $\nu_\mu$  disappearance analyses  
22 which are in turn used to build energy spectra on an event-by-event basis.

23 Currently the classification algorithm categorizes each event as either  $\nu_e$ -CC,  $\nu_\mu$ -CC, or NC. Events  
24 with a candidate muon are classified as  $\nu_\mu$ -CC. Events without a candidate muon, but with a can-  
25 didate electron/positron are classified as  $\nu_e$ -CC. Events without a candidate muon or a candidate  
26 electron/positron are classified as NC. A  $\nu_\tau$ -CC classification, which would identify  $\tau$  candidates  
27 is under development.

28 A muon candidate is defined as a minimum ionizing particle (MIP)-like track that is greater than  
29 2.0 m long, and is not consistent with the behavior of a charged pion. Charged pions will often  
30 "shower", depositing a relatively large amount of energy in the detector at the end of its track, as  
31 compared to a muon. There are several situations in which a pion topology will be indistinguishable  
32 from a muon: (1) the pion stops at the end of its range without interacting, (2) the kinetic energy of  
33 the pion is sufficiently small when it showers, (3) the pion is absorbed cleanly by a nucleus with  
34 no hadronic debris, (4) the pion decays in flight, and (5) the track exists the detector. The 2.0 m cut  
35 was chosen because the probability of (1) or (2) is very small for pion tracks above this threshold.

36 An additional selection probability is enforced for low-energy tracks to simulate acceptance losses  
37 due to increased difficulty in particle identification for short tracks, especially in high-multiplicity  
38 events. (The falling edge of the selection probability is well below the energy required to generate

1 a 2.0-m track, minimizing the effect of this criterion.)

2 An electron candidate is defined as the highest momentum electromagnetic (EM) shower in an  
3 event that is not consistent with a photon. An EM shower is identified as a photon (1) if it converts  
4 2.0 cm or more from the event vertex, (2) if it can be matched with another EM shower in the  
5 events to reconstruct the  $\pi^0$  mass ( $135 \pm 40$  MeV), or (3) if  $dE/dx$  information from the first sev-  
6 eral planes of the track is more photon-like than  $e^\pm$ -like. The latter is determined on a probabilistic  
7 basis as a function of EM shower energy and hadronic shower multiplicity. Signal and background  
8 efficiencies from the  $dE/dx$   $e/\gamma$  discriminant are based on MicroBooNE simulations. Cut values  
9 are tuned to preserve 95% of the signal across all neutrino energies. As with muon candidates a  
10 low energy selection probability is enforced to account for acceptance losses at low EM shower en-  
11 ergies, especially in high-multiplicity events. For the electron candidates this selection probability  
12 is tuned to agree with hand scan studies.

13 An event with no muon candidate and no electron candidate is assumed to be a NC interaction.  
14 Preliminary studies evaluating the use of transverse momentum imbalance to identify  $\nu_\tau$ -CC in-  
15 teraction candidates have shown promising results for identifying NC candidates as well, and are  
16 likely to be included in the near future.

17 Currently no attempt is made to identify tau lepton candidates in order to isolate a  $\nu_\tau$ -CC sample.  
18 A preliminary algorithm to remove  $\tau \rightarrow \mu + \nu + \nu$  and  $\tau \rightarrow e + \nu + \nu$  backgrounds has recently  
19 been incorporated in the Fast MC. This algorithm may also prove useful for isolating a sample of  
20  $\nu_\tau$ -CC interactions, in which the tau decays to a lepton. Development of an algorithm to identify  
21 taus that decay to hadrons is under discussion.

22 All of the selection criteria can easily be updated to reflect improved simulations or new under-  
23 standing of particle identification capabilities and analysis sample acceptances. Changes can also  
24 be made to investigate alternate analysis techniques, or more conservative or optimistic assump-  
25 tions on signal acceptance and/or background rejection rates. Furthermore, the information re-  
26 quired to simulate effects related to particle identification is available in the Fast MC files and  
27 users are encouraged to construct and evaluate their own selection criteria.

28 A preliminary algorithm for removing  $\nu_\tau$ -CC-induced backgrounds from from the  $\nu_\mu$ -CC and the  
29  $\nu_e$ -CC samples has been developed. It employs a k-Nearest Neighbor (kNN) machine-learning  
30 technique as implemented in the ROOT TMVA package. The inputs to the kNN are (1) the sum  
31 of the transverse momentum with respect to the incoming neutrino direction, (2) the reconstructed  
32 energy of the incoming neutrino, and (3) the reconstructed energy of the resulting hadronic shower.  
33 Figure A.6 (right) shows the distribution of the output discriminant for true  $\nu_e$ -CC signal events,  
34 and for true  $\nu_\tau$ -CC-induced backgrounds. The algorithm is still being optimized but initial results  
35 are promising. As can be seen in Figure A.6 (left), cuts on the discriminant that preserve 90% of  
36 the signal remove roughly 60% of the  $\nu_\tau$ -CC-induced background in the  $\nu_e$ -CC sample. Similar  
37 results are expected for the  $\nu_\tau$ -CC-induced background in the  $\nu_\mu$ -CC sample.

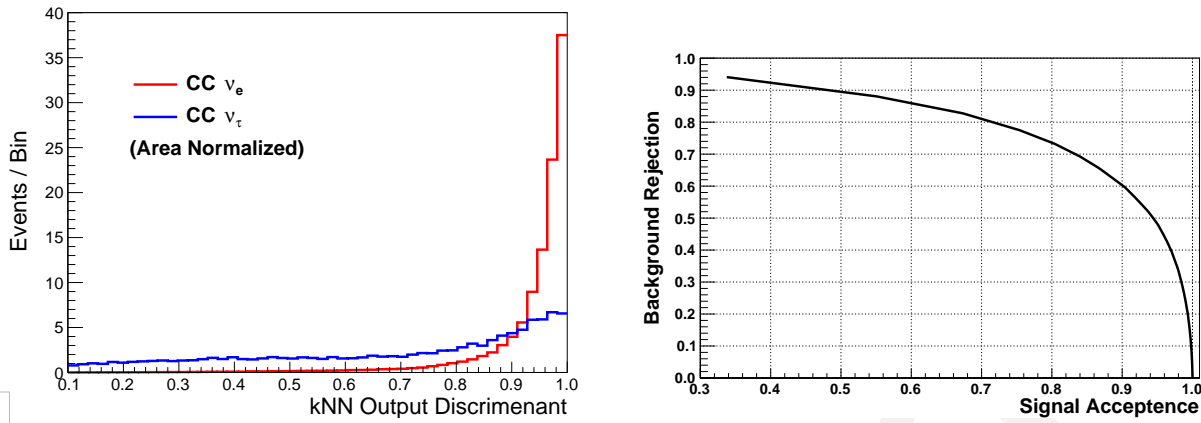


**Figure A.6:** The output discriminant of a kNN (left) created to remove  $\nu_\tau$ -CC-induced backgrounds from the  $\nu_\mu \rightarrow \nu_e$  oscillation analysis sample. Signal events (red) tend toward high values, while the  $\nu_\tau$ -CC-induced background events (blue) are more evenly distributed. The fraction of  $\nu_\tau$ -CC-induced backgrounds removed from the  $\nu_\mu \rightarrow \nu_e$  appearance candidate sample as a function of the corresponding signal efficiency (right). The curve is generated by varying the cut value on the kNN discriminant.

- 1 A similar approach is being studied to isolate the  $\nu_\tau$ -CC sample for the  $\nu_\tau$ -CC appearance analysis.
- 2 Current efforts are focused on identifying a set of reconstructed quantities that separate  $\nu_\tau$ -CC
- 3 interactions from potential backgrounds. For leptonic decay channels the quantities used in the
- 4 above kNN are prime candidates. Attempts to reconstruct a  $\rho$  mass from tracks originating at the
- 5 vertex are expected to help to isolate hadronic  $\tau$  decays. The parameterized pion response will
- 6 allow for selection of high-energy charged pions produced in hadronic  $\tau$  decays.

7 Figures A.7 and A.8 show the Fast MC reconstructed energy spectra of the signal and background  
 8 for the  $\nu_e$  appearance and the  $\nu_\mu$  disappearance samples, respectively. As an example of the cross  
 9 section and nuclear effect systematics that can be studied, the black histograms and the bottom  
 10 insert in each plot show the variation of the spectrum for each event type induced by changing the  
 11 value of CC  $M_A^{res}$  by  $+1\sigma$  (+15%, 2014 GENIE official uncertainty). CC  $M_A^{res}$  is the axial mass  
 12 parameter appearing in the axial form factor describing resonance production interactions in GE-  
 13 NIE. This particular example demonstrates a spectral distortion that is not a simple normalization  
 14 and is different for signal and for background. The effect of varying CC  $M_A^{res}$  on the  $\nu_\mu \rightarrow \nu_e$   
 15 analysis sample exhibits a strong correlation with the changes induced in the  $\nu_\mu \rightarrow \nu_\mu$  analysis  
 16 sample.

17 The left-hand side plots of Figures A.9 and A.10 show the acceptance (efficiency) of the signal and  
 18 the background for the Fast MC  $\nu_e$  appearance and  $\nu_\mu$  disappearance selections, respectively. The  
 19 effects of the low-energy selection probabilities induce the observed low-energy fall off in the  $\nu_e$   
 20 appearance sample. On the other hand, the 2.0-m track length requirement is mainly responsible  
 21 for the low-energy behavior in the  $\nu_\mu$  disappearance sample. The corresponding plots on the right-  
 22 hand side show the relative fraction (purity) of the signal and each background sample for the Fast  
 23 MC  $\nu_e$  appearance and  $\nu_\mu$  disappearance selections. The increased wrong-sign contamination is

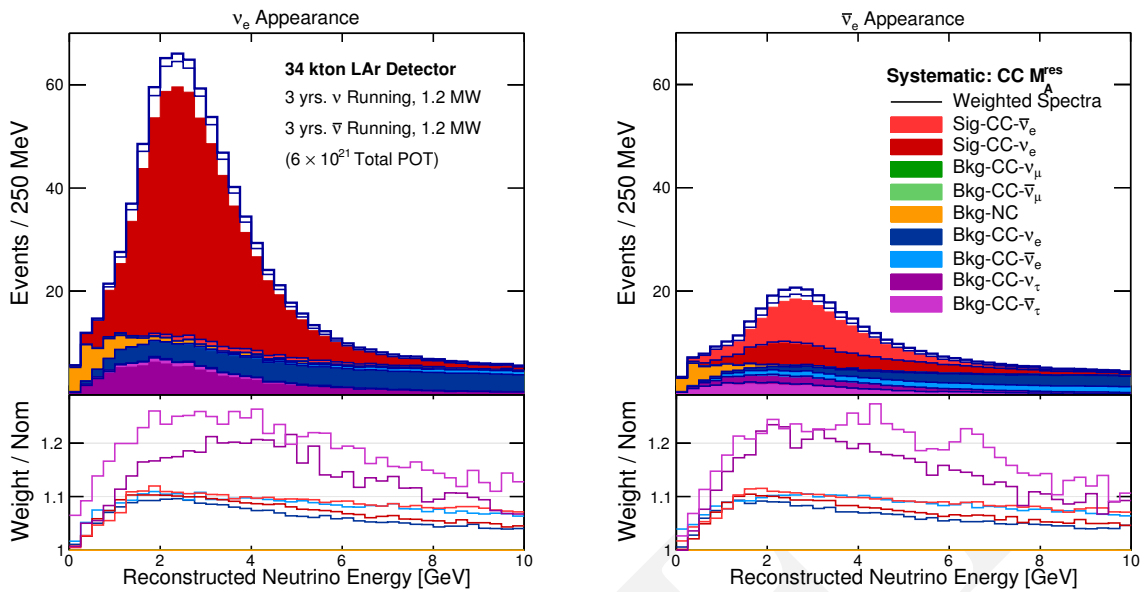


**Figure A.7:** The reconstructed energy distributions for the signals and backgrounds in the  $\nu_{e^-}$ - (left) and  $\bar{\nu}_e$  appearance (right) samples, as predicted by the Fast MC. The black histograms and bottom insert in each plot shows, for each event type, the variation in the spectrum that is induced by changing the value of  $CC M_A^{res}$  by +15%.

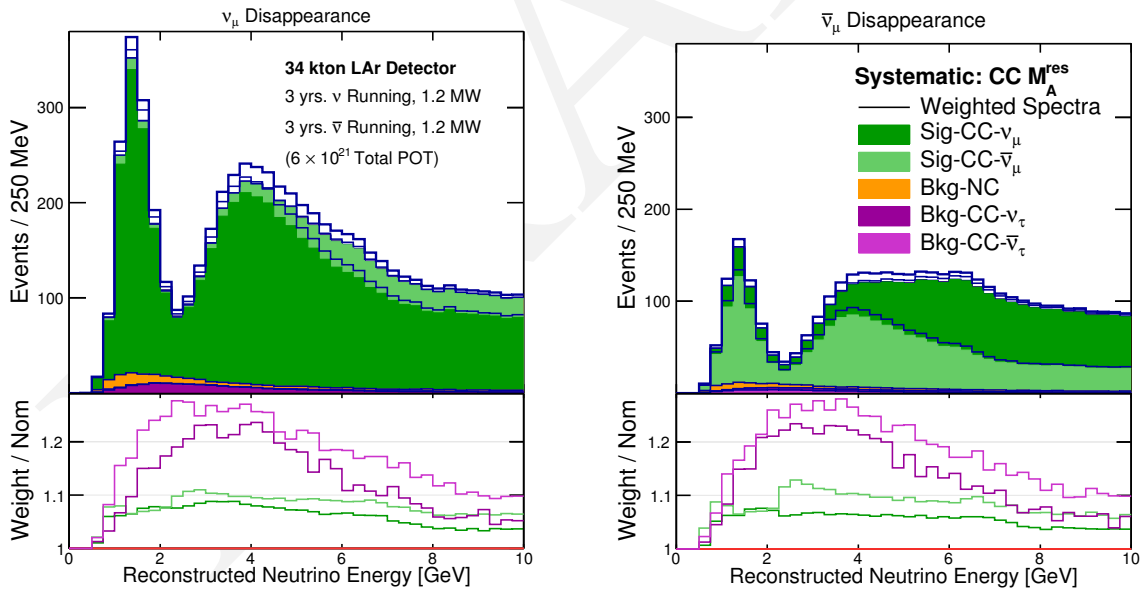


**Figure A.8:** The reconstructed energy distributions for the signals and backgrounds in the  $\nu_{\mu^-}$ - (left) and  $\bar{\nu}_{\mu}$  disappearance (right) samples, as predicted by the Fast MC. The black histograms and bottom insert in each plot shows, for each event type, the variation in the spectrum that is induced by changing the value of  $CC M_A^{res}$  by +15%.

- 1 evident in the  $\bar{\nu}$  beam samples as compared to the  $\nu$  beam samples. No attempt has been made to
- 2 reduce the tau background in these plots.
- 3 The output of the Fast MC is a file containing the information one would expect from a full MC

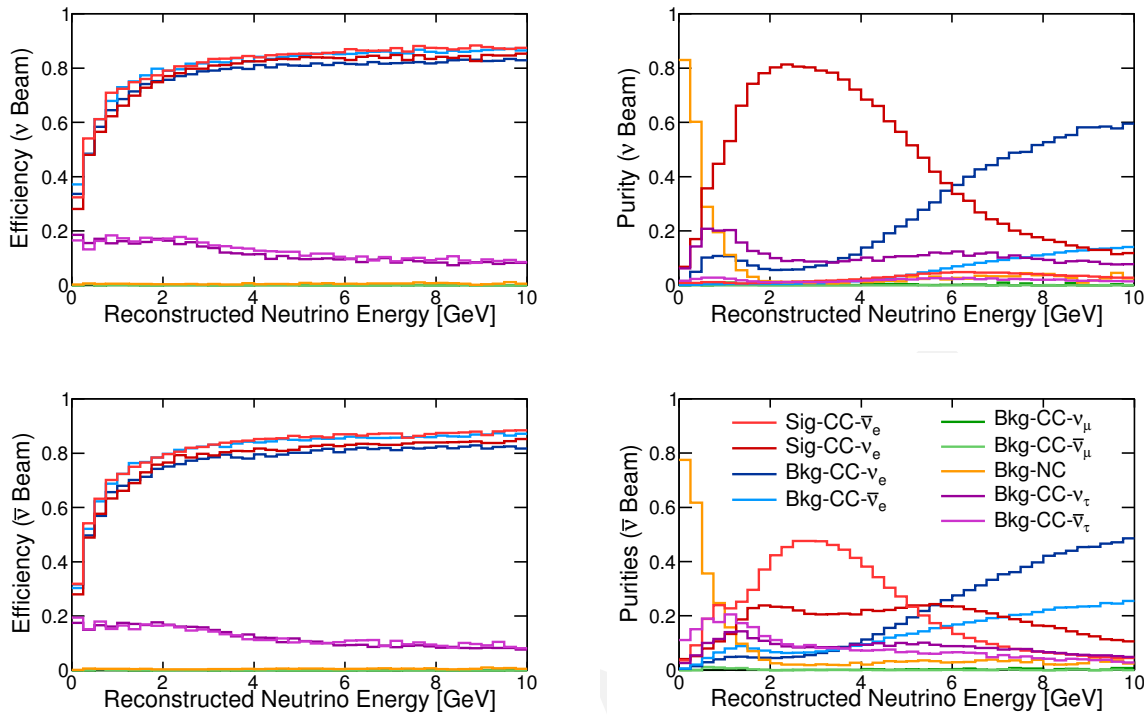


**Figure A.9:** The expected efficiencies and purities of selecting  $\nu_e$  appearance events in a LArTPC, obtained from the Fast MC.

1 simulation. There are truth level quantities that describe the generated event, and reconstructed  
 2 quantities that are calculated from simulated observables. The latter mimic the information that is  
 3 expected to be available from reconstructing data or full simulation and can be used in designing  
 4 analyses aimed at measuring physics parameters. Analyses based on the simulated reconstruction  
 5 produce event samples that can be used to estimate the sensitivity of LBNE to physics model  
 6 parameters, specifically the parameters of the PMNS matrix, as a function of a variety of input  
 7 parameters. Currently these studies are done using the GLOBES [121] software package. However,  
 8 instead of constructing the event rate spectra as a function of true neutrino energy from predictions  
 9 of the flux and neutrino interaction cross sections, they are built event-by-event from the Fast MC.  
 10 Similarly, smearing functions that give the distribution of measured (reconstructed) neutrino en-  
 11 ergies as a function of the true neutrino energy are built event-by-event from the Fast MC, rather  
 12 than estimated from external sources. In addition to the usual GLOBES inputs the Fast MC can pro-  
 13 vide systematic uncertainty response functions, which encode the expected changes to the energy  
 14 spectra when input model parameters are varied within their uncertainties. These response func-  
 15 tions, along with an augmented version of GLOBES, can be used to propagate realistic systematic  
 16 uncertainties in sensitivity studies.

17 The systematic uncertainty response functions are calculated from weights stored in the Fast MC  
 18 output files. Each weight corresponds to the probability of producing the event with an alternate

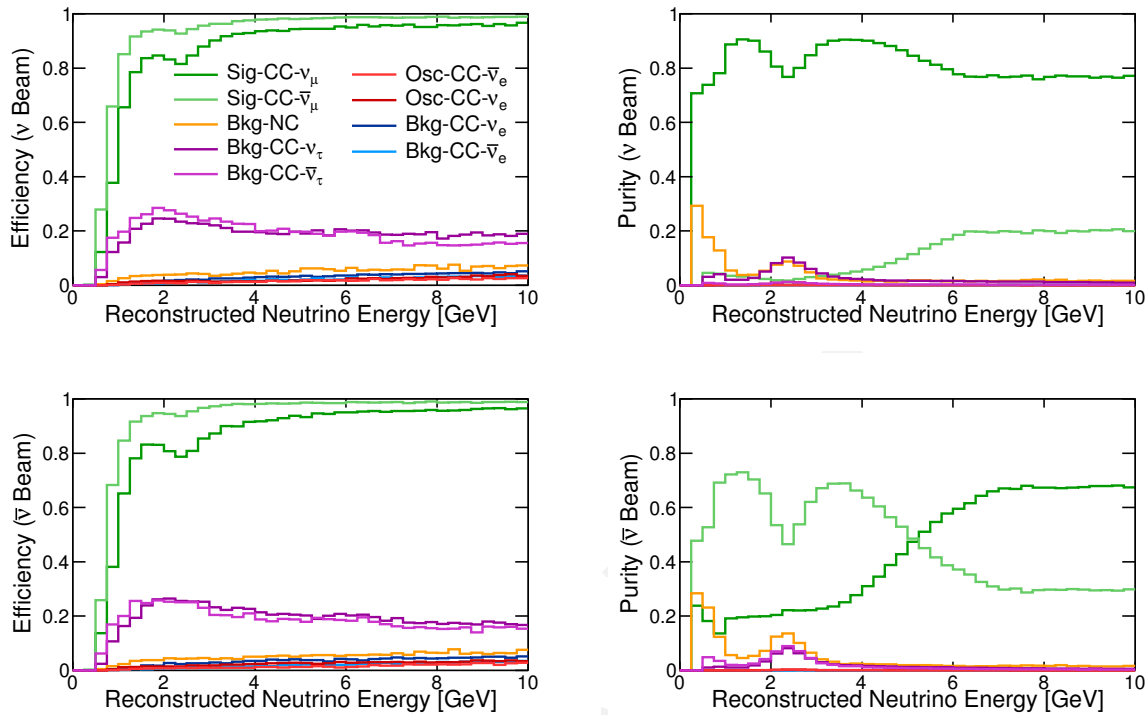


**Figure A.10:** The expected efficiencies and purities of selecting  $\nu_\mu$  disappearance events in a LArTPC obtained from the Fast MC.

1 physics model as compared to the model used to generate the sample. Currently the Fast MC  
 2 generates weights for parameters in interaction models that can be reweighted in GENIE as well  
 3 as a variety of parameters related to the neutrino flux. The flux parameters come in three varieties  
 4 related to: changes to the beamline design, tolerances in the beamline design, and uncertainties in  
 5 the physics models used in the simulations. The latter two contribute to systematic uncertainties  
 6 while the first can be used to evaluate the impact of design optimizations.

7 Propagation of systematic uncertainties through LBNE sensitivity studies using the Fast MC will  
 8 require inclusion of new, and improvements to existing reweighting algorithms. This includes (1)  
 9 the introduction of new models into GENIE, (2) adding to and improving the reweighting func-  
 10 tions currently in GENIE, (3) constructing flux files that correspond to the changes in the three  
 11 aforementioned categories, (4) implementing a system for reweighting individual events based on  
 12 changes to the models of hadronization from proton-target interactions, and (5) introducing de-  
 13 tector parameterizations representing alternate detector designs, detector design tolerances, and  
 14 model choices used in detector simulations.

15 The current focus of Fast MC studies is to estimate the effect of model uncertainties on sensitivity  
 16 projections. This includes several steps, the first of which is to look at the changes in the analy-  
 17 sis sample spectra induced by propagating individual systematic uncertainties. These studies are

1 benchmarked by calculating the  $\chi^2$  between the nominal and altered spectra. In the second step,  
 2 sensitivities are calculated for combined fits of the four main analysis samples ( $\nu_\mu/\bar{\nu}_\mu$  disappear-  
 3 ance,  $\nu_e/\bar{\nu}_e$  appearance). These studies must be done carefully to allow for realistic constraints of  
 4 systematic uncertainties across analysis samples within GLOBES. Input covariance matrices can  
 5 also be used to enforce external constraints on the relations between sources of systematic uncer-  
 6 tainty. The results of these studies will inform the investigators as to which model uncertainties  
 7 cause significant degradation of the sensitivities and therefore must be constrained by other meth-  
 8 ods. Methods to constrain these parameters will be sought from currently running experiments,  
 9 proposed intermediate experiments, and from the LBNE beam monitoring and the LBNE near de-  
 10 tector. Estimates of these constraints can then be propagated to sensitivity calculations to estimate  
 11 the degree to which they mitigate the decline in sensitivity.

12 Current studies focus on propagating uncertainties in flux and GENIE model parameters via reweight-  
 13 ing techniques. A example study shown in Figure A.11 illustrates the effect of including the un-  
 14 certainty on CC  $M_A^{res}$  in the calculation of sensitivity to CP violation. The sensitivity studies are  
 15 performed for (1) a fit to the  $\nu_e$  appearance sample (three years of  $\nu$ -beam running), (2) a combined  
 16 fit of the  $\nu_e$  appearance sample and the  $\bar{\nu}_e$  appearance sample (three years of  $\nu$ -beam plus three  
 17 years of  $\bar{\nu}$ -beam running), and (3) a combined fit of the  $\nu_e/\bar{\nu}_e$  appearance samples along with the  
 18 corresponding  $\nu_\mu/\bar{\nu}_\mu$  disappearance samples. All three studies are done in two ways: with no al-  
 19 lowance for non-oscillation parameter systematic variation, and with allowed 15% (width gaussian  
 20 PDF) variations in CC  $M_A^{res}$ .

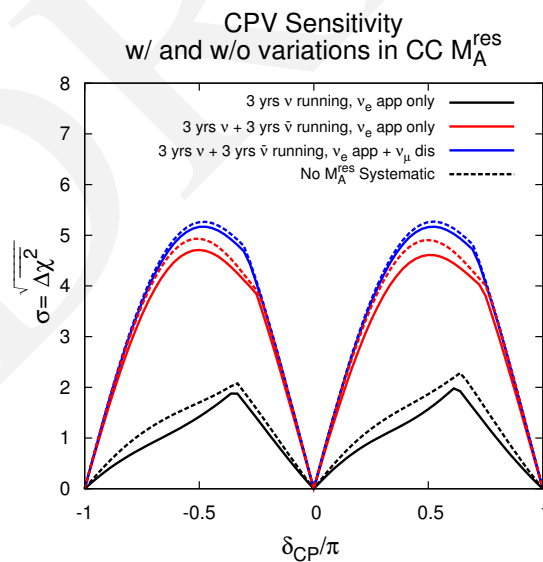


**Figure A.11:** The sensitivity to CP violation calculated using the energy spectra generated by the Fast MC. The sensitivities were generated with (solid) and without (dashed) allowed variations in the CC  $M_A^{res}$  resonance production model parameter in GENIE. The allowed variation degrades the sensitivity, however combined fits of multiple analysis samples provide additional constraints and reduce the impact.

As Figure A.11 shows, the inclusion of allowed variations in CC  $M_A^{res}$  degrades the sensitivity. However, combined fits of multiple analysis samples provide additional constraints and reduce the impact. The effect of these sample-to-sample constraints are dependent on the sample statistics and the curves in Figure A.11 include the statistical limitations on sample-to-sample constraints from a six-year (three years  $\nu$  + three years  $\bar{\nu}$  running) exposure. However, the software also allows for the inclusion of other possible limitations on sample-to-sample constraints related to the relative lack of experimental constraints on cross section ratios (i.e.,  $\sigma_{\nu_e}/\sigma_{\nu_\mu}$ ,  $\sigma_{\nu_\tau}/\sigma_{\nu_\mu}$ , and  $\sigma_{\bar{\nu}}/\sigma_{\nu}$ ), as well as theoretical considerations.

The preliminary Fast MC spectra shown in Figures A.7 and A.8 were generated with a different beam configuration than the ones shown in Figures 4.2 and 4.3. Consequently the sensitivities to CPV shown in Figure A.11 cannot be directly compared to the corresponding figures in Section 4.2. However, both the Fast MC and the methods discussed in Section 4.2 have been used to generate comparable spectra and to perform a series of sensitivity studies. The two methods were consistent, except regarding known differences between the two simulations, e.g., the inclusion of  $\nu_\tau$ -CC-induced backgrounds. These differences are well understood, as are their impact on oscillation parameter sensitivities.

Eventually the Fast MC seeks to incorporate near detector and atmospheric neutrino analyses and directly perform combined fits with the long-baseline neutrino analysis samples. These studies will provide the most accurate estimate of the ultimate sensitivity of LBNE, and provide a template for future data analysis procedures.

## A.4 Simulation of Cosmic-Ray Background for a 10-kt Surface Detector

A preliminary study of the background events expected from cosmic rays in the 10-kt far detector installed near the surface at the Sanford Underground Research Facility is detailed in [217]. The study simulated cosmic-ray interactions in the far detector and focused on cosmic-ray induced events from neutrons and muons that mimic electron-neutrino interactions in the detector. These include electromagnetic cascades from knock-on electrons, muon bremsstrahlung, and hadronic cascades with electromagnetic components from photons and  $\pi^0$ 's. The background from decays of neutral hadrons into electrons such as  $K_L^0 \rightarrow \pi e \nu$  were also studied. The energy of the cascades was required to be  $> 0.1$  GeV.

These initial studies indicate that a combination of simple kinematic and beam timing cuts will help in significantly reducing the cosmic-ray background event rate in this far detector configuration. In particular:

1. Only electromagnetic cascades with energies greater than 0.25 GeV are considered background. For the neutrino oscillation sensitivity calculations, only neutrino energies  $\geq 0.5$  GeV

1 are considered.

- 2 2.  $e^\pm$  background candidates are tracked back to the parent muon; the distance between the  
3 muon track and the point-of-closest-approach (PoCA) to the muon track is required to be  
4  $> 10$  cm.
- 5 3. The vertex of the  $e^\pm$  shower is required to be within the fiducial volume of the detector  
6 (defined as 30 cm from the edge of the active detector volume).
- 7 4. The  $e^\pm$  cascade is required to be within a cone around the beam direction (determined from  
8 the angular distribution of the beam signal  $e^\pm$  and the incoming neutrino beam).
- 9 5. It is assumed that EM showers initiated by  $\gamma$ 's and  $\pi^0 \rightarrow \gamma\gamma$  can be effectively distinguished  
10 from primary electron interactions using particle ID techniques such as  $dE/dX$ .
- 11 6. Events are timed with a precision of  $\leq 1 \mu\text{s}$  using the photon detection system, which limits  
12 background to events occurring within the  $10 \mu\text{s}$  of the beam spill.

13 The result of applying these selection criteria to the electromagnetic showers initiated by cosmic  
14 rays is summarized in Table A.1 and Figure A.12. The background rates given in Table A.1 include  
15 the recalculation for the cosmic flux at 1,500 m above sea level, which was not included in the  
16 previous study [217] (and is not included in Figure A.12). In the table, the initial background event  
17 rate is calculated for one calendar year assuming a 1.4-ms drift time per beam pulse, a beam pulse  
18 every 1.33 seconds and  $2 \times 10^7$  s/year of running. The expected event rate/yr after various selection  
19 criteria is applied from left to right in the table. The rates in all columns except the last are given  
20 for a time window of 1.4 ms, corresponding to the maximum electron drift time. The last column  
21 shows the rate reduction assuming an efficient photon detection system. The first three rows show  
22 events with a muon in the detector where a PoCA cut (column 3) can be applied. The row labeled  
23 'Missing  $\mu$ ' shows events without a muon in the detector; as there is no muon track, a PoCA cut  
24 can not be applied. The detector is assumed to be on the surface with 3 m of rock overburden.

25 The dominant background is from  $\pi^0 \rightarrow \gamma \rightarrow e^\pm$ , which contributes 12 out of the 16 total events  
26 per year and comes from  $\pi^0$ 's originating in cosmic showers. The study does not yet include spe-  
27 cific  $\pi^0$  reconstruction, only individual  $e/\gamma$  separation. More sophisticated reconstruction tech-  
28 niques should further reduce the  $\pi^0$  background. The studies indicate that application of these  
29 selection criteria coupled with a more detailed background event reconstruction can potentially  
30 reduce the background from cosmic rays to a few events per year — mostly in the energy region  
31  $< 1$  GeV.

32 In Figure A.12, black filled circles show events before any cuts are applied. The other point icons  
33 represent successively applied cuts in the order listed below and in the figure's legend.

- 34 1. Blue squares: PoCA to the muon track greater than 30 cm

**Table A.1:** Cosmic-ray-induced background (at 1,500 m above sea level) to the beam  $\nu_e$ -CC signal in the 10-kt detector.

tab:cosmic

Processes	$E_e > 0.25 \text{ GeV}$	PoCA $> 10 \text{ cm}$ and D $> 30 \text{ cm}$	Beam angle	$e/\gamma$ PID	Beam timing
$\pi^0 \rightarrow \gamma \rightarrow e^\pm$	$2.2 \times 10^6$	$9.7 \times 10^4$	$4.8 \times 10^4$	$1.7 \times 10^3$	12
$\mu \rightarrow \gamma \rightarrow e^\pm$	$7.1 \times 10^6$	12	0	0	$< 0.003$
Ext $\gamma \rightarrow e^\pm$	$1.9 \times 10^6$	660	340	13	0.1
$\pi^0, K^0 \rightarrow e^\pm$	$1.4 \times 10^6$	810	240	240	1.7
Missing $\mu$	$1.3 \times 10^6$	$1.8 \times 10^3$	580	20	0.1
Atm $n$	$2.9 \times 10^6$	$1.6 \times 10^4$	$6.5 \times 10^2$	240	1.7
<b>Total</b>	<b><math>1.1 \times 10^7</math></b>	<b><math>1.2 \times 10^5</math></b>	<b><math>5.6 \times 10^4</math></b>	<b><math>2.2 \times 10^3</math></b>	<b>16</b>

- 1 2. Red triangles: angle with respect to the beam such that 99% of signal events are retained
- 2 3. Green triangles: application of energy-dependent  $e/\gamma$  discrimination
- 3 4. Magenta open circles: application of efficient photon detection, assumed to allow the re-
- 4 duction of the time window from a maximum drift time of 1.4 ms down to a beam spill of
- 5  $10 \mu\text{s}$

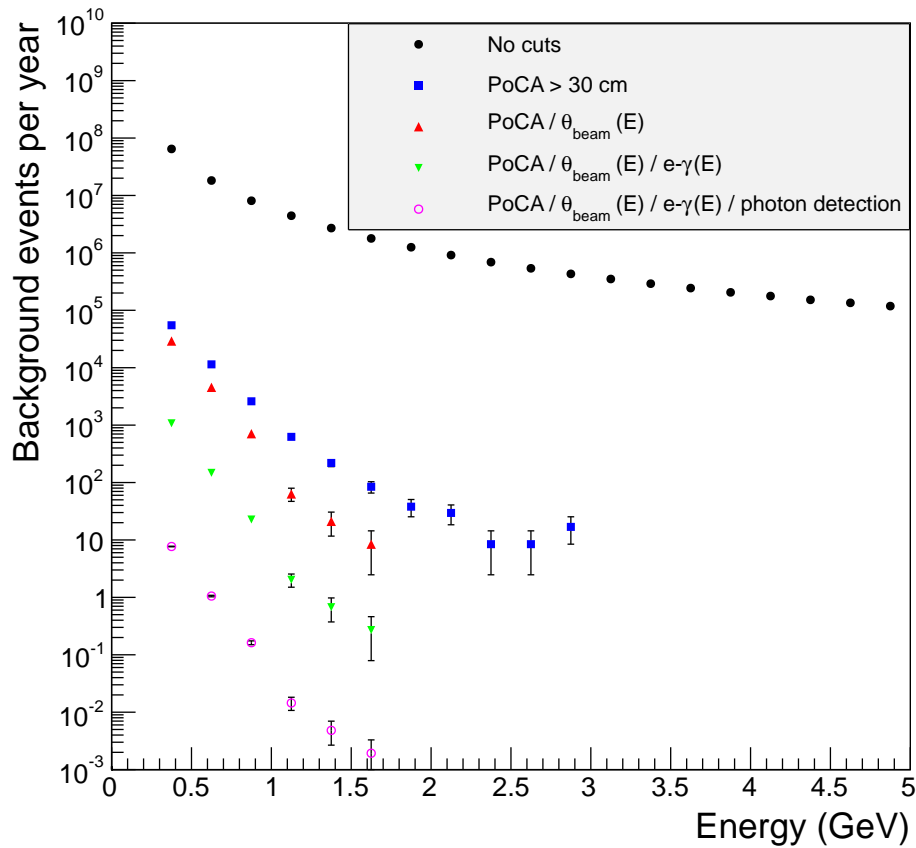


**Figure A.12:** Energy spectra of muon-induced background events for successively applied background rejection cuts. Simulations have been done for a muon spectrum at sea level. Correction for an altitude of 1,500 m above sea level has not been applied to the data on this graph.

# Appendix B

# Neutrino-Nucleon Scattering Kinematics

app-dis

2 The following explanation of neutrino-nucleon scattering kinematics is adapted from [345]:

Accardi:2012qut

1

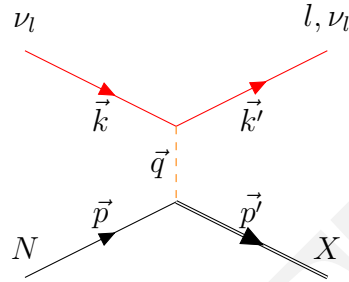


fig:nuscatter

**Figure B.1:** A schematic diagram of a neutrino-nucleon scattering process

3 The expression  $\nu_l + N \rightarrow \nu_l, l + X$  describes the scattering of a neutrino,  $\nu_l$  off a nucleon,  $N$ .  
 4 This interaction proceeds through the exchange of a  $W^\pm$  or  $Z^0$  boson, depending on whether it is  
 5 a CC or NC interaction, respectively. For the case of neutrino scattering, the incoming lepton is a  
 6 neutrino and the outgoing lepton is either a neutrino (NC) or a charged lepton,  $l$  (CC).  $X$  denotes  
 7 the resultant hadronic system.

8 The nucleon mass,  $M$ , is neglected where appropriate; the lepton mass is neglected throughout.  
 9 The following kinematic variables describe the momenta and energies involved in the scattering  
 10 process:

- 11 ○  $\vec{k}, \vec{k}'$  are the four-momenta of the incoming and outgoing lepton
- 12 ○  $\vec{p}$  is the initial four-momentum of the nucleon
- 13 ○  $E_\nu$  is the energy of the incoming neutrino
- 14 ○  $E_N$  is the energy of the nucleon

15 The Lorentz invariants are:

- 16 ○ the squared  $\nu+N$  collision energy  $s = (|\vec{p} + \vec{k}|)^2 = 4E_N E_\nu$
- 17 ○ the squared momentum transfer to the lepton  $Q^2 = -q^2 = -(|\vec{k} - \vec{k}'|)^2$ , equal to the virtuality  
 18 of the exchanged boson. Large values of  $Q^2$  provide a hard scale to the process, which allows  
 19 resolution of quarks and gluons in the nucleon.

- 1     ○ the Bjorken variable  $x_B = Q^2/(2\vec{p} \cdot \vec{q})$  is often simply denoted by  $x$ . It determines the  
 2     momentum fraction of the parton (quark or gluon) on which the boson scatters. Note that  
 3      $0 < x < 1$  for  $\nu+N$  collisions.
- 4     ○ the inelasticity  $y = (\vec{q} \cdot \vec{p})/(\vec{k} \cdot \vec{p})$  is limited to values  $0 < y < 1$  and determines in particular  
 5     the polarization of the virtual boson. In the lab frame, the energy of the scattered lepton is  
 6      $E_l = E_\nu(1 - y) + Q^2/(4E_\nu)$ ; detection of the scattered lepton thus typically requires a cut  
 7     on  $y < y_{max}$ .

8     These invariants are related by  $Q^2 = xys$ . The available phase space is often represented in the  
 9     plane of  $x$  and  $Q^2$ . For a given  $\nu+N$  collision energy, lines of constant  $y$  are then lines with a slope  
 10    of 45 degrees in a double logarithmic  $x - Q^2$ -plot.

11    Two additional important variables are:

- 12    ○ the squared invariant mass of the produced hadronic system ( $X$ ), denoted by  $W^2 = (|\vec{p} +$   
 13     $\vec{q}|)^2 = Q^2(1 - 1/x)$ . Deep-inelastic scattering (DIS) is characterized by the Bjorken limit,  
 14    where  $Q^2$  and  $W^2$  become large at a fixed value of  $x$ . Note: for a given  $Q^2$ , small  $x$  corre-  
 15    sponds to a high  $W, Z - N$  collision energy.
- 16    ○ the energy lost by the lepton (i.e., the energy carried away by the virtual boson) in the nucleon  
 17    rest frame, denoted  $\nu = \vec{q} \cdot \vec{p}/M = ys/(2M)$

18    For scattering on a nucleus of atomic number  $A$ , the nucleon momentum  $\vec{p}$  would be replaced by  
 19     $\vec{P}/A$  in the definitions, where  $\vec{P}$  is the momentum of the nucleus. Note that the Bjorken variable is  
 20    then in the range  $0 < x < A$ .

# Acknowledgments

acknowl

2 This report is the result of an initial collaboration-wide effort to prepare a whitepaper for the APS  
 3 Division of Particles and Fields Community Summer Study 2013 [1]. The paper has evolved into  
 4 LBNE's formal science document due to the hard work of many LBNE Collaboration and Project  
 5 members. We thank those colleagues who made significant contributions and provided excellent  
 6 feedback on drafts of this document. The following is a non-exhaustive list of LBNE collaborators  
 7 who made major contributions to this document. A major contribution is defined as  $\geq$  a section  
 8 and/or a study reported in a figure prepared for this document:

Contribution	LBNE Collaborator(s)
<i>Overall editing</i>	<i>Anne Heavey, Mary Bishai, Jon Urheim, Brett Viren, Maury Goodman</i>
<b>Technical/Figures</b>	Brett Viren
<i>Original content</i>	<i>Bob Wilson (Editor of the 2010 Interim Physics Report)</i>
<b>General Guidance</b>	Milind Diwan, Bob Wilson, Jim Strait, Sam Zeller, Bill Louis, Hank Sobel, Josh Klein, Nick Samios
Major Contributors by Chapter. A * indicates the chapter editor(s)	
<b>Chapter 1</b>	Jon Urheim*, Jim Strait, Bob Wilson
<b>Chapter 2</b>	Mary Bishai*, Elizabeth Worcester*, Jon Urheim, Kate Scholberg, Ed Kearns, Bill Marciano, Xin Qian.
<b>Chapter 3</b>	Mary Bishai*, Jim Strait, Elaine McCluskey, Kevin Lesko, Jim Stewart, Vaia Papadimitriou, Kevin Yarritu, Bill Louis
<b>Chapter 4</b>	Elizabeth Worcester*, Mary Bishai*, Matt Bass, Andy Blake, Xin Qian, Jon Urheim, Lisa Whitehead
<b>Chapter 5</b>	Ed Kearns*, Jon Urheim,* Vitaly Kudryavtsev
<b>Chapter 6</b>	Kate Scholberg,* Vic Gehman, Alex Friedland
<b>Chapter 7</b>	Roberto Petti*, Sanjib Mishra, Jaehoon Yu
<b>Chapter 8</b>	Michael Smy*, Mary Bishai*, Jaehoon Yu
<b>Chapter 9</b>	Jon Urheim*, Jim Strait
<b>Appendix A</b>	Dan Cherdack*, Tom Junk*, Andy Blake, Vitaly Kudryavtsev, Zepeng Li, Kate Scholberg
<b>Appendix B</b>	Mary Bishai*, Roberto Petti

10 We would also like to express our gratitude to the following non-LBNE collaborators who sup-  
 11 plied us with invaluable information: **Elke Aschenauer (Brookhaven Lab)**, the main editor of  
 12 the Electron Ion Collider (EIC) whitepaper [345] which inspired the look and style of this doc-  
 13 ument; **Joachim Kopp (Max-Planck Institute, Heidelberg)** for his study of LBNE's sensitivity

1 to Non-Standard Interactions summarized in Section 4.7.1; **Pilar Coloma (Virginia Tech)** for  
2 her studies comparing LBNE’s sensitivities to other proposed neutrino experiments shown in Fig-  
3 ures 4.34 and 4.36; **Patrick Huber (Virginia Tech)** for a long and fruitful collaborative effort, and  
4 his critical role in developing the case for a very long-baseline neutrino oscillation experiment over  
5 the past decade; **JJ Cherry (LANL)** and **Huaiyu Duan (U. of New Mexico)** for major input on  
6 the supernova studies shown in Chapter 6; **Dmitry Gorbunov (Institute for Nuclear Research,**  
7 **Moscow)** for his studies on LBNE sensitivities to  $\nu$ MSM heavy neutrinos shown in Figure 7.5;  
8 **Diana Brandonisio (Fermilab VMS)**, our graphic designer for her gorgeous cover design and  
9 invaluable design advice.

10 And last, but most importantly, our effusive thanks to **Anne Heavey** (AKA the **FIXME** monster)  
11 — our devoted general editor — for her dogged insistence on clarity and quality, her hard work  
12 well above and beyond the call of duty, and for being such an absolute pleasure to work with.

13 This work was supported in part by the U.S. Department of Energy (DOE), the National Science  
14 Foundation (NSF), the Sanford Underground Research Facility and the South Dakota Science and  
15 Technology Authority (SDSTA); the Brazilian Federal Agency for the Support and Evaluation of  
16 Graduate Education (CAPES), the Sao Paulo Research Foundation (FAPESP) and the National  
17 Council for Scientific and Technological Development (CNPq); the UK Science and Technology  
18 Facilities Council (STFC); the Italian government’s Istituto Nazionale di Fisica Nucleare (INFN);  
19 the Indian Department of Atomic Energy (DAE) and the Department of Science and Technology  
20 (DST), Ministry of Science and Technology.

# References

ref

- 2 1. “APS Division of Particles and Fields Community Summer Study 2013,” 2013.  
3 <http://www.snowmass2013.org>.
- 4 2. N. R. C. Neutrino Facilities Assessment Committee, *Neutrinos and Beyond: New Windows*  
5 *on Nature*. The National Academies Press, 2003. ISBN 0-309-08716-3.
- 6 3. Interagency Working Group on the Physics of the Universe. National Science and  
7 Technology Council Committee on Science, “A 21<sup>st</sup> Century Frontier of Discovery: The  
8 Physics of the Universe, a Strategic Plan for Federal Research at the Intersection of Physics  
9 and Astronomy.”. February, 2004.  
10 [http://pcos.gsfc.nasa.gov/docs/Physics\\_of\\_the\\_Universe.pdf](http://pcos.gsfc.nasa.gov/docs/Physics_of_the_Universe.pdf).
- 11 4. N. R. C. Committee on Elementary Particle Physics in the 21st Century, *Revealing the*  
12 *Hidden Nature of Space and Time: Charting the Course for Elementary Particle Physics*.  
13 The National Academies Press, 2006. ISBN 0-309-66039-4.
- 14 5. Neutrino Scientific Assessment Group, “Recommendations to the Department of Energy  
15 and the National Science Foundation on a Future U.S. Program in Neutrino Oscillations.  
16 Report to the Nuclear Science Advisory Committee and the High Energy Physics Advisory  
17 Board.”. July, 2007. [http://science.energy.gov/~media/hep/pdf/files/pdfs/  
18 nusagfinalreportjuly13\\_2007.pdf](http://science.energy.gov/~media/hep/pdf/files/pdfs/nusagfinalreportjuly13_2007.pdf).
- 19 6. Particle Physics Project Prioritization Panel, “U.S. Particle Physics: Scientific  
20 opportunities, a plan for the next ten years.”. May, 2008. [http:  
21 //science.energy.gov/~media/hep/pdf/files/pdfs/p5\\_report\\_06022008.pdf](http://science.energy.gov/~media/hep/pdf/files/pdfs/p5_report_06022008.pdf).
- 22 7. Ad Hoc Committee to Assess the Science Proposed for a Deep Underground Science and  
23 Engineering Laboratory (DUSEL); National Research Council, *An Assessment of the Deep*  
24 *Underground Science and Engineering Laboratory*. The National Academies Press, 2012.  
25 ISBN 978-0-309-21723-1.
- 26 8. HEPAP Facilities Subpanel, “Major High Energy Physics Facilities 2014-2024. Input to the  
27 prioritization of proposed scientific user facilities for the Office of Science.”. March, 2013.  
28 [http://science.energy.gov/~media/hep/hepap/pdf/Reports/HEPAP\\_  
29 facilities\\_letter\\_report.pdf](http://science.energy.gov/~media/hep/hepap/pdf/Reports/HEPAP_facilities_letter_report.pdf).
- 30 9. CERN Council, “The European Strategy for Particle Physics, Update 2013.”.  
31 CERN-Council-S/106, May, 2013.  
32 <http://council.web.cern.ch/council/en/EuropeanStrategy/esc-e-106.pdf>.
- 33 10. DOE Office of Science, Office of High Energy Physics, “Mission Need Statement for a  
34 Long-Baseline Neutrino Experiment (LBNE),” DOE, LBNE-doc-6259, 2009.
- 35 11. A. S. Kronfeld, R. S. Tschirhart, U. Al-Binni, W. Altmannshofer, C. Ankenbrandt, *et al.*,  
36 “Project X: Physics Opportunities,” FERMILAB-TM-2557,  
37 BNL-101116-2013-BC-81834, JLAB-ACP-13-1725, UASLP-IF-13-001, SLAC-R-1029,  
38 ANL-PHY-13-2, PNNL-22523, LBNL-6334E, arXiv:1306.5009 [hep-ex], 2013.

12. A. de Gouvea *et al.*, **Intensity Frontier Neutrino Working Group**, “Neutrinos,” FERMILAB-CONF-13-479-E, arXiv:1310.4340 [hep-ex], 2013.
13. K. Babu, E. Kearns, U. Al-Binni, S. Banerjee, D. Baxter, *et al.*, “Baryon Number Violation,” arXiv:1311.5285 [hep-ph], 2013.
14. Derwent, P. and others, “Proton Improvement Plan II,” Project X-doc-1232, November, 2013.
15. S. Holmes, R. Alber, B. Chase, K. Gollwitzer, D. Johnson, *et al.*, “Project X: Accelerator Reference Design,” FERMILAB-TM-2557, BNL-101116-2013-BC-81834, JLAB-ACP-13-1725, PNNL-22523, SLAC-R-1020, UASLP-IF-13-001, arXiv:1306.5022 [physics.acc-ph], 2013.
16. “Final Report, Director’s Independent Conceptual Design and CD-1 Readiness Review of the LBNE Project,” LBNE-doc-5788, March, 2012.
17. Y. K. Kim *et al.*, “LBNE Reconfiguration: Steering Committee Report,” 2012. [http://www.fnal.gov/directorate/lbne\\_reconfiguration/index.shtml](http://www.fnal.gov/directorate/lbne_reconfiguration/index.shtml).
18. “Department of Energy Review Committee Report on the Technical, Cost, Schedule, and Management Review of the Long Baseline Neutrino Experiment (LBNE),” October, 2012. [http://www.fnal.gov/directorate/OPMO/Projects/LBNE/DOERev/2012/10\\_30/1210\\_LBNE\\_rpt.pdf](http://www.fnal.gov/directorate/OPMO/Projects/LBNE/DOERev/2012/10_30/1210_LBNE_rpt.pdf).
19. “Independent Cost Review Closeout for the Long Baseline Neutrino Experiment (LBNE) Project,” LBNE-doc-6522, November, 2012.
20. “Critical Decision 1 Approve Alternative Selection and Cost Range of the Long Baseline Neutrino Experiment (LBNE) Project,” LBNE-doc-6681, December, 2012.
21. L. P. M. Team, “LBNE Conceptual Design Report, Volume 1: The LBNE Project,” LBNE-doc-5235, 2012.
22. L. P. M. Team, “LBNE Conceptual Design Report, Volume 2: The Beamline at the Near Site,” LBNE-doc-4317, 2012.
23. L. P. M. Team, “LBNE Conceptual Design Report, Volume 3: Detectors at the Near Site,” LBNE-doc-4724, 2012.
24. L. P. M. Team, “LBNE Conceptual Design Report, Volume 4: The Liquid Argon Detector at the Far Site,” LBNE-doc-4892, 2012.
25. L. P. M. Team, “LBNE Conceptual Design Report, Volume 5: Conventional Facilities at the Near Site (MI-10 Shallow),” LBNE-doc-4623, 2012.
26. L. P. M. Team, “LBNE Conceptual Design Report, Volume 6: Conventional Facilities at the Far Site,” LBNE-doc-5017, 2012.
27. R. J. Wilson, “Long-Baseline Neutrino Experiment, presentation, November 2013,” 2013. <https://indico.fnal.gov/getFile.py/access?contribId=25&sessionId=7&resId=0&materialId=slides&confId=7485>.
28. Marx-Reichanadter Committee, “Department of Energy Office of Science Review of Options for Underground Science.”. June, 2011. [http://science.energy.gov/~media/np/pdf/review\\_of\\_underground\\_science\\_report\\_final.pdf](http://science.energy.gov/~media/np/pdf/review_of_underground_science_report_final.pdf).

- 1 29. Grannis, P. and Green, D. and Nishikawa, K. and Robertson, H. and Sadoulet, B. and Wark,  
2 D., “The LBNE Science Capability Review,” LBNE-doc-5333, December, 2011.
- 3 30. M. Messier, **NOvA Collaboration** , “Extending the NOvA Physics Program,”  
4 FERMILAB-CONF-13-308-E, arXiv:1308.0106 [hep-ex], 2013.
- 5 31. P. Huber and J. Kopp, “Two experiments for the price of one? – The role of the second  
6 oscillation maximum in long baseline neutrino experiments,” *JHEP* **1103** (2011) 013,  
7 arXiv:1010.3706 [hep-ph].
- 8 32. E. Kearns, “Future Experiments for Proton Decay. Presentation at ISOUPS (International  
9 Symposium: Opportunities in Underground Physics for Snowmass), Asilomar, May 2013,”  
10 2013.
- 11 33. J. Strait, “Physics Research Goals After Reconfiguration,” LBNE-doc-3056, 2011.
- 12 34. R. Mohapatra, S. Antusch, K. Babu, G. Barenboim, M.-C. Chen, *et al.*, “Theory of  
13 neutrinos: A White paper,” *Rept.Prog.Phys.* **70** (2007) 1757–1867,  
14 arXiv:hep-ph/0510213 [hep-ph].
- 15 35. G. Aad *et al.*, **ATLAS Collaboration** , “Observation of a new particle in the search for the  
16 Standard Model Higgs boson with the ATLAS detector at the LHC,” *Phys.Lett.* **B716**  
17 (2012) 1–29, arXiv:1207.7214 [hep-ex].
- 18 36. S. Chatrchyan *et al.*, **CMS Collaboration** , “Observation of a new boson at a mass of 125  
19 GeV with the CMS experiment at the LHC,” *Phys.Lett.* **B716** (2012) 30–61,  
20 arXiv:1207.7235 [hep-ex].
- 21 37. DNP/DPF/DAP/DPB Joint Study on the Future of Neutrino Physics, “The Neutrino  
22 Matrix.”. November, 2004. [http:](http://www.aps.org/policy/reports/multidivisional/neutrino/upload/main.pdf)  
23 [//www.aps.org/policy/reports/multidivisional/neutrino/upload/main.pdf](http://www.aps.org/policy/reports/multidivisional/neutrino/upload/main.pdf).
- 24 38. F. An *et al.*, **Daya Bay Collaboration** , “Improved Measurement of Electron Antineutrino  
25 Disappearance at Daya Bay,” *Chin. Phys.* **C37** (2013) 011001, arXiv:1210.6327  
26 [hep-ex].
- 27 39. A. Aguilar-Arevalo *et al.*, **LSND Collaboration** , “Evidence for neutrino oscillations from  
28 the observation of anti-neutrino(electron) appearance in a anti-neutrino(muon) beam,”  
29 *Phys.Rev.* **D64** (2001) 112007, arXiv:hep-ex/0104049 [hep-ex].
- 30 40. A. Aguilar-Arevalo *et al.*, **MiniBooNE Collaboration** , “Improved Search for  $\bar{\nu}_\mu \rightarrow \bar{\nu}_e$   
31 Oscillations in the MiniBooNE Experiment,” *Phys.Rev.Lett.* **110** no. 16, (2013) 161801,  
32 arXiv:1207.4809 [hep-ex].
- 33 41. A.A.Aguilar-Arevalo *et al.*, **MiniBOONE** *Phys. Rev. Lett.* no. 98, (2007) . 231801,  
34 arXiv:0704.1500 [hep-ex].
- 35 42. G. Mention, M. Fechner, T. Lasserre, T. Mueller, D. Lhuillier, *et al.*, “The Reactor  
36 Antineutrino Anomaly,” *Phys.Rev.* **D83** (2011) 073006, arXiv:1101.2755 [hep-ex].
- 37 43. S. F. King, A. Merle, S. Morisi, Y. Shimizu, and M. Tanimoto, “Neutrino Mass and  
38 Mixing: from Theory to Experiment,” arXiv:1402.4271 [hep-ph], 2014.
- 39 44. P. Harrison, D. Perkins, and W. Scott, “Tri-bimaximal mixing and the neutrino oscillation  
40 data,” *Phys.Lett.* **B530** (2002) 167, arXiv:hep-ph/0202074 [hep-ph].

- 1 45. C. H. Albright and M.-C. Chen, “Model Predictions for Neutrino Oscillation Parameters,”  
2 *Phys.Rev.* **D74** (2006) 113006, arXiv:hep-ph/0608137 [hep-ph].
- 3 46. G. Fogli, E. Lisi, A. Marrone, D. Montanino, A. Palazzo, *et al.*, “Global analysis of  
4 neutrino masses, mixings and phases: entering the era of leptonic CP violation searches,”  
5 *Phys.Rev.* **D86** (2012) 013012, arXiv:1205.5254 [hep-ph].
- 6 47. J. Beringer *et al.*, **Particle Data Group**, “Review of Particle Physics (RPP),” *Phys.Rev.*  
7 **D86** (2012) 010001.
- 8 48. C. Jarlskog, “A Basis Independent Formulation of the Connection Between Quark Mass  
9 Matrices, CP Violation and Experiment,” *Z.Phys.* **C29** (1985) 491–497.
- 10 49. A. Meroni, S. Petcov, and M. Spinrath, “A SUSY SU(5)<sub>X</sub>T’ Unified Model of Flavour with  
11 large  $\theta_{13}$ ,” *Phys.Rev.* **D86** (2012) 113003, arXiv:1205.5241 [hep-ph].
- 12 50. G.-J. Ding, S. F. King, and A. J. Stuart, “Generalised CP and  $A_4$  Family Symmetry,” *JHEP*  
13 **1312** (2013) 006, arXiv:1307.4212.
- 14 51. C. Luhn, “Trimaximal  $TM_1$  neutrino mixing in  $S_4$  with spontaneous CP violation,”  
15 *Nucl.Phys.* **B875** (2013) 80–100, arXiv:1306.2358 [hep-ph].
- 16 52. G.-J. Ding and Y.-L. Zhou, “Predicting Lepton Flavor Mixing from  $\Delta(48)$  and Generalized  
17 CP Symmetries,” arXiv:1312.5222 [hep-ph], 2013.
- 18 53. S. Antusch, S. F. King, and M. Spinrath, “Spontaneous CP violation in  $A_4 \times SU(5)$  with  
19 Constrained Sequential Dominance 2,” *Phys.Rev.* **D87** no. 9, (2013) 096018,  
20 arXiv:1301.6764 [hep-ph].
- 21 54. S. F. King, “A model of quark and lepton mixing,” *JHEP* **1401** (2014) 119,  
22 arXiv:1311.3295 [hep-ph].
- 23 55. E. Kolb and M. Turner, *The Early Universe*. Westview Press, 1994. ISBN  
24 978-0201626742.
- 25 56. S. Weinberg, *Cosmology*. Oxford University Press, USA, first ed., April, 2008. ISBN  
26 978-0198526827.
- 27 57. G. Steigman, “Primordial Nucleosynthesis in the Precision Cosmology Era,”  
28 *Ann.Rev.Nucl.Part.Sci.* **57** (2007) 463–491, arXiv:0712.1100 [astro-ph].
- 29 58. M. Fukugita and T. Yanagida, “Baryogenesis Without Grand Unification,” *Phys.Lett.* **B174**  
30 (1986) 45.
- 31 59. T. Yanagida, “Horizontal Symmetry and Masses of Neutrinos,” *Prog.Theor.Phys.* **64** (1980)  
32 1103.
- 33 60. S. Pascoli, S. Petcov, and A. Riotto, “Leptogenesis and Low Energy CP Violation in  
34 Neutrino Physics,” *Nucl.Phys.* **B774** (2007) 1–52, arXiv:hep-ph/0611338 [hep-ph].
- 35 61. F. Capozzi, G. Fogli, E. Lisi, A. Marrone, D. Montanino, *et al.*, “Status of three-neutrino  
36 oscillation parameters, circa 2013,” arXiv:1312.2878 [hep-ph], 2013.
- 37 62. P. Adamson *et al.*, **MINOS Collaboration**, “Search for the disappearance of muon  
38 antineutrinos in the NuMI neutrino beam,” *Phys.Rev.* **D84** (2011) 071103,  
39 arXiv:1108.1509 [hep-ex].
- 40 63. S. Mikheev and A. Y. Smirnov, “Resonance Amplification of Oscillations in Matter and  
41 Spectroscopy of Solar Neutrinos,” *Sov.J.Nucl.Phys.* **42** (1985) 913–917.

- 1 64. L. Wolfenstein, “Neutrino Oscillations in Matter,” *Phys.Rev.* **D17** (1978) 2369–2374.
- 2 65. G. Bellini *et al.*, **Borexino Collaboration**, “Measurement of the solar 8B neutrino rate  
3 with a liquid scintillator target and 3 MeV energy threshold in the Borexino detector,”  
4 *Phys.Rev.* **D82** (2010) 033006, arXiv:0808.2868 [astro-ph].
- 5 66. G. Bellini, J. Benziger, D. Bick, S. Bonetti, G. Bonfini, *et al.*, “Precision measurement of  
6 the 7Be solar neutrino interaction rate in Borexino,” *Phys.Rev.Lett.* **107** (2011) 141302,  
7 arXiv:1104.1816 [hep-ex].
- 8 67. B. Aharmim *et al.*, **SNO Collaboration**, “Combined Analysis of all Three Phases of Solar  
9 Neutrino Data from the Sudbury Neutrino Observatory,” *Phys.Rev.* **C88** (2013) 025501,  
10 arXiv:1109.0763 [nucl-ex].
- 11 68. A. Renshaw *et al.*, **Super-Kamiokande Collaboration**, “First Indication of Terrestrial  
12 Matter Effects on Solar Neutrino Oscillation,” arXiv:1312.5176 [hep-ex], 2013.
- 13 69. M. Freund, “Analytic approximations for three neutrino oscillation parameters and  
14 probabilities in matter,” *Phys.Rev.* **D64** (2001) 053003, arXiv:hep-ph/0103300  
15 [hep-ph].
- 16 70. W. Marciano and Z. Parsa, “Intense neutrino beams and leptonic CP violation,”  
17 *Nucl.Phys.Proc.Suppl.* **221** (2011) 166–172, arXiv:hep-ph/0610258 [hep-ph].
- 18 71. B. Viren, “libnuosc++ - A library for calculating 3 neutrino oscillation probabilities..”  
19 <https://github.com/brettviren/nuosc>.
- 20 72. A. Dziewonski and D. Anderson *Phys. Earth, Planet, Interiors* **25** (1981) 297.
- 21 73. R. Brun, F. Bruyant, M. Maire, A. McPherson, and P. Zancarini, “GEANT3,”  
22 CERN-DD-EE-84-1, 1987.
- 23 74. M. Bass *et al.*, **LBNE Collaboration**, “Baseline optimization for the measurement of CP  
24 violation and mass hierarchy in a long-baseline neutrino oscillation experiment,”  
25 FERMILAB-PUB-13-506-E, arXiv:1311.0212 [hep-ex], 2013.
- 26 75. J. Appel *et al.*, “Physics Working Group Report to the LBNE Reconfiguration Steering  
27 Committee,” 2012. [http://www.fnal.gov/directorate/lbne\\_reconfiguration/  
28 files/LBNE-Reconfiguration-PhysicsWG-Report-August2012.pdf](http://www.fnal.gov/directorate/lbne_reconfiguration/files/LBNE-Reconfiguration-PhysicsWG-Report-August2012.pdf).
- 29 76. M. Raidal, “Relation between the neutrino and quark mixing angles and grand unification,”  
30 *Phys.Rev.Lett.* **93** (2004) 161801, arXiv:hep-ph/0404046 [hep-ph].
- 31 77. H. Minakata and A. Y. Smirnov, “Neutrino mixing and quark-lepton complementarity,”  
32 *Phys.Rev.* **D70** (2004) 073009, arXiv:hep-ph/0405088 [hep-ph].
- 33 78. A. Y. Smirnov, “Neutrino mass, mixing and discrete symmetries,” *J.Phys.Conf.Ser.* **447**  
34 (2013) 012004, arXiv:1305.4827 [hep-ph].
- 35 79. J. Harada, “Non-maximal  $\theta_{23}$ , large  $\theta_{13}$  and tri-bimaximal  $\theta_{12}$  via quark-lepton  
36 complementarity at next-to-leading order,” *Europhys.Lett.* **103** (2013) 21001,  
37 arXiv:1304.4526 [hep-ph].
- 38 80. B. Hu, “Trimaximal-Cabibbo neutrino mixing: A parametrization in terms of deviations  
39 from tribimaximal mixing,” *Phys.Rev.* **D87** no. 5, (2013) 053011, arXiv:1212.4079  
40 [hep-ph].

- 1 81. P. Ramond, “Fundamental Physics Underground. Presentation at ISOUPS (International  
2 Symposium: Opportunities in Underground Physics for Snowmass), Asilomar, May 2013,”  
3 2013.
- 4 82. S. Antusch, C. Biggio, E. Fernandez-Martinez, M. Gavela, and J. Lopez-Pavon, “Unitarity  
5 of the Leptonic Mixing Matrix,” *JHEP* **0610** (2006) 084, arXiv:hep-ph/0607020  
6 [hep-ph].
- 7 83. X. Qian, C. Zhang, M. Diwan, and P. Vogel, “Unitarity Tests of the Neutrino Mixing  
8 Matrix,” arXiv:1308.5700 [hep-ex], 2013.
- 9 84. J. C. Pati and A. Salam, “Is Baryon Number Conserved?,” *Phys.Rev.Lett.* **31** (1973)  
10 661–664.
- 11 85. H. Georgi and S. Glashow, “Unity of All Elementary Particle Forces,” *Phys.Rev.Lett.* **32**  
12 (1974) 438–441.
- 13 86. S. Dimopoulos, S. Raby, and F. Wilczek, “Proton Decay in Supersymmetric Models,”  
14 *Phys.Lett.* **B112** (1982) 133.
- 15 87. P. Langacker, “Grand Unified Theories and Proton Decay,” *Phys.Rept.* **72** (1981) 185.
- 16 88. W. de Boer, “Grand unified theories and supersymmetry in particle physics and  
17 cosmology,” *Prog.Part.Nucl.Phys.* **33** (1994) 201–302, arXiv:hep-ph/9402266  
18 [hep-ph].
- 19 89. P. Nath and P. Fileviez Perez, “Proton stability in grand unified theories, in strings and in  
20 branes,” *Phys.Rept.* **441** (2007) 191–317, arXiv:hep-ph/0601023 [hep-ph].
- 21 90. S. Raby, T. Walker, K. Babu, H. Baer, A. Balantekin, *et al.*, “DUSEL Theory White Paper,”  
22 SLAC-PUB-14734, FERMILAB-PUB-08-680-T, arXiv:0810.4551 [hep-ph], 2008.
- 23 91. G. Senjanovic, “Proton decay and grand unification,” *AIP Conf.Proc.* **1200** (2010)  
24 131–141, arXiv:0912.5375 [hep-ph].
- 25 92. T. Li, D. V. Nanopoulos, and J. W. Walker, “Elements of Fast Proton Decay,” *Nucl.Phys.*  
26 **B846** (2011) 43–99, arXiv:1003.2570 [hep-ph].
- 27 93. E. Noether, “Invariant Variation Problems,” *Gott.Nachr.* **1918** (1918) 235–257,  
28 arXiv:physics/0503066 [physics].
- 29 94. R. Bionta, G. Blewitt, C. Bratton, D. Casper, A. Ciocio, *et al.*, “Observation of a Neutrino  
30 Burst in Coincidence with Supernova SN 1987a in the Large Magellanic Cloud,”  
31 *Phys.Rev.Lett.* **58** (1987) 1494.
- 32 95. K. Hirata *et al.*, **KAMIOKANDE-II Collaboration**, “Observation of a Neutrino Burst  
33 from the Supernova SN 1987a,” *Phys.Rev.Lett.* **58** (1987) 1490–1493.
- 34 96. E. Alekseev, L. Alekseeva, V. Volchenko, and I. Krivosheina, “Possible Detection of a  
35 Neutrino Signal on 23 February 1987 at the Baksan Underground Scintillation Telescope  
36 of the Institute of Nuclear Research,” *JETP Lett.* **45** (1987) 589–592.
- 37 97. K. Scholberg, “Supernova neutrino detection,” *Nucl.Phys.Proc.Suppl.* **221** (2011) 248–253,  
38 arXiv:astro-ph/0701081 [astro-ph].
- 39 98. A. Dighe, “Physics potential of future supernova neutrino observations,” *J.Phys.Conf.Ser.*  
40 **136** (2008) 022041, arXiv:0809.2977 [hep-ph].

- 1 99. G. Pagliaroli, F. Vissani, E. Coccia, and W. Fulgione, “Neutrinos from Supernovae as a  
2 Trigger for Gravitational Wave Search,” *Phys. Rev. Lett.* **103** (2009) 031102,  
3 arXiv:0903.1191 [hep-ph].
- 4 100. C. Ott, E. O’Connor, S. Gossan, E. Abdikamalov, U. Gamma, *et al.*, “Core-Collapse  
5 Supernovae, Neutrinos, and Gravitational Waves,” *Nucl.Phys.Proc.Suppl.* **235-236** (2013)  
6 381–387, arXiv:1212.4250 [astro-ph.HE].
- 7 101. G. A. Tammann, W. Loeffler, and A. Schroder, “The Galactic supernova rate,” *Astrophys. J.*  
8 *Suppl.* **92** (1994) 487–493.
- 9 102. E. Cappellaro, R. Evans, and M. Turatto, “A new determination of supernova rates and a  
10 comparison with indicators for galactic star formation,” *Astron.Astrophys.* **351** (1999) 459,  
11 arXiv:astro-ph/9904225 [astro-ph].
- 12 103. A. Mirizzi, G. Raffelt, and P. Serpico, “Earth matter effects in supernova neutrinos: Optimal  
13 detector locations,” *JCAP* **0605** (2006) 012, arXiv:astro-ph/0604300 [astro-ph].
- 14 104. S. Choubey, B. Dasgupta, A. Dighe, and A. Mirizzi, “Signatures of collective and matter  
15 effects on supernova neutrinos at large detectors,” arXiv:1008.0308 [hep-ph], 2010.
- 16 105. G. G. Raffelt, “Astrophysical axion bounds: An Update,” arXiv:astro-ph/9707268  
17 [astro-ph], 1997.
- 18 106. S. Hannestad and G. Raffelt, “New supernova limit on large extra dimensions,”  
19 *Phys.Rev.Lett.* **87** (2001) 051301, arXiv:hep-ph/0103201 [hep-ph].
- 20 107. P. Antonioli *et al.*, “Snews: The supernova early warning system,” *New J. Phys.* **6** (2004)  
21 114, astro-ph/0406214.
- 22 108. K. Scholberg, “The SuperNova Early Warning System,” *Astron. Nachr.* **329** (2008)  
23 337–339, arXiv:0803.0531 [astro-ph].
- 24 109. K. Scholberg, “Future supernova neutrino detectors,” *J.Phys.Conf.Ser.* **203** (2010) 012079.
- 25 110. “Sanford Underground Research Facility.” <http://www.sanfordlab.org>.
- 26 111. B. Cleveland, T. Daily, J. Davis, Raymond, J. R. Distel, K. Lande, *et al.*, “Measurement of  
27 the solar electron neutrino flux with the Homestake chlorine detector,” *Astrophys.J.* **496**  
28 (1998) 505–526.
- 29 112. F. Gray, C. Ruybal, J. Totushek, D.-M. Mei, K. Thomas, *et al.*, “Cosmic Ray Muon Flux at  
30 the Sanford Underground Laboratory at Homestake,” *Nucl.Instrum.Meth.* **A638** (2011)  
31 63–66, arXiv:1007.1921 [nucl-ex].
- 32 113. W. Roggenthen and A. Smith, “U, Th, K contents of materials associated with the  
33 Homestake DUSEL site, Lead, South Dakota,” *Private Communication* .
- 34 114. D. Akerib *et al.*, **LUX Collaboration** , “First results from the LUX dark matter experiment  
35 at the Sanford Underground Research Facility,” arXiv:1310.8214 [astro-ph.CO],  
36 2013.
- 37 115. M. Bishai and Y. Lu, “Conceptual Designs for a Wide-Band Low-Energy Neutrino Beam  
38 Target,” LBNE-doc-3151, November, 2010.
- 39 116. B. Lundberg, “A beginner guide to horn design and history of LBNE horn design,”  
40 LBNE-doc-8398, November, 2014.

- 1 117. D. Ayres *et al.*, **NOvA Collaboration**, “The NOvA Technical Design Report,”  
2 FERMILAB-DESIGN-2007-01, 2007.  
3 <http://lss.fnal.gov/archive/design/fermilab-design-2007-01.pdf>.
- 4 118. E. Worcester, “Potential Sensitivity Improvements with 10 kT LBNE,” 2012.
- 5 119. S. Mishra, R. Petti, and C. Rosenfeld, “A High Resolution Neutrino Experiment in a  
6 Magnetic Field for Project-X at Fermilab,” *PoS NUFACT08* (2008) 069,  
7 arXiv:0812.4527 [hep-ex].
- 8 120. B. Choudhary *et al.*, **Indian Institutions and Fermilab Collaboration**, “LBNE-India  
9 Detailed Project Report (DPR) submitted to DAE, India,” LBNE-doc-6704, 2012.
- 10 121. P. Huber, M. Lindner, and W. Winter, “Simulation of long-baseline neutrino oscillation  
11 experiments with GLOBES (General Long Baseline Experiment Simulator),”  
12 *Comput.Phys.Commun.* **167** (2005) 195, arXiv:hep-ph/0407333 [hep-ph].
- 13 122. P. Huber, J. Kopp, M. Lindner, M. Rolinec, and W. Winter, “New features in the simulation  
14 of neutrino oscillation experiments with GLOBES 3.0: General Long Baseline Experiment  
15 Simulator,” *Comput.Phys.Commun.* **177** (2007) 432–438, arXiv:hep-ph/0701187  
16 [hep-ph].
- 17 123. S. Agostinelli *et al.*, **GEANT4**, “GEANT4: A simulation toolkit,” *Nucl. Instrum. Meth.*  
18 **A506** (2003) 250–303.
- 19 124. C. Andreopoulos, **GENIE Collaboration**, “The GENIE neutrino Monte Carlo generator,”  
20 *Acta Phys.Polon.* **B40** (2009) 2461–2475.
- 21 125. K. Abe *et al.*, **T2K Collaboration**, “The T2K Experiment,” *Nucl.Instrum.Meth.* **A659**  
22 (2011) 106–135, arXiv:1106.1238 [physics.ins-det].
- 23 126. **NuMI-MINOS**. <http://www-numi.fnal.gov/>.
- 24 127. A. Rubbia, “LAGUNA-LBNO: Design of an underground neutrino observatory coupled to  
25 long baseline neutrino beams from CERN,” *J.Phys.Conf.Ser.* **408** (2013) 012006.
- 26 128. J.-P. Delahaye, C. Ankenbrandt, A. Bogacz, S. Brice, A. Bross, *et al.*, “Enabling Intensity  
27 and Energy Frontier Science with a Muon Accelerator Facility in the U.S.: A White Paper  
28 Submitted to the 2013 U.S. Community Summer Study of the Division of Particles and  
29 Fields of the American Physical Society,” FERMILAB-CONF-13-307-APC,  
30 arXiv:1308.0494 [physics.acc-ph], 2013.
- 31 129. A. Longhin, “Optimization of neutrino beams for underground sites in Europe,”  
32 arXiv:1206.4294 [physics.ins-det], 2012.
- 33 130. S. Amoruso *et al.*, **ICARUS Collaboration**, “Measurement of the mu decay spectrum  
34 with the ICARUS liquid argon TPC,” *Eur.Phys.J.* **C33** (2004) 233–241,  
35 arXiv:hep-ex/0311040 [hep-ex].
- 36 131. T2K Collaboration, “A Proposal for a Detector 2km Away from the T2K Neutrino  
37 Source.”. 2005. <http://www.phy.duke.edu/~cwalter/nusag-members/2km-proposal-05-05-30.pdf>.
- 38 132. A. Ankowski *et al.*, **ICARUS Collaboration**, “Measurement of through-going particle  
39 momentum by means of multiple scattering with the ICARUS T600 TPC,” *Eur.Phys.J.* **C48**  
40 (2006) 667–676, arXiv:hep-ex/0606006 [hep-ex].  
41

- 1 133. P. Adamson *et al.*, **MINOS Collaboration**, “Electron neutrino and antineutrino  
2 appearance in the full MINOS data sample,” *Phys.Rev.Lett.* **110** no. 17, (2013) 171801,  
3 arXiv:1301.4581 [hep-ex].
- 4 134. M. J. Murtagh, **E734 Collaboration**, “A Search for muon-neutrino to electron-neutrino  
5 oscillations using the E734 detector,” BNL-39667, 1987.
- 6 135. R. Seto, “BNL E776: A Search for neutrino oscillations,” *AIP Conf.Proc.* **176** (1988)  
7 957–963.
- 8 136. L. Borodovsky, C. Chi, Y. Ho, N. Kondakis, W.-Y. Lee, *et al.*, “Search for muon-neutrino  
9 oscillations muon-neutrino to electron-neutrino (anti-muon-neutrino to  
10 anti-electron-neutrino in a wide band neutrino beam,” *Phys.Rev.Lett.* **68** (1992) 274–277.
- 11 137. P. Astier *et al.*, **NOMAD Collaboration**, “Search for  $\nu(\mu) \rightarrow \nu(e)$  oscillations in the  
12 NOMAD experiment,” *Phys.Lett.* **B570** (2003) 19–31, arXiv:hep-ex/0306037  
13 [hep-ex].
- 14 138. A. Aguilar-Arevalo *et al.*, **MiniBooNE Collaboration**, “Unexplained Excess of  
15 Electron-Like Events From a 1-GeV Neutrino Beam,” *Phys.Rev.Lett.* **102** (2009) 101802,  
16 arXiv:0812.2243 [hep-ex].
- 17 139. K. Abe *et al.*, **T2K Collaboration**, “Observation of Electron Neutrino Appearance in a  
18 Muon Neutrino Beam,” arXiv:1311.4750 [hep-ex], 2013.
- 19 140. X. Qian, A. Tan, W. Wang, J. Ling, R. McKeown, *et al.*, “Statistical Evaluation of  
20 Experimental Determinations of Neutrino Mass Hierarchy,” *Phys.Rev.* **D86** (2012) 113011,  
21 arXiv:1210.3651 [hep-ph].
- 22 141. M. Blennow, P. Coloma, P. Huber, and T. Schwetz, “Quantifying the sensitivity of  
23 oscillation experiments to the neutrino mass ordering,” arXiv:1311.1822 [hep-ph],  
24 2013.
- 25 142. R. Cousins, “Private communication,” 2013.
- 26 143. R. Cousins, J. Mumford, J. Tucker, and V. Valuev, “Spin discrimination of new heavy  
27 resonances at the LHC,” *JHEP* **0511** (2005) 046.
- 28 144. P. Adamson *et al.*, **MINOS Collaboration**, “Improved search for muon-neutrino to  
29 electron-neutrino oscillations in MINOS,” *Phys.Rev.Lett.* **107** (2011) 181802,  
30 arXiv:1108.0015 [hep-ex].
- 31 145. P. Adamson *et al.*, **MINOS Collaboration**, “Neutrino and Antineutrino Inclusive  
32 Charged-current Cross Section Measurements with the MINOS Near Detector,” *Phys.Rev.*  
33 **D81** (2010) 072002, arXiv:0910.2201 [hep-ex].
- 34 146. Q. Wu *et al.*, **NOMAD Collaboration**, “A Precise measurement of the muon  
35 neutrino-nucleon inclusive charged current cross-section off an isoscalar target in the  
36 energy range  $2.5 < E(\nu) < 40$ -GeV by NOMAD,” *Phys.Lett.* **B660** (2008) 19–25,  
37 arXiv:0711.1183 [hep-ex].
- 38 147. V. Lyubushkin *et al.*, **NOMAD Collaboration**, “A Study of quasi-elastic muon neutrino  
39 and antineutrino scattering in the NOMAD experiment,” *Eur.Phys.J.* **C63** (2009) 355–381,  
40 arXiv:0812.4543 [hep-ex].

- 1 148. A. Bodek, U. Sarica, K. Kuzmin, and V. Naumov, “Extraction of Neutrino Flux with the  
2 Low  $\nu$  Method at MiniBooNE Energies,” *AIP Conf.Proc.* **1560** (2013) 193–197,  
3 arXiv:1207.1247 [hep-ex].
- 4 149. P. Adamson *et al.*, **MINOS Collaboration**, “A Study of Muon Neutrino Disappearance  
5 Using the Fermilab Main Injector Neutrino Beam,” *Phys.Rev.* **D77** (2008) 072002,  
6 arXiv:0711.0769 [hep-ex].
- 7 150. M. Bishai, “Determining the Neutrino Flux from Accelerator Neutrino Beams,”  
8 *Nucl.Phys.Proc.Suppl.* **229-232** (2012) 210–214.
- 9 151. B. Osmanov, **MINERvA Collaboration**, “MINERvA Detector: Description and  
10 Performance,” arXiv:1109.2855 [physics.ins-det], 2011.
- 11 152. A. Korzenev, **NA61/SHINE**, “Hadron production measurement from NA61/SHINE,”  
12 arXiv:1311.5719 [nucl-ex], 2013.
- 13 153. P. Adamson *et al.*, **MINOS Collaboration**, “Measurement of the neutrino mass splitting  
14 and flavor mixing by MINOS,” *Phys.Rev.Lett.* **106** (2011) 181801, arXiv:1103.0340  
15 [hep-ex].
- 16 154. T. Yang, **ArgoNeuT Collaboration**, “New Results from ArgoNeuT,”  
17 FERMILAB-CONF-13-510-E, arXiv:1311.2096 [hep-ex], 2013.
- 18 155. M. Day and K. S. McFarland, “Differences in Quasi-Elastic Cross-Sections of Muon and  
19 Electron Neutrinos,” *Phys.Rev.* **D86** (2012) 053003, arXiv:1206.6745 [hep-ph].
- 20 156. K. Abe *et al.*, **Super-Kamiokande Collaboration**, “Search for Differences in Oscillation  
21 Parameters for Atmospheric Neutrinos and Antineutrinos at Super-Kamiokande,”  
22 *Phys.Rev.Lett.* **107** (2011) 241801, arXiv:1109.1621 [hep-ex].
- 23 157. F. An *et al.*, **Daya Bay Collaboration**, “Spectral measurement of electron antineutrino  
24 oscillation amplitude and frequency at Daya Bay,” arXiv:1310.6732 [hep-ex], 2013.
- 25 158. P. Adamson *et al.*, **MINOS Collaboration**, “Measurement of Neutrino and Antineutrino  
26 Oscillations Using Beam and Atmospheric Data in MINOS,” *Phys.Rev.Lett.* **110** (2013)  
27 251801, arXiv:1304.6335 [hep-ex].
- 28 159. V. Agrawal, T. Gaisser, P. Lipari, and T. Stanev, “Atmospheric neutrino flux above 1-GeV,”  
29 *Phys.Rev.* **D53** (1996) 1314–1323, arXiv:hep-ph/9509423 [hep-ph].
- 30 160. A. Ankowski *et al.*, “Energy reconstruction of electromagnetic showers from  $\pi^0$  decays  
31 with the icarus t600 liquid argon tpc,” *Acta Physica Polonica B* **41** no. 1, (2010) 103,  
32 arXiv:0812.2373 [hep-ex].
- 33 161. F. Arneodo *et al.*, **The ICARUS-Milano Collaboration**, “Performance of a liquid argon  
34 time projection chamber exposed to the cern west area neutrino facility neutrino beam,”  
35 *Phys. Rev. D* **74** (Dec, 2006) 112001.  
36 <http://link.aps.org/doi/10.1103/PhysRevD.74.112001>.
- 37 162. C. Rubbia *et al.*, “Underground operation of the ICARUS T600 LAr-TPC: first results,”  
38 *JINST* **6** (2011) P07011, arXiv:1106.0975 [hep-ex].
- 39 163. S. Davidson, C. Pena-Garay, N. Rius, and A. Santamaria, “Present and future bounds on  
40 nonstandard neutrino interactions,” *JHEP* **0303** (2003) 011, arXiv:hep-ph/0302093  
41 [hep-ph].

- 1 164. M. Gonzalez-Garcia and M. Maltoni, “Phenomenology with Massive Neutrinos,”  
2 *Phys.Rept.* **460** (2008) 1–129, arXiv:0704.1800 [hep-ph].
- 3 165. C. Biggio, M. Blennow, and E. Fernandez-Martinez, “General bounds on non-standard  
4 neutrino interactions,” *JHEP* **0908** (2009) 090, arXiv:0907.0097 [hep-ph].
- 5 166. H. Davoudiasl, H.-S. Lee, and W. J. Marciano, “Long-Range Lepton Flavor Interactions  
6 and Neutrino Oscillations,” *Phys.Rev.* **D84** (2011) 013009, arXiv:1102.5352 [hep-ph].
- 7 167. P. Adamson *et al.*, **MINOS Collaboration**, “Search for sterile neutrino mixing in the  
8 MINOS long baseline experiment,” *Phys.Rev.* **D81** (2010) 052004, arXiv:1001.0336  
9 [hep-ex].
- 10 168. P. Machado, H. Nunokawa, F. P. d. Santos, and R. Z. Funchal, “Large Extra Dimensions  
11 and Neutrino Oscillations,” arXiv:1110.1465 [hep-ph], 2011.
- 12 169. P. Coloma, P. Huber, J. Kopp, and W. Winter, “Systematic uncertainties in long-baseline  
13 neutrino oscillations for large  $\theta_{13}$ ,” *Phys.Rev.* **D87** no. 3, (2013) 033004,  
14 arXiv:1209.5973 [hep-ph].
- 15 170. K. Abe, T. Abe, H. Aihara, Y. Fukuda, Y. Hayato, *et al.*, “Letter of Intent: The  
16 Hyper-Kamiokande Experiment — Detector Design and Physics Potential —,”  
17 arXiv:1109.3262 [hep-ex], 2011.
- 18 171. A. Stahl, C. Wiebusch, A. Guler, M. Kamiscioglu, R. Sever, *et al.*, “Expression of Interest  
19 for a very long baseline neutrino oscillation experiment (LBNO),” CERN-SPSC-2012-021,  
20 SPSC-EOI-007, 2012.
- 21 172. M. Apollonio, A. Bross, J. Kopp, and K. Long, **IDS-NF Collaboration**, “The International  
22 Design Study for the Neutrino Factory,” *Nucl.Phys.Proc.Suppl.* **229-232** (2012) 515.
- 23 173. E. Christensen, P. Coloma, and P. Huber, “Physics Performance of a Low-Luminosity Low  
24 Energy Neutrino Factory,” arXiv:1301.7727 [hep-ph], 2013.
- 25 174. E. Kearns *et al.*, **Hyper-Kamiokande Working Group**, “Hyper-Kamiokande Physics  
26 Opportunities,” arXiv:1309.0184 [hep-ex], 2013.
- 27 175. S. Agarwalla *et al.*, **LAGUNA-LBNO Collaboration**, “The mass-hierarchy and  
28 CP-violation discovery reach of the LBNO long-baseline neutrino experiment,”  
29 arXiv:1312.6520 [hep-ph], 2013.
- 30 176. M. Bishai, M. Diwan, S. Kettell, J. Stewart, B. Viren, *et al.*, “Precision Neutrino Oscillation  
31 Measurements using Simultaneous High-Power, Low-Energy Project-X Beams,”  
32 BNL-101234-2013-CP, FERMILAB-FN-0962, arXiv:1307.0807 [hep-ex], 2013.
- 33 177. J. L. Raaf, **Super-Kamiokande Collaboration**, “Recent Nucleon Decay Results from  
34 Super-Kamiokande,” *Nucl.Phys.Proc.Suppl.* **229-232** (2012) 559.
- 35 178. A. Bueno, Z. Dai, Y. Ge, M. Laffranchi, A. Melgarejo, *et al.*, “Nucleon decay searches with  
36 large liquid argon TPC detectors at shallow depths: Atmospheric neutrinos and cosmogenic  
37 backgrounds,” *JHEP* **0704** (2007) 041, arXiv:hep-ph/0701101 [hep-ph].
- 38 179. D. Stefan and A. M. Ankowski, “Nuclear effects in proton decay,” *Acta Phys.Polon.* **B40**  
39 (2009) 671–674, arXiv:0811.1892 [nucl-th].
- 40 180. S. Amerio *et al.*, **ICARUS Collaboration**, “Design, construction and tests of the ICARUS  
41 T600 detector,” *Nucl.Instrum.Meth.* **A527** (2004) 329–410.

- 1 181. M. Antonello, B. Baibussinov, P. Benetti, E. Calligarich, N. Canci, *et al.*, “Precise 3D track  
2 reconstruction algorithm for the ICARUS T600 liquid argon time projection chamber  
3 detector,” *Adv.High Energy Phys.* **2013** (2013) 260820, arXiv:1210.5089  
4 [physics.ins-det].
- 5 182. A. Bernstein, M. Bishai, E. Blucher, D. B. Cline, M. V. Diwan, *et al.*, “Report on the Depth  
6 Requirements for a Massive Detector at Homestake,” FERMILAB-TM-2424-E,  
7 BNL-81896-2008-IR, LBNL-1348E, arXiv:0907.4183 [hep-ex], 2009.
- 8 183. V. Kudryavtsev *et al.*, “Cosmic rays and cosmogenics. report to the lbne collaboration.”  
9 LBNE-doc-5904, 2012.
- 10 184. K. Kobayashi *et al.*, **Super-Kamiokande Collaboration**, “Search for nucleon decay via  
11 modes favored by supersymmetric grand unification models in Super-Kamiokande-I,”  
12 *Phys.Rev.* **D72** (2005) 052007, arXiv:hep-ex/0502026 [hep-ex].
- 13 185. H. Gallagher, “Private communication.”
- 14 186. H.-T. Janka, “Explosion Mechanisms of Core-Collapse Supernovae,”  
15 *Ann.Rev.Nucl.Part.Sci.* **62** (2012) 407–451, arXiv:1206.2503 [astro-ph.SR].
- 16 187. T. Fischer, S. Whitehouse, A. Mezzacappa, F.-K. Thielemann, and M. Liebendorfer,  
17 “Protoneutron star evolution and the neutrino driven wind in general relativistic neutrino  
18 radiation hydrodynamics simulations,” *Astron.Astrophys.* **517** (2010) A80,  
19 arXiv:0908.1871 [astro-ph.HE].
- 20 188. M. Wurm *et al.*, **LENA Collaboration**, “The next-generation liquid-scintillator neutrino  
21 observatory LENA,” *Astropart.Phys.* **35** (2012) 685–732, arXiv:1104.5620  
22 [astro-ph.IM].
- 23 189. H. Minakata, H. Nunokawa, R. Tomas, and J. W. Valle, “Parameter Degeneracy in  
24 Flavor-Dependent Reconstruction of Supernova Neutrino Fluxes,” *JCAP* **0812** (2008) 006,  
25 arXiv:0802.1489 [hep-ph].
- 26 190. I. Tamborra, B. Muller, L. Hudepohl, H.-T. Janka, and G. Raffelt, “High-resolution  
27 supernova neutrino spectra represented by a simple fit,” *Phys.Rev.* **D86** (2012) 125031,  
28 arXiv:1211.3920 [astro-ph.SR].
- 29 191. H. Duan, G. M. Fuller, and Y.-Z. Qian, “Collective neutrino flavor transformation in  
30 supernovae,” *Phys.Rev.* **D74** (2006) 123004, arXiv:astro-ph/0511275 [astro-ph].
- 31 192. G. L. Fogli, E. Lisi, A. Marrone, and A. Mirizzi, “Collective neutrino flavor transitions in  
32 supernovae and the role of trajectory averaging,” *JCAP* **0712** (2007) 010,  
33 arXiv:0707.1998 [hep-ph].
- 34 193. G. G. Raffelt and A. Y. Smirnov, “Self-induced spectral splits in supernova neutrino  
35 fluxes,” *Phys.Rev.* **D76** (2007) 081301, arXiv:0705.1830 [hep-ph].
- 36 194. G. G. Raffelt and A. Y. Smirnov, “Adiabaticity and spectral splits in collective neutrino  
37 transformations,” *Phys.Rev.* **D76** (2007) 125008, arXiv:0709.4641 [hep-ph].
- 38 195. A. Esteban-Pretel, A. Mirizzi, S. Pastor, R. Tomas, G. Raffelt, *et al.*, “Role of dense matter  
39 in collective supernova neutrino transformations,” *Phys.Rev.* **D78** (2008) 085012,  
40 arXiv:0807.0659 [astro-ph].

- 1 196. H. Duan and J. P. Kneller, “Neutrino flavour transformation in supernovae,” *J.Phys.G* **G36**  
2 (2009) 113201, arXiv:0904.0974 [astro-ph.HE].
- 3 197. B. Dasgupta, A. Dighe, G. G. Raffelt, and A. Y. Smirnov, “Multiple Spectral Splits of  
4 Supernova Neutrinos,” *Phys.Rev.Lett.* **103** (2009) 051105, arXiv:0904.3542 [hep-ph].
- 5 198. H. Duan, G. M. Fuller, and Y.-Z. Qian, “Collective Neutrino Oscillations,”  
6 *Ann.Rev.Nucl.Part.Sci.* **60** (2010) 569–594, arXiv:1001.2799 [hep-ph].
- 7 199. H. Duan and A. Friedland, “Self-induced suppression of collective neutrino oscillations in  
8 a supernova,” *Phys.Rev.Lett.* **106** (2011) 091101, arXiv:1006.2359 [hep-ph].
- 9 200. J. F. Cherry, J. Carlson, A. Friedland, G. M. Fuller, and A. Vlasenko, “Halo Modification  
10 of a Supernova Neutronization Neutrino Burst,” *Phys.Rev.* **D87** (2013) 085037,  
11 arXiv:1302.1159 [astro-ph.HE].
- 12 201. J. F. Beacom, R. Boyd, and A. Mezzacappa, “Black hole formation in core collapse  
13 supernovae and time-of-flight measurements of the neutrino masses,” *Phys.Rev.* **D63**  
14 (2001) 073011, arXiv:astro-ph/0010398 [astro-ph].
- 15 202. T. Fischer, S. C. Whitehouse, A. Mezzacappa, F. K. Thielemann, and M. Liebendorfer,  
16 “The neutrino signal from protoneutron star accretion and black hole formation,”  
17 arXiv:0809.5129 [astro-ph], 2008.
- 18 203. R. C. Schirato and G. M. Fuller, “Connection between supernova shocks, flavor  
19 transformation, and the neutrino signal,” LA-UR-02-3068, arXiv:astro-ph/0205390  
20 [astro-ph], 2002.
- 21 204. F. Hanke, A. Marek, B. Muller, and H.-T. Janka, “Is Strong SASI Activity the Key to  
22 Successful Neutrino-Driven Supernova Explosions?,” *Astrophys.J.* **755** (2012) 138,  
23 arXiv:1108.4355 [astro-ph.SR].
- 24 205. F. Hanke, B. Mueller, A. Wongwathanarat, A. Marek, and H.-T. Janka, “SASI Activity in  
25 Three-Dimensional Neutrino-Hydrodynamics Simulations of Supernova Cores,”  
26 *Astrophys.J.* **770** (2013) 66, arXiv:1303.6269 [astro-ph.SR].
- 27 206. A. Friedland and A. Gruzinov, “Neutrino signatures of supernova turbulence,”  
28 LA-UR-06-2202, arXiv:astro-ph/0607244 [astro-ph], 2006.
- 29 207. T. Lund and J. P. Kneller, “Combining collective, MSW, and turbulence effects in  
30 supernova neutrino flavor evolution,” arXiv:1304.6372 [astro-ph.HE], 2013.
- 31 208. G. G. Raffelt, “Particle Physics from Stars,” *Ann. Rev. Nucl. Part. Sci.* **49** (1999) 163–216,  
32 arXiv:hep-ph/9903472.
- 33 209. A. Bueno, I. Gil Botella, and A. Rubbia, “Supernova neutrino detection in a liquid argon  
34 TPC,” ICARUS-TM-03-02, arXiv:hep-ph/0307222 [hep-ph], 2003.
- 35 210. K. Scholberg *et al.*, “SNOWGLOBES: SuperNova Observatories with GLOBES.”  
36 <http://www.phy.duke.edu/~schol/snowglobes>.
- 37 211. E. D. Church, “LArSoft: A Software Package for Liquid Argon Time Projection Drift  
38 Chambers,” arXiv:1311.6774 [physics.ins-det], 2013.
- 39 212. T. Totani, K. Sato, H. E. Dalhed, and J. R. Wilson, “Future detection of supernova neutrino  
40 burst and explosion mechanism,” *Astrophys. J.* **496** (1998) 216–225,  
41 arXiv:astro-ph/9710203.

- 1 213. J. Gava, J. Kneller, C. Volpe, and G. C. McLaughlin, “A dynamical collective calculation  
2 of supernova neutrino signals,” *Phys. Rev. Lett.* **103** (2009) 071101, arXiv:0902.0317  
3 [hep-ph].
- 4 214. L. Hudepohl, B. Muller, H.-T. Janka, A. Marek, and G. Raffelt, “Neutrino Signal of  
5 Electron-Capture Supernovae from Core Collapse to Cooling,” *Phys.Rev.Lett.* **104** (2010)  
6 251101, arXiv:0912.0260 [astro-ph.SR].
- 7 215. A. Cherry, A. Friedland, and H. Duan, “Private communication.”
- 8 216. M. T. Keil, G. G. Raffelt, and H.-T. Janka, “Monte Carlo study of supernova neutrino  
9 spectra formation,” *Astrophys.J.* **590** (2003) 971–991, arXiv:astro-ph/0208035  
10 [astro-ph].
- 11 217. E. Church *et al.*, “Muon-induced background for beam neutrinos at the surface,”  
12 LBNE-doc-6232, October, 2012.
- 13 218.
- 14 219. D. Casper, “The Nuance neutrino physics simulation, and the future,”  
15 *Nucl.Phys.Proc.Suppl.* **112** (2002) 161–170, arXiv:hep-ph/0208030 [hep-ph].
- 16 220. G. Zeller, “Nuclear Effects in Water vs. Argon,” LBNE-doc-740, 2010.
- 17 221. G. Zeller, “Expected Event Rates in the LBNE Near Detector,” LBNE-doc-783, 2010.
- 18 222. S.R.Mishra, Apr, 1990. Review talk presented at Workshop on Hadron Structure Functions  
19 and Parton Distributions, Fermilab.
- 20 223. R. Raja, “The Main injector particle production experiment (MIPP) at Fermilab,”  
21 *Nucl.Instrum.Meth.* **A553** (2005) 225–230, arXiv:hep-ex/0501005 [hep-ex].
- 22 224. J. Formaggio and G. Zeller, “From eV to EeV: Neutrino Cross Sections Across Energy  
23 Scales,” *Rev.Mod.Phys.* **84** (2012) 1307, arXiv:1305.7513 [hep-ex].
- 24 225. W. J. Marciano and Z. Parsa, “Neutrino-Electron Scattering Theory,” *J. Phys.* **G29** (2003)  
25 2629–2645, arXiv:hep-ph/0403168.
- 26 226. S. Mishra, K. Bachmann, R. Bernstein, R. Blair, C. Foudas, *et al.*, “Measurement of  
27 Inverse Muon Decay  $\nu_\mu + e \rightarrow \mu^- + \nu_e$  at Fermilab Tevatron Energies 15-GeV -  
28 600-GeV,” *Phys.Rev.Lett.* **63** (1989) 132–135.
- 29 227. S. Mishra, K. Bachmann, R. Blair, C. Foudas, B. King, *et al.*, “Inverse Muon Decay,  
30  $\nu_\mu e \rightarrow \mu^- \nu_e$ , at the Fermilab Tevatron,” *Phys.Lett.* **B252** (1990) 170–176.
- 31 228. P. Vilain *et al.*, **CHARM-II Collaboration**, “A Precise measurement of the cross-section  
32 of the inverse muon decay muon-neutrino + e-  $\rightarrow$  mu- + electron-neutrino,” *Phys.Lett.*  
33 **B364** (1995) 121–126.
- 34 229. O. Samoylov *et al.*, **NOMAD**, “A Precision Measurement of Charm Dimuon Production  
35 in Neutrino Interactions from the NOMAD Experiment,” *Nucl.Phys.* **B876** (2013)  
36 339–375, arXiv:1308.4750 [hep-ex].
- 37 230. G. Zeller *et al.*, **NuTeV Collaboration**, “A Precise determination of electroweak  
38 parameters in neutrino nucleon scattering,” *Phys.Rev.Lett.* **88** (2002) 091802,  
39 arXiv:hep-ex/0110059 [hep-ex].

- 1 231. H. Abramowicz, R. Belusevic, A. Blondel, H. Blumer, P. Bockmann, *et al.*, **CDHS**  
2 **Collaboration**, “A Precision Measurement of  $\sin^2\theta_W$  from Semileptonic  
3 Neutrino Scattering,” *Phys.Rev.Lett.* **57** (1986) 298.
- 4 232. J. Allaby *et al.*, **CHARM Collaboration**, “A Precise Determination of the Electroweak  
5 Mixing Angle from Semileptonic Neutrino Scattering,” *Z.Phys.* **C36** (1987) 611.
- 6 233. P. Reutens, F. Merritt, D. MacFarlane, R. Messner, D. Novikoff, *et al.*, **CCFR**  
7 **Collaboration**, “Measurement of  $\epsilon^2 \theta_W$  and  $\rho$  in Deep Inelastic Neutrino - Nucleon  
8 Scattering,” *Phys.Lett.* **B152** (1985) 404–410.
- 9 234. S. Alekhin, S. A. Kulagin, and R. Petti, “Modeling lepton-nucleon inelastic scattering from  
10 high to low momentum transfer,” *AIP Conf.Proc.* **967** (2007) 215–224, arXiv:0710.0124  
11 [hep-ph].
- 12 235. S. Alekhin, S. A. Kulagin, and R. Petti, “Update of the global fit of PDFs including the  
13 low-Q DIS data,” arXiv:0810.4893 [hep-ph], 2008.
- 14 236. S. Alekhin, S. A. Kulagin, and R. Petti, “Determination of Strange Sea Distributions from  
15 Neutrino-Nucleon Deep Inelastic Scattering,” *Phys.Lett.* **B675** (2009) 433–440,  
16 arXiv:0812.4448 [hep-ph].
- 17 237. A. Arbuzov, D. Y. Bardin, and L. Kalinovskaya, “Radiative corrections to neutrino deep  
18 inelastic scattering revisited,” *JHEP* **0506** (2005) 078, arXiv:hep-ph/0407203  
19 [hep-ph].
- 20 238. S. A. Kulagin and R. Petti, “Global study of nuclear structure functions,” *Nucl.Phys.* **A765**  
21 (2006) 126–187, arXiv:hep-ph/0412425 [hep-ph].
- 22 239. S. A. Kulagin and R. Petti, “Neutrino inelastic scattering off nuclei,” *Phys.Rev.* **D76** (2007)  
23 094023, arXiv:hep-ph/0703033 [HEP-PH].
- 24 240. S. Kulagin and R. Petti, “Structure functions for light nuclei,” *Phys.Rev.* **C82** (2010)  
25 054614, arXiv:1004.3062 [hep-ph].
- 26 241. P. Vilain *et al.*, **CHARM-II Collaboration**, “Precision measurement of electroweak  
27 parameters from the scattering of muon-neutrinos on electrons,” *Phys.Lett.* **B335** (1994)  
28 246–252.
- 29 242. A. Czarnecki and W. J. Marciano, “Polarized Moller scattering asymmetries,”  
30 *Int.J.Mod.Phys.* **A15** (2000) 2365–2376, arXiv:hep-ph/0003049 [hep-ph].
- 31 243. S. Bennett and C. Wieman, “Erratum: Measurement of the  $6s \rightarrow 7s$  Transition  
32 Polarizability in Atomic Cesium and an Improved Test of the Standard Model [Phys. Rev.  
33 Lett. 82, 2484 (1999) ],” *Phys.Rev.Lett.* **82** (1999) 4153–4153.
- 34 244. W. Yao *et al.*, **Particle Data Group**, “Review of Particle Physics,” *J.Phys.* **G33** (2006)  
35 1–1232.
- 36 245. P. Anthony *et al.*, **SLAC E158 Collaboration**, “Precision measurement of the weak  
37 mixing angle in Moller scattering,” *Phys.Rev.Lett.* **95** (2005) 081601,  
38 arXiv:hep-ex/0504049 [hep-ex].
- 39 246. J. H. Lee, “The Qweak: Precision measurement of the proton’s weak charge by parity  
40 violating experiment,” *Few Body Syst.* **54** (2013) 129–134.

- 1 247. Nuruzzaman, “Q-weak: First Direct Measurement of the Weak Charge of the Proton,”  
2 arXiv:1312.6009 [nucl-ex], 2013.
- 3 248. R. D. Young, J. Roche, R. D. Carlini, and A. W. Thomas, “Extracting nucleon strange and  
4 anapole form factors from world data,” *Phys.Rev.Lett.* **97** (2006) 102002,  
5 arXiv:nucl-ex/0604010 [nucl-ex].
- 6 249. D. B. Leinweber, S. Boinepalli, I. Cloet, A. W. Thomas, A. G. Williams, *et al.*, “Precise  
7 determination of the strangeness magnetic moment of the nucleon,” *Phys.Rev.Lett.* **94**  
8 (2005) 212001, arXiv:hep-lat/0406002 [hep-lat].
- 9 250. L. Ahrens, S. Aronson, P. Connolly, B. Gibbard, M. Murtagh, *et al.*, “Measurement of  
10 Neutrino - Proton and anti-neutrino - Proton Elastic Scattering,” *Phys.Rev.* **D35** (1987) 785.
- 11 251. G. Garvey, W. Louis, and D. White, “Determination of proton strange form-factors from  
12 neutrino p elastic scattering,” *Phys.Rev.* **C48** (1993) 761–765.
- 13 252. W. Alberico, M. Barbaro, S. M. Bilenky, J. Caballero, C. Giunti, *et al.*, “Strange  
14 form-factors of the proton: A New analysis of the neutrino (anti-neutrino) data of the  
15 BNL-734 experiment,” *Nucl.Phys.* **A651** (1999) 277–286, arXiv:hep-ph/9812388  
16 [hep-ph].
- 17 253. A. Aguilar-Arevalo *et al.*, **MiniBooNE Collaboration**, “Measurement of the Neutrino  
18 Neutral-Current Elastic Differential Cross Section on Mineral Oil at  $E_\nu \sim 1$  GeV,”  
19 *Phys.Rev.* **D82** (2010) 092005, arXiv:1007.4730 [hep-ex].
- 20 254. L. Bugel *et al.*, **FINeSSE Collaboration**, “A Proposal for a near detector experiment on  
21 the booster neutrino beamline: FINeSSE: Fermilab intense neutrino scattering scintillator  
22 experiment,” FERMILAB-PROPOSAL-0937, arXiv:hep-ex/0402007 [hep-ex], 2004.
- 23 255. W. Leung, P. Quintas, S. Mishra, F. Sciulli, C. Arroyo, *et al.*, “A Measurement of the  
24 Gross-Llewellyn-Smith sum rule from the CCFR x(F3) structure function,” *Phys.Lett.*  
25 **B317** (1993) 655–659.
- 26 256. A. Bodek and A. Simon, “What Do Electron and Neutrino Experiments Tell Us About  
27 Nuclear Effects in the Deuteron,” *Z.Phys.* **C29** (1985) 231.
- 28 257. G. Jones *et al.*, **Birmingham-CERN-Imperial Coll.-MPI(Munich)-Oxford-University**  
29 **Coll. Collaboration**, “A Measurement of the Proton Structure Functions From Neutrino  
30 Hydrogen and Anti-neutrino Hydrogen Charged Current Interactions,” *Z.Phys.* **C44** (1989)  
31 379–384.
- 32 258. J. Berge, H. Burkhardt, F. Dydak, R. Hagelberg, M. Krasny, *et al.*, “A Measurement of  
33 Differential Cross-Sections and Nucleon Structure Functions in Charged Current Neutrino  
34 Interactions on Iron,” *Z.Phys.* **C49** (1991) 187–224.
- 35 259. D. Allasia *et al.*, **WA25 Collaboration**, “Measurement of the Neutron and Proton  
36 Structure Functions From Neutrino and Anti-neutrinos Scattering in Deuterium,”  
37 *Phys.Lett.* **B135** (1984) 231.
- 38 260. D. Allasia, C. Angelini, A. Baldini, L. Bertanza, A. Bigi, *et al.*, “ $Q^2$  Dependence of the  
39 Proton and Neutron Structure Functions from Neutrino and anti-neutrinos Scattering in  
40 Deuterium,” *Z.Phys.* **C28** (1985) 321.

- 1 261. U.-K. Yang *et al.*, **CCFR/NuTeV Collaboration**, “Measurements of  $F_2$  and  $xF_3^\nu - xF_3^{\bar{\nu}}$   
2 from CCFR  $\nu_\mu$ -Fe and  $\bar{\nu}_\mu$ -Fe data in a physics model independent way,” *Phys.Rev.Lett.*  
3 **86** (2001) 2742–2745, arXiv:hep-ex/0009041 [hep-ex].
- 4 262. U.-K. Yang *et al.*, **CCFR/NuTeV Collaboration**, “Extraction of  $R = \sigma(L) / \sigma(T)$   
5 from CCFR Fe-neutrino(muon) and Fe-anti-neutrino(muon) differential cross-sections,”  
6 *Phys.Rev.Lett.* **87** (2001) 251802, arXiv:hep-ex/0104040 [hep-ex].
- 7 263. M. Tzanov *et al.*, **NuTeV Collaboration**, “Precise measurement of neutrino and  
8 anti-neutrino differential cross sections,” *Phys.Rev.* **D74** (2006) 012008,  
9 arXiv:hep-ex/0509010 [hep-ex].
- 10 264. G. Onengut *et al.*, **CHORUS Collaboration**, “Measurement of nucleon structure  
11 functions in neutrino scattering,” *Phys.Lett.* **B632** (2006) 65–75.
- 12 265. R. Petti and O. Samoylov, “Charm dimuon production in neutrino-nucleon interactions in  
13 the NOMAD experiment,” *Phys.Part.Nucl.Lett.* **8** (2011) 755–761.
- 14 266. T. Sekiguchi, “Neutrino facility and neutrino physics in J-PARC,” *PTEP* **2012** (2012)  
15 02B005.
- 16 267. J. Dudek, R. Ent, R. Essig, K. Kumar, C. Meyer, *et al.*, “Physics Opportunities with the 12  
17 GeV Upgrade at Jefferson Lab,” *Eur.Phys.J.* **A48** (2012) 187, arXiv:1208.1244  
18 [hep-ex].
- 19 268. N. Mondal, “India-Based Neutrino Observatory (INO),” *Eur.Phys.J.Plus* **127** (2012) 106.
- 20 269. A. Butkevich, “Quasi-elastic neutrino charged-current scattering off medium-heavy nuclei:  
21 40Ca and 40Ar,” *Phys.Rev.* **C85** (2012) 065501, arXiv:1204.3160 [nucl-th].
- 22 270. A. Butkevich and S. A. Kulagin, “Quasi-elastic neutrino charged-current scattering cross  
23 sections on oxygen,” *Phys.Rev.* **C76** (2007) 045502, arXiv:0705.1051 [nucl-th].
- 24 271. A. M. Ankowski and J. T. Sobczyk, “Construction of spectral functions for medium-mass  
25 nuclei,” *Phys.Rev.* **C77** (2008) 044311, arXiv:0711.2031 [nucl-th].
- 26 272. T. Asaka and M. Shaposhnikov *Phys. Rev. Lett.* **B** no. 620, (2005) 17.  
27 arXiv:hep-ph/0505013.
- 28 273. D. Gorbunov and M. Shaposhnikov, “How to find neutral leptons of the  $\nu$ MSM?,” *JHEP*  
29 **0710** (2007) 015, arXiv:0705.1729 [hep-ph].
- 30 274. A. Boyarsky, O. Ruchayskiy, and M. Shaposhnikov, “The Role of sterile neutrinos in  
31 cosmology and astrophysics,” *Ann.Rev.Nucl.Part.Sci.* **59** (2009) 191–214,  
32 arXiv:0901.0011 [hep-ph].
- 33 275. S. Dodelson and L. M. Widrow, “Sterile-neutrinos as dark matter,” *Phys.Rev.Lett.* **72**  
34 (1994) 17–20, arXiv:hep-ph/9303287 [hep-ph].
- 35 276. A. Atre, T. Han, S. Pascoli, and B. Zhang, “The Search for Heavy Majorana Neutrinos,”  
36 *JHEP* **0905** (2009) 030, arXiv:0901.3589 [hep-ph].
- 37 277. M. Shaposhnikov, “The nuMSM, leptonic asymmetries, and properties of singlet  
38 fermions,” *JHEP* **0808** (2008) 008, arXiv:0804.4542 [hep-ph].
- 39 278. E. K. Akhmedov, V. Rubakov, and A. Y. Smirnov, “Baryogenesis via neutrino oscillations,”  
40 *Phys.Rev.Lett.* **81** (1998) 1359–1362, arXiv:hep-ph/9803255 [hep-ph].

- 1 279. A. M. Cooper-Sarkar *et al.*, **WA66 Collaboration**, “SEARCH FOR HEAVY NEUTRINO  
2 DECAYS IN THE BEBC BEAM DUMP EXPERIMENT,” *Phys.Lett.* **B160** (1985) 207.
- 3 280. F. Bergsma *et al.*, **CHARM Collaboration**, “A Search for Decays of Heavy Neutrinos in  
4 the Mass Range 0.5-GeV to 2.8-GeV,” *Phys.Lett.* **B166** (1986) 473.
- 5 281. A. Vaitaitis *et al.*, **NuTeV Collaboration, E815 Collaboration**, “Search for neutral heavy  
6 leptons in a high-energy neutrino beam,” *Phys.Rev.Lett.* **83** (1999) 4943–4946,  
7 arXiv:hep-ex/9908011 [hep-ex].
- 8 282. G. Bernardi, G. Carugno, J. Chauveau, F. Dicarolo, M. Dris, *et al.*, “SEARCH FOR  
9 NEUTRINO DECAY,” *Phys.Lett.* **B166** (1986) 479.
- 10 283. G. Bernardi, G. Carugno, J. Chauveau, F. Dicarolo, M. Dris, *et al.*, “Further Limits on  
11 Heavy Neutrino Couplings,” *Phys.Lett.* **B203** (1988) 332.
- 12 284. L. Canetti and M. Shaposhnikov, “Baryon Asymmetry of the Universe in the NuMSM,”  
13 *JCAP* **1009** (2010) 001, arXiv:1006.0133 [hep-ph].
- 14 285. C. Kullenberg *et al.*, **NOMAD Collaboration**, “A Search for Single Photon Events in  
15 Neutrino Interactions in NOMAD,” *Phys.Lett.* **B706** (2012) 268–275, arXiv:1111.3713  
16 [hep-ex].
- 17 286. C. Volpe, N. Auerbach, G. Colo, T. Suzuki, and N. Van Giai, “Neutrino C-12 reactions and  
18 the LSND and KARMEN experiments on neutrino oscillations,” *Phys. Atom. Nucl.* **64**  
19 (2001) 1165–1168.
- 20 287. M. Maltoni and T. Schwetz, “Sterile neutrino oscillations after first MiniBooNE results,”  
21 *Phys.Rev.* **D76** (2007) 093005, arXiv:0705.0107 [hep-ph].
- 22 288. P. Ade *et al.*, **Planck Collaboration**, “Planck 2013 results. XVI. Cosmological  
23 parameters,” arXiv:1303.5076 [astro-ph.CO], 2013.
- 24 289. C. Bennett *et al.*, **WMAP**, “Nine-Year Wilkinson Microwave Anisotropy Probe (WMAP)  
25 Observations: Final Maps and Results,” *Astrophys.J.Suppl.* **208** (2013) 20,  
26 arXiv:1212.5225 [astro-ph.CO].
- 27 290. B. Batell, M. Pospelov, and A. Ritz, “Exploring Portals to a Hidden Sector Through Fixed  
28 Targets,” *Phys.Rev.* **D80** (2009) 095024, arXiv:0906.5614 [hep-ph].
- 29 291. P. deNiverville, M. Pospelov, and A. Ritz, “Observing a light dark matter beam with  
30 neutrino experiments,” *Phys.Rev.* **D84** (2011) 075020, arXiv:1107.4580 [hep-ph].
- 31 292. P. deNiverville, D. McKeen, and A. Ritz, “Signatures of sub-GeV dark matter beams at  
32 neutrino experiments,” *Phys.Rev.* **D86** (2012) 035022, arXiv:1205.3499 [hep-ph].
- 33 293. R. Dharmapalan *et al.*, **MiniBooNE Collaboration**, “Low Mass WIMP Searches with a  
34 Neutrino Experiment: A Proposal for Further MiniBooNE Running,”  
35 FERMILAB-PROPOSAL-1032, arXiv:1211.2258 [hep-ex], 2012.
- 36 294. H. Bethe, “Energy production in stars,” *Phys.Rev.* **55** (1939) 434–456.
- 37 295. C. Weizsäcker, “Über Elementumwandlungen im Innern der Sterne II,” *Physik.Z.* **39** (1938)  
38 633–646.
- 39 296. J. N. Bahcall, A. M. Serenelli, and S. Basu, “New solar opacities, abundances,  
40 helioseismology, and neutrino fluxes,” *Astrophys.J.* **621** (2005) L85–L88,  
41 arXiv:astro-ph/0412440 [astro-ph].

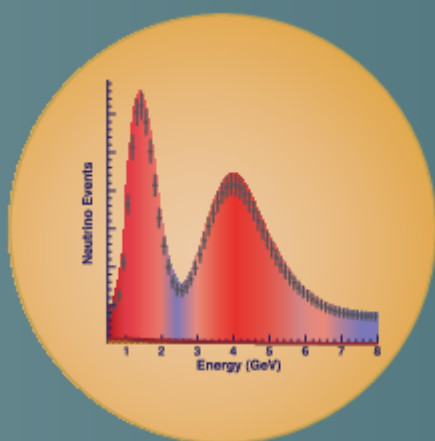
- 1 297. S. Fukuda *et al.*, **Super-Kamiokande Collaboration**, “Solar B-8 and hep neutrino  
2 measurements from 1258 days of Super-Kamiokande data,” *Phys.Rev.Lett.* **86** (2001)  
3 5651–5655, arXiv:hep-ex/0103032 [hep-ex].
- 4 298. Q. Ahmad *et al.*, **SNO Collaboration**, “Measurement of the rate of  $\nu/e + d \rightarrow p + p + e^-$   
5 interactions produced by B-8 solar neutrinos at the Sudbury Neutrino Observatory,”  
6 *Phys.Rev.Lett.* **87** (2001) 071301, arXiv:nucl-ex/0106015 [nucl-ex].
- 7 299. G. Bellini, J. Benziger, D. Bick, S. Bonetti, G. Bonfini, *et al.*, “Precision measurement of  
8 the  $^7\text{Be}$  solar neutrino interaction rate in Borexino,” *Phys.Rev.Lett.* **107** (2011) 141302,  
9 arXiv:1104.1816 [hep-ex].
- 10 300. C. Kraus, **SNO+**, “SNO with liquid scintillator: SNO+,” *Prog. Part. Nucl. Phys.* **57** (2006)  
11 150–152.
- 12 301. H. Sekiya, **Collaboration for the Super-Kamiokande**, “Solar neutrino analysis of  
13 Super-Kamiokande,” arXiv:1307.3686, 2013.
- 14 302. G. Bellini *et al.*, **Borexino Collaboration**, “First evidence of pep solar neutrinos by direct  
15 detection in Borexino,” *Phys.Rev.Lett.* **108** (2012) 051302, arXiv:1110.3230 [hep-ex].
- 16 303. G. Bellini *et al.*, **Borexino Collaboration**, “Measurement of the solar  $^8\text{B}$  neutrino rate  
17 with a liquid scintillator target and 3 MeV energy threshold in the Borexino detector,”  
18 *Phys.Rev.* **D82** (2010) 033006, arXiv:0808.2868 [astro-ph].
- 19 304. A. Guglielmi, **ICARUS Collaboration**, “Status and early events from ICARUS T600,”  
20 *Nucl.Phys B (Proc. Suppl.)* **229-232** (2012) 342–346.
- 21 305. A. Gando *et al.*, **KamLAND Collaboration**, “Reactor On-Off Antineutrino Measurement  
22 with KamLAND,” arXiv:1303.4667 [hep-ex], 2013.
- 23 306. J. Silk, K. A. Olive, and M. Srednicki, “The Photino, the Sun and High-Energy Neutrinos,”  
24 *Phys.Rev.Lett.* **55** (1985) 257–259.
- 25 307. M. Cirelli, N. Fornengo, T. Montaruli, I. A. Sokalski, A. Strumia, *et al.*, “Spectra of  
26 neutrinos from dark matter annihilations,” *Nucl.Phys.* **B727** (2005) 99–138,  
27 arXiv:hep-ph/0506298 [hep-ph].
- 28 308. J. LoSecco, J. Van der Velde, R. Bionta, G. Blewitt, C. Bratton, *et al.*, “Limits on the Flux  
29 of Energetic Neutrinos from the Sun,” *Phys.Lett.* **B188** (1987) 388.
- 30 309. M. Aartsen *et al.*, **IceCube collaboration**, “Search for dark matter annihilations in the Sun  
31 with the 79-string IceCube detector,” *Phys.Rev.Lett.* **110** (2013) 131302,  
32 arXiv:1212.4097 [astro-ph.HE].
- 33 310. M. Blennow, M. Carrigan, and E. F. Martinez, “Probing the Dark Matter mass and nature  
34 with neutrinos,” *JCAP* **1306** (2013) 038, arXiv:1303.4530 [hep-ph].
- 35 311. T. Totani, K. Sato, and Y. Yoshii, “Spectrum of the supernova relic neutrino background  
36 and evolution of galaxies,” *Astrophys.J.* **460** (1996) 303–312, arXiv:astro-ph/9509130  
37 [astro-ph].
- 38 312. K. Sato, T. Totani, and Y. Yoshii, “Spectrum of the supernova relic neutrino background  
39 and evolution of galaxies,” 1997.
- 40 313. D. Hartmann and S. Woosley, “The cosmic supernova neutrino background,”  
41 *Astropart.Phys.* **7** (1997) 137–146.

- 1 314. R. Malaney, “Evolution of the cosmic gas and the relic supernova neutrino background,”  
2 *Astropart.Phys.* **7** (1997) 125–136, arXiv:astro-ph/9612012 [astro-ph].
- 3 315. M. Kaplinghat, G. Steigman, and T. Walker, “The Supernova relic neutrino background,”  
4 *Phys.Rev.* **D62** (2000) 043001, arXiv:astro-ph/9912391 [astro-ph].
- 5 316. S. Ando, J. F. Beacom, and H. Yuksel, “Detection of neutrinos from supernovae in nearby  
6 galaxies,” *Phys.Rev.Lett.* **95** (2005) 171101, arXiv:astro-ph/0503321 [astro-ph].
- 7 317. C. Lunardini, “Testing neutrino spectra formation in collapsing stars with the diffuse  
8 supernova neutrino flux,” *Phys.Rev.* **D75** (2007) 073022, arXiv:astro-ph/0612701  
9 [astro-ph].
- 10 318. M. Fukugita and M. Kawasaki, “Constraints on the star formation rate from supernova relic  
11 neutrino observations,” *Mon.Not.Roy.Astron.Soc.* **340** (2003) L7,  
12 arXiv:astro-ph/0204376 [astro-ph].
- 13 319. P. Vogel and J. F. Beacom, “Angular distribution of neutron inverse beta decay,  
14 anti-neutrino(e) + p  $\rightarrow$  e+ + n,” *Phys.Rev.* **D60** (1999) 053003, arXiv:hep-ph/9903554  
15 [hep-ph].
- 16 320. A. Strumia and F. Vissani, “Precise quasielastic neutrino nucleon cross section,” *Phys. Lett.*  
17 **B564** (2003) 42–54, arXiv:astro-ph/0302055.
- 18 321. W. E. Ormand, P. M. Pizzochero, P. F. Bortignon, and R. A. Broglia, “Neutrino capture  
19 cross-sections for Ar-40 and Beta decay of Ti-40,” *Phys. Lett.* **B345** (1995) 343–350,  
20 arXiv:nucl-th/9405007.
- 21 322. E. Kolbe, K. Langanke, G. Martinez-Pinedo, and P. Vogel, “Neutrino nucleus reactions and  
22 nuclear structure,” *J. Phys.* **G29** (2003) 2569–2596, arXiv:nucl-th/0311022.
- 23 323. M. Sajjad Athar and S. K. Singh, “ $\nu/e$  (anti- $\nu/e$ ) - Ar-40 absorption cross sections for  
24 supernova neutrinos,” *Phys. Lett.* **B591** (2004) 69–75.
- 25 324. A. Cocco, A. Ereditato, G. Fiorillo, G. Mangano, and V. Pettorino, “Supernova relic  
26 neutrinos in liquid argon detectors,” *JCAP* **0412** (2004) 002, arXiv:hep-ph/0408031  
27 [hep-ph].
- 28 325. R. Abbasi *et al.*, **IceCube Collaboration**, “Search for Relativistic Magnetic Monopoles  
29 with IceCube,” *Phys.Rev.* **D87** (2013) 022001, arXiv:1208.4861 [astro-ph.HE].
- 30 326. M. Aartsen *et al.*, **IceCube Collaboration**, “The IceCube Neutrino Observatory Part IV:  
31 Searches for Dark Matter and Exotic Particles,” arXiv:1309.7007 [astro-ph.HE],  
32 2013.
- 33 327. K. Ueno *et al.*, **Super-Kamiokande Collaboration**, “Search for GUT Monopoles at  
34 Super-Kamiokande,” *Astropart.Phys.* **36** (2012) 131–136, arXiv:1203.0940 [hep-ex].
- 35 328. M. Aartsen *et al.*, **IceCube Collaboration**, “Search for non-relativistic Magnetic  
36 Monopoles with IceCube,” arXiv:1402.3460 [astro-ph.CO], 2014.
- 37 329. M. Ambrosio *et al.*, **MACRO Collaboration**, “Final results of magnetic monopole  
38 searches with the MACRO experiment,” *Eur.Phys.J.* **C25** (2002) 511–522,  
39 arXiv:hep-ex/0207020 [hep-ex].
- 40 330. R. Mohapatra, “Neutron-Anti-Neutron Oscillation: Theory and Phenomenology,” *J.Phys.*  
41 **G36** (2009) 104006, arXiv:0902.0834 [hep-ph].

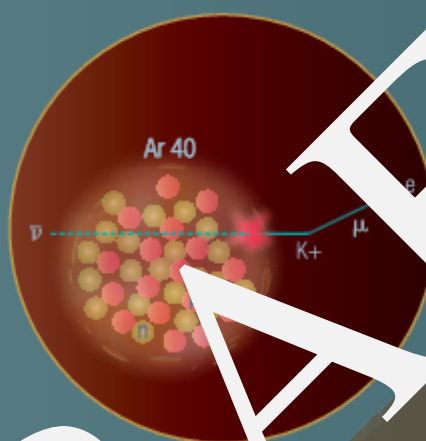
- 1 331. The United States Department of Energy, “Program and Project Management for the  
2 Acquisition of Capital Assets,” DOE, DOE O 413.3B, November, 2010.
- 3 332. J. Strait, R. Wilson, and V. Papadimitriou, “LBNE Presentations to P5,” LBNE-doc-8694,  
4 November, 2013.
- 5 333. S. Bilenky and C. Giunti, “Neutrinoless double-beta decay: A brief review,”  
6 *Mod.Phys.Lett.* **A27** (2012) 1230015, arXiv:1203.5250 [hep-ph].
- 7 334. L. P. M. Team, “LBNE Conceptual Design Report: The LBNE Water Cherenkov Detector,”  
8 LBNE-doc-5118, 2012.
- 9 335. J. Hewett, H. Weerts, K. Babu, J. Butler, B. Casey, *et al.*, “Planning the Future of U.S.  
10 Particle Physics (Snowmass 2013): Chapter 2: Intensity Frontier,”  
11 FERMILAB-CONF-14-019-CH02, arXiv:1401.6077 [hep-ex], 2014.
- 12 336. C. Green, J. Kowalkowski, M. Paterno, M. Fischler, L. Garren, *et al.*, “The art framework,”  
13 *J.Phys.Conf.Ser.* **396** (2012) 022020.
- 14 337. T. Katori, **MicroBooNE Collaboration**, “MicroBooNE, A Liquid Argon Time Projection  
15 Chamber (LArTPC) Neutrino Experiment,” *AIP Conf.Proc.* **1405** (2011) 250–255,  
16 arXiv:1107.5112 [hep-ex].
- 17 338. M. Soderberg, **ArgoNeuT Collaboration**, “ArgoNeuT: A Liquid Argon Time Projection  
18 Chamber Test in the NuMI Beamline,” FERMILAB-CONF-09-516-E, arXiv:0910.3433  
19 [physics.ins-det], 2009.
- 20 339. D.Huffman, “A Method for the Construction of Minimum-Redundancy Codes,” in  
21 *Proceedings of the IRE.* 1952.
- 22 340. M. Szydagis, N. Barry, K. Kazkaz, J. Mock, D. Stolp, *et al.*, “NEST: A Comprehensive  
23 Model for Scintillation Yield in Liquid Xenon,” *JINST* **6** (2011) P10002,  
24 arXiv:1106.1613 [physics.ins-det].
- 25 341. C. Hagman, D. Lange, J. Verbeke, and D. Wright, “Cosmic-ray Shower Library (CRY),”  
26 Lawrence Livermore National Laboratory, UCRL-TM-229453, March, 2012.  
27 [http://nuclear.llnl.gov/simulation/doc\\_cry\\_v1.7/cry.pdf](http://nuclear.llnl.gov/simulation/doc_cry_v1.7/cry.pdf).
- 28 342. R. P. Sandhir, S. Muhuri, and T. Nayak, “Dynamic Fuzzy c-Means (dFCM) Clustering and  
29 its Application to Calorimetric Data Reconstruction in High Energy Physics,”  
30 *Nucl.Instrum.Meth.* **A681** (2012) 34–43, arXiv:1204.3459 [nucl-ex].
- 31 343. R. E. Kalman, “A new approach to linear filtering and prediction problems,” *Transactions*  
32 *of the ASME—Journal of Basic Engineering* **82** no. Series D, (1960) 35–45.
- 33 344. J. Marshall and M. Thomson, “The Pandora software development kit for particle flow  
34 calorimetry,” *J.Phys.Conf.Ser.* **396** (2012) 022034.
- 35 345. A. Accardi, J. Albacete, M. Anselmino, N. Armesto, E. Aschenauer, *et al.*, “Electron Ion  
36 Collider: The Next QCD Frontier - Understanding the glue that binds us all,”  
37 BNL-98815-2012-JA, JLAB-PHY-12-1652, arXiv:1212.1701 [nucl-ex], 2012.



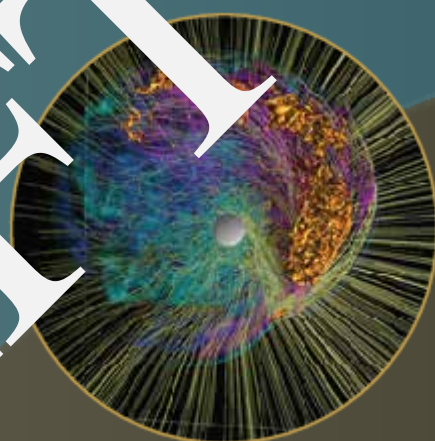




Through precise studies of neutrino flavor oscillations enabled by an intense, optimized beam and advanced detectors, LBNE aims to shed light on the mystery of the matter-antimatter asymmetry in the Universe.



With the world's largest cryogenic particle detector deep underground, LBNE will probe the stability of matter and its relation to the Grand Unification of forces.



LBNE's observation of thousands of neutrinos from a core-collapse supernova in the Milky Way would allow us to peer inside a newly-formed neutron star and potentially witness the birth of a black hole.